The Origin of Primitive Ocean Island and Island Arc Basalts

by

Stephen Eggins B.App.Sc. (Hons), U.N.S.W

submitted in fulfilment of the requirements for the degree of

Doctor of Philosophy

University of Tasmania

November, 1989.

This thesis contains no material which has been accepted for the award of any other degree or diploma in any University and, to the best of my knowledge and belief, contains no copy or paraphrase of material previously published or written by another person, except where due reference is made in the text of this thesis.

Stephen Eggins

November, 1989.

Abstract

Fundamental aspects concerning the origin of ocean island basalts and primitive island arc magmas are addressed using examples from the Vanuatu Arc, Hawaii, and the Tasmantid Seamounts.

A suite of alkali-olivine to tholeiitic basalts, newly dredged from the Tasmantid Seamounts, are possible primary and near-primary compositions (e.g. $Mg^{\#}$'s 61-70, Ni = 221-322 ppm). Their bulk compositions correspond with those produced by experimental melting of peridotite between ~1.0GPa (for tholeiites) and ~2.5GPa (for alkali-olivine basalts), leaving residual mineralogies of (spinel) lherzolite and harzburgite. The inferred absence of residual garnet necessitates magma generation from sources with middle/heavy REE values >chondrites to account for the fractionated REE patterns of the Tasmantid basalts.

An experimental liquidus study on a new Kilauea primary melt estimate (16wt% MgO), based on the most Mg-rich olivine phenocrysts occurring in Hawaiian lavas (i.e. $Mg^{\#}$ 90.5), demonstrates equilibrium with mantle peridotite (harzburgite) at 2.0GPa and ~1450°C. Garnet is not a liquidus phase below ~3.5GPa, reaffirming previous interpretations based on experimental studies, for shallow garnet-absent generation of Hawaiian olivine tholeiite and picrite primary magma estimates.

In an effort to reconcile phase equilibria evidence for shallow melt segregation and trace element geochemistry arguments for deep garnet-present melting, geochemical models for dynamic melt segregation from an upwelling mantle plume have been assessed. These models are found to have little or no capacity to reproduce the geochemical characteristics of Hawaiian, or other ocean island tholeiites, if melting proceeds beyond the garnet peridotite stability field to shallower levels.

Two possible models may account for the geochemical characteristics of ocean island tholeiites:

(1) melting occurs entirely within the presence of residual garnet, requiring the generation of ultramagnesian primary melts (>20wt% MgO) that are capable of equilibrating at high temperature and pressure (>3.0GPa) with garnet peridotite;

(2) melting of an incompatible element enriched source, bearing a "residual garnet" geochemical signature, occurs at relatively shallow levels (~1-2GPa) to produce olivine tholeiite/picritic primary melts. A suitable source enriched in incompatible elements is the oceanic lithosphere, fertilised by small melt fractions migrating from the underlying mantle, as is consistent with peridotite-C-H-O phase equilibria and melt segregation considerations.

Ambae is a site of voluminous eruptions of primitive olivine and clinopyroxene phenocryst-rich lavas in the Vanuatu Arc. Three distinct lava suites, all erupted in the previous 100Ka, can be identified on the basis of stratigraphy, phenocryst mineralogy, and geochemistry. The youngest suite, which mantles much of the island, ranges from high-alumina basalt through to picritic compositions with up to ~20 wt% MgO. Geochemical variation in this suite is controlled by fractional crystallisation (and accumulation) of magnesian olivine (to $Mg^{\#}$ 93.4) and clinopyroxene (to $Mg^{\#}$ 92), and accessory Cr-rich spinel. The liquid line of descent can be traced from an Mg-rich picritic parent ($Mg^{\#}$~81) to high-alumina basalts, in which crystallise calcic plagioclase (to An ~90), relatively Fe-rich olivine ($Mg^{\#}$~80) and clinopyroxene ($Mg^{\#}$~80), and titanomagnetite.

The dominant basaltic lava suites erupted throughout the Vanuatu Arc are notable for their primitive phenocryst assemblages, which comprise magnesian olivine and clinopyroxene, Cr-rich spinel, and calcic plagioclase. These assemblages enable identification of a range of Mg-rich parent magmas ($Mg^{\#}$ 75-82), spanning low-K tholeiites to high-K alkali picrites, from which the spectrum of more evolved high-alumina basalts and andesites occurring in the arc are derived by fractionation processes. The primitive nature of the parent compositions provide unequivocal evidence for melt derivation from upper mantle peridotite. They require high temperature (>~1300°C) melting of peridotite between ~2 and ~4 GPa, conditions which are likely to exist only within the core of the mantle wedge.

Incompatible element geochemistry in the Vanuatu Arc parent magmas is dominated by the interaction of two components, which are separately responsible for LILE enrichment over LREE, and HFSE depletion relative to LREE. The enrichment of LILE over LREE, which dominates the low-K tholeiitic compositional end-member, is consistent with the introduction into the arc source of an LILE (and Pb) -rich fluid, released from the dehydration of amphibole. The other component, which dominates high-K alkaline end-member, is associated with strong enrichment of both LILE and LREE but not of HFSE, characteristics which suggest contamination of the source by a small melt fraction generated in the presence of a residual HFSE-bearing phase.

A third source component, equivalent to the regional upper mantle (N-MORB source) peridotite, is recognised from the affinity of several lava suites to the N-MORB basalts of the North Fiji Basin. The majority of lava suites in the Vanuatu Arc, however, have very low HFSE and HREE (and sometimes also LREE) abundances (0.2-0.5x N-MORB), which require their upper mantle protoliths to be considerably more refractory and depleted in incompatible elements than an N-MORB source.

Acknowledgements

In the completion of this thesis I owe much to all members of the Geology Department, and the CSL, who have combined to make a pleasant and fruitful work environment. To each and everyone of these people I extend my gratitude.

A number of persons deserve special mention for their contributions to this work, including:

Dave Green for his insight, example, ability to unravel the unreadable, and efforts in establishing and maintaining the petrology research group;

Tony Crawford for his guidance, particularly in directing me toward the problems of magmagenesis in island arcs;

Phil Robinson for his dedication toward maintaining the analytical facilities;

Graeme Wheller for his generosity with ideas, and the provision of geochemical database and plotting programs;

Bas Hensen for sharing his enthusiasm and encouraging me to proceed with research;

Ian MacDougall for his companionship and persistence in attempting to retrieve material from the Tasmantid Seamounts;

Mark Barsdell for selflessly making available his unpublished data on the Vanuatu Arc;

John Stephenson for providing me with his field notes, samples, and analyses of lavas from Ambrym;

Russell Sweeney and **Joe Stolz** for critically reading parts of this thesis;

All members of the Petrology Group, past and present, for their insights into aspects of this and their own research work. In particular, I thank **Steve Foley, Graeme Wheller**, and **Scott Kuehner** for guidance in my early "plastic pants" years, and **Joe**

Stolz, Wayne Taylor, Nic Odling, John Adam, Trevor Falloon, Margaret Wallace, Chris Ballhaus, Vanessa Guthrie, Ai Yang and **Mike Seitz** for taking over where they left off. **Rick Varne** is thanked for sharing his enthusiasm, and for using me as target practice for his constant stream of ideas.

Field work in Vanuatu was enabled with the kind help of staff of the Vanuatu Department of Mines, Geology, and Rural Water Supply who provided logistical support including assistance in the field. Special thanks are due to **Colin Clarke, Stanley Temacon, Alex Tari,** and **Willy Harrison.** I am also indebted to **Ray Carpenter** for sharing the experience of six weeks field work on Ambrym, and the peoples of Ambae and Ambrym for their hospitality and generosity.

In addition, I thank all persons involved in dredging of the Tasmantid Seamounts with the "RV Franklin", and the Department of Education for making available a Commonwealth Postgraduate Scholarship.

Finally, I thank Nic, Kate, Garry, and Trish for their much valued friendship, and also my parents for their continuing support, which has often included the odd couple of hundred dollars every now and then to keep me solvent.

Table of Contents

PART 2

Petrogenesis of Primitive Island Arc Basalts

CHAPTER 5

The Geology of Ambae, and an Outline of the Geology of the Vanuatu Arc 120

CHAPTER 6

The Crystallisation of Primitive Arc Magmas from Ambae, Vanuatu 136

Table of Contents

CHAPTER 7

The Geochemical Evolution of Lavas from Ambae, Vanuatu 185

CHAPTER 8

The Geochemical Evolution of Primary Magmas in the Vanuatu Arc 221

Introduction

This thesis is divided into two parts, the first addressing the PT conditions of formation of ocean island basalts, and the second addressing the origin of primitive island arc basalts. Though the scope of this study was initially limited to magmagenesis in island arcs, prior to embarking on a field-based sampling programme in Vanuatu, an opportunity to work on newly dredged material from the Tasmantid Seamounts was made available. This revealed some important unresolved problems associated with current models for hotspot magmatism, which warranted closer examination.

Part 1 focuses on establishing the depth of origin of ocean island tholeiites, and the resultant implications for the geochemical character of their source regions and associated models for hotspot magmatism. Chapter 1 documents the geochemistry and mineralogy of the Tasmantid Seamounts and, in so doing, outlines evidence for shallow conditions of melting for the primitive tholeiites present. Chapter 2 re-evaluates previously established PT conditions for the generation of ocean island tholeiites, through a liquidus study upon a new parent melt estimate for Hawaii. Finding close agreement between conclusions based on existing studies and the new data, for the shallow origin of tholeiite primary magmas, the possibility that dynamic melt segregation effects may account for garnet-present, deep melting geochemical signature occurring in bulk compositions reflecting shallow garnet-absent levels of melting, is pursued in Chapter 3. A synthesis of available geochemical data, modelled partial melting effects, and phase equilibria constraints on the origin of ocean island tholeiites is assembled in Chapter 4, which is concluded with two possible competing models for the generation of tholeiitic magmas at hotspots.

Part 2, concerning the generation of primitive magmas in island arcs, is based on examples of primitive lava suites occurring in the Vanuatu Arc, in particular those found on Ambae. This is introduced with an outline of the geology of Ambae and the Vanuatu Arc in Chapter 5. A detailed appraisal of the phenocryst mineralogy and conditions of crystallisation of lavas erupted on Ambae is made in Chapter 6, upon which parent melt

compositions are established. Chapter 7 continues with an analysis of the causes of geochemical variation in the Ambae lavas. This is expanded in Chapter 8 to include a full assessment of the geochemistry and origin of parent melt compositions which can be identified throughout the Vanuatu Arc.

PART 1

Petrogenesis of Primitive Ocean Island Tholeiites

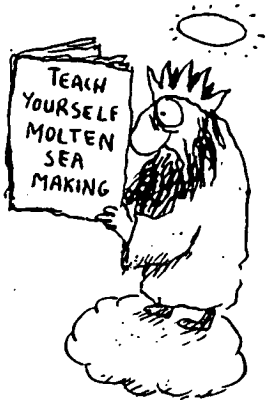

CHAPTER 1

Petrology and Geochemistry of the Tasmantid Seamounts

1.1 INTRODUCTION

The nature and origin of the mantle sources of hotspot-style volcanism remain poorly understood, despite continued growth of geochemical, isotopic, and geophysical data. Several recent syntheses (Feigenson, 1986; Frey and Roden, 1987) have produced petrogenetic models constrained principally by data from the Hawaiian Islands. None have drawn on experimental constraints for magma generation, although in separate work, Wyllie (1988) has proposed a phase equilibria-based model within a hot upwelling mantle plume framework. Most current models have endeavoured to be consistent with evidence from trace element modelling for the melting of garnet peridotite sources. There is, however, little concensus in these models on the P (pressure) and T (temperature) of magma generation, degree of partial melting, residual mineralogy, or the relative contributions from lithosphere, asthenosphere, or even deep mantle sources. Important new results stemming from fluid dynamical modelling of melt segregation processes (e.g. McKenzie, 1984) are claimed by some to resolve several lines of previously conflicting evidence; in particular, the firmly held arguments for deep origins (in the presence of residual garnet) and the equally firmly held arguments for relatively shallow melting (~1.5 GPA; for this rationale see Thompson, 1987).

In this study an integrated approach has been pursued using a combination of experimental, trace element, and isotopic techniques to evaluate the petrogenesis of the newly sampled Tasmantid Seamounts. This approach highlights the existing deep versus shallow melting controversy, and serves to introduce further detailed examination of the problem in Chapters 2, 3, and 4.

1.2 GEOLOGICAL SETTING

The Tasmantid Seamounts form a north-south trending chain of submarine volcanoes subparallel to the east Australian continental margin (Fig. 1.1). They are constructed on deep oceanic crust (>4000m) of the Tasman Sea basin. K-Ar and $^{40}Ar/^{39}Ar$ isotopic dates document progressive younging of the volcanism towards the south (McDougall and Duncan, 1988), confirming earlier hypotheses for a hospot-related origin based upon observations of increasing seamount subsidence to the north (Vogt and Connolly, 1971). Migration has been quantified at 67 ± 5mm/yr over the period 24 to 6 Ma between Queensland and Gascoyne seamounts, though seamounts occurring farther to the north probably predate this interval of volcanism (McDougall and Duncan, 1988).

Individual seamounts may be conical or elongate in the direction of plate motion. Normal to the plate motion direction the volcanoes are up to 60 km in diameter at their bases. Flat summits on several larger seamounts indicate previous planation to sea level by erosion.

Basalts previously recovered from several Tasmantid Seamounts were identified as alkali olivine basalts (Slater and Goodwin, 1973). The basalts in this study, obtained by dredging with the R/V Franklin during 1985 and 1986, comprise water worn basaltic cobbles from Derwent-Hunter and Gascoyne seamounts, and glassy blocks, clasts, and hyaloclastite material from Gascoyne, Taupo, and Britannia seamounts.

The recovery by dredging of altered volcanic material during 1988 from Nova and Argo Banks (on the parallel Lord Howe Island seamount chain to the east)has also confirmed a volcanic origin for that feature. Presently, the only available dated material is from Lord Howe Island which is ~7Ma (McDougall et al., 1981).

1.3 PETROLOGY OF THE TASMANTID BASALTS

1.3.1 Petrography

Two groups of lavas are identified on the basis of phenocryst mineralogy. One is dominated by an olivine+Cr-spinel phenocryst assemblage, and the other by plagioclase and clinoyroxene phenocrysts. The first group are representative of Gascoyne and

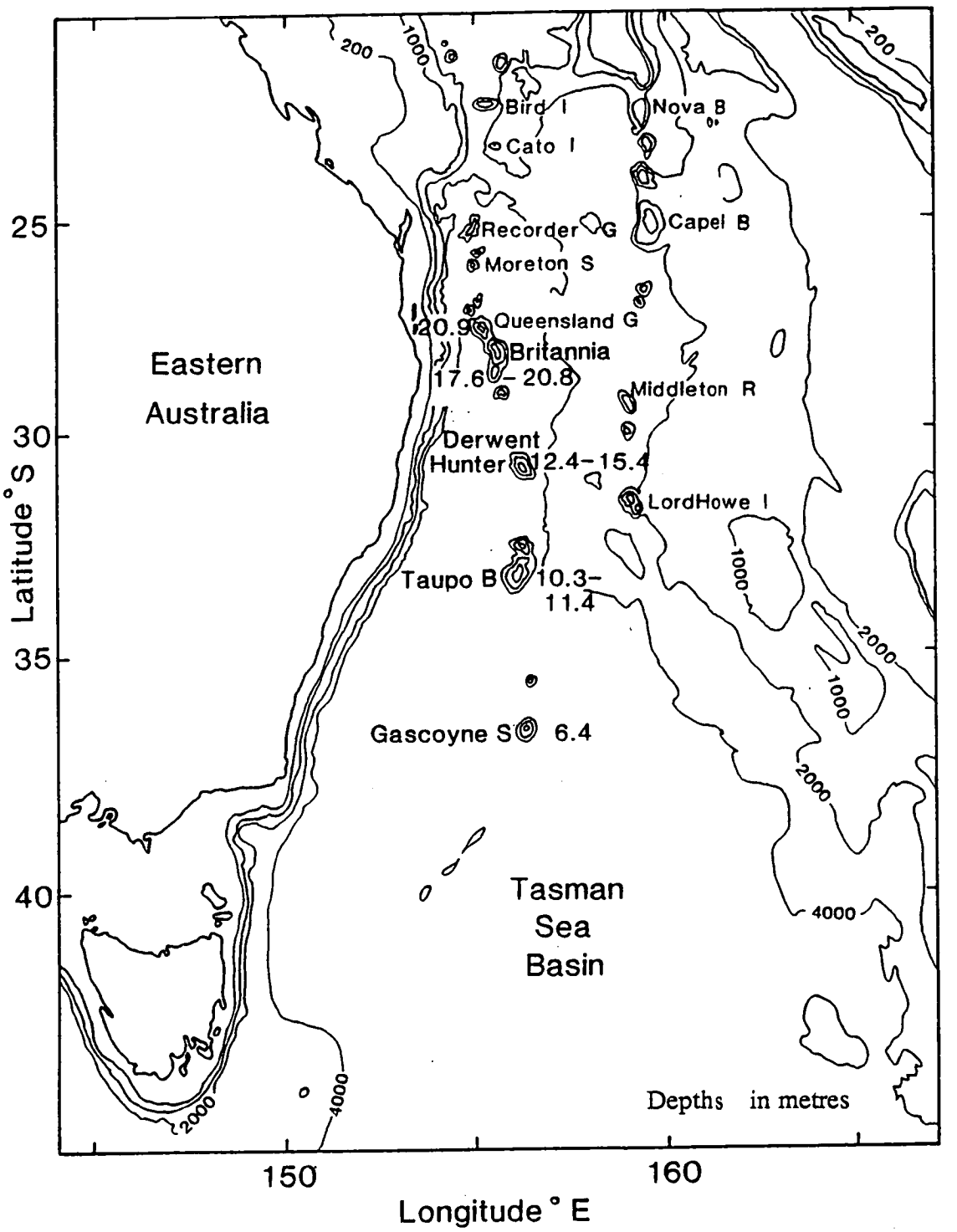

Figure 1.1 Bathymetric map of the Tasman Sea region. Larger seamounts of the subparallel Tasmantid and Lord Howe seamount chains are labelled, and adjacent numerals in bold type give K/Ar age determinations in Ma (after McDougall and Duncan, 1988). Seamount name abbreviations include G (guyot), S (seamount), B (bank), R (reef), and I (island).

Britannia basalts whereas the plagioclase+clinopyroxene-phyric group dominates Derwent Hunter samples. The small Taupo sample selection contains variants of both groups.

The glassy, olivine and Cr-spinel-phyric basalts may be divided into two subsets on the presence/absence of plagioclase microphenocrysts. Less common orthopyroxene and rare clinopyroxene phenocrysts (xenorcysts?) also occur in a number of samples. These invariably display disequilibrium textures, either in the form of coronal olivine microphenocrysts or resorbed crystal margins. Orthopyroxene exsolution lamellae are present in one Taupo clinopyroxene phenocryst (sample #85-175).

The plagioclase+clinopyroxene-phyric lavas display a wide variety of textures and phenocryst modal abundances (<1% to 20%). They typically have crystalline groundmasses of plagioclase+clinopyroxene+Fe-Ti oxides+olivine, and minor interstitial glass. Low-Ca-pyroxene occurs rarely as a groundmass phase, though orthopyroxene phenocrysts are common in these basalts recovered from Taupo Bank.

Altered rinds occur about kernels of fresh basalt in many samples, with carbonate and zeolite minerals sometimes filling cracks and vesicles. Glass may be devitrified, particularly when a constituent of partially crystalline groundmasses, however, glassy pillow margins tend to be fresh.

1.3.2 Mineral Chemistry

Mineral chemistry data is summmarised in Table 1.1, and selected analyses are given in Table 1.2. All analyses were obtained using a Jeol JXA-50A electron microprobe with EDAX attachment, housed in the Central Science Laboratory at the University of Tasmania.

Olivine

In most lavas a spectrum of olivine compositions occurs, with a common maximum Mg# (100Mg/(Mg+Fe^{2+}) of 85-86 being observed in the olivine+Cr-spinel-phyric group of basalts. Olivine-liquid Fe/Mg exchange relationships place most olivine phenocrysts near expected equilibrium compositions (i.e. assuming $K_D^{Fe/Mg}{}_{Ol\text{-}liq} = 0.30$; e.g. Roeder and Emslie, 1970) with respect to their host glass/groundmass compositions (Fig. 1.2). The overall range of olivine compositions in individual samples generally falls between equilibrium Mg# values (100Mg/(Mg+Fe^{2+}) predicted for glass/groundmass and

Table 1.1 Mineralogy of Tasmantid basalts listed in Table 1.3.

Seamount	Sample#	Mineralogy
Gascoyne	65821	Olivine (12%[a]; $Mg^{\#}$ [b] = 79.9-84.4) + Cr-spinel + plagioclase (3%; An[c] 55.9-65.3) + groundmass ($MG^{\#}$ [d] = 48.1, $Ca^{\#}$ [e] = 60.9)
	65809	Olivine (6%; $Mg^{\#}$ = 74.6-84.2) + Cr-spinel + xenocrystic(?) orthopyroxene (<1%; $Mg^{\#}$ = 78.3-85.1) + clinopyroxene (wehrlite cumulate glomerocryst: $Mg^{\#}$ = 77.3) + groundmass ($MG^{\#}$ = 51.3, $Ca^{\#}$ = 53.4)
	65811	Olivine (12%) + Cr-spinel + plagioclase (2.5%)
	65808	Olivine (10%; $Mg^{\#}$ 82.1-84.7) + chrome spinel + groundmass ($MG^{\#}$ = 53.5, $Ca^{\#}$ = 58.3).
	85-170	Olivine + Cr-spinel + plagioclase
Derwent Hunter	65828	Olivine (11%; $Mg^{\#}$ = 80.9-84.4) + Cr-spinel + plagioclase (2%; An 59.3-65.4) + clinopyroxene (<1%; $Mg^{\#}$ = 72.7-77.5) + groundmass ($MG^{\#}$ = 47.2, $Ca^{\#}$ = 59.4).
	65835	Plagioclase (1.4%; An 63.5-70.1) + clinopyroxene (<1%; $Mg^{\#}$ = 72.3-84.9) + ilmenite (<1%) + groundmass ($MG^{\#}$ = 45.6, $Ca^{\#}$ = 59.8).
	65836	Plagioclase (1.8%; An 45.3-53.0) + clinopyroxene (<1%; $Mg^{\#}$ = 74.7-77.9) + ilmenite + titano-magnetite + groundmass ($MG^{\#}$ = 37.9, $Ca^{\#}$ = 47.8).
Taupo	65839	Plagioclase (7.1%; An 45.3-56.9) + olivine (3.4%; $Mg^{\#}$ ~67-74.6) + orthopyroxene xenocrysts(?) (1.6%; $Mg^{\#}$ = 76.9-82.9) + groundmass ($MG^{\#}$ = 40.0, $Ca^{\#}$ = 52.4).
	85-175	Olivine ($Mg^{\#}$ = 79.1-82.3) + plagioclase (~An 50) + clinopyroxene ($Mg^{\#}$ ~80) + clinopyroxene xenocryst ($Mg^{\#}$ = 81.0_{rim}-92.3_{core}) with orthopyroxene lamellae ($Mg^{\#}$ = 90.8-91.0) + groundmass.
Britannia	68644	Olivine (8.9%; $Mg^{\#}$ = 81.5-85.5) + Cr-spinel + groundmass ($MG^{\#}$ = 54.2, $Ca^{\#}$ = 59.9).

a Modal volumes in percent.
b $Mg^{\#}$ = $100Mg/(Mg+Fe^{2+})$
c An = mole% anorthite in plagioclase.
d $MG^{\#}$ = $100Mg/(Mg+Fe^{tot})$
e $Ca^{\#}$ = 100Ca/(Ca+Na)

Table 1.2. Selected ferromagnesian phenocryst analyses.

Phenocryst	Olivine				Pyroxene			
Sample#	85-169	85-169	85-169	65809	85-175	65839	65809	85-169
Analysis#	1	2	3	4	5[a]	6	7	8
wt%								
SiO_2	41.09	39.93	39.37	37.53	57.56	53.47	55.72	53.83
TiO_2						0.47		
Al_2O_3					3.86	2.78	1.37	4.10
Cr_2O_3					0.37	0.21	0.34	0.56
Fe_2O_3						1.50	1.16	
FeO	13.81	15.84	17.30	21.02	6.05	12.92	8.86	2.50
NiO	0.40	0.35	0.31					
MgO	46.33	44.90	43.02	40.19	34.02	27.39	31.50	16.94
CaO				0.16	0.92	2.00	1.27	22.78
Na_2O								0.34
Total	101.63	101.02	100.00	98.91	102.78	100.74	100.21	101.04
Cations								
Si	1.008	0.996	0.999	0.983	1.928	1.907	1.952	1.927
Ti						0.011		
Al					0.152	0.117	0.057	0.173
Cr					0.010	0.006	0.009	0.016
Fe^{3+} [b]						0.040	0.031	
Fe^{2+}	0.283	0.331	0.367	0.460	0.170	0.386	0.260	0.075
Ni	0.008	0.007	0.006					
Mg	1.694	1.670	1.628	1.569	1.699	1.457	1.645	0.904
Ca				0.005	0.033	0.076	0.048	0.874
Na								0.024
Total	2.993	3.004	3.000	3.017	3.992	4.000	4.000	3.993
$Mg\#$[c]	85.7	83.5	81.6	77.3	90.9	79.1	86.4	92.3

a Exsolution lamellae in clinopyroxene (analysis# 8).
b Fe^{3+} based on stoichiometry.
c $Mg\# = 100Mg/(Mg+Fe^{2+})$

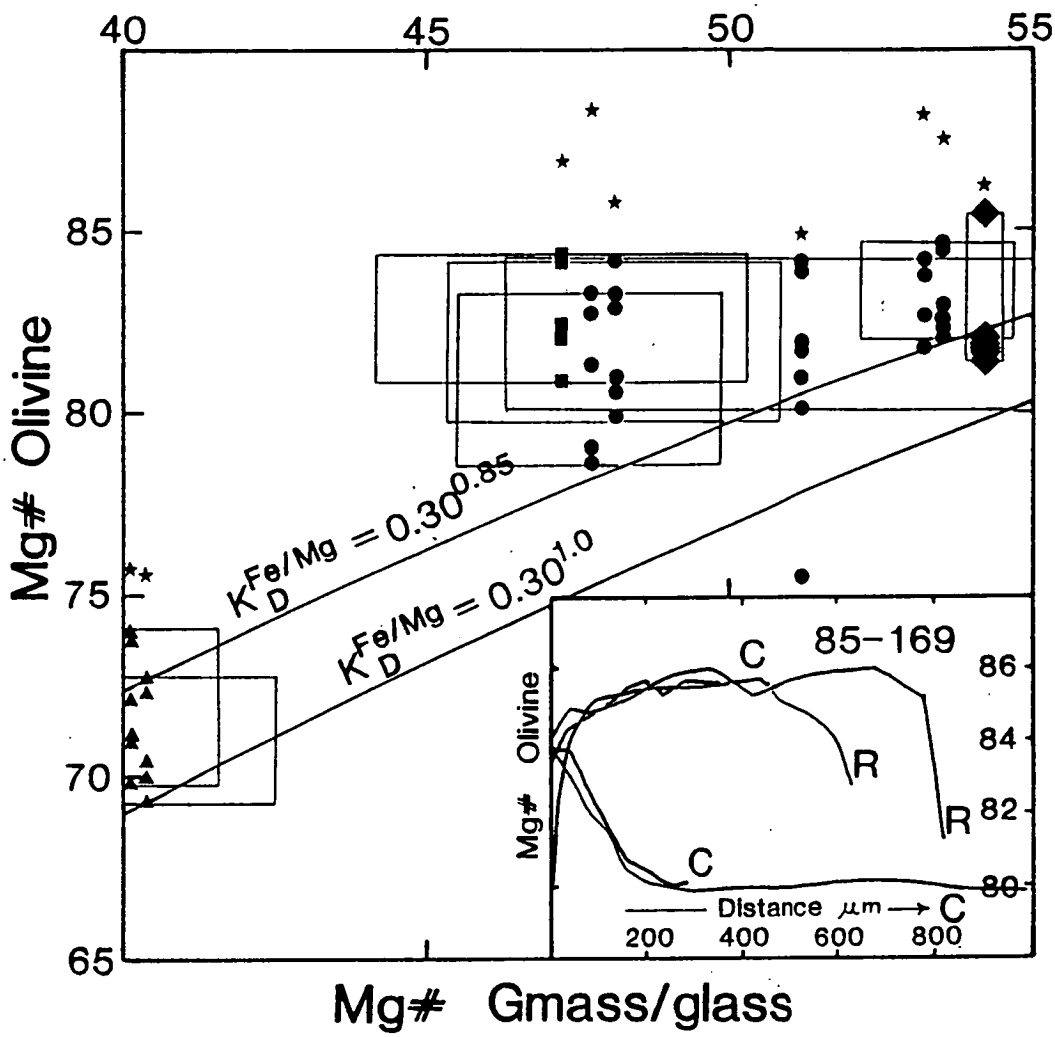

Figure 1.2 Mg# of olivine phenocrysts versus MG# of host-rock glass (or groundmass). Curved lines illustrate equilibrium relationships calculated using $K_D^{Fe/Mg}{}_{Ol\text{-}Liq} = 0.30$ (Roeder and Emslie, 1970) for assumed melt Fe^{2+}/Fe^{tot} values of 0.85 and 1.0 (as denoted by superscripts). Boxes outline 1σ errors for melt MG# values, as determined from multiple, defocused-beam, electron probe analyses of glass/groundmass compositions. Stars are equilibrium olivine compositions for whole-rock compositions calculated assuming $Fe^{2+}/Fe^{tot} = 0.85$ and $K_D^{Fe/Mg} = 0.30$. Symbols used include circles (Gascoyne), squares (Derwent Hunter), diamonds (Britannia), and triangles (Taupo). The inset illustrates olivine Mg# zonation profiles for five olivine phenocrysts in Gascoyne sample #85-169. Distance is measured in microns from phenocryst rims; C indicates a traverse is ended in the phenocryst core, whereas R indicates the opposing rim.

whole-rock compositions. Single olivine phenocrysts may be normal or reverse zoned, usually about unzoned core regions. Distinct populations of olivine phenocrysts may be identified, on such a basis, in single lavas (see inset in Fig. 1.2). The most Mg-rich olivines are notable for their high NiO contents, between 0.25 and 0.40 wt% (Table 1.2).

Orthopyroxene

The orthopyroxene phenocrysts (xenocrysts?), which are mainly restricted in occurrence to a number of primitive alkali olivine basalts, vary widely in composition within individual samples (e.g. in #65809 $Mg^{\#}$ = 78.3-85.1 and in #65839 $Mg^{\#}$ = 67.6-82.9). Single phenocrysts, however, span only a small fraction of this range. These phenocrysts have moderately high Al_2O_3 contents (1.37-3.33 wt%; see Table 1.2), as also have orthopyroxene lamellae (3.75-3.99 wt%) exsolved from a rounded (resorbed) clinopyroxene phenocryst in a Taupo alkali-olivine basalt (sample #85-175). This particular mineralogical association is distinguished by very magnesian compositions ($Mg^{\#}_{opx}$ = 91, $Mg^{\#}_{cpx}$ = 92).

Other Phenocryst Phases

Other phenocryst phases for which compositional data have collated include Cr-spinel, which falls within the range $Mg^{\#}$=31-55, $Cr^{\#}$ (100Cr/(Cr+Al)) = 50-69, and $100Fe^{3+}/(Fe^{3+}+Al+Cr)$ = 5-18. These values resemble those of Cr-spinel occurring in Hawaiian tholeiites (c.f. the Basaltic Volcanism Study Project (BVSP), 1981). Plagioclase phenocrysts vary between An45 and An70. This range probably reflects the spectrum of magma compositions from which plagioclase has crystallised, as phenocryst compositions correlate broadly the $Ca^{\#}$ (Ca/(Ca+Na)) values of their host glass/groundmass (see Table 1.1). Clinopyroxene phenocrysts also span a wide spectrum of compositions (Table 1.1), again in accord with the diversity of host basalt compositions in which they have crystallised.

1.4 GEOCHEMISTRY

Whole-rock major, trace element, and REE geochemistry has been determined by XRF techniques (REE after Robinson et al., 1986) using an automated Phillips PW1410 spectrometer (for details of sample preparation, analytical procedure, and precision

estimates see Appendix 1). Representative analyses are listed in Table 1.3, and a complete data set (31 samples) is provided in Appendix 2.

1.4.1 Classification and Grouping of Basalts: Major Elements, Ni and Cr

The dredged Tasmantid basalts are compositionally diverse, varying from slightly Quartz to Nepheline normative (Fig. 1.3). This variation corresponds with the geochemical transition from tholeiitic through transitional, to alkali-olivine basalt compositions, as indicated by the compositional range observed either side of the tholeiite-alkaline discriminant (MacDonald and Katsura, 1961) on a total-alkalis versus SiO_2 diagram (Fig. 1.4).

The basalts are readily grouped into primitive and evolved suites on the basis of $Mg^{\#}$ ($100Mg/(Mg+Fe^{2+})$) and transition element abundances. The suite of primitive basalts generally have $Mg^{\#}$ >61, and have Ni abundances between 238 and 322ppm (Fig. 1.5), whereas evolved suite samples have low $Mg^{\#}$ (39-55) and low transition element abundances (e.g. Ni 34-101ppm). Most evolved basalts may also be distinguished by their higher incompatible element abundances (see Table 1.3).

Among the primitive basalts, decreasing SiO_2 and increasing incompatible major/minor element abundances (TiO_2, Na_2O, K_2O, and P_2O_5) accompany the trend from tholeiitic to alkali olivine basalt compositions. The tholeiites are similar in composition to 'average Hawaiian tholeiite' at equivalent MgO contents, though they tend to have slightly higher SiO_2, Al_2O_3, and alkali contents, and have lower TiO_2, CaO and $Fe_2O_3^{tot}$ contents. These differences are most marked for the Britannia tholeiite (sample #68644; see Table 1.3 for a comparison).

1.4.2 Trace Elements

Incompatible trace element characteristics are summarised in a series of multi-element diagrams in Figure 1.6 (normalising values after Thompson, 1982). These plots form smooth convex-up patterns with higher abundance levels of the more highly incompatible elements (e.g. Ba, Rb, K, Nb, La), as is commonly found for intraplate basalts. Overall, increasing abundance levels of the incompatible trace elements coincide with the transition from tholeiitic to alkaline olivine basalt compositions. Other notable features of the incompatible element geochemistry include :

Table 1.3. Whole-rock geochemistry of selected Tasmantid basalts.

	Gascoyne					D-Hunter			Taupo		Brit.[a]	Hawaii[b]
Sample Number	65821	65809	65808	65811	85-170	65828	65835	65836	65839	85-175	68644	
wt.%												
SiO_2	48.85	48.67	49.67	50.25	51.39	50.32	47.73	49.56	50.08	45.86	51.48	48.98
TiO_2	1.84	2.48	1.89	1.72	2.27	1.80	3.46	3.67	3.04	2.81	1.31	2.41
Al_2O_3	13.79	14.51	13.66	13.46	13.74	13.30	15.15	16.00	14.98	15.14	13.90	13.09
Fe_2O_3	11.57	11.16	11.13	10.87	11.02	10.51	11.26	10.03	11.97	11.93	11.44	12.40
MnO	0.16	0.14	0.15	0.15	0.13	0.15	0.13	0.12	0.15	0.14	0.14	0.17
MgO	11.37	8.15	10.12	10.08	7.47	8.99	4.87	3.61	4.84	6.76	9.26	9.91
CaO	8.70	8.11	8.44	8.26	7.89	9.27	9.35	8.13	7.61	8.17	8.25	10.18
Na_2O	2.89	3.52	2.92	2.77	3.16	2.84	3.28	4.17	3.95	3.36	2.80	2.16
K_2O	0.54	1.19	0.85	0.75	1.18	0.57	1.15	2.30	1.23	1.17	0.44	0.46
P_2O_5	0.37	0.73	0.53	0.30	0.53	0.28	1.64	0.87	0.59	0.78	0.31	0.26
LOI[c]	0.56	0.59	0.50	0.77	0.68	2.21	1.84	1.87	1.22	3.68	0.39	
Total	100.64	99.25	99.86	99.38	99.46	100.24	99.86	100.33	99.66	99.80	99.72	100.02
ppm												
Rb	7	19	13	12	18	10	33	20	20	10	8	
Ba	160	296	207	143	255	103	340	602	249	417	122	
Sr	446	626	551	442	585	416	609	711	538	920	293	
La	13.8	28.0	16.2	11.0	21.8	11.1	32.6	38.0	30.3	36.6	8.22	
Ce	29.8	62.0	36.6	25.7	47.0	26.3	71.8	91.8	51.1	77.2	20.0	
Pr	3.75	7.62	4.55	3.40	6.30	3.45	9.32	11.6	7.36	9.82	2.71	
Nd	18.7	34.0	22.0	16.4	28.4	17.2	41.8	50.7	32.3	41.9	12.4	
Sm	4.64	7.36	5.01	3.88	6.34	4.62	9.64	10.5	8.20	8.55	3.54	
Eu	1.75	2.53	1.92	1.84	2.33	1.69	3.41	3.40	2.84	3.00	1.48	
Gd	4.96	6.94	5.19	3.99	5.97	5.22	9.65	9.77	8.66	7.77	4.03	
Dy	4.07	5.10	4.08	3.67	4.70	4.31	7.46	7.56	6.45	5.99	3.83	
Er	1.88	2.11	1.85	1.93	2.01	2.01	3.75	3.74	2.71	3.09	2.21	
Yb	1.47	1.58	1.38	1.42	1.51	1.59	2.73	2.73	1.89	1.83	1.72	
Y	18	25	20	19	24	22	37	38	30	28	19	
Zr	121	242	149	119	201	125	282	346	236	279	97	
Nb	15	36	17	12	29	13	39	41	30	51	8	
Sc	25	18	22	21	20	20	22	21	16	17	23	
V	185	177	174	167	179	179	266	249	168	199	172	
Cr	553	317	484	503	361	559	49	20	83	273	499	
Ni	314	254	301	274	247	322	59	34	76	238	302	
Mg#[d]	69.6	63.0	67.9	68.3	61.2	66.6	50.2	45.6	48.5	56.9	64.3	

a Brit. = Britannia

b Average Hawaiian tholeiite at ~10 wt% MgO (Maaloe, 1979)

c LOI = Loss on ignition

d $Mg^{\#} = 100Mg/(Mg+Fe^{2+})$, assuming $Fe^{2+}/Fe^{tot} = 0.85$.

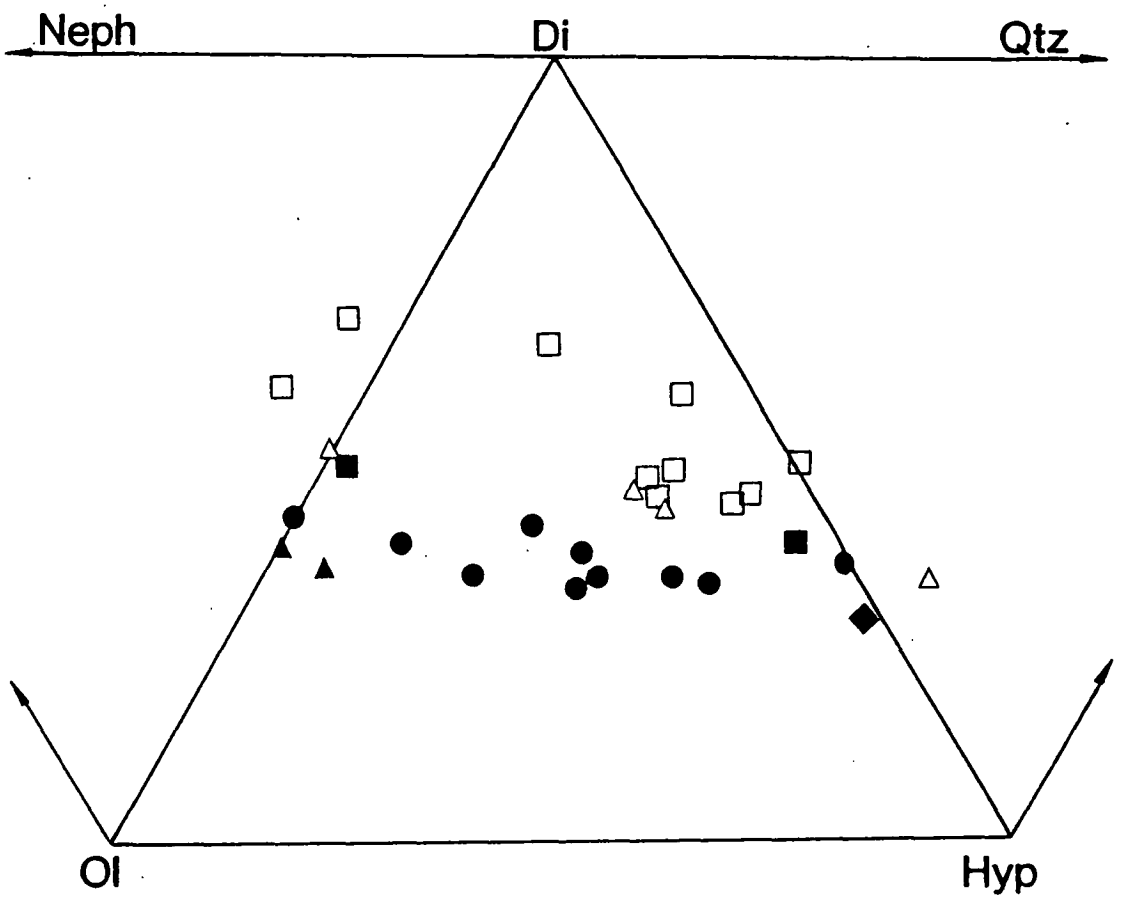

Figure 1.3 Normative mineralogy of Tasmantid basalts. Symbols used are circles (Gascoyne), squares (Derwent Hunter), diamonds (Britannia), and triangles (Taupo). Filled and unfilled symbols denote basalts belonging to the primitive and evolved compositional groups respectively (see text for details).

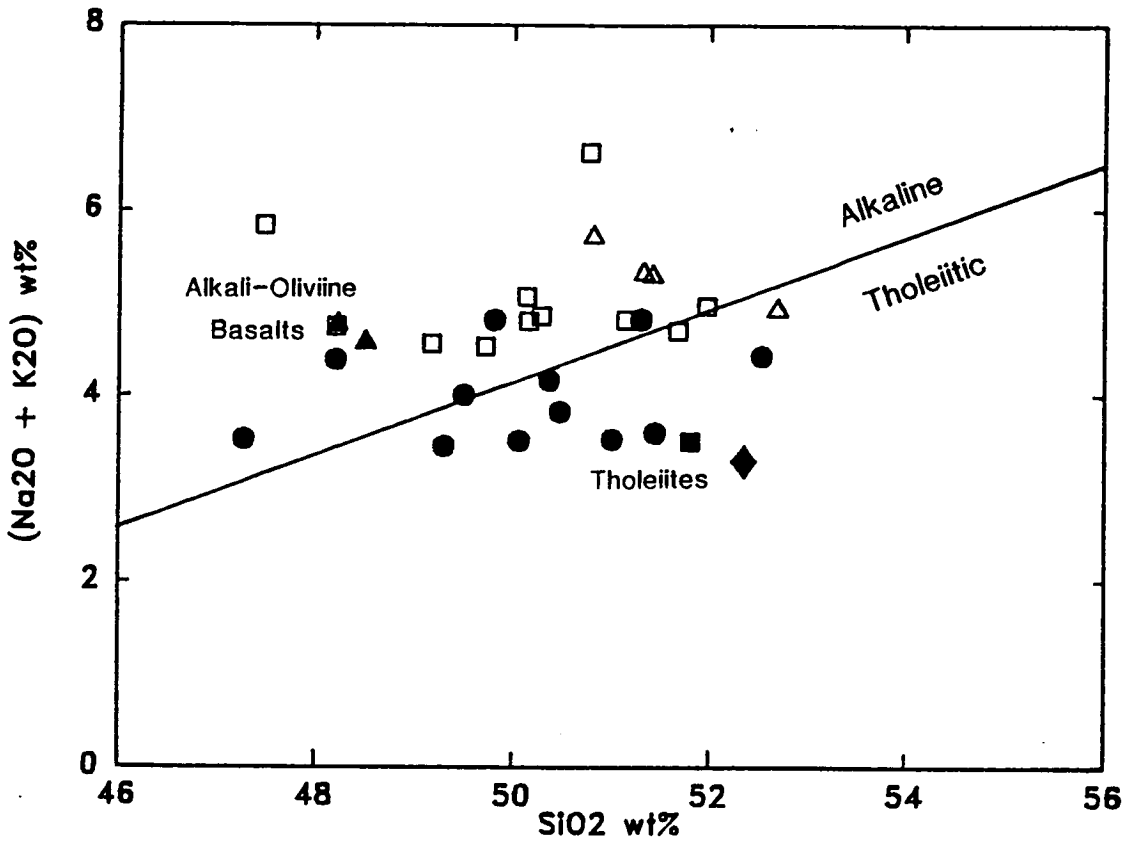

Figure 1.4 Total alkalis versus SiO_2 variation diagram for Tasmantid basalts. Tholeiite-alkaline discriminant is after MacDonald and Katsura (1961). Symbols as for Figure 1.3.

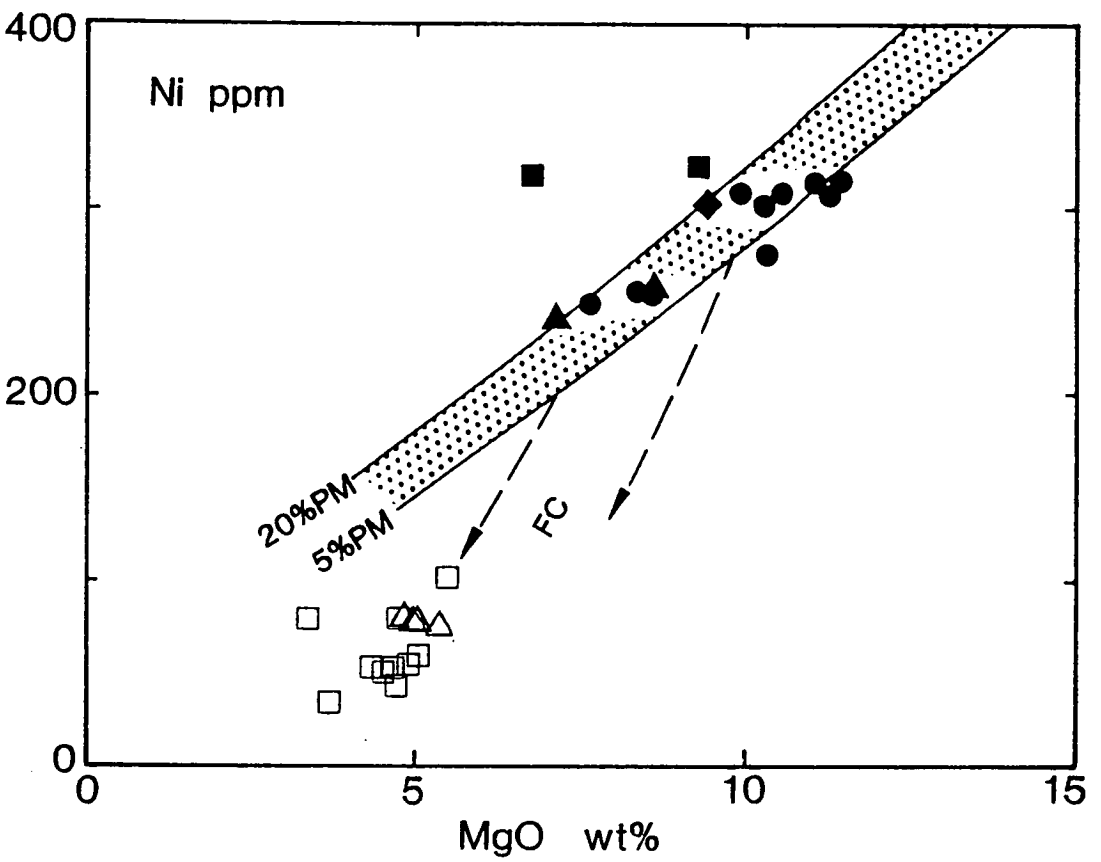

Figure 1.5 Ni versus MgO covariation in Tasmantid basalts. Curves labelled "5%PM" and "20%PM" bound the partial melt compositions of a peridotite source with 2000ppm estimated by Hart and Davis (1978). Dashed lines show approximate liquid evolution paths produced by shallow level olivine-dominated crystal fractionation (FC). Symbols as for Figure 1.3.

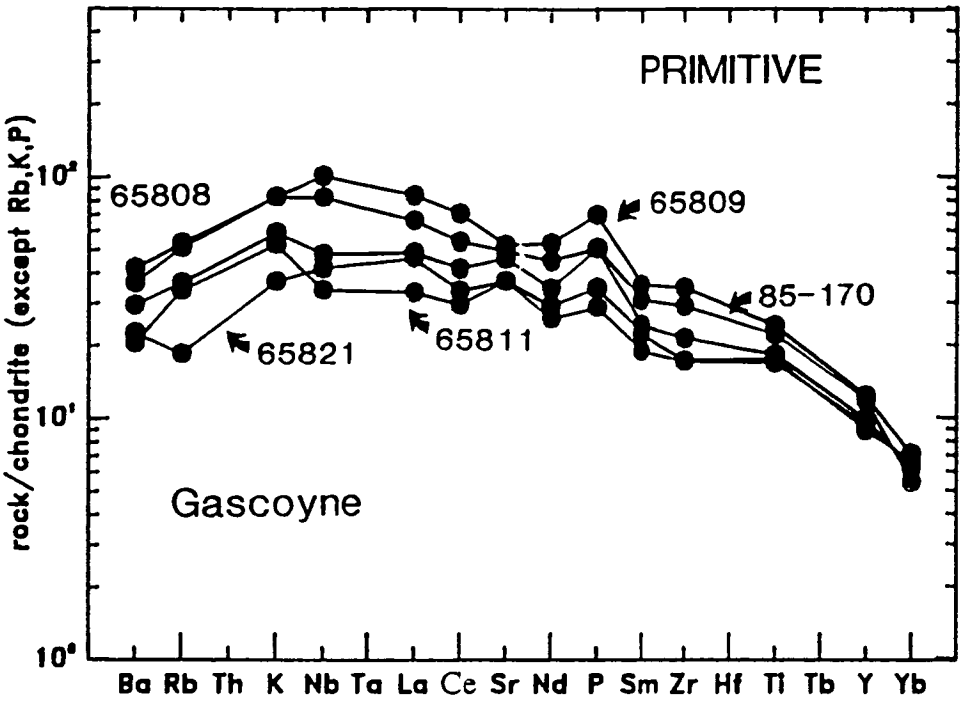
PRIMITIVE
65808
65809
85-170
65821
65811
Gascoyne
rock/chondrite (except Rb,K,P)
Ba Rb Th K Nb Ta La Ce Sr Nd P Sm Zr Hf Ti Tb Y Yb

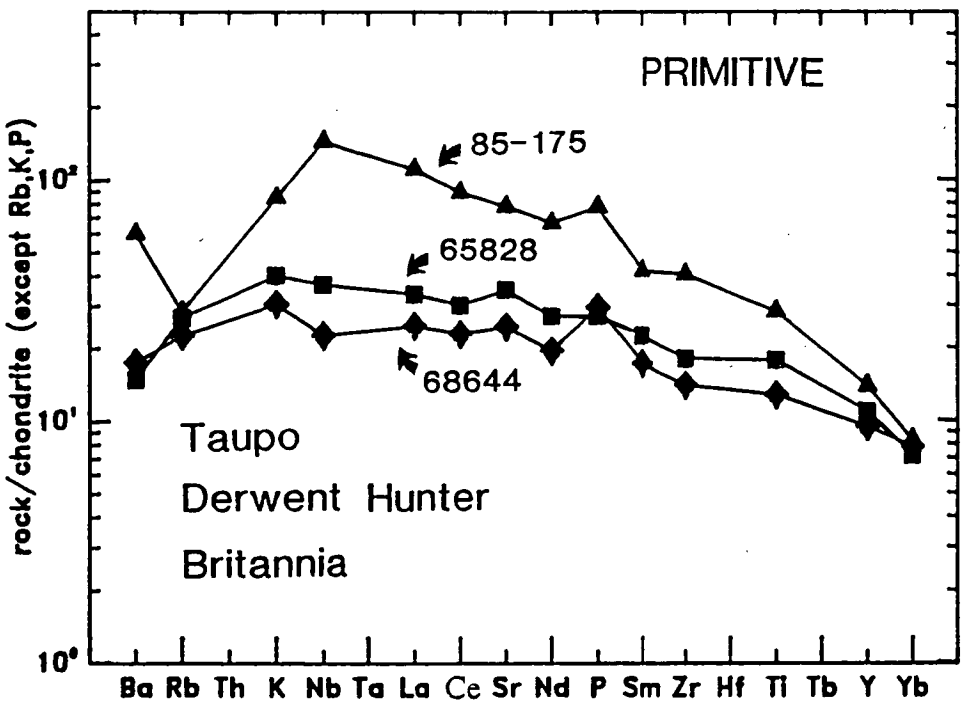
PRIMITIVE
85-175
65828
68644
Taupo
Derwent Hunter
Britannia
rock/chondrite (except Rb,K,P)
Ba Rb Th K Nb Ta La Ce Sr Nd P Sm Zr Hf Ti Tb Y Yb

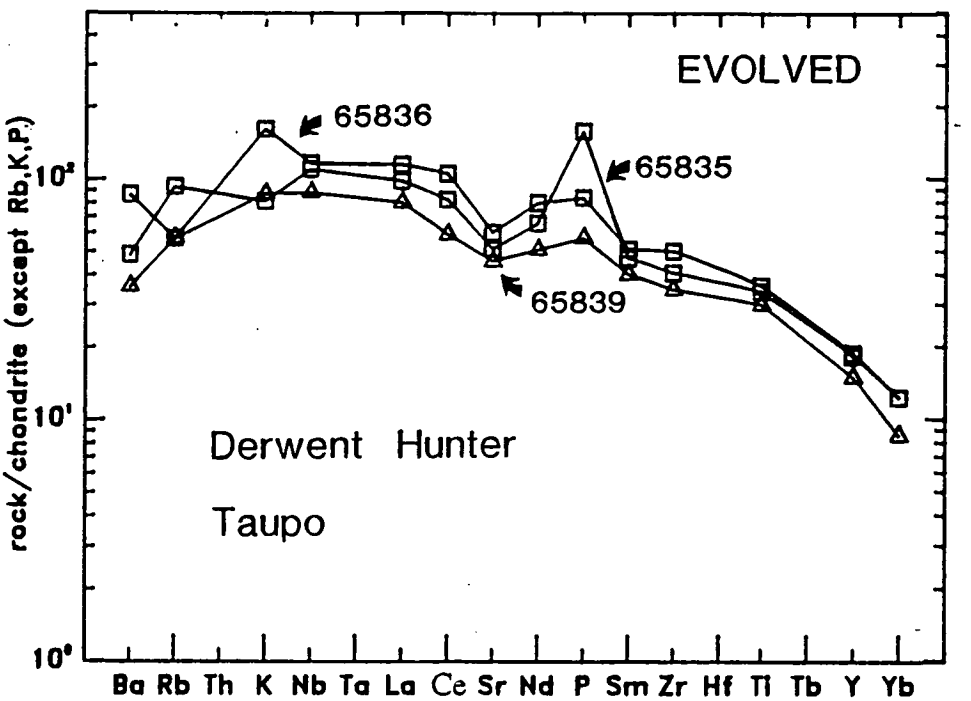

Figure 1.6 Multi-element diagrams for Tasmantid basalts listed in Table 1.3 (normalising values after Thompson, 1982). Symbols as for Figure 1.3.

1) variable relative abundance levels of the highly incompatible elements Rb, Ba, K, Nb, and La,

2) anomalous P and Sr abundances, which are observed as "positive spikes" in several samples.

The REE patterns of the Tasmantid tholeiites (e.g. sample #'s 68644, 65821, 65828) are characterised by slight to moderate LREE enrichment (La/Sm_{CN} = 1.45-2.37) and fractionated HREE (Gd/Yb_{CN} = 1.92-3.52), resembling closely the distinctive "kinked" patterns of Hawaiian tholeiites (Fig. 1.7). The transition to alkali olivine basalt compositions is marked by increasing absolute and relative abundances of the LREE.

1.4.3 Alteration

Only the freshest material available was chosen for geochemical analysis, however, some of the geochemical variability observed in the Tasmantid basalts may be attributed to alteration by seawater. In general, this appears to be restricted to the LIL elements (mainly Rb and K) and sometimes also Na_2O, as these elements do not behave systematically relative to other similarly incompatible, immobile elements (e.g. LREE, Zr, Nb), particularly as indicators of alteration (e.g. loss on ignition values) increase. A case also exists for an alteration-related overabundance of P_2O_5 relative to Nd in some basalts (see Figure 1.8). This appears to be restricted to several evolved suite basalts from Derwent Hunter, each of which lacks fresh glass and has a relatively coarsely crystalline groundmass.

1.5 ISOTOPE GEOCHEMISTRY

Sr and Nd isotope values of selected Tasmantid basalts (Fig. 1.9), which have been determined by McCulloch (1988), exhibit a large range in $^{87}Sr/^{86}Sr$ (0.70379 to 0.70472) and εNd values (+3.0 to -3.3). The most radiogenic Sr and unradiogenic Nd isotope values occur in the tholeiites, whereas the converse applies to the alkali olivine basalts (though note that the Queensland Guyot sample which has the highest $^{87}Sr/^{86}Sr$ and lowest εNd values has not been analysed for major and trace elements). Transitional basalts from Gascoyne have intermediate isotopic compositions between these extremes.

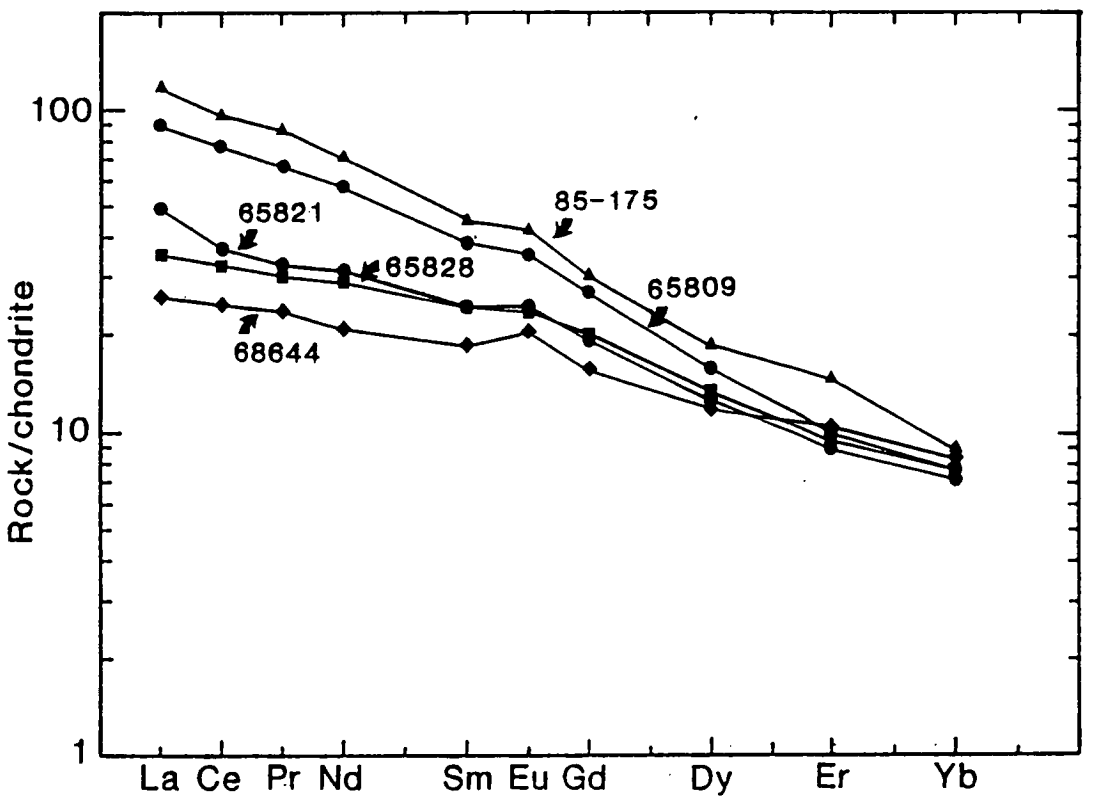

Figure 1.7 REE patterns for selected Tasmantid primitive basalts. Note the fourfold increase in LREE abundance levels as bulk compositions progress from tholeiites (#68644 and #65828) to alkali olivine basalts (e.g. #85-175). Symbols as for Figure 1.3.

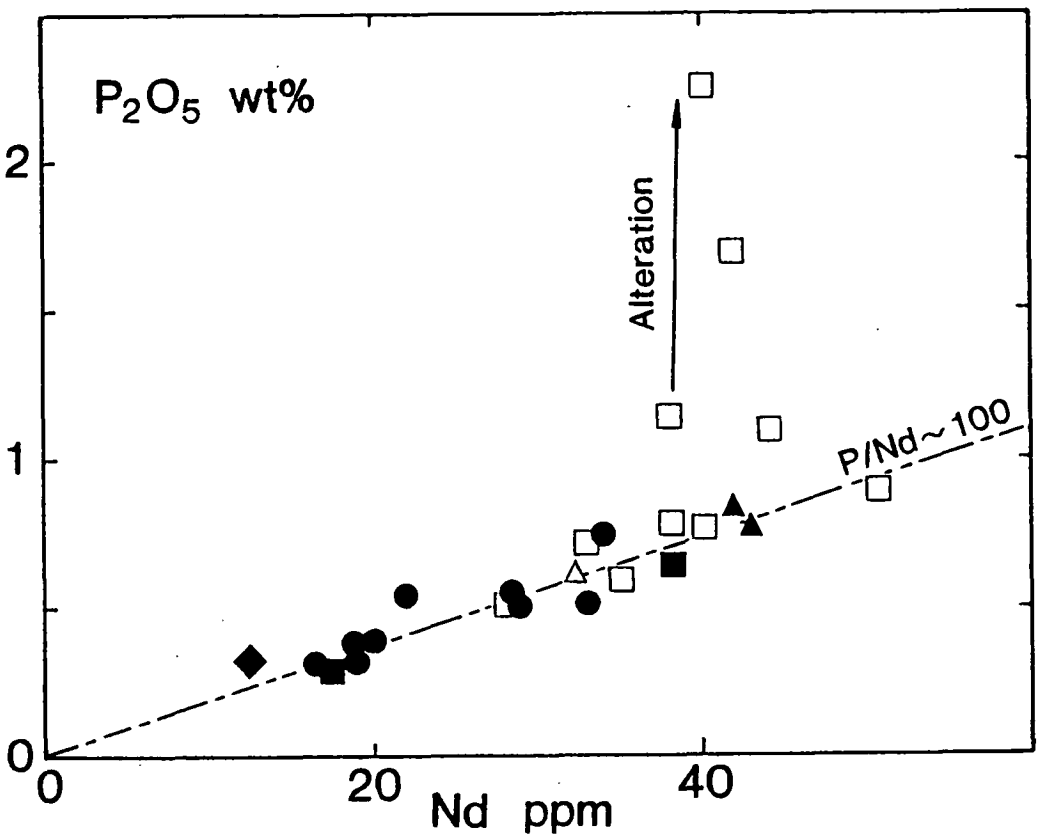

Figure 1.8 P_2O_5 versus Nd co-variation in Tasmantid basalts. Note the constant P/Nd value (~100), except for several evolved samples from Derwent Hunter. The anomalous P in these particular basalts is probably alteration derived. Symbols as for Figure 1.3.

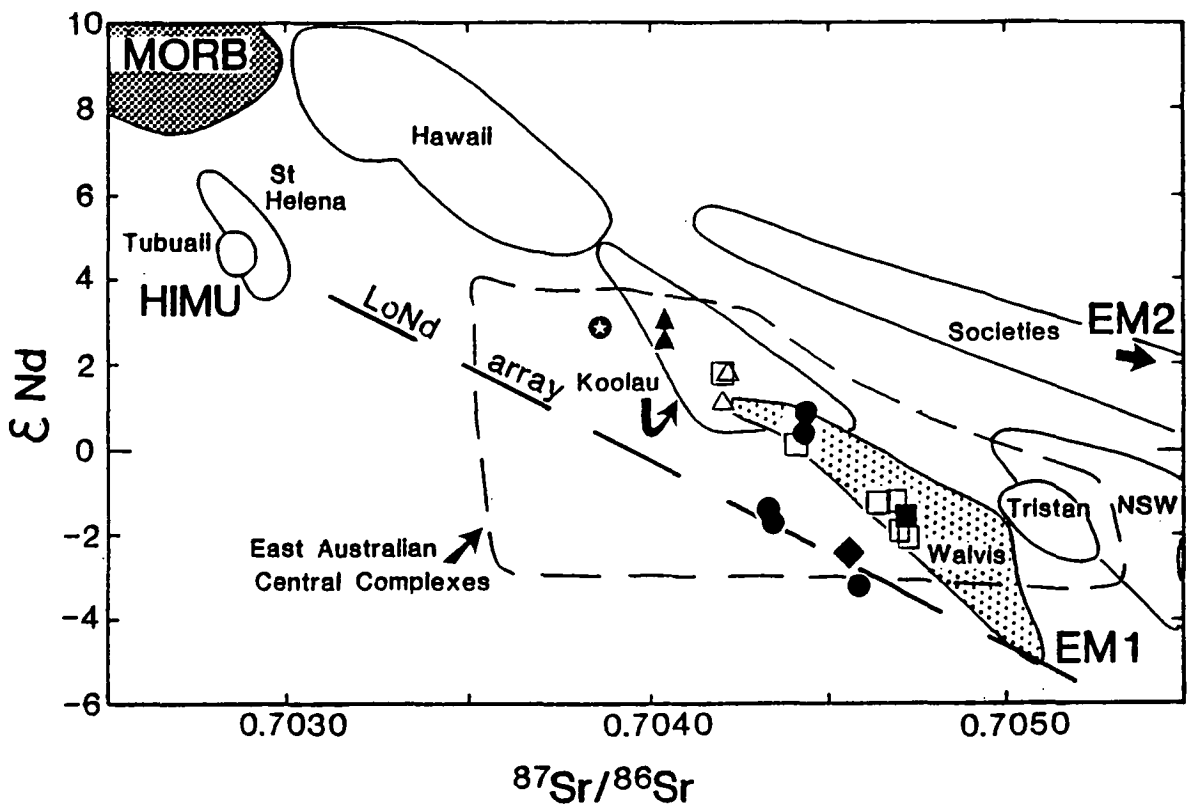

Figure 1.9 Nd and Sr isotope co-variation in Tasmantid basalts (data from McCulloch, 1988). Fields for MORB, Societies, St. Helena, Tubuaii, Tristan da Cunha (Tristan), and Walvis Ridge are from Hart et al. (1986); New South Wales leucitites (NSW) and east Australian central complexes are from Ewart et al. (1988); and Hawaii and Koolau are from Stille et al. (1986). HIMU, EM1, and EM2 mantle components, and the LoNd array, are as defined by Hart et al. (1986) and Zindler and Hart (1986). The circled five-point star represents a single sample recovered from Queensland Guyot, otherwise symbols are as for Figure 1.3.

The Tasmantid isotope data are somewhat unusual among the global population of OIB (ocean island basalts), being similar only to OIB from Tristan da Cunha and Walvis Ridge (Richardson et al. 1982; Hart, 1976). They also resemble and overlap with some east Australian Cenozoic Province basalts, particularly samples from the central volcano complexes and the New South Wales leucitites (Ewart et al., 1988). These particular isotopic characteristics trend off the main mantle array toward the EM1 mantle end-member, which forms a low $^{87}Sr/^{86}Sr$ part of the DUPAL mantle anomaly (Hart, 1984; Zindler and Hart, 1986) coincident with the so called LoNd array (Hart et al., 1986).

1.6 ORIGIN OF TASMANTID PRIMITIVE MAGMAS

1.6.1 Evidence for Primary/Near-Primary Magma Compositions

The high transition element abundances (238-322 ppm Ni; 320-560ppm Cr) and high $Mg^{\#}$'s (predominantly 61-70; $Fe^{2+}/Fe^{tot} = 0.85$) of the suite of primitive Tasmantid basalts are consistent with widely accepted geochemical criteria for near-primary and primary mantle-derived magma compositions. This assertion is supported by the elevated NiO content and $Mg^{\#}$ of olivine phenocrysts (see Table 1.2. & Fig. 1.2), which overlap with peridotitic olivine compositions, indicating that the phenocrysts probably represent the early crystallisation products of near-primary peridotite-derived melts (e.g. Takahashi et al., 1987). Collectively, these features document the primitive nature of the Tasmantid basalts, and support the interpretation of a primary/near primary origin for these compositions. Moreover, the suite of primitive basalts are also concordant with the field of compositions produced by experimental melting of peridotite, as illustrated in Figure 1.10 using the projection schemes of Falloon and Green (1988), and Falloon et al. (1988).

1.6.2 PT Conditions of Melt Generation, and Residual Source Mineralogy

A framework, based on peridotite melting experiments, now exists for interpreting the pressure of melt segregation and the residual mantle phase mineralogy of volatile-poor primary magma compositions. Projection of the primitive Tasmantid basalts onto the cotectic grid scheme for melting of Hawaiian pyrolite (proposed source composition of Hawaiian tholeiites) determined by Falloon and Green (1988) and Falloon et al. (1988), reveals that these compositions are in equilibrium with peridotite residues (mainly

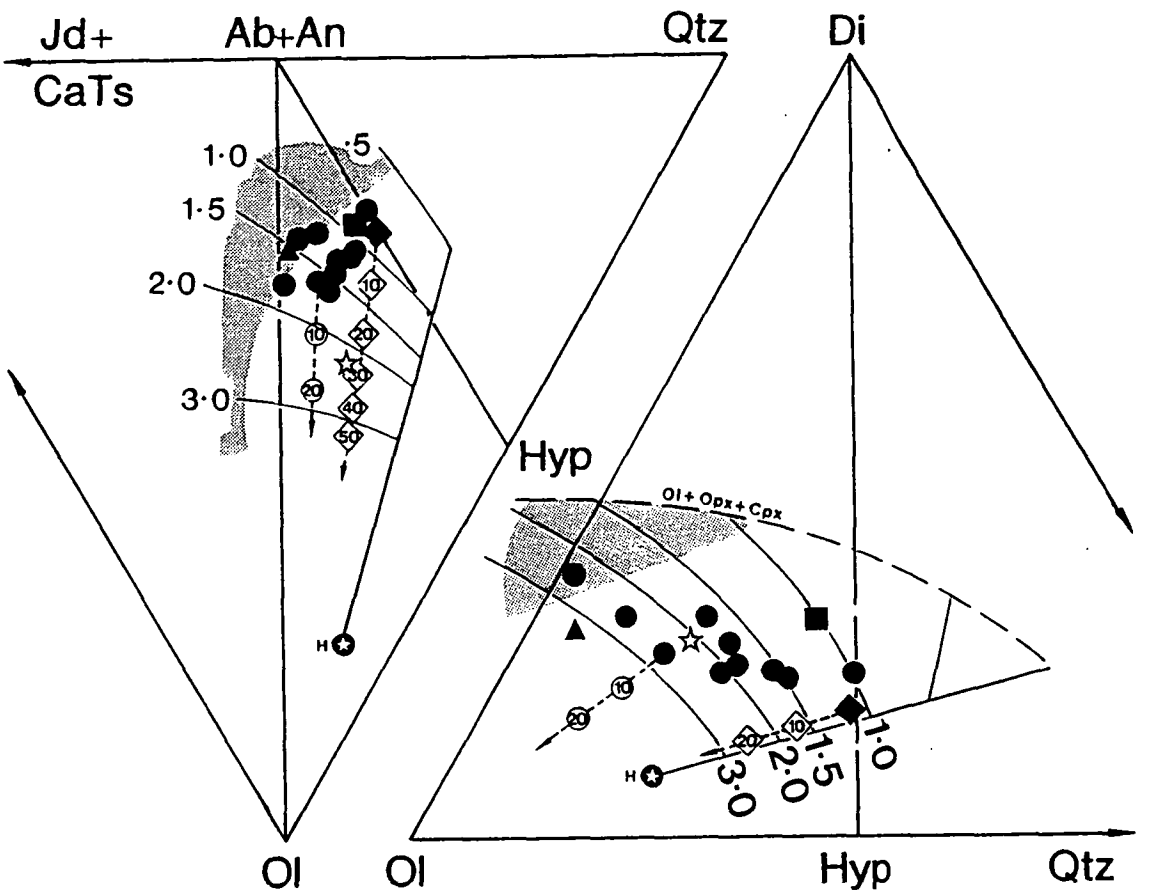

Figure 1.10 Tasmantid primitive basalt compositions projected onto the Ol-Jd+CaTs-Qtz and Ol-Di-Qtz faces of the CIPW molecular normative basalt tetrahedron, following the methods of Green (1970) and Falloon and Green (1988). Numbered grids are the high pressure melting cotectics (in GPa) determined from high pressure experimental melting studies on "Hawaiian pyrolite" by Falloon et al. (1988). The shaded regions indicate melt compositions in equilibrium with lherzolite residua at pressures between 0.5 and >3.0GPa on the Ol-Jd+CaTs-Qtz projection, and at >1.0GPa on the Ol-Di-Qtz projection. The 5-point star is the projected composition of a new Kilauea Iki parent estimate (see Chapter 2), otherwise symbols are as for Figure 1.3. Unfilled symbols linked by dashed lines illustrate the trend toward higher pressure compositions as olivine is added incrementally to several samples (#68644 and #65809). The total %mass of olivine added is indicated by the numerals enclosed within the symbols.

harzburgite) at pressures between 0.8GPa and ~2.5GPa (Fig. 1.10). Only the alkali olivine basalts lie near the field of melt compositions potentially deriving from *lherzolitic* residues at pressures >1.0GPa (see stippled fields in Fig. 1.10). These predictions are relatively robust, as only small variations in pressure estimates (+0.2GPa) occur on the Jd+CaTs-Qtz-Ol projection cotectics with variation in source bulk composition, and slight expansion of the residual lherzolite field occurs as source bulk composition becomes less fertile (Falloon et al., 1988). Finally, the ability of these projection methods to predict peridotite melting conditions, is supported by the closely matching result obtained from the projection method, and that determined experimentally for an Hawaiian primary melt estimate in Chapter 2 (i.e. 2.0GPa and Ol+Opx residue; see Fig. 1.10)

The principal uncertainty in the conditions of magma generation predicted here, lies with the assumed primary nature of the primitive Tasmantid basalts. Based on phase equilibria considerations and geochemical observations in other suites of primitive OIB (e.g. Hawaii; see Chapter 2), it is reasonable to expect that the true primary melt compositions will lie on olivine-controlled fractionation,or accumulation vectors passing through the projected primitive Tasmantid basalt compositions. Little potential exists for olivine accumulation in the Tasmantid basalts (12% maximum modal abundance; see Table 1.1), hence lower pressure derivation from lherzolite residues is unlikely. More magnesian (olivine-rich) primary melt compositions, on the other hand, may originate at higher pressure from harzburgite residues, as indicated by the olivine-addition vectors shown for selected samples in Figure. 1.10. How much olivine may reasonably be added to the already primitive compositions of the Tasmantid basalts is not constrained, apart perhaps from possible limits to the abundance of transition elements able to be generated by melting of mantle peridotite. Primary melt compositions modelled using the $D^{Ni}_{Ol\text{-}Liq}$ relationship of Hart and Davis (1978), for 5 to 20% partial melting of a peridotite source containing 2000 ppm Ni (Fig. 1.5), are coincident with the existing primitive Tasmantid basalts, indicating that appreciably more Ni-rich, and thus more olivine-rich and deeply-derived primary melts are unlikely.

The aluminous orthopyroxene and/or clinopyroxene phenocrysts present in some alkali olivine basalts may result from prior crystallisation at elevated pressure. This can be

demonstrated using the cotectic grids in Figure 1.10, which clearly show that orthopyroxene and/or clinopyroxene saturation is more likely to occur at higher pressures as the olivine phase volume contracts. Equilibration of these alkali olivine basalts with lherzolite/harzburgite assemblages at high pressure is also consistent with the more evolved nature (i.e. lower Mg#) of these orthopyroxene "xenocryst" bearing basalts (i.e. sample #'s 65809, 85-175, 65839; see Table 1.3). Accordingly, the primary melt compositions from which these particular samples have evolved are less likely to fall on simple olivine-addition trends.

The distribution of Tasmantid basalts in Fig. 1.10 outlines a PT path which is consistent with progressive decompression melting of peridotite occurring up to shallow levels (~1.0GPa). This simple melting scheme is supported by the transition from incompatible element-rich alkali olivine basalts at the highest pressures (i.e 2.5GPa) to more incompatible element-poor tholeiites segregated at lower pressures.

1.6.3 Implications for the Presence of Residual Garnet

A shallow melting origin (<2.5 GPa) for the Tasmantid primitive magmas would confine their derivation to (spinel) lherzolite and harzburgite phase assemblages. These low pressures preclude equilibrium with garnet-peridotite residues, as is indicated by the high pressure liquidus mineralogy of similar basalt compositions which have been studied experimentally (e.g. Green and Ringwood, 1967a; Ito and Kennedy, 1968; Green et al, 1979; Chapter 2). These studies also show that garnet is a liquidus phase for anhydrous tholeiitic and alkali-olivine basalt compositions at pressures >2.5-3.5 GPa, and that the only co-liquidus phase at these conditions is clinopyroxene. Highly magnesian compositions are necessary to achieve garnet-peridotite equilibrium, as illustrated by the quantity of added equilibrium olivine (e.g. #68644 + 40wt% olivine) required to attain olivine+orthopyroxene saturated cotectics at high pressures suitable for garnet-saturation (see Fig. 1.10). The already high transition element abundances in the Tasmantid primitive basalts (Fig 1.5) do not support their evolution by such large amounts of olivine fractionation. The observed olivine phenocrysts are very Ni-rich (Table 1.2), and their involvement in an olivine-fractionation-correction procedure will result in extremely high Ni concentrations in more olivine-rich primary compositions.

1.7 TASMANTID SOURCE GEOCHEMISTRY

Knowing the residual mineralogy of the Tasmantid mantle source allows calculation of the source geochemistry by applying a simple batch partial melting model, and using appropriate solid-liquid trace element partition coefficients and residual phase proportion estimates. An even simpler first-order approach may recognise that :

1) minor phases are unlikely to persist to the high degrees of melting believed to give rise to the tholeiites, as is consistent with the smooth pattern of relative element abundances observed in Fig. 1.6,

2) and that the residual mineralogy is dominated by olivine and orthopyroxene, with clinopyroxene either nearing or having been completely melted out.

Incompatible element bulk partition coefficients, between peridotite residues and primary melts, are therefore likely to be governed by the low to very low partition coefficients for olivine and orthopyroxene, resulting in highly incompatible behaviour, i.e.

$$Ci_S = Ci_l.f \qquad (1.1)$$

where Ci_S = trace element abundance in source,

Ci_l = trace element abundance in liquid,

f = degree of partial melting.

The increasing incompatible element abundances occurring in the Tasmantid primitive basalts, from tholeiites through to alkali olivine basalts, can be expected to derive from decreasing degrees of partial melting and/or alkali olivine basalt source regions more enriched in incompatible elements. Importantly, the relative abundances of incompatible trace elements are likely to be inherited unchanged from values existing in the magma source regions.

1.7.1 Evidence for Source Heterogeneity

The relative abundances of highly incompatible elements,and elements with similar bulk paritition coefficients, are known to be little affected during partial melting or magmatic differentiation. This certainly will be the case if the residual phase mineralogy is harzburgitic as indicated above. Consequently, variation in the ratio values of highly and

similarly incompatible elements will provide a measure of chemical heterogeneity occurring in the magma source region. Among the Tasmantid primitive basalts, considerable variation of (and covariation between) such element ratios (e.g. Ba/Nb, La/Nb, Sr/Nd) occurs, as do correlations with other element ratios which are more prone to the effects of variable degrees of partial melting (e.g. La/Y, see Table 1.4 and Fig. 1.11). From the preceding arguments this geochemical variability can be interpreted confidently in terms of magma source region heterogeneity.

1.7.2 Nature of the Geochemical Heterogeneity

The Tasmantid basalts which have the lowest Ba/Nb values (~8) have trace element characteristics broadly akin to the composition of average OIB compiled by Sun and McDonough (1988; see Table 1.4 and Fig. 1.11). This average OIB geochemistry, which includes strong LREE enrichment, fractionated (non-chondritic) middle/heavy REE abundances (e.g. $Dy/Yb_{CN} > 1$), Ba/Nb~8, La/Nb~1, and Sr/Nd~17, is best developed in the more incompatible element-rich alkali-olivine basalts, which as noted earlier are also characterised by the lowest $^{87}Sr/^{86}Sr$ values (<0.7038) and the highest εNd values (>+3) among the Tasmantid basalts (Fig. 1.9).

A prominent departure from the average OIB geochemical characteristics occurs as compositions become more tholeiitic and incompatible element-poor, a trend which is accompanied by increasing Ba/Nb values up to ~15. This transition is marked by increasing LREE/HFSE (e.g.La/Nb), LILE/HFSE (e.g. Ba/Nb, K/Nb), LILE/LREE (e.g. Ba/La, Sr/Nd), and Zr/Nb values, and by decreasing LREE enrichment (e.g. decreasing La/Sm and La/Y values) and middle/heavy REE (e.g. Dy/Yb) values. Furthermore, it should be recalled that the tholeiites have the highest $^{87}Sr/^{86}Sr$ and lowest εNd values of the Tasmantid basalts.

The alkali-olivine basalts may clearly be associated with the petrogenetic processes, and mantle sources, that give rise to the common geochemical character of many OIB. The high Ba/Nb values of the Tasmantid tholeiites, however, are restricted in association to a few DUPAL anomaly OIB, particularly seamounts in the South Atlantic Ocean (Weaver et al., 1986; Hawkesworth et al., 1987; Sun and McDonough, 1988), neighbouring continental volcanics in South America and southern Africa (e.g. Hawkesworth et al.,

Table 1.4. Incompatible element ratios for selected Tasmantid basalts, ranging from tholeiite to alkali-olivine basalt in composition, and comparative values for average OIB and some high Ba/Nb lithologies.

Sample	OIB[a]	85-175	65809	65821	65808	68644	IAB[b]	PAWMS[c]	PC[d]
Ba/Nb	7.3	8.2	8.2	10.7	12.2	15.3	214	1070	164
Ba/La	9.46	11.4	10.6	10.4	12.8	14.8	30.1	51.9	54.8
La/Nb	0.77	0.72	0.78	0.92	0.95	1.03	7.1	20.6	3.0
K/Nb	250	190	274	299	415	457	6170	----	1790
Zr/Nb	5.83	5.5	6.7	8.1	8.8	12.1	28.6	17.3	10.7
Sr/Nd	17.1	22.0	18.4	23.9	25.0	23.6	42	59.3	0.44
Dy/Yb	2.59	3.3	3.2	2.8	3.0	2.2	1.5	0.10[e]	1.95
La/Sm	3.7	4.3	3.8	3.0	3.2	2.3	3.45	5.86	5.25
La/Y	1.28	1.3	1.1	0.77	0.86	0.43	0.67	0.50[f]	1.05

a Average ocean island basalt (Sun and McDonough, 1988)
b Average island arc basalt (Sun, 1980).
c PAWMS (a pelagic sediment composite for the western Pacific, from Hole et al., 1984).
d Average pelagic clay (Taylor and McClennan, 1985).
e Dy/Yb value estimated assuming $Dy_{CN} = Tb_{CN}$.
f La/Y estimated assuming $Y_{CN} = Yb_{CN}$.

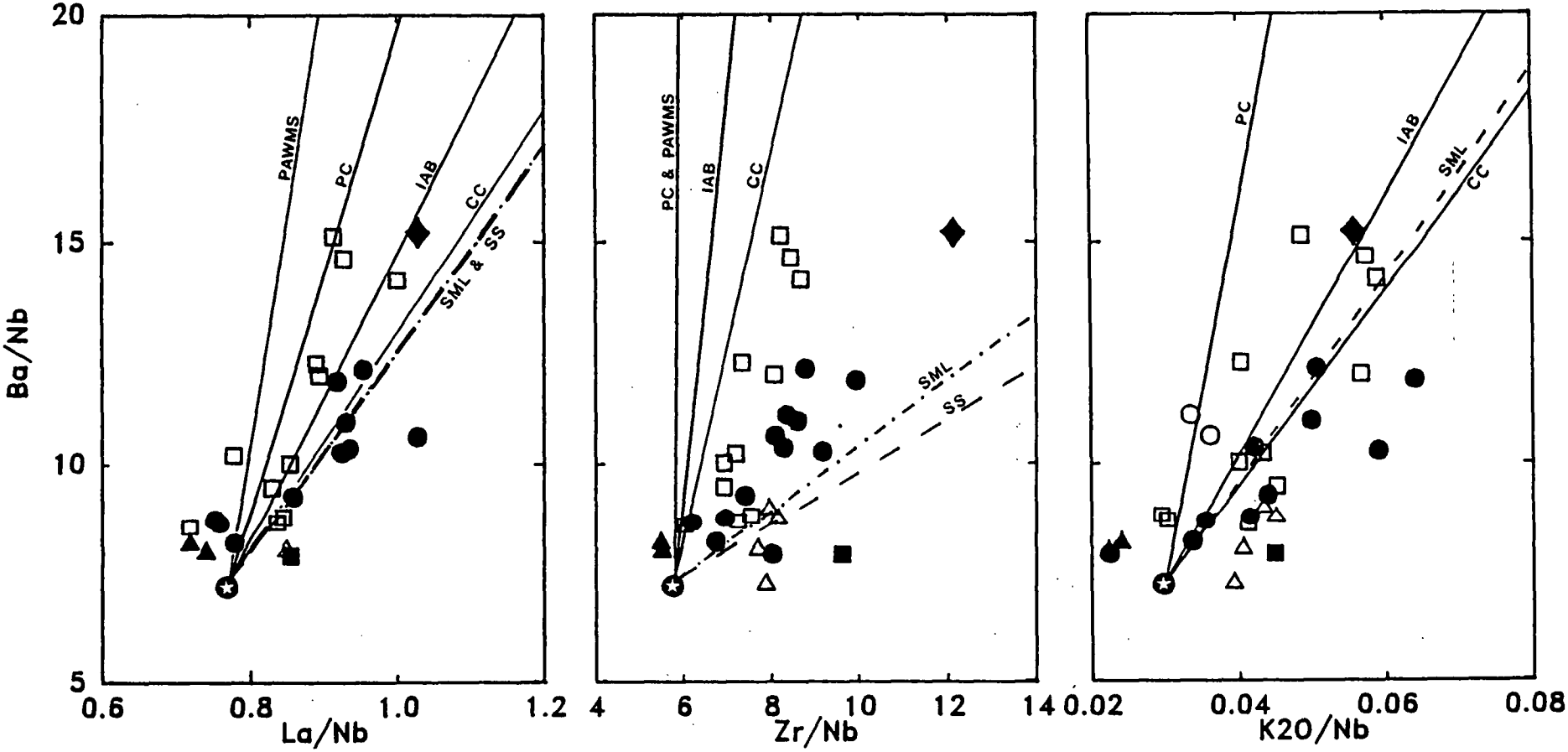
Ba/Nb
20
15
10
5
PAWMS
PC
IAB
CC
SML & SS
0.6
0.8
1.0
1.2
La/Nb
PC & PAWMS
IAB
CC
SML
SS
4
6
8
10
12
14
Zr/Nb
PC
IAB
SML
CC
0.02
0.04
0.06
0.08
K2O/Nb

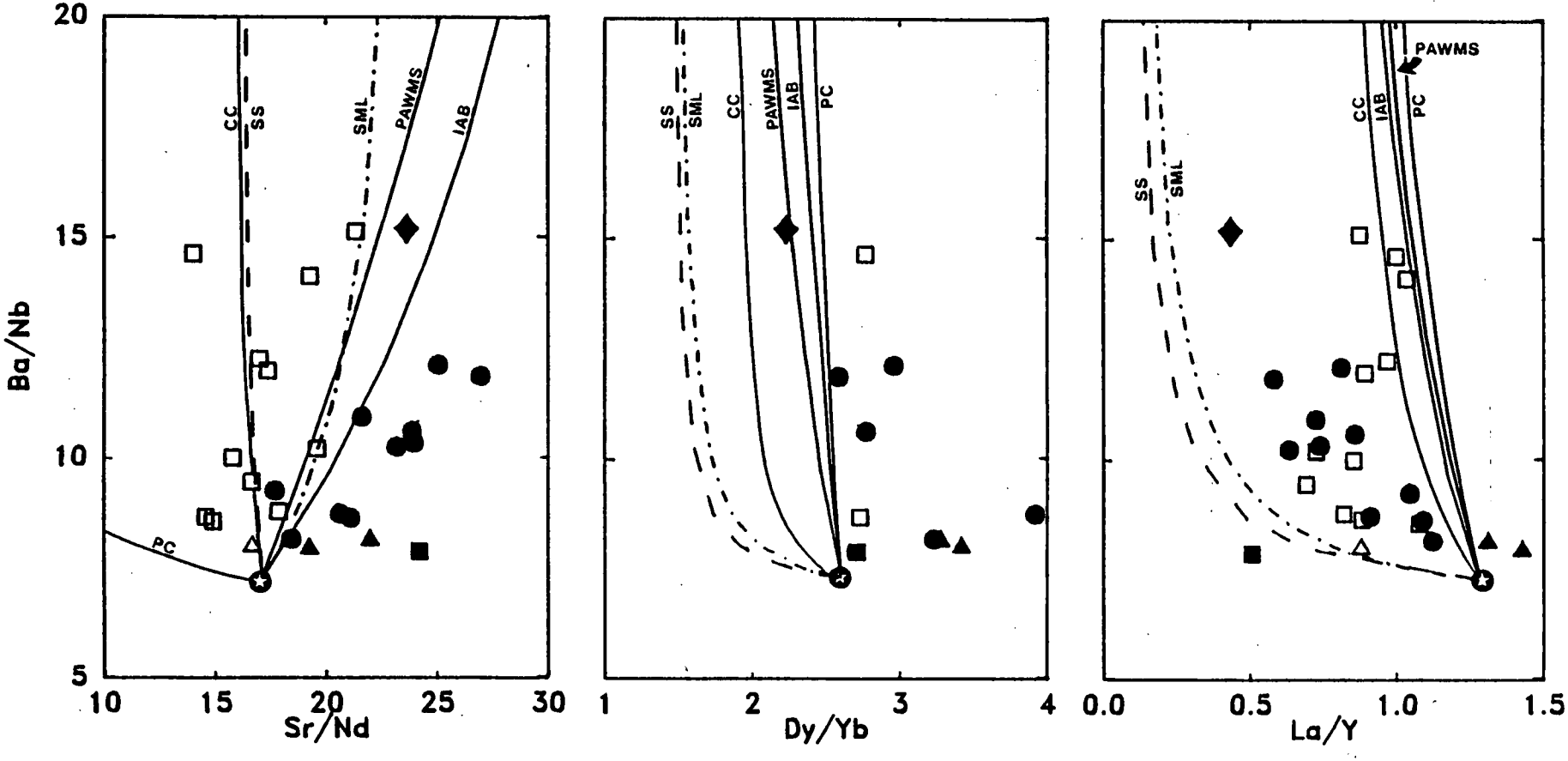

Figure 1.11 Covariation between selected incompatible trace element ratios (La/Nb, K/Nb, Zr/Nb, Sr/Nd, Dy/Yb, and La/Y) and increasing Ba/Nb values in Tasmantid basalts. Solid lines illustrate mixing systematics between an OIB source estimate (circled star) and possible high Ba/Nb source components (PAWMS, Pelagic clay [PC], island arc basalt [IAB], and continental crust [CC]). Dashed lines show additional mixing systematics for addition of subducted ocean crust (SS) and subduction modified lithosphere (SML) compositions to the OIB source estimate (see text and Fig. 1.13 for details). Symbols as for Figure 1.3.

1986; Duncan et al., 1984; Hawkesworth et al., 1987), and also some East Australian Cenozoic basalts (Ewart et al., 1988; see Fig. 1.12). The OIB which possess high Ba/Nb values (e.g. Gough, Tristan da Cunha, and Walvis Ridge basalts) are notable for their low $^{87}Sr/^{86}Sr$ at low $^{143}Nd/^{144}Nd$ values, and high $^{208}Pb/^{204}Pb$ and $^{207}Pb/^{204}Pb$ at equivalent $^{206}Pb/^{204}Pb$ values compared to other OIB (Hawkesworth et al.,1987; Hart et al.,1986). These features are characteristic of the distinctive EM1 mantle reservoir designated by Zindler and Hart (1986). The Sr and Nd isotope values of the Tasmantid tholeiites clearly support a common genetic link with other high Ba/Nb (EM1) OIB.

The mantle sources of high Ba/Nb OIB have been ascribed a variety of origins, including partial modification of primitive mantle (Hart et al., 1986), subduction-related enrichment of a sub-continental lithospheric source (Ewart et al., 1988), source contamination by pelagic sediment (Weaver et al.,1986; Richardson et al., 1982; Hawkesworth et al., 1987), and also crustal contamination (Ewart et al., 1988). In particular, Weaver et al. (1986) have presented a strongly argued case for the incorporation of ancient pelagic sediments into the mantle sources of the South Atlantic OIB. The timing and physical processes postulated for the evolution of these source geochemical and isotopic characteristics vary,from ancient sediment incorporation via subduction into the deep mantle (Weaver et al., 1986), to delamination of old geochemically-enriched lithosphere into the deep mantle, or similarly, the dispersion of old continental lithosphere into the convecting mantle during continental breakup events (Hawkesworth et al., 1986).

1.7.3 Possible Mixing Origins for Tasmantid Geochemical Variability

The geochemical variations illustrated in Fig. 1.11 are broadly consistent with the mixing of two discrete geochemical components: (1) a low Ba/Nb end-member with trace element characteristics like average OIB, and (2) a high Ba/Nb end-member with geochemical and isotopic characteristics similar to some DUPAL OIB. From the illustrated geochemical sytematics, the high Ba/Nb end-member is constrained to have high LREE/Nb (La/Nb>1), LILE/Nb (K/Nb>500), Zr/Nb (>12), and Sr/Nd values (>25); and low Dy/Yb (<2.2), La/Sm(<2.3) and La/Y values (<0.5). These characteristics are common only to island arc basalts and some pelagic carbonate-bearing sediment compositions (see Table 1.4), though many, but not all of these features, are also shared with pelagic clays,

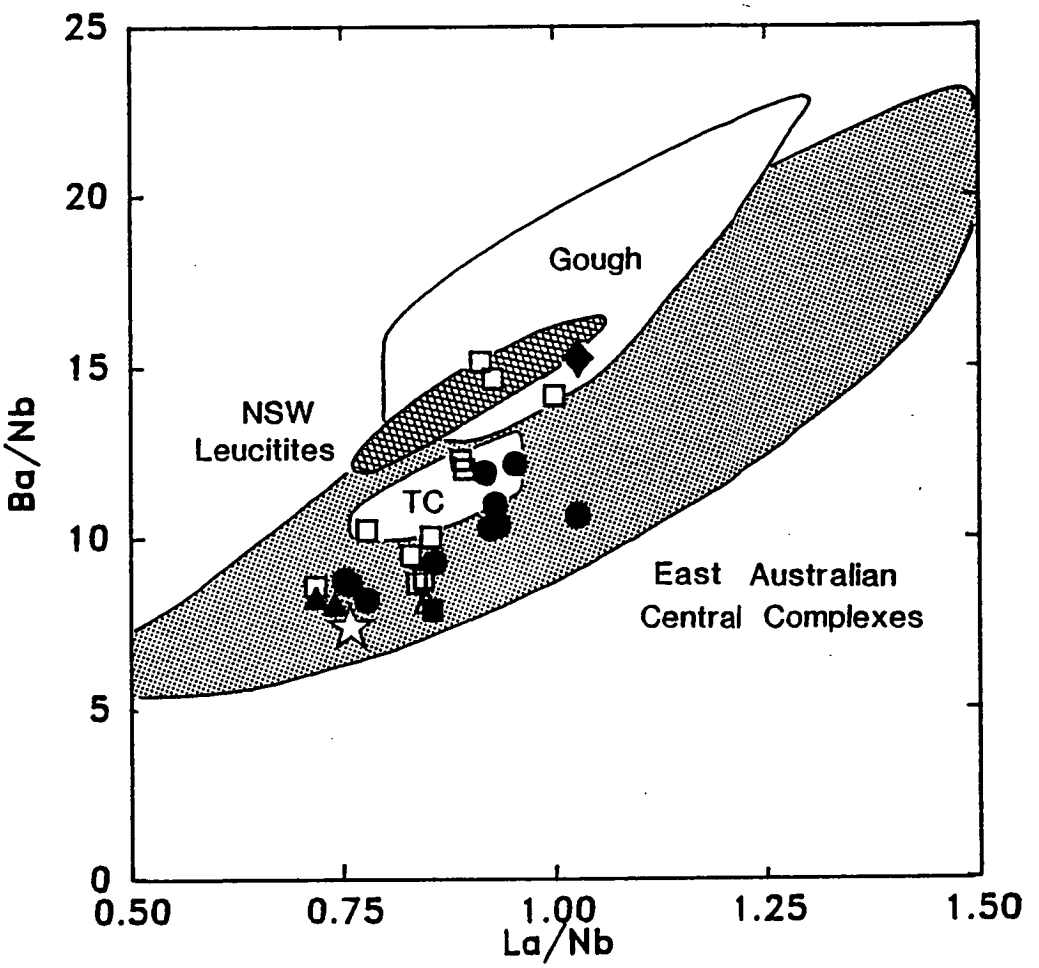

Figure 1.12 Ba/Nb versus La/Nb variation in Tasmantid basalts, and a comparison with other high Ba/Nb intraplate basalts from Gough, Tristan da Cunha (TC), New South Wales leucitites, and east Australian central complexes (data fields from Weaver et al., 1986; and Ewart et al., 1988). Large 5-point star is the composition of average OIB (Sun and McDonough, 1988). Symbols as for Figure 1.3.

sub-continental lithosphere, and the continental crust. Importantly, the high Ba/Nb end-member also must have radiogenic Sr ($^{87}Sr/^{86}Sr > 0.7047$) and non-radiogenic Nd isotopic values ($\varepsilon Nd < -3$).

In order to gain insight into the origin of the high Ba/Nb geochemistry in the Tasmantid basalts, a series of experiments modelling the addition of possible high Ba/Nb contaminants to an OIB source composition have been performed. The admixed contaminants used in these experiments include estimates for the compositions of average pelagic clay and continental crust from Taylor and McLennan (1985), an average island arc basalt from Sun (1980), and PAWMS, a pelagic carbonate-bearing sediment composite compiled by Hole et al. (1984). An estimate for the OIB source end-member has been obtained by assuming the average OIB composition of Sun and McDonough (1988) is generated by 5% partial melting, with all incompatible elements behaving in a highly incompatible manner (i.e. according to equation 1.1).

Only the addition of IAB, and possibly also PAWMS, are consistent with the sense of incompatible element variation occurring in the Tasmantid basalts (see Fig. 1.11). The IAB addition model generally provides the closest solution to the observed geochemical systematics, however, the mixing lines for both this, and the other contaminants, are considerably steeper than the natural trends. This inconsistency could result from the unsuitable nature of the "average" compositions modelled, where regional or individual IAB, sediment, crustal compositions, or a more appropriate OIB source composition,may be more suited to reproduction of the natural data trends.

In an attempt to produce more realistic models for the mixing of plausible mantle source reservoirs, an additional set of experiments have been performed using analogues for subducted ocean crust (SS = N-MORB + PAWMS) and subduction modified lithosphere (SML = MORB source +IAB), both of which have featured in previous hypotheses for the origin of high Ba/Nb OIB sources. To obtain estimates of these "hybrid" high Ba/Nb source components, the equations for mixing between N-MORB (from Sun and McDonough, 1988) and sediment (i.e. PAWMS), and between N-MORB source (from Wood, 1979) and IAB, have been solved simultaneously with the regression line describing Ba/Nb versus La/Nb variation in the Tasmantid primitive basalts i.e.

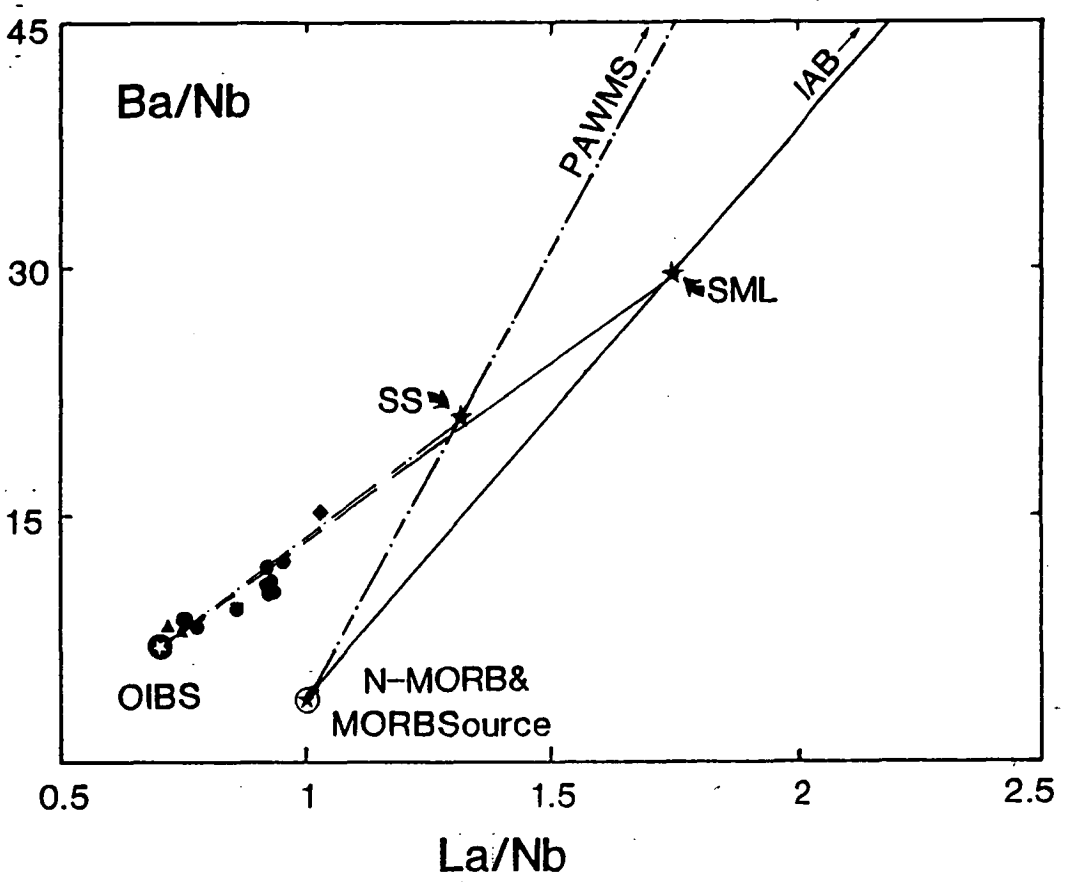

Figure 1.13 A schematic template, based on Ba/Nb versus La/Nb covariation, illustrating the methodology used to estimate subducted ocean crust (SS) and subduction modified lithosphere (SML) compositions. The proportions of N-MORB and pelagic sediment (PAWMS), or N-MORB source and island arc basalt (IAB), which comprise SS and SML compositions, are defined simply where intersection of the natural data trend occurs with the mixing lines between the individual SML and SS components.

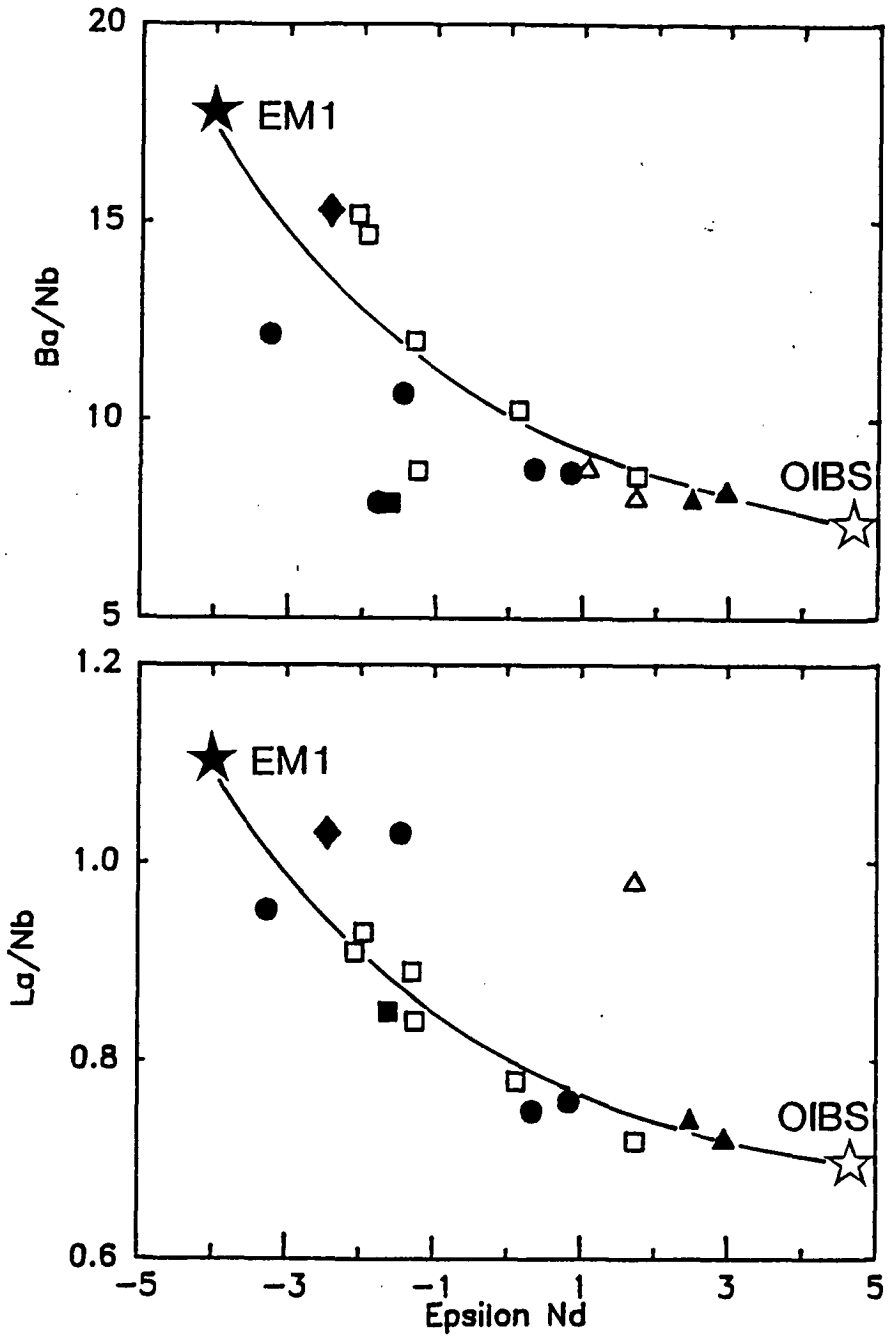

Figure 1.14 Covariation between both Ba/Nb and La/Nb, and Nd isotope values in the Tasmantid basalts. OIBS and EM1 indicate approximate compositions of OIB source and high Ba/Nb mantle source components, and curves illustrate trends for mixing between these components if EM1 has Nd/Nb greater than OIB source. The match occurring between the mixing lines illustrated and the natural data trends, provides support for a mantle source mixing origin for the geochemical variation occurring in the Tasmantid basalts.

$$Ba/Nb = 21.3La/Nb - 7.7 \quad (1.2)$$

This methodology is illustrated schematically in Figure 1.13. The mixing trends for addition of the resultant SML (97% N-MORB source + 3% IAB) and SS (96.6% N-MORB + 3.4% PAWMS) compositions to the OIB source are shown as dashed lines in Figure 1.11. It is worth pointing out that these particular mixing lines will also approximate magma mixing between partial melts derived separately from high Ba/Nb and low Ba/Nb mantle sources.

The SML mixing model forms a reasonably successful match to the natural data (see Fig. 1.11). If an OIB source composition more appropriate for the low Ba/Nb end-member (i.e. with La/Nb~0.7, Zr/Nb~5, Dy/Yb~3.5, and La/Y~1.5) were substituted into the mixing models, then even closer agreement would result. Unfortunately, the poorly constrained nature of the modelled source components does not facilitate any objective selection of a "best" model. It is clear, however, that average continental crust and pelagic clay compositions are unsuitable source components due to their inability to enrich Sr over LREE.

1.7.4 Isotopic Constraints on Mixing Models

The systematic variation in Nd isotope values accompanying variation in Ba/Nb and La/Nb ratio values (Fig. 1.14), facilitates the estimation of Nd isotope values and Nd model ages for the high Ba/Nb contaminant using appropriate trace element mixing constraints. For example, consider mixing between the OIB source and a high Ba/Nb contaminant (e.g. SML) to produce the variation in Ba/Nb and εNd values observed in the Tasmantid basalts i.e.

$$R_{Tas} = \frac{[(1-x).i_{OIBS}.R_{OIBS} + x.i_{HBa}.R_{HB}\ ]}{[(1-x).i_{OIBS} + x.i_{HB}\ ]} \quad (1.3)$$

where R = isotope or trace element ratio value (Ba/Nb or εNd),

i = trace element abundance of the numerator of R (i.e. Nb or Nd),

x = mass fraction of the high Ba/Nb contaminant added to the OIB source

and OIBS, HB and Tas are subscripts referring to the OIB source, the Tasmantid basalts, and the high Ba/Nb source component/contaminant.

Rearrangement and combination of solutions for εNd and Ba/Nb from (1.3) gives

$$\varepsilon Nd_{HB} = \frac{[(1-x).Nd_{OIBS}+x.Nd_{HB}].\varepsilon Nd_{Tas}-(1-x).Nd_{HB}.\varepsilon Nd_{OIBS}}{x.Nd_{HB}} \quad (1.4)$$

where $$x = \frac{Nb_{OIBS}.(Ba/Nb_{OIBS}-Ba/Nb_{Tas})}{[Ba/Nb_{Tas}.(Nb_{HB}-Nb_{OIBS})+Ba/Nb_{OIBS}.Nb_{OIBS}-Ba/Nb_{HB}.Nb_{HB}]} \quad (1.4a)$$

which may be solved by furnishing an estimate for εNd_{OIBS}, and by substituting appropriate trace element abundance values for the OIB source, high Ba/Nb source component/contaminant, and individual Tasmantid basalts (ideally those which have the highest Ba/Nb values). Results for each of the previously proposed high Ba/Nb source components, based on the Britannia tholeiite (sample #68644) which has an εNd value of ~-2.5 (McCulloch, 1988), and assuming the low Ba/Nb OIB source has εNd ~+5, are listed in Table 1.5. In addition, Nd model ages have been determined for each of the high Ba/Nb contaminants using modelled Sm/Nd values of the respective high Ba/Nb contaminants. For SML and SS source components, an additional set of model Nd ages have also been calculated, based on the assumption that these high Ba/Nb contaminants have formed recently. In these cases, the model Nd ages are calculated specifically for the IAB and PAWMS components (results in parentheses in Table 1.4), by assuming an εNd value of +10 for the N-MORB source and N-MORB components.

Strikingly old model Nd ages, and very low εNd values, are obtained for each of the modelled high Ba/Nb source components. Though a guide only, these results indicate an ancient origin for the high Ba/Nb geochemical component. In contrast, for the OIB source a depleted mantle model Nd age (i.e. T_{DM}) of only ~420Ma is calculated.

If mixing of low and high Ba/Nb mantle sources has occurred recently (i.e. during magmagenesis), the results obtained for the pelagic sediment models preclude contamination by modern examples of these sediments, which do not attain such low εNd values (i.e. εNd <-40). Likewise, the option of recent formation of SML and SS source components requires contributions from high Ba/Nb contaminants with even more extreme, and therefore unlikely, isotopic compositions.

Even though few firm constraints can be placed on the genesis of the high Ba/Nb geochemistry, Nd model ages imply that it derives from a long-lived geochemically-enriched source. This is an important result, for it probably mitigates against addition of

Table 1.5. Nd isotope values and model ages for hypothetical high Ba/Nb contaminants of an OIB source estimate.

High Ba/Nb Contaminant	x[a]	Sm/Nd_{HB}	εNd	T_{DM}	T_{CHUR}
IAB	6.5	0.220	-18	2.6Ga	2.2Ga
PAWMS	1.4	0.228	-54	6.2Ga	7Ga
Pelagic clay	0.9	0.195	-40	3.9Ga	3.9Ga
Continental Crust	0.184	0.219	-6	1.5Ga	0.8Ga
SML (Subduction Modified Lithosphere)	80	0.322	-5.4	5.4Ga	21Ga
	---	(0.22)[b]	(-38)	(44Ga)	(4.6Ga)
SS (Subducted Ocean Crust)	53	0.349	-4.1	18Ga	---
	---	(0.228)	(-2.5)	(16Ga)	(19Ga)
OIB Source	0	0.204	~+5	~0.4Ga	---

a x = mass fraction of high Ba/Nb contaminant added to OIB source to generate Ba/Nb value of sample 68644 (i.e. ~15)

b Values in parentheses are results for sediment and IAB components of SML and SS composite sources, assuming their formation immediately prior to generation of the Tasmantid Seamounts (N-MORB and N-MORB-source components assumed to have $\varepsilon Nd = +10$ at time of formation).

$T_{DM} = \lambda Sm^{-1}.\ln[1 + (0.511836(\varepsilon Nd_{HB}/10000 + 1) - 0.51235)/(0.605.Sm/Nd_{HB} - 0.217)]$

$T_{CHUR} = \lambda Sm^{-1}.\ln[1 + (0.511836(\varepsilon Nd_{HB}/10000))/(0.605.(Sm/Nd)_{HB} - 0.1967)]$

Mesozoic or younger carbonate-bearing pelagic sediments (e.g. PAWMS) as an explanation for the unusual high Ba/Nb geochemistry in the Tasmantid basalts.

1.7.5 The Origin of OIB Source Characteristics

The elevated incompatible element abundances and fractionated REE patterns (i.e. middle $REE/HREE_{CN}$ >1) of the low Ba/Nb basalts could be interpreted to result from small degrees of melting, in the presence of garnet, of an upper mantle source with an unfractionated REE pattern (i.e. middle $REE/HREE_{CN}$ = 1). This possibility may be accomodated within a framework of high pressure melting (i.e >~2.5GPa) for the generation of the alkali-olivine basalts. This option, however, is inconsistent with the development of similar geochemical features in the shallowly-derived tholeiites, unless tholeiite magmagenesis also involves mixing with deeply-derived (garnet-equilibrated) melt fractions. Alternatively, these geochemical characteristics can be considered to derive from mixing of mantle sources, as modelled above, where the low Ba/Nb (OIB) source is geochemically-enriched and has chondrite-normalised middle REE/HREE (e.g. Dy/Yb_{CN}) values >1.

In effect, these possibilities reduce to the problem of whether intraplate magma chemistry reflects shallow melting of incompatible element-rich sources, or deeper garnet-present melting of more geochemically-depleted (MORB-like?) mantle sources.

Recent workers have tended to compromise these two possibilites by invoking dynamic partial melting processes. In these models, primary mantle melts are viewed as comprising an integration of melt fractions deriving from throughout the partially molten mantle source volume. Incompatible element-rich melt fractions, generated in the presence of garnet at depth, are envisaged to mix with more shallowly-derived melt fractions, to impart their geochemical characteristics onto otherwise apparently low pressure melt bulk compositions, which are determined by equilibration with peridotite at shallow levels. This proposal, however, is largely unfounded for it can be demonstrated through modelling of dynamic melting trace element behaviour that residual garnet geochemical signatures (i.e. Dy/Yb_{CN} >1) are unlikely to develop in primary melts comprising melt fractions generated outside the stability field of residual garnet (see Chapter 3). It also is unlikely that the systematic geochemical variation documented in the

Tasmantid basalts (Fig. 1.11) could be attributed to chance mixing with garnet-equilibrated melts. In view of these considerations, and the compelling evidence for shallow generation of the Tasmantid basalts, the residual garnet geochemical signatures occurring in the Tasmantid basalts are best interpreted to result from mixing of two mantle sources, with one (OIB mantle source) providing the geochemical enrichments characteristic of residual garnet.

Earlier workers who have emphasised the control of source composition on intraplate magma geochemistry (e.g. Frey et al., 1978; Green, 1970; Wright, 1984), have argued for geochemical enrichment of lithospheric sources through addition of incompatible element-rich, silica-undersaturated liquids (and fluids) migrating from the underlying asthenosphere. This proposal can be shown to be consistent with high PT peridotite-C-H-O phase equilibria (see Chapter 4), and also interpretations of the Low Velocity Zone as a region of incipient melting in the shallow oceanic asthenosphere (e.g. Green and Lieberman, 1976). The young Nd model age obtained for the modelled Tasmantid OIB mantle source is in accordance with this proposal requiring enrichment of the Tasmantid oceanic lithosphere since its formation (between 75 and 53Ma; Weissel and Hayes, 1977) and prior to Tasmantid magmagenesis.

1.8 A MODEL FOR THE PETROGENESIS OF THE TASMANTID SEAMOUNTS

The basis of this model recognizes two discrete mantle sources contributing to the Tasmantid Seamount's geochemistry. One source is characterised by typical OIB-type geochemistry found in alkali-olivine basalts, and the other by a series of geochemical enrichments associated with the trend toward anomalously high Ba/Nb ratios in the tholeiitic basalts. Combined geochemical and isotopic data are consistent with the OIB source component being young "metasomatically enriched" oceanic lithosphere, whereas the high Ba/Nb component is a distinct mantle source characterised by an ancient geochemical enrichment. I propose the high Ba/Nb component is sourced in asthenosphere-derived diapirs, as this would be consistent with higher degrees of melting and liquidus temperatures for the generation of tholeiites compared to alkali-olivine basalts, and their corresponding adiabatic-derivation from deeper mantle levels. Mixing of

the two sources is probably effected during migration of deep hotspot-initiated diapirs into the over-riding lithosphere. General elements of this model are similar to those proposed by Chen and Frey (1983) and McDonough et al. (1985). In this framework, the diapir cores undergo the largest degrees of melting as they decompress to shallow levels, and generate tholeiitic melts. Toward the diapir margins, greater relative interaction occurs with geochemically-enriched oceanic lithosphere results in cooler temperatures, smaller degrees of melting, and the generation of alkali-olivine basalts.

Interpretation of experimental studies which have modelled the interaction of hot rising diapirs with overlying cool lithosphere (Griffiths, 1986), indicates that lithospheric material is most likely to contribute to magmagenesis during the early and late stages of a diapir's interaction. This may explain the the temporal distribution of alkaline volcanism at individual Hawaiian volcanoes, and also the partial capping of the Tasmantid seamounts by alkaline basalts, if in both cases these magmas are derived mainly from an oceanic lithosphere source.

Residence of the high Ba/Nb component in the asthenosphere beneath the Tasman Sea could be related to dispersion of old eastern Australian lithosphere into the convecting mantle during craton rifting and opening of the Tasman Sea. Alternatively, discrete long-lived mantle reservoirs (e.g. delaminated sub continental lithosphere) may be incorporated into, or may even form, the deeply-sourced diapirs.

1.9 IMPLICATIONS FOR EAST AUSTRALIAN CENOZOIC VOLCANISM

Migrating hotspot trails that are contemporaneous with, and parallel to, the Tasmantid Seamounts (McDougall and Duncan, 1988) are a feature of the extensive East Australian Volcanic Province. These have been identified principally on the basis of progressive northward ageing of central volcano complexes (Wellman and McDougall, 1974). This greater region of volcanic activity, however, also comprises additional lava field subprovinces which are of less certain affinity to the hotspot trails.

The mafic lavas which dominate the East Australian Province span a complete compositional spectrum from leucitites, melilitites, and nephelinites, through to olivine tholeiites and quartz tholeiites. Samples representative of the central volcano complexes

(i.e. the focus of hotspot magmatic activity), however, tend to be less variable in composition (comprising hawaiites, transitional, and tholeiitic basalts), less primitive, and generally more silica saturated than the lava field basalts (Ewart et al., 1988).

Trace element and isotopic studies have documented distinctive high Ba/Nb and EM1 mantle source characteristics (see Figs. 1.9 and 1.12), particularly among the central volcano complexes. These closely match those found for the Tasmantid Seamounts. Ewart et al. (1988) attribute these particular characteristics to AFC processes (crustal contamination) during magma ascent, or alternatively, a mantle source involving subduction-modified east Australian subcontinental mantle. Considering the obvious similarities between the Tasmantid and East Australian magma source geochemistries, it may be warranted to redress the origin of these geochemical and isotopic enrichments in terms of a common deep asthenospheric source. On the other hand, if Ewart et al. (1988) are correct in their assertion that the high Ba/Nb characteristics are derived from the east Australian continental lithosphere or crust, then such material is likely to have been incorporated into the convecting upper mantle during rifting of the Tasman Sea.

1.10 CONCLUSIONS

1. The suite of primitive basalts recovered from the Tasmantid Seamounts span a compositional range from tholeiitic, through transitional, to alkali-olivine basalts. Major and trace element geochemistry, and mineral chemistry, support a near primary/primary origin for these compositions. Estimated conditions of melt generation based on peridotite melting experiments, range between 0.8 and ~2.5 GPa.

2. Garnet is not an equilibrium phase at the pressures and temperatures of melt segregation determined for the Tasmantid basalts. This requires geochemical traits nominally attributed to melting in the presence of garnet to be source inherited.

3. Geochemical and isotopic sytematics indicate that mixing of two distinct mantle sources dominates the Tasmantid basalt geochemistry.

a. One source component closely matches the geochemical character of average OIB, and is found largely in the alkaline-olivine basalts. It is proposed that this component is oceanic lithosphere enriched in incompatible elements by small garnet-equilibrated melt fractions migrating from the underlying Low Velocity Zone.

b. The other mantle source is dominated by geochemical characteristics similar to island arc basalts (or island arc source regions) and some modern, carbonate-bearing, pelagic sediments (e.g. PAWMS). Available geochemical and isotopic evidence point to a close link with other OIB which possess similar,unusually high,Ba/Nb values and EM1 mantle reservoir isotope characteristics. Estimated εNd values and model Nd age calculations, determined for various high Ba/Nb component source contamination models, favour an ancient origin for the development of this particular source component, and probably rule out mantle contamination by modern pelagic (carbonate-bearing) sediments such as PAWMS.

4. A mantle source mixing model is consistent with the migration of deeply-derived diapirs and into the overlying oceanic lithosphere. The diapir cores undergo the largest degrees of melting as they decompress to shallow levels, to generate tholeiitic melts. Toward the diapir margins greater interaction occurs with geochemically-enriched oceanic lithosphere, resulting in cooler temperatures, smaller degrees of melting, and the generation of alkali-olivine basalts.

CHAPTER 2

Petrogenesis of Hawaiian Tholeiites - Phase Equilibria Constraints

2.1 INTRODUCTION

Hawaiian and other hotspot-related volcanism is notable for a trace element fingerprint that implies the presence of residual garnet during partial melting. Garnet-present melting models form the basis of recent syntheses of Hawaiian magmagenesis by Feigenson (1986), Frey and Roden (1987), and Wyllie (1988), which find support in the many previous studies that have concluded melting occurs within the garnet peridotite stability field (e.g. Hofmann et al., 1984; Budahn and Schmitt, 1984). In so doing, Hawaiian magmas are perceived to originate at deep levels beneath the lithosphere, from which independence of the magma source is implied by the "fixed" nature of hotspot volcanism within the framework of plate tectonics, as was initially proposed by Wilson (1963).

High pressure phase equilibria studies of Hawaiian primary melt composition estimates, however, provide evidence for relatively shallow (<1.7 GPa) melt segregation leaving residual harzburgite (Green and Ringwood, 1967a; Green, 1970). The conclusions of the phase equilibria approach and the trace element geochemical modelling are mutually exclusive, and have not been reconciled in any of the recent syntheses. New experimental data are obtained in this study to re-evaluate the importance of phase equilibria constraints on Hawaiian magmatism. Whether melting occurs at deep (garnet-present) levels or shallow levels (Ol+Opx+Cpx residues) is likely to have profound implications for Hawaiian source geochemistry and also the origin of magmatism. Herein,solutions are considered within a framework of simple equilibrium melting, whereas Chapter 3 pursues the problem through alternative models based on recently advocated dynamic melting processes (e.g. McKenzie, 1984; Ribe, 1988; McKenzie and Bickle, 1988).

2.2 HAWAIIAN PRIMARY MELT COMPOSITIONS

Hawaiian tholeiites have retained remarkable compositional uniformity through time since formation of the older Emperor Seamounts (>60Ma; e.g. Dalrymple et al., 1980) until the present (Wright, 1984; Frey and Roden, 1987). This obviously requires more or less constant conditions of melting and source compositions throughout this period. Most attention, however, has focused on the more subtle second-order trace element and isotopic variations observed between and within individual volcanoes. These secondary characteristics have been attributed largely to systematic variation in degrees of melting, occurring with passage of the magma source beneath the lithosphere, and to fluctutations in the contributions from discrete mantle source components,characterised by varying degrees and histories of relative incompatible element enrichments (e.g. Chen and Frey, 1985; Clague and Frey, 1982; Lanphere and Frey, 1987; Frey and Clague, 1983; Hofmann et al., 1987).

Experimental phase equilibria studies are capable of testing the pressure of origin of basaltic liquids if accurate estimates for primary compositions are available. In the case of Hawaiian tholeiites, these vary widely from a 7 wt% MgO low quoted by Feigenson (1986), to compositions with >20 wt% MgO, as invoked by Wright (1984) and Budahn and Schmitt (1984). This range largely reflects the different criteria on which the estimates have been established, and their associated uncertainties. For example, some commonly used criteria, such as Ni content and $Mg^{\#}$ of primary magmas suitable for equilibrium with mantle olivine, even though widely accepted, are subject to imprecision due to uncertainties in element partitioning behaviour and variability in mantle source compositions.

Alternatively, evidence for primitive liquid compositions can be derived from magnesian olivine phenocrysts occurring in Hawaiian lavas. The melt compositions from which these olivines have crystallised may be estimated using the well established Fe/Mg distribution relationship between olivine and basaltic liquid (e.g. Roeder and Emslie, 1970; Ulmer, 1987). This requires correcting available primitive melt compositions (glass or aphyric whole-rocks) for the effects of olivine fractionation,which is known to dominate the geochemical evolution of primitive Hawaiian magmas (e.g Macdonald and Katsura,

1961; Gunn, 1971; Wright, 1971). Based on this rationale Wilkinson and Hensel (1988) have proposed primary liquids with 12 to 14 wt% MgO to match the most Mg-rich olivines they have observed ($Mg^{\#}$ 88 to 89). A comprehensive survey of Hawaiian olivine phenocrysts, however, reveals the occurrence of even more magnesian compositions with $Mg^{\#}$ up to 90.5 (Maaloe and Hansen, 1982; A. Sobolev, pers. comm., 1987; S.Eggins and D.H. Green, unpublished data). It is notable that these magnesian phenocrysts also have Ni concentrations equal to and exceeding those of olivine in mantle xenoliths, up to a maximum of ~0.60wt% NiO.

Clearly, at least some Hawaiian tholeiites have evolved from parent melts capable of crystallising the most Mg-rich olivine phenocryst compositions. An ideal method of reconstructing such primitive melt compositions is by adding small increments (e.g. 1% mass) of equilibrium olivine (i.e. $K_D^{Fe/Mg}{}_{Ol\text{-}Liq} = 0.30$; e.g Roeder and Emslie, 1970) to primitive liquid compositions until the olivine-fractionation-corrected bulk composition is in equilibrium with olivine of $Mg^{\#}$ 90.5. At each step, fO_2 constraints on Fe^{3+}/Fe^{2+} speciation may be calculated from bulk composition dependent expressions of the type developed by Sack et al. (1980), and Kilinc et al. (1983), by assuming a prevailing oxygen fugacity appropriate for crystallisation of Hawaiian magmas (i.e. QFM; Sack et al., 1980; Greenland, 1988), and by substituting liquidus temperature estimates also based on bulk compositional parameters (e.g. Ramsay et al. 1984).

2.3 PREVIOUS EXPERIMENTAL STUDIES

High pressure liquidus experiments on primitive Hawaiian lava compositions have been conducted previously by Green and Ringwood (1967a) and Green (1970). In most cases, the equilibrium peridotite phase assemblage found has been a harzburgite, occurring at a pressure of 1.0 GPa for an olivine basalt (12.37 wt% MgO), 1.2 GPa for an olivine tholeiite (14.55 wt% MgO), and pressures of 1.7 GPa and 2.2GPa for two picritic tholeiite compositions (~16.0 wt% MgO and 18.79 wt% MgO respectively, see Fig. 2.1). Clinopyroxene occurs usually as a subliquidus phase some tens of degrees below the harzburgite-saturated liquidus temperature. Garnet has been found as a liquidus phase only at pressures more than 1.0 GPa above (i.e.~30km deeper) the pressure of harzburgite

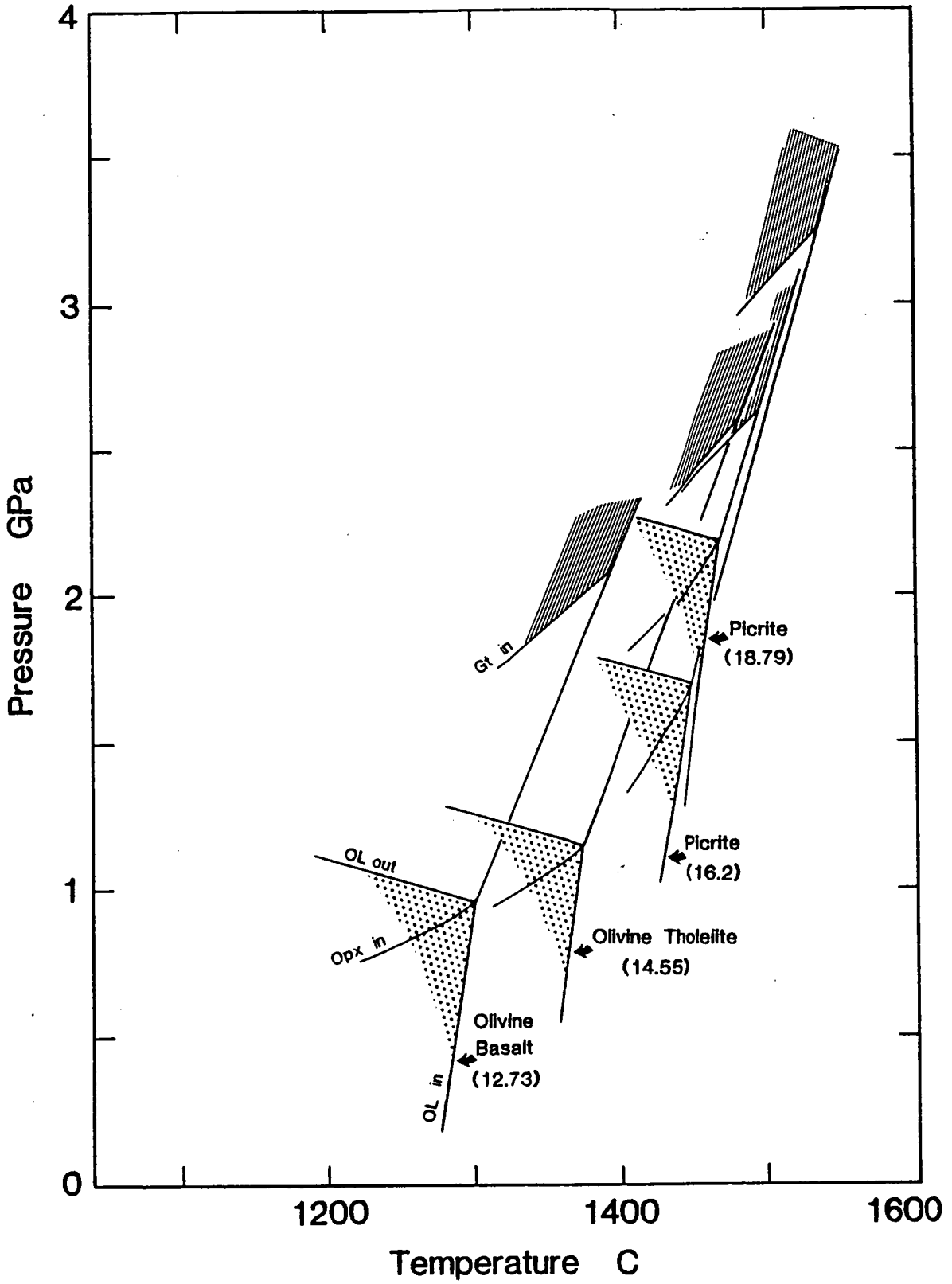

Figure 2.1 High PT phase relationships of experimentally-studied Hawaiian parent magma compositions (after Green and Ringwood, 1967a; and Green, 1970). Shown are the multiple phase (peridotite) saturation points, the garnet stability fields, and the high PT extent of the olivine phase volume. Numerals in parentheses denote the MgO content of the various parent magma compositions.

saturation, except for the most Mg-rich picrite where garnet occurs ~0.5 GPa above the multiple saturation point (Fig. 2.1). These phase relations clearly conflict with the trace element geochemistry-based claims for segregation of primary Hawaiian tholeiites from garnet peridotite residues.

Several observations concerning these early experiments dictate that caution be used in drawing precise interpretations from their results. The use of Pt capsules, for example, resulted in significant Fe-loss (~20-25%, Green and Ringwood, 1967a), a process known to stabilise orthopyroxene relative to olivine and shift the multiple saturation point (Ol+Opx+Liq) to lower pressure. Moreover, the bulk compositions chosen for study are not accurate representatives of primitive Hawaiian tholeiite compositions. They have been established mainly, from a Kilauea iki parent composition estimated by MacDonald and Katsura (1961), using olivine-addition calculations. When compared at similar MgO contents to more recent studies of both Kilauea Iki and averaged Hawaiian tholeiite compositions, they are found to be considerably enriched in CaO and Al_2O_3, and depleted in SiO_2, K_2O, and FeO^{tot} (see Table 2.1). These compositional differences could be expected to create significant changes in the high pressure phase equilibria. For example, the high alumina and calcium contents of the olivine tholeiite and picrite compositions are likely to enlarge the stability field of garnet beyond that of more appropriate parent compositions, and the low SiO_2 contents may reduce the orthopyroxene field (possibly counteracting the Fe-loss effect). The phase relations presented by Green and Ringwood (1967a) and Green (1970) are therefore only broadly applicable to Hawaii. Their use in a predictive capacity, however, is supported as the phase relations determined by Green and Ringwood (1967a) and Green (1970) match those indicated by recent peridotite melting studies. Projection of the various, experimentally-studied, olivine tholeiite and picrite compositions onto the cotectic grids for melting of Hawaiian Pyrolite (Falloon et al., 1988), following the methodology of Green (1970) and Falloon and Green (1988) places these compositions on residual harzburgite cotectics at pressure ~0.5GPa above those established by the liquidus experimental studies. Like in the earlier liquidus studies, clinopyroxene is not a predicted liquidus phase and neither is garnet, which only occurs in the peridotite melting experiments at pressures >3.0 GPa (Fig. 2.2).

Table 2.1 A comparison of previously studied experimental compositions with Kilauea Iki and average Hawaiian tholeiite compositions.

	1 olivine basalt	2 olivine tholeiite	3 picrite	4 picrite	5 Macdonald & Katsura	6 Murata & Richter	7 Gunn	8 Maaloe
SiO_2	47.05	46.95	46.6	45.51	46.9	48.13	48.54	48.16
TiO_2	2.31	2.02	1.92	1.93	2.3	2.25	2.14	2.16
Al_2O_3	14.17	13.10	12.5	12.44	12.9	11.26	10.65	11.34
FeO^{tot}	11.0	10.99	10.9	9.5	11.5	11.58	11.37	11.61
MnO	0.16	0.15	0.15	0.15	0.18	0.16	0.17	
MgO	12.73	14.55	16.2	18.79	14.6	14.55	14.55	14.55
CaO	9.87	10.16	9.7	9.67	9.9	9.52	9.82	9.28
Na_2O	2.21	1.73	1.64	1.64	1.5	1.85	1.91	1.86
K_2O	0.44	0.08	0.08	0.08	0.40	0.45	0.45	0.39
P_2O_5		0.21	0.20	0.20	0.22	0.21	0.24	
Total	99.94	99.94	99.89	100.0	99.91	99.99	99.80	99.76

1. Olivine basalt (Green and Ringwood, 1967a).
2. Olivine tholeiite (Green and Ringwood, 1967a).
3. Picrite (Green, 1970); olivine tholeiite + 5% Fo90 olivine).
4. Picrite (Green and Ringwood, 1967a).
5. Kilauea Iki primary composition (MacDonald and Katsura, 1961).
6. Kilauea Iki composition with 14.55 wt% MgO (from regression data of Murata and Richter, 1966).
7. KI0051 (Gunn, 1971); fractionation corrected to 14.55 wt% MgO.
8. Hawaiian tholeiite with 14.55 wt% MgO (from regression data of Maaloe, 1979).

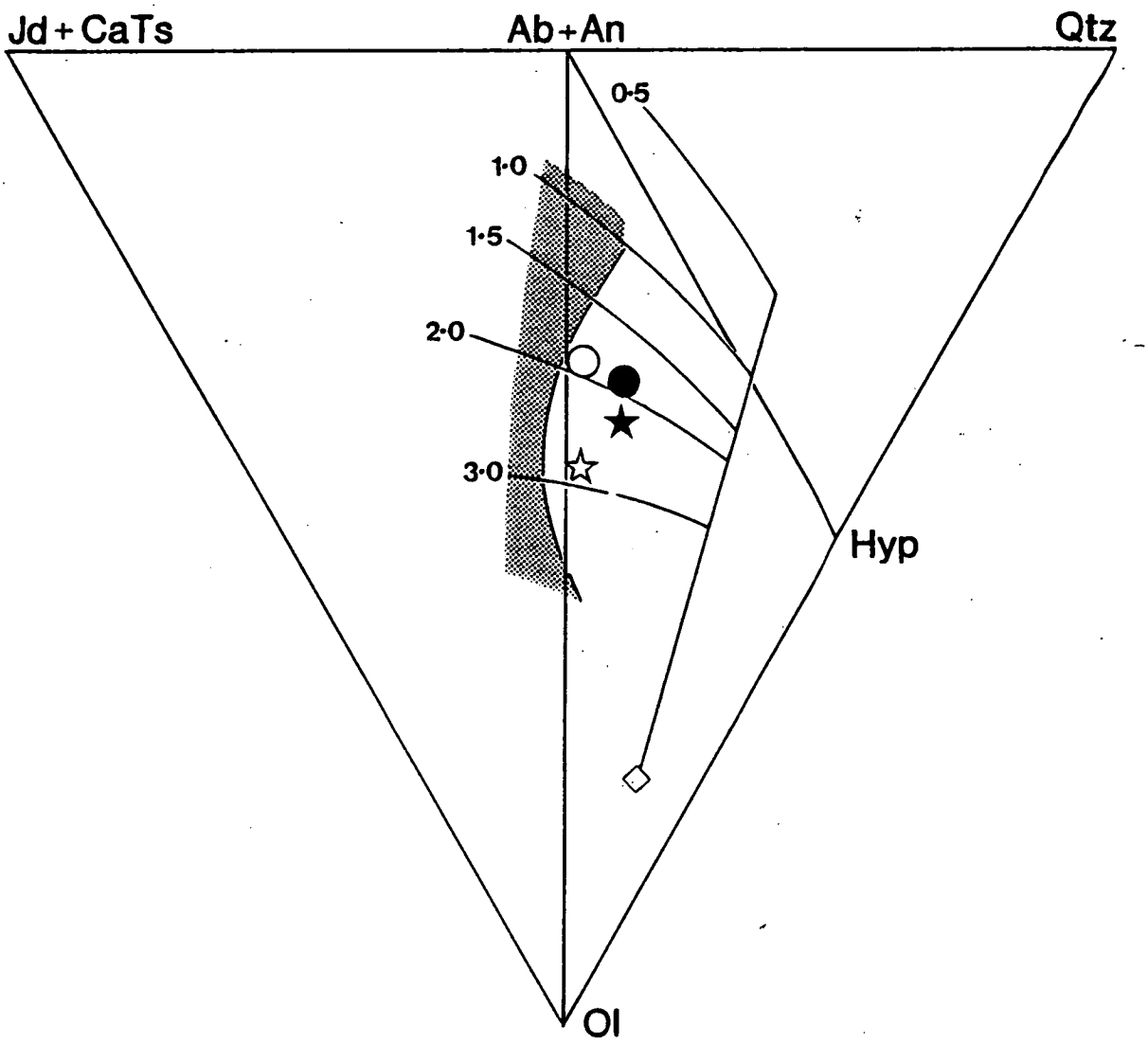

Figure 2.2 Projection of previously studied Hawaiian parent magma compositions (see Figure 2.1 and Table 1.1) onto the Ol-Jd+CaTs-Qtz cotectic grids for melting of "Hawaiian pyrolite" (after Falloon et al., 1988). Numerals in bold type indicate the pressure (in GPa) of the various cotectics. The stippled region outlines the field of compositions in equilibrium with lherzolite residua, and the cotectics labelled "Ol+Opx" indicate where melts are in equilibrium with harzburgite residues. Symbols used include; circle (olivine basalt), filled circle (olivine tholeiite), filled 5-point star (picrite; Green, 1970), and 5-point star (picrite; Green and Ringwood, 1967a).

2.4 NEW EXPERIMENTAL DATA FOR A KILAUEA IKI PRIMARY MELT ESTIMATE

An experimental study has been made using a new parent magma composition estimate to complement the existing experimental data. The composition chosen is parental to the Kilauea Iki eruption, which is a well documented example of olivine fractionation/accumulation controlled geochemical variation (e.g. Murata and Richter, 1966; Gunn, 1971), and possibly one of the most thoroughly studied volcanic events.

The parent magma composition has been calculated by adding percentage mass increments of equilibrium olivine to an olivine phenocryst-poor,low MgO (~9.5 wt% MgO) tholeiite (sample #KI0051; Gunn, 1971) until a bulk composition in equilibrium with olivine of $Mg^{\#}$ 90.5 was achieved. At each step an olivine-liquid $K_D^{Fe/Mg}$ value of 0.30 was applied (Roeder and Emslie, 1970), which is consistent with the maximum value observed for olivine in the Kilauea Iki eruptives (Fig. 2.3), and an Fe^{3+}/Fe^{2+} ratio of the bulk composition was determined for the QFM buffer using the expression of Kilinc et al. (1983).

The calculated Kilauea Iki parent magma composition is found to differ significantly from an equivalent composition calculated using the regression data for the Kilauea Iki eruption of Murata and Richter (1966). To hedge against an inappropriate composition, these estimates were averaged (see Table 2.2). NiO was then added for the purpose of future Ni partitioning experiments, and also a component equivalent to ~0.5 wt% chrome spinel to compensate for minor fractionation of that phase. Perhaps coincidentally, but important in terms of general application to Hawaiian tholeiite magmagenesis, the resultant composition matches closely that of an equivalently MgO-rich, "average", Hawaiian tholeiite calculated using the regression data of Maaloe (1979; see Table 2.2).

2.4.1 Experimental Technique

The Kilauea Iki parent composition was mixed from high purity oxides and carbonates, ground under acetone, and fired at 1000°C for 8 hours. Fayalite was added

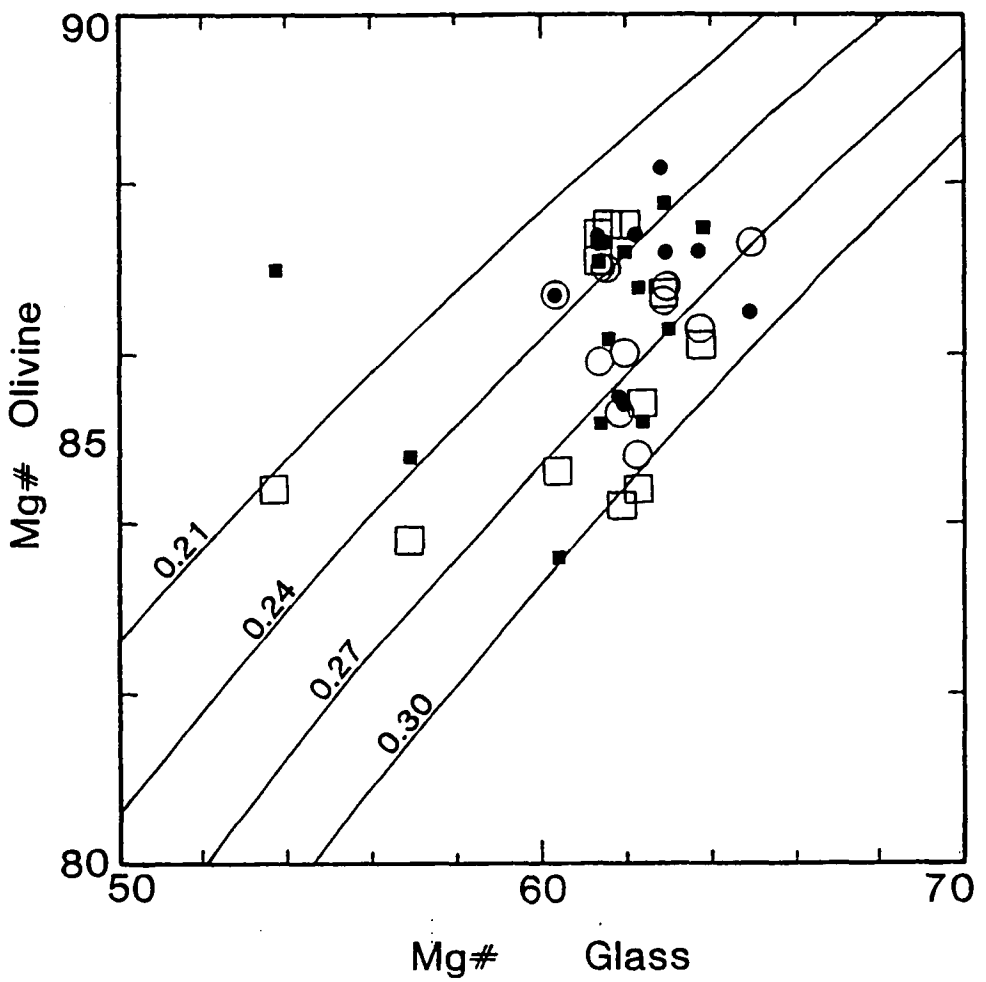

Figure 2.3 Relationships between the Mg# of natural glasses and the Mg# of olivine phenocrysts in Kilauea Iki lavas. Data points are average core (filled symbols) and rim (unfilled symbols) compositions of the Group 2 (circles) and Group 1, 3, 4, and 5 olivine phenocryst (squares) populations identified by Helz (1987). Fe^{2+} concentrations in the glasses have been calculated by the methods of Kilinc et al. (1983), at fO_2 values equivalent to the QFM oxygen buffer and temperatures measured at the eruption of the individual samples (see Helz, 1987). Labelled curves illustrate lines of equivalent $K_D^{Fe/Mg}{}_{Ol\text{-}Liq}$ values.

Table 2.2 Kilauea Iki parent melt estimate and comparative Hawaiian tholeiite compositions.

	1 KI0051 ($Mg^{\#}$=90.5)	2 M&R 16%MgO	3 average of 1&2	4 Maaloe 16% MgO	5 Starting comp.	6 Analysed glass
SiO_2	48.32	47.77	48.00	47.75	47.76	48.07
TiO_2	2.06	2.12	2.08	2.07	2.09	2.05
Al_2O_3	10.26	10.77	10.51	10.76	10.53	10.50
FeO^{tot}	11.33	11.64	11.49	11.69	11.61	11.33
MnO	0.14	0.15	0.15	0.17	0.15	0.15
MgO	15.97	16.03	16.0	16.0	15.98	16.27
CaO	9.46	9.15	9.31	8.96	9.26	9.31
Na_2O	1.84	1.75	1.80	1.76	1.79	1.72
K_2O	0.43	0.42	0.43	0.37	0.43	0.36
P_2O_5	0.20	0.19	0.20	0.23	0.20	0.26
NiO					0.10	
Cr_2O_3					0.13	
Total	100.01	99.99	99.97	99.76	100.03	100.02

1. Olivine-fractionation-corrected parent melt in equilibrium with $Mg^{\#}$ 90.5 olivine (based on sample #KI0051; Gunn, 1971).
2. Kilauea Iki composition at ~16 wt% MgO (from regression data of Murata and Richter, 1966).
3. Average of columns 1 and 2.
4. Hawaiian tholeiite composition at ~16 wt% MgO (Maaloe, 1979).
5. Kilauea Iki parent composition (Column 3 + 0.5 wt% chrome spinel + 0.10 wt% NiO).
6. Average electron microprobe analysis (n = 20) of Ir-strip-heater-prepared fused glass of the starting composition (column 5).

prior to regrinding and firing. The resultant starting mix is an anhydrous, CO_2-free, cryptocrystalline powder.

All experiments were performed in piston cylinder apparatus at the University of Tasmania. The piston-in technique was applied with a pressure correction of -10% of nominal load pressure, and temperature was controlled to within 7°C of the quoted run temperature using Pt/Pt90Rh10 thermocouples. Only graphite capsules were used during the course of these experiments, thus excluding Fe-loss/gain problems. As a consequence of the sample assembly used, fO_2 is constrained to fall on or below the GCO surface, which lies between 1 and 2 log units below the QFM oxygen buffer for most run conditions. The outer assembly consisted of a dehydrated talc/pyrex sleeve.

Phase equilibria were investigated over a pressure range from 1.0 to 3.5 GPa at above-solidus conditions. Each experimental charge was examined optically prior to electron microprobe analysis of all coexisting phases.

2.4.2 Experimental Results

Pertinent experimental details and equilibrium phase assemblages are provided in Table 2.3, and the chemistry of the coexisting phases is listed in Appendix 3. The construction of a liquidus phase diagram using these results (Fig. 2.4), illustrates that olivine is the liquidus phase to pressures near 2.0 GPa, where it is replaced at the multiple (peridotite) saturation point (~2.0 GPa, 1450°C) by orthopyroxene, which occupies a narrow liquidus field up to 2.5 GPa. Clinopyroxene, in turn, is the liquidus phase from 2.5 to ~3.5 GPa, where it is joined by garnet some 1.5 GPa above the peridotite saturation point. At pressures lower than the multiple saturation point (Ol+Opx+Liq), olivine occupies a progressively expanded liquidus field prior to co-saturation with orthopyroxene and clinopyroxene at lower temperature. Plagioclase is a near-solidus phase at ~ 1 GPa or less.

These phase relationships match closely those determined previously for the picritic bulk compositions studied by Green and Ringwood (1967a) and Green (1970; cf. Figs. 2.1 and 2.4), with only a minor shift of the multiple saturation point (Ol+Opx+Liq) occurring toward higher pressure. Importantly, the liquidus garnet field has also shifted to higher pressure, with a very large gap (~1.5GPa) occurring between the peridotite

Table 2.3. Experimental run conditions and phase equilibria.

Run no.	P (GPa)	Temp(C) (°C)	Time (mins)	Phase assemblage
T-2580	1.0	1200	120	ol+opx+cpx+plag+l
T-2578	"	1240	120	ol+opx+cpx+l
T-2350	"	1280	60	ol+opx+cpx+l
T-2343	"	1320	60	ol+l
T-2230	"	1400	20	ol+l
T-2241	"	1420	20	l
T-2212	1.5	1320	100	ol+opx+cpx+l
T-2572	"	1340	140	ol+opx+cpx+l
T-2204	"	1360	90	ol+opx+cpx+l
T-2242	"	1380	60	ol+opx+l
T-2200	"	1400	45	ol+opx+l
T-2203	"	1440	30	ol+l
T-2206	"	1455	20	l
T-2248	1.8	1450	10	ol+l
T-2220	2.0	1400	100	ol+cpx+opx?+l
T-2227	"	1420	105	ol+cpx+opx+l
T-2216	"	1440	45	ol+opx+l
T-2222	"	1460	40	opx+l
T-2218	"	1480	35	l
T-2577	2.15	1465	30	opx+l
T-2341	2.2	1450	40	cpx+Opx?+l
T-2245	2.2	1475	25	l
T-2336	2.5	1440	150	cpx+l
T-2252	"	1460	85	cpx+l
T-2224	"	1480	30	cpx+l
T-2251	"	1490	20	opx+l
T-2226	"	1500	30	l
T-2253	2.8	1505	25	cpx+l
T-2348	3.0	1490	60	cpx+l
T-2334	"	1520	25	cpx+l
T-2586	3.5	1540	30	cpx+gt+l

ol = olivine, opx = orthopyroxene, cpx = clinopyroxene, plag = plagioclase, and l = liquid

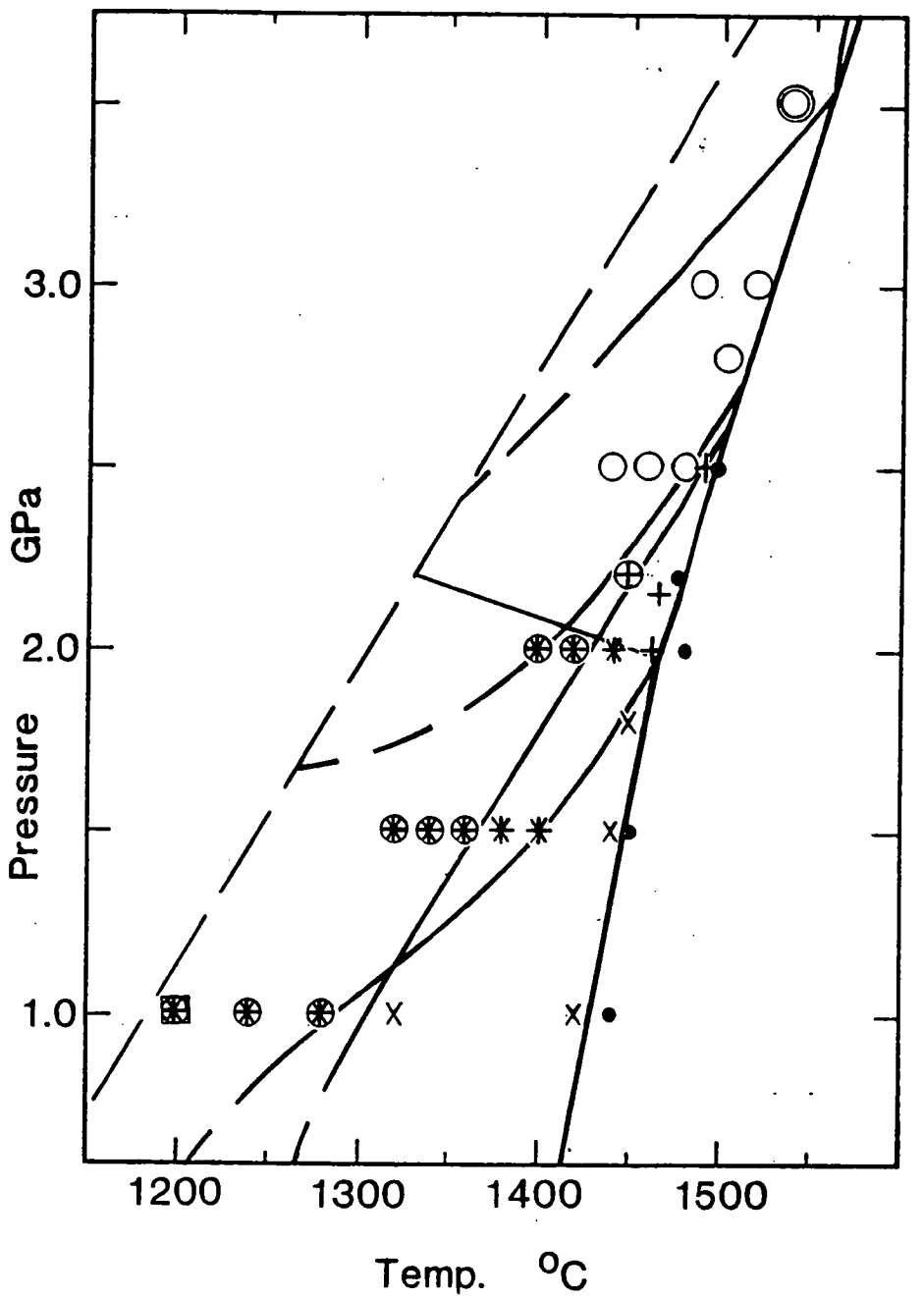

Figure 2.4 High pressure phase relationships determined for the new Kilauea Iki parent melt estimate of this study. Equilibrium phases are indicated as follows: ●-above liquidus, O-clinopyroxene, X-olivine, ┼-orthopyroxene, O-garnet, and □- plagioclase. Note that all experiments are above the solidus. Constrained phase boundaries are shown as solid lines, and inferred boundaries as dashed lines.

saturation point and the liquidus garnet field. Finally, it is worth noting, the pressure and residual phase mineralogy (i.e. harzburgite) of the multiple saturation point compares favourably with an estimate derived from the peridotite melting studies of Falloon et al. (1988; Fig. 2.5).

2.5 IMPLICATIONS FOR THE PETROGENESIS OF HAWAIIAN THOLEIITES

The experimental results obtained here reaffirm the conflict existing between previous phase equilibria studies and trace element geochemistry-based models for Hawaiian magmagenesis, which argue for and against a residual garnet peridotite phase mineralogy. To sustain the trace element-based arguments, either the parent compositions studied are not representative of Hawaiian primary magma compositions, or the experimental conditions used (both liquidus and peridotite melting studies) do not provide an adequate approximation of the upper mantle melting environment beneath Hawaii. Conversely, the geochemical evidence for residual garnet is based solely upon an assumed Hawaiian mantle source comprising chondritic relative abundances of REE. This is neither defensible from observations on the geochemistry of mantle xenoliths (e.g. O'Reilly and Griffin, 1988), nor from other evidence for incompatible element-enriched intraplate magma sources (e.g. Wedepohl, 1985). Following discussions in this study pursue these possibilities, and serve to establish a forum for the application of dynamic melting models in an effort to resolve this dichotomy in Hawaiian magmagenesis (see Chapter 3).

2.6 A CASE FOR MORE OLIVINE-RICH PRIMARY COMPOSITIONS?

Experimental studies of peridotite melting behaviour demonstrate that basaltic liquids are saturated with liquidus garnet in the company of other essential peridotite phases (i.e. Ol+Opx) only at elevated pressure. The liquids found coexisting with garnet peridotite phase assemblages are rich in normative olivine (e.g. Takahashi, 1986), in accordance with contraction of the olivine phase volume with increasing pressure (Green and Ringwood, 1967a; O'Hara, 1968; Falloon and Green, 1988; see Fig. 2.2).

Given that addition of olivine to a basaltic bulk composition will expand the olivine phase volume to higher pressure (as illustrated in Fig. 2.1), the phase diagram for

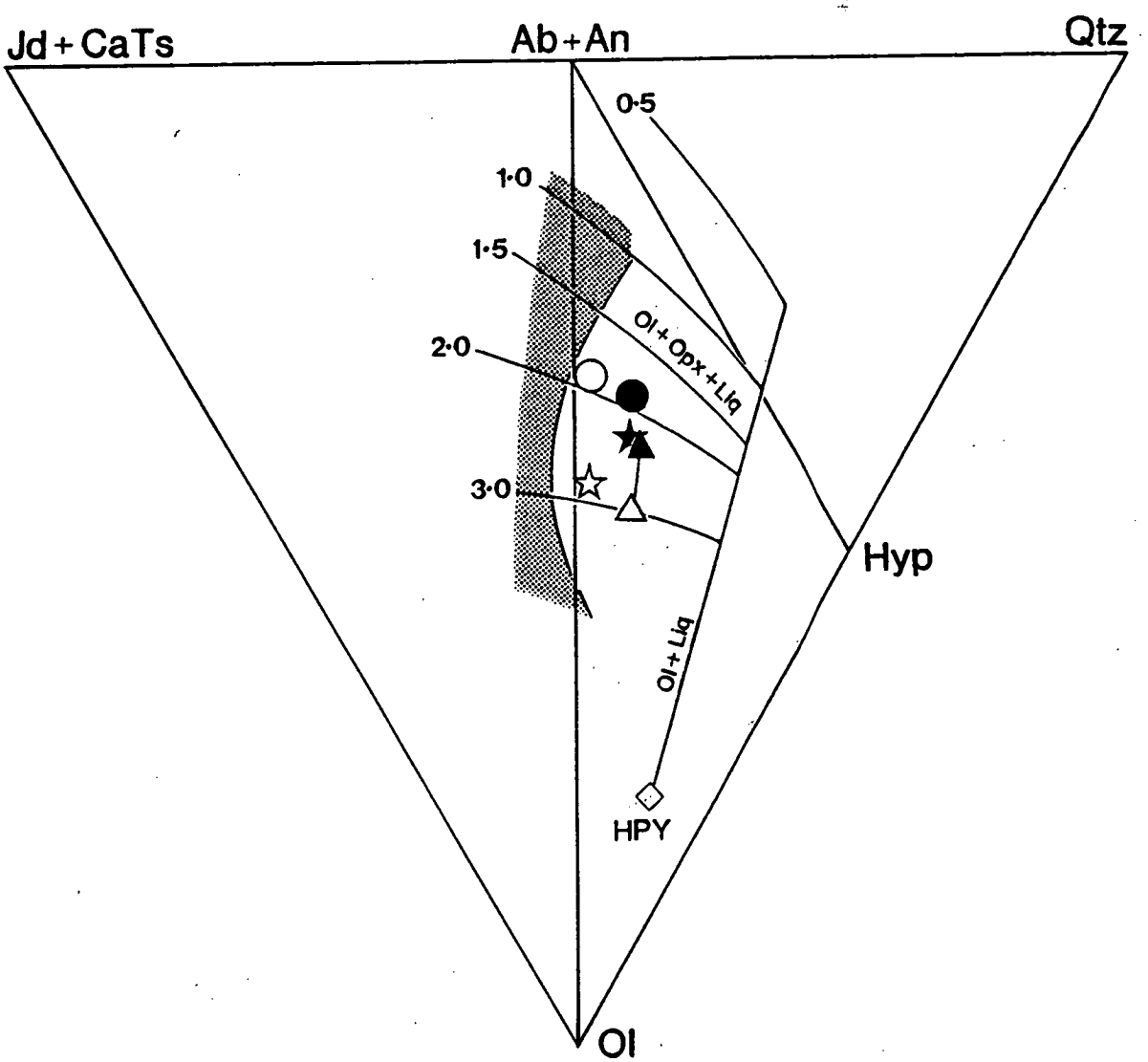

Figure 2.5 Projection of the new Kilauea Iki parent melt composition estimate (filled triangle) onto the Ol-Jd+CaTs-Qtz cotectic grids for melting of "Hawaiian pyrolite" (after Falloon et al., 1988). The unfilled triangle shows a parent melt estimate consistent with peridotite equilibrium at 3.0GPa, that has been generated by the further addition of 13wt% olivine. Symbols for previously studied Hawaiian parent melt estimates, and the cotectic pressures, are as in Fig. 2.2.

the Kilauea Iki parental picrite (Fig. 2.4) suggests that garnet is unlikely to be a liquidus phase in the presence of olivine and orthopyroxene until pressures >~ 3.0 GPa and temperatures exceeding ~1500°C. Falloon and Green (1988) and Falloon et al. (1988) have established comparable conditions for garnet peridotite saturation in melting experiments on Hawaiian Pyrolite (i.e. 3.0 GPa, 1550°C) and MORB pyrolite (i.e. 3.5 GPa, 1600°C).

The position of the garnet-spinel transition provides a means for establishing more accurately the conditions where garnet-peridotite may be a residual mantle phase assemblage. Experiments in, and theoretical analysis of, simple systems (MAS; MacGregor, 1964; Obata, 1976: CMAS; O'Hara et al., 1971) indicate progressive increase in the slope (dP/dT) of the garnet-spinel transition with increasing temperature, from near zero values at T<1000°C and P~1.5-2.0 GPa. At temperatures appropriate for melting of primary Hawaiian tholeiite magmas (i.e. >~1450°C), the garnet-spinel transition for CMAS is very steep with garnet being unstable below ~2.5 GPa (Fig. 2.6). The effect of adding other components is poorly known, apart from FeO which will slightly reduce the transition pressure (by ~0.1-0.2 GPa), and Cr which is likely to produce a marked opposing effect (O'Neill, 1981). Experimental data available for Hawaiian pyrolite (proposed Hawaiian source composition), and other peridotite compositions studied by O'Hara et al. (1971), Takahashi (1986), and T.J. Falloon (unpublished data), show that in the upper mantle the garnet-spinel transition closely follows that in the CMAS system, but at slightly higher pressure (~0.2GPa), particularly when T>1400°C (see Fig. 2.6).

If the olivine phase volume determined for the picritic Kilauea Iki parent melt estimate is plotted on Figure 2.6, it becomes clear that the olivine phase volume must be considerably enlarged to achieve garnet peridotite saturation. Phase equilibrium considerations (e.g. Fig. 2.1) indicate this is most reasonably achieved by further addition of olivine. The amount of additional olivine required to create a primitive parent melt composition capable of equilibrium with peridotite at higher pressure, where garnet may be residual phase, can be calculated from the cotectic grids of Falloon and Green (1988) and Falloon et al. (1988). Using the Ol-Jd+CaTs-Qtz projection, on which the cotectic grids are relatively robust to bulk compositional variation, ~13 wt% additional olivine is required to place the studied Kilauea Iki parent composition over the 3.0 GPa cotectic of

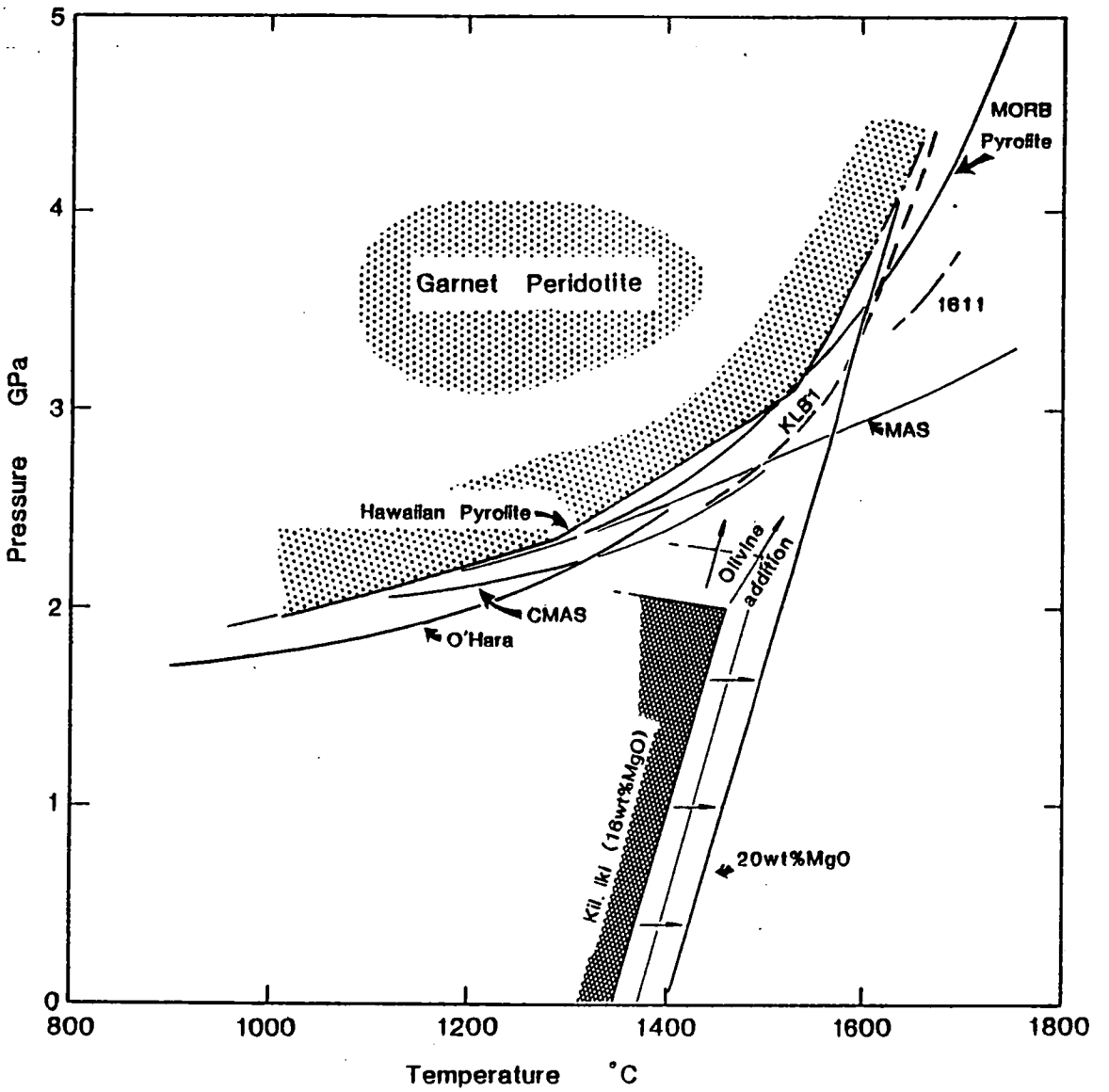

Figure 2.6 The garnet peridotite stability field for Hawaiian pyrolite (stippled field; after Green and Ringwood, 1967b), and other experimentally-studied simple system and natural peridotite compositions. These include the systems MAS (MacGregor, 1964; Obata, 1976) and CMAS (O'Hara et al., 1971), and the peridotite compositions of KLB1 (Takahashi, 1986), MORB pyrolite (T.J. Falloon, pers. comm., 1988), 1611 (Mysen and Kushiro, 1977), and those studied by O'Hara et al. (1971). The hatched field outlines the olivine phase volume for the new Kilauea Iki parent melt estimate, and small arrows indicate the expansion of this volume occurring with further olivine addition up to a bulk composition containing ~20 wt% MgO.

Hawaiian Pyrolite (Fig. 2.5). It is worth noting that these calculations are insensitive to choice of acceptable olivine-liquid Fe/Mg partition relationships (i.e. $K_D^{Fe/Mg_{Ol\text{-}Liq}}$ = 0.27-0.35). This 3.0 GPa parent melt estimate has a very high MgO content (~20 wt%; Mg#>78) and is capable of crystallising olivine of Mg#~92.5 (assuming $K_D^{Fe/Mg_{Ol\text{-}Liq}}$ of 0.30).

On the basis of established relationships between the liquidus temperature of anhydrous basaltic liquids and their bulk compositions (e.g. Ramsay et al., 1984), the liquidus temperature of a melt with 20 wt% MgO can be estimated to be ~60°C higher than a picritic composition with 16 wt% MgO. By extrapolating an appropriate liquidus slope for the 20 wt% MgO parent to higher pressure, parallel to the picrite liquidus slope, the garnet peridotite stability field is intersected at between 3.3 and 4.0 GPa (see Fig. 2.6). Consequently, this 3.0 GPa parent melt composition is also unlikely to be in equilibrium garnet peridotite. Small amounts of dissolved volatiles occurring in Hawaiian magmas, however, may depress anhydrous liquidus temperatures by several tens of degrees, to promote garnet satuaration. Even considering this possibility, it appears unlikely that Hawaiian primary melt compositions will be garnet peridotite saturated at pressures <3.0GPa. Such, potentially garnet saturated, primary melt compositions with ~20 wt% MgO or more, shall be referred to as ultramafic parent melts.

Evidence for more olivine-rich (ultramafic) primary melt compositions than the studied Kilauea Iki parent could be concealed in a number of ways. Foremost, and perhaps the most difficult to establish, is the potential for crystallisation of primary melts during transfer from source region to sub-volcanic magma reservoirs. Heat conduction into wallrocks from dykes propagating through cooler lithosphere may, if the tendency toward superheating on adiabatic ascent is overcome, lead initially to crystallisation of liquidus olivine along conduit walls. Helz (1987) has suggested that populations of deformed/strained olivine found in erupted magmas have originated from such sites. However, neither these particular olivines, nor those found in deep-crystallised dunite xenoliths (Sen and Presnall, 1986), are more magnesian than other Hawaiian phenocrysts. Consequently, unless they have crystallised at very high pressures (1 to 3GPa), where equilibrium olivine compositions may be more Fe-rich than at low pressure (Ulmer, 1989),

they do not provide evidence for the crystallisation of more primitive compositions than the picritic Kilauea Iki parent melt calculated herein. Another possibility arises from consideration of rapid intracrystalline diffusion rates in olivine, which can accomodate re-equilibration of Fe and Mg components of even large olivine phenocrysts with their surrounding melt, within periods as short as months or years (Maaloe and Hansen, 1982; Helz, 1987). Olivine phenocrysts may therefore crystallise initially as compositions more magnesian than observed. The common, unzoned Mg# profiles of many Hawaiian olivines may be interpreted as evidence for diffusive Fe/Mg exchange having kept pace with phenocryst growth rates, but they are not definitive as they could also indicate these phenocrysts have grown from essentially constant melt compositions (e.g. Maaloe and Hansen, 1982).

2.7 TRANSITION ELEMENT CONSTRAINTS ON PRIMARY MELT COMPOSITIONS

The suitability of the competing picritic tholeiite and ultramafic parent melt estimates as Hawaiian primary melt compositions,may be tested using known partitioning behaviour of the transition elements, in particular Ni. On such a basis, Feigenson (1986) has argued previously that even picritic primary compositions (i.e. 14-16 wt% MgO) are inconsistent with the observed high Ni and Cr abundances in less Mg-rich Hawaiian tholeiites. This viewpoint is re-examined here after first establishing what the Ni contents of the proposed parent melt compositions are likely to be.

The Ni abundances of parent magmas evolving by olivine-dominated crystal fractionation can be assessed by using established expressions for Ni partitioning between olivine and basaltic liquids (e.g. Hart and Davis, 1978; Takahashi et al., 1987). By choosing suitable primitive Hawaiian glass compositions (e.g. Iki-9 from Helz, 1987), estimated to contain between ~75 and 90ppm Ni based on a compilation of Ni contents of Hawaiian tholeiites with ~7 wt% MgO content (Fig. 2.7), the Ni contents of picritic tholeiite and ultramafic parent melt compositions can be calculated by applying a similar incremental olivine-fractionation-correction procedure to that applied to major elements. This procedure is found to reproduce the Ni versus Mg# variation of Hawaiian olivine

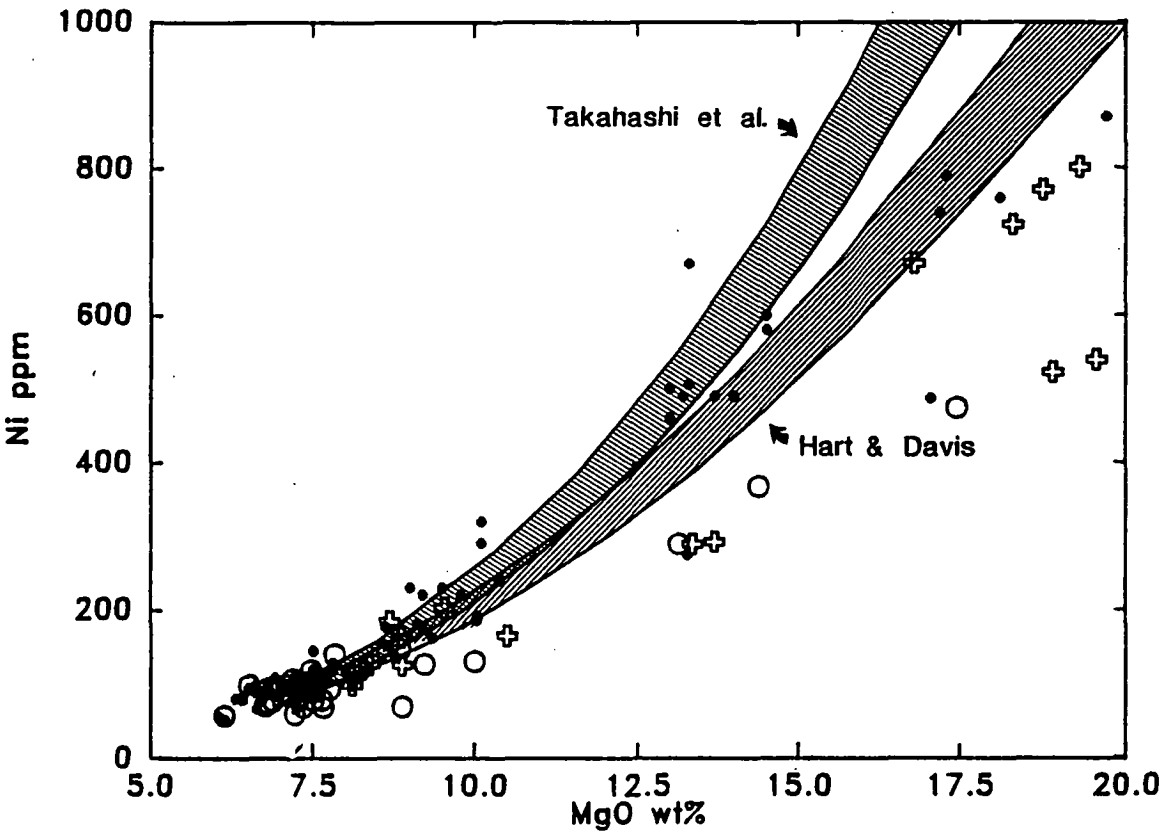

Figure 2.7 Ni versus MgO covariation in Hawaiian lavas compared to fields for olivine-fractionation-corrected parent compositions modelled using the Ni partitioning expressions of Takahashi et al. (1987) and Hart and Davis (1978; see text for details). Compiled Hawaiian tholeiites include samples from Mauna Loa (circles), Kilauea (dots), and the Kilauea Iki eruption (Swiss crosses). Data sources include Gunn (1971), the BVSP (1981), Budahn and Schmitt (1984), Feigenson et al. (1983), Casadevall and Dzurisin (1987), and Tilling et al. (1987).

phenocrysts rather well (Fig. 2.8), and also the Ni concentrations in most olivine-rich, Hawaiian lavas with between 10 and 20 wt% MgO (Fig. 2.7). The discrepancy occurring for those samples falling below the modelled parent compositions trends, may reflect the accumulation of relatively Ni-poor olivine phenocrysts in the magmas, or the combined effects of equilibrium crystallisation and magma mixing.

The calculated Ni contents of ultramafic parent melts (at 20 wt% MgO) range between 985 and 1180 ppm using the $D^{Ni}_{Ol\text{-}Liq}$ relationship of Takahashi et al. (1987), and between 1350 and 1640 ppm using the expression of Hart and Davis (1978). The calculated equilibrium olivine Ni contents for these compositions are 0.55-0.65 and 0.88-1.06 wt% respectively. For the picritic parent compositions (~16 wt% MgO) these estimates reduce to 580-700 and 735-880 ppm Ni in the melts and, 0.43-0.51 and 0.60-0.73 wt% NiO in the equilibrium olivine. Application of the olivine-fractionation-correction procedure to sample #KI0051, which has 211ppm Ni content at 9.54wt% MgO (Gunn, 1971), results in estimates at the Ni-rich end of these ranges.

These parent melt Ni contents may be tested for consistency with a primary derivation from peridotitic sources if the Ni partitioning relationships, upon which the fractionation modelling is based, are also assumed to apply to partial melting. By assuming that the residual phases other than olivine will combine to produce a partial bulk partition coefficient for D^{Ni}_S of ~ 1 (i.e. $D^{Ni}_{Ol\text{-}Opx}$ ~$D^{Ni}_{Ol\text{-}Cpx}$ ~5; Duke, 1976), then the equilibrium partial melting equation (Shaw, 1970) can be rearranged to solve for the mass fraction of residual olivine present in the peridotite residue i.e.

$$X^{Ol}_S = \frac{[\{(C^{Ni}_S/C^{Ni}_l) - f\} \times 1.25]}{[D^{Ni}_{OL\text{-}Liq}.(1-f)] - 0.25} \qquad (2.1)$$

where X^{Ol}_S = olivine fraction in the residue

C^{Ni}_S = Ni concentration in the source (i.e. 2000ppm)

C^{Ni}_l = Ni concentration in primary melt

f = degree of partial melting

The X^{Ol}_S values obtained should comply with olivine mass fractions occurring in peridotites (i.e. X^{Ol}_S ~0.50-0.80). Results calculated by substituting the Ni concentrations estimated for the picritic and ultramafic parent compositions are shown as functions of the

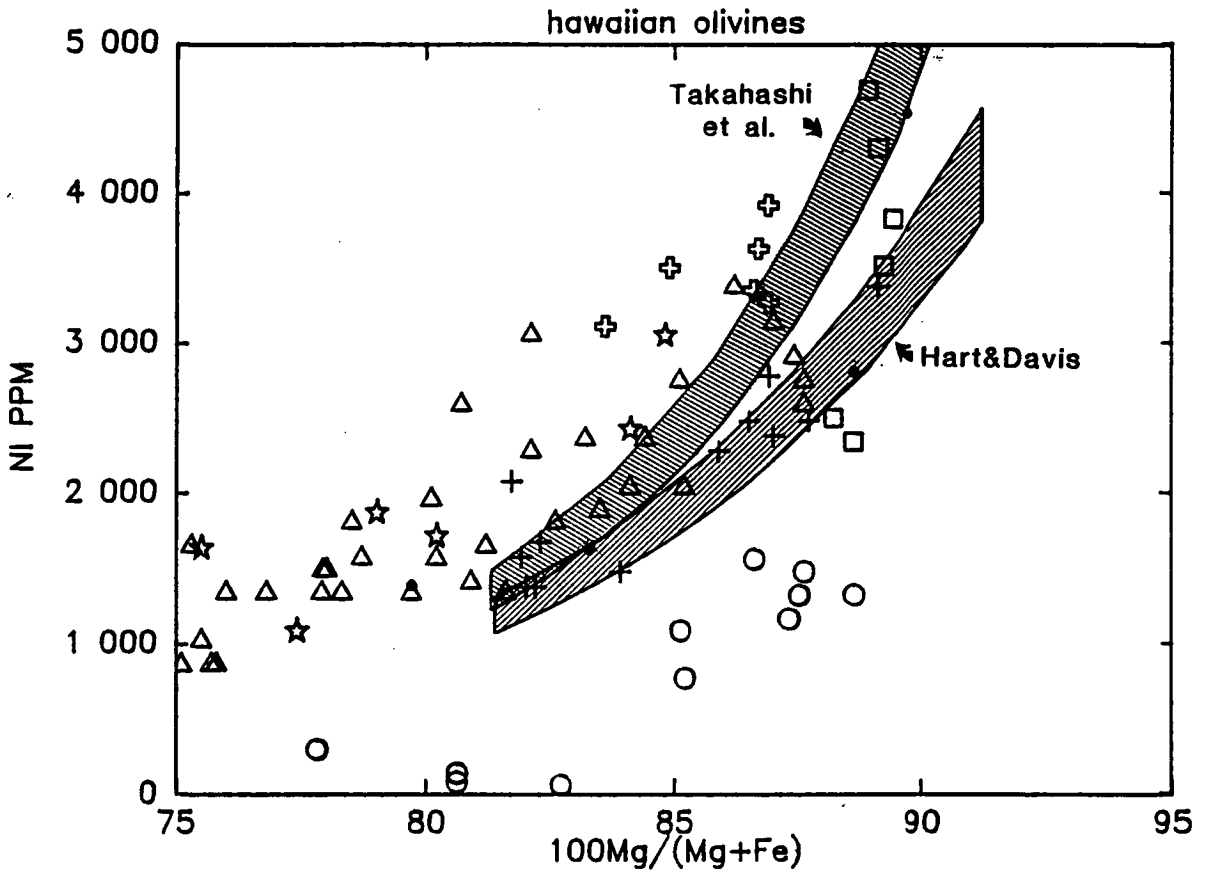

Figure 2.8 Hawaiian olivine phenocryst Ni contents compared to olivine Ni contents in equilibrium with olivine-fractionation-corrected Hawaiian tholeiite parent melt compositions (see Fig. 2.7). Compositions are modelled using the Ni partitioning expressions of Takahashi et al. (1987) and Hart and Davis (1978). Hawaiian olivine compositions are from Helz (1987; circles), Fodor et al. (1977; 5-point stars), Wilkinson and Hensel (1988; filled circles), Hawkins and Melchior (1983; crosses), Leeman and Scheidegger (1977; Swiss crosses), Nicholls and Stout (1988; triangles), and Eggins and Green (unpublished data).

degree of partial melting in Figure 2.9. Only the picritic parent estimates yield acceptable results, and then only using the $D^{Ni}_{Ol\text{-}Liq}$ relationship of Takahashi et al. (1987).

Some limited experimental data shows, however, that $D^{Ni}_{Ol\text{-}Liq}$ values may decrease with increasing pressure in basaltic compositions (Bickle et al., 1977; Irvine and Kushiro, 1976). The data of Bickle et al. (1977) suggest that appropriate $D^{Ni}_{Ol\text{-}Liq}$ values for ultramafic liquids (~20 wt% MgO) at 3.0 GPa are ~3 (but not less than 2), in which case the X^{Ol}_{s} values calculated for both the Hawaiian picritic and ultramafic parent compositions would be shifted to higher and possibly more acceptable values. Clearly, the potential exists for constraining primary melt compositions if Ni partitioning can be accurately determined as a function of T, P, and bulk composition. Unfortunately, at present, Ni abundances cannot be applied as definitive criteria on which the selection of high pressure Hawaiian primary melt compositions can be made.

A compelling argument against garnet-saturated ultramagnesian parent compositions is provided by the Tasmantid Seamount tholeiites. These have formed in a similar intraplate setting and are geochemically akin to Hawaiian tholeiites (Chapter 1), and thus by association, can be considered to share a common petrogenesis. The primitive glassy Tasmantid basalts show no evidence for significant olivine accumulation (Chapter 1), yet are significantly more Ni-rich than Hawaiian counterparts with similar MgO contents. Their olivine phenocryst Ni contents also overlap with peridotitic olivine (i.e >0.30 wt%), and X^{Ol}_{s} values calculated on the basis of the natural whole-rock compositions are consistent with a peridotite source derivation (see Fig. 2.9). In contrast, when subjected to the Ni modelling procedure outlined above, and melt compositions suitable for equilibrium with garnet peridotite at ~3GPa are calculated, parent melt Ni concentration estimates fall between 1500 and 3000ppm Ni. The corresponding X^{Ol}_{s} values are reduced to less than 0.05 for reasonable degrees of partial melting between 0 and 35%. In this case, Ni is required to behave as an incompatible element $D^{Ni}_{Ol\text{-}Liq} < 1$ during melt generation. This seems most improbable, and makes garnet equlibrated primary melt compositions unlikely for the Tasmantid tholeiites, as previously argued in Chapter 1.

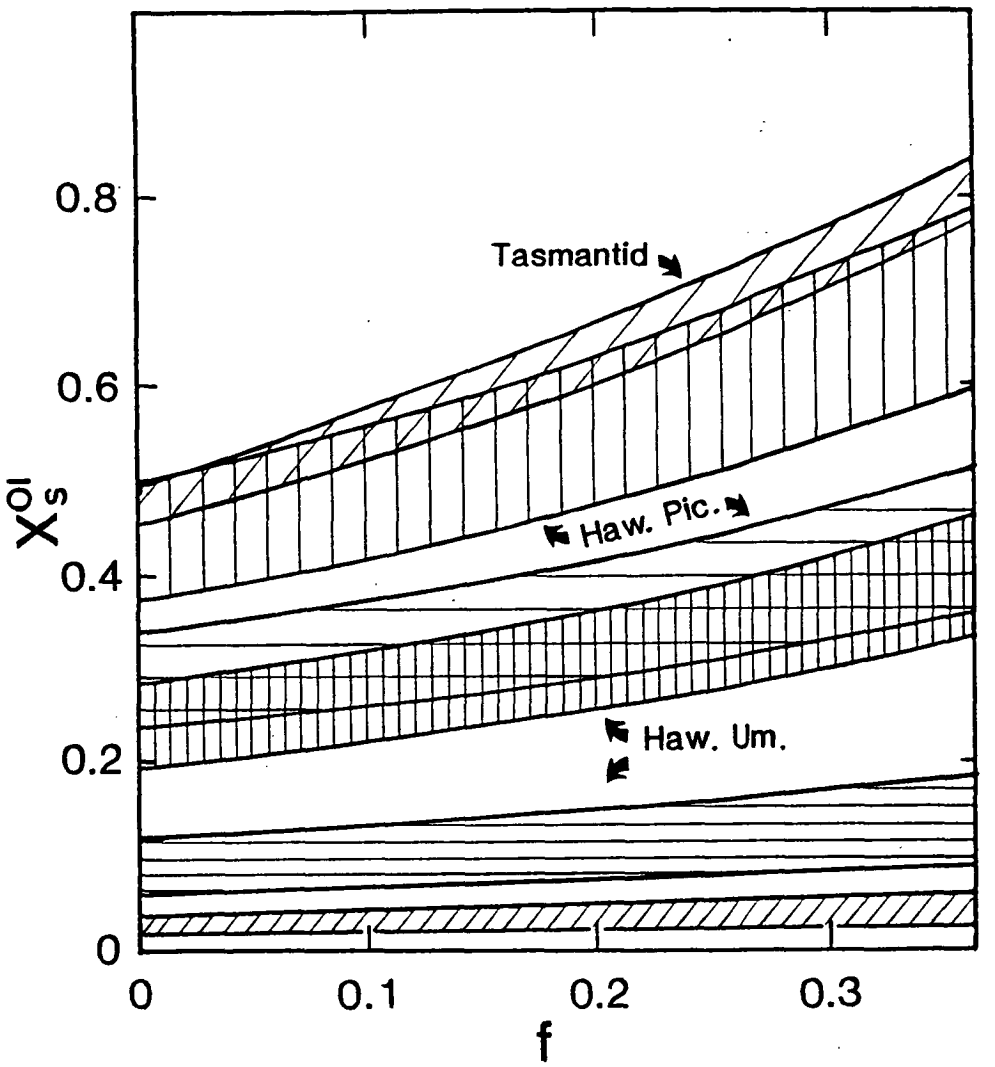

Figure 2.9 Calculated residual olivine fractions in the Hawaiian source for competing ultramafic primary melt and picritic primary melt models. Modelling is based on caculated parent melt Ni contents (see Fig. 2.7 and text for details) and equation 2.1. Two sets of results are shown, corresponding to the Ni partitioning expression of Takahashi et al. (1987; vertical ruled fields) and the expression of Hart and Davis (1978; horizontally ruled fields). Ultramafic primary melt solutions (Haw. Um.) are ruled with twice the density of the picritic primary melt solutions (Haw. Pic.). Also shown are results calculated (using the Takahashi et al. partitioning expression only) for Tasmantid primitive basalts (which have between 238 and 322 ppm Ni, see Chapter 1; diagonally ruled field) and corresponding high pressure (3.0 GPa) olivine-fractionation-corrected parent composition estimates (double density diagonally ruled field).

In summary, there is currently no basis for an unequivocal selection of primary melt compositions for Hawaiian tholeiites. On the basis of available evidence some Hawaiian primary melt compositions must be at least ~16wt% MgO, but may well be >20wt% MgO. Magnesian olivine phenocrysts provide the only firm evidence for the composition of primitive melts, but they only account for compositions with up to ~16 wt% MgO.

2.8 IMPLICATIONS FOR THE SOURCE OF HAWAIIAN THOLEIITES

Experimental phase relations demonstrate that picritic Hawaiian parent compositions are in equilibrium with peridotite residues (Ol+Opx) at depths exceeding the deepest earthquake focii (~45-60 km; e.g. Eaton, 1962; Klein et al., 1987). These observations may be consistent with partial melt existing at and beneath that depth. Moreover, they provide evidence that substantially less magnesian (olivine-poor) compositions than those capable of equilibrating with peridotite at depths of ~60 km (~1.7 GPa) are inappropriate primary magma compositions. In this light, Hawaiian primary melt compositions are required to be at least picritic in composition (>14 to 16wt% MgO).

2.8.1 Evidence for a Hot Mantle Source

Irrespective of whether a picritic tholeiite or an ultramafic primary melt model is invoked, the liquidus temperatures of multiple saturation points for picrites (~1450°C) and ultramafic liquids with ~20 wt% MgO (~ 1550°C), indicate that melting is occurring at anomalously high mantle temperatures. If the latent heat of fusion is also taken into account, these estimates are likely to correspond to mantle temperatures about 200°C above those believed by some to be ambient conditions for the upper mantle (see McKenzie and Bickle, 1988). This supports previous hypotheses for the existence of an anomalously hot mantle source beneath Hawaii.

2.8.2 Hawaiian Source Geochemistry

The geochemistry of the Hawaiian source is likely to be strongly dependent upon the choice between picritic and ultramafic primary melts. A harzburgite residue in the case of picritic primary compositions will be refractory to the large majority of trace elements which are highly incompatible in olivine and orthopyroxene. The source abundances of

these elements (including the REE) will mimic those of Hawaiian tholeiites at concentration levels determined by the degree of melting as follows :

$$C^i_0 = f.C^i_l \qquad (2.2)$$

where C^i_0 = concentration of element i in the source

C^i_l = concentration of element i in the liquid.

Clearly, the source of Hawaiian tholeiites would be required to be enriched in the more incompatible elements and possess a pre-existing residual garnet signature (e.g. Dy/Yb_{CN} >1).

In contrast, ultramafic primary melts segregating from garnet-peridotite residues may derive from a source less enriched in incompatible elements, and possibly possessing chondritic middle REE/HREE values. The relationship between the source and the primary melt composition in this case is likely to be a complex function of,the degree of melting, proportions of residual phases, solid-liquid partition coefficients, and the nature of the melt segregation process, as indicated by the equilibrium batch melting equation (Shaw, 1970) i.e.

$$C^i_0 = C^i_l.[D^i_0 + f(1 - D^i_0)] \qquad (2.3)$$

where $D^i_0 = X_j.D^i_j$

D^i_j = partition coefficient for element i between phase j and liquid

X_j = fraction of phase j in the residue

This expression may be employed to calculate trace element abundances in the Hawaiian source if X_j and f values can be estimated. To evaluate the different source geochemistry required by the picrite and ultramafic primary melt models, these parameters have been approximated using least squares methods (e.g. GENMIX program of LeMaitre, 1980) to constrain the mass balance between peridotite bulk compositions, proposed primary melt compositions, and appropriate residual phases (i.e. for picrites, the 2.0 GPa liquidus olivine and orthopyroxene compositions determined in this study, and for ultramafic melts, the 3.5 GPa olivine, orthopyroxene, clinopyroxene and garnet compositions reported by Takahashi, 1986). A variety of peridotite source compositions, which include Primitive Upper Mantle (PUM; Jagoutz et al., 1979), Bulk Silicate Earth (BSE: Zindler and Hart, 1986), MORB

pyrolite (Falloon and Green, 1988), Tinaquillo Lherzolite (Jacques and Green, 1980), KLB1 (Takahashi, 1986), an average spinel lherzolite from Maaloe and Aoki (1977), and the average of 10 Fe-rich lherzolites reported by Kuno and Aoki (1970), have been employed in the GENMIX modelling in order to span a possible range from fertile to refractory source compositions. The minor elements K_2O, MnO, and P_2O_5 have been excluded from the modelling to avoid the weighting of solutions to these components. The GENMIX modelling results obtained for the picritic and ultramafic primary melt models are listed in Table 2.4.

Melting models for the generation of picritic primary melt compositions produce solutions for the degree of partial melting (f) varying between 6% and 19%, as peridotite fertility increases from the average spinel lherzolite composition to BSE, PUM, and MORB pyrolite compositions. Even larger estimates for the degree of melting are obtained for the ultramafic primary melt compositions, ranging up to between 22 and 26% for PUM, BSE, and MORB pyrolite. The more refractory peridotite compositions (e.g. average spinel lherzolite and average Fe-rich lherzolite), however, appear to be unsuitable sources for ultramafic primary melts as negative solutions are obtained for residual garnet and clinopyroxene. The fraction of residual olivine calculated varies little between 63 and 79% for the picrite primary melt model, and between 62 and 73% for the ultramafic primary melt model. In the latter model, residual garnet accounts for only a small proportion of the residual phase assemblage (0 to 6.4%), orthopyroxene between 16 and 30%, and clinopyroxene between 6 and 13%.

The REE geochemistry of the Hawaiian source is readily calculated according to equation (2.3) from the acquired GENMIX results, by substituting suitable partition coefficients (i.e. Set 3 from Frey et al., 1978) and appropriate "primary" melt REE abundance estimates. For this purpose the "primary" melt REE chemistry has been established by correcting representative Mauna Loa and Kilauea Iki tholeiite compositions (i.e sample #'s HAW-9 and HAW-24: BVSP, 1981) for the mass of added olivine needed to reproduce the picritic and ultramafic parent compositions. Somewhat different source characteristics arise from the two competing primary melt models (Fig. 2.10). The primary picrite melt models produce a range of LREE-enriched source estimates with strongly

Table 2.4 Least squares mixing model results for mass balance between picritic and ultramafic primary melt, peridotite source, and residual phase compositions.

Peridotite Source[a]	PUM	BSE	MPY90	Fe-rich	TQ	SpLhz
Picrite Primary Melt Model						
Residual Phases[b]						
Olivine	0.709	0.619	0.734	0.786	0.705	0.750
Orthopyroxene	0.291	0.381	0.266	0.214	0.295	0.250
Melt fraction (%)	18.7	16.8	19.3	18.7	12.0	5.5
RSS[c]	8.7	8.4	11.8	0.26	8.8	4.7
Ultramafic Primary Melt Model						
Residual Phases[d]						
Olivine	0.702	0.620	0.683	--	0.726	--
Orthopyroxene	0.160	0.302	0.125	--	0.181	--
Clinopyroxene	0.121	0.061	0.128	--	0.097	--
Garnet	0.017	0.017	0.064	--	--	--
Melt Fraction (%)	25.9	24.4	22.0	--	21.4	--
RSS	0.14	0.12	0.08	--	0.20	--

a. Peridotite compositions are PUM = Primitive Upper Mantle, BSE = Bulk Silicate Earth, MPY90 = MORB pyrolite, Fe-rich = average of 10 Fe-rich lherzolites, TQ = Tinaquillo lherzolite, and SpLhz = average spinel lherzolite, see text for data sources.
b. Residual phase compositions are liquidus olivine and orthopyroxene at 2.0GPa 1450°C in Kilauea Iki picrite parent melt, from this study (see Appendix 2).
c. RSS = residual sum of squares
d Residual phase compositions are those at 3.5GPa 1550°C, for peridotite KLB1 (Takahashi, 1986).

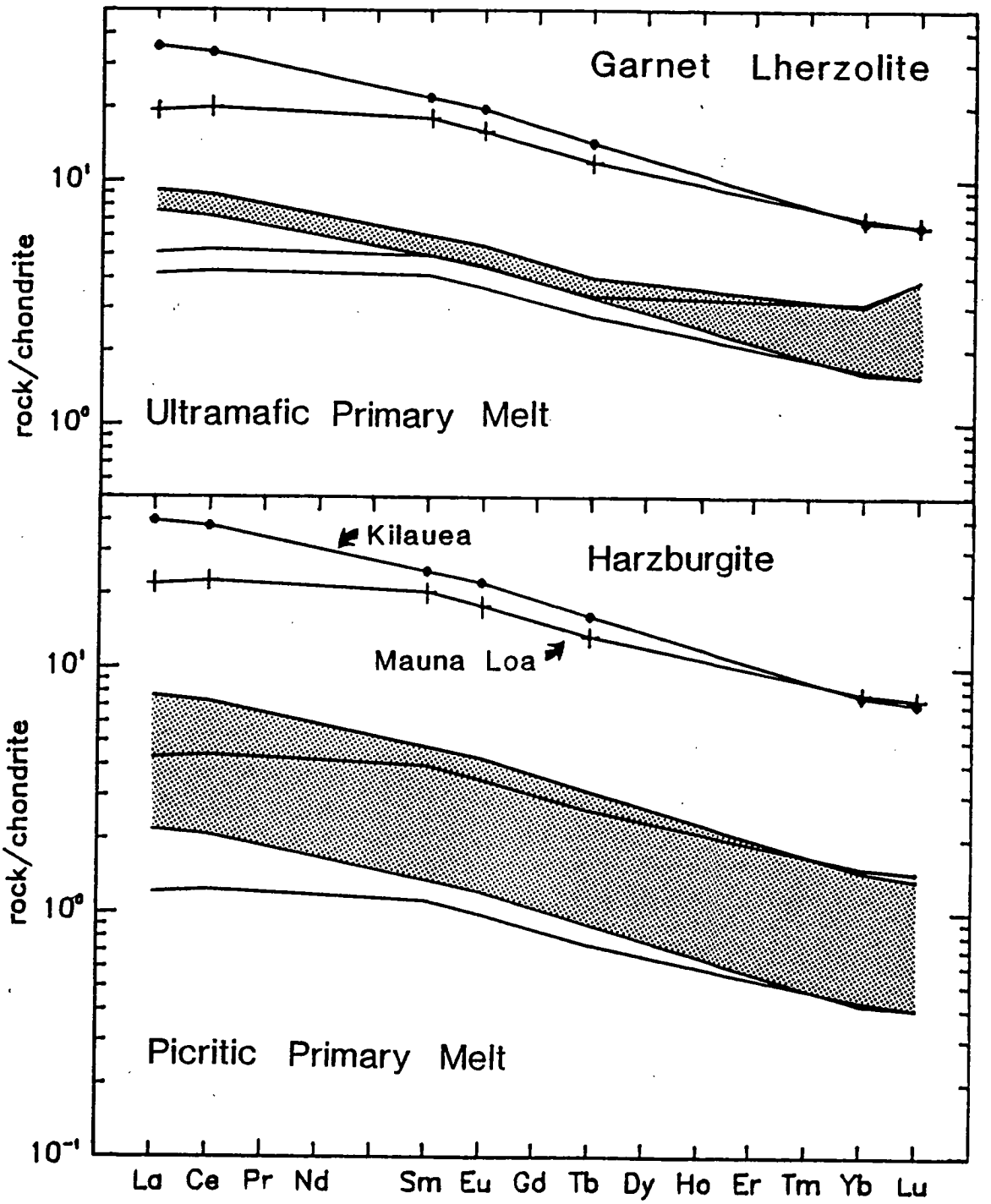

Figure 2.10 Chondrite-normalised Hawaiian source REE abundances for deep garnet-present (ultramafic primary melt) and shallow garnet-absent (picritic primary melt) melting models. Results are based on olivine-fractionation-corrected REE abundances in primitive Kilauea and Mauna Loa basalts compositions (i.e. #HAW-24 and #HAW-9 in the BVSP, 1981). The modelled Kilauea source is shown in stipple and the Mauna Loa source as a plain field (see text for details of calculation procedure).

fractionated REE abundances (i.e. $Gd/Yb_{CN} > 1$) identical to the basalt REE patterns. The ultramafic primary melt (garnet lherzolite source) model, on the other hand, results in some source estimates with near chondrite-relative REE abundances, particularly for the Mauna Loa source, and appreciably higher HREE abundances than the picrite source models.

The results illustrated in Figure 2.10 should be treated as a guide only, as some parameters (e.g. partition coefficients) are poorly constrained. In particular, X^i_j and f values are very sensitive to minor variations in the residual phase and source compositions employed in the GENMIX modelling. Nonetheless, this forward modelling approach serves to illustrate the potential differences in source geochemistry that may arise from the two competing primary melt composition models.

2.8.3 The Origin of an Enriched Mantle Source

If Hawaiian primary melts are picritic, then the origin of an incompatible element enriched source bearing a "residual garnet" signature demands explanation. Considering the Sr and Nd isotopic characteristics of Hawaiian lavas (e.g. Stille et al., 1986), which will support their derivation from a source with time integrated depletions of incompatible trace elements, this enrichment is required to have occurred relatively recently. Most incompatible element enrichment models for intraplate oceanic magma sources have argued for migration of small melt fractions or fluids into the oceanic lithosphere, as proposed by Green (1971), Green and Lieberman (1976), and Wright (1984). Bulk addition of incompatible element-rich melt or fluid fractions, however, is likely to develop a source geochemistry highly enriched in LREE, which will be inconsistent with the comparatively slight level of LREE enrichment observed in Hawaiian tholeiites (e.g. Fig. 2.10). Instead, a preferable mechanism may be found in selective geochemical enrichment processes, similar to those modelled by Wright (1984), and as observed in metasomatically enriched mantle nodules (e.g. O'Reilly and Griffin, 1988) where the added geochemical components are determined by the stable phase assemblage during metasomatism. In the oceanic lithosphere, at depths <100km, the peridotite-C-H-O solidus (at fO_2 >IW+2 log units) is raised by amphibole stability to form a geochemical trap for rising incompatible element-rich melt or fluid (Green and Lieberman, 1976, Green and Wallace, 1988). Newly formed or pre-existing amphibole, clinopyroxene, and other possible minor phases will

control the partitioning of elements from the melt/fluid phases. This may produce the incompatible element-enriched source characteristics required, particularly if the most incompatible elements are removed to higher levels by continuing migration of the melt/fluid phase, as is likely to result if a carbonatitic melt is generated in this environment (Wallace and Green, 1988). Oceanic lithosphere may be considered to become enriched in this manner as it cools and thickens with age away from the mid ocean ridges systems. This pre-enriched base of the lithosphere may become incorporated into the Hawaiian magma source as an adjunct to lithospheric erosion by a hot upwelling mantle plume.

2.9 CONCLUSIONS

1. The most magnesian olivine phenocrysts in Hawaiian lavas (Mg# = 90.5) provide evidence for the crystallisation of primitive Hawaiian parent melts with Mg#~75. Fe/Mg partitioning between olivine and liquid ($K_D^{Fe/Mg_{Ol\text{-}Liq}} = 0.30$) and assumed fO_2 conditions of crystallisation equivalent to the QFM oxygen buffer, constrain these parent melts to be picritic with ~16 wt% MgO. These primitive compositions are candidates for Hawaiian tholeiite primary melts.

2. Experimentally-determined high pressure phase equilibria for a picritic Kilauea Iki parent composition estimate,demonstrate multiple saturation with olivine and orthopyroxene at ~2.0 GPa and 1450°C. Garnet is not a liquidus phase at pressures below ~3.5 GPa. Consequently, if Hawaiian primary melt compositions are picritic they cannot have equilibrated with residual garnet at a level of melt segregation near ~60. This result conflicts with trace element geochemistry-based models for Hawaiian magmagenesis which argue for garnet-peridotite residues.

3. Garnet-peridotite may be considered a residual phase assemblage only if Hawaiian primary melts are even more magnesian (olivine-rich) then the proposed picrite parent compositions. The stability field of garnet peridotite requires such melt compositions to be ultramafic with 20 wt% MgO or more. Even though these ultramafic compositions are estimated to have extremely high Ni contents (~1000ppm), they cannot be ruled out on the basis of available constraints on Ni partitioning at high P and T.

4. The proposed picrite primary compositions require a Hawaiian magma source enriched in the incompatible trace and minor elements, with relative abundances closely matching the patterns observed in the Hawaiian tholeiites. The favoured origin for such a source is one formed by open-system geochemical enrichment involving migration of small fraction silicate melts, or fluids, into the oceanic lithosphere. This proposal is in keeping with phase equilibria based models for the growth and geochemical enrichment of lithosphere with age and cooling. This source of incompatible elements must be tapped during Hawaiian magmagenesis, possibly as a result of lithospheric erosion by an upwelling mantle plume.

5. Ultramafic primary melts, with ~20 wt% MgO or more, are potentially consistent with magmagenesis at high pressures (>3.0 GPa) leaving a garnet-bearing peridotite residue. Simple forward modelling shows that such primary melt compositions may derive from sources possessing near chondritic relative abundances of the middle and HREE, as assumed in trace element-based models for Hawaiian magmatism.

CHAPTER 3

Petrogenesis of Hawaiian Tholeiites - Aspects of Dynamic Melt Segregation.

3.1 INTRODUCTION

Picritic tholeiites with 14-16 wt% MgO are widely favoured as the primary melt compositions giving rise to Hawaiian tholeiites (Irvine, 1979; Wilkinson and Hensel, 1988; Nicholls and Stout, 1988, Thompson, 1987; Chapter 2). The high pressure phase relationships of these picritic compositions, however, are inconsistent with established geochemical arguments for melt segregation leaving residual garnet (Frey and Roden, 1987; Chapter 2). A possible resolution to this conflict may exist in the relatively new concepts developed for dynamic melt segregation during decompression melting of peridotite (Turcotte and Ahern, 1978; McKenzie, 1984; McKenzie, 1985b; Thompson, 1987). In such models, the initial incompatible element-rich melt fractions, formed at depth in the presence of residual garnet, are transferred more rapidly than the peridotite residue to shallower garnet-absent levels of melting. It has been proposed that this process imparts a "residual garnet" geochemical signature onto the primary melt bulk compositions, which are determined largely by phase equilibria at shallow levels in the partially molten region.

It is the objective of this study to test whether the existing models for dynamic melting are capable of reconciling the incompatible trace element geochemistry-based arguments for deep garnet-present melting, and the phase-equilibria-based evidence for shallow garnet-absent melting (Chapter 2). I will begin by redressing the conflict arising from the application of simple equlibrium melting models for the petrogenesis of Hawaiian tholeiites, after which progressively more complex dynamic melting models will be employed in an effort to reproduce the geochemical characteristics of Hawaiian tholeiites.

3.2 SIMPLE EQUILIBRIUM BATCH MELTING MODELS

Most previous investigations of ocean island tholeiite (OIT) magmagenesis and their source region geochemistry have relied largely on simple batch melting models. The widespread application of these models has arisen from the combined abilities of (1) experimentally-determined phase equilibria and (2) simple expressions for modal and non-modal batch melting (i.e. equations 3.1 and 3.2 below) to reproduce the observed spectrum of basalt compositions from established upper mantle peridotite compositions (e.g. Frey et al., 1978; Wedepohl, 1985). The familiar equations for trace element behaviour during batch melting are (after Shaw, 1970),

$$C^i_l = C^i_s/[D^i_0+f(1-D^i_0)] \qquad (3.1)$$

where C^i_l is the concentration of element *i* in the melt

C^i_s is the concentration of element *i* in the source

f is the degree of partial melting

D^i_0 is the bulk partition coefficient of element *i* with respect to the solid residue

and,

$$C^i_l = C^i_s/[D^i_0+f(1-P^i)] \qquad (3.2)$$

where P^i is the bulk partition coefficient based on the phase proportions entering the melt

Notable geochemical and isotopic differences occurring between primitive Hawaiian tholeiites and MORB have received considerable attention within the framework of these simple batch melting models. Compared to MORB,Hawaiian tholeiites have:

(1) higher abundances of incompatible elements (e.g. LREE, LILE, TiO_2, P_2O_5, etc.);

(2) fractionated REE patterns characterised by both enriched LREE (e.g. $La/Sm_{CN} > 1$) and fractionated HREE (e.g. $Dy/Yb_{CN} > 1$), whereas MORB usually have strongly depleted LREE ($La/Sm_{CN} < 1$) and chondritic relative abundances of middle and HREE (i.e. $Dy/Yb_{CN} = 1$),

(3) Sr and Nd isotope ratios recording a source history of depletion in the more incompatible elements, but to a lesser degree of depletion than occurring in MORB sources.

Qualitatively, from equations 3.1 and 3.2, the elevated incompatible abundance levels in Hawiian tholeiites may result from either smaller degrees of melting of a source compositionally similar to the MORB source, or by melting of a source which is enriched in these particular elements relative to the MORB source. Moreover, if a chondrite-based geochemical source model is *assumed* for the Hawaiian source, then the characteristics of incompatible element partitioning between mantle phases and basaltic liquids dictate that garnet is a residual phase during melting (e.g. Frey and Roden, 1987). The presence of residual garnet in the Hawaiian source, but not in the MORB source, allows explanation of the fractionation occurring between middle and heavy REE (i.e. $Dy/Yb_{CN} > 1$) in Hawaiian tholeiites.

The isotopic differences occurring between MORB and Hawaiian tholeiites indicate that the Hawaiian source has been more enriched in incompatible elements than the MORB source on a time-integrated basis, but that both sources have been depleted in incompatible elements relative to bulk Earth models. The mismatch between measured parent/daughter element ratios (i.e. $Sm/Nd_{CN} < 1$) and the ratio values necessary to sustain the long term evolution of Sr and Nd isotopes (i.e. $Sm/Nd_{CN} > 1$) can be explained only if the parent/daughter ratios have been fractionated during partial melting, or if the Hawaiian source has been recently enriched in more incompatible elements.

Phase equilibria studies on proposed Hawaiian picritic primary melt compositions serve to clarify these observations, for they support garnet-absent shallow levels of melting leaving a residue of harzburgite (Green and Ringwood, 1967a; Green, 1970; Chapter 2). This evidence favours melting of a source recently enriched in incompatible elements (see Chapter 2 and 4). The only plausible alternative, within a simple batch melting framework, is if the primary melt compositions are considerably more magnesian (olivine-rich) than the picrite primary melt estimates. Ultramafic primary melts (~20 wt% MgO) are necessary for melting to occur at deeper levels (>3 GPa) in the presence of residual garnet. However, it is not possible using available data to choose between a model based on

primary picrite (~16 wt% MgO) melt compositions and a model based on primary ultramafic (>~20 wt% MgO) melt compositions.

3.3 DYNAMIC MELTING MODELS

It is now widely regarded that melting of peridotite under upper mantle conditions may be a dynamic process, possibly resulting in geochemical characteristics not predicted by simple equilibrium melting models (McKenzie, 1984; Richter, 1986; Ribe, 1988). Evidence supporting the assertions of fluid dynamical theory for the dynamic segregation of melt comes from two main sources.

(1) ^{238}U decay-series data on MORB and OIT indicate fractionation of U from Th during melting, a feature consistent with the presence of only very small melt fractions (i.e. <2%; McKenzie, 1985a; Williams and Gill, 1989) throughout the melting of the mantle source.

(2) Experimental determinations of the wetting characteristics of melt/fluid distributed in peridotite matrices (e.g. Waff and Balau, 1979) indicate that partial melting generated porosity may become connected, and thus allow melt migration to occur, at very small amounts of melting (as low as ~0.001%), particularly when carbonatite or other similar volatile-rich melt fractions are formed (e.g. Hunter and McKenzie, 1989).

To grasp an appreciation of the important processes occurring in these dynamic melting models it is useful to consider a column of mantle within a larger volume of upwelling mantle (see Fig. 3.1). Let the base of the column correspond to where the peridotite solidus is intersected and melting begins, and let the top be the highest level of ascent, the limit of decompression, and where the maximum extent of melting is reached. The degree of melting will be a function of decompression and thus of the height within the mantle column. The amount of melt present, however, will be less than the degree of melting, as determined by the porosity which also is likely to be dependent upon the height within the mantle column (e.g. Ribe, 1985).

Both melt buoyancy and, of less certain importance in regard to upwelling mantle plumes, matrix compaction force melt to migrate within and from partially molten zones (e.g. Ribe, 1987). These two processes have important implications for the means by which

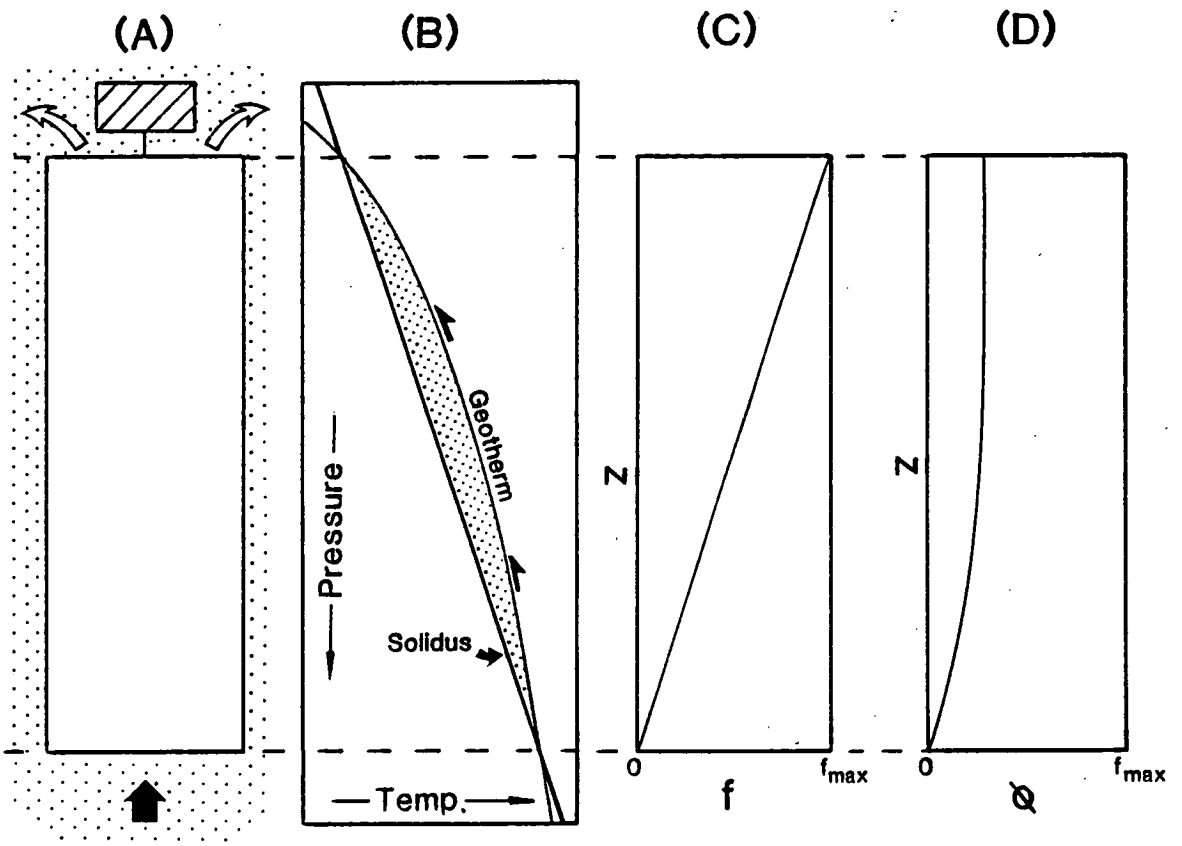

Figure 3.1 A schematic presentation of melting and melt accumulation in an ascending column of mantle. The partially molten column is shown as a plain field in (A), the derivative melt from which is collected in a reservoir (striped box) at the top of the column. The relationship between the peridotite solidus and the adiabatic ascent path is illustrated in (B), with the above solidus interval of melting indicated by the stippled field. (C) shows a simple relationship between the degree of melting occurring with decompression and reduced height (z) within the column. A similar relationship between z and the melt fraction present within the peridotite matrix (i.e. the porosity [ϕ]) in a mantle column undergoing dynamic melt segregation is shown in (D). Note that ϕ is less than f_{max} in this case.

melt migration and accumulation occurs, and their relative roles during melting may be crucial in determining the chemistry of derivative melts (Ribe and Smooke, 1987).

If melt percolates through the matrix, the melt composition derived will be that existing in equilibrium with the matrix at the top of the mantle column (at f_{max}). On the other hand, if melt segregation occurs via channels upward through the partially molten column, the melt composition extracted will be an integration of all melt increments entering the channel network. The primary melt composition generated may be assessed as either an instantaneous aggregate of melt increments entering the channel network at all levels within the column, or the aggregate of melt increments deriving from a unit volume of mantle (e.g. the column itself) as it passes completely through the zone of melting. The contrasting nature of percolation and channel segregation melting processes are illustrated schematically in Figure 3.2.

Recent advances in the understanding of magma segregation processes have resulted in quantification of the geochemical behaviour both of trace elements (e.g. McKenzie, 1985a; Ribe, 1988) and major elements (McKenzie and Bickle, 1988) during decompression mantle melting. These may be grouped into :

(1) percolation melting (PM) models, governed principally by Darcy's Law, (e.g. Ribe, 1985; Ribe and Smooke, 1987), and

(2) channel segregation melting (CSM) models, which have been invoked generally as solutions to matrix compaction driven melt segregation models (e.g. McKenzie, 1985a; Williams and Gill, 1989).

Appropriate geochemical solutions for trace element behaviour in a mantle plume produced by PM are given by Ribe (1988), and for CSM models by McKenzie (1985a) and Williams and Gill (1989). Other more complex segregation processes, such as the development of wave-forms (solitons/magmons) in porosity profiles within partially molten regions (Scott and Stevenson, 1986), and three dimensional melting effects (e.g. O'Hara, 1985; Holness and Richter, 1989), have even higher order implications for the composition of melts generated. The established PM and CSM models are used extensively in this study to evaluate the behaviour of incompatible trace elements during dynamic melting, with particular attention being focused on their ability to generate Hawaiian REE

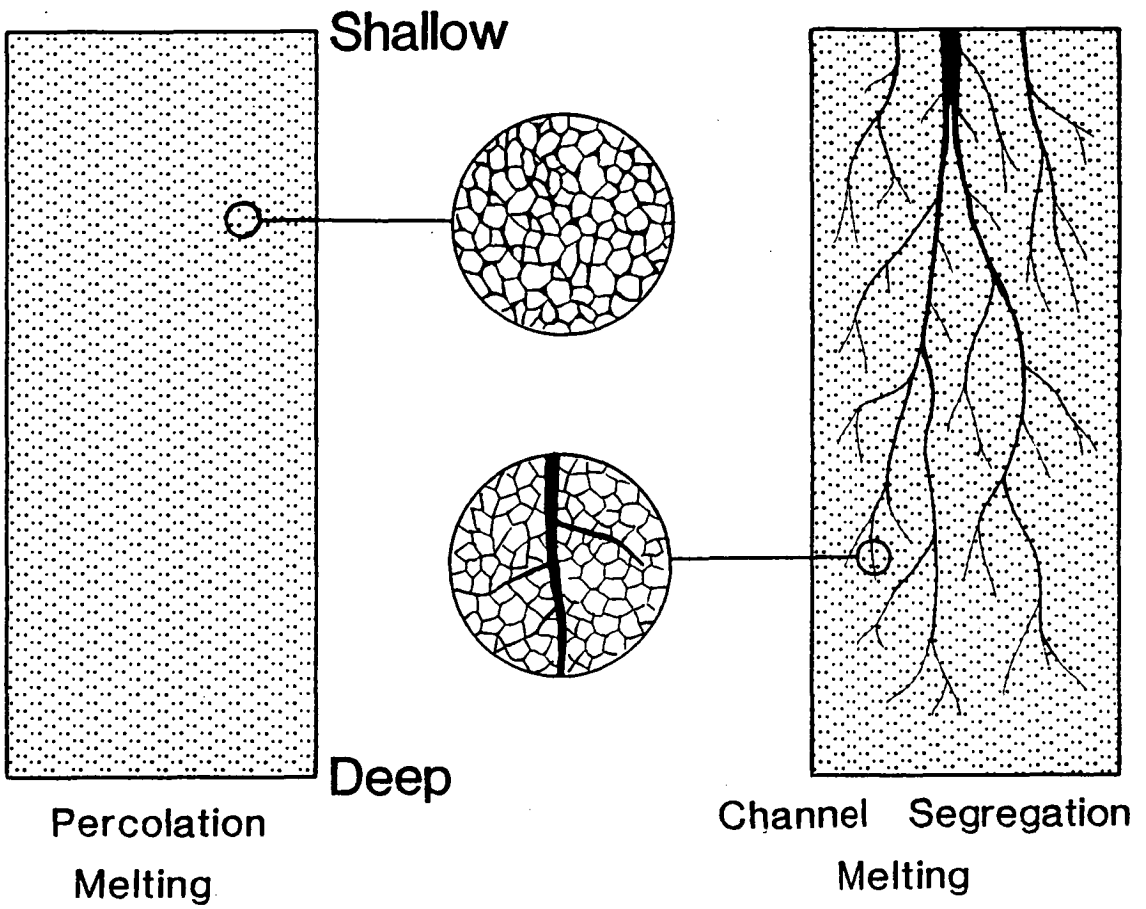

Figure 3.2 Schematic presentation of contrasting percolation and channel segregation melting models. (A) illustrates a percolation dominated melting system where the melt always remains distributed within the peridotite matrix, and (B) illustrates a system in which channel-ways are the dominant means of melt movement through the matrix. These channels coalesce to form a network of "dykes" via which melt migrates out of the partially molten region. In this case, the melt chemistry will be controlled by chemical equilibrium with the matrix until entering the channel-ways, after which it is determined by the integration of melt increments entering the dyke. Dots represent the distribution of melt-filled porosity occurring in each case.

characteristics. The results acquired are compared with those predicted by batch melting (BM; equations 3.1 and 3.2) and fractional (Rayleigh) melting models. It is worth pointing out that the CSM models treat melt migration as occurring through channelways within the partially molten mantle region, even though such a process is not formally accounted for in existing theoretical analyses of melt segregation.

3.3.1 Channel Segregation Melting (CSM)

Trace Elements

For the endmember case of CSM where there exists no porosity, the melt is segregated instantaneously into channelways where it cannot re-equilibrate with the surrounding matrix. The distribution of a trace element, as a function of the degree of melting, is governed by the equation for fractional melting (Shaw,1970).

$$C_{i_l} = C_{i_s}.(D_{i_0})^{-1}.(1-f)^{(1/D_o^*-1)} \qquad (3.3)$$

The concentration of element *i* in an aggregate melt, comprising an integration of all melt increments produced instantaneously within a melting column of mantle, or from a unit volume of mantle passing through the melting region, is given by the equation for an accumulated fractional melt (Shaw, 1970) i.e.

$$C_{i_l} = 1/f.(1-(1-f)^{1/D_o^*}) \qquad (3.4)$$

In reality, porosity will develop from the onset of melting, which based on observations from ^{238}U decay-series equilbria and dihedral angle measurements in melting experiments (e.g. McKenzie, 1985a), has been argued to be a low value, probably <2-3%. The concentration of a trace element in the aggregate melt, in this case, is given by the so-called accumulated continuous melt (ACM) equation of Williams and Gill (1989: after McKenzie, 1985a) i.e.

$$C_{i_l} = (1/X).G.C_{i_s}.[1-(1-X)^{(G(1-D_0^*)+1)}]/[G.(1-D_{i_0})+1] \qquad (3.5)$$

$$\text{where } G = [p_l.\phi+p_s(1-\phi)]/[p_l.\phi+p_s(1-\phi).D_{i_0}] \qquad (3.6)$$

ϕ = porosity

X = mass fraction of melt extracted (X = f-ϕ, if ϕ-->0 then X~f)

p_l = density of liquid (~2.8×10^3 g/cm^3)

p_s = density of matrix (~3.3×10^3 g/cm^3)

Both the porosity (ϕ) and the bulk partition coefficients (D^i_0) are likely to vary during mantle melting as functions of the degree of melting (i.e. with changing bulk composition and residual mineralogy). These variations may be accomodated if equation (3.5) is implemented incrementally.

Major Elements

The bulk composition of a primary melt produced by CSM will comprise an integration of melt increments forming within a partially melting column of mantle. The inital (low f) melt increments, formed at the highest temperature and pressure, will be incompatible element and volatile-rich, probably highly silica undersaturated compositions. As melting progresses with decompression to shallower levels, more incompatible element-poor melt increments will derive from the increasingly depleted (and refractory) matrix residue. The major element composition of these progressive melt increments will be determined by the changing peridotite phase equilibria with ascent and the decreasing fertility of the bulk composition (for a schematic presentation see Falloon et al., 1988). Using existing data from experimental peridotite melting studies, McKenzie and Bickle (1988) have quantified this process,for a zero porosity case, to produce what is in effect an accumulated fractional melting model for primary melt bulk compositions. Their primary melt composition is constrained to represent an intermediate PT bulk composition, between the first (f=0) and final (f_{max}) melt increment bulk compositions formed on the adiabatic melting path at the highest and lowest pressure respectively. This underlies the reasoning used by McKenzie and Bickle (1988) to refer to their derivative primary melt as the point-depth average composition. Clearly, if a liquidus study were performed on a melt generated by this process, a multiple saturation point representative of the "average" conditions of melting would be obtained. Consequently, the PT conditions determined for multiple phase (peridotite) saturation would provide evidence for melting at *both higher and lower pressures and temperatures.*

3.3.2 Percolation Melting

Trace Elements

Ribe (1988) has developed a solution for trace element behaviour which is specific to the melting of a buoyant upwelling mantle plume. Melt migration occurs by

percolation through the matrix, facilitating the maintenance of chemical equilibrium between the segregating melt and the residual matrix throughout melting. The porosity is variable and increases toward a maximum value with increasing degree of melting, which depending upon the ease with which the melt is able to percolate, may be considerably less than the total degree of melting.

The concentration of a trace element in the derivative melt is solved (after Ribe, 1988) from the equation

$$Ci_l = Ci_s.(1/Di_0).\exp\{-(1-Di_0).$$
$$-d\int^z\{[G.(B+A.dT/dz)]/[G+(1-Di_0)(1-\phi)(R\phi^3-G)]\}\} \quad (3.7)$$

where T = temperature in °C

A and B are constants relating the degree of melting to variation in T and P (values used here are those employed by Ribe;i.e. A = 2.5×10^{-3}/°C and B = 9.7×10^{-6}/m)

d = depth of initial melting

z = a vertical co-ordinate in metres

R is a measure of the rate ("ease") at which melt migrates (reasonable values ranging between R = 10^3 and 105; Ribe, 1988). A value of 1000 is used here.

G is a constant, which is a function of z i.e.

$$G(z) = 2/3.Di_0 - (1-Di_0).(z/d) - Di_0/(3.z^3/d)^3 \quad (3.8)$$

Suggested numerical methods for solving these equations are given by Ribe (1988). The degree of melting can be controlled by choosing appropriate values of z and d.

Major Elements

Due to the maintenance of equilibrium between the matrix and melt during PM, the primary melt composition will be determined by the equilibrium phase relationships of the bulk composition (matrix + melt) at the PT conditions existing at the top of the upwelling plume (or mantle column as viewed in Figure 3.1). The bulk composition may be related to the original source composition by mass balance using the porosity, total degree of melting, and the primary melt composition derived at the top of the mantle plume i.e.

$$BULK_{PT} \sim (BULK_S - [(f-\phi)BULK_{pm})/(1-f+\phi)] \quad (3.9)$$

where $BULK_{PT}$ and $BULK_S$ = the bulk compositions existing at the top of the plume, and in the source prior to melting

$BULK_{pm}$ = primary melt bulk composition

If $f>>\phi$ the bulk composition may be very infertile, else if $O\rightarrow f$, or if $\phi>f$, as may be possible when high porosities develop due to solitary wave phenomena (e.g. Scott and Stevenson, 1986), a fertile bulk composition may result. This uncertainty in the bulk composition may preclude the use of composition dependent peridotite melting studies to accurately determine the PT conditions of melt segregation. However, the liquidus phase relationships of a PM primary magma will reflect the PT conditions and residual phase mineralogy at which it last equilibrated at the plume top, regardless of the bulk composition (matrix + melt) present.

3.4 A COMPARISON OF CSM AND PM MODELS

The trace element abundances formed by both CSM and PM models have been calculated as a function of degree of melting for a range of varying bulk partition coefficients (D^i_0 values). In both cases, absolute incompatible element concentrations are greater than or equal to concentrations produced by equivalent degrees of batch melting (Fig. 3.3). Several differences, however, distinguish the CSM and PM models.

(1) In PM models the more incompatible elements are always more enriched than less incompatible elements compared to batch melting. In CSM models this only occurs at relatively low degrees of melting (<5 to 10%), and is very sensitive to the porosity (ϕ). Where the changeover occurs to greater relative enrichment of a less incompatible element, is largely a function of the relative differences in partition coefficients of the two elements. The occurrence of these crossovers is very important, for it demonstrates an error in the widely held belief that dynamic melting processes result in greater relative enrichments of more incompatible elements when compared to batch melting. This is readily borne out by illustrating examples of parent/daughter ratios of common isotopic systems (see Fig. 3.4), and also two further examples of REE ratios which, as will be seen below, have implications for the melting of garnet peridotite source (Figure 3.5).

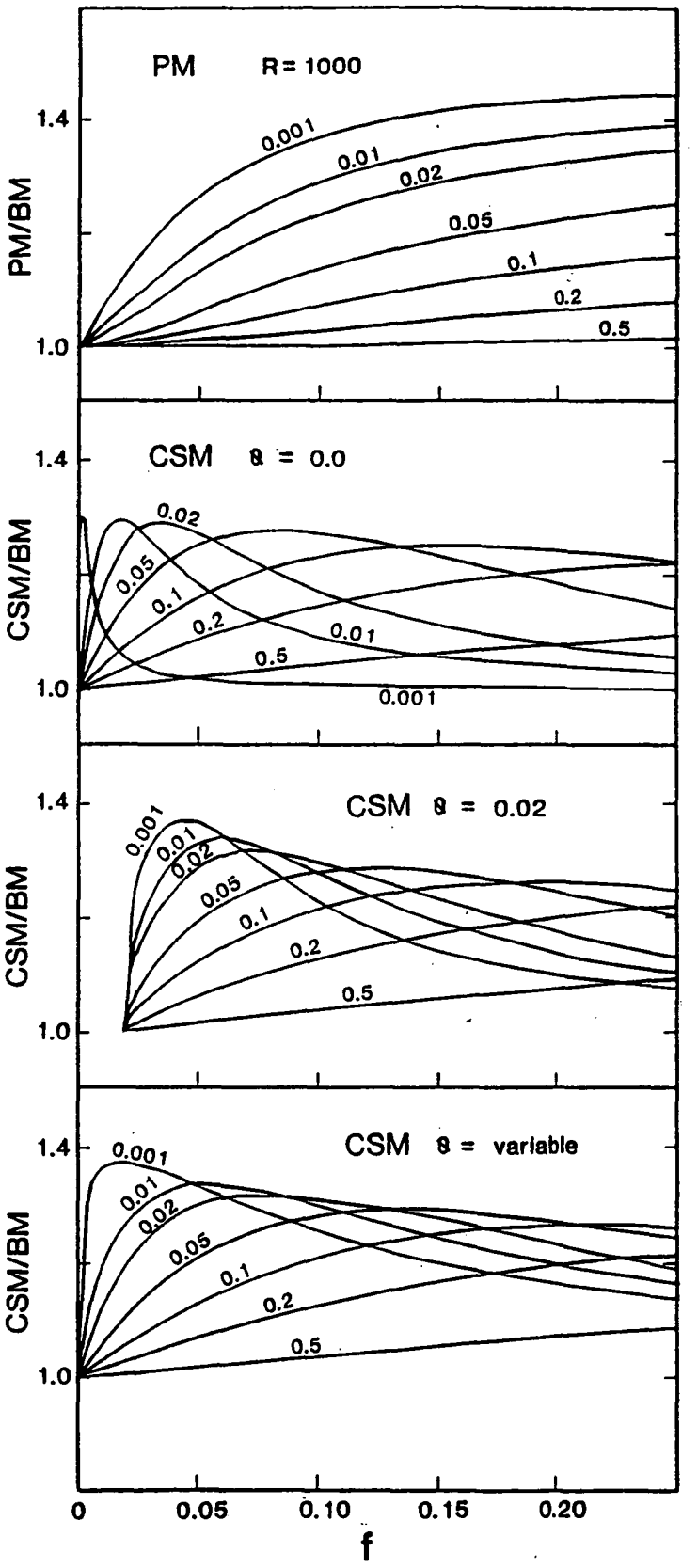

Figure 3.3 Batch melting normalised concentrations of incompatible trace elements generated by variable degrees (f) of PM and CSM. Results are illustrated for a range of element incompatibilities (Di_0 = 0.001-0.5), and a range of porosity values for the CSM models.

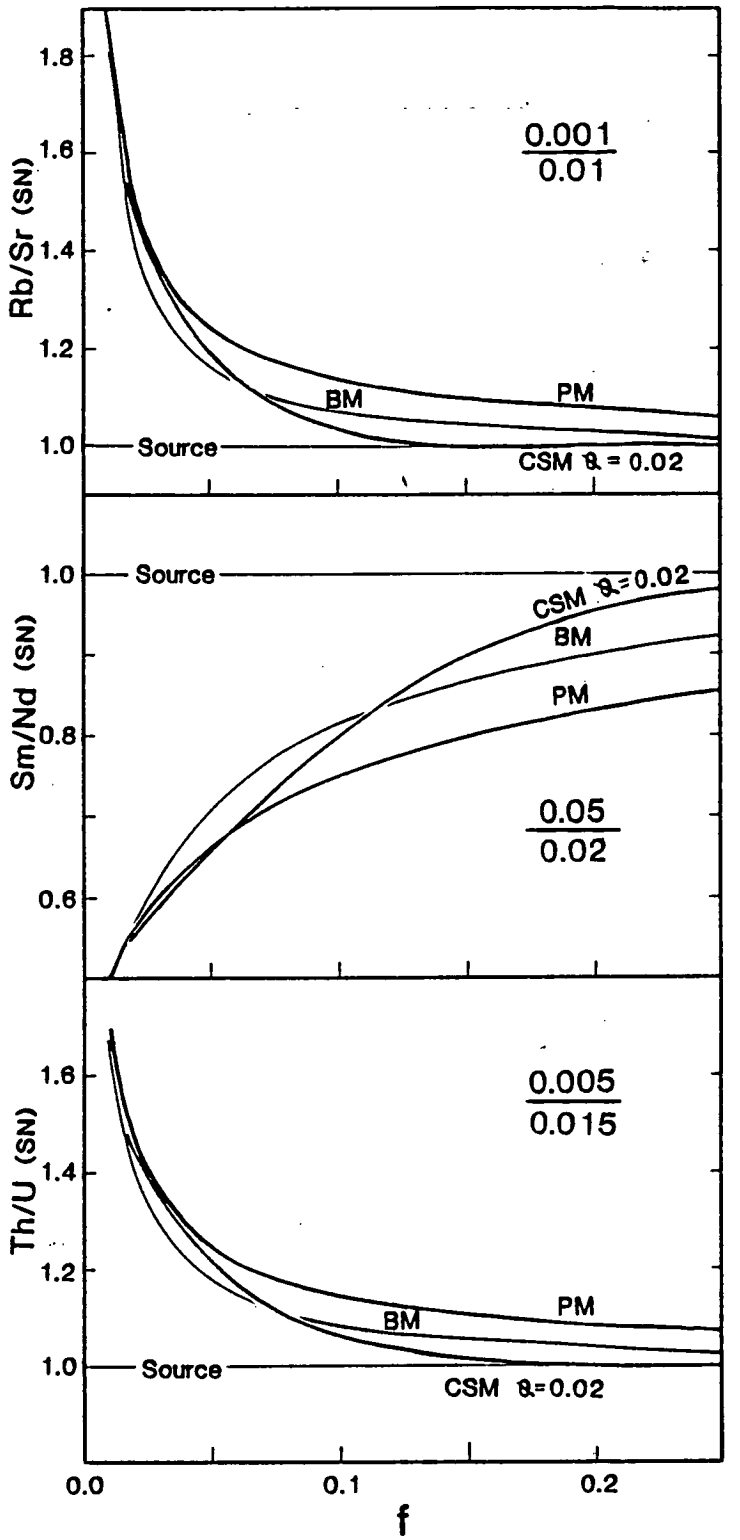

Figure 3.4 A comparison of the incompatible trace element behaviour produced by variable degrees of CSM, PM, and batch melting (BM) for several radiogenic isotope parent-daughter element pairs. The D^i_S values assigned to the parent-daughter pairs of each example are shown as ratioed values. Note that in CSM, parent-daughter ratio values approach the source values (i.e. SN = 1) more closely than either PM or BM at moderate to large degrees of melting (>5 to 10%).

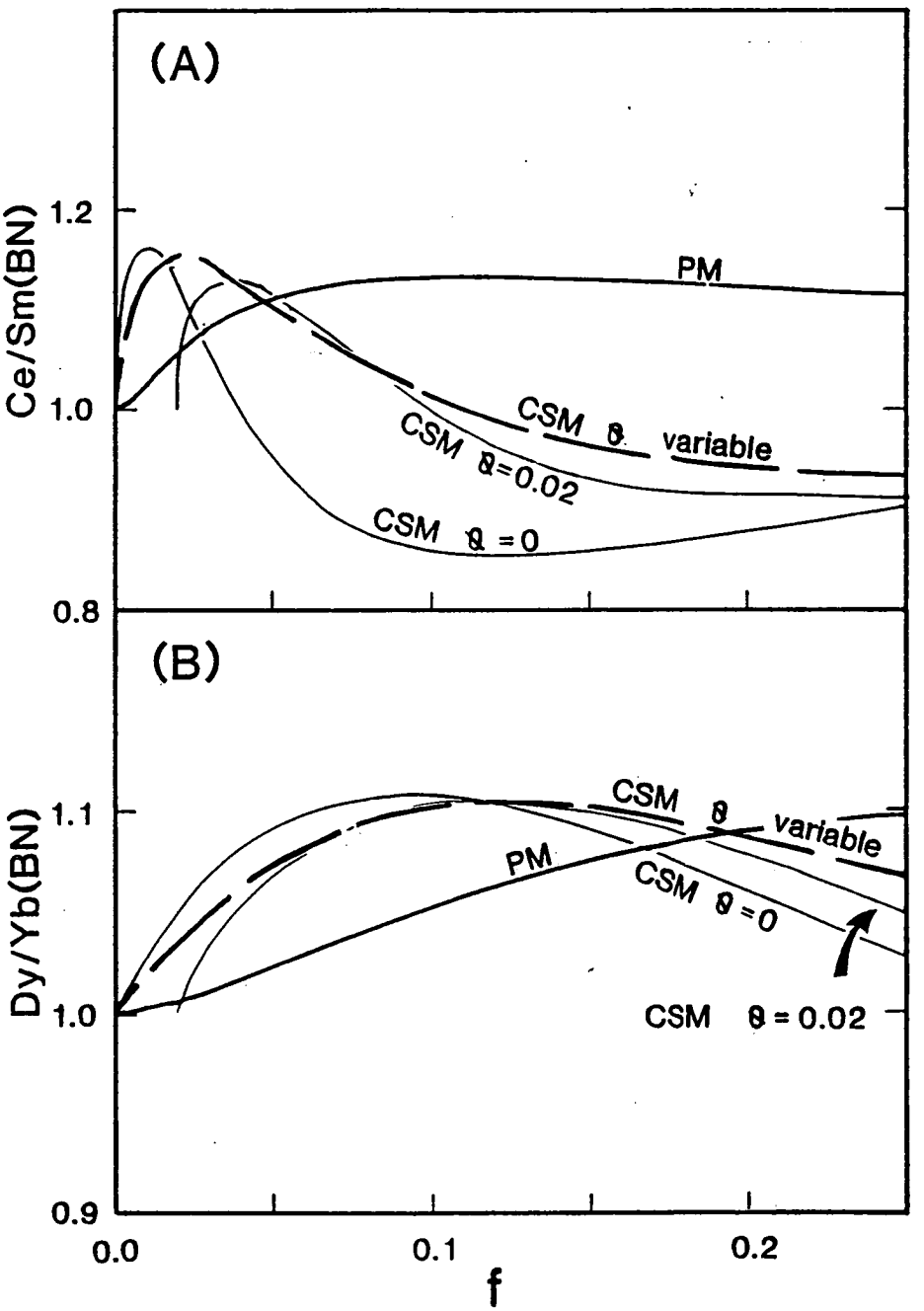

Figure 3.5 Behaviour of selected REE ratios produced by PM and CSM of a model garnet peridotite source. Ratio values are normalised to those produced by batch melting at equivalent degrees of melting. (A) compares results for Ce/Sm, a measure of LREE enrichment, whereas (B) illustrates the behaviour of a middle REE/HREE pair which is suitable as a measure of the fractionation of HREE. Note the more LREE-depleted nature of melts forming by CSM than by either batch melting or PM at small to high degrees of melting (i.e f >0.05). This contrasts with the similar HREE fractionation produced by CSM and PM over a large range in melting degree. Bulk partition coefficients used are $D_o^{Ce} = 0.01$, $D_o^{Sm} = 0.05$, $D_o^{Dy} = 0.10$, and $D_o^{Yb} = 0.25$, which are based on a source mode of 65% olivine, 20% orthopyroxene, 10% clinopyroxene, and 5% garnet.

(2) The moderately incompatible elements (D^i_0= 0.1-1.0) are gradually enriched relative to BM in both CSM and PM models. The highly incompatible elements are also progressively enriched relative to BM in PM models, however, in CSM models they pass through a maximum enrichment at low f values, prior to decreasing to absolute abundance levels near those produced by BM.

3.4.1 PM and CSM models and the Generation of Hawaiian REE Patterns

To facilitate modelling of Hawaiian REE characteristics using PM and CSM models, the standard chondrite-normalised REE plots have been reduced to a bivariate plot which, in effect, provides a measure of LREE enrichment (i.e. Ce/Sm_{CN}) against a measure of HREE fractionation (e.g. Dy/Yb_{CN} or Tb/Yb_{CN}). To aid visualising the corresponding REE patterns a series of REE patterns are provided in insets in Figure 3.6.

A comparison of the variation in REE patterns arising from variable degrees of PM, CSM (o = 0.02), and batch melting (BM) is illustrated in Figure 3.6. Calculations have been performed assuming a chondritic source (i.e. $Ce/Sm_{CN} = Tb/Yb_{CN} = Dy/Yb_{CN} = 1.0$) and partition coefficients for Ce, Sm, Tb, Dy, and Yb which are appropriate for modal melting of a garnet peridotite source (see Fig. 3.6 for details). The different melting models produce reasonable separation of derivative melt compositions at 10 to 20% partial melting, but the scatter observed in the Hawaiian data is such that no basis exists for preference of one melting model over another. It is also apparent that slight variations in source LREE characteristics (i.e. Ce/Sm_{CN} values) are sufficient to swamp the effects which might distinguish between the melting models.

3.5 DYNAMIC MELTING WITH VARIABLE BULK PARTITION COEFFICIENTS

Melting models which do not consider variable D^i_0 values during partial melting are potentially misleading. During decompression melting both clinopyroxene and garnet, the major repositories of REE in peridotite, will play diminishing roles as residual phases for they are preferentially consumed by non-modal melting and/or solid-solid reactions. Consequently, the bulk partition coefficients of many incompatible trace elements are likely to decrease markedly as melting progresses.

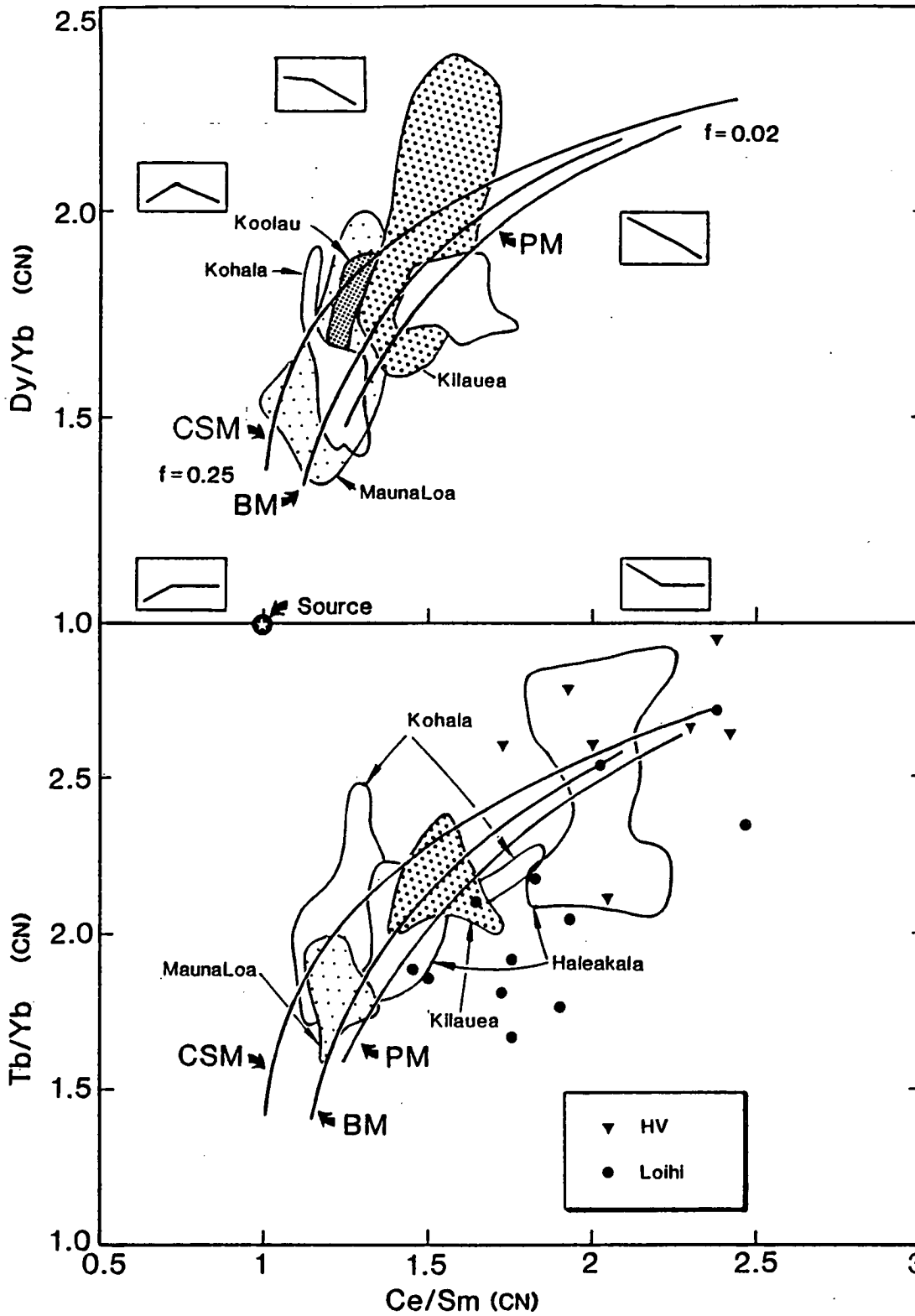

Figure 3.6 A comparison of REE characteristics generated by PM, CSM, and batch melting over a range of melting degrees from 2 to 25%, of a source with chondritic relative abundances of REE. Insets illustrate the shape of REE patterns in various regions of the diagram. Fields of chondrite-normalised data for individual Hawaiian volcanoes have been compiled from Budahn and Schmitt (1984), the BVSP (1981), Casadavell and Dzurisin (1987), Chen and Frey (1985), Clague and Frey (1982), Feigenson et al. (1983), Feigenson (1984), Frey and Clague (1983), Hofmann et al. (1984), Hofmann et al. (1987), Lanphere and Frey (1987), Roden et al. (1984), and Tilling et al. (1987). Note the generally similar pattern of REE behaviour in each of the melting models, and the transition from alkaline (e.g. Honolulu Volcanics) to tholeiitic (e.g. Mauna Loa) REE patterns occurring with increasing degree of melting.

If the CSM equations are used incrementally they can be adapted to account for variable D^i_0 values. Conveniently, the moderately incompatible elements, which are most sensitive to the presence/absence of residual garnet (i.e. middle and HREE), behave similarly at moderate to large (5-25%) degrees of melting in both PM and CSM models (Fig. 3.5). The results acquired by modelling CSM should thus also apply to PM.

To test the suitability of picritic compositions as primary Hawaiian melts, it should first be recognised from preceding arguments that to generate these compositions, decompression melting must continue until levels at or shallower than the experimentally-determined multiple (peridotite) saturation points of picritic compositions (i.e ~2.0 GPa, 1450°C). At such shallow levels and high temperatures the residues are likely to be harzburgitic, with garnet having melted-out with decompression near or >3.0 GPa (Chapter 2). Bulk partition coefficients (PC's) may be calculated for the peridotite residue during melting if the residual phase proportions are assumed to vary simply as a function of degree of melting (f). For simplicity, it will be assumed here that they vary linearly with f. In accordance with experimental evidence for residual harzburgite, clinopyroxene is somewhat arbitrarily set to be melted-out at the maximum degree of melting (f_{max}). Garnet exhaustion, on the other hand, is allowed to vary freely within the limits of melting (i.e. between f = 0 and f_{max}).

To account for a wide range of possible REE partitioning behaviour between residual phases (i.e. olivine, orthopyroxene, clinopyroxene, and garnet) and liquids, a number of PC sets are employed in the following modelling, including PC sets 1, 3, and 5 from Frey et al. (1978), and the PC set used by Hofmann et al. (1984). These REE PC's are selected on the basis of relatively low $D_0^{HREE}{}_{Gt\text{-}Liq}$ values, to be consistent with the trend toward decreasing $D_0^{HREE}{}_{Gt\text{-}Liq}$ values with increasingly high temperatures (e.g. Nicholls and Harris, 1980). In fact, the $D_0^{HREE}{}_{Gt\text{-}Liq}$ values of the PC sets used may be regarded as maximum values, for they are based on determinations made at temperatures up to several hundred degrees below (i.e. 1200-1340°C) the inferred melting conditions of the primary Hawaiian picrites (i.e. ~1450°C). Likewise clinopyroxene REE PC's decrease with increasing temperature, but conversely increase with pressure (Green and Pearson, 1985). These authors suggest the use of $D_0^{HREE}{}_{Cpx\text{-}Liq}$ values for mantle melting between 0.6 and

1.1 (at T ~1300°C), however, extrapolation of their high pressure data to ~1450°C results in $D_0^{HREE}{}_{Cpx\text{-}Liq}$ between 0.4 and 0.7. On this basis, PC set 5 of Frey et al. (1978) and the PC set employed by Hofmann et al. (1984), probably provide the best estimates available for modelling melting beneath Hawaii.

Prior to presentation of results of numerical experiments, it is informative to reconsider the role of garnet during decompression melting, and where it can be expected to be a residual phase. For PM models the final pressure of melting will correspond to the multiple saturation point of picritic Hawaiian tholeiites (~2.0 GPa), and for CSM models melting is required to extend to even lower pressures given the rationale for the "point and depth average composition" outlined above. Consequently, decompression melting is required to proceed beyond the high temperature garnet peridotite stability limit (i.e. ~3.0 GPa at 1500°C; Chapter 2) by at least 1.0 GPa. Peridotite melting rate estimates of ~12%/GPa (Klein and Langmuir, 1987; after Turcotte and Ahern, 1978), 12-16%/GPa (Ribe, 1988), and 8-10%/GPa (McKenzie, 1984) indicate that garnet-out will be surpassed by a further 8-16% partial melting. A very conservative value of 5% melting past garnet-out shall be adopted here, but a value nearer 10% may be more appropriate.

To allow for possible variation in peridotite bulk compositions two source models (A&B), comprising different starting mineralogies corresponding to fertile and depleted compositions, have been modelled (see Fig. 3.7 for details). Curves marked "Gt-out" in Figure 3.7 correspond to variable degrees of melting (from 3 to 20%) at the point of garnet exhaustion (i.e. garnet-out), as modelled using the four separate PC sets. The curves marked "Gt-out+5" represent 5% melting past garnet-out at corresponding further degrees of melting varying between 8 to 25%. These curves demonstrate that as the degree of melting exceeds where garnet ceases to be a residual phase, the primary melt REE patterns rapidly approach the source REE characteristics. This arises mainly from the integration of melt increments forming near, and immediately after garnet exhaustion, which have middle $REE/HREE_{CN} << 1$ and Yb concentrations greater than the aggregate melt composition contributed from the garnet-present interval of melting. It is clear that the fractionated REE patterns of Hawaiian tholeiites (e.g. Dy/Yb_{CN} ~1.5-2.0) cannot be explained by dynamic melting processes as modelled here, unless melting occurs entirely

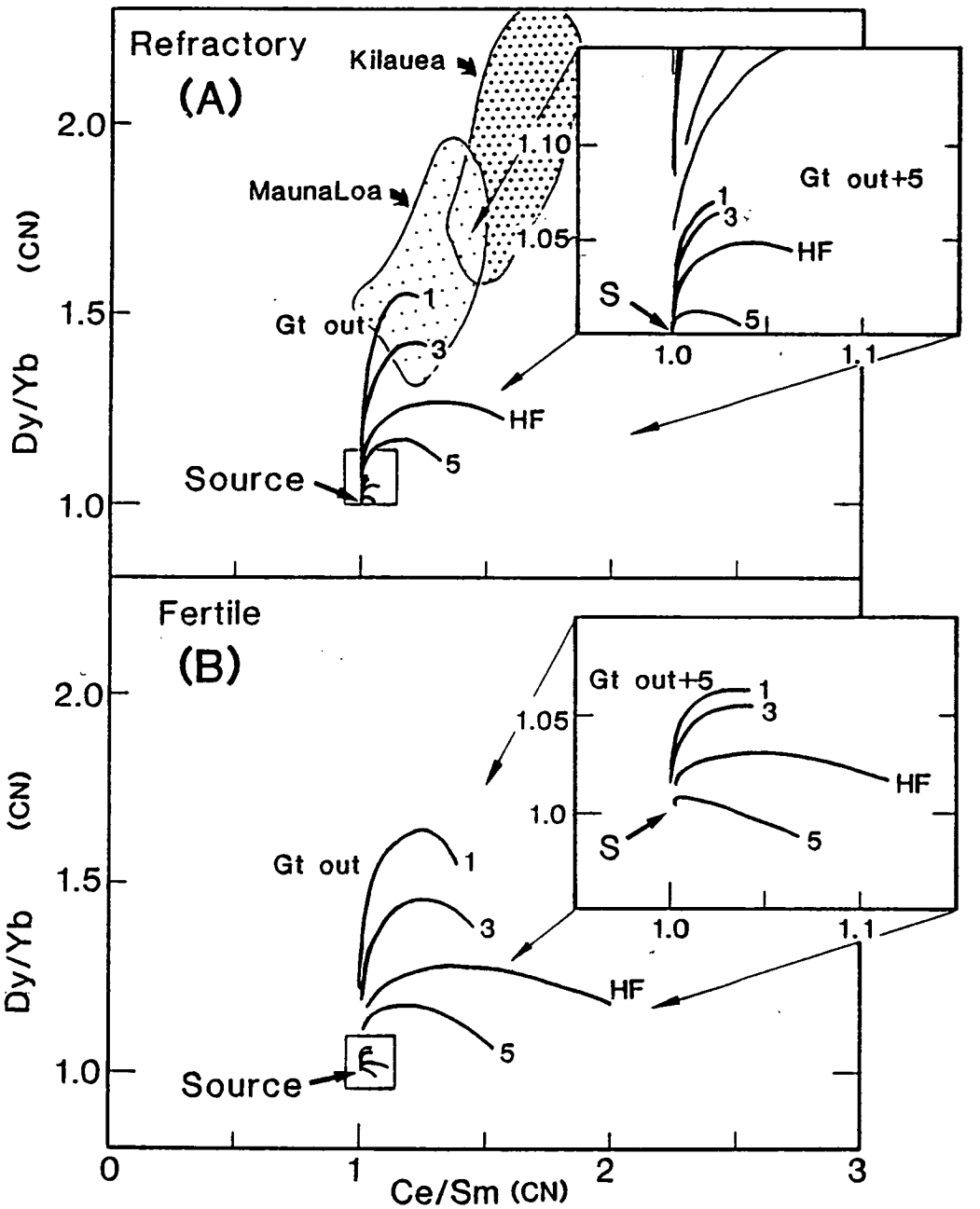

Figure 3.7 REE characteristics (patterns) produced by non-modal dynamic melting (i.e variable D^i_S values) of depleted (A) and fertile (B) garnet peridotite sources possessing chondritic relative REE abundances. Curves with arrows outline the trend in REE patterns generated by increasing absolute degrees of melting (5 to 25%) at the point where garnet is eliminated as a residual phase (marked "Gt-out"), and where elimination of garnet is exceeded by a further 5% melting (marked "Gt-out+5"). The numerals 1, 3, 5, and HF refer to the partition coefficient sets used to calculate each curved trend. Insets show an expanded portion of each diagram to illustrate the close approach of REE characteristics to those of the source when melting exceeds garnet-out by an additional 5%. In all calculations it has been assumed that f = X; a reasonable approximation for large degrees of melting when o is small (here assumed to be 0.02). Kilauea and Mauna Loa reference fields are shown as shaded regions in (A).

within the presence of residual garnet (i.e. at P >3.0GPa). Alternatively, the source is required to have middle $REE/HREE_{CN}$ values >1.

3.6 DYNAMIC MELTING WITH MELT ACCUMULATION IN THREE DIMENSIONS

O'Hara (1985) outlined a need to consider the three dimensional (3D) effects of magma accumulation from partially molten mantle volumes. For a hot upwelling mantle plume, now the most commonly proposed model for Hawaii, a radial decrease in temperature away from the plume core may be expected. The relationship between mantle flow lines, temperature distribution, and the mantle solidus within the plume is likely to influence the degree of melting such that it will diminish toward the plume's margin. The degree of melting undergone by a unit mass of mantle, passing along a particular flow line through the plume, may be considered to vary as a function of the flow line's radial distance from the plume centre (i.e. plume's vertical axis). No compelling evidence exists for the selection of a particular "melting shape", which will be a complex function of the peridotite solidus, plume form, and melt accumulation process. In order to evaluate the effects of plausible 3D melting and melt accumulation schemes, a variety of functions F(f,r) describing the radial variation in the degree of melting have been modelled, including

$$\text{Shape 1} \quad F(f,r) = f_{max} - f_{max}.r^2 \tag{3.10}$$

$$\text{Shape 2} \quad F(f,r) = f_{max} - f_{max}.r \tag{3.11}$$

$$\text{Shape 3} \quad F(f,r) = f_{max} - 2.f_{max}.r + f_{max}.r^2 \tag{3.12}$$

$$\text{Shape 4} \quad F(f,r) = 0.5.f_{max}.\cos(\pi.r) + 0.5.f_{max} \tag{3.13}$$

Schematic cross sections through partially molten regions with these shapes are depicted in Figure 3.8.

The concentration of a trace element *i*, formed by the aggregation of melt increments forming within these partially molten volumes, have been calculated using a simple numerical integration procedure. This involves division of the mantle plume into a sufficiently large number (n = 20) of cylindrical pipes (as outlined in Fig. 3.9), for each of which the average degree of melting is calculated by integrating F(f,r) between the

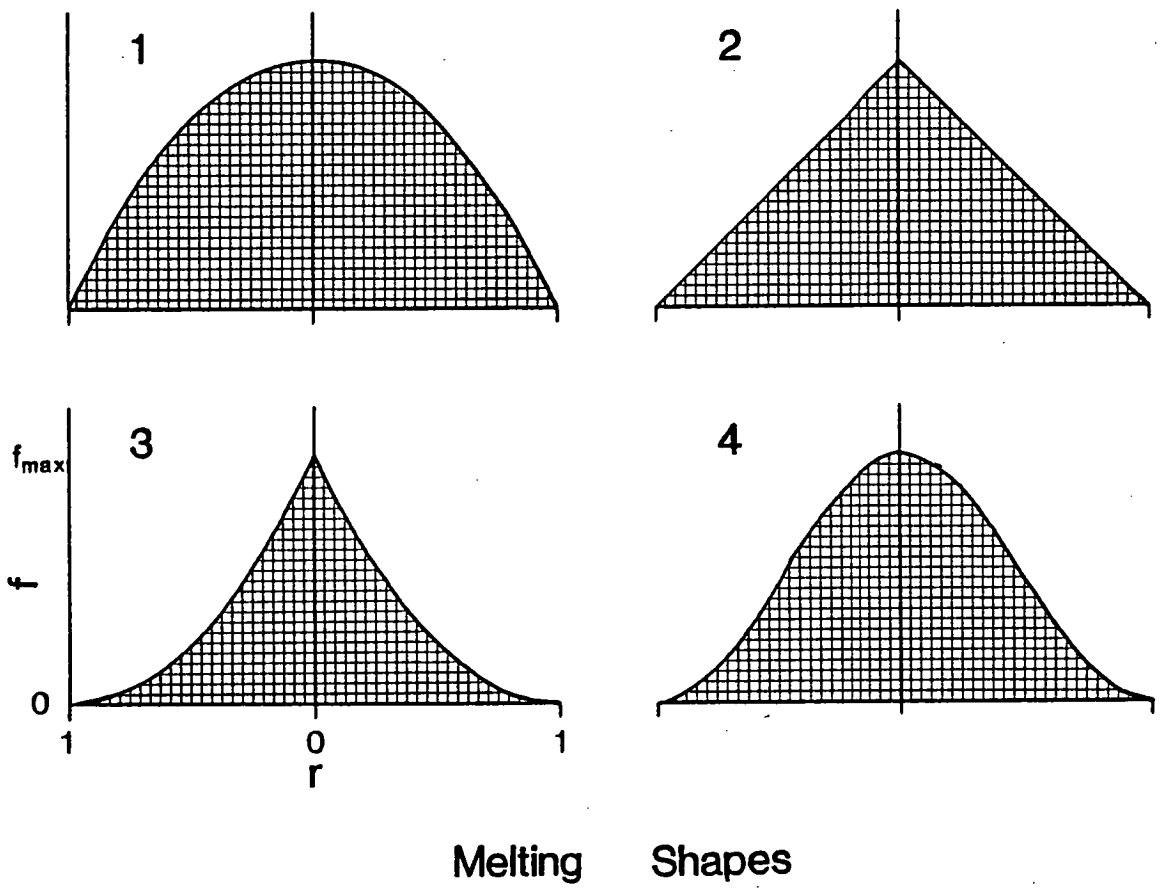

Figure 3.8 A comparison of cross sections through three dimensional melting shapes investigated in this study. Numerals refer to the shapes described by equations 3.10 to 3.13.

individual cylinders' inner and outer radii. The average concentration of a trace element *i* produced by melting in any particular cylinder is derived, as previously, from equation (3.5). The melt fractions from each cylinder are then integrated by taking into account the relative mass of melt derived from each cylinder i.e.

$$M_n = \pi . X_n . (r_{n(outer)}^2 - r_{n(inner)}^2) \qquad (3.14)$$

where M_n = relative mass of melt derived from cylinder n

X_n = fraction of melt extracted from cylinder n

$r_{n(outer)}$ and $r_{n(inner)}$ = inner and outer radii of cylinder n

to give the concentration of *i* in the three dimensional dynamic melt i.e.

$$C^{3i} = \sum_{1}^{n} (C^{i}_{n} . M_n) / \sum_{1}^{n} M_n \qquad (3.15)$$

where C^{i}_{n} = the concentration of *i* in melt derived from cylinder n.

A range of 3D dynamic melt compositions have been calculated following the procedure of the earlier and simpler numerical experiments, by varying the maximum degree of melting at r = 0 between 10 and 25%, and by allowing the degree of melting where garnet ceases to be a residual phase, to vary within these limits. Results for selected combinations of the four melting shape models, four PC sets, two mantle sources (A&B), and variable degrees of melting exceeding garnet-out are displayed in Figure 3.10.These illustrate the marked effect that 3D "melting shapes" have on trace element characteristics compared to simpler melting schemes. They again illustrate how important the parameter "degree of melting past garnet-out" is in determining the REE characteristics of the derivative melt.

The models most consistent with Hawaiian REE patterns are those combining the more fertile source regions, PC sets where garnet discriminates more between the middle and HREE (e.g. Set 1), melting shapes that have disproportionately large contributions from low melting fraction peripheral regions (e.g. Shapes 2 and 3), and also when the degree of melting exceeding garnet-out is relatively small. Regardless of these efforts to reproduce the Hawaiian tholeiite REE patterns from a source with chondritic relative REE abundances, many of the 3D solutions are unsuccessful (see Fig.3.10), including a preferred model based on PC set 5 and larger (>5%) degrees of melting past garnet-out.

Whether the 3D melt segregation and accumulation processes are capable of homogenising all melt formed in a partially molten mantle volume is of critical importance

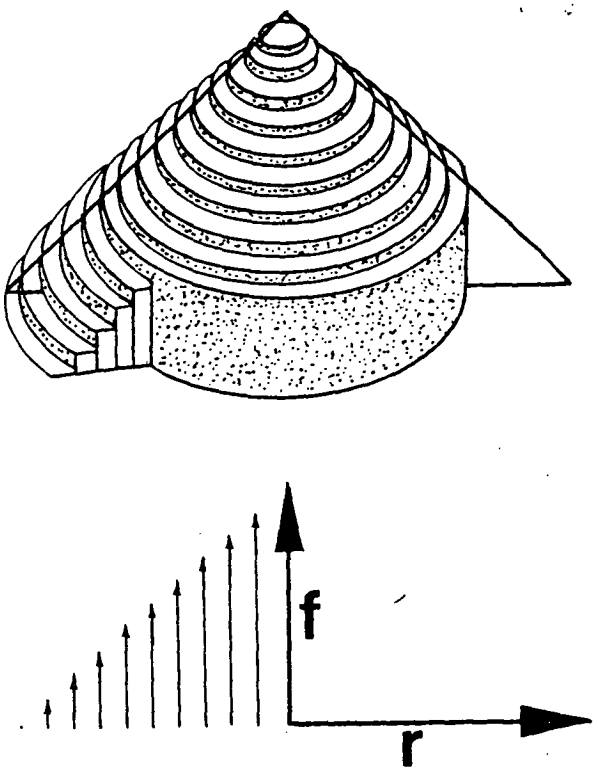

Figure 3.9 A schematic illustration of the method used to calculate three dimensional dynamic melt compositions. The partially molten mantle volume is divided into multiple cylinders, within which the degree of melting is then treated as a function of the radial distance from the centre of the molten region (i.e. central axis of the upwelling plume).

Figure 3.10 A comparison of REE characteristics (patterns) produced by comprehensive three dimensional dynamic melting models over a range of absolute degrees of melting from ~10 to 25%. The following is a list of parameters used in each example:

(a) melting shapes 1, 2, 3, and 4 (as labelled), and partition coefficient (PC) set 3, source model A, and 5% melting past garnet-out;

(b) PC sets 1, 3, 5, and HF, 5% melting past garnet-out, source model A, and melting shape 4;

(c) refractory source model A (thin lines) and fertile source model (B) with all other parameters as for (a);

(d) REE characteristics at 5, 7, and 9% melting past garnet-out, calculated for PC set 3, source model A, and melting shape 4.

Reference fields for Mauna Loa and Kilauea are taken from Figure 3.5.

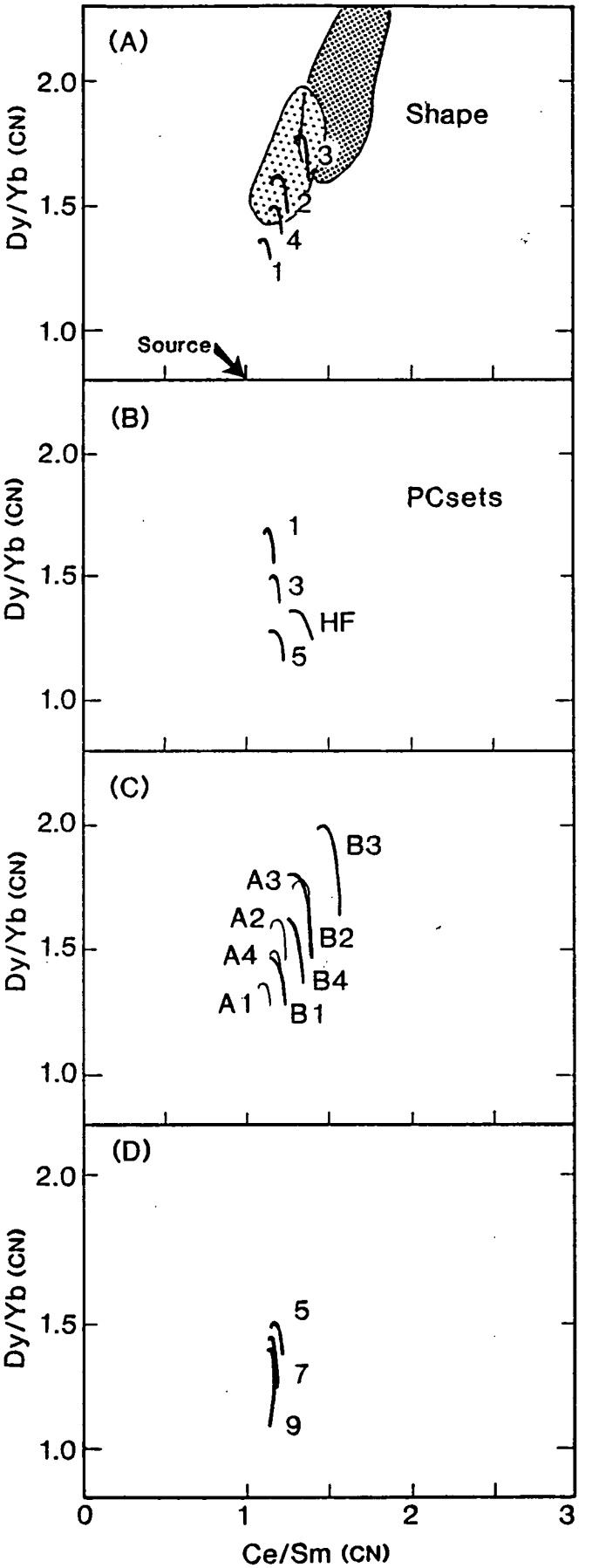
(A)
Shape
Source
(B)
PCsets
HF
(C)
(D)
Dy/Yb (CN)
Ce/Sm (CN)
2.0
1.5
1.0
0
1
2
3

if these models are to be endorsed. Fluid dynamical modelling of melt and matrix flow at the top of a mantle plume by Ribe and Smooke (1987), indicates that melt segregating from the upwelling plume is not drawn toward the plume centre, but rather tends to migrate away from the plume centre with the advective matrix flow. Even if unaccounted for non-hydrostatic pressure gradients were to force melt toward the plume centre, it would be unlikely that such a process could draw melt formed beyond a certain radial distance from the plume centre, as has been demonstrated for melt extraction beneath mid ocean ridges where *large* suction forces may exist (Spiegelman and McKenzie, 1986; Ribe, 1987). Significant contributions of peripheral melts therefore seem to be unlikely on fluid mechanical grounds.

The fluid dynamical model of Ribe and Smooke (1987) suggests that the composition of primary melts deriving from upwelling (buoyant) mantle plumes is probably best considered in terms of simple vertical (though their model is strictly two dimensional) melt accumulation models. Given these arguments it becomes clear that dynamic melt extraction processes are incapable of generating the residual garnet geochemical signatures observed in Hawaiian tholeiites from a source with chondritic relative abundances of the middle and HREE, unless melting occurs entirely within the field of garnet stability. This matches the conclusions deduced previously from batch melting models.

3.6.1 Some Observations from Hawaii

An important observation, with implications for melt accumulation processes beneath Hawaii, can be made from the spatial distribution of magmas representing lower degrees of melting (e.g. alkali olivine basalt, basanites, nephelinites, melililitites), which are erupted at both the leading and trailing edges of the Hawaiian hotspot (e.g. Feigenson, 1986; Clague, 1988). This provides *apriori* evidence against the incorporation of peripheral small melt fractions into an aggregate composition representing the 3D volume of partially molten mantle. Potential indicators of the degree of melting (e.g. $Ce/Sm_{(CN)}$ ratio values) vary systematically from high values (small f) in suites of peripherally erupted lavas, to minimum values (maximum f) for Mauna Loa (Fig. 3.11). On this basis, Mauna Loa may represent the Hawaiian hotspot/mantle plume focus. The spatial variation

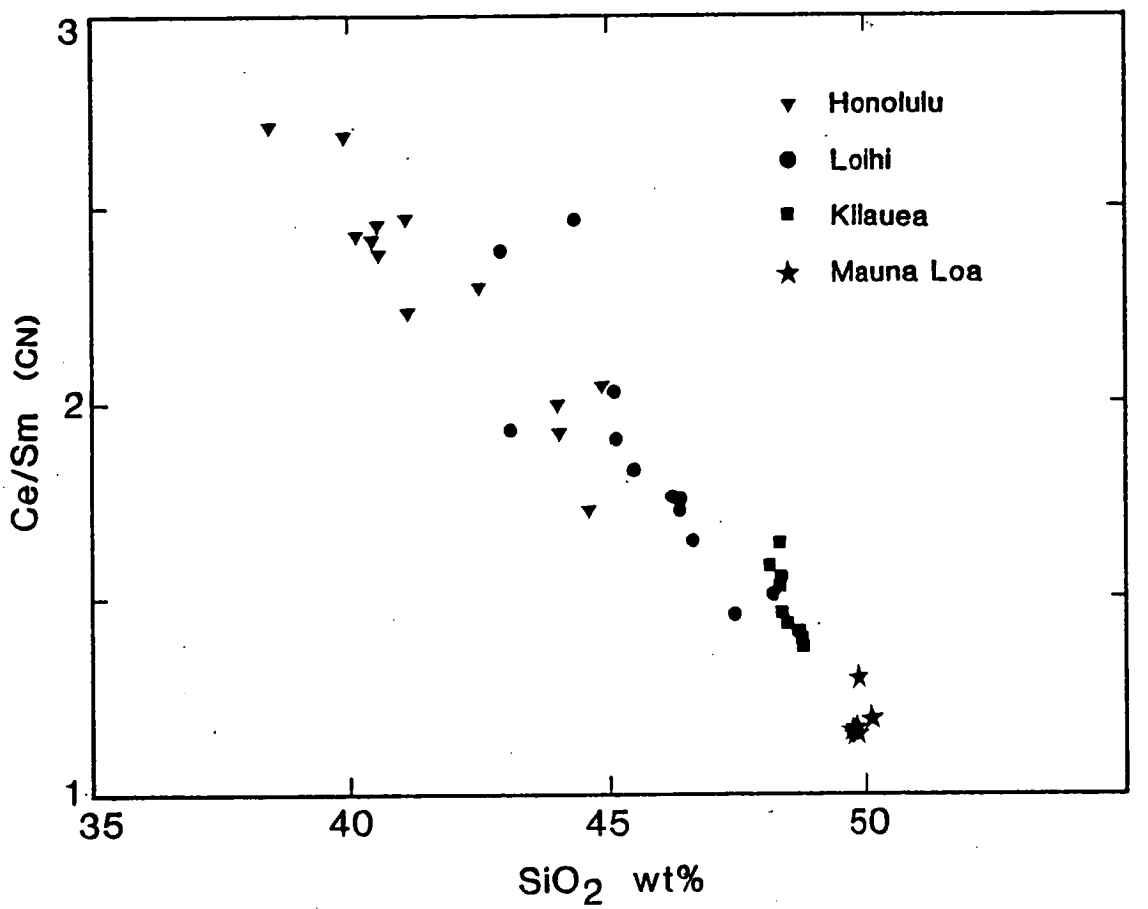

Figure 3.11 Chondrite-normalised Ce/Sm versus SiO_2 covariation in representative suites of Hawaiian parent compositions. All SiO_2 values have been corrected for olivine-fractionation in order to produce "equally" primitive bulk compositions with ~16wt% MgO. The methods used in this fractionation-correction procedure are outlined in Chapter 2. Data sources include the BVSP (1981), Clague and Frey (1982), and Frey and Clague (1983).

in Hawaiian melt chemistry is thus consistent with the theoretical model of Ribe and Smooke (1987), which predicts predominantly vertical melt flow with a slightly divergent flow component away from the plume centre.

In conclusion, little theoretical or observational evidence supports a 3D melt accumulation and melting model for the generation of Hawaiian tholeiites. Instead, numerical solutions based on vertical migration of melt should provide the best estimates of trace element behaviour observed in Hawaiian and other hotspot-related basalts. The role for 3D melting effects is most likely restricted to explaining radial (horizontal) variations in the degree of melting occurring in plan sections through upwelling mantle plumes.

3.7 IMPLICATIONS FOR HAWAIIAN MAGMAGENESIS

Mantle plume models provide a foundation for petrologic, geochemical, and geophysical models for Hawaiian volcanism. A principle uncertainty in these models is the extent to which lithospheric material contributes to the source of Hawaiian magmas. Determining the depth of origin of primary melts is a key to understanding this problem. This study provides an important contribution to this debate by ruling out dynamic melting as a mechanism via which possible picritic primary melts segregated at shallow levels (~2.0 GPa) can be equated with chondrite-based source geochemical models. The origin of Hawaiian tholeiites thus remains, as previously resolved by simple batch partial melting models, polarised between :

(1) shallower melting of incompatible element enriched sources to produce primary picritic melts, and

(2) deep garnet-present melting (~3 GPa) models, involving sources with chondritic relative middle and HREE abundances,which result in the generation of ultramafic primary melts (Chapter 2).

Geophysical estimates indicate the oceanic lithosphere is about 90-100km thick near Hawaii (e.g. Dettrick and Crough, 1978). This has several important implications for the competing picritic and ultramafic Hawaiian primary melt models, as outlined in Chapter 2. Deeply-derived ultramafic melts, with ~20 wt% MgO or more, will segregate

beneath the oceanic lithosphere, and may have little interaction with the lithosphere apart from minor fractionation and assimilation processes occurring during magma ascent to shallow storage reservoirs. Primary picritic melts (~16wt% MgO), on the other hand, require considerable erosion of the oceanic lithosphere during magmagenesis. In this case, the lithosphere may contribute significantly to the magma source volume, and may provide the recent source enrichments in incompatible elements necessitated by this model. Further implications stemming from these competing models, for the nature of the magma source regions of ocean island tholeiites, are addressed in greater detail in Chapter 4.

3.8 DISCUSSION

Numerous previous studies addressing the geochemical effects of dynamic melt segregation processes have noted a similarity in results to those returned by simple batch melting models (e.g. Richter and McKenzie, 1984). This is particularly true for the less incompatible elements in both PM and CSM models, and also the behaviour of more incompatible elements in CSM at moderate to large degrees (5-25%) of melting. On the other hand, highly incompatible elements at moderate to large degrees of PM, become increasingly enriched relative to BM models. An important feature of CSM models is that relative enrichment of more incompatible elements over less incompatible elements is considerably less than in BM at similar, moderate to large, degrees of melting. This is contrary to the widely perceived behaviour of trace elements during dynamic melting processes.

The differences in the geochemistry of melts produced by CSM and PM may exceed those occurring between either CSM or PM and BM. It can be shown that BM models will provide a more accurate representation of certain geochemical parameters produced during mantle melting (i.e. incompatible element ratios), than in the event that the melt segregation process is unknown. Furthermore, if melt segregation occurs via a mix of CSM and PM processes, BM may provide the best approximation to the behaviour of incompatible element ratios.

Whether melt-filled channels (dykes) can form in partially molten mantle is a matter of some debate (Sleep, 1988). Moreover, whether such channels can be continuous

and capable of transferring melt to considerably higher levels within molten regions is also unknown. These uncertainties are of critical importance if CSM models are to be applied to mantle melting with confidence, as is required for the modelling of McKenzie and Bickle (1988) and also Williams and Gill (1989). Otherwise, to be successful, melting models must take into account the re-equilibration of melt with the matrix as both ascend to higher levels.

Finally, the possible need to consider 3D melting effects need only apply to partially molten mantle regions where lateral migration and accumulation of melt fractions can take place prior to eruption. This may occur where sufficient gradients in non-hydrostatic pressure exist, such as in models for melt segregation beneath mid ocean ridges (and other rift environments), where the divergent plate motion, in effect, sucks melt toward the axis of spreading (e.g. Spiegelman and McKenzie, 1987; Ribe, 1987). Similar forces may also affect melt segregation within the sub-arc mantle due to the influence of a slab-drag-induced mantle counterflow (Spiegelman and McKenzie, 1987). In both the arc and mid-ocean-ridge cases, the shape of the partially molten mantle region may be treated as being semi-infinite along one horizontal axis, which effectively reduces the melt segregation and accumulation problem to two dimensions (e.g. Holness and Richter, 1989). In upwelling mantle plumes, on the other hand, melt segregation is likely to be forced predominantly by its own buoyancy (Ribe and Smooke, 1987), with a small component of laterally divergent melt migration occurring in association with the advective matrix flow away from the plume top. Geochemical models in the plume case can be treated largely in terms of melt accumulation in a single (vertical) dimension. Given these observations, any consideration of melting in terms of three dimensional melt accumulation models is probably an over-assessment of geochemical problems associated with mantle melting.

3.9 CONCLUSIONS

1. The results of experiments performed here reveal that Hawaiian REE patterns are incompatible with claims, based on dynamic melting models, that primary picritic tholeiites (~16 wt% MgO) can be generated from source regions with chondritic relative abundances of REE.

2. Three dimensional dynamic melting and accumulation models requiring admixture of large volumes of low melting fraction peripheral melts can reproduce the REE characteristics of Hawaiian tholeiites in some instances. This ability is dependent upon the choice of partition coefficients for residual mantle phases, the degree of melting, source bulk compositions (fertile versus refractory), and the degree to which melting exceeds the melting out of garnet. These 3D melting models, however, may be ruled out on the basis of fluid dynamic considerations of melts and matrix flow within a partially molten mantle plume (Ribe and Smooke, 1987) and also the spatial geochemical variation observed in Hawaiian volcanism.

3. Possible models for the generation of Hawaiian magmas remain polarised between options for,

a) primary ultramafic melts derived from chondrite model-based peridotite source compositions, and

b) primary picrite melts derived by melting of incompatible element-rich source regions.

4. Dynamic melting processes do not necessarily lead to the generation of greater enrichment of more incompatible elements over less incompatible elements than that produced by equivalent degrees of batch melting.

CHAPTER 4

The Origin of Ocean Island Tholeiites - A Synthesis

4.1 INTRODUCTION

Tholeiites form the silica-rich end of the compositional spectrum of ocean island basalts, and their low relative abundances of incompatible elements show that they must correspond to the largest extent of partial melting if source composition is not the controlling factor in ocean island basalt suite geochemistry. The compelling evidence for "fixed hotspots" in plate tectonic models argues that the ultimate cause of hotspot volcanism is the presence of upwelling convective plumes representing both material and anomalous heat flow from deep within the mantle. If this model is correct then the petrogenesis of ocean island tholeiites provides an insight into the upper temperature limits to melting in the modern convective mantle and into the origins and characteristics of deep-seated mantle plumes.

A minority view argues that "hotspots" are caused by an excessive volatile (C-H-O) rather than an excessive heat flux from the underlying mantle. In this model, ocean island tholeiites are products of melt extraction from source volumes with elevated volatile elements, particularly C-H-O but also highly incompatible elements, compared to the sources for mid-ocean-ridge tholeiites. In terms of relative temperatures, the mid-ocean-ridges with their steady-state sampling of the asthenosphere would represent an upper limit for temperatures in the modern mantle.

Establishing ocean island tholeiite primary melt compositions and their PT conditions of origin is a major step toward reaching an understanding of convective activity in the mantle and in the processes responsible for "hotspot" volcanism.

4.2 THE NATURE OF PRIMITIVE OCEAN ISLAND THOLEIITES

Primary mantle melts can be expected to have $Mg^{\#}>67$ and relatively high Ni concentrations (200-600ppm; e.g. Hart and Davis, 1978). Possible variation in mantle source olivine compositions from $Mg^{\#}$ 87 to 92, and the pressure-dependent behaviour of Fe/Mg and Ni(?) partitioning over a range of conditions at which mantle may be partially melted, preclude a unique estimation of primary melt composition using these criteria alone.

On the other hand, firm evidence for the composition of primitive melts is available from olivine phenocrysts present in primitive lavas. Phase equilibria dictate that olivine will be the liquidus phase of primary mantle melts at depths less than the depth of magma segregation, and that it will dominate (+ minor Cr-spinel) the low pressure crystallisation of primitive tholeiites, as is confirmed by both petrographic observations and geochemical studies, in particular those documenting Hawaiian tholeiites (e.g. Wright and Helz, 1987). The most Mg-rich olivine phenocrysts occurring in OIT from Hawaii ($Mg^{\#}$ = 90.5; Chapter 2), Reunion ($Mg^{\#}$ = 89; Fiske et al., 1988), and the Tasmantid Seamounts ($Mg^{\#}$ = 86; Chapter 1) thus provide evidence for the most primitive melts sampled in these examples of tholeiitc volcanism. These parental compositions can be estimated in each case by correcting the compositions of observed or inferred liquids (e.g. glasses, crystal-poor whole rocks) for prior olivine fractionation until the calculated compositions are in equilibrium with the Mg-rich olivine phenocrysts (for details see Chapter 2). The high $Mg^{\#}$ (67-74) and Ni contents (300-720ppm) of parent melts calculated in this way (Table 4.1a) satisfy the criteria necessary for equilibrium with upper mantle peridotite noted above. The primary/near-primary nature of these compositions is further supported by the Ni-rich nature of the most magnesian olivine phenocrysts occurring in Hawaiian, Reunion, and Tasmantid lavas, which overlap with mantle olivine compositions, and match closely the modelled parent melt equilibrium olivine compositions (Table 4.1).

Table 4.1 Ocean island tholeiite parent melt composition estimates.

	Kilauea Iki	Mauna Loa	Reunion	Britannia	Gascoyne
Olivine Mg#	90.5[a]	90.5[a]	89[b]	86[c]	86[c]
SiO_2	48.19	49.57	47.57	52.41	50.54
TiO_2	2.05	1.63	2.17	1.33	1.92
Al_2O_3	10.19	10.77	12.19	14.15	13.90
Fe_2O_3	1.60	1.49	1.67		
FeO	9.85	9.73	9.90	10.48	10.19
MnO	0.16	0.17	0.17	0.14	0.15
MgO	16.05	15.91	13.49	9.43	10.30
CaO	9.39	8.38	9.65	8.40	8.59
Na_2O	1.83	1.80	2.22	2.85	2.97
K_2O	0.43	0.29	0.69	0.45	0.86
P_2O_5	0.20	0.19	0.25	0.32	0.54
Total	99.94	99.93	99.97	99.96	99.96
Nippm	850		620	302	301
Ni in Ol	0.53		0.47	0.42	0.39
3.0GPa parent compositions					
SiO_2	47.40	48.46	46.74	48.78	47.98
TiO_2	1.83	1.42	1.90	0.92	1.42
Al_2O_3	9.08	9.37	10.71	9.77	10.29
Fe_2O_3	1.48	1.38	1.55	1.26	1.29
FeO	9.62	9.45	9.76	8.86	8.65
MnO	0.15	0.16	0.17	0.13	0.14
MgO	19.71	20.38	17.81	21.70	20.42
CaO	8.37	7.29	8.48	5.80	6.36
Na_2O	1.63	1.57	1.94	1.97	2.20
K_2O	0.38	0.25	0.61	0.31	0.64
P_2O_5	0.18	0.16	0.22	0.22	0.40
Total	99.83	99.89	99.89	99.72	99.79
Ni ppm	1440		1300	2840	1850
Ni in Ol	0.66		0.63	1.10	0.85

Kilauea compositions are based on sample #KI0051 (Gunn, 1971), Mauna Loa on sample #HAW-9 (BVSP, 1981), Reunion on sample #GB1976 (Albarede and Tamagnan, 1988), Britannia on sample #68644 (Chapter 1), and Gascoyne on sample #65808 (Chapter 1). For details of olivine-fractionation-correction procedure see Chapter 2.

a Maximum olivine Mg# in Hawaiian tholeiites (Chapter 2).

b Maximum olivine Mg# in Reunion tholeiites (Fiske et al., 1988).

c Maximum olivine Mg# in Tasmantid basalts (Chapter 1).

4.3 THE RESIDUAL GARNET PARADOX!

4.3.1 Evidence from Phase Equilibria

High pressure liquidus studies on olivine tholeiite and picrite compositions, matching or similar to the calculated parents, demonstrate their equilibrium with mantle peridotite phase assemblages (usually harzburgite) at pressures between ~1.0 and ~2.2 GPa (Green and Ringwood, 1967a; Green, 1970; and Chapter 2: see Fig. 4.1). Confirmation of these results comes from peridotite melting studies (Falloon and Green, 1988; and Falloon et al., 1988), which predict equilibrium of the tholeiite parent compositions established here (Table 4.1) with harzburgite (or lherzolite in the Reunion case) at pressures between ~1.0 and 2.3 GPa (Fig. 4.2).

An assumed primary (or near-primary) origin for these parent melt compositions would imply that generation of ocean island tholeiites occurs by shallow melting, and does not involve equilibrium with residual garnet. Both liquidus and peridotite melting studies confirm that garnet-peridotite (olivine+garnet+orthopyroxene+clinopyroxene) can only be a residual phase assemblage for primitive volatile-poor tholeiite liquids at pressures >3.0GPa. To achieve garnet-peridotite saturation, the primary melts need to be more magnesian (olivine-rich) than the parent melt compositions estimated herein on the basis, of the most Mg-rich olivine phenocrysts occurring in these ocean island tholeiites.

4.3.2 Evidence from Trace Element Geochemistry

Middle REE/HREE ratio values greater than chondritic values are a ubiquitous feature of ocean island basalts (e.g. Frey and Roden, 1987; Liotard et al., 1986; Palacz and Saunders, 1986; Chapter 1) and intraplate volcanics generally. If it is assumed that the mantle sources of these basalts have chondritic middle REE/HREE values, consistent with both bulk earth geochemical models and upper mantle source compositions based on MORB chemistry, it becomes necessary for melting to occur in the presence of garnet to create the relative fractionation of middle and HREE observed in OIT (e.g. Frey and Roden, 1987). Moreover, small garnet-equilibrated melt fractions are a means of explaining LREE enriched compositions which are accompanied by Nd isotope signatures implying sources with time-integrated depletion of more incompatible elements (e.g Rb and LREE), as is the case for Hawaiian and Reunion tholeiites, and also for the more incompatible element-rich Tasmantid alkaline basalts (Chapter 1).

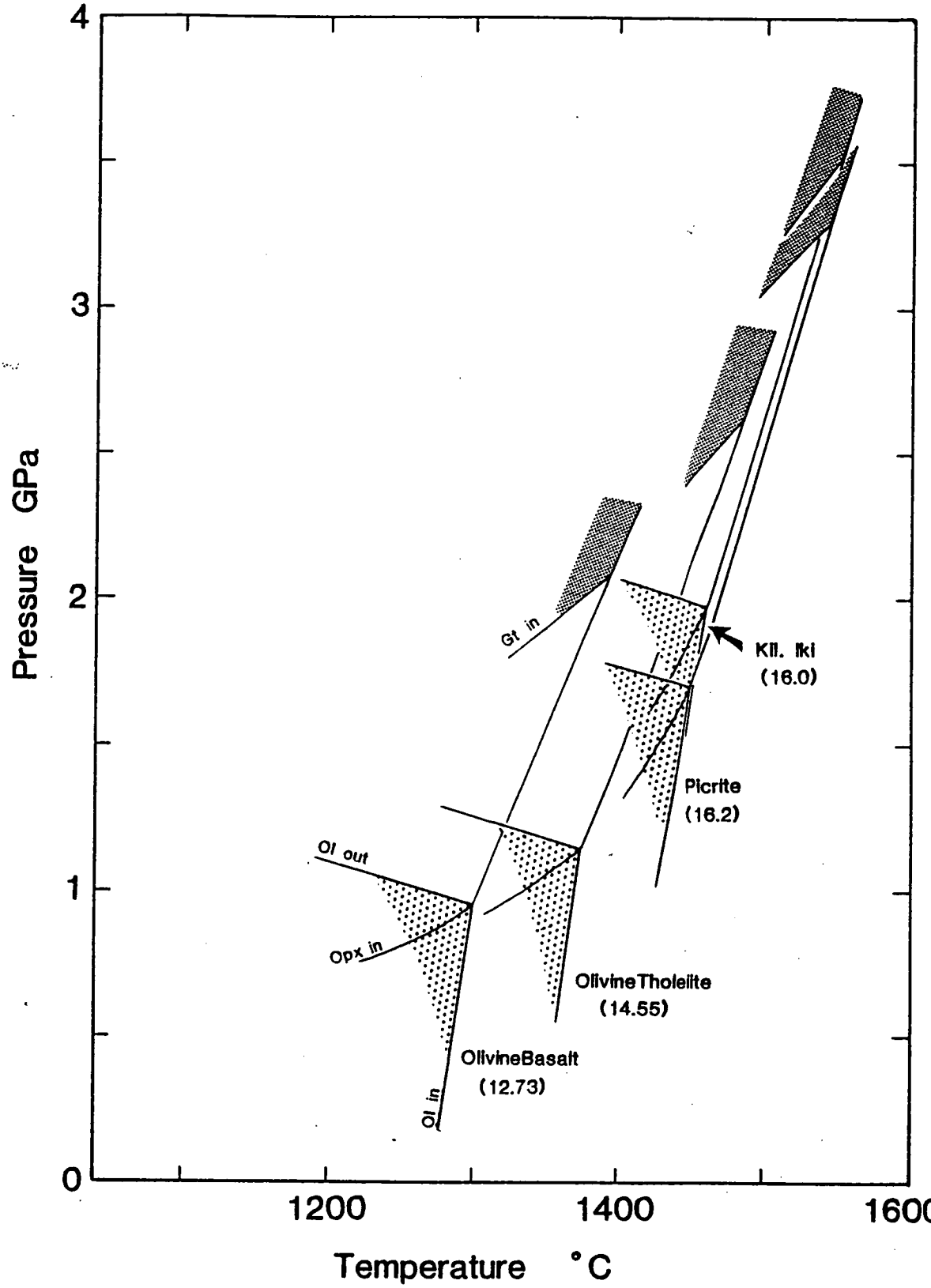

Figure 4.1 High PT phase relationships of experimentally-studied Hawaiian parent magma compositions (after Green and Ringwood, 1967a; Green, 1970; and Chapter 2). Stippled fields mark the PT maximum of the olivine phase volume, and the more heavily shaded fields indicate the closest approach of the liquidus garnet field to the multiple (peridotite) saturation point (Ol+Opx+Liq). "In" and "out" refer to the appearance and disappearance of phases with increasing pressure. Bracketed values are the MgO contents of the experimentally-studied bulk compositions.

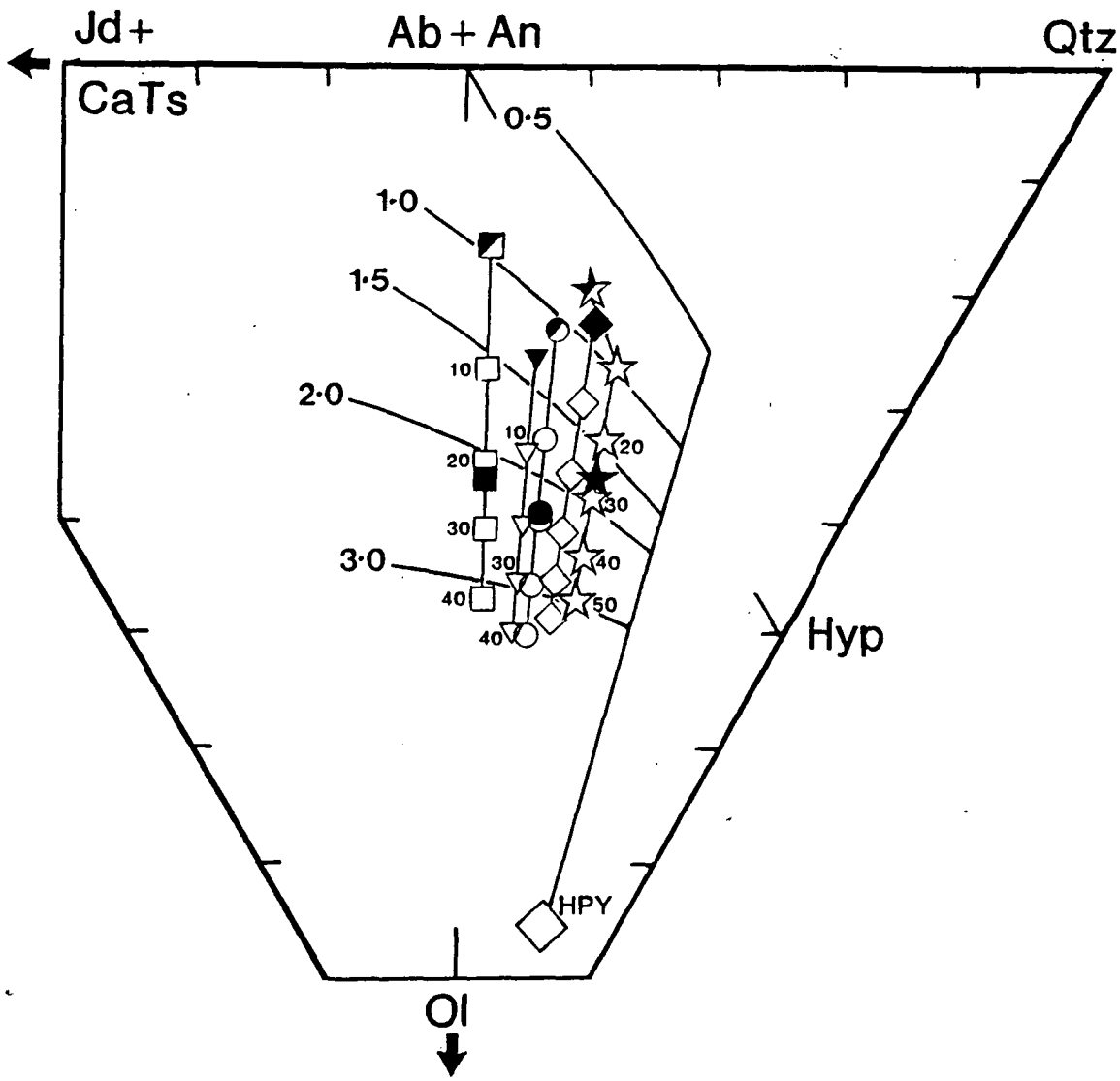

Figure 4.2 Potential Mg-rich primary melt compositions for ocean island tholeiites as defined by olivine-addition vectors deriving from representative low MgO (7-11wt%) tholeiites. Labelled curves are the high pressure cotectics (in GPa) for melting of Hawaiian pyrolite (after Falloon et al., 1988) plotted on the Ol-Jd+CaTs-Qtz projection following the method of Green (1970). The ocean island tholeiite starting compositions used include Reunion (half-filled square, #GB1976; Albarede and Tamagnan, 1988), Kilauea Iki (half-filled circle, #Ki0051; Gunn, 1971), Mauna Loa (half-filled star, #Haw-9; the BVSP, 1981), solid triangle (Gascoyne, #65808; Chapter 1), and Britannia (filled diamond, #68644; Chapter 1). Calculated parent melt compositions for each example (solid symbols), are based on equilibrium with the most Mg-rich olivine phenocrysts occurring in Reunion, Hawaiian, and Tasmantid tholeiites. Numerals adjacent symbols indicate the %mass of olivine added to each starting composition. Note the large amounts of additional olivine required to attain 3.0GPa cotectics where garnet-peridotite may be considered a residual phase assemblage.

The application of inverse modelling techniques to suites of ocean island basalts has generally, but not always, provided evidence for the presence of residual garnet during melting (Feigenson et al., 1983, Hofmann et al., 1984; Budahn and Schmitt, 1984; Albarede, 1983). However, a recent analysis of Reunion lavas by Albarede and Tamagnan (1988), using an improved modelling technique, provides compelling evidence for garnet-absent harzburgite residues and a source recently enriched in incompatible elements.

4.4 THE ROLE OF DYNAMIC MELTING ?

It has been suggested that melt accumulation might occur by a process of "dynamic melting", enabling the imprinting of a high pressure geochemical signature (e.g. $Dy/Yb_{CN} > 1$) of residual garnet through the mixing of melt increments (Galer and O'nions, 1986; Thompson, 1987). The hypothesis proposes that picritic or olivine tholeiite primary melts, with major element compositions determined by relatively large degrees of melting of incompatible-element depleted peridotite residues at low pressure. Their incompatible element abundances, however, are dominated by the mixing in of small melt fractions formed at deeper levels in equilibrium with garnet. Attempts to evaluate this hypothesis must model the behaviour of trace elements which are sensitive to the presence and then absence of residual garnet during progressive melting. This in turn requires incremental use of the available dynamic melting equations (e.g. McKenzie, 1985a; Williams and Gill, 1989) to account for variation in bulk partition coefficients due to the effects of non-modal melting of the garnet-lherzolite assemblages.

The consideration of experimentally-determined phase equilibria, and rates of melting during decompression (i.e ~1% melting per 0.1GPa), indicates that primary olivine tholeiite or picritic tholeiite (10-16wt% MgO) are likely to be generated by a further 10% melting (to <2.0GPa) beyond garnet exhaustion at ~3.0GP (Chapter 3). Appropriate dynamic melting models (i.e. equation A.12 of Williams and Gill, 1989) have been employed assuming :

(1) a source with chondritic relative REE abundances;

(2) pre-melting garnet lherzolite mineralogies with 5-10% garnet, 10-20% clinopyroxene, and 10-20% orthopyroxene ;

(3) various REE partition coefficient sets including sets 1, 3, and 5 from Frey et al. (1978) and the set used by Hofmann et al. (1984),

(4) a porosity estimate of 2%, and the integration of 1% melt increments. These comprehensive melting models define fields of REE patterns for possible primary melts formed by dynamic melting, which are summarised for various degrees of melting relative to garnet exhaustion in Fig. 4.3 (see also Chapter 3).

At 5% melting past garnet-out (i.e. f_{max} at ~2.5GPa) the REE characteristics of dynamic melts are almost identical to the mantle source, and very unlike Hawaiian, Reunion, or Tasmantid tholeiites (Fig 4.3). At 10% melting past garnet-out (i.e. f_{max} ~3.0GPa) the partial melt REE characteristics are indistinguishable from those of the source. The only melting model variants capable of reproducing the REE characteristics of the OIT, are those where melt extraction occurs entirely within the field garnet stability (i.e at garnet-out and smaller degrees of melting; e.g. garnet-out-2% melting). This result is equivalent to that deduced from simple equilibrium melting models. From experimental studies, and also the consideration of melt segregation processes (Chapter 3), garnet-equilibrated primary melts are constrained to derive from >~3.0GPa, which requires them to be considerably more olivine-rich, and thus even more magnesian than the calculated parent melt compositions based on olivine phenocryst compositions.

Alternatively, more complex three dimensional dynamic melting and accumulation models (e.g. O'Hara, 1985) are capable of reproducing OIT REE characteristics, but only if disproportionately large volumes of low degree (garnet-equilibrated) melt fractions are incorporated from peripheral regions (Chapter 3). This possibility is contrary to theoretical considerations which show that both matrix and melt flow will be divergent away from an upwelling plume's centre (Ribe and Smooke, 1987). In addition, the eruption of magmas respresenting smaller melting fractions (e.g. nephelinites, basanites, alkali-olivine basalts) with increasing distance away from the present tholeiitic focus of Hawaiian volcanism (e.g. Clague, 1988; Feigenson, 1986) supports a divergent flow of matrix and melt within a melting mantle plume.

Ocean island magma geochemistry is thus probably best modelled in terms of two dimensional (~vertical) melt segregation models, combined with lateral variation in the

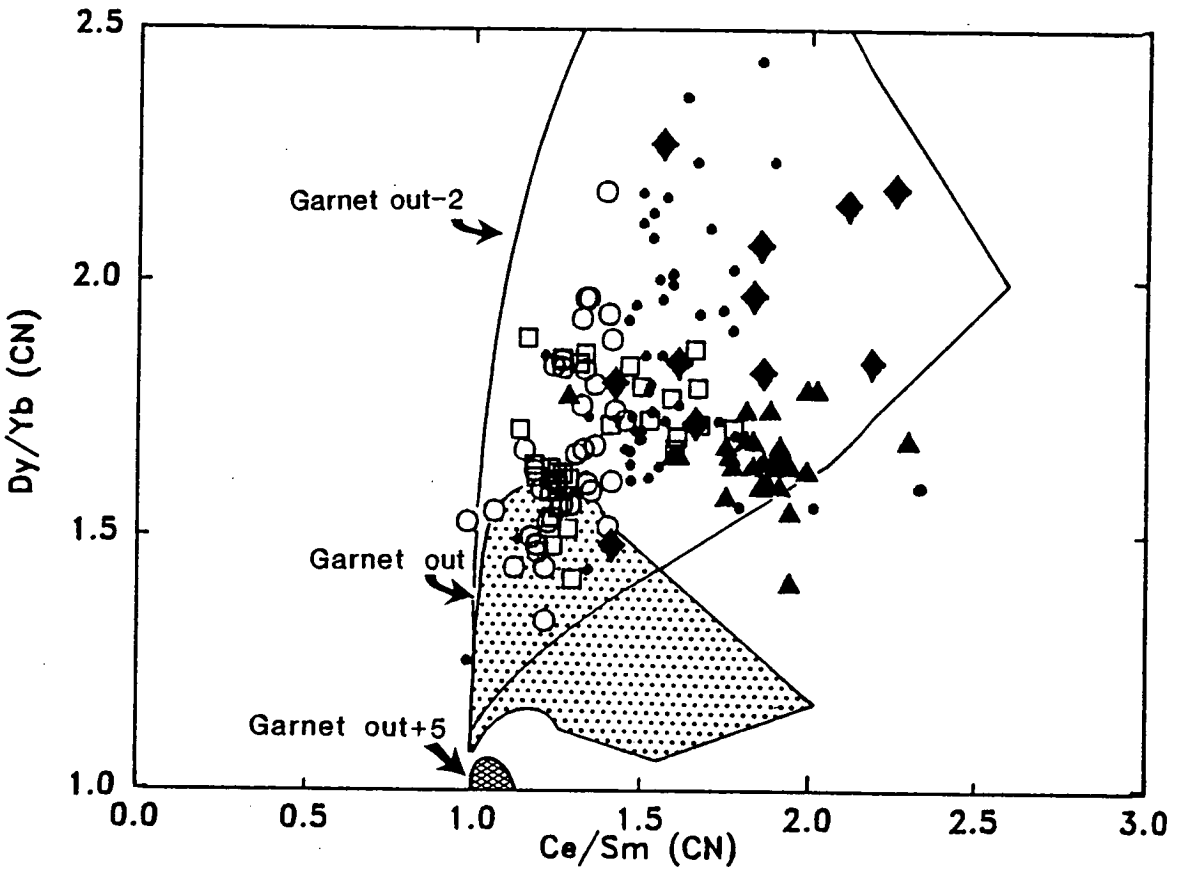

Figure 4.3 A comparison between the REE characteristics of ocean island tholeiites and those predicted for dynamic melting of garnet-peridotite in an upwelling mantle plume. The field marked "Garnet-out+5" refers to the field of melt compositions formed by 5% melting beyond the limit of garnet stability, "Garnet-out" to compositions generated where garnet ceases to be a residual phase (stippled field), and "Garnet-out-2" to compositions formed at 2% melting prior to reaching the elimination of residual garnet. For full details of the modelling procedure see text and Chapter 2. Plotted ocean island basalt suites are Mauna Loa (circles), Kilauea (dots), Koolau and Kohala (squares), Reunion (triangles), and the Tasmantid Seamounts (diamonds). Data sources include Albarede and Tamagnan (1988), Budahn and Schmitt (1984), the BVSP (1981), Casadavell and Dzurisin (1987), Feigenson et al. (1983), Hofmann et al. (1984), Hofmann et al. (1987), Lanphere and Frey (1987), Ludden (1978), Roden et al. (1984), Tilling et al. (1987), and Chapter 1.

absolute degree of melting to account for the spatial variation in magma type and incompatible element enrichment. OIT REE geochemical characteristics require either melting entirely within the presence of garnet to fractionate the middle REE from the HREE, *or* melting at shallower garnet-absent levels involving source volumes which are pre-enriched in LREE and middle REE, and possessing a "residual garnet signature" (i.e. Dy/Yb_{CN} >1.5 to 2.5).

4.5 HOW Mg-RICH NEED GARNET-EQUILIBRATED PRIMARY THOLEIITES BE ?

The composition of primary tholeiites which could be generated in the presence of garnet at >3.0GPa, may be gauged by correcting the existing parent melt estimates to produce compositions lying on the 3.0 GPa peridotite melting cotectics (see Fig. 4.2). This is best achieved by olivine-addition (i.e. correction for olivine fractionation), as based on the rationale outlined above and phase equilibria considerations (see Chapter 2). The large amounts of additional olivine needed result in highly magnesian and Ni-rich compositions (18 to 22 wt% MgO, and 1000 to >2000 ppm Ni), closely resembling basaltic komatiites (see Table 4.1b).

4.6 PLUME MODELS FOR HOTSPOT VOLCANISM

The high temperatures at which picritic and basaltic komatiite-like magmas are in equilibrium with peridotite (e.g. Fig. 4.1), support the existence of thermal anomalies within the mantle beneath the Hawaiian, Reunion, and Tasmantid hotspots. Most recent models for hotspot volcanism are based on upwelling of buoyant hot mantle plumes (e.g. Wyllie, 1988). A comparison of the high pressure liquidus temperatures of picritic and ultramafic basalt compositions, with the decompression melting paths modelled by McKenzie and Bickle (1988), places their pre-melting mantle source temperatures about 200°C above those considered to be ambient values for the upper mantle by McKenzie and Bickle (1988).

A comprehensive framework already exists for melting processes associated with pressure release in hot upwelling mantle plumes (see Wyllie, 1988). Some important

qualifications of these schemes can be made in view of the two competing possibilities for the origin of OIT geochemical characteristics.

4.6.1. A Model for the Generation of Ultramafic Primary Melts

In this model (refer to Fig. 4.4a), the source is assumed to have chondrite-relative middle and HREE values, requiring major melting to occur wholly within the stability field of garnet in order to account for the REE character of ocean island tholeiites. The hotspot magma source, which is fixed with respect to the over-riding lithosphere, is provided by an upwelling mantle plume as it intersects the peridotite solidus. Within individual plumes, variation in the degree of melting is likely to result from lateral variation in temperature, which will probably decrease away from the plume core. At the plume's central apex, at >3GPa, highly magnesian primary melts (>20 wt% MgO) accumulate prior to transfer through the lithosphere. Primary melts evolve by 25 to 40% crystallisation of olivine, prior to eruption of magmas with compositions which commonly fall between 7 and 10 wt% MgO. To account for the absence of olivine phenocrysts recording the earlier stages of this differentiation (i.e. with $Mg^{\#}$~92), early fractionation may be partly hidden at deeper lithospheric depths, or intracrystalline diffusion may be instrumental in the re-equilibration of olivine phenocrysts to more Fe-rich compositions.

The lithosphere, though not viewed as an important magma source volume, may play an important role in the melting process by forming a barrier to the upward plume flow. This effectively limits plume decompression, and thus provides a control on the degree of melting and also the pressure-dependent phase equilibria during melt segregation. The model can be adapted for plumes rising beneath thin oceanic lithosphere, for example near mid-ocean-ridge environments, where melting may proceed to shallower garnet-absent levels. In such an event, fractionated REE patterns could not be anticipated.

4.6.2 A Model for Olivine Tholeiite/Picrite Primary Melts

In this model, the primary melts are assessed as olivine-rich tholeiites to picrites, requiring melt segregation at low pressures (i.e 1-2GPa) leaving garnet-absent residues (Chapter 2, Figs. 4.1&4.2). An important variation upon the plume-dominated melting process outlined above, involves thermal erosion and melting of the overlying oceanic lithosphere (refer to Fig. 4.4b). In fact, thin lithosphere will be necessary to facilitate the

Figure 4.4 Schematic cross-sections through the upper mantle source region of ocean island tholeiites for two competing magma generation models based on formation of (A) deeply derived ultramafic primary melts or (B) more shallow-deriving picritic/olivine tholeiite primary melts. Both models illustrated are based on decompression melting of a hot upwelling mantle plume, though for (B) it may be possible to replace a hot material flux with a volatile-rich plume (e.g. Green et al., 1987). Also shown are approximate oceanic geotherms and corresponding regions of melt generation consistent with peridotite-C-H-O phase equilibria (solidii taken from Takahashi, 1986; and Green and Wallace, 1988). In detail, (A) is a deep garnet-present melting model where ultramagnesian primary melts are generated, these being necessary for equilibration with garnet-peridotite residues. Significant volumes of melt are formed as the hot ascending mantle plume (jet) intersects the "anhydrous" peridotite solidus at depth, between ~150 and 100km. Continued plume ascent is restricted by the overlying oceanic lithosphere, which limits melting to deep levels entirely within the stability field of garnet. Primary melts (~basaltic komatiite in composition) released from near the plume apex fractionate large quantities of olivine prior to surface eruption of typical tholeiite lava compositions with between 6 and 10 wt% MgO. In contrast, (B) is a shallow-level (residual garnet-absent) melting model where picritic or olivine-tholeiite primary melt compositions are segregated at depths <~60-70km. In this case, significant lithosphere erosion is necessary, occurring either through scouring by the plume, or melting in response to heating or volatile infiltration from the plume. Melting of a mixed lithosphere-asthenosphere source results. The lithosphere provides a major source of incompatible elements, pre-enriched there by small melt/fluid fractions migrating from the underlying asthenosphere (see small arrows), during growth and cooling of the oceanic lithosphere as it ages away from the mid-ocean ridges, and possibly also during arrival of the leading margin of the "hotspot". In this process, the highly incompatible elements (e.g. LREE) are removed to higher levels of the lithosphere by continuing migration of melt/fluid phases, thus creating a lower lithosphere (60-100km) with relative element abundances suitable as a source of ocean island tholeiites. This geochemical layer of the oceanic lithosphere appears to be consistent with the effects of formation of a carbonatite melt phase in the region of amphibole-peridotite stability at P >2.1GPa (see hatched field; after Wallace and Green, 1988). The ready migration of this melt phase will strip the region between 60 and 100km of elements which are incompatible in phases stable there (i.e. amphibole, clinopyroxene), and transport them to higher levels (i.e P <2.1GPa) where the carbonatite melt phase breakdowns. The predicted REE characteristics of the resultant layered oceanic lithosphere are illustrated as a series of insets in (B).

(a) Ultramagnesian Primary Melts (~20wt% MgO)

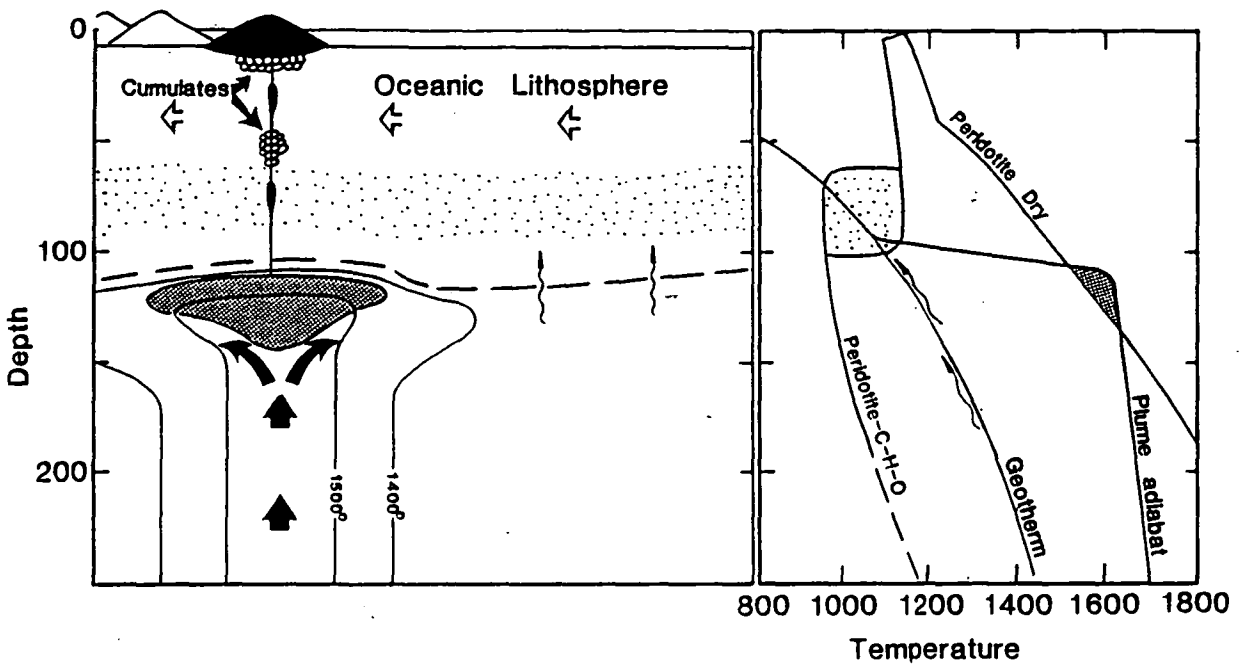

(b) Olivine Tholeiite/Picrite Primary Melts

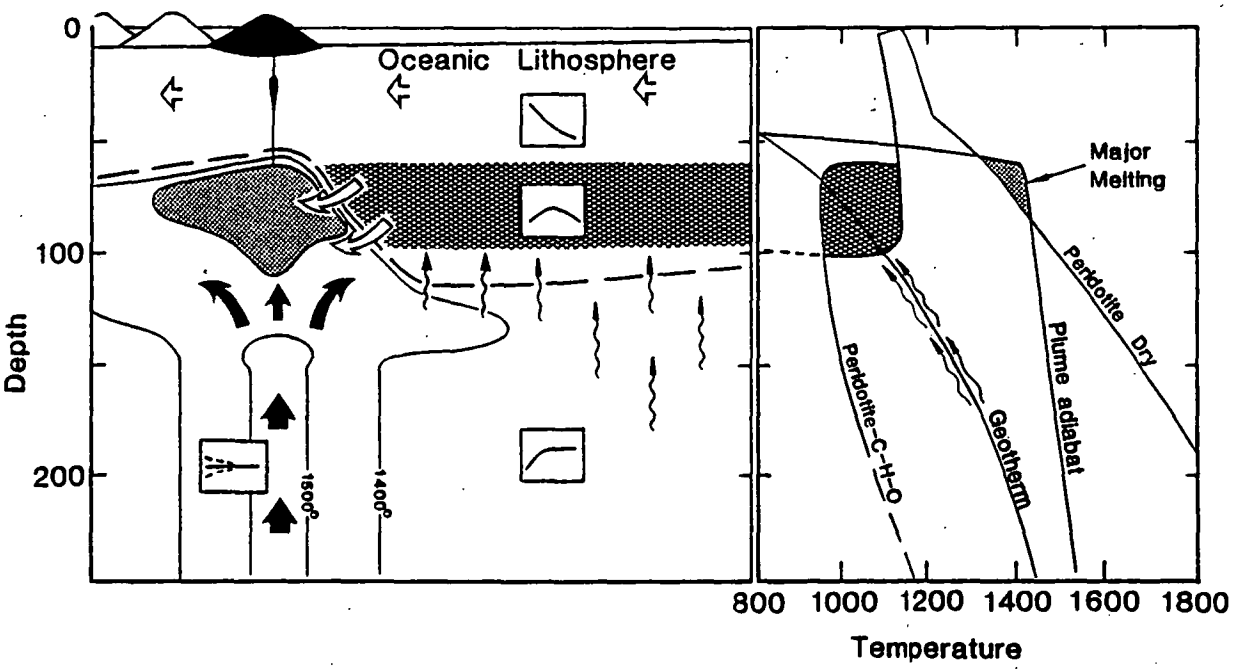

shallow levels of melting indicated by the olivine tholeiite and picrite primary melts. This proposal is supported by an aseismic region at depths >60 km beneath Hawaii (e.g. Eaton, 1962; Klein et al., 1987), which may signify the presence of melt at that depth. In terms of age of lithosphere and distance from the ridge crest, the lithosphere near Hawaii is expected to be ~100km (Dettrick and Crough, 1978), requiring the removal of ~40km from the basal lithosphere in the Hawaiian case. Theoretical models for the erosion of lithospheric plates by mantle plumes, such as those commonly advocated to explain hotspot swells, can produce this magnitude of lithospheric thinning (e.g. Liu and Chase, 1989). Significant plume-lithosphere interaction/mixing may be expected to accompany any such lithosphere thinning process.

An essential requirement of this model is a source enriched in incompatible elements, bearing a "residual garnet signature". Conveniently, the oceanic lithosphere can fulfil this requirement through its potential for enrichment by prior infiltration of incompatible element-rich silicate melts (or fluids: e.g. Green, 1971; Green and Lieberman, 1976; Wright, 1984). This may be viewed as a natural consequence of lithosphere development as it cools and thickens with age away from the mid-ocean-ridge environment, and the ease with which small volatile-rich melt fractions or fluids escape from the mantle (McKenzie, 1985a; Hunter and McKenzie, 1989). In fact, this style of geochemical enrichment is predicted from the distinctive shape of the peridotite-C-H-O solidius (fO_2>IW+2log units) at depths <100km due to the stability field of amphibole (Green, 1971; Green et al., 1987). The resultant solidus ledge creates an effective trap for small degree melts/fluids migrating from the extensive region of incipient melting (low velocity zone), which is also predicted to occur in the underlying asthenosphere.

The enrichment process is envisaged to be open-system, involving preferential extraction of moderately incompatible elements (e.g. middle and HREE) into newly formed or pre-existing amphibole and clinopyroxene from migrating melt/fluid. The resulting pargasite-lherzolite would not have excessive LREE enrichment, as would result from the simple addition of an incompatible element-rich melt/fluid, but instead will form a weak to moderately LREE-enriched source with $Dy/Yb_{CN} > 1$. This process may be enhanced by the presence of a carbonatitic melt at >2.1GPa in the presence of amphibole,

which will transport incompatible elements (e.g. LREE) to higher levels (<2.1GPa). A geochemically-zoned lithosphere results, enriched between ~60 and ~95km depth in those incompatible elements partitioned into amphibole and clinopyroxene, and at shallower levels in LREE, P, and CO_2 bubbles due to the destabilisation of escaping carbonatite melt at P <2.1GPa (Green and Wallace, 1988).

It is proposed that the deeper "amphibole" enriched zone may provide a significant portion of the incompatible element budget of OIT.

4.7 DISCUSSION

In the past, strong arguments have been made against both the models outlined above, on the basis of the unconstrained and variable nature of metasomatic enrichment processes (e.g. Frey and Roden, 1987) and the very high transition element abundances of very olivine-rich primary melts (e.g. Feigenson, 1986). It is likely that models relying on an enriched lithospheric source will remain unsubstantiated until a much better understanding of metasomatic enrichment processes exists. However, such models are apparently consistent with both peridotite-C-H-O equilibria, the thermal evolution of the oceanic upper mantle away from mid ocean ridges, and with models for the extraction of incipient melt/fluid from the mantle. They should not be dismissed lightly. Moreover, though not a compelling argument in itself, it is this model which is consistent with the composition of the most primitive OIT parent melts based on early crystallising phenocryst phases. In respect to the other criticism, our knowledge of transition element concentrations in primary melts derives mainly from low pressure (usually 1atm) experimental studies. It is well established that partitioning of Ni between olivine and basaltic melts decreases markedly with increasing temperature (i.e. more MgO-rich melt compositions), a trend which, if augmented by an additional pressure effect, could result in very Ni-rich primary melts if generated at depth from an anomalously hot mantle plume. Consequently, picritic and, even more importantly, ultramafic primary melt compositions cannot be ruled out on the basis of their apparently excessive Ni contents.

Along both the Hawaiian and Tasmantid hotspot tracess it is the more incompatible element-rich alkaline lavas that are associated with the more "depleted

source" isotopic characteristics. These basalts lie between the MORB field and the more radiogenic Sr and unradiogenic Nd values of the tholeiites (Frey and Roden, 1987; Stille et al., 1986; Chapter 1). Stille et al.(1986) have interpreted Hawaiian alkaline magma sources as oceanic lithosphere, recently (<100Ma) enriched in incompatible elements, and the tholeiite magma source as a mixture of plume and enriched lithosphere components. These mixing trends, however, are also broadly consistent with a predominantly plume melting model, where increased involvement of cooler upper mantle (MORB source?) toward the plume margins, results in lower degrees of partial melting, more incompatible element-rich alkaline magmas, and a more pronounced "depleted mantle" (MORB source) isotopic signature there. Though partly inconclusive to date, integrated studies combining isotopic and geochemical systematics within a framework of phase equlibrium constraints, are probably capable of unravelling much of the unresolved detail of the melting processes occurring at hotspots.

PART 2

Petrogenesis of Primitive Island Arc Basalts

CHAPTER 5

The Geology of Ambae, and an Outline of the Geology of the Vanuatu Arc

5.1 RATIONALE FOR STUDY

Little is known about the nature of primary melts in island arc environments, and few constraints can be placed upon the physio-chemical processes associated with their generation. A possible exception is the group of primitive boninite-type rocks (eg. Crawford et al., 1989), but these cannot be considered parental to typical products of arc volcanism.

In principle, primary and parent melt compositions can be determined by accounting for the modifications which have resulted in derivative magma compositions. In arc environments, however, the complexity of processes such as crystal fractionation, phenocryst accumulation, and magma mixing, and the potential for crustal contamination, dictate that this is no easy task. This problem is further compounded by a lack of criteria for ascertaining what constitutes a primary arc magma composition. This study aims to evaluate the nature and origin of primitive (primary?) island arc magmas, and their links with the more evolved products of arc volcanism with which they are associated. Primitive lava occurrences in the Vanuatu Arc, particularly on the island volcano of Ambae (formerly Aoba, in Warden, 1970; Gorton, 1974 & 1977; Ramsay et al., 1984), have been targeted for this purpose.

Ambae is perhaps the best example of "picritic" (olivine-rich) volcanism in an active island arc environment (Ramsay et al., 1984). Other notable occurrences of primitive arc volcanism include Oshima-Oshima in Japan (Yamamoto, 1988), Merelava and Western Epi in Vanuatu (Barsdell, 1988; Barsdell and Berry, in press), various restricted localities in the Aleutian Islands (e.g. Gust and Perfit, 1987; Reid and Nye,

1987), and the now inactive New Georgia Group in the Solomon Islands (Ramsay et al., 1984).

5.2 TECTONIC FRAMEWORK OF THE VANUATU ARC

The Vanuatu Arc is located in a tectonically complex region of the southwest Pacific, comprising several microplates sandwiched between the Indo-Australian and Pacific plates. The complexity of the region arises from the effects of opposing zones of subduction; west-dipping along the Tonga-Kermadec and east-dipping along the Vanuatu-Solomon Islands-New Britain arc-trench systems. Linking these opposed subduction zones, between southern Vanuatu and northern Tonga-Fiji, is the sinistral Hunter Fracture Zone, which separates active sites of back-arc spreading in the North Fiji and Lau Basins (Fig. 5.1).

The Vanuatu Arc extends more than 1000km toward the NNW from the Hunter Fracture Zone in the south, until reaching a sharp dog-leg bend to the west where it joins the Solomon Islands Arc (Fig. 5.1). The Vanuatu Arc is notable for its steeply inclined (~70°) Benioff zone, with convergence occurring on an azimuth of N75°E (Pascal, 1978) at a rate of ~120mm year (Dubois et al., 1977). A well developed trench runs the length of the arc, except for where the d'Entrecasteaux Fracture Zone (DFZ), a positive feature on the subducting Indo-Australian Plate, abuts the arc (Fig. 5.1).

5.2.1 Development of the Vanuatu Arc

Initiation of subduction along the Vanuatu Arc can be related to disruption of the Vitiaz Arc, which once marked a continous zone of westward subduction along the perimeter of the Pacific Plate. This ancient plate boundary is now identifiable as an inactive trench-volcanic arc remnant aligned between Fiji and New Ireland to the northwest of the Solomon Islands (Brocher, 1985; Fig. 5.1). The termination of westward Vitiaz Arc subduction at about 12Ma (e.g. Brocher, 1985), is believed to be a consequence of collision between the Vitiaz Arc and Ontong Java Plateau (Kroenke, 1972), an anomalously thick and extensive area of Pacific ocean crust now located to the rear of the Solomons Arc. This event, and the initiation of subduction of the Indo-Australian Plate to the north, may be associated with ophiolite emplacement in the Solomon Islands (Parrot

Figure 5.1 Tectonic elements in the Vanuatu Arc region of the southwest Pacific. Shown are the spatial relationships between, and orientation of, active and previously active arc-trench systems, as well as sites of back-arc spreading in the North Fiji and Lau basins. Relative plate and microplate motions are indicated by arrows, and regions of rifting occurring behind the Vanuatu Arc (e.g. Coriolis and Vot Tande troughs) are shown as horizontally striped areas.

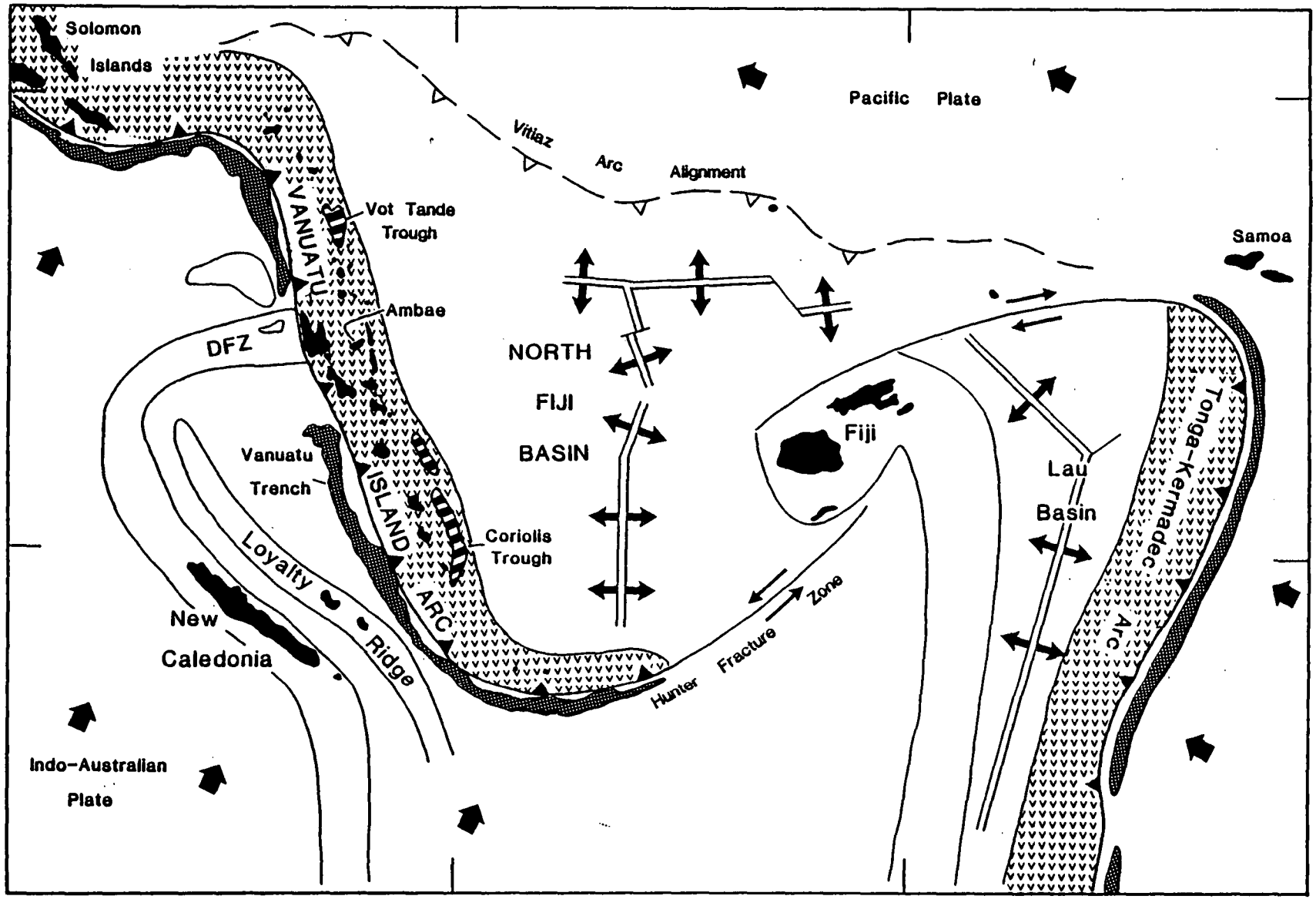
Solomon
Islands
Pacific Plate
Vitiaz
Arc
Alignment
VANUATU
Vot Tande
Trough
Ambae
Samoa
DFZ
NORTH
FIJI
BASIN
Fiji
Vanuatu
Trench
ISLAND
ARC
Coriolis
Trough
Lau
Basin
Tonga-Kermadec
Arc
Loyalty
Ridge
New
Caledonia
Hunter
Fracture
Zone
Indo-Australian
Plate

and Dugas, 1980) and also on Pentecost in the Vanuatu Arc. The timing of, and relationships between, events associated with subduction zone reversal remain poorly constrained and the subject of ongoing debate. In the Vanuatu Arc the major sequence of geological events during this period are :

(1) the accumulation of a thick (>4-6km) sequence of Vitiaz Arc-related, late Oligocene to early Miocene, volcanics preserved in the Western Belt islands of Malekula, Santo and the Torres Islands (Fig. 5.2); followed by

(2) a volcanically "dormant" period (~14-8Ma) dominated by thick greywacke accumulations in tensional grabens in the Western Belt (Malekula and Santo) and deep water sedimentation in the Eastern Belt islands of Pentecost and Maewo.

(3) the re-establishment of volcanism by ~8Ma, with the eruption of a basaltic island arc lava association in the Eastern Belt (Carney et al., 1985), which probably accompanied the initial stages of development of the North Fiji Basin (see Fig. 5.3);

(4) a westward shift (~50km) in the locii of volcanism, to the present line of Central Chain volcanoes, then occurred at ~3Ma, possibly in conjunction with steepening of the Benioff zone (Carney et al., 1985).

For more detailed accounts of the geological evolution of the Vanuatu Arc see either Carney and MacFarlane (1982), Carney et al. (1985), or the concise summary by Kroenke (1984).

5.2.2 The North Fiji Basin

Incipient rifting of the North Fiji Basin probably began around 10Ma (Auzende et al., 1988), resulting in separation of the Vanuatu Arc from Fiji and the Vitiaz Arc remnants. Its subsequent development has accompanied clockwise rotation of the Vanuatu Arc to its present NNW-SSE alignment (Fig. 5.3). The North Fiji Basin is currently the site of several active spreading ridge segments (Auzende et al., 1988), running almost the length of the basin and subparallel to the Vanuatu Arc. Dredged basalts are dominated by N-MORB types, but also include incompatible element-rich alkaline basalts (Price et al., submt.; Aggrey et al., 1985). Isotopic data confirm the derivation of magmas from a geochemically-depleted MORB-like source, as $^{87}Sr/^{86}Sr$ ranges between 0.7028 and 0.7033, and εNd between +7.4 and +10.4 (Boespflug et al., 1989).

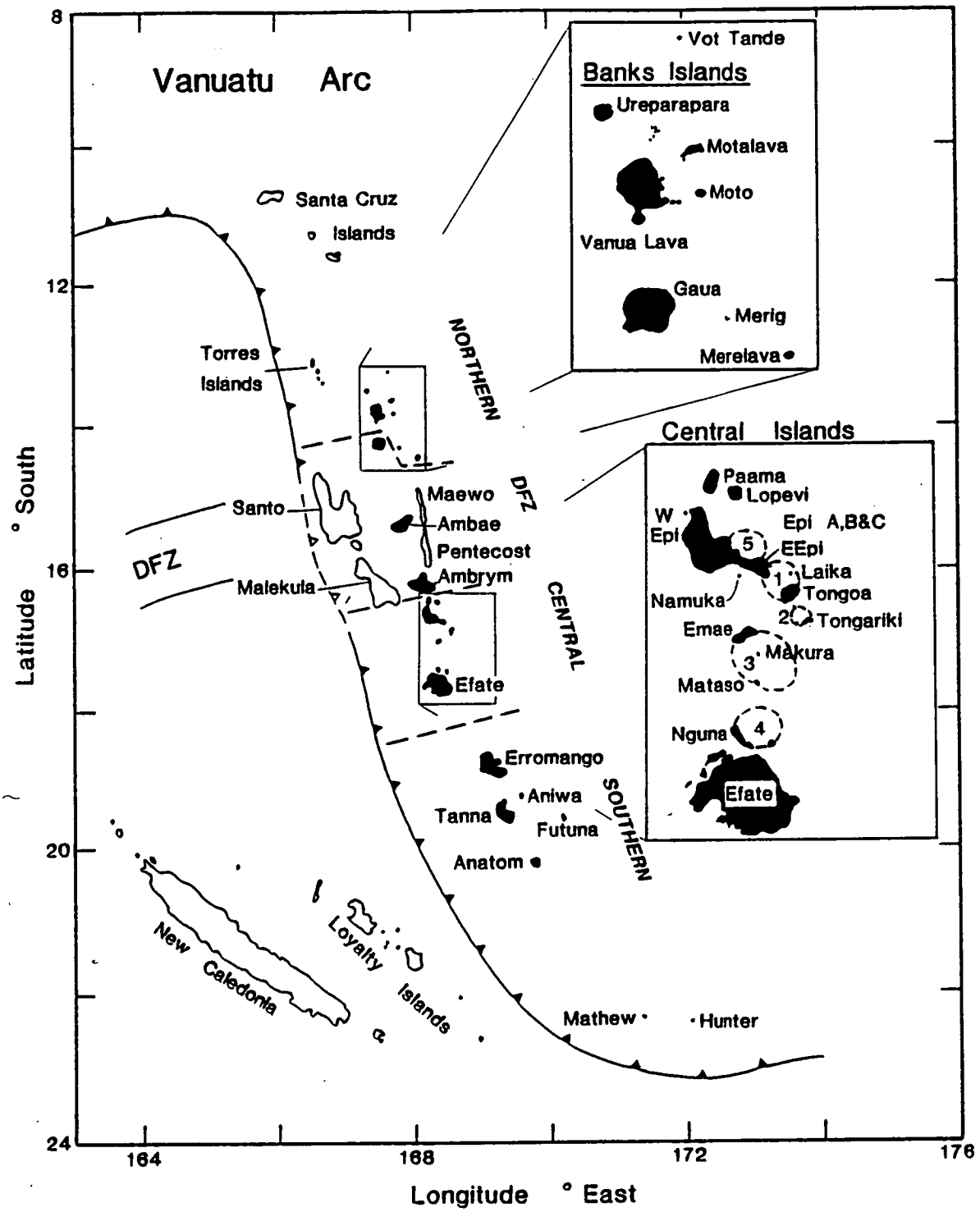

Figure 5.2 A map illustrating island locations in the Vanuatu Arc. Islands forming part of the "active" Central Chain volcanic alignment are shown in black, and the division of the arc into four principal segments is indicated by the dashed lines trending normal to the strike of the arc. Numbers encompassed by dashed circles indicate large caldera structures occurring in and around the Central Islands (after Crawford et al., 1988).

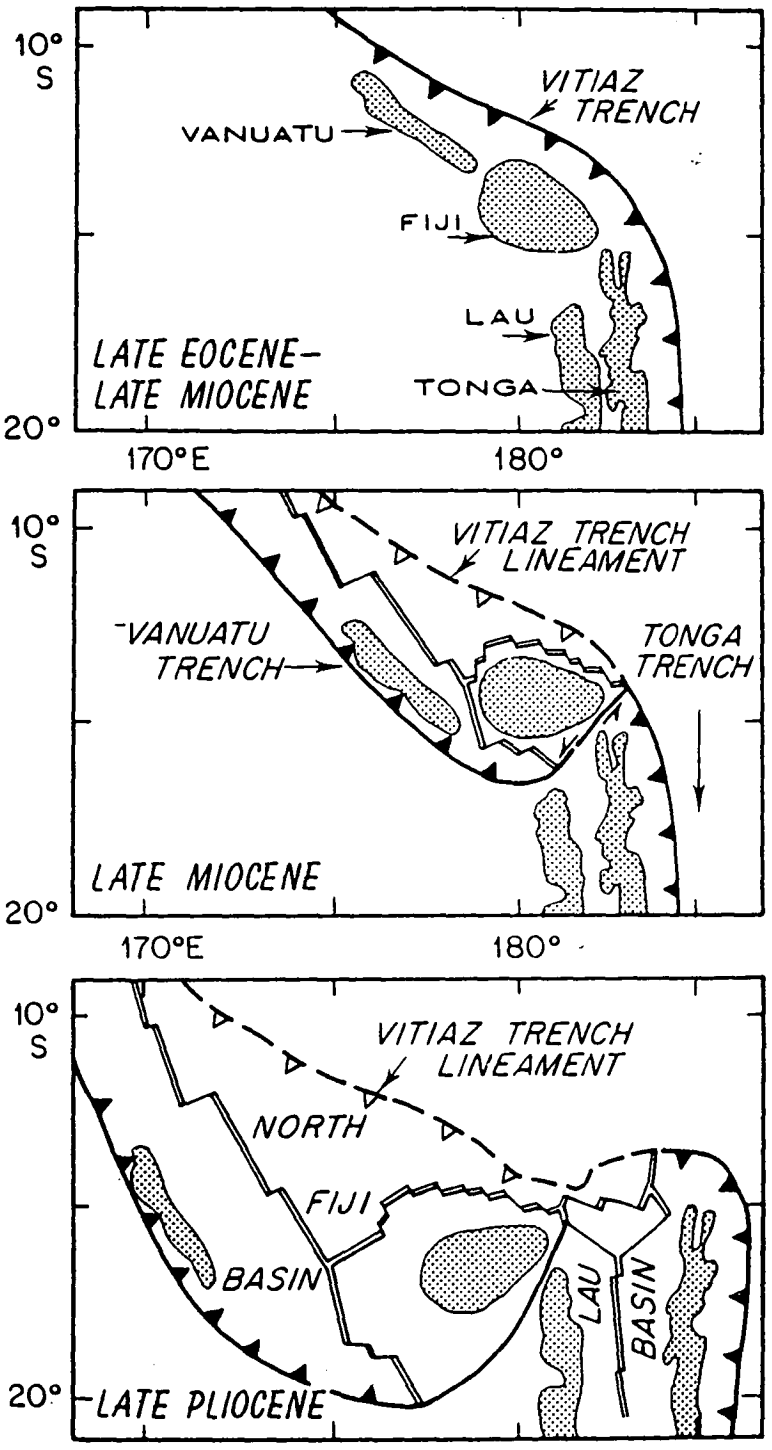

Figure 5.3 Stages in the development of the North Fiji Basin, and the accompanying clockwise rotation of the Vanuatu Arc away the original Vitiaz Arc alignment (after Falvey, 1978).

5.2.3 The d'Entrecasteaux Fracture Zone (DFZ)

The DFZ is a complex structure continuous with, and possibly geologically related to, the New Caledonia-Loyalty Islands archipelago to the south. Its morphology is complicated by a series of horsts and grabens, which may be linked to a phase of extension after about Middle Miocene time (Maillet et al., 1983). Sediment of variable thickness (up to 2.3 seconds two-way time) infills the graben structures, where it is notable for greater thicknesses than on the surrounding abyssal plains (Maillet et al., 1983). Basalts dredged from the horst scarps are of Eocene age and have MORB geochemical affinites (Maillet et al., 1983). On the southeastern flank of the DFZ occur several seamounts (e.g. Sabine Bank) which are postulated to be part of a previously active (Eocene) island arc that possibly included the basement of the Loyalty islands (Maillet et al. 1983). In this context, by analogy with the Hunter Fracture Zone termination of the Vanuatu Arc, it has been proposed that the DFZ forms an old transcurrent plate boundary terminating the northern end of the earlier New Caledonia-Loyalty Islands subduction/obduction zone (Daniel et al., 1977).

5.3 GEOLOGICAL ELEMENTS OF THE VANUATU ARC

The Vanuatu Arc is marked by an alignment of active and recently active volcanic centres (the Central Chain Volcanoes) which run much of the length of the arc (see Fig. 5.2). To the east and west of these volcanoes lie the uplifted and older islands of the Eastern Belt (Pentecost and Maewo) and the Western Belt (Malekula, Santo, and the Torres islands). The Vanuatu Arc is also divisible into a number of distinctive segments by an anomalous zone, centred between 14°30'S and 17°00'S, which is related to collision/coupling of the subducting DFZ with the arc. North and south of this segment, a typical arc-trench system has developed, in association with extension/rifting of the rear-arc flanks to form the Coriolis, Vot Tande, and associated trough systems (Fig. 5.1). These narrow complex rift zones have been interpreted to be incipient back-arc spreading centres on the basis of bathymetry, and geophysical evidence which is consistent with the effusion of basaltic lava (e.g. high heat flow, magnetic, and gravity anomalies: e.g. Dubois et al., 1978; Kroenke, 1984). Recent studies of dredged samples from these zones by Monjaret

(1989) confirm this hypothesis, and indicate that these rear-arc regions have been sites of periodic volcanic activity since ~6.5Ma.

The anomalous DFZ segment of the arc is physiographically distinct from other regions of the arc. It is marked by extensive recent uplift in both forearc (Santo-Malekula) and rear-arc areas (Maewo-Pentecost), which are separated by the Ambae (Aoba) Basin, an intervening downwarped region and site of sedimentation since Mio-Pliocene time (e.g. Karig and Mammerickx, 1972). Evidence for east-west compressive deformation of this central segment is manifested as folding and thrusting within the sediment pile (Collot et al., 1985). This is supported by observations relating to the orientation of the maximum horizontal compression and focal mechanism solutions for shallow earthquakes occurring in this region (Roca, 1978; Collot et al., 1985). The principle stress direction is observed to rotate parallel to the strike of the arc both to the north and to the south of this central region. Collot et al. (1985) argue that this strain pattern is consistent with a simple indentation model, where the effects of coupling/collision between the DFZ and the Vanuatu Arc is analogous to a rigid die impinging on a long narrow plastic body (Fig. 5.4). This model infers transcurrent movement along cross-arc faults, culminating in eastward shunting of the central arc segment. This model is also advanced by Collot et al. (1985) as an explanation for the development of tensional rifts in rear-arc regions to the north and south of the DFZ collision-affected region (Fig. 5.4).

5.3.1 Petrology and Geochemistry of the Central Chain Volcanics

Geochemistry

Petrological studies of the Central Chain Volcanics in the Vanuatu Arc have documented a wide range of lava compositions, from picritic through high-alumina basalts, to andesites, and in some cases also dacites. Many authors have drawn attention to the dominance of basaltic compositions. K_2O contents vary widely across a spectrum from low-K to high-K compositions (e.g. 1 to 5 wt% at 60 wt% SiO_2, Carney et al., 1985), with considerable variation occurring even on individual islands (e.g. Erromango, Colley and Ash, 1971; Western Epi, Gorton, 1977). The low-K magmatic suites have generally been associated with island arc tholeiite compositions (e.g. Merelava, Barsdell, 1988) whereas the highest K suites have been assigned transitional to alkaline affinties (e.g. Ambae,

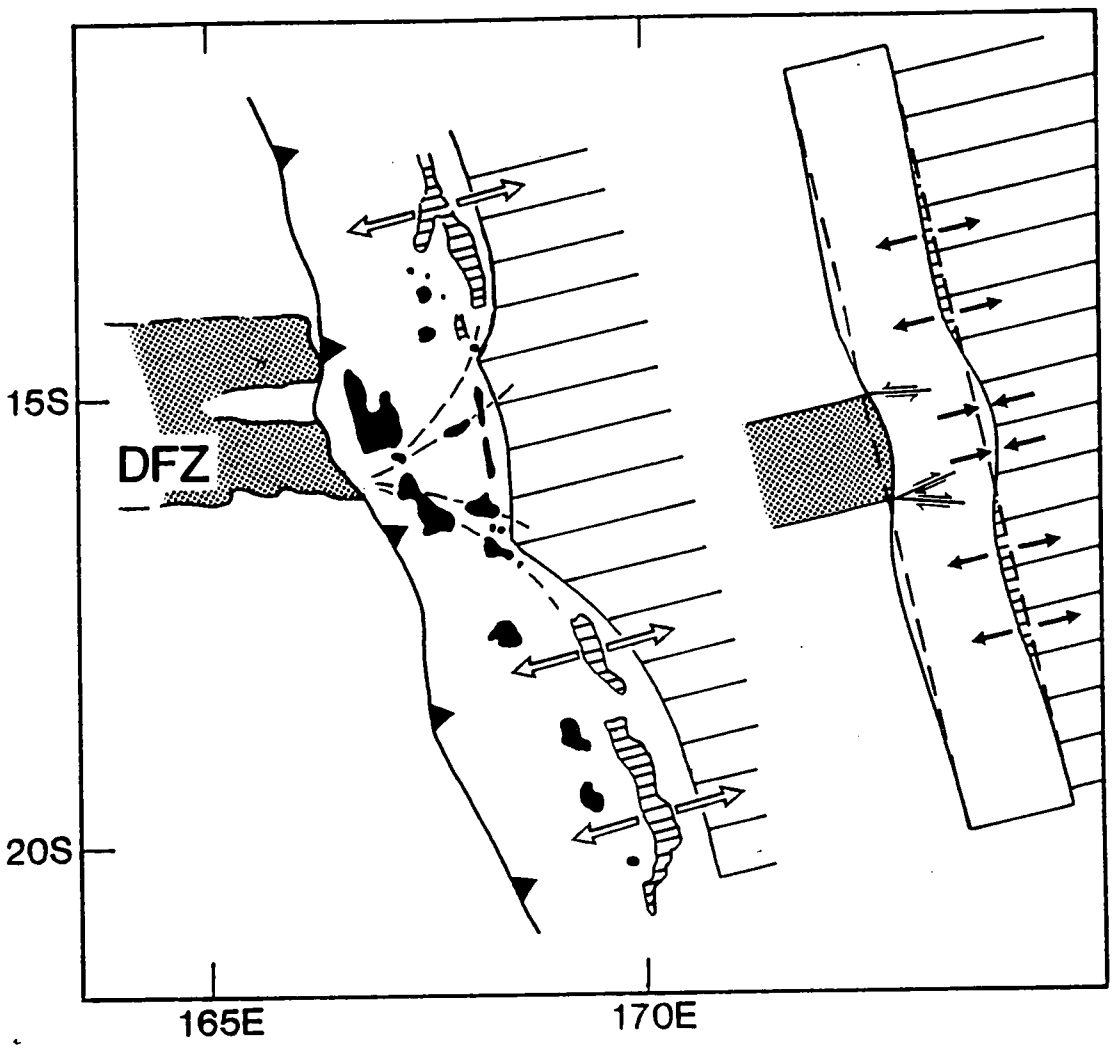

Figure 5.4 A comparison between the physiography of the Vanuatu Arc and the effects of indenting a solid beam (DFZ analogue) on a long plastic body (Vanuatu Arc analogue). Note the concurrence of predicted tensional areas with the rear-arc rifts which occur both to the north and south of the DFZ affected arc segment. This figure is adapted from Figures 13 and 16 in Collot et al. (1985).

Ambrym, Gaua; Mallick, 1973). A lateral decrease in K_2O contents across the northern part of the arc away from the trench (i.e. Gaua-Merig-Merelava), contrary to the Hatherton-Dickenson relationship, was first noted by Mallick (1973) and later the subject of further discussion by Barsdell et al. (1982) who ascribed it to source enrichment under the previous west-facing Vitiaz Arc subduction regime. Gorton (1977), on the other hand, has argued that similar K content ranges occurring elsewhere in the arc, arise from variable degrees of melting of an LILE-enriched source.

Detailed trace element studies show that the Vanuatu Arc magmas are characterised by relative enrichments of LILE and depletion in HFSE compared to N-MORB (Gorton, 1977; Dupuy et al., 1982). They also reveal a wide range in incompatible element abundance levels in basalts of similar bulk composition. Dupuy et al. (1982) have demonstrated an inverse relationship between the relative enrichment of LILE over LREE and LREE enrichment over HREE, matching that found in island arc basalts elsewhere (e.g. Perfit et al., 1980). On the basis of low HFSE and HREE abundance levels in Vanuatu Arc basalts, both Gorton (1977) and Dupuy et al. (1982) have also argued for large degrees of melting of a MORB source protolith that has been enriched by LILE derived from the subducting ocean crust.

Mineralogy

Accounts of the petrography of virtually all of the Central Chain volcanic suites (excluding Ambrym) are available, among other sources, in the various reports of the New Hebrides Geological Survey (now the Vanuatu Department of Mines, Geology, and Rural Water Supply). These sources are summarised in Table 5.1. Detailed mineral chemistry data is also available for Merelava (Barsdell, 1988), the Banks Islands (Barsdell, 1980), Western Epi (Barsdell and Berry, in press), Erromango (Marcelot et al., 1983), and Mathew and Hunter (Maillet et al., 1986). These studies reveal a similar sequence of crystallisation throughout the arc, beginning with magnesian olivine (+ minor Cr-spinel) and magnesian clinopyroxene in the most mafic basalts, joined later by plagioclase and magnetite in more evolved basalts and andesites, and commonly also orthopyroxene, though rarely in basaltic compositions. Amphibole is a relatively rare phase, occurring in

Table 5.1 Phenocryst mineralogy of Central Chain volcanic suites in the Vanuatu Arc.

Island	Basalts <52wt% SiO_2	Andesites 52-63wt% SiO_2	Dacites >63wt% SiO_2
Vot Tande	Ol+Cpx+Pl+(Opx)	Pl+Cpx+Opx+(Hb)	---
Ureparpara	Ol+Cpx+Pl	Pl+Cpx+Opx+Hb	---
Vanua Lava	Ol+Cpx+(Pl)	Pl+Cpx+Opx+(Ol)	---
Gaua	Ol+(Cpx+Pl)	Pl+Cpx+(Ol)	---
Motalava	Ol+Cpx+Pl	---	---
Merelava	Ol+Cpx+(Pl)	---	---
Ambae	Ol+Cpx+(Pl)	---	---
Ambrym	Ol+Cpx+(Pl)	Pl+Cpx+(Ol)	---
Western Epi	Ol+Cpx+(Pl)	Pl+Cpx+(Opx)	---
Central Islands[a]	Cpx+Pl+(Ol)	Pl+Cpx+(Opx+Ol)	---
Karua Epi A,B&C	Ol+Cpx+Pl+(Opx)	---	Pl+Opx+(Cpx+Ol)
Efate	Ol+Cpx+Pl	Pl+Cpx+Opx+(Ol)	Pl+Cpx+(Opx)
Erromango	Ol+Cpx+Pl	Pl+Cpx+Opx	---
Tanna	Ol+Cpx+Pl	Pl+Cpx+(Ol+Hb)	---
Anatom	Ol+Cpx+Pl	Pl+Cpx+Opx+Hb	---
Futuna	Ol+Cpx+(Pl)	Pl+Cpx+Opx+(Hb+Ol)	---
Hunter & Mathew	---	Cpx+Opx+Pl+(Ol)	Cpx+Opx+Pl+(Ol)

a Includes all Central Islands except Western Epi, Karua, and the submarine Epi volcanoes (i.e. Epi A,B, and C).

Note oxide phases are not listed, but that Cr-spinel and titanomagnetite are common phases in basalts and that titanomagnetite is common in andesites and dacites. Parentheses designate phases which may or may not be present. Data sources include Ash et al. (1978), Ash et al. (1980), Barsdell (1980), Barsdell (pers. comm., 1988), Barsdell et al. (1982), Carney and MacFarlane (1979), Crawford et al. (1988), Gorton (1974), Maillet et al., (1986), Mallick and Ash (1975), Marcelot et al. (1983), and Warden (1967, 1970).

some andesites/dacites in a few localities (Futuna, Merig, Ureparapara, Tanna, Anatom), and then often only in intrusive rocks (e.g. Anatom, Merig).

5.4 GEOLOGY OF AMBAE

Ambae is a large shield volcano rising more than 3700m above the surrounding sea floor (1500m above sea level) and exceeding 400km^2 in subaerial extent. The island is elliptical in outline, with a long NE-SW axis being formed by two rift structures radiating from the island's central volcanic summit. A nested caldera structure (~7km in diameter) crowns the summit and is the site of several lakes (Fig. 5.5).

Ambae's shield is dotted with numerous scoria cones, particularly in locations scattered along the rift zones, with some the largest examples being up to several hundred metres high. These are replaced by phreatomagmatic cones near sea level, clusters of which are found where the axial rift zones enter the sea at the island's north-eastern and south-western tips. Several fissure zones of variable length (up to to several km) are marked by scoria ramparts coincident with the strike of the rift zones. Examination of aerial photographs reveals that abundant lava flows have issued from both the summit caldera region and from the rift zones (e.g. Warden, 1970). Most of these flows have autobrecciated surfaces, though ropey flow tops also occur, usually in association with aphyric lavas. Individual flows are of variable thickness, the greatest (~5-6m) being observed on shallow sloping rift flanks. In these flank areas marked pressure ridges running normal to the coastline are commonplace.

Generally thin (<1m) pyroclastic deposits, comprised of weathered ash and lapilli horizons, are subordinate to lava flows throughout the exposed volcanic sequence. The only exceptions are the Lomalla Pyroclastics (Warden, 1970), a relatively thick sequence (tens to possibly 100m) of pyroclastics exposed on the northern flank of the main shield (Fig. 5.5), and a sequence of buff coloured tuffs of ~3m thickness, which mantle much of the island.

Warden (1970) noted a correlation between basalt type and stratigraphic position, particularly in regard to the dominance of olivine and clinopyroxene phenocryst-rich lavas (termed picrite basalts by Warden, 1970) erupted subsequent to the deposition of the

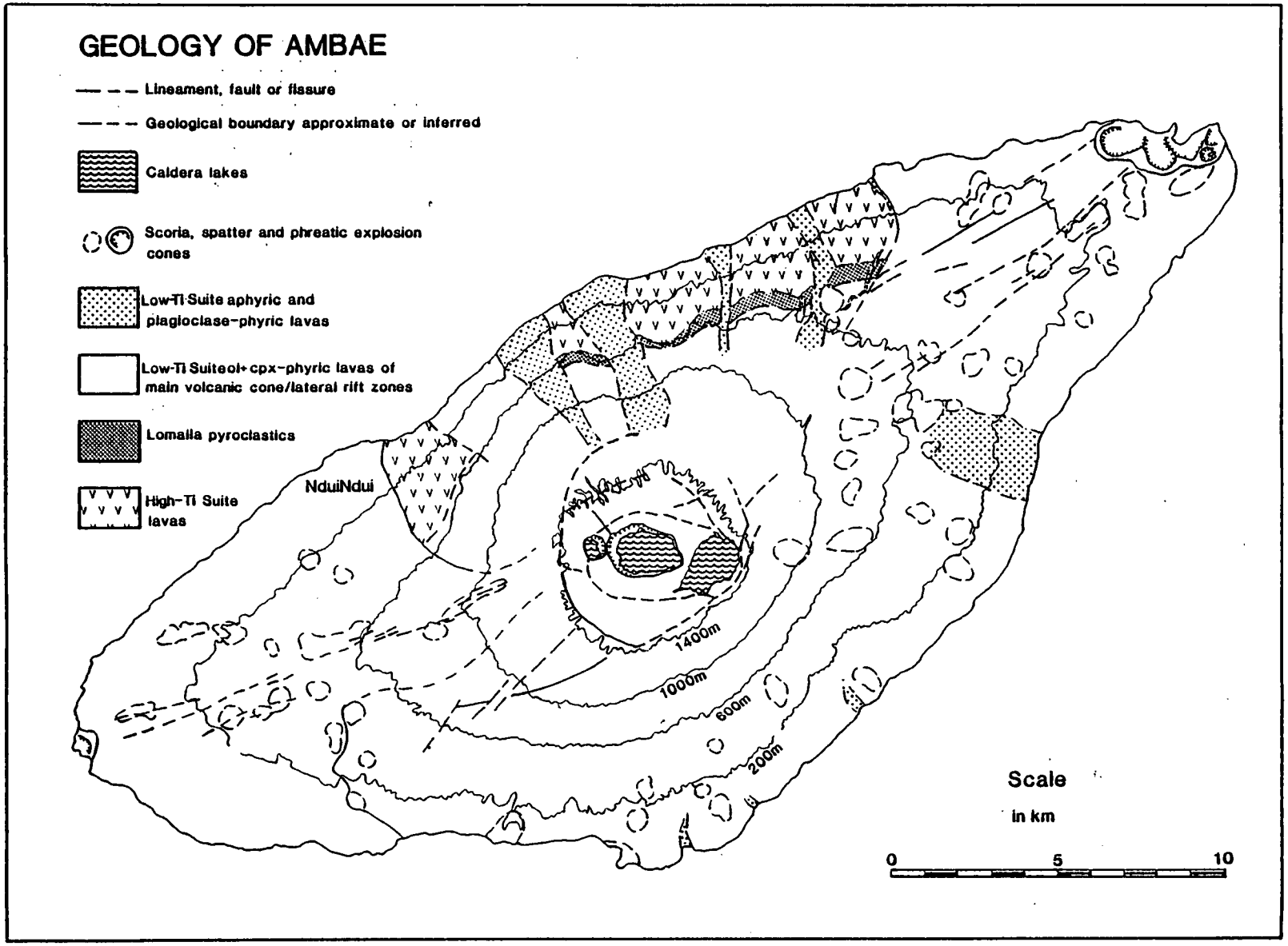

Figure 5.5 Geological map of Ambae.

Lomalla Pyroclastics. This group of phenocryst-rich lavas are intercalated with other more sparsely phyric lavas containing an identical phenocryst assemblage. They, in turn are partly overlain by light grey-coloured aphyric and plagioclase microphenocryst-phyric lavas, which are often confined to stream courses. These are among the most recent lavas erupted on Ambae, the youngest of which were erupted in the Ndui Ndui area about 300 years ago (Warden, 1970). The oldest lavas, occurring beneath the Lomalla Pyroclastics, outcrop along a restricted section of the northern coast (Fig 5.5.). They are easily distinguished from all later lavas by their ubiquitous large (2-3mm) phenocrysts of plagioclase. K/Ar dates place eruption of these basalts at about 100Ka (Gorton, 1974).

The basaltic nature of Ambae's eruptives was first documented by Warden (1970), and later confirmed by analysis of a comprehensive set (44 samples) of lavas by Gorton (1974). Warden also noted a variety of compositions from high-alumina to picritic basalts, that was later shown by Gorton (1977) to be a continuous spectrum of compositions between these end-members. Gorton (1977) suggested that the tight linear geochemical trends observed could be largely accounted for by the accumulation/fractionation of olivine phenocrysts. However, the scatter in K_2O contents found by Gorton (1977), upon which he defined a high and low K suite, could not be reconciled with the sorting of phencocryst phases present in the Ambae lavas.

5.4.1 An Analogy with Hawaiian Volcanism

A number of parallels can be drawn between Ambae and Hawaiian volcanism. In both these examples, the voluminous eruption of fluidal basalts has resulted in the construction of large volcanic shields with shallow sloping sides. Ambae's nested summit calderas are also similar in both form and size to those of Kilauea (Fig. 5.6), and in this light, the outline and steep sided nature of the Ambae's summit lakes are reminiscent of the physiography of Hawaiian lava lakes. Perhaps the most significant likeness to Hawaiian volcanism is the well developed rift zones, which radiate from the summit caldera and have provided the locus of eruptions forming the rift flank regions of Ambae. The fissure and scoria rampart association attest to eruption styles similar to the curtain of fire stage of Hawaiian eruptions, and the large scoria cones may equate with locii of fire

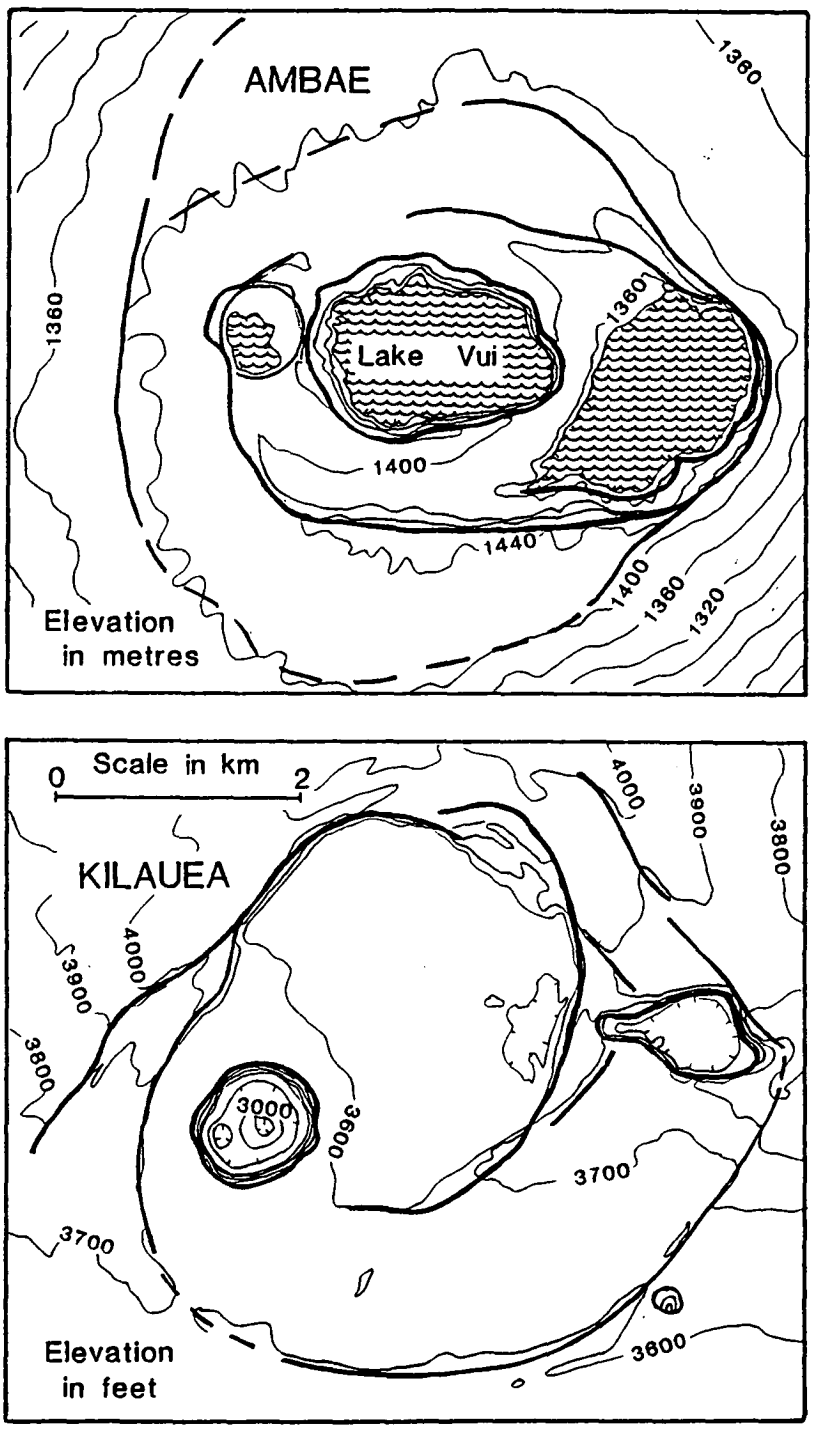

Figure 5.6 A comparison of the summit caldera topography of Ambae and Kilauea. Note the similar dimensions of both structures (fault structures indicated by thick lines), and also the size and shape of the very prominent, smaller, nested-calderas. Scales are equal for both maps.

fountaining, an interpretation consistent with the observation that these cones are often breached by lava flows on their downslope sides (Warden, 1970).

The NE-SW development of Ambae's rift zones has been attributed to alignment of volcanic activity along deep crustal fractures, enabling easy surface access to deeply-derived primitive magmas (Ramsay et al., 1984). These rift orientations, however, are more likely to represent the propagation directions of magma-filled dykes along the orientation of maximum horizontal stress within the volcano. Ryan (1987) has demonstrated for Hawaii that after failure of a (central) magma chamber, dykes migrate radially at shallow levels along a horizon of neutral magma buoyancy. This occurs between ~2 and 4km below the surface due to a density crossover, which results in the magma density exceeding that of the surrounding rock at shallower levels. Repeated episodes of dyke injection create extension (and thus a rift zone) in the near surface environment, normal to the direction of dyke emplacement (i.e. maximum horizontal stress direction). Depending on the physical environment controlling this process, dyke emplacement may at times be associated with surface eruptions as magma propagates at depth beneath the rift zones (Ryan, 1987). In this context, the northeast to southwest alignment of Ambae's rift zones is consistent with existence of compression across this segment of the arc due to collision of the DFZ.

CHAPTER 6

The Crystallisation of Primitive Arc Magmas from Ambae, Vanuatu

6.1 INTRODUCTION

The origin of parental and primitive magmas in island arcs is not well understood, as borne out by the many contrasting models existing for arc-magma genesis (e.g. Nicholls and Ringwood, 1971; Arculus and Powell, 1986; Tatsumi, 1988; Brophy and Marsh, 1987; Westercamp, 1987). Notable recent debate has centred on a fundamental question of whether primary melts are derived from the subducted ocean plate or from the overlying peridotite wedge (see Gust and Perfit, 1987; Crawford et al., 1987; Brophy and Marsh, 1987). This dichotomy can be attributed to contrasted interpretation of the voluminous andesites and high-alumina basalts present in many arcs, as either "evolved" or "primary" magmas, and the poorly established links between the comparatively rare examples of considerably more magnesian (primitive) arc magmas and their evolved counterparts. To shed light on the role of primitive Mg-rich magmas in arc magmagenesis, the nature and evolution of primitive lavas erupted on Ambae, Vanuatu, are assessed. The mineral chemistry and mineralogical data compiled in this study provide an important contribution to the as yet fragmentary documentation of the early crystallisation stages of primitive arc magmas.

6.2 THE GEOLOGICAL SETTING AND GEOLOGY OF AMBAE - AN OVERVIEW

Ambae is one the active Central Chain volcanoes in the Vanuatu Arc. It is located on a tectonically anomalous central arc segment undergoing compression due to coupling between the arc and the d'Entrecasteaux Fracture Zone (DFZ), a positive topographic feature on the subducting Indo-Australian Plate (see Fig. 5.1, Chapter 5.1). Ambae forms a

voluminous volcanic shield (~10000 km^3) that is elongate in a northeast to southwest orientation due to the focus of magmatic activity along rift zones radiating from the central summit caldera region in these directions (Fig. 6.1).

On the basis of phenocryst mineralogy and whole-rock geochemistry (Chapter 7), the volcanic stratigraphy of Ambae can be divided into two principal lava suites, which are separated in time by a comparatively thin (~100m) intervening pyroclastic sequence (the Lomalla Pyroclastics; Warden, 1970). The lava stratigraphy (see Fig. 6.1) comprises:

(1) an older sequence of plagioclase+clinopyroxene+olivine+ titanomagnetite-phyric lavas which have high relative abundances of high field strength (HFS) elements (which will be referred to here as the high-Ti Suite or HTS, see Chapter 7),

(2) a younger sequence of olivine+clinopyroxene (and rarely plagioclase)-phyric to aphyric lavas characterised by relatively low HFS element abundances (here called the low-Ti suite or LTS).

The LTS has been further subdivided to distinguish a minor group of intercalated lavas which have high relative concentrations of K-group elements (the high-K suite or HKS; see Chapter 7). A single analysis of a volcanic bomb from the Lomalla Pyroclastics, indicates a chemical relationship with the older HTS lava sequence.

6.3 PETROGRAPHY

6.3.1 Low-Ti Suite

The LTS lavas comprise a continuum from crystal-rich to crystal-poor and aphyric basalts. Phenocrysts, when present, always include olivine, which predominates over clinopyroxene and accessory Cr-spinel. Plagioclase and titanomagnetite also occur in some of the more crystal-poor and compositionally evolved samples.

Olivine

Olivine phenocrysts are dominantly euhedral in outline, though their corners and apices are frequently rounded. Embayed or strained and fragmented crystals form subordinate populations in several samples, but are usually absent. Optical zoning is apparent only as narrow (~100μm) rims, and less commonly as concentric zones, or crystal cores, littered with microlites and inclusions. Cr-spinels are abundant inclusions in many

Figure 6.1 Simplified geological map of Ambae illustrating the location of sites sampled in this study. Samples collected from the younger lava sequence are indicated by circles (LTS) and diamonds (HKS), and from the older lava sequence (HTS) by squares. Filled symbols denote those samples which have been analysed for major and trace elements (see Chapter 7). Numbers are Tasmania University catalogue suffixes for the sequence #68561 to #68642.

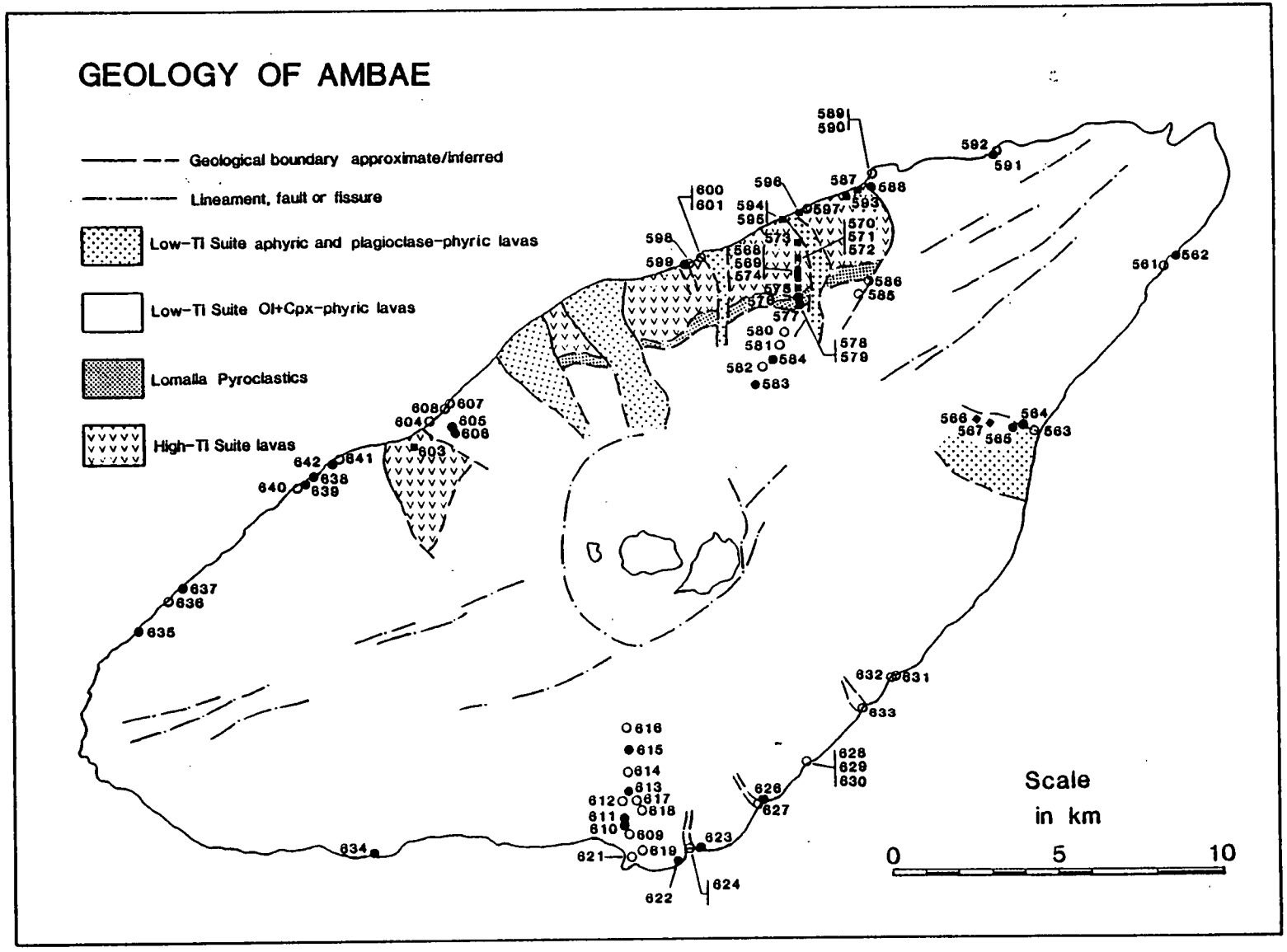
GEOLOGY OF AMBAE
Geological boundary approximate/inferred
Lineament, fault or fissure
Low-Ti Suite aphyric and plagioclase-phyric lavas
Low-Ti Suite Ol+Cpx-phyric lavas
Lomalla Pyroclastics
High-Ti Suite lavas
Scale
in km
0
5
10

olivines, as are trapped melt pools now comprised of matted quench crystals. A large proportion of the Cr-spinel inclusions are encased within a film of enclosing glass or matted quench crystals.

Analysis of the size distribution of olivine phenocrysts in several thin sections (cf. Marsh, 1988), reveals there is continuity in olivine crystal size (i.e. seriate texture) ranging from the matrix up to the largest phenocrysts which exceed 10mm in length. Several large olivine megacrysts, up to 28mm in length, have been sampled from brecciated flow tops and scoria accumulations. The largest of these is distinctive, having an homogeneous core ~5x10mm that is mantled by an optically-continous, skeletal overgrowth composed of rotated domains somewhat like the blades of a fan. Many of the other megacrysts sampled tend to be highly strained.

Clinopyroxene

Clinopyroxene phenocrysts occur as a variety of euhedral shapes in thin section, reflecting the varied orientation of prismatic forms in thin section. The distribution of crystal sizes is similar to that of olivine, with the largest phenocrysts again exceeding 10mm in length. In contrast to olivine, most clinopyroxene crystals have well developed growth zoning, which is often oscillatory and finely spaced. Usually, growth zones are concentrically arranged and continuous on all crystal sides. Resorbed and truncated growth zones are commonplace, as are coarsely mottled core regions that host irregularly shaped and variably crytallised melt inclusions. Immediately around these inclusions brownish straw-yellow clinopyroxene has crystallised, in contrast to the weak brown-green colouration of the host proper. Small olivine and titanomagnetite crystals are additional phases sometimes found included in clinopyroxene. Sector zoned crystals also occur, though infrequently (<1% of phenocrysts).

Spinel

Cr-spinel occurs as small (usually <200μm) euhedral microphenocrysts, and as abundant similarly sized euhedral to anhedral inclusions in olivine phenocrysts. It rarely occurs as inclusions in clinopyroxene. The microphenocrysts are zoned under reflected light from grey-brown cores to lighter grey-white titanomagnetite rims. Titanomagnetite

microphenocrysts do occur in some LTS samples, but are usually subordinate to the more abundant Cr-spinels.

Plagioclase

Plagioclase phenocrysts occur as relatively small (<1mm) laths and glomerocrysts in a number of the olivine and clinopyroxene phenocryst-poor lavas, in which they sometimes are the dominant phenocryst phase. Abundant plagioclase (>10 modal %), however, is present only in a few of the very youngest lava flows of the LTS. Oscillatory growth zoning is common, and is often accompanied by concentrations of microlites and/or dark coloured melt inclusions.

Cumulate Blocks and Polycrystalline Aggregates

A small number of cognate cumulate nodules (5mm-5cm) that have been sampled, exhibit a range in texture from heteradcumulate to orthocumulate. Phases present are dominated by olivine and/or clinopyroxene, along with accessory Cr-spinel, and in a few cases also plagioclase. Common glomerocrysts and crystal aggregates are possibly the disaggregation products of larger cumulate nodules, some of which in thin section appear to be disintegrating due to melt penetration along grain boundaries.

Groundmass Phases

The groundmasses of LTS samples are comprised of clinopyroxene, olivine, plagioclase laths, abundant small magnetite euhedra, and interstitial alkali feldspar. Low-Ca pyroxenes have not been identified.

6.3.2 High-K Suite

The two HKS lava samples (#68566 and #68567) are petrographically indistinguishable from the crystal-rich LTS lavas, apart from the infrequent presence of small pockets of phlogopite dispersed within their groundmasses.

6.3.3 High-Ti Suite

These lavas are predominantly crystal-rich with phenocrysts of plagioclase, clinopyroxene, olivine, titanomagnetite, and often also Cr-spinel. The relative abundances of the individual phenocryst phases differs markedly among these lavas, with plagioclase being abundant in olivine-poor samples and less common in more olivine-rich samples. The modal proportion of clinopyroxene invariably dominates over that of olivine.

Olivine and Clinopyroxene

The petrographic features of olivine and clinopyroxene are similar to those described for the LTS, apart from a relatively common discolouration of very thin rims (<20μm) about olivine phenocrysts, due to formation of a red brown phase, possibly hematite.

Plagioclase

The ubiquitous plagioclase phenocrysts in the HTS form small to medium sized (up to 3-4mm) euhedral laths or glomerocrysts. They are often complexly zoned, and like plagioclase in the LTS, many crystals are riddled with melt inclusions.

Titanomagnetite

Titanomagnetite often occurs as relatively large (up to 1-2mm) euhedral phenocrysts, that are sometimes skeletal in outline with deep embayments. Under reflected light these crystals have uniform grey-brown cores surrounded, across a narrow transition zone, by silver-grey rims.

The groundmass mineralogy of the HTS lavas is petrographically similar to the LTS.

6.4 PHASE CHEMISTRY

6.4.1 Analytical Techniques

The composition of phases occurring in selected samples, representative of each of the lava suites, have been determined by routine analysis using a Jeol JXA-50A electron microprobe with EDAX analytical facility, operating at 15kV and calibrated on pure Cu. All phenocryst phases were analysed with a focused beam (~2-3μm), whereas a defocused beam (or rastered focused beam) has been employed to measure the bulk composition of groundmasses and phenocryst-enclosed melt inclusions. Lowered detection limits for analysis of Ni contents in olivine were achieved by operating at higher beam current (20kV), and by employing wavelength dispersive analytical techniques.

The chemistry of the individual phases are discussed separately below, noting differences in phase chemistry between the various lava suites where appropriate. Representative analyses of all phases are listed in Tables 6.1 to 6.6.

Table 6.1 Selected olivine analyses (wavelength dispersive method).

Analysis#	1 Meg1	2 Meg1	3	4	5	6 CUM1	7 CUM1
SiO_2	40.87	40.93	40.67	40.44	39.96	40.29	40.29
FeO	6.73	6.75	8.78	9.7	11.49	10.32	10.24
MnO	--	--	--	--	--	--	--
FeO	52.06	51.59	50.04	49.25	47.63	48.82	49.20
CaO	--	0.11	0.18	0.12	0.19	0.22	0.18
NiO	0.17	0.20	0.16	0.16	0.10	0.09	0.08
Total	100.0	100.0	100.0	100.0	100.0	100.0	100.0
Mg#	93.2	93.3	91.0	90.1	88.1	89.5	89.5

(energy dispersive method)

	8	9	10	11	12	13	14	15	16
SiO_2	41.83	41.13	40.54	39.85	39.77	39.22	39.13	38.48	36.72
FeO	6.99	11.04	12.74	14.06	14.35	16.63	17.92	20.14	28.88
MnO	--	--	--	0.21	0.21	--	0.32	0.35	0.79
MgO	51.04	47.57	46.44	45.62	45.30	43.95	42.41	40.87	33.47
CaO	0.14	0.21	0.28	0.28	0.37	0.19	0.22	0.16	0.14
Total	100.0	100.0	100.0	100.0	100.0	100.0	100.0	100.0	100.0
Mg#	92.9	88.4	86.7	85.3	84.9	82.6	80.8	78.3	75.4

6.4.2 Olivine

Olivine phenocrysts in the Ambae lavas are notable for their restricted range of very magnesian compositions. A compilation of $Mg^{\#}$ ($100Mg/(Mg+Fe^{2+})$) values of individual phenocryst cores in the LTS lavas results in a normal distribution with a distinct mode at $Mg^{\#}$ ~87 (Fig. 6.2). The maximum $Mg^{\#}$ of olivine phenocrysts is 93.1, however, the largest olivine megacryst (#MEG1) extends the $Mg^{\#}$ range to 93.4. In the HTS lavas the maximum $Mg^{\#}$ of olivine is 89.9. The HTS in contrast to the LTS exhibits a bimodal distribution of compositions (Fig. 6.2) with many olivines being relatively Fe-rich, mostly within the range $Mg^{\#}$ 63-80. All analysed olivine phenocrysts are normally zoned with narrow (~100μm) Fe-rich rims, where $Mg^{\#}$ commonly falls below 80.

CaO and MnO contents are lowest in the most Mg-rich olivine, increasing up to 0.4 wt% CaO and ~1.0 wt% MnO in the more Fe-rich compositions. NiO contents are highest in the most magnesian olivines, which have values up to ~0.20 wt% (see Table 6.1). Compared to primitive olivine phenocrysts occurring in suites of oceanic basalts, which commonly have NiO contents above 0.30 wt% and up to 0.60 wt% in less magnesian olivine (e.g. see Chapter 2), these Ni contents are surprisingly low.

Several olivine phenocrysts with differing core $Mg^{\#}$ values were chosen for analysis of $Mg\text{-}Fe^{2+}$ zonation profiles, which have been constructed by analysis at set intervals. In each case, normal zoning occurs about a central region of almost constant $Mg^{\#}$, with the more Fe-rich rims ($Mg^{\#}$ 70-80) being uniformly narrow (~100μm: Fig. 6.3).

Relationships between the $Mg^{\#}$ of olivine and the bulk composition of host lavas have been sought through a systematic analysis of phenocryst core populations within individual lava samples of widely varying bulk composition (Fig. 6.4). No correlation was found in the LTS, where the majority of olivine compositions fall between Mg# 84 and 87 irrespective of host composition, nor in the HTS, where the bimodal distribution of olivine compositions noted earlier is also a characteristic of the individual lavas. The majority of the olivine phenocrysts are too Fe-rich to be in equilibrium with their host bulk rock compositions on the basis of established Fe/Mg partitioning relationships between olivine and basaltic melts (e.g. Roeder and Emslie, 1970; see Fig. 6.4).

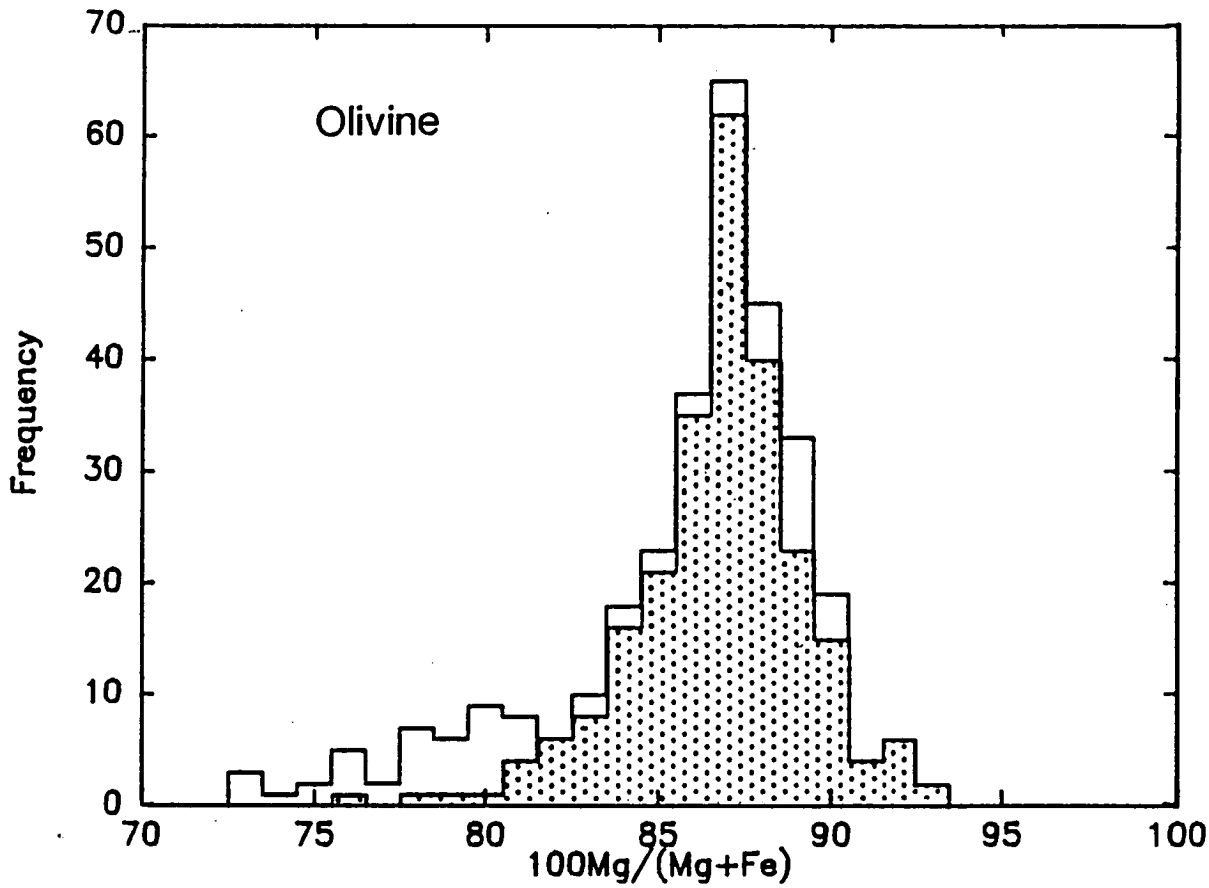

Figure 6.2 Cumulative frequency histogram of Mg# of individual olivine phenocryst cores in Ambae lavas. The contribution from olivine in the younger lavas (LTS and HKS) is stippled, whereas that from the HTS is plain.

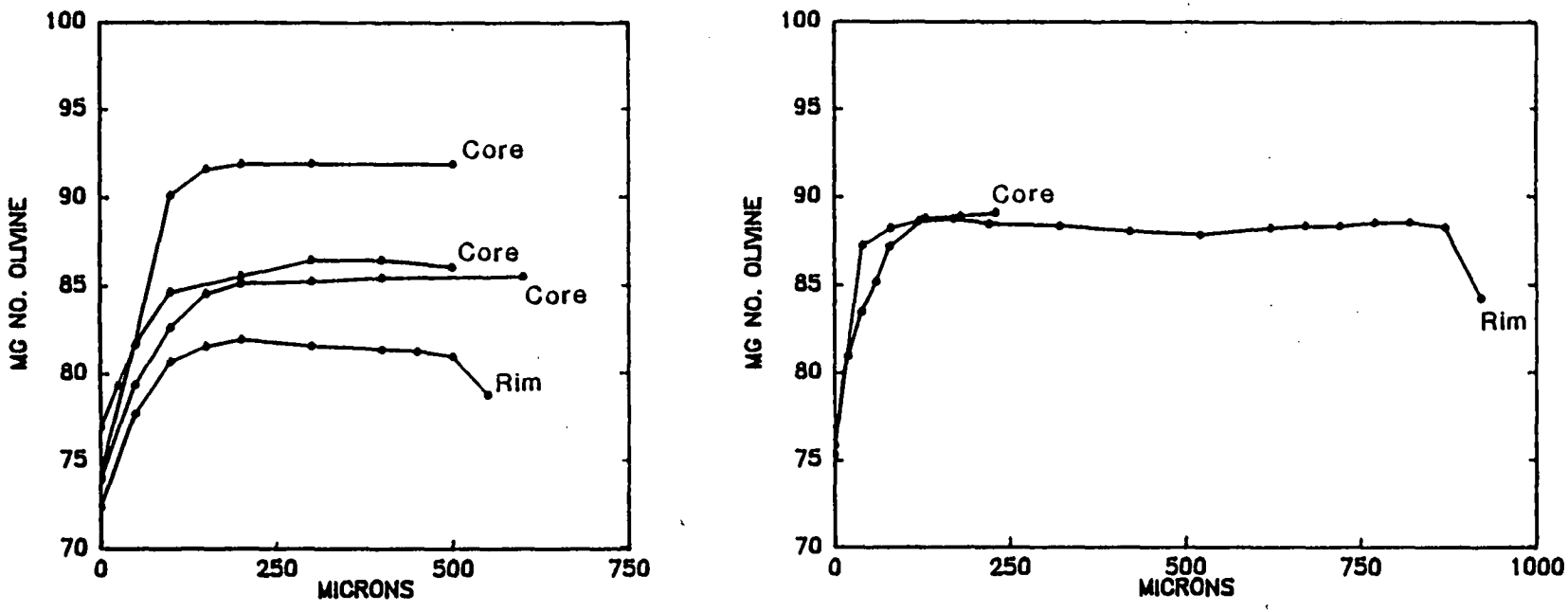

Figure 6.3 Olivine Mg# zonation profiles across several LTS-hosted olivine phenocrysts. Distance is measured in microns from the phenocryst rim, and "Core" and "Rim" denote traverses which have been ended in the crystal core or at the opposing rim.

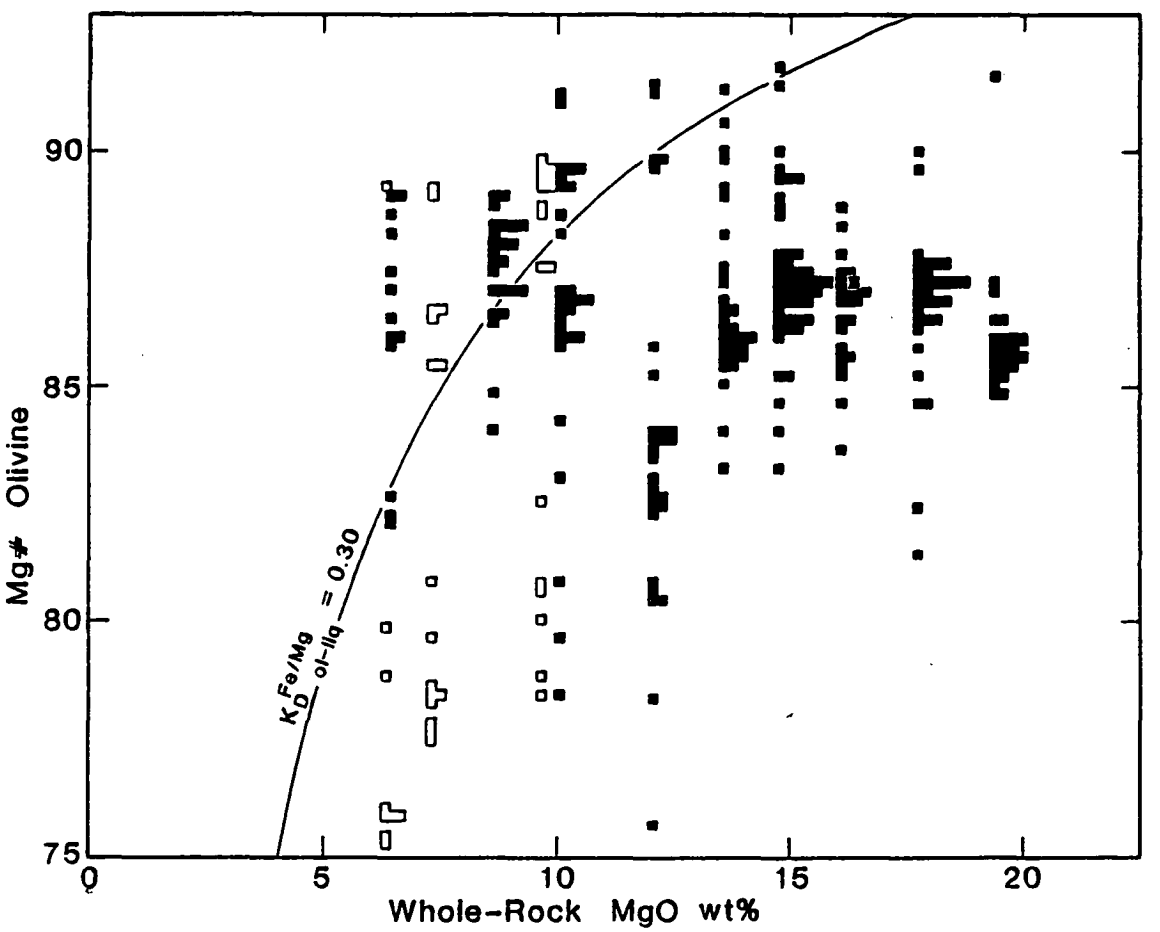

Figure 6.4 Cumulative frequency histograms for Mg# of individual olivine phenocryst cores, which have been compiled for individual lavas of the LTS and HKS (filled histograms) and the HTS (unfilled histograms). In each case, the histograms are plotted on baselines determined by the MgO content (in wt%) of the host lava. The curved line is the equilibrium olivine composition estimated for host lava bulk compositions assuming $Fe^{3+}/Fe^{2+} = 0.80$, $FeO^{tot} = 10$ wt%, and $K_D^{Fe/Mg}{}_{Ol\text{-}Liq} = 0.30$ (e.g. Roeder and Emslie, 1970).

6.4.3 Clinopyroxene

Clinopyroxene phenocrysts span a compositional range from diopside through to augite and salite (Fig. 6.5). A distinct relationship is observed between decreasing silica saturation levels of host lavas and increasing wollastonite component in clinopyroxene, particularly as compositions become more Fe-rich (Fig. 6.5). Clinopyroxene $Mg^{\#}$ (Fe^{2+} calculation based on stoichiometry) varies from very magnesian values near 92 (LTS_{max} = 92.4, HTS_{max} = 91.5) down to about $Mg^{\#}$ = 80 in the LTS, and $Mg^{\#}$ = 75 in the HTS. Unlike the distribution of olivine $Mg^{\#}$ a well defined modal value does not occur, though a rather diffuse frequency maximum does occupy a band between $Mg^{\#}$ 84 and 88 (cf. Figs. 6.2 and 6.6). Representative analyses are listed in Table 6.2.

The majority of minor elements follow broad systematic variation paths with decreasing $Mg^{\#}$ (Fig. 6.7). These trends are largely conchordant between the lava suites, with the exception of higher Ti contents and extension to lower $Mg^{\#}$ in the HTS clinopyroxenes. Among the behaviour of the individual elements, Cr alone decreases with $Mg^{\#}$ from maximum concentrations exceeding 1.0 wt% Cr_2O_3. All other minor components (Ti, Fe^{3+}, Al^{IV}, Al^{VI}, and probably Na) increase with Fe-enrichment until at least $Mg^{\#}$ ~84, after which Al^{IV}, Al^{VI}, and Fe^{3+} decrease with further reduction in $Mg^{\#}$.

Considerable geochemical variability within individual clinopyroxene phenocrysts is exposed by random spot analyses. Detailed core to rim profiles (Fig. 6.8) reveal this to be part of complex geochemical zoning matching the optical zonation of these crystals. This zoning entails oscillations back and forth along the chemical evolution paths outlined in Figure 6.7. Of note in this regard is the sensitivity of Cr content to variations in $MG^{\#}$ ($100Mg/(Mg+Fe^{tot})$), with small increases in $MG^{\#}$ resulting in doubling or even trebling of clinopyroxene Cr contents.

The zonation patterns are highly variable in form, ranging from largely unzoned regions (mainly Mg-rich cores) to intense oscillatory variation, which petrographic observations indicate may be much finer (<10μm) than the resolution of the analysis spacing employed (i.e. 25 or 50μm).

The majority of clinopyroxenes found coexisting with olivine compare favourably with Fe/Mg partitioning occurring between olivine and clinopyroxene in 1 atm experimental melting studies (e.g. Grove and Bryan, 1983), but many are too Fe-rich

Table 6.2 Selected clinopyroxene analyses.

Anal.#	1	2	3	4	5	6	7	8	9
Suite	LTS CUM1	LTS	LTS	LTS	LTS	LTS	LTS	LTS	LTS
SiO_2	54.19	53.98	53.60	53.27	53.32	52.60	51.72	51.51	50.87
TiO_2			0.24		0.18	0.28	0.33	0.34	0.41
Al_2O_3	1.06	1.37	1.49	1.79	1.88	2.38	3.25	3.43	4.05
Cr_2O_3	0.63	0.82	0.94	0.82	0.76	0.72	1.01	0.56	0.63
FeO	2.63	2.66	2.85	3.62	3.91	4.46	4.71	5.36	5.84
MnO									
MgO	17.88	17.40	17.51	17.05	16.91	16.49	16.02	15.78	15.31
CaO	23.61	23.77	23.37	23.45	23.04	23.07	22.96	23.02	22.89
Na_2O									
Total	100.0	100.0	100.0	100.0	100.0	100.0	100.0	100.0	100.0
MG#[b]	92.4	92.1	91.6	89.4	88.5	86.8	85.8	84.0	82.4
Fe_2O_3[a]	--	--	--	0.39	--	0.32	0.61	1.20	1.38
FeO	2.63	2.66	2.85	3.27	3.91	4.17	4.16	4.27	4.59
Mg#[c]	92.4	92.1	91.6	90.3	88.5	87.6	87.3	86.8	85.6

Anal.#	10	11	12	13	14	15	16	17	18
Suite	LTS	LTS	LTS	LTS	LTS	HKS	HKS	HKS	HKS
SiO_2	50.61	50.73	49.12	50.95	49.86	53.25	52.45	52.07	51.63
TiO_2	0.46	0.48	0.81	0.47	0.68		0.23	0.24	0.31
Al_2O_3	4.05	4.30	5.79	3.85	4.62	1.83	2.40	2.73	3.36
Cr_2O_3	0.26	0.40	0.41			1.20	0.97	0.79	0.79
FeO	6.57	6.55	7.25	7.83	8.72	3.64	3.68	4.33	4.90
MgO	15.15	15.13	13.99	14.91	14.24	17.13	16.45	16.33	15.74
CaO	22.89	22.41	22.63	21.98	21.87	22.96	23.83	23.52	23.28
Na_2O									
Total	100.0	100.0	100.0	100.0	100.0	100.0	100.0	100.0	100.0
MG#	80.8	80.4	77.5	77.2	74.4	89.4	88.9	87.0	85.1
Fe_2O_3	2.20	1.26	1.90	1.36	2.09	--	0.67	1.20	0.84
FeO	4.58	5.41	5.53	6.60	6.83	3.64	3.07	3.24	4.14
Mg#	85.5	83.3	81.8	80.1	78.8	89.4	90.5	90.0	87.1

Anal.#	19	20	21	22	23	24	25	26	27
Suite	HTS	HTS	HTS	HTS	HTS	HTS	HTS	HTS	HTS
SiO_2	53.87	53.89	53.13	52.63	51.22	50.25	49.14	50.35	49.41
TiO_2			0.31	0.33	0.60	0.64	0.88	0.81	1.22
Al_2O_3	1.39	1.39	1.66	2.15	3.40	4.10	5.12	3.90	4.48
Cr_2O_3	1.03	0.53	0.43	0.34	0.36	0.41	0.43		
FeO	2.93	3.43	3.97	4.74	5.41	6.15	7.07	8.93	9.00
MnO									0.25
MgO	17.58	17.43	16.89	16.50	15.59	15.24	14.10	14.56	13.82
CaO	23.20	23.35	23.61	23.32	23.42	23.21	23.27	21.19	21.57
Na_2O								0.26	0.25
Total	100.0	100.0	100.0	100.0	100.0	100.0	100.0	100.0	100.0
MG#	91.5	90.1	88.3	86.1	83.7	81.5	78.1	74.4	73.2
Fe_2O_3	--	--	0.58	0.90	1.57	2.64	2.74	2.57	2.76
FeO	2.93	3.43	3.45	3.93	3.99	3.75	4.58	6.59	6.49
Mg#	91.5	90.1	89.7	88.2	87.4	87.9	84.6	79.7	79.1

a Fe_2O_3 content based on stoichiometry
b $MG^{\#} = Mg/(Mg+Fe^{tot})$
c $Mg^{\#} = Mg/(Mg+Fe^{2+})$

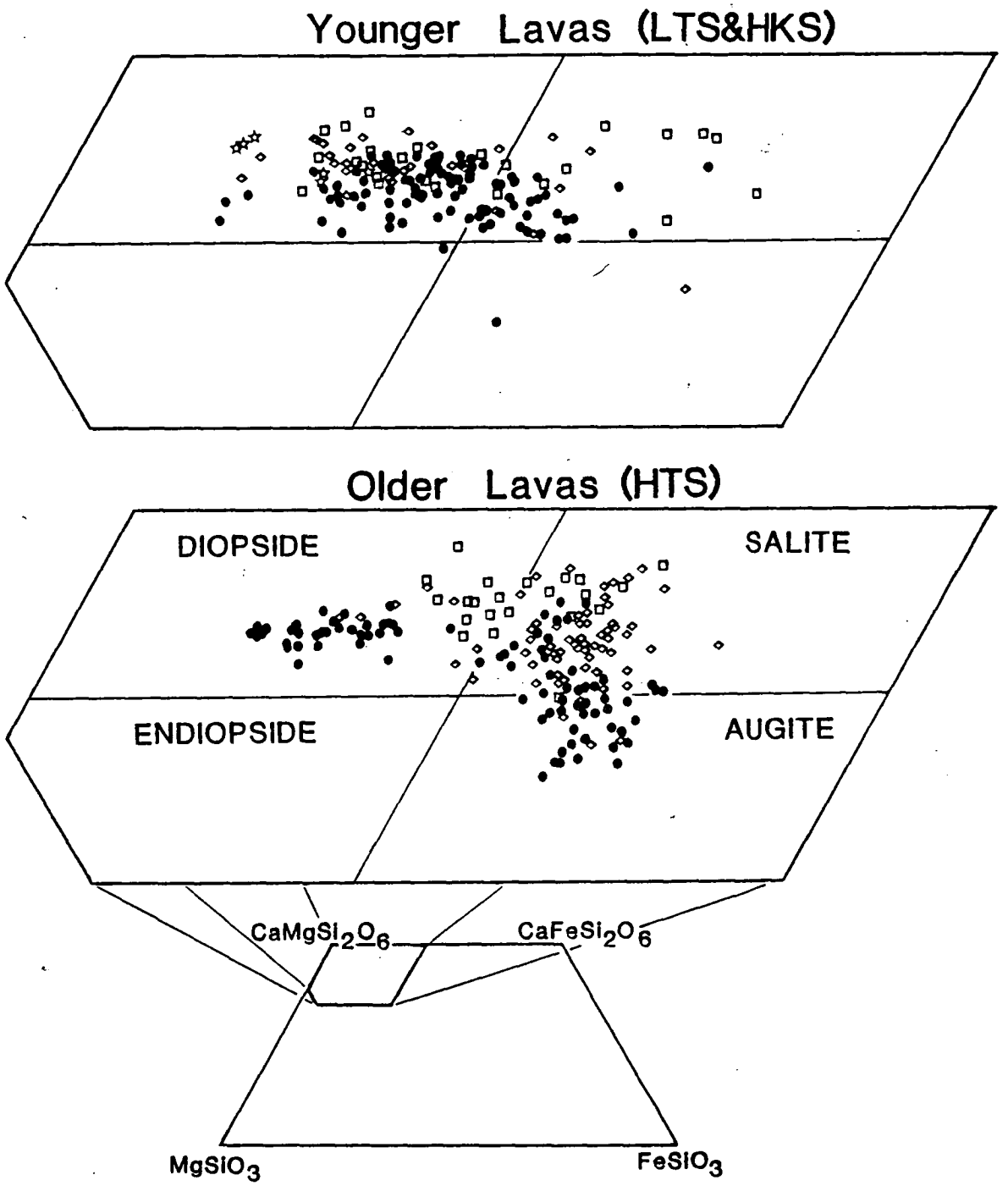

Figure 6.5 Quadrilateral components of clinopyroxene phenocrysts occurring in (A) the younger lava sequence (LTS and HKS) and (B) the older lava sequence (HTS). All Fe is calculated as Fe^{2+}. Symbol usage is based on the normative mineralogy of host lava bulk compositions (see Figure 7.3 in Chapter 7). Filled circles indicate >1% normative Hypersthene, filled diamonds indicate <2% normative Nepheline and <1% normative Hypersthene, and squares indicate >2% normative Nepheline. Clinopyroxene compositions occurring in cumulate nodules are plotted as five-point stars. Note the trend occurring toward wollastonite-rich compositions as the clinopyroxenes become more Fe-rich in the more silica undersaturated bulk compositions.

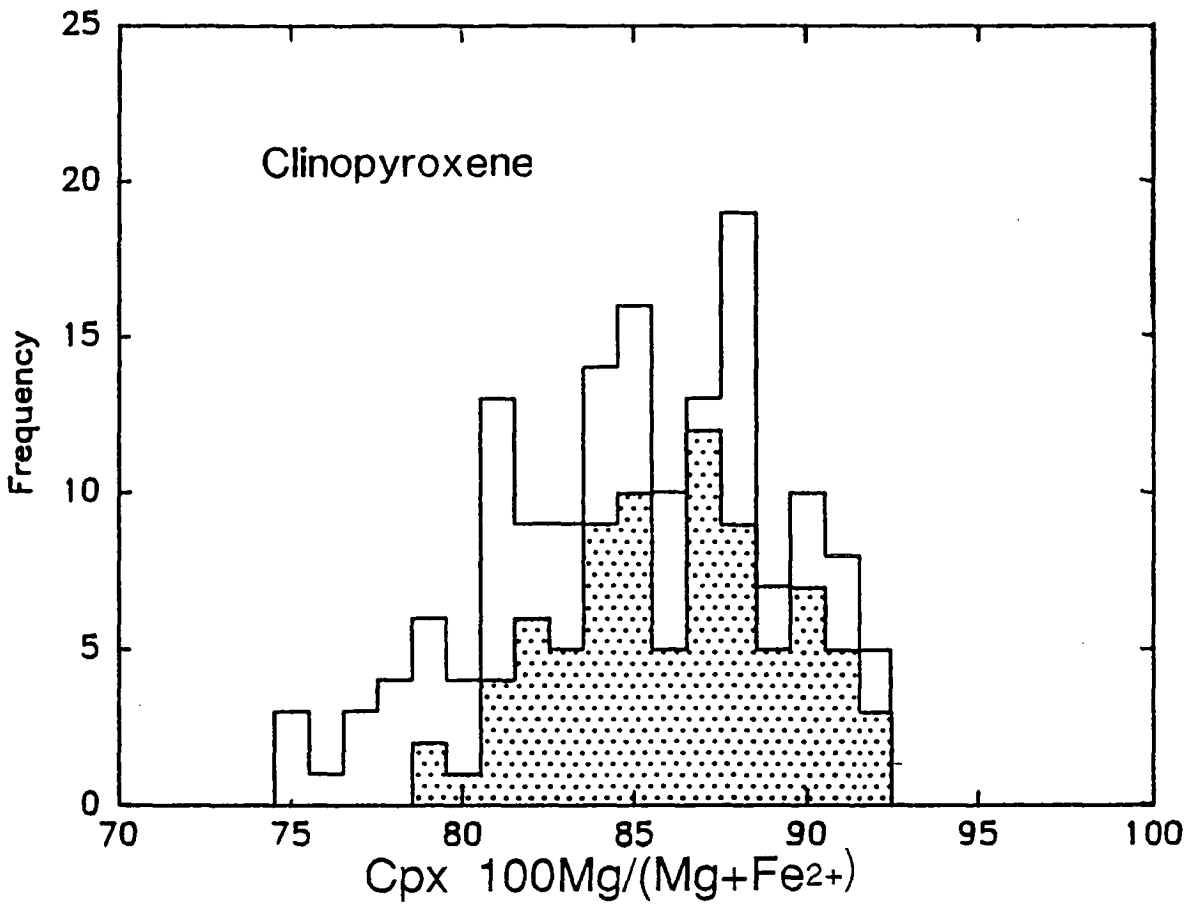

Figure 6.6 A cumulative frequency histogram for Mg# of clinopyroxene phenocrysts (single analyses only) occurring in the LTS and HKS (stippled), and in the HTS (plain).

Figure 6.7 Variation of cations versus $Mg^{\#}$ in Ambae clinopyroxene phenocrysts (Fe^{2+} and Fe^{3+} based on stoichiometry). Clinopyroxene occurring in the LTS and HKS is plotted as filled circles, and in the HTS as open squares. Arrows outline compositional evolution paths occurring with Fe-enrichment. Note the higher Ti contents of clinopyroxene occurring in the HTS than in the LTS and HKS.

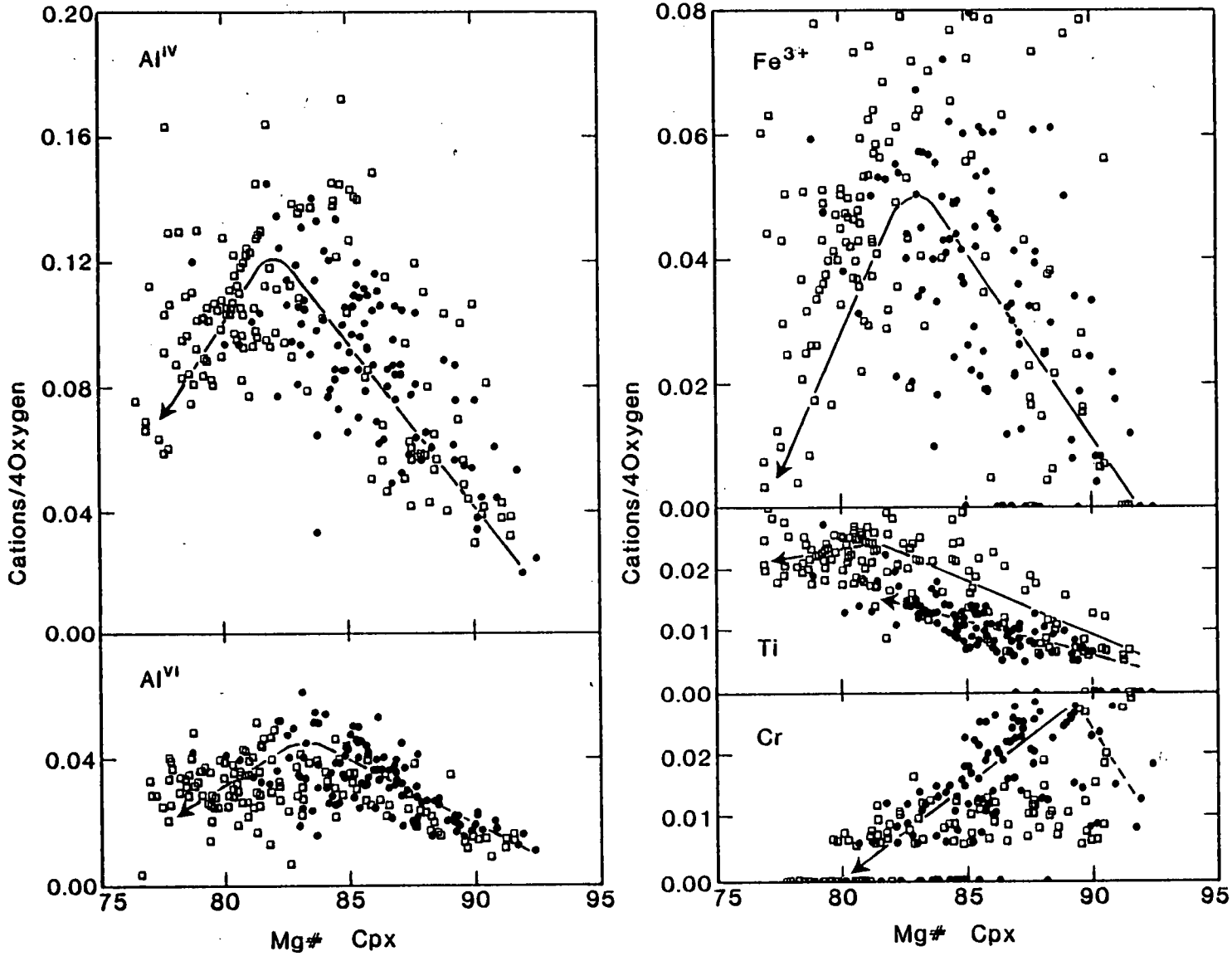
Al^IV
Al^VI
Fe3+
Ti
Cr
Cations/4Oxygen
Mg# Cpx
0.20
0.16
0.12
0.08
0.04
0.00
0.06
0.02
0.01
75
80
85
90
95

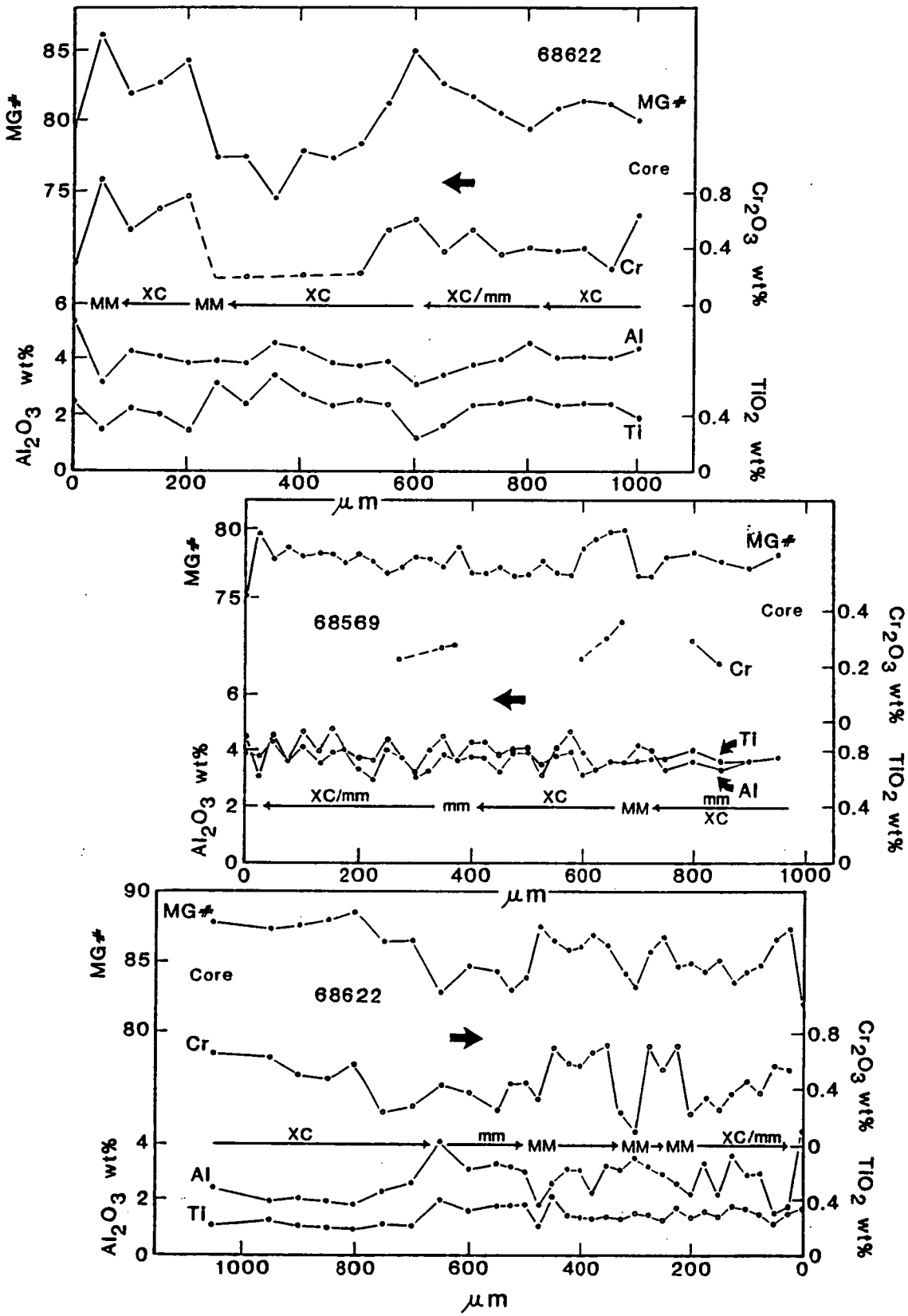
68622
MG#
Core
Cr
Al
Ti
MM
XC
XC/mm
Cr_2O_3 wt%
Al_2O_3 wt%
TiO_2 wt%
μm
68569
mm

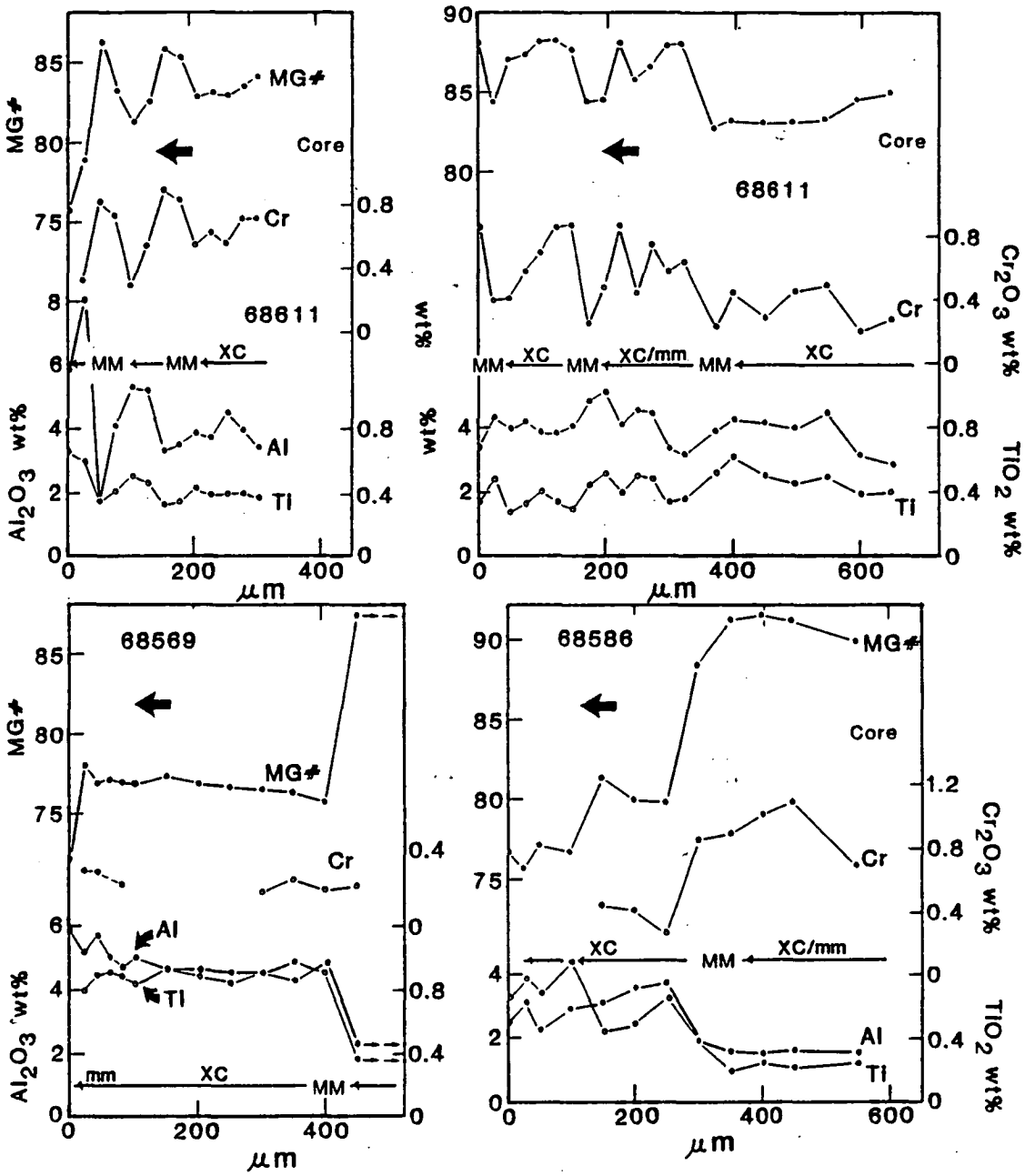

Figure 6.8 Chemical zonation profiles of MG#, TiO_2, Al_2O_3, and Cr_2O_3, for rim to core traverses across selected clinopyroxene phenocrysts (host sample# is shown in bold type). Distances are measured in microns from the phenocryst rim, and the arrows indicate the direction of crystal growth. See text for a discussion of the origin of zoning, and for interpretation of regions marked XC, mm, and MM.

when compared to an empirical calibration of olivine-clinopyroxene equilibria based on primitive arc magmas from nearby Merelava volcano (eg. Barsdell, 1988: see Fig. 6.9). Notably, the best match with the partitioning relationship documented by Barsdell, occurs for coexisting Mg-rich clinopyroxene and olivine in a single heteradcumulate nodule, which on the basis of textural criteria can be regarded as the best available example of equilibrium between these two phases.

Groundmass clinopyroxenes extend the phenocryst geochemical trends to lower $Mg^{\#}$, Al, and Fe^{3+}, and higher Ti contents. The only examples of low-Ca pyroxenes found are groundmass pigeonites occurring in several HTS lavas (#68587 and #68673).

6.4.4 Spinel

Cr-spinels,occurring as inclusions in magnesian olivine phenocrysts (i.e. $Mg^{\#}>80$) and as microphenocrysts in the LTS lavas, but less commonly in the HTS lavas, form an extensive solid solution of Cr-rich compositions (Fig. 6.10). These fall mainly within the compositional limits of $Cr^{\#}$ ($100Cr/(Cr+Al)$) = 45-78, $Mg^{\#}$ = 19-68, and $Fe^{3\#}$ ($100Fe^{3+}/(Fe^{3+}+Al+Cr)$) = 10-37, though several small populations extend the $Cr^{\#}$ range to 84, and $Fe^{\#}$ to between 3.5 and 42. The Cr-spinels are compositionally separated from the Ti-magnetite solid-solution spinels that occur predominantly as phenocrysts in HTS lavas, overgrowths on Cr-rich spinel microphenocrysts, and in the groundmass of both the HTS and LTS lavas. Representative analyses from this diverse range of compositions are listed in Table 6.3.

The Ambae spinels broadly overlap with compositions occurring in other island arc basalts and some primitive intraplate lava suites (e.g. Hawaii, Tasmantid Seamounts). The crystals with the highest $Cr^{\#}$ examples match spinels crystallised in magmas believed to derive from refactory mantle sources, such as the Troodos Upper Pillow Lavas and some boninitic lavas (see Fig. 6.11). Ambae and MORB spinels are almost mutually exclusive in terms of $Cr^{\#}$ and $Mg^{\#}$ (Fig. 6.11a), and the higher $Fe^{3\#}$ and lower Ti contents of the Ambae spinels distinguish them from Hawaiian spinels (Fig. 6.10 & 6.11b).

Decreasing Cr content (56.2 to ~20 wt% Cr_2O_3) in Cr-spinel is accompanied by increasing Fe^{3+}, Ti, and Al (7.4 to 19.3 wt% Al_2O_3). The Ti contents of HTS spinels

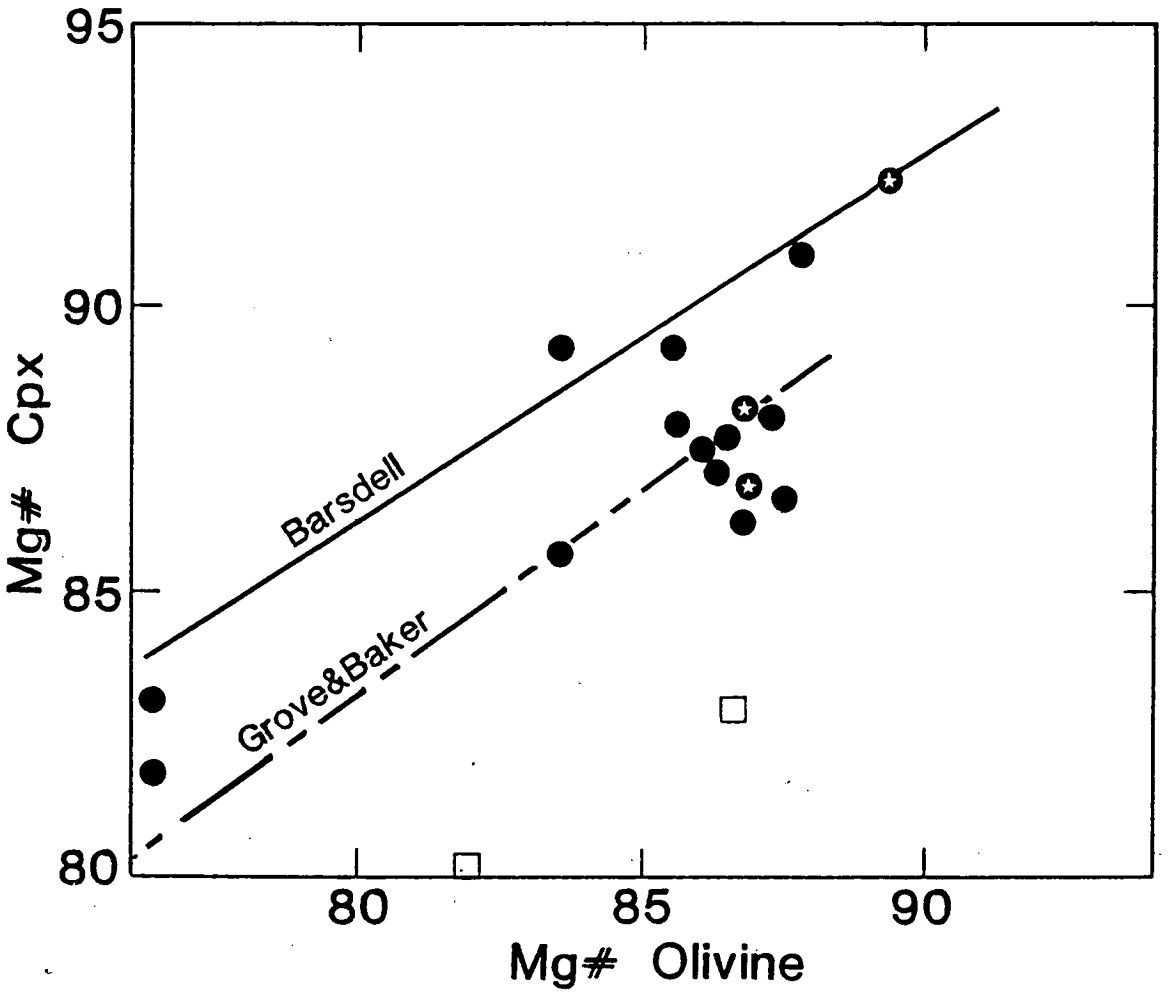

Figure 6.9 The relationship between Mg# of coexisting clinopyroxene and olivine in Ambae lavas. Circles denote olivine-clinopyroxene pairs occurring in LTS and HKS lavas, squares those found in HTS lavas, and circled stars those occurring in cumulate nodules. Lines marked Barsdell and GB are equilibrium relationships determined for coexisting clinopyroxene and olivine in lavas from Merelava, Vanuatu, by Barsdell (1988), and in 1atm melting experiments on primitive MORB basalts by Grove and Bryan (1983).

Table 6.3 Representative spinel analyses (compositions normalised to 100 wt%).

Analysis#	1	2	3	4	5	6	7	8	9
Suite	LTS	LTS	LTS	LTS	LTS	LTS	LTS	LTS	LTS
TiO_2	0.22	0.45	0.52	0.50	0.48	0.66	0.53	0.79	0.32
Al_2O_3	7.56	9.19	9.51	9.89	10.20	10.90	12.32	12.20	16.97
Cr_2O_3	55.13	52.40	48.68	44.38	44.81	46.27	51.59	43.40	51.96
Fe_2O_3[a]	9.40	9.62	13.79	16.82	16.29	14.19	8.91	16.50	2.63
FeO	17.08	18.06	15.54	18.19	17.57	16.30	12.11	13.33	15.13
MgO	10.61	10.28	11.96	10.22	10.65	11.68	14.54	13.80	12.98
MnO	–	–	–	–	–	–	–	–	–
$Mg^{\#}$	52.6	50.4	57.8	50.1	51.9	56.1	68.2	64.9	60.5
$Cr^{\#}$	83.0	79.3	77.4	75.1	74.7	74.0	73.7	70.5	67.3
$Fe^{3\#}$	11.9	12.2	17.3	21.3	20.6	17.8	10.8	20.3	8.8
$Mg^{\#}_{Ol}$[b]	86.8	91.2	89.4	87.0	88.4	91.4	92.8	91.4	91.3
T°C[c]	1099	841	1067	1030	998	908	1010	1067	850
ΔQFM[d]	1.27	2.21	2.30	2.38	2.53	2.84	2.13	2.90	-0.16
ΔQFM[e]	-0.66	0.66	0.48	0.54	0.76	1.28	0.66	1.31	-1.73

Analysis#	10	11	12	13	14	15	16	17	18
Suite	LTS	LTS	LTS	HTS	HTS	HTS	HTS	HTS	LTS
TiO_2	1.95	1.15	1.33	0.90	1.35	8.94	18.90	14.23	7.27
Al_2O_3	19.04	13.43	13.42	14.74	12.34	6.00	2.80	2.39	4.30
Cr_2O_3	25.31	33.61	26.0	41.58	42.33	1.19	0.25		4.02
Fe_2O_3	22.42	23.00	28.94	15.25	15.72	45.46	30.00	40.00	47.36
FeO	21.44	17.53	21.55	13.38	15.54	34.67	46.12	40.37	34.18
MgO	9.85	11.47	8.76	14.12	12.71	3.73	1.94	2.41	2.87
MnO	–	–	–	–	–	–	–	0.59	–
$Mg^{\#}$	45.1	54.1	42.0	65.3	59.3	16.1	7.0	9.6	13.0
$Cr^{\#}$	47.1	62.7	56.5	65.4	69.7	11.7	5.6	–	38.5
$Fe^{3\#}$	28.5	29.1	37.4	18.5	19.8	81.0	86.6	91.4	81.2
$Mg^{\#}_{Ol}$	84.4	85.8	84.7	89.7	89.5	75.8	–	–	–
T°C	914	1135	959	1143	1058	910			
ΔQFM[d]	2.77	2.69	3.21	2.38	2.52				
ΔQFM[e]	0.97	0.81	1.15	0.77	0.89	1.06			

a Fe_2O_3 based on stoichiometry.

b $Mg^{\#}$ of host olivine phenocryst

c Olivine spinel temperature calculated after O'Neill and Wall (1987)

d log of fO_2 relative to the QFM oxygen buffer calculated using equation 6.6 (Ballhaus et al., in press)

e ΔQFM calculated following O'Neill and Wall (1987) assuming log $aSiO_2$ = -0.5

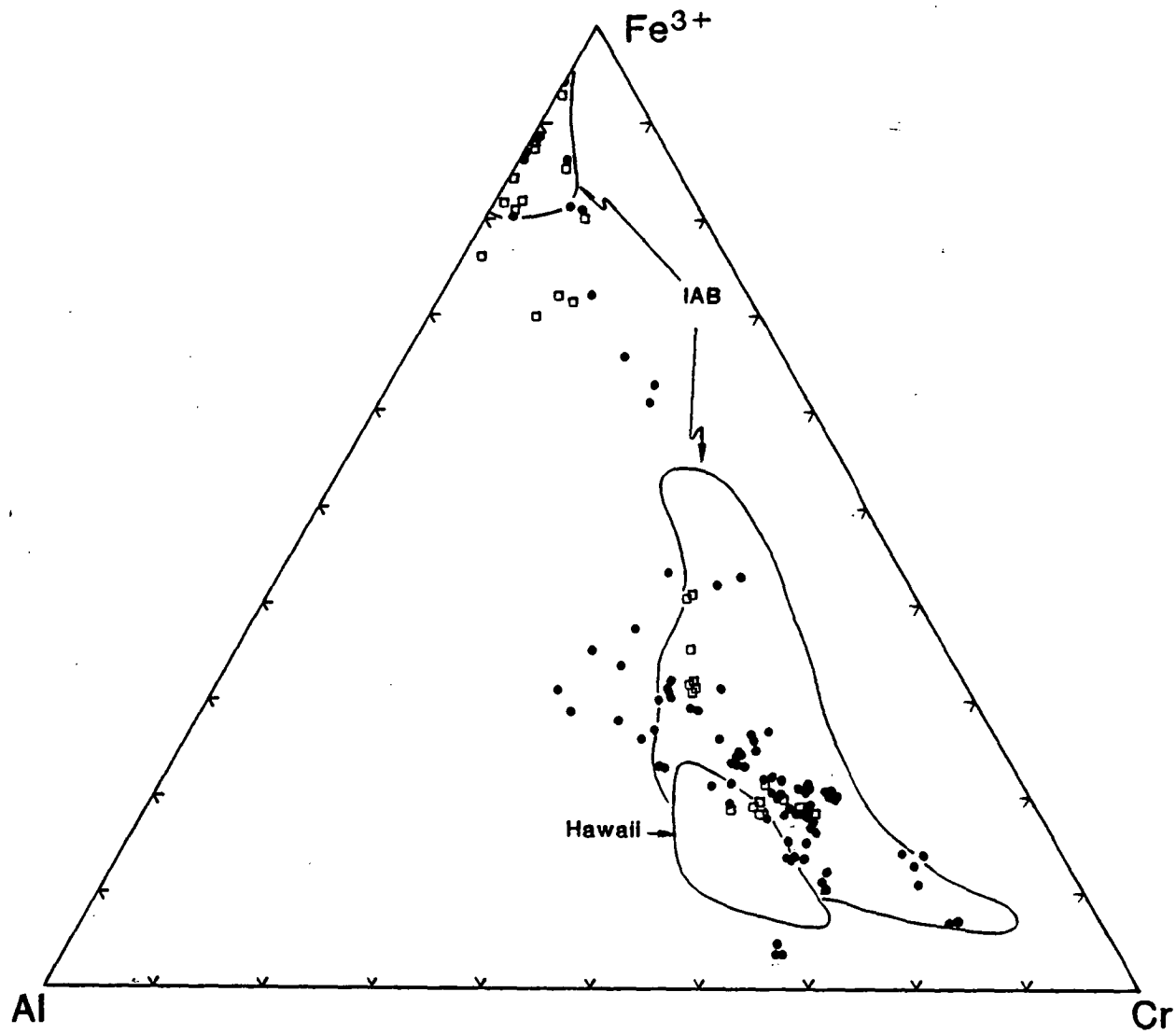

Figure 6.10 Trivalent cation proportions (Fe^{3+} based on stoichiometry) of Cr-spinel and magnetite occurring as microphenocrysts and inclusions in phenocrysts in Ambae lavas. Examples in LTS and HKS lavas are shown as solid circles and in the HTS lavas as squares. The field for primitive IAB is compiled from Yamamoto (1984), Johnson et al. (1985), Nye and Reid (1986), and Ramsay et al. (1984); and the field for Hawaii is compiled from the BVSP (1981), Hawkins and Melchior (1983), Sen and Presnall (1986), Wilkinson and Hensel (1987), Nicholls and Stout (1988), and Eggins and Green (unpublished data).

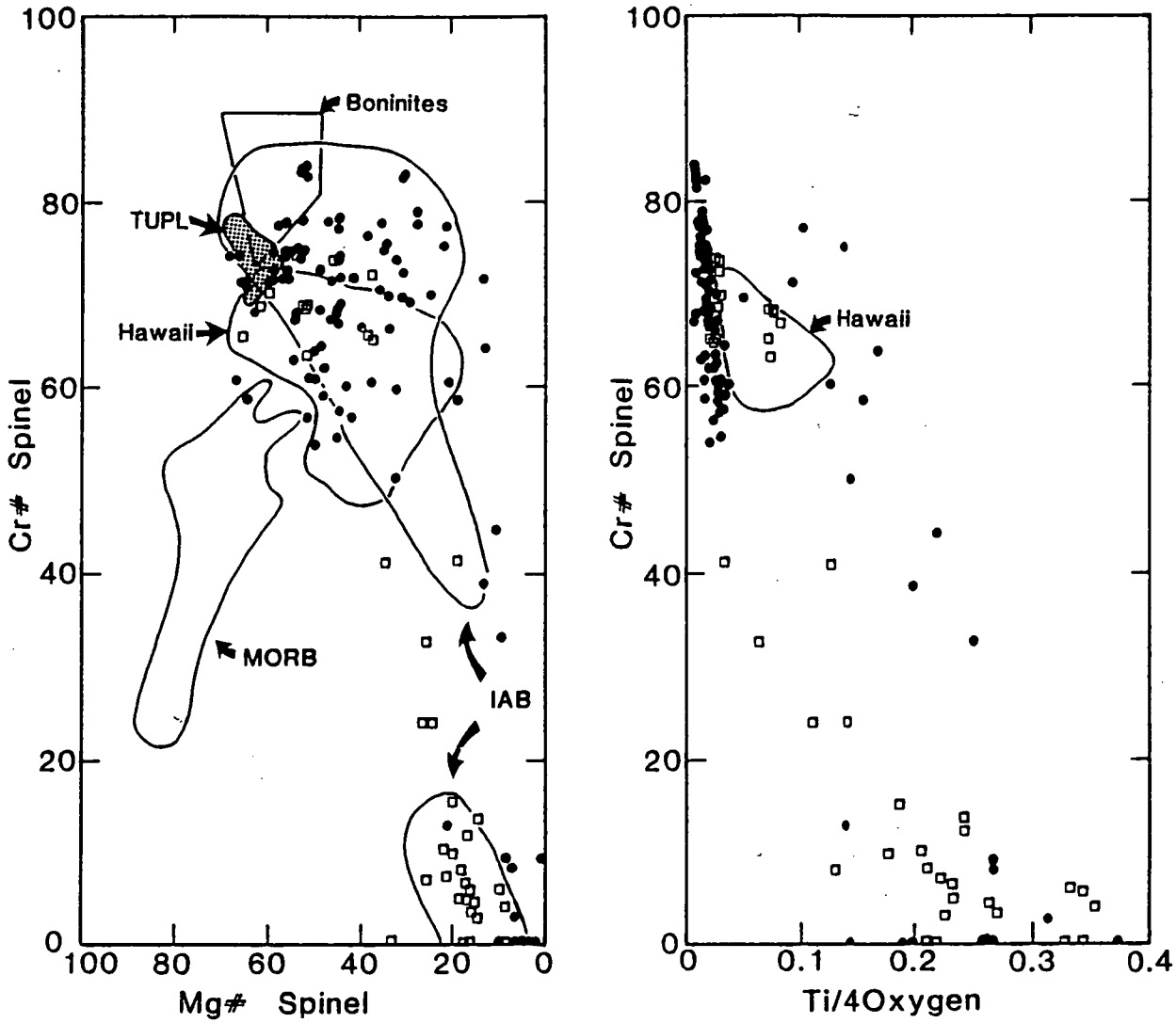

Figure 6.11 Cr# versus Mg#, and Cr# versus Ti content, of Cr-spinel and titanomagnetite occurring in Ambae lavas. Symbols as for Figure 6.10. The fields for N-MORB and Troodos Upper Pillow Lavas (TUPL) are from Dick and Bullen (1984), and the data sources for Hawaii and primitive IAB fields are listed in Figure 6.10.

appear to evolve along trends at slightly higher Ti contents than the LTS spinels (Fig. 6.12b).

Compositional zoning in most Cr-spinels is restricted mainly to variations in Mg and Fe^{2+}, with $Mg^{\#}$ decreasing toward crystal rims. Relative enrichment of Fe^{2+} over Mg is greatest in the rims of microphenocrysts, and also spinels only partially included in olivine, with both types having lower rim $Mg^{\#}$ (20-30) than Cr-spinels fully enclosed by olivine ($Mg^{\#}$ of rims typically >35).

Coexisting Cr-spinel and olivine exhibit a weak positive correlation between $Mg^{\#}_{Ol}$ and the $Mg^{\#}_{Sp}$, and also between $Mg^{\#}_{Ol}$ and $Cr^{\#}_{Sp}$ (not shown).

TiO_2 contents of titanomagnetite phenocrysts range from 2.4 to 20.2 wt%, which occurs concurrently with decreasing Al_2O_3 (10.5 to 1.45 wt%), $Mg^{\#}$ (30 to 3), and Cr_2O_3 content (~2.0 to 0 wt%), and increasing MnO content (up to 0.90 wt%). Groundmass titanomagnetites are similar in composition to the phenocrysts.

6.4.5 Plagioclase

Plagioclase phenocrysts span a range of calcic compositions from $Ca^{\#}$ [100Ca/(Ca+Na)] 66 to 94.5, although the majority (>70%) occupy a more restricted range between $Ca^{\#}$ 82 and 91 (Fig. 6.12). Most plagioclase phenocrysts contain <1 mole % $KAlSi_3O_8$ component, and have relatively high FeO^{tot} contents, between 0.7 and 1.0 wt%. Decreasing $Ca^{\#}$ is correlated with a slight increase in $KAlSi_3O_8$ component, but bears no systematic relation to FeO^{tot} contents. Compositional zoning can exceed 10 $Ca^{\#}$ units, and may be either reverse, normal, or oscillatory in nature. Selected analyses are listed in Table 6.4.

6.4.6 Groundmass Chemistry

Groundmass compositions of selected samples have been obtained by electron microprobe analysis of polished glass chips, fused by Ir-strip heater from groundmass powders drilled from thin (1-2mm) rock slivers. Duplicates of each sample were prepared in this way, and the mean values of multiple (n = 8-10) defocused beam analyses of each were averaged. In the few cases where duplicate analyses did not match within analytical error, it was assumed that contamination by the dominant ferromagnesian phenocrysts had occurred, and the most magnesian glass composition was discarded. Results for 20 samples analysed by this method are listed in Table 6.5.

Table 6.4 Selected plagioclase analyses.

No.	1	2	3	4	5	6	7
Suite	HTS	HTS	LTS	LTS	HTS	LTS	HTS
SiO_2	46.25	44.99	46.31	46.45	46.51	47.11	50.38
Al_2O_3	33.88	34.58	33.48	33.94	33.41	33.14	31.04
FeO	0.73	0.93	0.90	0.88	1.01	0.96	0.87
MgO		0.19					
CaO	18.30	18.32	17.97	17.27	17.43	16.74	14.30
Na_2O	0.84	0.98	1.34	1.46	1.49	1.88	3.20
K_2O					0.16	0.17	0.20
Total	100.0	100.0	100.0	100.0	100.0	100.0	100.0
Ca#[a]	92.3	91.2	88.1	86.8	85.8	82.2	70.4

a $Ca^{\#} = 100Ca/(Ca+Na)$

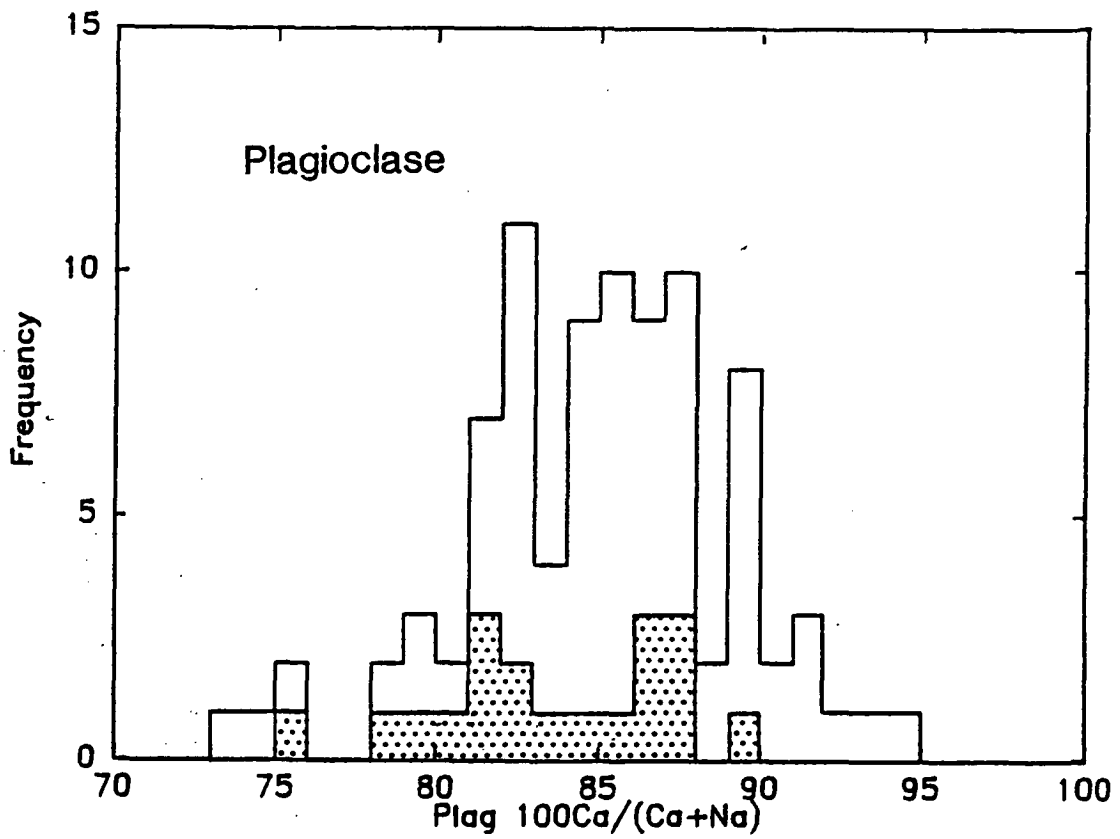

Figure 6.12 A cumulative frequency histogram for $Ca^{\#}$ (100Ca/(Ca+Na)) of plagioclase phenocrysts occurring in Ambae lavas, compiling examples from both the LTS (stippled) and the HTS (plain).

Groundmass compositions were also estimated by averaging multiple (n = 5-20) defocused beam analyses of groundmass regions within individual thin sections. When compared to XRF bulk composition analyses of available duplicate aphyric lavas, and also to compositions obtained by the Ir-strip fused glass technique, this method results in anomalously high Al_2O_3, and low FeO^{tot} and MgO concentrations (Table 6.5). On this basis, the analysis of groundmass compositions by this method is considered unreliable.

6.4.7 Melt Inclusions

Trapped pools of melt which occur in many phenocrysts are a potential source of information regarding the melt compositions from which their host phases have crystallised. However, it has proved difficult to obtain homogeneous compositions from such inclusions by repeated defocused beam analyses, due largely to the formation of coarsely crystalline quench phases, particularly for those inclusions enclosed by olivine and clinopyroxene.

All analysed melt inclusions, relative to aphyric whole-rock and groundmass compositions, are enriched in components incompatible in their host phase and depleted in host-compatible components (Table 6.6). Several extreme cases of this type of melt modification are found in clinopyroxene phenocrysts as pools of alkali feldspar, which are bordered by very Fe, Al, Ti, and Na-rich clinopyroxene. Nonetheless, it has been possible to obtain information about the primary inclusion compositions from those elements which have been conserved within the inclusions. In plagioclase these are Ti, Fe, Mg, P, and possibly also K, whereas inclusions in olivine conserve Ti, Al, Ca, Na, K, and P. Ratios of these elements are considered to reflect those of the inclusions at the time of entrapment, and are amenable for comparison with the groundmass/whole-rock geochemical evolution trends..For example, a plot of (2Ca+Na)/Ti versus Al/Ti (Fig. 6.13), which serves to distinguish between the chemistry of the major lava suites and also the effects of fractionation of various phenocryst phases present, illustrates an affiliation between the LTS olivine-hosted melt inclusions and the LTS lava compositions. Similarly, a plot of Ti/Fe versus $MG^{\#}$ for HTS plagioclase-hosted melt inclusions reveals their association with the low $MG^{\#}$ (40-45) whole–rock compositions of the HTS suite (Fig. 6.13b). These plagioclase-hosted inclusions are also shown in Figure 6.13a to illustrate their consistency

Table 6.5 Groundmass compositions for 20 Ambae lavas. Analyses determined by electronprobe analysis of Ir-strip fused glasses are compared with averaged broadbeam analyses of groundmass, and aphyric whole-rock bulk compositions.

number	68638g	68605g	68567g	68591g	68564g	68642g	68584g	68562g	68578g	68634g
SiO2	49.00	48.65	49.01	49.20	48.94	49.17	49.36	49.40	47.87	50.12
TiO2	0.62	0.74	0.69	0.80	0.72	0.68	0.78	0.85	1.18	0.82
Al2O3	13.23	14.00	13.60	13.48	13.84	14.46	14.65	14.91	15.68	16.61
Fe2O3										
FeO	10.09	10.35	9.63	9.64	9.92	9.80	9.70	9.82	11.68	9.84
MnO	0.20	0.20	0.20	0.20	0.20	0.20	0.20	0.24	0.20	0.20
MgO	10.91	10.50	9.64	9.56	9.72	9.33	8.27	7.82	7.82	6.28
CaO	12.46	11.58	12.60	12.91	12.57	12.42	12.64	12.36	11.73	11.09
Na2O	2.24	2.42	2.14	2.42	2.43	2.39	2.70	2.69	2.62	3.11
K2O	0.98	1.23	2.03	1.36	1.38	1.22	1.22	1.50	0.92	1.59
P2O5	0.28	0.32	0.45	0.42	0.28	0.32	0.48	0.40	0.30	0.35
L.O.I.										
H2O-										
rest										
total	100.01	99.99	99.99	99.99	100.00	99.99	100.00	99.99	100.00	100.01

Broadbeam

number	68638		68567	68591	68564	68642				68634
SiO2	50.48		50.14	50.48	50.75	51.46				50.30
TiO2	0.65		0.52	0.62	0.69	0.55				0.67
Al2O3	16.88		18.58	17.83	19.23	19.23				21.85
Fe2O3										
FeO	8.45		8.90	7.89	8.22	7.20				7.69
MnO										
MgO	7.16		5.01	6.08	4.68	4.97				4.22
CaO	12.37		11.59	12.32	11.07	11.97				10.33
Na2O	2.50		2.74	2.74	3.11	2.99				3.03
K2O	1.32		2.11	1.67	1.91	1.62				1.65
P2O5	0.20		0.41	0.36	0.34					0.26
L.O.I.										
H2O-										
rest										
total	100.01		100.00	99.99	100.00	99.99				100.00

Aphyric whole-rock

number	68638						68584			68634
SiO2	49.45						50.02			50.32
TiO2	0.66						0.76			0.84
Al2O3	13.39						15.06			16.26
Fe2O3										
FeO	10.09						9.99			9.99
MnO	0.18						0.19			0.18
MgO	10.55						7.74			6.44
CaO	12.26						12.50			10.97
Na2O	2.22						2.25			3.16
K2O	1.01						1.27			1.55
P2O5	0.18						0.23			0.29
L.O.I.										
H2O-										
rest										
total	99.99						100.01			100.00

Table 6.5 cont'd.

number	68606g	68632g	68593g	68573g	68588g	68587g	68596g	68570g	68574g	68576g
SiO2	50.23	50.07	51.59	48.09	50.04	51.90	48.57	48.69	48.91	50.17
TiO2	0.92	0.86	1.23	1.48	0.91	1.31	1.66	1.62	1.21	1.05
Al2O3	16.46	16.65	16.34	16.25	16.65	16.93	16.77	16.50	16.02	16.78
Fe2O3										
FeO	10.04	10.10	9.63	11.26	10.37	9.43	11.18	11.52	12.10	11.27
MnO	0.20	0.20	0.20	0.20	0.20	0.24	0.23	0.28	0.26	0.20
MgO	6.09	5.89	5.38	6.14	5.54	4.67	5.23	5.33	5.58	4.95
CaO	10.78	10.93	10.42	12.22	11.03	9.73	10.92	10.91	11.24	10.41
Na2O	3.11	3.28	3.43	2.85	3.12	3.77	3.27	3.11	3.04	3.29
K2O	1.77	1.65	1.40	1.10	1.73	1.57	1.58	1.57	1.31	1.51
P2O5	0.41	0.38	0.38	0.42	0.40	0.46	0.58	0.48	0.32	0.38
L.O.I.										
H2O-										
rest										
total	100.01	100.01	100.00	100.01	99.99	100.01	99.99	100.01	99.99	100.01

Broadbeam

number		68632	68593	68573	68588	68587	68596	68570	68574	
SiO2		51.07	53.31	49.71	50.05	54.70	50.50	50.32	49.71	
TiO2		0.73	1.15	1.34	0.76	1.15	1.32	1.39	1.34	
Al2O3		20.02	19.02	18.75	20.39	18.58	18.30	18.34	18.75	
Fe2O3										
FeO		8.03	8.46	9.99	8.57	7.70	9.40	9.70	9.99	
MnO										
MgO		4.69	3.13	4.24	4.27	3.11	4.16	4.13	4.24	
CaO		10.04	8.14	10.88	10.33	8.12	10.24	10.30	10.88	
Na2O		3.26	4.35	3.39	3.31	4.18	3.53	3.41	3.39	
K2O		1.86	1.95	1.34	2.00	1.98	1.92	1.86	1.34	
P2O5		0.30	0.48	0.37	0.32	0.48	0.63	0.56	0.37	
L.O.I.										
H2O-										
rest										
total		100.00	99.99	100.01	100.00	100.00	100.00	100.01	100.01	

Aphyric whole-rock

number	68606			68588		68570		68576
SiO2	50.03			50.12		49.05		50.54
TiO2	0.86			0.86		1.63		1.02
Al2O3	16.64			16.71		17.04		17.28
Fe2O3								
FeO	10.14			10.58		11.36		11.15
MnO	0.19			0.20		0.21		0.21
MgO	6.35			5.47		4.94		4.66
CaO	10.86			10.99		10.88		10.30
Na2O	2.96			2.97		2.87		3.06
K2O	1.65			1.78		1.56		1.48
P2O5	0.32			0.30		0.46		0.30
L.O.I.								
H2O-								
rest								
total	100.00			99.98		100.00		100.00

Note, samples are normalised to 100.0% assuming all Fe as Fe^{2+}.

Table 6.6 Selected analyses of melt inclusions in olivine, clinopyroxene, and plagioclase.

	1	2	3	4	5	6	7	8	9
Host	Ol	Ol	Ol	Ol	Plag	Plag	Plag	Plag	Cpx
Mg#orCa#	90.5	88.2	86.6	84	92.3	82.6	86.6	91.2	83.9
SiO_2	51.01	51.22	49.42	52.37	44.46	48.62	47.89	44.51	60.80
TiO_2	0.71	0.65	0.87	0.80	2.37	2.30	1.89	2.70	0.19
Al_2O_3	18.19	16.68	17.69	18.01	15.40	10.35	10.10	5.71	24.00
FeO^{tot}	7.86	6.42	6.22	5.95	15.46	15.80	15.02	23.20	0.61
MnO						0.35	0.23	0.54	
MgO	6.47	5.24	6.22	2.53	6.53	6.35	6.66	10.69	
CaO	11.36	14.45	13.11	14.70	12.96	11.25	11.10	9.86	5.98
Na_2O	3.06	2.73	3.75	3.45	0.82	1.95	4.00	1.30	6.05
K_2O	0.99	2.28	2.37	1.75	1.07	2.59	2.63	0.80	2.36
P_2O_5	0.35	0.33	0.34	0.44	0.93	0.41	0.47	0.68	
Total	100.0	100.0	100.0	100.0	100.0	100.0	100.0	100.0	100.0

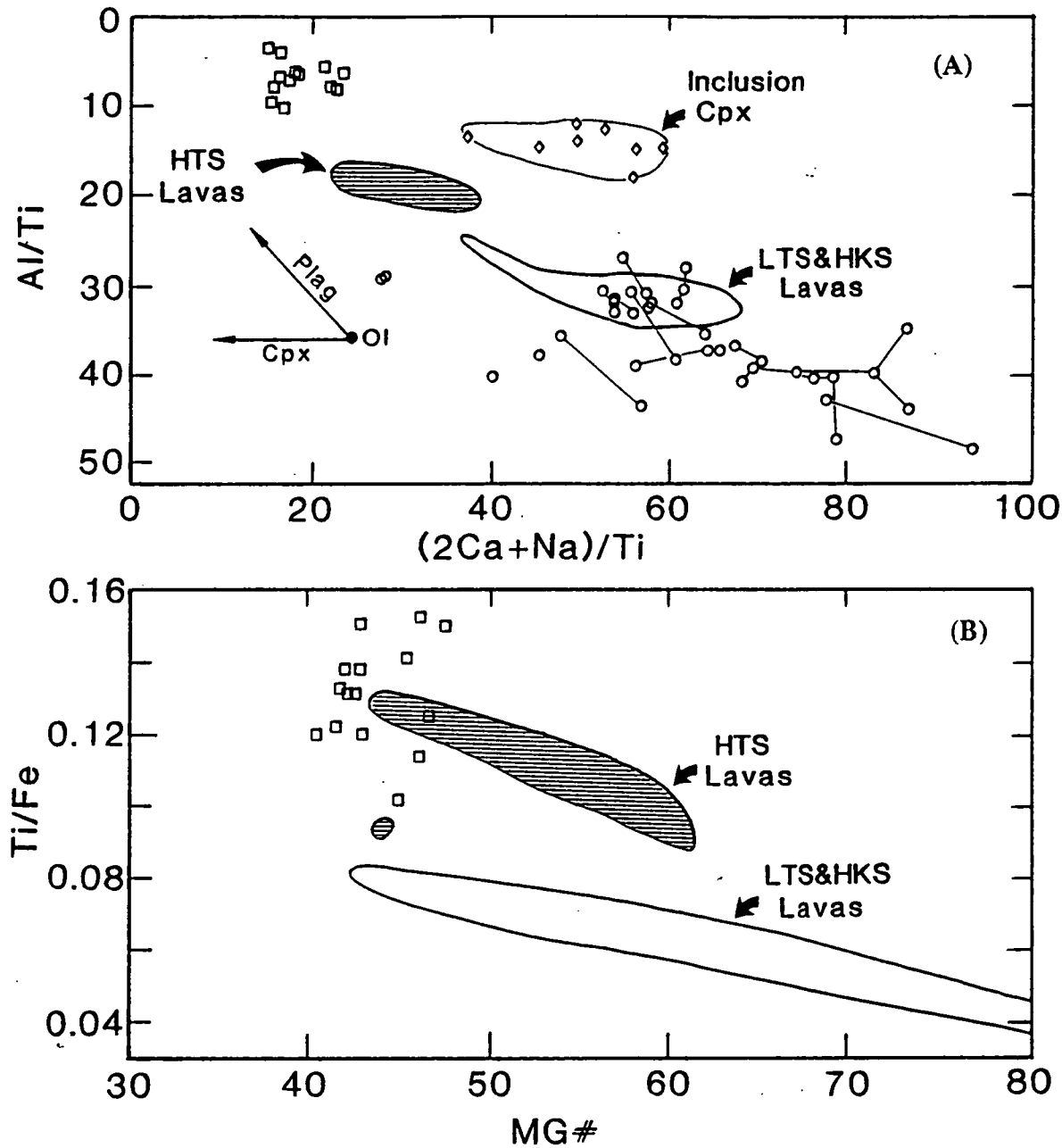

Figure 6.13 Plots of conserved element ratios for melt inclusions occurring in plagioclase phenocrysts (open squares) and in olivine phenocrysts (open circles). Bulk composition fields for the HTS (striped) and the younger lavas (both LTS and HKS; plain) are shown for comparison, as well as an additional field encompassing clinopyroxene (diamonds) occurring within olivine-hosted melt inclusions. Tie lines joining multiple analyses of individual inclusions illustrate the extent of analytical variation encountered. The labelled vectors indicate the direction of compositional variation arising from fractionation of various phenocryst phases present in the Ambae lavas.

with the removal of host (plagioclase) compatible components from melts equivalent to the HTS whole-rock compositions.

6.5 SEQUENCE OF CRYSTALLISATION

A general sequence of crystallisation of the LTS magmas can be linked to the evolution of melt compositions through the well established Fe/Mg partitioning relationship between olivine and basaltic liquids (i.e. $K_D^{Fe/Mg} = 0.30$; Roeder and Emslie, 1970). The principal reference points in the sequence are (as summarised in Fig. 6.14):

(1) the most primitive liquidus phase is olivine of $Mg^{\#} = 93.4$ ($Mg^{\#}_{Liq} = 80.9$);

(2) Cr-spinel accompanies olivine crystallisation from at least $Mg^{\#}_{Ol} = 93.1$ (i.e. $Mg^{\#}_{Liq}$ 80.2) to more Fe-rich compositions;

(3) diopsidic clinopyroxene of $Mg^{\#}$ ~92 first crystallises in the presence of olivine of $Mg^{\#} = 89.4$ (i.e $Mg^{\#}_{liq} = 71.7$), as established from coexisting olivine and clinopyroxene in the cognate cumulate nodule CUM1 (Tables 6.1 and 6.2);

(4) the onset of plagioclase crystallisation may be linked to a decrease in Al^{IV} and Al^{VI} in clinopyroxene at $Mg^{\#}_{Cpx}$ ~83-85, in response to the reaction

$$CaAl_2SiO_6^{Cpx} + SiO_2^{Liq} \text{ <----> } CaAl_2Si_2O_8^{Plag} \qquad (6.1)$$

which in turn can be related through the Fe/Mg partitioning relationships between clinopyroxene and olivine, and between olivine and liquid, to melts with $Mg^{\#}_{Liq}$ of ~47-52. [this is in close agreement with the $Mg^{\#}$ of melt compositions from which HTS plagioclase have crystallised, as demonstrated using melt inclusion compositions (i.e. $MG^{\#}$ = 40-47 ~$Mg^{\#}$ = 46-53, assuming $Fe^{2+}/Fe^{tot} = 0.80$)],

(5) titanomagnetite crystallisation is poorly constrained, but occurs more or less concurrently with plagioclase, possibly after an interval during which no spinel phase is stable.

Apart from minor differences in the chemistry of phases crystallising in the LTS and HTS (e.g. higher Ti contents in HTS clinopyroxenes), the phenocryst assemblages and overall phase compositions are very similar, which points to a parallel sequence of crystallisation in both suites. The major distinction between the crystallisation of these two

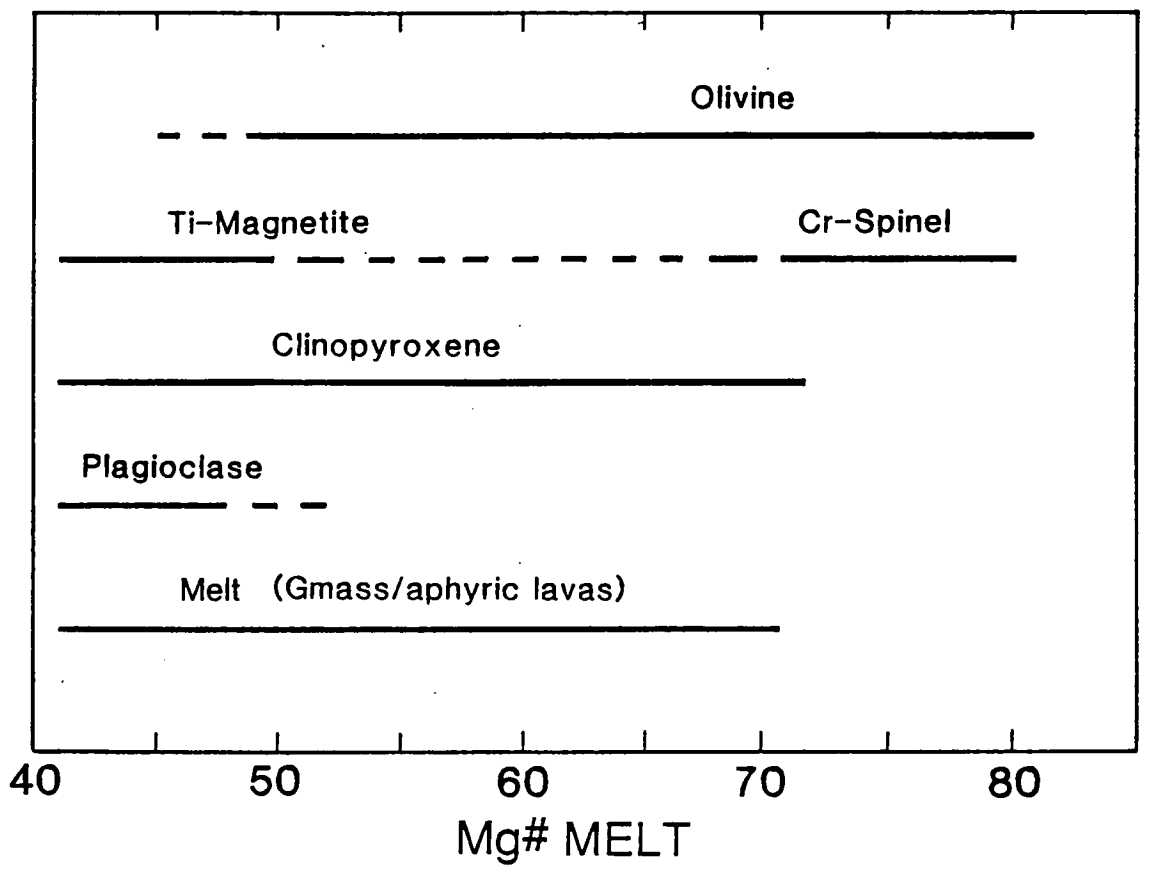

Figure 6.14 Schematic illustration of the intervals of crystallisation of phenocrysts crystallising in the LTS magmas as melt Mg# varies. The range in melt Mg# is based on measured groundmass and aphyric whole-rock compositions, assuming Fe^{2+} = $0.8Fe^{tot}$. Note that the most magnesian melt compositions are consistent with evolution by olivine crystallisation (+ minor Cr-spinel) from more primitive melt compositions with Mg# up to ~81.

lava suites is in the evolution of the HTS phenocrysts to more evolved (Fe-rich) compositions.

6.6 MAGMA CRYSTALLISATION CONDITIONS

6.6.1 Temperature

Olivine-Spinel Thermometry

Estimates for the temperature of equilibrium of olivine-spinel pairs have been obtained using the O'Neill and Wall (1987) calibration for the olivine-spinel Fe^{2+}-Mg exchange geothermometer, which is based on the reaction

$$Fe_2SiO_4^{Ol} + 2MgAl_2O_4^{Sp} \text{ <----> } Mg_2SiO_4^{Ol} + 2FeAl_2O_4^{Sp} \qquad (6.2)$$

Resultant temperatures scatter widely between 635 and 1170°C (see Table 6.3), and are often strongly dependent on the variable Mg# of the individual spinels. Fe-rich spinel rims in particular, which are often in contact with groundmass and possibly out of equilibrium with their olivine hosts, are up to 400°C lower than core temperatures, and often result in temperature estimates falling below acceptable magmatic values (ca. 1000°C). There is a high probability that all olivine-spinel pair temperatures have been effected by subsolidus diffusion of Fe^{2+}-Mg, as only relatively short times are required to alter the primary Mg# of spinel cores by diffusive processes (Ozawa, 1983). Indeed, the rapid cooling rates necessary to freeze-in magmatic temperatures may not be attainable during the cooling of subaerially erupted lavas. For example, the closure temperatures for Fe^{2+}-Mg diffusion in spinel can be approximated using the equation for volume diffusion in a sphere (Dodson, 1973)

$$T_c = (R/Q).\ln\{-[55RT_c^2D_0]/[a^2Q(dT/dt)]\} \qquad (6.3)$$

where T_c= closure temperature in °K

R = 8.3143 J/°K

D_0 = diffusion rate of component

a ~ crystal radius (in m)

Q = activation energy in J

dT/dt = cooling rate °K/s

By assuming, as a first approximation, that the Fe^{2+}-Mg interdiffusion rate can be equated with the self-diffusion rates of Fe^{2+} and Mg in spinel (Jurewicz and Watson, 1988), the closure temperatures estimated for spinels of 100μm radius, cooled at rates appropriate for lava flows (e.g. ~0.01 to 10°C/hr),fall between 802 and 1119°C. This range is consistent with the variation in temperature estimates calculated for Ambae olivine-spinel pairs. It also emphasises the rapid cooling necessary for this phase assemblage to record magmatic temperatures.

Thermometry from Melt Bulk Compositions

Another means of estimating magmatic temperatures comes from relationships established between compositional parameters and the experimentally determined liquidus temperatures of basaltic melts (e.g. Ramsay et al, 1983; Sack et al., 1987). Little difference occurs between temperatures estimates derived from either the expression developed by Ramsay et al. (1984) i.e.

$$T°C = 16.3MgO(wt\%) + 1083 \quad (6.4)$$

or that of Sack et al. (1987) i.e.

$$T°C = -468.8(FeO_{tot}/(FeO_{tot}+MgO)) + 1392 \quad (6.5)$$

Both predict a similar temperature range for Ambae groundmass and aphyric whole-rock compositions (Table 6.5 and Chapter 7), between 1155 and 1253°C for the LTS examples, and 1155 to 1204°C for the HTS examples. It is notable that, when applied to Hawaiian glasses, these expressions result in temperature estimates about 30 to 40°C higher than their measured eruption temperatures (e.g. Helz, 1987). This observation probably underscores the importance of volatiles in reducing the liquidus temperatures of natural basalts.

Water is likely to be an important dissolved volatile phase in the Ambae magmas, as in other island arc magmas, and a corresponding depression of the liquidus temperatures calculated using equations 6.4 and 6.5 can be expected. Estimates for the water content of Ambae magmas using alkaline-earth-element/H_2O values observed in oceanic basaltic glasses (e.g. Michael and Chase, 1987; Michael, 1988) may indicate H_2O concentrations of ~1wt%, but it must be uncertain as to whether such relationships hold also in island arc magmas. The maximum temperatures recorded by olivine-spinel pair thermometry,

however, can be used to imply a small liquidus temperature depression of <70°C from the anhydrous liquidus temperature estimates calculated above. This corresponds to a liquidus temperature depression produced by ~1wt% dissolved H_2O (e.g. Green, 1974; Brophy, 1986). These relatively low water contents are consistent with the absence of hydrous phenocryst phases crystallising in the Ambae magmas.

6.6.2 Oxygen Fugacity

The olivine-spinel reaction:

$$3Fe_2SiO_4^{Ol} + O_2 <----> 2Fe_3O_4^{Sp} + 3SiO_2^{Liq} \qquad (6.6)$$

has been the subject of several recent oxygen barometer calibrations (Ballhaus et al., in press; O'Neill and Wall, 1987; Mattioli and Wood, 1986). The calibration by Ballhaus et al. can be considered the best curently available, producing close agreement with fO_2 estimates based on measured Fe^{3+}/Fe^{2+} in basaltic glasses and the fO_2 under which spinels have been grown in independent experimental studies (Ballhaus et al., in press). Ballhaus et al. have experimentally synthesised spinels over a wide range of P, T, fO_2, and bulk compositions, to formulate a simple expression for the calculation of fO_2 relative to the QFM oxygen buffer:

$$\Delta\log(fO_2)QFM = 0.27 + 2505/T - 400P/T - 6\log(XFe_{Ol}) - 3200(1-XFe_{Ol})^2/T + 2\log(XFe^{2+}_{Sp}) + 4\log(XFe^{3+}_{Sp}) + 2630(XAl_{Sp})^2/T \qquad (6.6)$$

where T is in °K, P is in GPa, XFe_{Ol} and XFe^{2+}_{Sp} are the cation ratios of $Fe^{2+}/(Mg+Fe^{2+})$ in olivine and spinel, and XFe^{3+}_{Sp} and XAl_{Sp} are the $Fe^{3+}/\sum R^{3+}$ and $Al/\sum R^{3+}$ ratios in spinel. fO_2 estimates for olivine-spinel pairs in the Ambae lavas based on equation 6.6 (assuming P = 0.1GPa and calculating T from the olivine-spinel geothermometer of O'Neill and Wall (1987)) cluster around QFM+2.5 log units, despite covering a range from below to more than 3 log units above the QFM oxygen buffer (Table 6.3). These values are between 1.5 and 2 log units more oxidising than values determined from the O'Neill and Wall oxygen barometer (Table 6.3), using an $aSiO_2$ estimate for the Ambae magmas of -0.5 log units (inferred by comparison with similar silicate melt compositions modelled by Ghiorso and Carmichael, 1987). The fO_2 estimate of QFM+2.5 log units indicates very oxidising crystallisation conditions for the Ambae magmas, consistent with the high oxidation states

generally considered to distinguish island arc magmas from other oceanic tectonic settings (e.g. Carmichael, 1989; Gill, 1981).

6.7 Primary melt compositions

The highly magnesian olivine phenocrysts in LTS lavas record the crystallisation of very primitive melt compositions with $Mg^{\#}$ up to ~81 (assuming $K_D^{Fe/Mg}{}_{Ol\text{-}Liq} = 0.30$). These particular phenocrysts form the extreme end of a continuous phenocryst spectrum spanning more Fe-rich compositions, consistent with the melt from which they have crystallised being parental to the LTS lavas.

In order to reconstruct the compositions of such primitive parent melts, the efects of crystal fractionation need to be taken into account. this is a relatively simple task for the LTS, as the most primitive melt composition observed (#68638, Table 6) has an Mg# higher than the melt composition at which clinopyroxene (the second major liquidus phase) first crystallises (i.e. Mg# = 71.4). This requires the composition of #68638 to be corrected only for olivine fractionation, given that minor Cr-spinel is the only other crystallising phase at Mg#Liq>71.4. The correction of olivine fractionation effects has been facilitated by adding small increments (0.1 wt%) of equilibrium olivine ($K_D^{Fe/Mg}{}_{Ol\text{-}Liq} = 0.30$) until a bulk composition capable of crystallising the most Mg-rich olivine (Mg# = 93.4) is produced. At each increment, temperature and fO_2 control on Fe^{3+}/Fe^{2+} speciation have been determined using the expressions of Kilinc et al. (1983) and Ramsay et al. (1984; -50°C to adjust for dissolved volatiles) in accordance with an fO_2 value of QFM+2.5 log units. The resultant parent melt estimate has ~15 wt% MgO (Table 6.7) and an Mg# of 81, making it an excellent candidate for primary derivation from mantle peridotite. A parallel calculation based on an fO_2 value of QFM+1 log unit, as determined by the O'Neill and Wall (1987) oxygen barometer for Ambae olivine-spinel pairs, produces an extremely magnesian parent melt composition with ~19 wt% MgO (Table 6.7).

6.8 THE ORIGIN OF PHENOCRYST ZONING

The composition of phases crystallising in slowly cooled silicate melts is likely to be controlled by equilibrium crystallisation, as determined by bulk composition of the melt and reaction governing intensive parameters (e.g. P, T, fO_2, fH_2O). The possibility, however, remains that disequilibrium reactions (often brought about by undercooling) may cause departure from equilibrium relationships, and make links between phenocryst and

Table 6.7
Fractionation-corrected LTS parent melt estimates.

fO_2 = QFM+2.5			
	#68638	to	Parent
SiO_2	49.23		48.25
TiO_2	0.66		0.58
Al_2O_3	13.372		11.74
Fe_2O_3	4.10		3.82
FeO	6.36	+13.4wt%	6.39
MnO	0.18	Olivine	0.18
MgO	10.55		15.27
CaO	12.20		10.76
Na_2O	2.21		1.95
K_2O	1.01		0.89
P_2O_5	0.18		0.16

fO_2 = QFM+1log unit			
	#68638	to	Parent
SiO_2	49.32		47.57
TiO_2	0.66		0.52
Al_2O_3	13.34		10.57
Fe_2O_3	2.40		2.10
FeO	7.91	+26.2 wt%	7.86
MnO	0.18	Olivine	0.18
MgO	10.56		18.78
CaO	12.22		9.68
Na_2O	2.21		1.75
K_2O	1.01		0.80
P_2O_5	0.18		0.14

melt compositions difficult. Available evidence from the Ambae magmas, however, is consistent with equilibrium controlled crystal growth, as indicated by :

(1) euhedral crystal morphologies exhibiting a minimum surface area/volume, in contrast to rapidly cooled crystal morphologies (e.g. "hopper olivines");

(2) the crystallisation of extreme phase compositions, often approaching solid solution end-members (e.g. forsterite, diopside, anorthite), as opposed to compositions which tend to merge with melt compositional characteristics when large degrees of undercooling occur; and

(3) the close covariation between clinopyroxene chemistry and host whole-rock compositions (Figs. 6.5 & 6.8).

It follows that the range of phenocryst compositions documented result from the crystallisation of a corresponding spectrum of equilibrium melt compositions. Furthermore, the complex zonation patterns observed in clinopyroxene phenocrysts can be interpreted to reflect fluctuating melt compositions, and/or intensive variables during crystallisation.

Interestingly, from the systematic Fe/Mg partitioning relationships occurring between olivine, clinopyroxene, and basaltic liquids, and knowing that olivine and clinopyroxene have co-crystallised over a wide compositional interval (Fig. 6.14), it cannot be anticipated that these phenocrysts should display such different Mg# zonation patterns (cf. Figs. 6.3 and 6.8). This assessment does not, however, take into account the varying abilities of these different phases to re-equilibrate with the surrounding melt via intracrystalline diffusion processes. This process deserves close examination as it has implications for the preservation of early-formed phenocryst compositions in primitive magmas, and also the interpretation of magmatic history from phenocryst zoning characteristics.

6.8.1 The Role of Intracrystalline Diffusion

The ability of intracrystalline diffusion to modify the internal composition of a phenocryst out of equilibrium with its surrounding melt can be estimated from the equation for diffusion within a sphere (Crank, 1975),

$$\frac{C - Cp}{Cr - Cp} = 1 + \frac{2a}{\pi r} \sum_{n=1}^{\infty} [(-1)^n/n].\sin[n\pi r/a].\exp[-Dn^2\pi^2 t/a^2] \qquad (6.12)$$

where a = phenocryst radius (in metres)

r = radial distance from phenocryst core

D = diffusion or interdiffusion coefficient

C = "concentration" of component *i* (e.g. Mg, Fe^{2+}, Mg#) at r and time t

C^p = "concentration" of *i* in the phenocryst, which is assumed to be homogeneous, at t = 0

C^r = equilibrium "concentration" of *i* at the rim at t = 0

Olivine

Ignoring the narrow Fe-rich rims occurring about olivine phenocrysts, which may be interpreted as late quench overgrowths, the time required to produce their internally homogeneous compositions (Fig. 6.3) can be calculated from equation (6.12) using a set of solution curves given by Maaloe (1985; Fig. 6.16). Assuming an equilibrium composition at the crystal surface which is <5 Mg# units from the core composition (i.e. $C-C^p$ <5Mg#) at t = 0, and that the analytical precision is ~0.5 Mg# units, an olivine will be perceived to be homogeneous when $[(C - C^p)/(C^r - C^p)] > 0.9$, after time (t) $>0.3a^2/D$. For a typical Ambae olivine phenocryst 2mm in diameter, and a constant interdiffusion coefficient value (D_{Mg-Fe}) of $\sim 4.2 \times 10^{-11}$ (value at 1200°C, Buening and Buseck, 1973), this time period will be ~2.3 years (or ~10 years at 1100°C, or 230 days at 1300°C). These results match the worked examples of many other studies which show that olivine homogenisation times in basaltic magmas are *short*, occurring within periods ranging from days up to tens of years (e.g. Nicholls and Stout, 1988; Maaloe and Hansen, 1982; Jurewicz and Watson, 1988). Moreover, as diffusion will occur concurrently with crystal growth, even shorter periods may be taken to form the characteristically flat Mg# zonation profiles of the Ambae olivine phenocrysts (Fig. 6.3).

Clinopyroxene

Little data can be gleaned from the literature for cation diffusion rates in clinopyroxene (e.g. see review by Freer, 1981). If it is assumed that the fine scale (~10μm) chemical zoning observed in some clinopyroxenes has been subjected to equivalent magmatic temperatures and the time periods taken to homogenise olivine phenocrysts (ie. ~10 years), then diffusion coefficients for their constituent cations may be approximated

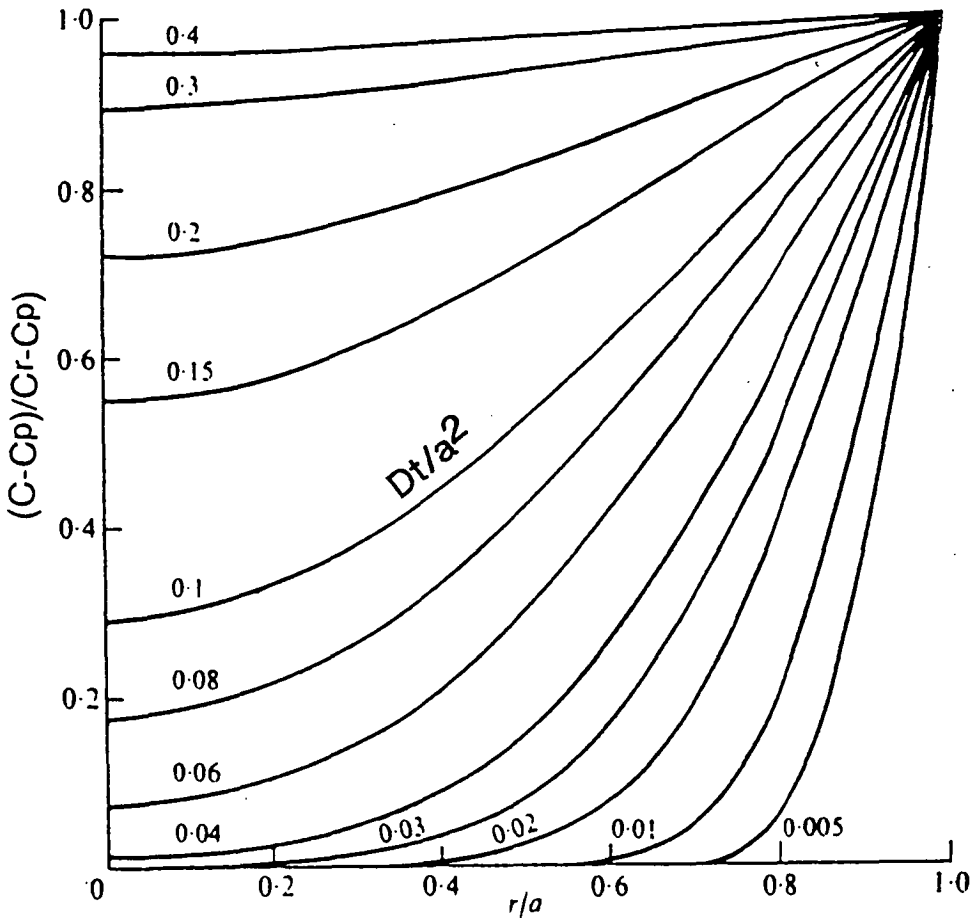

Figure 6.16 Curves for the evaluation Dt/a^2 for diffusion occurring in a sphere (i.e. equation 6.12). Dt/a^2 values are obtained by plotting the ratio of the distance from the phenocryst core to the phenocryst radius (r/a), against the proportional change in the phenocryst's composition there, from its initial composition at t = 0 toward the equilibrium composition at the phenocryst's rim.

using the solution for two-dimensional diffusion across a planar boundary (after Maaloe, 1985);

$$C(x,t) = [C_1 - C_0)/2][1\text{-erf}(x/2\sqrt{Dt})] \quad (6.13)$$

where x = distance from boundary

C_1 = concentration of component i at t=0, x<0

C_2 = concentration of component i at t=0, x>0

After 10 years at a distance 5μm from the boundary, >50% of the original compositional difference between the adjacent growth zones will be retained if the diffusion coefficient values for the relevant components are $<8.7\text{x}10^{-16}\text{cm}^2\text{s}^{-1}$. If >90% of the original compositional difference is retained then D will be $<1.5\text{x}10^{-16}\text{cm}^2\text{s}^{-1}$. These values match the interdiffusion coefficients for Ca-Mg in diopside at 1150°C ($0.5\text{-}2.0\text{x}10^{-16}\text{cm}^2\text{s}^{-1}$; Brady and McCallister, 1980), and also Al diffusion in augite at 1240°C ($\sim 6\text{x}10^{-16}\text{cm}^2\text{s}^{-1}$; Seitz, 1973). If an "average element" diffusion coefficient of $5\text{x}10^{-16}\text{cm}^2\text{s}^{-1}$ is substituted into equation (6.12), the estimated time for homogenisation of a clinopyroxene phenocryst 2mm in diameter is $\sim 10^5$ years.

Spinel

Spinel Mg-Fe^{2+} interdiffusion coefficients have been measured by Freer and O'Reilly (1980), and previously used by Ozawa (1983, 1984) to assess equilibria between spinel inclusions in olivine and the thermal history of peridotite xenoliths. From equation (6.12), using a $D_{Mg\text{-}Fe^{2+}}$ value of $2.6\text{x}10^{-10}\text{cm}^2\text{s}^{-1}$ (1200°C value determined by Freer and O'Reilly, 1980), the time estimated to reduce the core Mg# of a relatively large (200μm diameter) spinel to within 90% of its surface equilibrium value is ~1.3 days (or ~6 days at 1100°C). It can also be shown that preservation of the original Mg# of a spinel's core will only occur if $t < 0.03a^2D^{-1}$. This may be estimated to occur within 3.2 hours at 1200°C, or <14 hours at 1100°C. Similar results can be obtained for spinels included in olivine, where even large spinels (1mm diameter) may undergo core Mg# changes after a period of 10 days, and smaller spinels (~200μm diameter) after <1day (Ozawa, 1983). This ability for rapid re-equilibration of spinel in olivine re-emphasises the difficulty of obtaining magmatic crystallisation temperatures using olivine-spinel geothermometry.

6.9 IMPLICATIONS FOR MAGMATIC HISTORY

The continuous compositional ranges of phenocryst phases in the Ambae lavas are consistent with the evolution of melt compositions from very magnesian parents ($Mg^{\#}$ up to 81), to the high-alumina basalt compositions ($Mg^{\#}$~45) which are found as groundmasses and phenocryst-poor lavas (e.g. Table 6.5, and Chapter 7). The distinct phenocryst and groundmass compositions observed in the LTS and HTS support whole-rock geochemical evidence for the evolution of compositionally distinct parent melts in these two suites, with the HTS crystallising from more TiO_2-rich melt compositions. The crystallisation sequence followed by both magma suites, however, is very similar, beginning with Mg-rich olivine (+Cr-spinel), followed by Mg-rich clinopyroxene, and then calcic plagioclase and titanomagnetite from more evolved melts (i.e. $Mg^{\#}_{Liq}$<~50).

A record of highly variable crystallisation conditions is detailed by the complex zonation patterns preserved in clinopyroxene phenocrysts. These chemical zonation characteristics are consistent with variation arising from changes in melt composition, back and forth along their liquid line of descent. Processes identifiable in this evolution include:

(1) differentiation by fractional crystallisation, following the trends outlined in Figure 6.7 and resulting in reduced $Mg^{\#}$ and Cr content, and generally increased TiO_2 and Al_2O_3 contents in clinopyroxene (marked --XC--> in Fig. 6.8);

(2) magma mixing events, often producing abrupt compositional changes (marked MM in Fig. 6.8), or in some cases more gradual compositional variation due perhaps to repeated small or drawn out mixing events (denoted --mm--> in Fig 6.8),

(3) and also volatile degassing resulting in redox reactions, variation of Fe^{3+}/Fe^{2+} equilibria, and associated change in $Mg^{\#}_{Liq}$ [this may provide an alternative explanation for (1) and (2), but this process is not generally supported by accompanying variations of Fe^{3+} contents in clinopyroxene (not shown)].

Strong evidence for magma mixing also comes from the presence of distinct populations of olivine phenocrysts within the individual lavas (Fig. 6.4), in particular the bimodal distribution of olivine compositions occuring in the HTS. Moreover, these events may be linked to eruptive phases of volcanism, as the periods required for diffusive processes to modify olivine compositions indicate that mixing has probably occurred

immediately prior to eruption. Significant time periods between mixing and eruption of the sampled basalts would result in olivine phenocrysts with wide zoned rims merging toward a uniform rim Mg# value (excluding quench overgrowths). The abrupt changes to and from high Mg# in clinopyroxene, and the occurrence of highly Mg-rich olivine populations in many samples, indicate that mixing of primitive magma batches is a common phenomenon in the Ambae magmas. Moreover, the well developed olivine mode at Mg# 87 in the LTS lavas may be explained if melt compositions in this suite are buffered near $Mg\#_{Liq}$ ~67, possibly as a result of regular influxes of primitive magma.

6.10 A COMPARISON WITH OTHER PRIMITIVE ISLAND ARC BASALTS

Primitive (olivine-bearing) basalts are a relatively uncommon volcanic products in island arcs. However, several notable occurrences of primitive IAB are distributed throughout the global system of island arcs, of which the best documented examples include the New Georgia Group in the Solomon Islands (Ramsay et al., 1984), Oshima-Oshima in Japan (Yamamoto, 1984; Yamamoto, 1988), Okmok in the Aleutian Arc (Nye and Reid, 1986), Manam Island in Papua New Guinea (Johnson et al., 1985), Grenada in the Lesser Antilles (Arculus, 1978), and Merelava and Western Epi in the Vanuatu Arc (Barsdell, 1988; Barsdell and Berry, in press). Other significant occurrences also include Batu Tara (Stolz et al., 1988), Rinjani (Foden, 1984) and the Balukan Formation of Bali in the Indonesian Arc (Wheller, 1987) , Mt. Shasta in the Cascades (Anderson, 1974), Jorullo in Mexico (Luhr and Carmichael, 1985), and many of the Central Chain Volcanoes in the Vanuatu Arc (e.g. Barsdell, 1980; Gorton, 1974; Marcelot et al., 1983; Roca, 1978).

Collectively, these primitive IAB tend to contain phenocryst assemblages comprising magnesian olivine and clinopyroxene, Cr-rich spinel, and calcic plagioclase (Table 6.8). This generalisation applies across a wide compositional spectrum of host magmas, ranging from low-K island arc tholeiites (e.g. Manam, Merelava), to high-K basalts (e.g. Oshima-Oshima, Ambae) and even leucititic compositions (e.g. Batu Tara). Matching phenocryst assemblages are found in cumulate xenoliths entrained from deeper crustal and/or upper mantle levels in some island arc lavas (e.g. Conrad and Kay, 1984; Debari et al., 1987; Arculus and Wills, 1980), and in the exhumed roots of ancient island

Table 6.8 A compilation of extreme olivine, clinopyroxene, spinel, and plagioclase compositions occurring in arc magma suites.

Phenocryst	Olivine Mg#	Clinopyroxene Mg#	Cr-Spinel Cr#	Plagioclase Ca#
Locality				
Lesser Antilles				
Grenada	90	88	76	94
plutonic	90	90	--	100
Solomon Islands				
New Georgia	94	87	76	80
Indonesia				
Rinjani	93	92	72	95
Batu Tara	81	92	72	89
NZ & Tonga				
Ruapehu N.Z.	94	83	--	89
Metis Shoal	93	--	--	--
Vanuatu				
Merelava	92	94	81	--
Gaua	93	91	79	--
Ambrym	94	94	88	--
Ambae	93	92	94	--
Western Epi	92	94	86	--
Tanna	93	95	88	--
Anatom	93	94	79	--
New Britain				
Manam	92	89	81	86
New Britain	89	--	--	90
Mexico				
Jorullo	90	86	~60	85
Aleutians				
Okmok	93	88	81	--
Adak *plutonic*	93	93	92	--
Cascades				
Mt. Shasta	94	--	--	--
Japan				
Oshima-Oshima	94	92	--	84

Data sources include Anderson (1974), Arculus (1978), Arculus and Wills (1980), Barsdell (1988; pers. comm., 1988), Barsdell and Berry (in press), the BVSP (1981), Conrad and Kay (1984), Foden (1983), Graham and Hackett (1987), Johnson et al. (1985), Luhr and Carmichael (1985), Nye and Reid (1986), Ramsay et al. (1984), Stolz et al. (1988), Yamamoto (1984), and the author's unpublished data for Ambrym.

arcs (e.g. DeBari and Coleman, 1989). In some respects these phenocryst assemblages are similar to those of boninitic magmas, which often contain magnesian olivine and low-Ca-pyroxene, calcic plagioclase, and Cr-rich spinel (e.g. Crawford et al., 1989). It is clear from these observations that the Ambae phenocryst assemblages are not an isolated or anomalous occurrence of this nature. Ambae is unique, however, in terms of the dominance of primitive magmas and the presence of a complete record of crystallisation from ultramafic to more evolved high-alumina basalt compositions.

6.10.1 Primary Magmas in Island Arcs

The occurrence of highly magnesian olivine phenocrysts ($Mg^{\#}$ 90-94) in many arc lavas (Table 6.8) provides compelling evidence for the crystallisation of (primary?) melt compositions with $Mg^{\#}_{Liq}$ between 73 and 82 (assuming $K_D^{Fe/Mg}{}_{Ol\text{-}liq} = 0.30$). If olivine crystallisation has occurred at elevated pressures even more Mg-rich parent melt compositions may be required as $K_D^{Fe/Mg}{}_{Ol\text{-}Liq}$ will be >0.3 (Ulmer, 1989). Few studies have focused attention on this feature of primitive arc magmatism apart from Ramsay et al. (1984), who proposed primary melt compositions of $Mg^{\#}$ 75-76 for both Ambae and the New Georgia Group lavas, and Nye and Reid (1986), who calculated a parental picrite composition ($Mg^{\#}$ ~81) for Okmok (Aleutian Islands) with ~16 wt% MgO. Instead, other authors working within a peridotite melting framework have opted for primary melt compositions in equilibrium with acceptable but relatively "Fe-rich" mantle olivine compositions (i.e $Mg^{\#}_{Ol}$~87-89; e.g. Tatsumi et al., 1983; Gust and Perfit, 1987). Gust and Perfit (1987) have, however, on the basis of high pressure phase relationships, entertained the possibility that Aleutian primary magmas may be more Mg-rich (with ~14wt% MgO) than their experimentally-studied composition which had ~10 wt% MgO.

Without detailed studies of the evolution of suites of primitive arc basalts elsewhere, it is premature to speculate whether arc magmagenesis globally involves such primitive Mg-rich primary melt compositions. A systematic study of primitive magmatism in the Vanuatu Arc in Chapter 8 (compiling observations mainly from studies by Barsdell, 1980; Barsdell, 1988; Barsdell and Berry, in press; and Gorton, 1974) reveals that a majority of magma suites can be linked to parent compositions equally primitive to those determined for Ambae. Furthermore, the continuum of phenocrysts from the Mg-rich early

crystallising phases (i.e. olivine and clinopyroxene) to more evolved compositions, provides evidence for the evolution of "evolved" high-alumina basalt compositions (e.g. groundmass and phenocryst-poor lavas) from extremely Mg-rich parent melt compositions. The relatively Fe-rich olivine ($Mg^{\#}$ <~80) and clinopyroxene ($Mg^{\#}$ <~85), calcic plagioclase ($Ca^{\#}$ 70-95), and titanomagnetite bearing phenocryst assemblages which crystallise from the most evolved Ambae melt compositions, match those commonly found in high-alumina basalts and andesites elsewhere in island arcs (e.g. Brophy, 1986). These observations clearly support those models which treat high-alumina basalts as "evolved" mantle derived melts, rather than "primitive" ocean crust-derived primary melts. (e.g. Crawford et al., 1987). Finally, a simple but important deduction is that the principal site of magmagenesis for Ambae, and other magmas in the Vanuatu Arc, is the peridotitic mantle wedge.

6.11 CONCLUSIONS

1. Highly magnesian olivine ($Mg^{\#}$ 80-93) and clinopyroxene ($Mg^{\#}$ 80-92), Cr-rich spinel ($Cr^{\#}$ ~50-84), and calcic plagioclase ($Ca^{\#}$ = 80-94) dominate the phenocryst assemblages of Ambae lavas.

2. A similar crystallisation sequence occurs within the two principal lava suites identified (the LTS and HTS), beginning with Mg-rich olivine and Cr-spinel (at $Mg^{\#}_{Liq}$>72), later joined by Mg-rich clinopyroxene (at $Mg^{\#}_{Liq}$ <72), and then by plagioclase and titanomagnetite when $Mg^{\#}_{Liq}$<~50. Higher Ti contents in both clinopyroxene and the groundmass bulk compositions of the HTS, indicate the crystallisation of more Ti-rich melts than in the LTS.

3. The continuity in phenocryst compositions across the range observed in each suite are consistent with the evolution of magmas from primitive parent melt compositions ($Mg^{\#}$~75 in the HTS, and $Mg^{\#}$~81 in the LTS) to high-alumina basalt compositions.

4. The magmas have crystallised at oxygen fugacities near the NNO oxygen buffer, and in the presence of insufficient volatiles to stabilise hydrous phases.

5. An excellent primary melt candidate with ~19 wt% MgO ($Mg^{\#}$~81) is calculated for the LTS by correcting the most Mg-rich aphyric lava sample ($Mg^{\#}$~70, 10.5

wt% MgO) for olivine fractionation until capable of crystallising the most magnesian olivine phenocrysts observed.

6. The complex geochemical zonation of clinopyroxene phenocrysts and the multiple olivine phenocryst populations occurring in the Ambae lavas, provide evidence for episodes of magma mixing involving influxes of primitive magma batches and intervening periods of melt differentiation by fractional crystallisation.

7. The occurrence of complex geochemical zoning in clinopyroxene but not in co-crystallised olivine phenocrysts, is consistent with rapid (weeks to years) re-equilibration of olivine phenocrysts by intracrystalline diffusion at magmatic conditions.

8. Similar phenocryst assemblages to those documented for Ambae, comprising highly magnesian olivine and clinopyroxene, Cr-rich spinel, and calcic plagioclase, occur in primitive arc magmas elsewhere. This supports a more widespread generation of similar mafic melt compositions in the Vanuatu and other island arcs.

CHAPTER 7

The Geochemical Evolution of Lavas from Ambae, Vanuatu

7.1 INTRODUCTION

Most models for the petrogenesis of arc magmas now favour melting in the peridotitic mantle wedge overlying the subducting ocean crust. These models require the generation of primary melt compositions in equilibrium with mantle olivine (i.e. $Mg^{\#}_{Ol}$ = 87-92), and thus with $Mg^{\#}$ >67. Mafic magmas are rarely sampled by arc volcanism, hence their nature and links with the evolved magma compositions more typical of island arc volcanics (IAV) have remained largely unexplored. To shed light on the composition and differentiation of primary magmas in island arcs, the geochemical evolution of primitive Mg-rich lavas erupted on Ambae, Vanuatu, have been investigated. In a previous study of these lavas, Gorton (1977) illustrated a continuum between picritic and high-alumina basalt compositions, which was claimed to be related by olivine fractionation and accumulation to a primary melt with ~10.5 wt% MgO and $Mg^{\#}$ ~70.

7.2 GEOCHEMISTRY

7.2.1 Analytical techniques

Whole-rock analyses of 39 lavas and a single volcanic bomb (locations illustrated in Figure 6.1, Chapter 6) have been obtained by XRF techniques using a Philips 1410 spectrometer at the Geology Department, University of Tasmania. Major and trace element concentrations were determined by standard methods, after Norrish and Hutton (1969) and Norrish and Chappell (1977), and REE following Robinson et al. (1986). A complete list of analyses is given in Table 7.1, along with modal data for each sample. Details of sample preparation and analytical precision are documented in Appendix 1.

Table 7.1 Major and trace element analyses, and phenocryst modal data for Ambae lavas.

Sample#	68622	68591	68613	68639	68623	68583	68642	68626	68564	68605	68611	68635	68638	68562	68615	68584	68599	68565	68610	68634
Lava suite	LTS	LTS	LTS	LTS	LTS	LTS	LTS	LTS	LTS	LTS	LTS	LTS	LTS	LTS	LTS	LTS	LTS	LTS	LTS	LTS
Major elements																				
SiO2	46.90	47.33	47.66	47.76	47.43	47.68	48.01	48.17	48.01	48.10	47.81	48.92	48.79	48.96	49.03	49.59	48.70	50.38	49.30	49.87
TiO2	0.54	0.55	0.61	0.54	0.59	0.59	0.56	0.60	0.64	0.64	0.70	0.70	0.65	0.72	0.75	0.75	0.72	0.79	0.86	0.83
Al2O3	9.35	10.06	11.26	11.18	11.18	11.34	11.44	11.67	12.19	12.66	12.59	13.76	13.21	13.90	14.48	14.93	15.87	15.83	15.97	16.11
Fe2O3	11.61	11.14	11.38	11.19	11.20	11.39	11.14	11.11	11.07	11.39	11.29	11.19	11.06	11.13	11.16	11.01	10.93	10.52	11.85	11.00
FeO	0.00	0.00	0.00	0.00	0.00	0.00	0.00	0.00	0.00	0.00	0.00	0.00	0.00	0.00	0.00	0.00	0.00	0.00	0.00	0.00
MnO	0.20	0.18	0.19	0.19	0.19	0.19	0.20	0.19	0.19	0.19	0.19	0.20	0.18	0.20	0.18	0.19	0.19	0.18	0.20	0.18
MgO	19.35	17.75	16.16	15.61	14.85	14.83	14.74	14.27	13.49	13.02	12.08	10.77	10.41	9.95	8.62	7.67	7.53	6.58	6.51	6.38
CaO	9.97	10.54	9.74	11.15	10.94	11.15	11.53	10.63	11.20	11.04	11.86	11.21	12.10	11.50	12.14	12.39	12.04	11.68	11.17	10.87
Na2O	1.27	1.62	1.70	1.64	1.84	1.66	1.77	1.99	1.78	1.84	1.85	2.14	2.19	2.22	2.34	2.23	2.43	2.60	2.91	3.13
K2O	0.84	0.92	0.85	0.89	1.18	1.04	0.90	1.23	1.19	1.10	0.89	1.28	1.00	1.31	1.17	1.26	0.91	1.46	1.38	1.54
P2O5	0.17	0.22	0.17	0.18	0.23	0.22	0.17	0.23	0.23	0.23	0.18	0.26	0.18	0.26	0.25	0.23	0.20	0.26	0.27	0.29
L.O.I.	-0.21	-0.17	-0.09	-0.42	-0.32	-0.18	-0.49	-0.19	-0.10	-0.19	0.15	-0.23	-0.51	-0.23	0.16	0.03	0.54	-0.09	-0.03	-0.04
Total	99.99	100.14	99.63	99.91	99.31	99.91	99.97	99.90	99.89	100.02	99.59	100.20	99.26	99.92	100.28	100.28	100.06	100.19	100.39	100.16
Trace elements																				
Rb	12	17	13	15	21	20	15	19	20	16	13	23	15	22	17	18	14	23	18	23
Ba	329	258	347	330	470	347	363	415	417	375	345	446	366	445	430	485	359	500	513	543
Sr	490	488	493	526	641	557	542	643	683	632	583	763	585	673	710	732	578	748	727	790
La	8.13	10.1	9.0	10.7	12.8	12.7	7.9	12.4	11.2	12.4	9.57	15.4	8.74	13.40	12.9	12.1	10.0	12.8	12.9	15.5
Ce	19.00	23.5	15.9	16.5	29.3	24.0	18.9	26.0	25.9	24.3	22.50	29.3	21.10	30.20	22.7	25.9	17.5	26.4	29.7	34.1
Pr	2.49										2.98		2.83	3.71						
Nd	11.40	12.4	11.6	13.5	16.5	15.9	13.3	15.8	16.6	15.8	13.70	18.8	12.90	17.80	15.7	18.3	11.7	16.7	17.9	18.5
Sm	2.62										3.65		3.05	4.26						
Eu	0.83										1.15		1.08	1.21						
Gd	2.44										3.39		3.04	3.84						
Dy	2.10										3.22		2.96	3.53						
Er	1.24										1.83		1.96	1.94						
Yb	0.99										1.57		1.73	1.67						
Y	12	13	16	14	16	15	17	17	16	16	17	19	16	17	19	19	18	22	20	20
Zr	34	39	38	36	45	46	37	45	48	45	47	52	41	53	50	52	47	56	57	60
Nb	1	1	2	2	2	2	2	1	2	2	2	2	1	2	2	1	2	1	3	2
Sc	38	40	35	42	35	40	40	38	38	39	41	35	44	36	41	37	42	37	34	31
V	254	271	299	297	297	288	283	297	324	325	389	353	342	355	376	374	369	361	403	401
Cr	1208	1187	936	882	745	789	790	741	748	669	559	482	475	347	292	212	199	85	104	131
Ni	445	413	365	330	303	281	302	297	266	256	188	190	163	145	113	79	75	63	55	70
Phenocryst Modes																				
Ol	23.8	20.1	16.5	14.8	13.5	13.8	15	15.6	13	10.9	10.1	6	0.3	7.4	3.9	0.4	4.3	0	0.5	1.4
Cpx	13.1	4.7	5.7	7.1	5.1	6.7	7	8	9	2.1	8.9	3	0.5	5.7	2.9	1.2	6.5	0	4.1	0.5
Plag	0	0	0	0	0	0	0	0	0	0	0	0	0	0	0	0	3.7	0	2.5	0
Total	36.9	25.8	22.2	21.9	18.6	20.5	22	23.6	22	13	19	9	0.8	13.1	6.8	1.6	14.5	0	7.1	1.9
OL/(Ol+Cpx)	0.645	0.810	0.743	0.676	0.726	0.673	0.682	0.661	0.591	0.838	0.532	0.667	0.375	0.565	0.574	0.250	0.398	0.000	0.109	0.737

Sample#	68606	68627	68637	68588	68576	68566	68567	68578	68569	68571	68573	68595	68586	68593	68587	68603	68574	68596	68570	68577
Suite	LTS	LTS	LTS	LTS	LTS	HKS	HKS	HTS	HTS	HTS	HTS	HTS	HTS	HTS	HTS	HTS	HTS	HTS	HTS	HTS
Major elements																				
SiO2	49.49	49.09	50.02	49.37	49.65	47.11	47.18	47.74	47.79	47.76	47.31	47.66	49.03	49.99	49.94	49.67	48.75	48.11	48.50	55.95
TiO2	0.85	0.79	0.84	0.85	1.00	0.58	0.58	1.07	1.22	1.24	1.36	1.27	1.19	1.17	1.16	1.31	1.24	1.58	1.61	1.30
Al2O3	16.46	16.23	16.53	16.46	16.98	10.70	10.87	13.84	14.27	14.28	14.81	15.22	16.03	15.83	15.85	17.09	16.06	16.78	16.85	15.96
Fe2O3	11.15	11.52	10.97	11.58	12.17	11.24	11.14	12.10	11.65	11.70	12.16	11.60	11.39	10.96	10.88	10.90	13.16	12.54	12.48	9.35
FeO	0.00	0.00	0.00	0.00	0.00	0.00	0.00	0.00	0.00	0.00	0.00	0.00	0.00	0.00	0.00	0.00	0.00	0.00	0.00	0.00
MnO	0.19	0.20	0.19	0.20	0.21	0.19	0.19	0.21	0.21	0.21	0.22	0.21	0.22	0.20	0.21	0.18	0.23	0.23	0.21	0.21
MgO	6.28	5.91	5.90	5.39	4.58	15.60	16.05	9.65	8.56	8.60	8.05	7.35	6.90	6.34	6.12	5.28	5.26	4.99	4.88	2.47
CaO	10.74	11.54	10.78	10.83	10.12	11.29	11.11	12.34	12.58	12.72	12.67	12.19	10.91	10.45	10.40	10.86	10.95	10.93	10.76	5.85
Na2O	2.93	2.76	3.20	2.93	3.01	1.40	1.38	2.01	1.97	2.16	2.40	2.48	2.83	2.99	3.07	2.96	2.91	3.15	2.84	4.92
K2O	1.63	1.45	1.53	1.75	1.45	1.40	1.52	0.75	1.33	1.37	0.86	1.50	0.92	1.20	1.21	1.36	1.29	1.51	1.54	2.40
P2O5	0.32	0.27	0.27	0.30	0.29	0.31	0.34	0.20	0.37	0.33	0.28	0.37	0.30	0.31	0.32	0.35	0.31	0.45	0.45	0.66
L.O.I.	0.33	-0.11	0.04	0.22	0.25	0.06	-0.22	-0.21	-0.22	-0.07	-0.02	0.00	0.32	0.11	0.15	0.23	-0.02	0.00	0.13	0.45
Total	100.37	99.65	100.27	99.88	99.71	99.88	100.14	99.70	99.73	100.30	100.10	99.85	100.04	99.55	99.31	100.19	100.14	100.27	100.25	99.52
Trace elements																				
Rb	32	22	24	28	27	42	52	11	27	26	13	31	12	19	22	21	18	30	32	38
Ba	488	508	546	597	467	409	433	294	431	431	292	452	398	411	407	427	401	383	394	713
Sr	773	774	819	938	654	645	638	487	627	634	536	674	579	579	586	687	676	630	658	438
La	15.7	15.0	13.7	14.30	14.7	15.0	16.10	9.49	16.80	17.9	13.2	20.2	15.5	14.2	15.9	18.0	14.80	20.9	20.30	26.60
Ce	32.0	29.1	27.0	33.90	29.9	32.0	33.20	23.80	37.40	38.2	30.2	42.9	33.9	31.9	34.2	36.3	36.00	43.3	44.30	65.50
Pr				4.37			4.44	3.14	4.74								4.55		5.99	8.32
Nd	20.9	18.3	17.5	19.40	17.4	18.7	21.50	15.20	22.60	23.4	18.8	25.7	19.6	21.5	20.6	22.1	21.70	28.9	27.70	36.30
Sm				4.50			4.54	3.88	5.06								5.00		6.36	7.74
Eu				1.52			1.47	1.29	1.51								1.63		2.07	2.20
Gd				4.09			4.16	4.15	5.05								5.18		6.38	7.95
Dy				3.26			3.70	4.45	5.02								5.27		6.62	8.56
Er				1.73			2.11	2.58	2.82								3.13		3.96	5.47
Yb				1.48			1.92	2.35	2.60								2.77		3.47	5.14
Y	21	21	20	21	26	17	17	24	30	30	32	32	32	32	32	33	31	37	38	49
Zr	68	56	60	65	76	57	60	70	102	101	107	108	117	122	123	118	94	141	146	194
Nb	3	1	2	2	2	1	2	4	7	7	9	8	8	7	7	8	5	12	12	10
Sc	33	34	29	29	33	40	39	44	42	43	40	38	35	36	34	33	36	30	33	21
V	389	400	429	418	437	272	284	367	342	374	387	351	361	359	349	379	447	426	428	220
Cr	163	31	99	20	20	850	910	308	243	250	187	171	131	135	147	80	12	15	11	3
Ni	71	49	57	40	27	298	331	102	79	75	69	62	61	56	55	34	30	27	24	5
Phenocryst Modes																				
Ol	1.5	0	0.7	0	0	14.5	17.1	3.6	3.7	4	3.2	4.3	1.3	2.5	3.3	1.9	2	0	0.2	0
Cpx	1.9	0	0.5	0	0.3	17.3	9.1	12.1	12.8	13	10.7	9.6	13.6	7.7	8.8	4.5	5	0	0.5	0
Plag	3.1	0	1.8	0	5.2	0	0	2.3	3.2	3	3.1	4.7	9.3	9.5	8.8	9.4	9	2.7	4.9	0
Total	6.5	0	3	0	5.5	31.8	26.2	16	19.7	20	17	18.6	24.2	19.7	20.9	15.8	16	2.7	5.6	0
OL/(Ol+Cpx)	0.441	0.000	0.583	0.000	0.000	0.456	0.653	0.229	0.224	0.235	0.230	0.309	0.087	0.245	0.273	0.297	0.286	0.000	0.286	0.000

7.2.2 Geochemical Division and Classification of Lava Suites

All samples analysed are basalts, with the exception of a single andesite bomb from the Lomalla Pyroclastics. Compositions vary from high-alumina basalts (MgO <5wt% and Al_2O_3 >16wt%) to picrites with up to ~20 wt% MgO, and span an $Mg^{\#}$ range from 46 to 80 (Fe^{2+}/Fe^{tot} = 0.80).

Three geochemically distinct lava suites are recognised, and these conform with the stratigraphic division of lavas. The older lava sequence, beneath the Lomalla Pyroclastics, have higher TiO_2 contents (>1 wt%) than the overlying lavas which have TiO_2 generally <1wt%. A third relatively minor group of lavas is subdivided from among the younger lavas based on its higher K_2O contents. The separation of these three suites, the high-Ti suite (HTS), low-Ti suite (LTS), and high-K suite (HKS), is clearly shown in a plot of TiO_2/Al_2O_3 versus K_2O/Al_2O_3 (Fig. 7.1).

The LTS and HTS lavas both fall within the compositional fields of medium and high-K basalts, whereas the HKS lavas border on shoshonitic compositions (Fig. 7.2). These elevated alkali contents are manifested as normative mineralogies which straddle the plane of silica saturation, indicating a transitional to alkaline character for each suite (Fig. 7.3).

7.2.3 Minor and Trace Element Characteristics

The geochemical characteristics of the individual lava suites are summarised in multi-element diagrams in Figure 7.4. Each of the lava suites possesses the HFSE depleted and LILE enriched characteristics which are considered diagnostic of arc magmas. It is notable that HFSE and HREE abundances in the LTS and HKS are considerably lower than in N-MORB, but in the HTS are similar to N-MORB. LILE and LREE abundances, on the other hand, are much greater than those in N-MORB in all suites. REE patterns are LREE enriched and have moderate middle-HREE fractionation (Fig. 7.5).

7.3 GEOCHEMICAL VARIATION

Harker variation diagrams (Figs. 7.6 and 7.7) illustrate well defined differentiation trends for most elements, particularly among the LTS lavas, which vary continuously

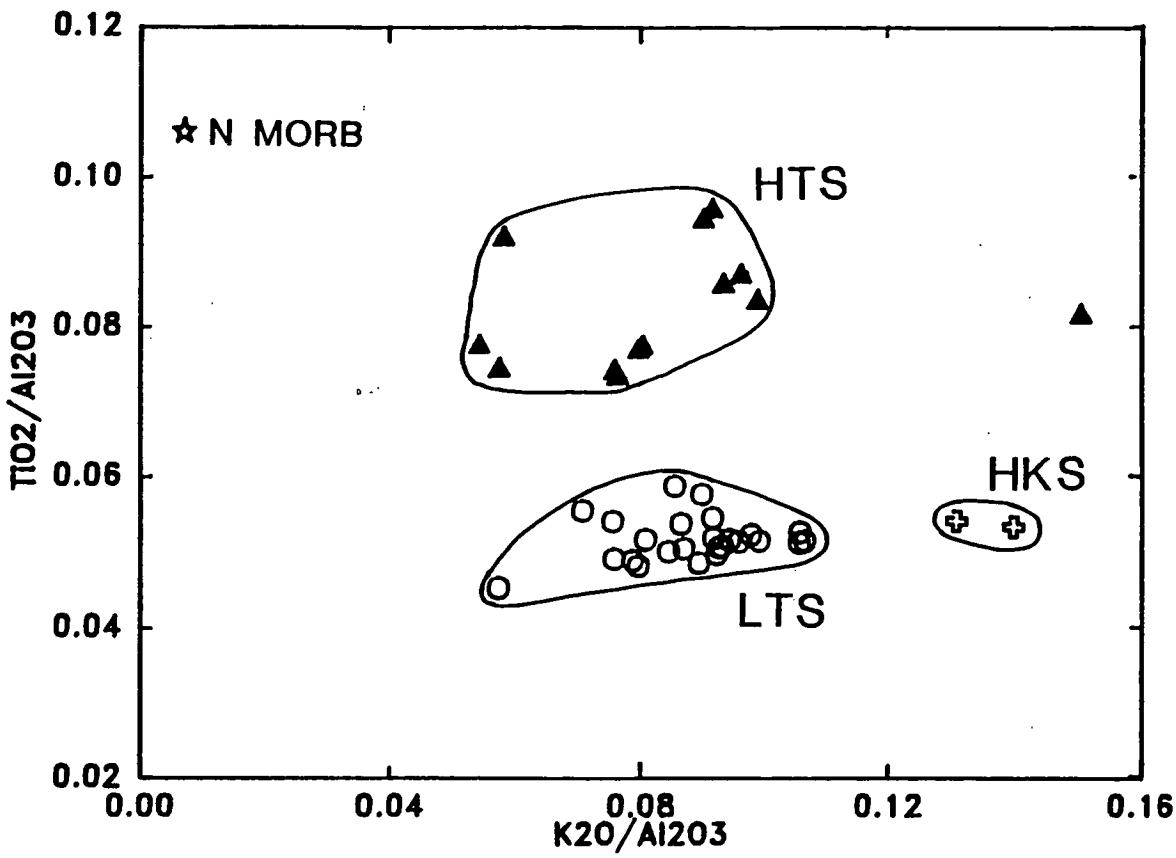

Figure 7.1 TiO_2/Al_2O_3 versus K_2O/Al_2O_3 variation in Ambae lavas, illustrating the distinctive geochemistry of the principal lava suites, the High-Ti Suite (filled triangles), the Low-Ti Suite (circles) and the High-K Suite (crosses). The outlying High-Ti Suite sample is an andesitic bomb from the Lomalla Pyroclastics. The average N-MORB composition compiled by Hofmann (1988) is shown for comparison.

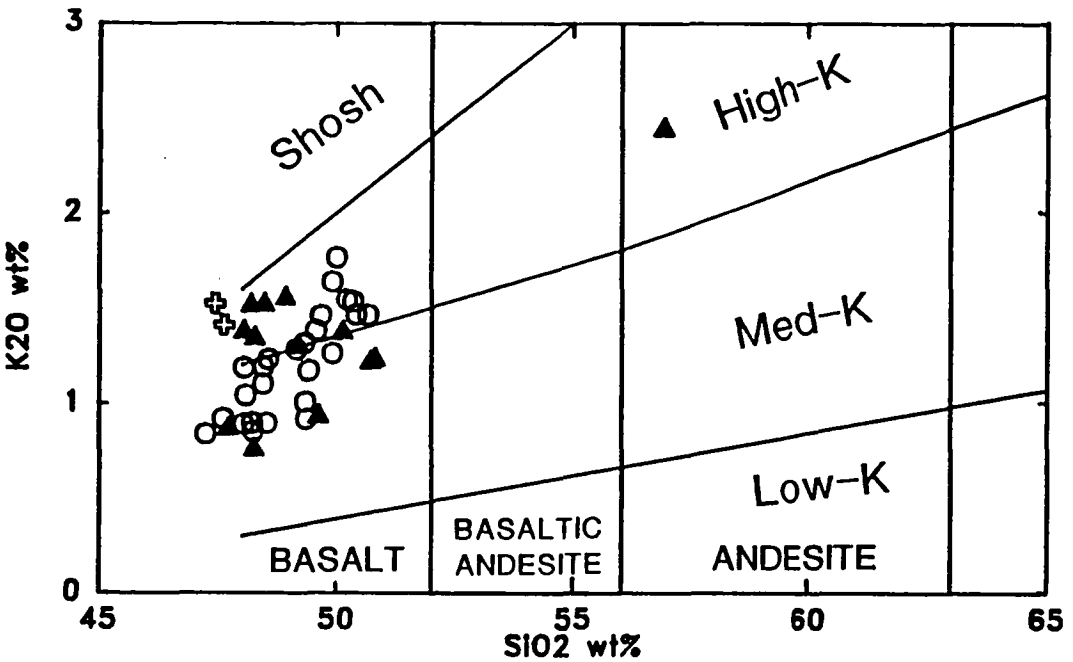

Figure 7.2 Classification of Ambae samples using a K_2O versus SiO_2 variation diagram and compositional fields from Peccerillo and Taylor (1976). Symbols as for Figure 7.1.

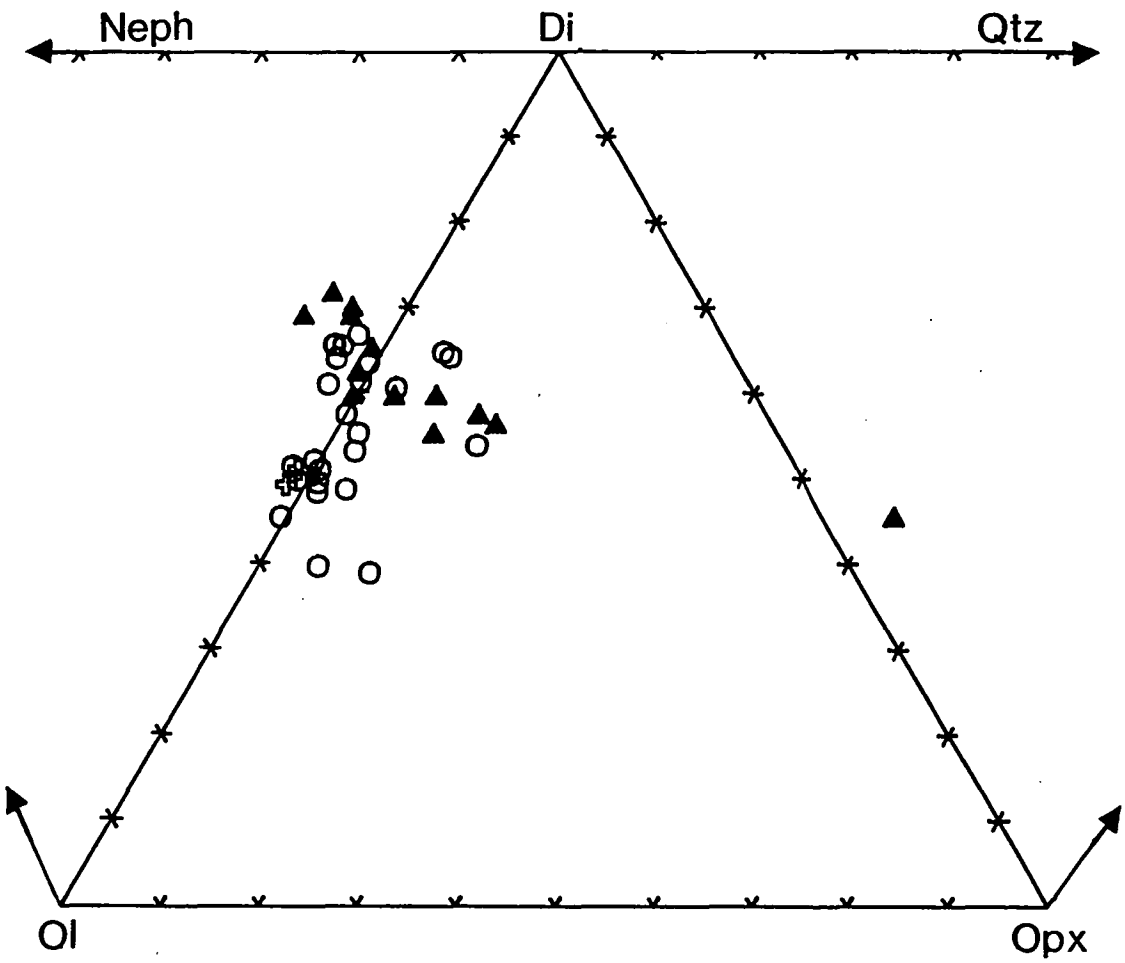

Figure 7.3 Normative Olivine-Diopside-Nepheline-Hypersthene-Quartz mineralogy of Ambae lavas. Symbols as for Figure 7.1.

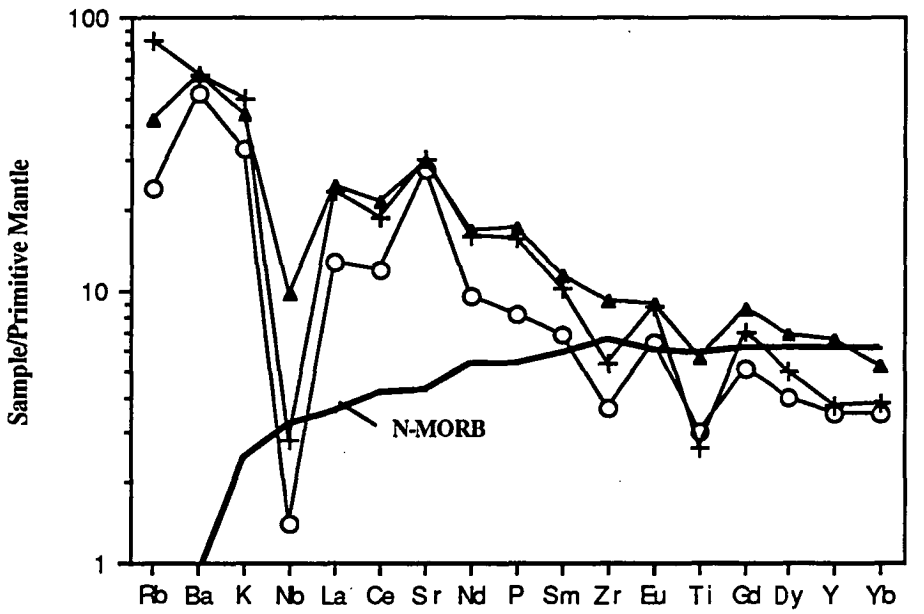

Figure 7.4 Multi-element diagram for representative LTS, HTS, and HKS samples, compared to average N-MORB (from Hofmann, 1988). Normalising values used are those of Sun and McDonough (1988).

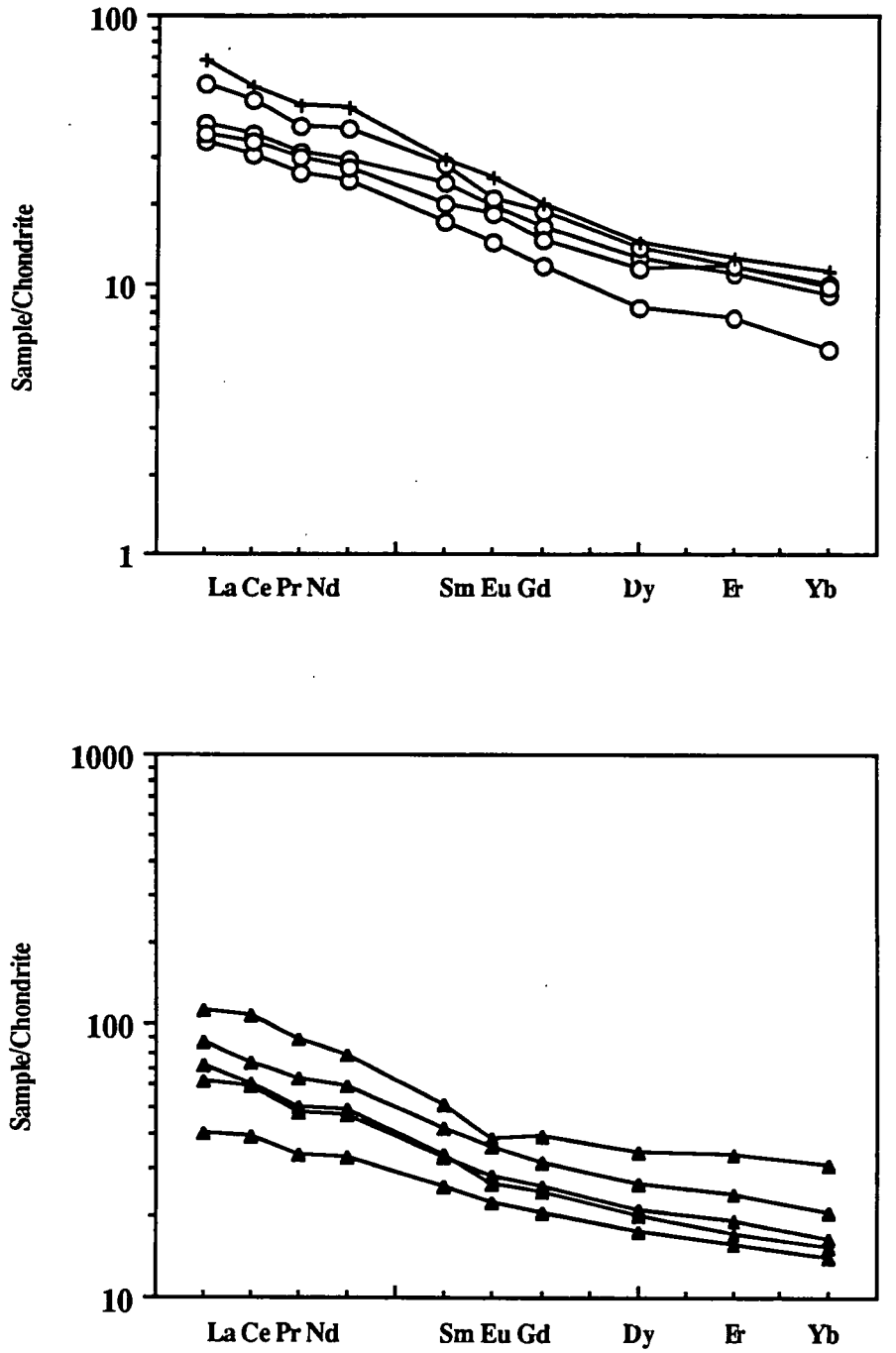

Figure 7.5 Chondrite-normalised REE diagrams for representative Ambae lavas (symbols as in Fig. 7.1). Note the more steeply inclined patterns of the LTS and HKS samples than the HTS samples.

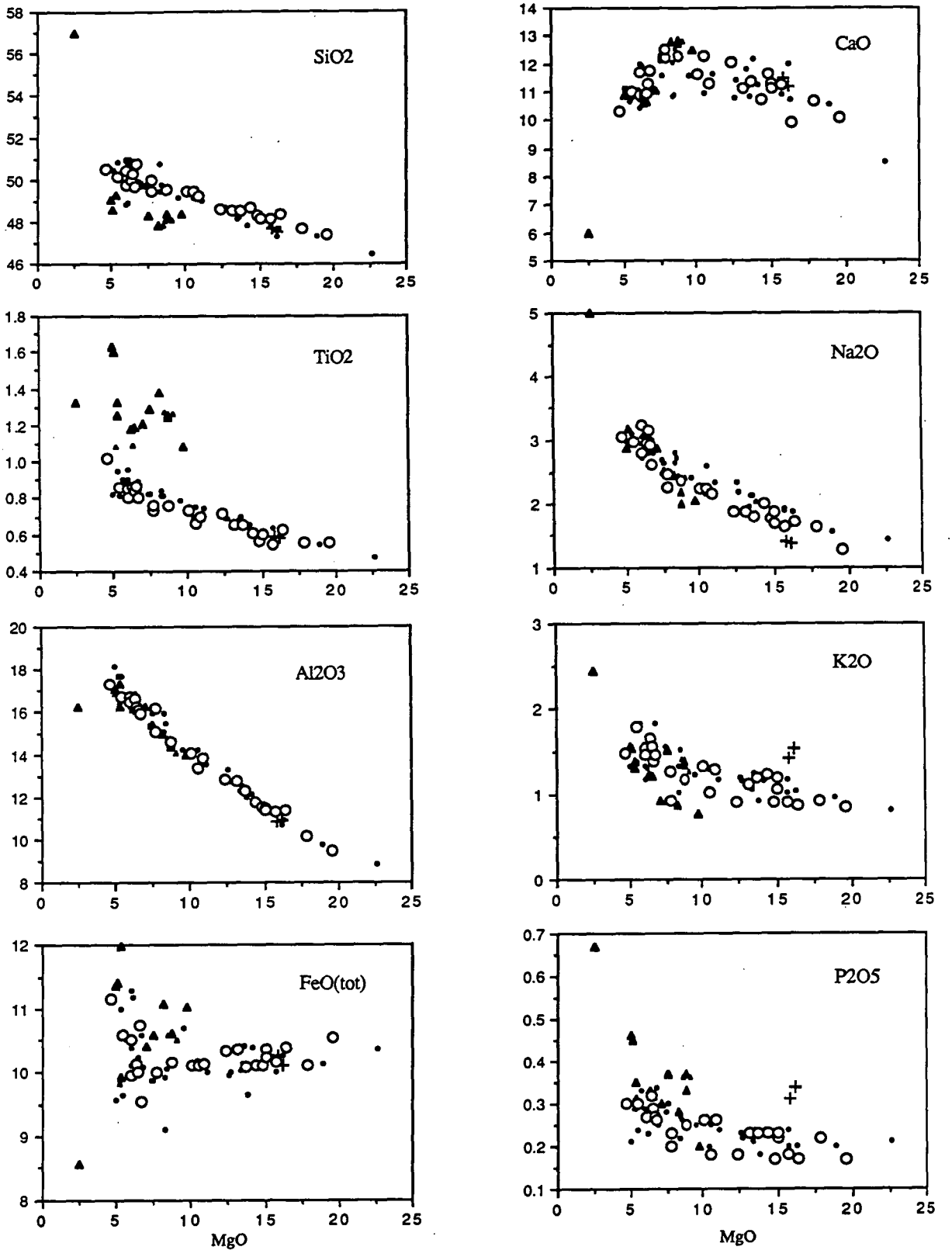

Figure 7.6 Major element covariation diagrams for Ambae lavas, including samples analysed by Gorton (1974). Note the tight linear compositional variation exhibited by the LTS and the distinctive geochemical characteristics of the individual suites. Symbols as for Figure 7.1, with Gorton's analyes shown as small filled circles and triangles.

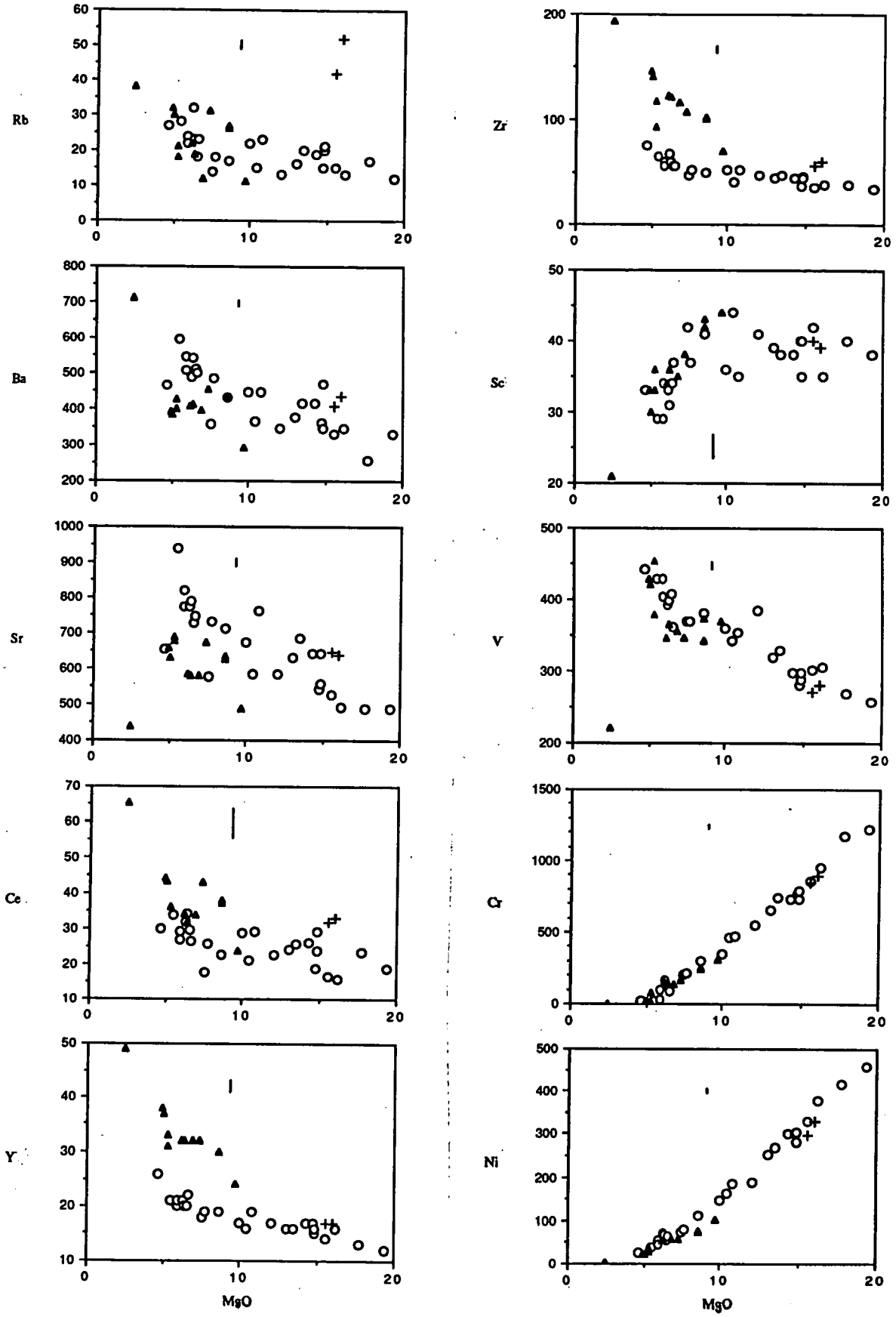

Figure 7.7 Trace element variation in Ambae lavas as a function of MgO content. Short vertical lines show typical 2σ error limits for trace element abundances in the LTS lavas, and symbols are as in Figure 7.1.

between high and low MgO end-members. The LILE trends are notable as a group for they tend to display scatter exceeding analytical error. Distinctly curved differentiation paths are followed only by CaO and Sc, which inflect toward lower concentrations at MgO contents <9wt%, though close inspection reveals that most other element trends also deviate near 9wt% MgO. The distinctive chemistries of the different lava suites are clearly demonstrated in these diagrams, in particular the high relative HFSE and REE abundances of the HTS lavas, and the high LILE abundances of the HKS (particularly Rb and K).

7.3.1 Origin of Geochemical Variation

Evaluating the role of phenocryst fractionation processes is a first step toward understanding geochemical evolution of the Ambae lavas. This is addressed here using least squares mass balance methods (i.e. GENMIX program of Le Maitre, 1980), with Pearce element ratio plots being employed to confirm and aid visualisation of results. Attention is focused on the extended and systematic variation of the LTS lavas, for this suite bridges the critical region of interest between primitive picrite and evolved high-alumina basalt compositions. Particular emphasis is placed on evaluating liquid evolution paths and the nature of the crystal and Mg-rich lavas

Whole-rock geochemical variation

Whole-rock geochemical variation in the LTS lavas can be divided into two linear trend segments, comprising:

(1) samples with >9wt% MgO, and

(2) samples with <9wt% MgO.

Regression analysis shows these segments closely approximate straight lines, facilitating calculation of end-member compositions and modelling by least squares methods. The compatability of crystal fractionation with these geochemical variation trends has been assessed using the model:

$$Magma_1 = Magma_2 + Phenocrysts$$

based on regressed compositions at 5, 9 and 20 wt% MgO, and "average" phenocrysts compositions in the LTS lavas. Low residual sum of squares values are obtained for both trend segments, indicating each is consistent with the addition/removal of phenocryst phases

(Table 7.2a&b). The mafic lava trend corresponds with olivine and clinopyroxene addition/subtraction in the proportions 7:3, in very close agreement with observed modal proportions of these phenocrysts (Table 7.1, Figure 7.8). The lavas with <9wt% MgO follow a fractionation trend in which clinopyroxene dominates over olivine (+minor oxide phase).

Liquid Evolution Trends

Liquid evolution paths, as defined by aphyric whole-rock and calculated groundmass compositions (phenocrysts subtracted), have also been modelled in terms of phenocryst fractionation. Results for the evolution of individual aphyric rocks, from the two most primitive aphyric samples (#68638 and #68584), are reported in Table 7.2c. The low residual sum of squares (RSS) values obtained indicate geochemical differences between the aphyric lavas are closely approximated by fractionation of the observed phenocrysts (olivine, clinopyroxene, and an oxide phase). It is notable that the relatively low proportion of clinopyroxene removed (up to 70%) with progressive fractionation of #68638 is at odds with the high proportion of clinopyroxene determined using #68584. This could reflect an interval of olivine-only fractionation during differentiation of #68638, an interpretation supported by the calculated equilibrium olivine Mg# for #68638 (i.e. 90.5, assuming fO_2 = QFM+2.5 log units), which exceeds that of olivine in equilibrium with the most magnesian clinopyroxene in the LTS.

The analysis of a more comprehensive set of liquid compositions is enabled by employing calculated groundmass compositions. The compositional trends formed by these data have also been analysed by regression analysis and used, as above, to define end-member compositions at 5 and 9 wt% MgO. Variation trends for groundmasses saturated with olivine and clinopyroxene (i.e. excluding plagioclase-phyric samples and #68638) are found to be consistent with the fractionation of these phases in the proportions 1:3 (Table 7.2d), in good agreement with a 1:4 prediction based on phase equilibria (e.g. Cox and Bell, 1972). Additional modelling involving the most evolved liquid compositions within the LTS, demonstrates plagioclase becomes a major fractionating phase toward the limit of differentiation of these lavas (see Table 7.2e).

Table 7.2
Least squares modelling of geochemical variation in LTS lavas.

a. Whole-rock variation trend from 20 to 9wt% MgO.

	20WR	=	9WR	+	Ol	+	Cpx	+	Cr-spinel	=	Product
Mass%	100.00		61.68		26.94		10.88		0.50		100.00
SiO2	47.26		49.59		40.36		52.50		0.00		47.17
TiO2	0.51		0.73		0.00		0.18		0.50		0.47
Al2O3	9.24		14.47		0.00		3.03		9.89		9.30
FeO	10.37		10.08		12.51		4.06		33.00		10.20
MnO	0.19		0.19		0.10		0.10		0.00		0.16
MgO	20.00		9.00		46.92		16.29		10.22		20.01
CaO	10.08		12.14		0.21		23.24		0.00		10.07
Na2O	1.34		2.30		0.00		0.10		0.00		1.43
K2O	0.84		1.26		0.00		0.00		0.00		0.78
P2O5	0.18		0.24		0.00		0.00		0.00		0.15

Residual Sum of Squares (RSS) = 0.0580

b. Whole-rock variation trend from 9 to 5wt% MgO.

	9WR	=	5WR	+	Ol	+	Cpx	+	Ti-mt	=	Product
Mass%	100.00		75.98		4.13		18.59		1.30		100.00
SiO2	49.92		50.44		40.36		52.50		0.00		49.75
TiO2	0.74		0.88		0.00		0.18		7.27		0.80
Al2O3	14.29		17.35		0.00		3.03		4.30		13.80
FeO	10.04		10.21		12.51		4.06		76.00		10.01
MnO	0.19		0.20		0.10		0.10		0.20		0.17
MgO	9.00		5.00		46.92		16.29		2.87		8.80
CaO	12.66		10.60		0.21		23.24		0.00		12.38
Na2O	2.12		3.34		0.00		0.10		0.00		2.56
K2O	1.13		1.70		0.00		0.00		0.00		1.29
P2O5	0.24		0.30		0.00		0.00		0.00		0.23

Residual Sum of Squares (RSS) = 0.5920

c. Least squares modelling of differences betweeen aphyric whole-rock compositions.

	Melt(wt%)	+	Ol	+	Cpx	+	Ti-mt	RSS	Ol/(Ol+Cpx)
#68638 to									
#68584	88.18		6.09		5.39		0.34	0.0790	0.470
#68565	80.15		6.91		11.46		1.48	0.1208	0.724
#68634	77.18		6.16		15.47		1.19	0.2584	0.715
#68627	78.93		7.83		13.02		0.22	0.0653	0.624
#68637	75.14		6.76		16.79		1.31	0.2288	0.713
#68588	75.41		7.73		16.30		0.56	0.2389	0.678
#68584 to									
#68565	90.87		0.93		6.91		1.29	0.1949	0.881
#68634	87.47		0.07		11.49		0.97	0.5718	0.994
#68627	89.49		1.97		8.67		-0.13	0.1007	0.815
#68637	85.16		0.75		12.99		1.11	0.5350	0.945
#68588	85.49		1.85		12.41		0.25	0.3875	0.870

d. Ol+Cpx saturated groundmass compositional variation from 9 to 5wt% MgO.

	9	=	5	+	Ol	+	Cpx	+	Ti-mt	=	Product
Mass%	100.00		79.50		5.55		14.00		0.95		100.00
SiO2	49.49		50.25		40.36		52.50		0.00		49.54
TiO2	0.75		0.87		0.00		0.18		7.27		0.79
Al2O3	14.22		16.96		0.00		3.03		4.30		13.95
FeO	10.27		10.37		12.51		4.06		76.00		10.24
MnO	0.20		0.20		0.10		0.10		0.20		0.17
MgO	9.00		5.00		46.92		16.29		2.87		8.89
CaO	12.56		10.50		0.21		23.24		0.00		12.41
Na2O	2.04		2.95		0.00		0.10		0.00		2.36
K2O	1.22		1.63		0.00		0.00		0.00		1.30
P2O5	0.26		0.30		0.00		0.00		0.00		0.24

Residual Sum of Squares (RSS) = 0.2232

e. Evolution of the most evolved plagioclase saturated groundmass composition.

	68588	=	68576g	+	Ol	+	Cpx	+	Ti-mt	+	Plag	=	Product
Mass%	100.00		77.82		0.98		5.35		0.27		15.57		100.00
SiO2	50.12		51.20		40.36		52.50		0.00		46.51		50.30
TiO2	0.86		1.19		0.00		0.18		7.27		0.00		0.96
Al2O3	16.71		14.68		0.00		3.03		4.30		33.41		16.80
FeO	10.58		12.86		12.51		4.06		76.00		1.01		10.71
MnO	0.20		0.25		0.10		0.10		0.20		0.00		0.20
MgO	5.47		5.38		46.92		16.29		2.87		0.00		5.53
CaO	10.99		9.06		0.21		23.24		0.00		17.43		11.01
Na2O	2.97		3.34		0.00		0.10		0.00		1.49		2.84
K2O	1.78		1.70		0.00		0.00		0.00		0.16		1.35
P2O5	0.30		0.35		0.00		0.00		0.00		0.00		0.27

Residual Sum of Squares (RSS) = 0.2746

f. Intersection between olivine-liquid line of descent and the Ol+Cpx cotectic.

	Ol(90)	+	68638	=	9G	+	5G	=	React's	=	Product
Mass%	-2.96		102.96		109.82		-9.82		100.00		100.00
SiO2	40.44		49.45		49.49		50.25		49.72		49.42
TiO2	0.00		0.66		0.75		0.87		0.68		0.74
Al2O3	0.00		13.39		14.22		16.96		13.79		13.95
FeO	9.70		10.09		10.27		10.37		10.10		10.26
MnO	0.00		0.18		0.20		0.20		0.19		0.20
MgO	49.25		10.55		9.00		5.00		9.40		9.39
CaO	0.12		12.26		12.56		11.50		12.62		12.66
Na2O	0.00		2.22		2.04		2.95		2.29		1.95
K2O	0.00		1.01		1.22		1.63		1.04		1.18
P2O5	0.00		0.18		0.26		0.30		0.19		0.26

Residual Sum of Squares = 0.2857

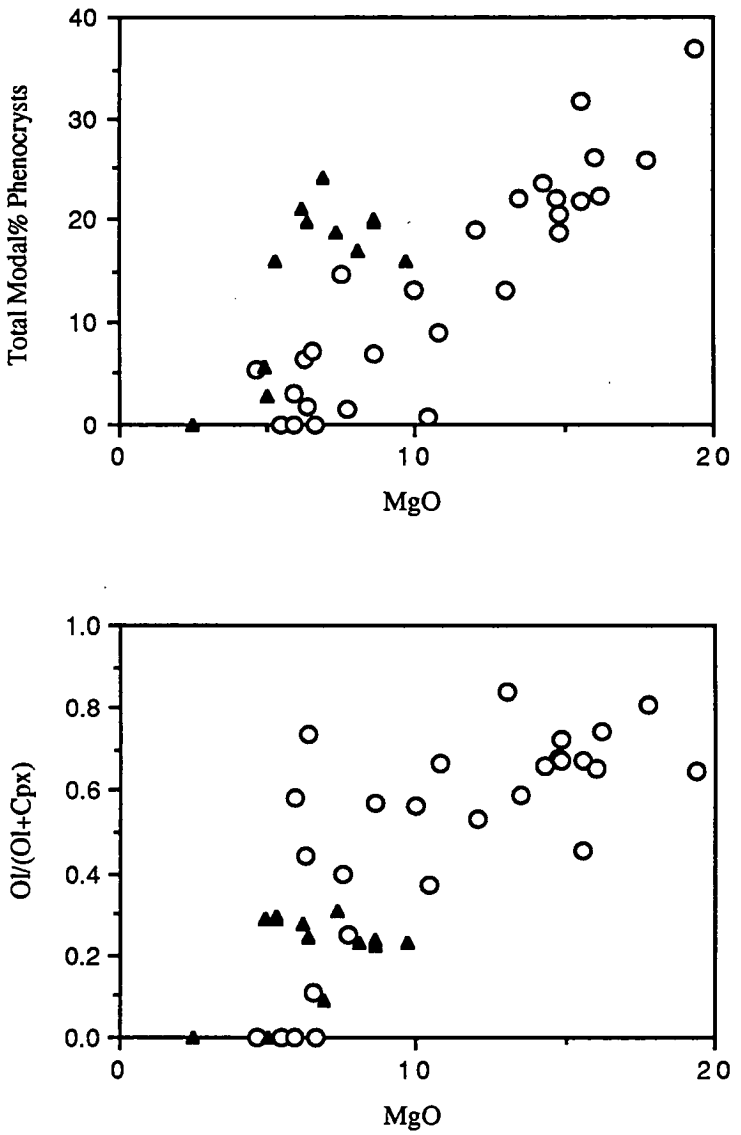

Figure 7.8 (a) Modal phenocryst content of the LTS lavas plotted against MgO content, and (b) variation in the modal proportions of olivine and clinopyroxene in the Ambae lavas as a function of MgO content.

The intersection of a linear combination of the most magnesian aphyric rock (#68638) and magnesian olivine (Mg# = 90), with the olivine-clinopyroxene cotectic defined by groundmass compositions, enables estimation of the melt composition where clinopyroxene first crystallises. Least squares modelling reveals this composition to have ~9.4wt% MgO. This is significant in terms of fO_2, for this composition will crystallise Mg# 89.4 olivine (i.e. that in equilibrium with the most magnesian clinopyroxene) if the fO_2 is near QFM+2.25 log units (calculation based on $K_D^{Fe/Mg}{}_{Ol/Liq} = 0.30$ and Fe^{3+}/Fe^{2+} determined following Kilinc et al., 1983). This in good agreement with the fO_2 inferred from the olivine-spinel oxygen barometer of Ballhaus et al. (in press), and suggests the O'Neill and Wall calibration considerably underestimates the fO_2 at which the Ambae magmas have crystallised.

The least squares modelling results above can be confirmed by plotting calculated groundmass and whole-rock compositions on Pearce element ratio diagrams designed to discriminate between fractionation of olivine and clinopyroxene (Fig. 7.9). These plots enable graphic illustration of the relative phenocrysts proportions which control geochemical variation, and facilitate quantitative determination of these proportions through regression analysis. The results obtained closely match those determined using least squares methods (see Fig 7.9).

In summary, liquid evolution paths for the LTS lavas are consistent with the following sequence of fractionation: olivine (+accessory Cr-spinel?), followed by olivine and clinopyroxene (+ minor oxide phase) in the proportions 1:4, and then plagioclase, clinopyroxene, olivine and magnetite. This sequence matches the low pressure phase relationships of compositionally similar basalts from the Solomon Islands (Brown and Schairer, 1968), and the proportions match those determined in relevant liquidus studies (Cox and Bell, 1972). The crystal-rich mafic lavas do not correspond with this low pressure fractionation trend but are consistent with fractionation or accumulation of the modal proportions of olivine and clinopyroxene in these lavas.

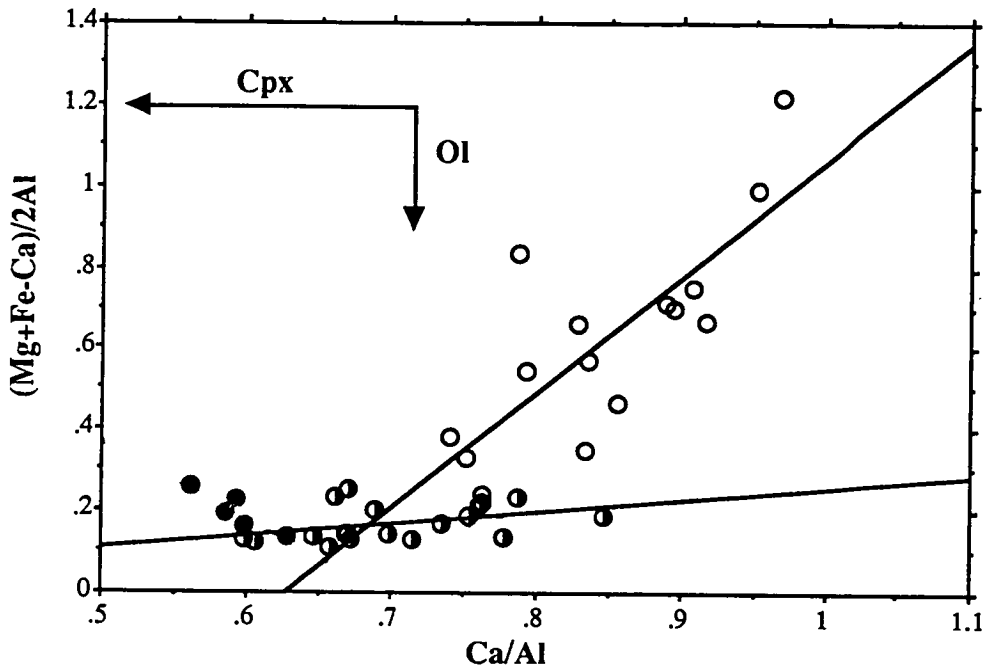

Figure 7.9 Pearce element ratio plot discriminating between olivine and clinopyroxene fractionation effects in the LTS lavas with >9wt% MgO (unfilled circles) and LTS groundmass compositions (half-filled and filled circles indicate samples unassociated and associated with plagioclase phenocrysts, respectively). Arrows indicate the effects of fractionating equivalent masses of olivine and clinopyroxene. Regression lines are shown for the crystal-rich lavas and the groundmass compositions unassociated with plagioclase phenocrysts. Fractionating olivine and clinopyroxene mass proportion estimates based on the best-fit regression slope values, are 66Ol:34Cpx for the crystal-rich lavas and 16Ol:84Cpx for the groundmass trend.

7.3.2 Origin of the crystal-rich lavas

Projection of the LTS lavas onto the Ol-Di-Plag plane of the normative basalt tetrahedron (Fig. 7.10) shows that the crystal-rich lavas form a mixing line between relatively evolved melts (marked L), falling mid-way along the Ol+Cpx cotectic, and an olivine-clinopyroxene mixture of 7:3 (marked S). These end-points correspond with the groundmass compositions and the modal proportions of olivine and clinopyroxene in the LTS lavas. This reaffirms a previous suggestion that addition or subtraction of observed phenocryst modal proportions controls bulk compositional variation in the LTS lavas, but the question remains as to what these phenocryst proportions represent?

The modal proportions of olivine and clinopyroxene in the crystal-rich LTS lavas are best attributed to an integration of phenocrysts crystallised over intervals of olivine-only and olivine+clinopyroxene crystallisation. For example, the phase relations in Figure 7.10 dictate that an olivine saturated primary or parent liquid, which lies on the compositional trend of mafic LTS lavas, will evolve to point L on the olivine and clinopyroxene cotectic after crystallising 70% olivine and 30% clinopyroxene. Alternatively, the 7:3 proportion of olivine and clinopyroxene could be attributed to;

(1) high pressure crystallisation where cotectics are more olivine rich, or

(2) selective accumulation of olivine, co-crystallised with clinopyroxene in the cotectic proportions 1:4.

The first of these possibilities is inconsistent with the low concentrations of jadeite and other pressure sensitive components in LTS clinopyroxenes (see Table 6.2), and the second seems an unlikely means of producing the relatively constant phenocryst proportions in the LTS lavas. At face value, a selective accumulation is supported by the observation that most phenocrysts in the LTS lavas are in equilibrium with relatively evolved olivine- and clinopyroxene-saturated melts (except olivine with Mg# >89.4): however, zoning profiles indicate primitive olivine phenocrysts are able to re-equilibrate with evolved melts compositions (Chapter 6).

A final problem worth discussing is whether the phenocrysts present are redistributed in origin (i.e. fractionated and accumulated), or have been retained, at least

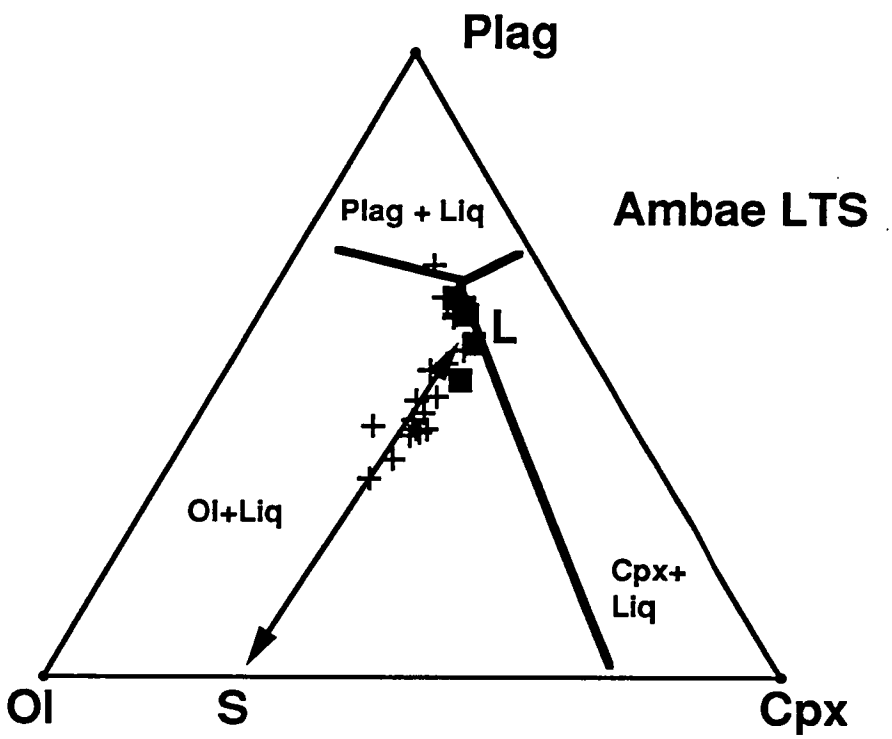

Figure 7.10 Projection of the normative mineralogies of LTS lavas onto the Ol-DI-Plag plane of the basalt tetrahedron, following re-distribution of normative orthopyroxene into its constituent olivine and quartz components. The phase boundaries shown are approximate only, after Cox and Bell (1972). Aphyric lavas are plotted as solid squares, and all other lavas as crosses. Normative mineralogies have been calculated assuming $Fe^{2+}/(Fe^{2+}+Fe^{3+}) = 0.80$. The double ended arrow is a mixing line between a liquid composition (L) lying on the Ol+Cpx cotectic and an olivine-clinopyroxene mixture (S) of 7Ol:3Cpx.

partly, in the magmas as they have cooled and crystallised. These competing possibilities are likely to be geochemically indistinguishable, yet have fundamentally different implications for magmatic differentiation and the origin of the crystal-rich magmas. To illustrate these differences, it is useful to consider crystal settling rates in the Ambae magmas.

Crystal settling velocities for typical (2mm diameter) olivine and clinopyroxene phenocrysts in the LTS will range from ~1m/hr for olivine in picritic melts to ~0.005m/hr in high-alumina basalt compositions (based on Stokes Law, melt viscosities calculated using the method of Shaw (1972), and appropriate densities for melt and phenocrysts). The time taken for these crystals to settle through a moderately large magma body (~1km thick), in the absence of convection, will increase from ~1 month to several tens of years as magmas become more evolved, from picrites to high-alumina basalts. These times will lengthen in the presence of large crystal concentrations (Marsh and Maxey, 1985), but are likely to remain short compared to the cooling times of moderate to large magma bodies, which are on the order of thousands, to tens of thousands, of years (e.g. Marsh and Maxey, 1985). It is further notable that recent fluid dynamic experiments show crystal settling probably remains effective even under conditions of turbulent convection (Nokes and Martin, 1990). These observations imply that mafic basaltic magma chambers are likely to be largely free of crystals. It is concluded that crystal-rich basaltic magmas form either by rapid cooling and crystallisation with insufficient time for settling to take place (e.g. Krishnamurthy and Cox, 1978), or by the redistribution and accumulation of phenocrysts within a volume of magma.

Crystal accumulation appears necessary to explain those crystal-rich LTS lavas which have more magnesian compositions than the LTS primary melt estimate. Recent investigations show that mafic crystal-rich (accumulative) magmas may be generated locally within the eruptable interiors of magma chambers, where convective flow opposes and exceeds (or equals) crystal settling velocities (Marsh and Maxey, 1985). The relative volume of crystal-rich magma produced will be small, unless convective flow velocities are high throughout the magma chamber or crystal sizes are small. This model has been used specifically to explain the formation of plagioclase phenocryst-rich high-alumina basalts in island arcs (Brophy, 1987). Another crystal settling (accumulation) process deserving

comment, given the similarity between the LTS magmas and the New Georgia picrites upon which it was developed, is compensated crystal settling (Cox and Bell, 1972). In this model, phenocrysts settling from horizons within the lower part of a magma body are replaced by phenocrysts settling from above. This results in a zone of compensated crystal settling where no apparent differentiation takes place. In the uppermost part of the magma body, differentiation occurs because settling crystals are not fully replaced from overlying magma, which becomes progressively depleted in crystals. In this region evidence occurs which distinguishes compensated crystal settling from other processes, for differentiation may be inconsistent with the fractionation of observed phenocryst assemblages (for a detailed discussion, see Cox and Bell, 1972). Given the consistency between bulk compositional variation and fractionation of the modal phenocryst proportions observed in the LTS lavas, no evidence exists to suggest the Ambae crystal-rich magmas have formed by this process.

Maaloe et al. (1986) have proposed a delayed fractionation model, in which retention of crystals occurs in magmas as they cool and crystallise during ascent from depth, followed by variable degrees of crystal fractionation upon ponding in shallow magma reservoirs prior to eruption. Advanced as a general model for the differentiation of tholeiitic and alkalic magmas (Maaloe et al., 1988), this proposal is consistent with theoretical models for the formation crystal-rich magmas during ascent (Huppert and Sparks, 1985). An identical outcome can be envisaged when a basaltic magma chamber is replenished by a more primitive magma batch. Possible formation of a layer of dense, hot, primitive magma beneath cooler resident magma, will promote rapid cooling and crystallisation of the primitive magma, followed by later mixing with the resident magma and fractionation (for details see Huppert and Sparks, 1980). Indeed, evidence for the rapid crystallisation of primitive magma batches in this manner is now established in layered intrusions (Ballhaus and Glikson, 1989). This provides an efficient means of transfering a primitive magma to a chemically evolved and crystal-rich state, in which crystal settling velocities will be slow. Ensuing eruptions are able to tap a slowly differentiating crystal-rich magma.

Both processes outlined above could be classified as rapid crystallisation models, given that any delay in fractionation is probably apparent only. They result in compositional

variation, due to subsequent crystal-liquid fractionation, between the melt evolved and phenocrysts formed during rapid crystallisation, and are, accordingly, consistent with the geochemical and modal variation in the LTS lavas (Figs. 7.8&10). Moreover, the patchy-zoned and skeletal diopside crystal cores in the LTS lavas (Chapter 6) may be readily explained by rapid growth, driven by undercooling, during the early stages of magma evolution by either of these process. The evidence cited for magma mixing in the Ambae lavas, though not conclusive, lends support to a magma chamber replenishment origin in the case of the crystal-rich LTS lavas.

In conclusion, crystal-liquid fractionation provides the foundation for understanding differentiation of the LTS lavas, and within this crystal-redistribution framework, accumulation is necessary to explain the occurrence of LTS lavas which have bulk compositions more magnesian than the primary melt estimate (i.e. >~15 wt% MgO). It follows therefrom, given the likely role of rapid-crystallisation in formation of the crystal-rich magmas, that both crystal-retention and crystal redistribution processes (involving fractionation and accumulation) are required to explain the compositional spectrum of LTS magmas.

7.3.3 Trace Element Evolution

Trace element variation in the Ambae LTS lavas is compared herein to fractional and equilibrium crystallisation models, based on the liquid line of descent determined above. These crystallisation models bound compositions arising in "steady-state" magma chambers through open-system differentiation involving influxes of primitive magma (Langmuir 1989), and can account for discrete magma mixing events and "rapid crystallisation" processes which will lie on lines constrained to connect, or pass through, points on the modelled trace element evolution paths. Most partition coefficients used in this modelling are specific to Ambae phenocrysts, as determined by Gorton (1974; Table 7.3) based on spark source mass spectrometry analyses of LTS phenocryst separates. Supplementary partition coefficients for phenocrysts and elements not analysed by Gorton have been compiled from Fujimaki et al. (1984), and Gill (1978; Table 7.3).

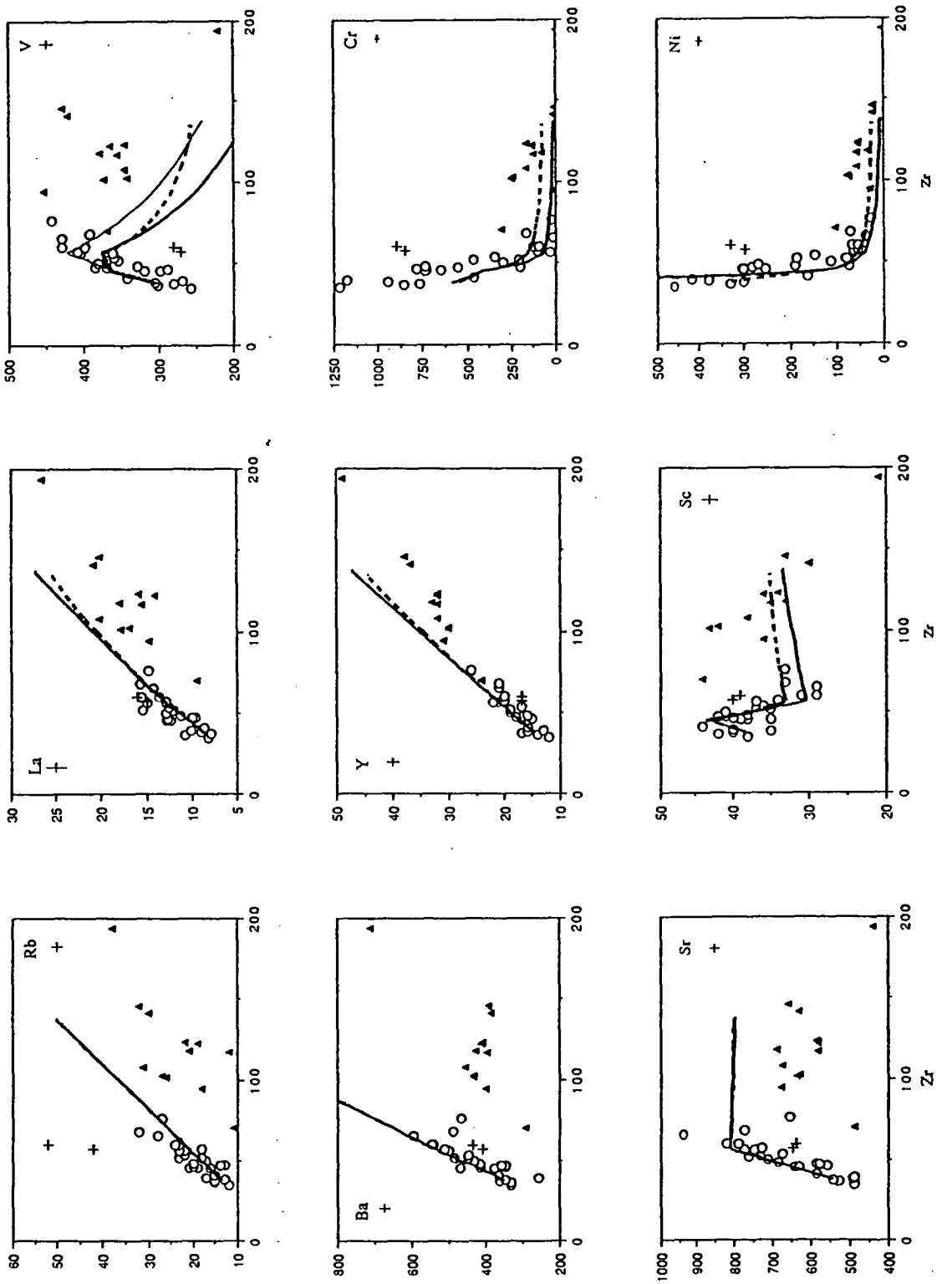

Figure 7.11 Trace element co-variation diagrams for Ambae lavas. Thick solid lines are modelled LTS fractional crystallisation paths, and dashed lines show equilibrium crystallisation paths. Details of the fractionation modelling are given in text. Error bars show analytical precision estimates (2σ) for typical LTS lavas, and the symbols used are as in Fig. 7.1.

Table 7.3
Phenocryst partition coefficients used in trace element fractionation modelling.

	Olivine	Clinopyroxene	Plagioclase	Ti-magnetite
Rb	0	0	0.07	0
Ba	0.001	0.004	0.16	0
Sr	0	0.114	1.8	0
La	0.002	0.064	0.3	0
Ce	0.002	0.097	0.22	0
Nd	0.002	0.194	0.15	0
Yb	0.009	0.269	0.07	0
Y	0.01	0.42	0.1	0
Zr	0	0.142	0	0
Nb	0	0.043	0	0
Sc	0.3	3	0	2
V	0	1.1	0	30
Cr	3	10	0	0
Ni	15	3	0	0

Data sources include Gorton (1974), Fujimaki et al. (1984), and the preferred values listed by Gill (1978). 0 values are used where partition coefficients are poorly constrained and elements are likely to be highly incompatible.

The modelling is progressed initially by olivine removal, constrained to pass through the composition of #68638 at ~13% crystallisation, and continued until the olivine-clinopyroxene cotectic is reached after ~16% crystallisation. Olivine and clinopyroxene fractionation proceeds thereafter in the proportions 1:4 for a further 22% crystallisation, and is then followed by olivine, clinopyroxene, plagioclase, and titanomagnetite fractionation in the modelled proportions 0.15: 0.25: 0.55: 0.05, until the total degree of crystallisation is ~75%. This has been continued beyond the modelled termination of evolution of the LTS lavas (at ~65ppm Zr and 40% crystallisation) in order to assess possible links between the principle lava suites through differentiation processes.

The modelled fractionation paths are observed to closely match the natural variation trends in the LTS lavas (Fig. 7.11). This affirms the control which crystal fractionation processes have on geochemical evolution of the Ambae lavas. It is notable that data scatter occurring beyond analytical error may be explained by mixing across curved fractionation trends (e.g. for Sc, Cr, and Ni) but not where these trends are straight (e.g. for Rb, Sr, Ba, LREE). The trace element modelling clearly shows the HTS or HKS lavas are unrelated to the LTS by differentiation, as the extended fractionation paths do not coincide with the LTS or HTS lava compositions.

7.4 GEOCHEMICAL HETEROGENEITY IN THE AMBAE LAVAS

The existence of distinct parent magma compositions for each of the major lava suites (LTS, HTS, and HKS) is implied by the inability of differentiation processes to account for their geochemical differences. The nature and extent of such heterogeneity can be assessed by examining variability of incompatible trace element ratios. A selection of appropriate element ratios are plotted in Figure 7.12, along with their modelled variation arising from protracted fractional crystallisation (see Figure 7.11). These differentiation paths do not exceed analytical error in many cases, and do not link the separate lava suites, thereby confirming the need for geochemically distinct parent/primary magma compositions for each suite.

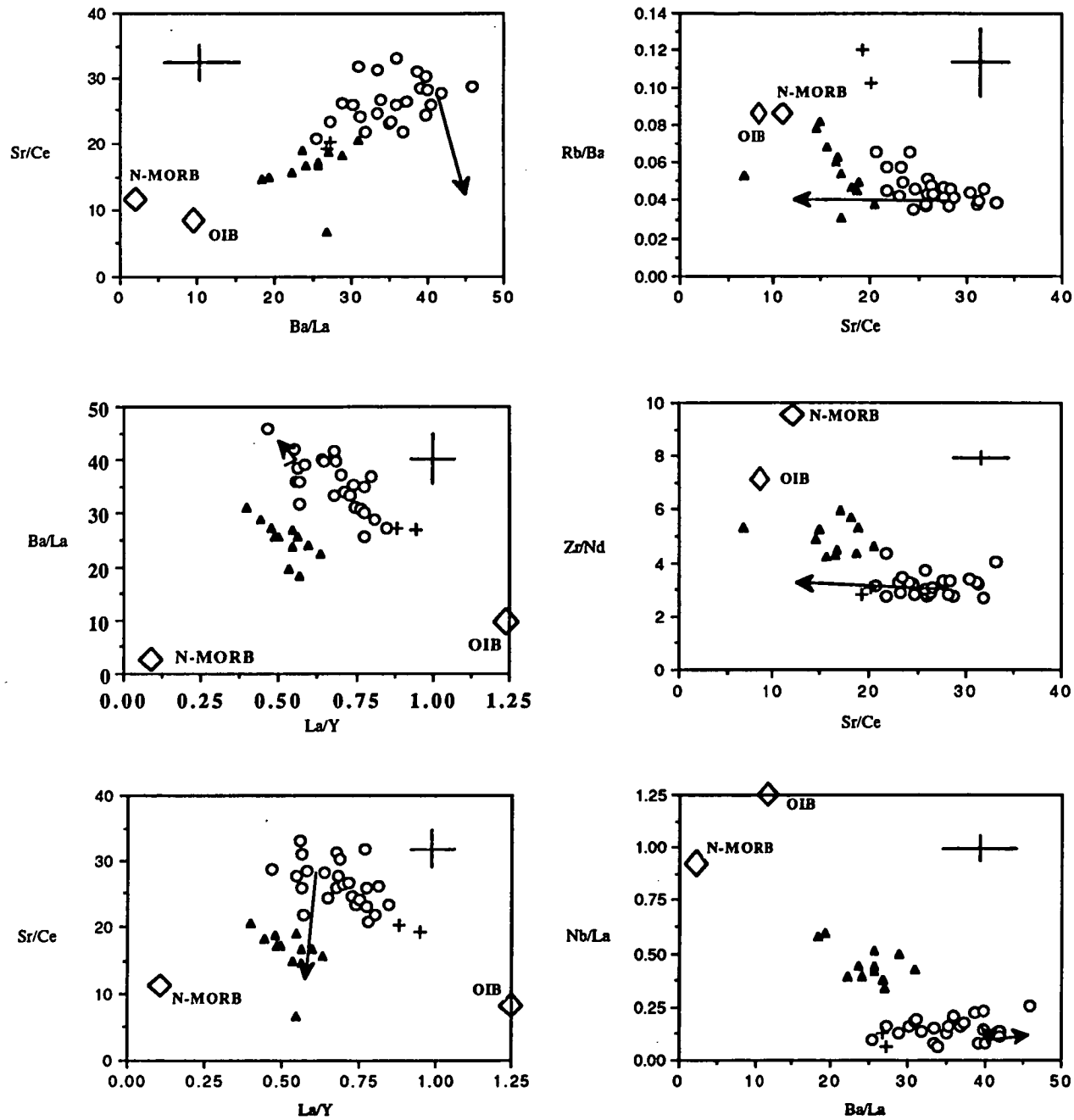

Figure 7.12 Covariation of selected incompatible element ratios in the Ambae lavas. Arrows illustrate the effect of 75% fractional crystallisation of a LTS primary melt estimate, as modelled in Figure 7.11. Symbols for Ambae lava samples are those used in Figure 7.1, and large diamonds are the average N-MORB and OIB compositions compiled by Sun and McDonough, 1988). Error bars show analytical precision estimates (1σ) for typical LTS ratio values.

A surprising revelation of Figure 7.12 is the occurrence of systematic and parallel variation trends within both the LTS and HTS. These trends are also discordant with the magnitude or direction of the fractionation paths, requiring a further need to consider the presence of geochemical heterogeneity within the individual lava suites. It is notable, in the context, that the HKS is consistently located as an extension to the LTS variation trends.

7.4.1 Origin of geochemical heterogeneity

The subduction zone geochemical character of the Ambae lavas is evident in Figure 7.12 as high LILE/LREE and low LREE/HFSE values relative to N-MORB. These subduction zone characteristics are developed most in the LTS lavas, which plot farthest from the oceanic basalt compositions. The HTS lavas exhibit a pattern of geochemical differences relative to oceanic basalts similar to that of the LTS lavas, such that they lie mid-way between the LTS and N-MORB. This relationship provides evidence for a greater contribution to the HTS from a geochemical component which determines the geochemical charatcter of N-MORB. This can be readily equated with the peridotitic source of MORB, which is widely believed to dominate the upper mantle.

The *parallel within suite* geochemical variation trends of the LTS (+HKS) and HTS are characterised by increasing LILE/LREE ratio values correlated with decreasing LREE enrichment (i.e.La/Y values), Rb/Ba values, and possibly also LREE/HFSE values. These trends can be extrapolated to the very high LILE/LREE values, low levels of LREE enrichment, and low Rb/Ba values observed in low-K island arc tholeiites in Vanuatu (Barsdell, 1988; Barsdell and Berry, 1990; Chapter 8) and elsewhere (e.g. Tafahi, Tonga; Ewart and Hawkesworth, 1987), and conversely extrapolated to the low LILE/LREE values, high levels of LREE enrichment, and high Rb/Ba levels which characterise high-K arc volcanics in Vanuatu (Chapter 8) and in other arcs (e.g. Batu Tara, Indonesia; Stolz et al., 1988). It is notable, in regard to intrasuite geochemical heterogeneity, that higher LILE/LREE values in Ambae lavas of otherwise similar bulk composition are associated with lower absolute K abundances (compare #68569 and #68578, and #68613 and #68567 in Table 7.1). These observations suggest the Ambae intrasuite variation trends are short segments of a larger spectrum of systematic geochemical variation occurring within the

Vanuatu Arc, and possibly also on a global scale, between low-K and high-K arc volcanics. This variation can be attributed to the interaction of two distinct components:

(1) an LILE-rich, but LREE and HFSE-poor component, responsible among other characteristics, for high LILE/LREE and low Rb/Ba values, and

(2) an LILE and LREE-rich, but HFSE-poor component, associated with enhanced incompatible element abundance levels (e.g. K), large degrees of LREE enrichment, and relatively low LILE/LREE values.

The interaction of these components within the LTS magmas may account for the data scatter noted previously in Figures 7.7 and 7.11, which is most marked for the LILE.

The origin of subduction zone geochemical characteristics remains unclear, apart from the concensus now developing for the origin of LILE enrichments observed in island arc tholeiites (i.e. component 1), which are believed to result from the introduction of LILE-rich aqueous fluids into their source regions (e.g. Ewart and Hawkesworth, 1987). This proposal coincides with the expected release of, and LILE solubility in, dehydration fluids from the subducting ocean crust (Jakes and Gill, 1970; Tatsumi. et al., 1986). The much larger incompatible element enrichments observed in high-K arc basalts, on the other hand, are attributed to source contributions from either subducted sediments, subcontinental lithosphere, or the geochemically-enriched mantle sources of OIB (e.g. Varne, 1986; Rogers et al., 1987), with the effects of very small degrees of partial melting also needing to be taken into account. A thorough evaluation of these possible origins for high K contents in the Ambae lavas is beyond the scope of this study, particularly in the absence of isotopic data able of discriminate between possible source contaminants.

7.4.2 Mixing Relationships

Two of the three distinctive geochemical components recognised in the Ambae lavas, (1) the high LILE/LREE, low-K component and (2) the LILE- and LREE-rich, high-K component, seem to be closely related, for they interact to produce the parallel intrasuite variation trends in the HTS and LTS (+ HKS). In contrast, the inferred upper mantle peridotite component (i.e. MORB source) is independent of these components, as indicated by its role in separating the subparallel HTS and LTS trends. A puzzling feature of these

relationships is why the HTS lavas should have higher concentrations of incompatible elements than the LTS, yet apparently possess the greatest proportion of incompatible element-poor source material (i.e. upper mantle peridotite). Conceivably, the higher trace element contents in the HTS may simply reflect lower degrees of partial melting than for the LTS. The HFSE and HREE abundances of the HTS lavas, however, are more or less equivalent to N-MORB, and could be used to infer similar degrees of melting to those producing N-MORB (i.e. 10-20%, Klein and Langmuir, 1987; Hofmann, 1988). Doubling or trebling these melting degree estimates to produce the much lower HFSE and HREE abundances in the LTS, makes a rather unlikely explanation for the difference in HFSE and HREE abundance levels between the LTS and HTS.

An more reasonable explanation can be developed if the peridotite source component of the LTS is even more depleted in incompatible elements than the (N-MORB) source protolith inferred for the HTS. In this case, the LTS source protolith would be more susceptible to relative geochemical enrichments by the introduction of LILE and LREE enriching agents. In fact, the existence of highly depleted peridotite sources in island arcs is consistent with the refractory phenocryst chemistry and extremely low abundance levels of many incompatible elements in island arc magmas, particularly IAT and boninites (e.g. Barsdell and Berry, 1990; Chapter 8). In this way, it may be argued that four geochemically distinct components are necessary to account for the geochemical heterogeneity in the Ambae magmas. Two components derive from the introduction of separate LILE and, LILE- and LREE-rich agents into the mantle source, whereas a third appears to arise from variable fertility (refractoriness) of the mantle wedge peridotite.

7.5 IMPLICATIONS FOR ISLAND ARC MAGMAGENESIS

The major result of this study is the demonstrated differentiation of evolved high-alumina basalts from primitive mantle-derived primary magmas. Although the high-alumina basalts are of high-K affinity, the similar evolution of low-K high-alumina basalts and more evolved compositions elsewhere in the Vanuatu Arc (e.g. Barsdell, 1988; Barsdell and

Berry, 1990), show that a spectrum of evolved island arc basalt and andesite compositions can be generated by differentiation of primitive mantle-derived arc magmas.

The formation of crystal-rich mafic magmas in island arcs, and elsewhere, probably reflects a rapid transition from hot primitive melts to cooler, more evolved, crystal-rich magmas in which crystal settling rates are low. Subsequent redistribution of phenocrysts through buoyancy driven crystal-settling and convection, cautions against the interpreting crystal-rich magmas as primary melt analogues.

Finally, the recognition of multiple, distinct, geochemical components in the Ambae lavas testifies to the existence of small length and large chemical scale heterogeneity within the Ambae mantle source. This could be regarded as unusual (?), but introduces the possibility that similar scales of heterogeneity may exist elsewhere.

7.6 CONCLUSIONS

Ambae is dominated by eruptions of primitive basalts, which span a range from high-alumina basalt to phenocryst-rich, picritic compositions. Two major lava suites are identified:

(1) an older plagioclase+clinpyroxene+olivine+Ti-magnetite phryic suite with high relative abundances of HFS and and HREE (the High Ti-Suite), and

(2) a younger olivine + clinopyroxene + Cr-spinel phyric suite (the Low Ti-Suite).

A third minor suite of lavas is subdivided from among the Low-Ti Suite lavas based on its higher LILE abundances. Collectively the Ambae lavas have medium to high K contents and may be regarded as transitional to alkaline in character.

The liquid line of descent in the Low Ti-Suite is consistent with low pressure phase relationships and the fractionation of observed phenocrysts, in the sequence olivine (+Cr-spinel), olivine+clinopyroxene, and then plagioclase+clinopyroxene+olivine+ Ti-magnetite. The mafic phenocryst-rich LTS lavas form a compositional trend between relatively evolved olivine-clinopyroxene saturated melts and a 7:3 mixture of olivine and clinopyroxene phenocrysts. This does not correspond to the liquid line of descent, but is consistent with the fractionation/ accumulation of olivine and clinopyroxene in the modal proportions present in

these lavas. This can be explained by an apparent delay in fractionation, brought about by an initial phase of rapid cooling and crystallisation of primitive magmas with insufficient time for crystal settling. Subsequent re-distribution of phenocrysts produces a compositional spectrum between the relatively melts formed and the phenocrysts crystallised.

The geochemical differences between the LTS, HTS, and HKS lavas cannot be attributed to differentiation processes. Variation in incompatible element ratios requires the existence of multiple geochemically distinct source components. Two components, associated with subduction zone geochemical characteristics in the Ambae lavas, probably derive from the introduction of separate LILE and, LILE- and LREE-rich agents into the mantle source, and a third can be attributed to variable fertility (refractoriness) of the peridotitic mantle source.

CHAPTER 8

The Geochemical Evolution of Primary Magmas in the Vanuatu Arc

8.1 INTRODUCTION

A diverse mix of protoliths and enriching agents have been suggested for the magmatic sources of island arc volcanics (IAV). Geochemical and isotopic data have contributed to a general appreciation of the complexity of subduction zone magma sources, yet have failed to define the processes responsible for the distinctive geochemistry of arc magmas.

The identification of primitive magma compositions promises a fundamental step toward resolving some existing contentions by:

(1) enabling the distinction between peridotite and subducted ocean crust magma sources, and

(2) providing a window into the arc magma source geochemistry, through inversion of partial melting effects.

The Vanuatu (formerly New Hebrides) Arc is ideal for a study of primitive arc magmatism, for it is unusual among modern island arcs in having highly magnesian magmas erupted from many of its active volcanoes (Gorton, 1977; Barsdell, 1980; Barsdell, 1988; Barsdell and Eggins, submt.; Barsdell and Berry, in press; Chapter 7).

8.2 OVERVIEW OF PETROCHEMICAL VARIATION IN THE VANUATU ARC

In excess of 800 whole-rock major element analyses, which are related to the presently active centres of volcanism in the Vanuatu Arc, have been compiled from the literature and unpublished analyses (see Appendix 4 for details). This study is based mainly on a subset of samples (~15%) for which comprehensive analyses are available, including trace and REE elements, from Gorton (1974, 1977), Barsdell (1977, 1988),

Barsdell and Berry (in press), Roca (1978), Dupuy et al. (1982), this study, and unpublished data of Barsdell (pers. comm., 1988). Approximately half of this subset have been analysed by XRF spectrometry at the University of Tasmania (for details see Appendix 1 and 4).

An introduction to geochemical variability in the Vanuatu Arc is provided by K_2O-SiO_2 variation (Fig. 8.1), for which data has been compiled into subregions of the arc. An additional grouping is also made for lavas that have been erupted in anomalous locations, off the alignment of the Central Chain volcanoes (Fig. 8.2). These plots illustrate marked regional geochemical variation encompassing a broad range of K_2O contents, from low to high-K and even shoshonitic compositions. High-K compositions are found to dominate only the d'Entrecasteaux Fracture Zone (DFZ) volcanoes of Gaua, Ambae, and Ambrym, whereas the remainder of the arc is characterised by variation mainly within both the medium and high-K fields defined by Peccerillo and Taylor (1976). Samples falling within low-K compositional fields are generally associated with anomalous sites of volcanism, mostly those occurring in rear-arc regions (i.e. Merelava, Merig, and Futuna), though the lowest K contents of all are found on Mathew and Hunter Islands,which form part of the southernmost extension of the arc.

The majority of analysed samples are tholeiitic (based on the FeO^{tot}/MgO versus SiO_2 discriminant of Miyashiro, 1974; not shown), apart from the K-rich suites erupted on the DFZ volcanoes of Gaua, Ambae, and Ambrym, which can be regarded as transitional to alkaline in terms of their lack of low-Ca groundmass pyroxenes, near or slightly nepheline normative compositions, and relatively high total alkali contents. The only compositions consistent with the calc-alkaline classification are from Futuna, Merig, Mathew, and Hunter Islands, all of which are grouped in this study as anomalous sites of magmatism within the Vanuatu Arc.

One of the most noteworthy features of magmas erupted in the Vanuatu Arc is the dominance of basalts (~70% of analyses), and virtual absence of highly evolved compositions. Andesites and dacites are also relatively uncommon, being erupted mainly in and around the Central Islands where several large submarine calderas are located (Crawford et al., 1988; see Fig. 8.2).

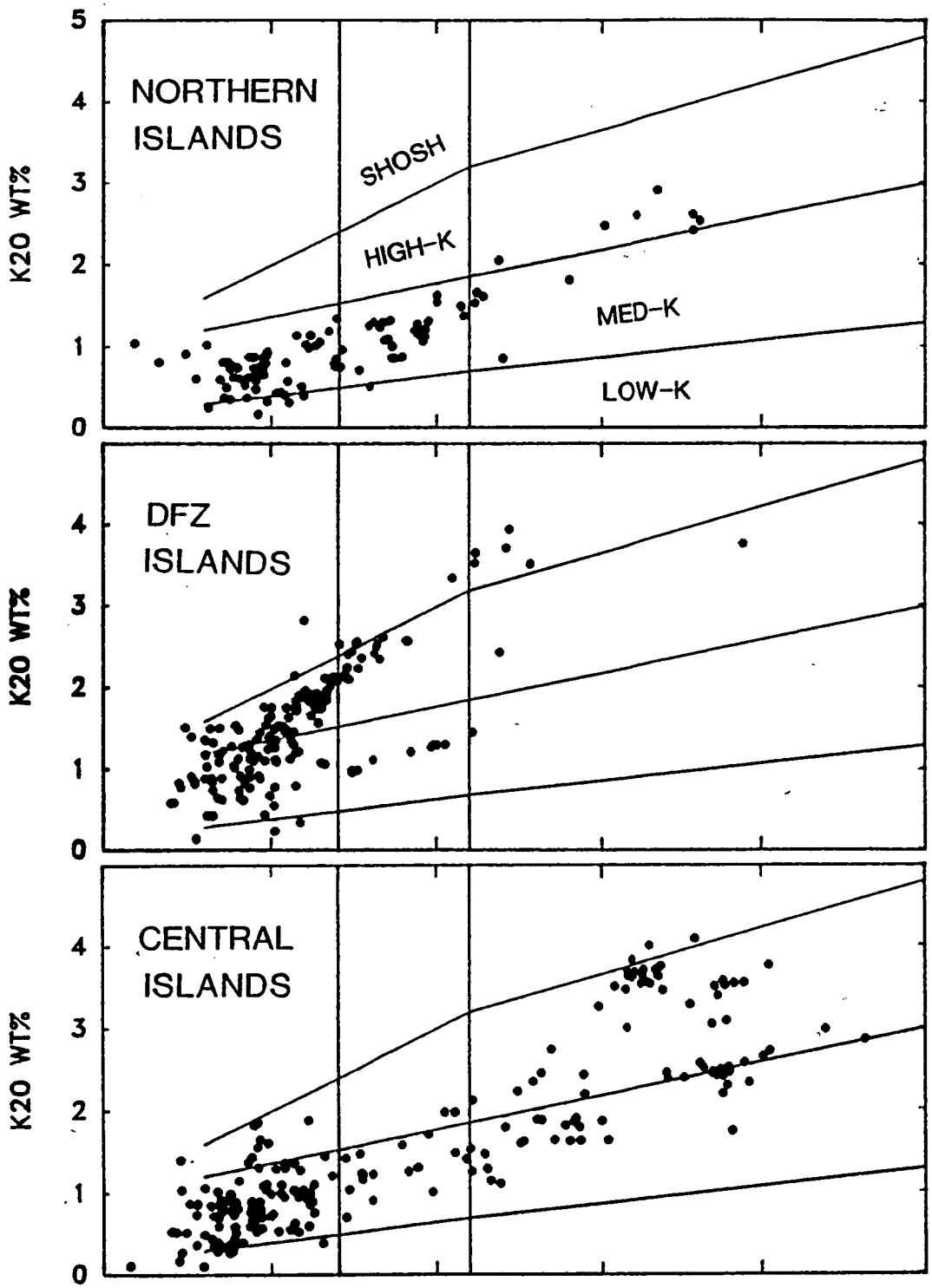
NORTHERN ISLANDS
SHOSH
HIGH-K
MED-K
LOW-K
DFZ ISLANDS
CENTRAL ISLANDS
K2O WT%
0
1
2
3
4
5

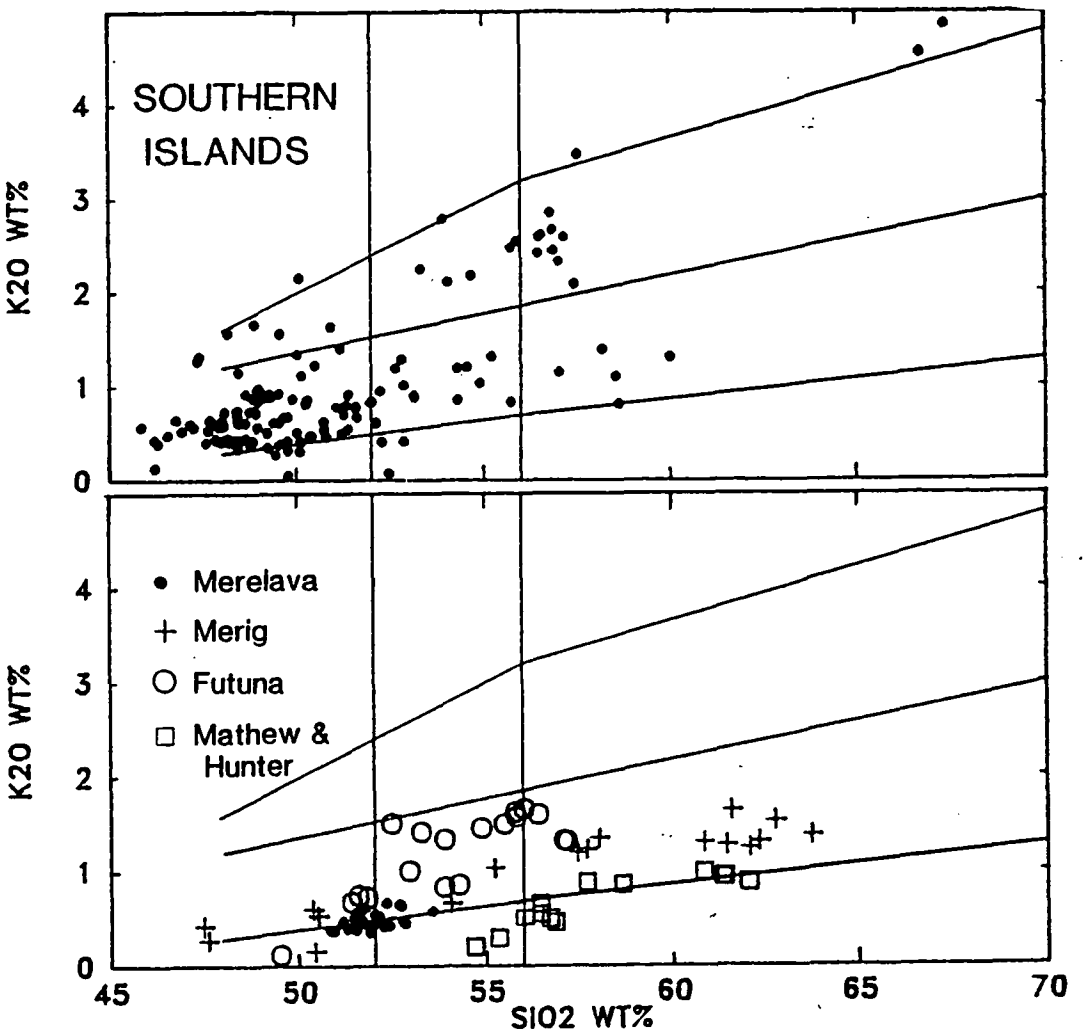

Figure 8.1 K_2O versus SiO_2 covariation diagrams for all analysed Central Chain volcanics, compiled into the principal segments of the Vanuatu Arc. K-group discrimination lines are from Peccerillo and Taylor (1976). Data sources include Ash et al. (1978), Ash et al. (1980), Barsdell (1980, 1988, and unpublished data), Barsdell and Berry (submt.), Barsdell et al. (1982), Carney and MacFarlane (1979), Colley and Ash (1971), Crawford et al. (1988), Dupuy et al. (1982), Gorton (1974, 1977), Maillet et al. (1986), Mallick and Ash (1975), Marcelot et al. (1983), P.J. Stephenson unpublished data, Roca (1978), Warden (1967, 1970), and the author's unpublished data for Ambrym. See Appendix 5 for a complete list of analyses.

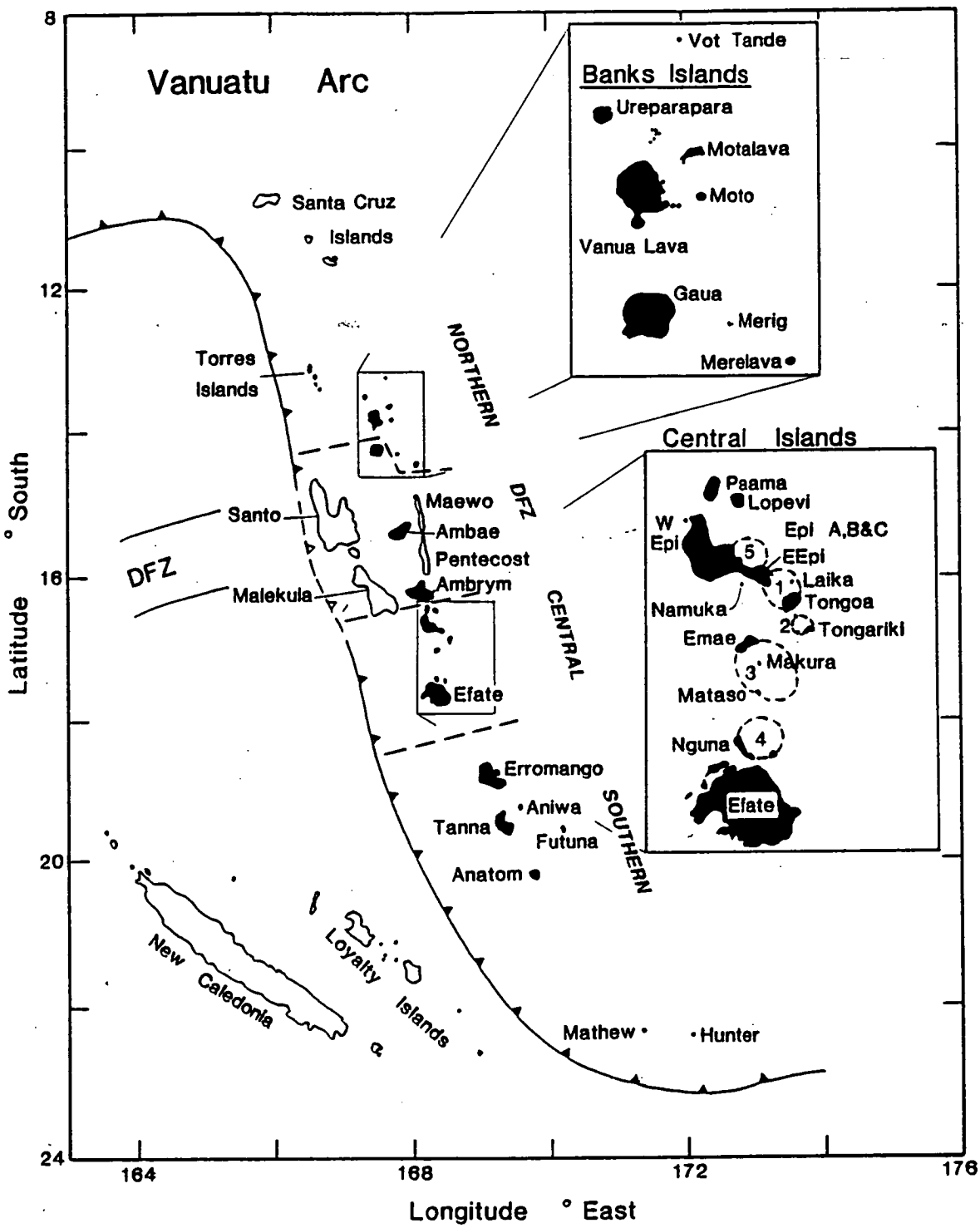

Figure 8.2 A simplified map of the Vanuatu Arc illustrating major tectonic elements, island locations, major caldera structures in the Central Islands, and the subdivision of Central Chain volcanics (marked by dashed lines) into four principal arc segments.

The geochemical evolution of Vanuatu basaltic suites, which have been studied in detail, are found to follow coherent geochemical trends consistent with the accumulation and/or fractionation of observed phenocryst phase assemblages. In many cases, these suites are dominated by crystallisation of magnesian olivine and clinopyroxene (Barsdell, 1988; Barsdell and Berry, in press; Chapter 6). A similar sequence of crystallisation is documented throughout most of the arc, following the order (see Table 5.1 in Chapter 5),

olivine+Cr-spinel+clinopyroxene --->
clinopyroxene+olivine+magnetite --->
clinopyroxene+plagioclase+magnetite+olivine+orthopyroxene+
hornblende

Significant differences in major and trace element geochemical evolution trends, which occur between the magma suites of the arc, can be ascribed to differing proportions of the fractionating phenocryst species. For example, bulk geochemical variation in the transitional-alkaline suites of Gaua and Ambae are approximated by the removal or the accumulation of olivine and clinopyroxene in the ratio 0.7:0.3 (Barsdell and Berry, in press; Chapter 7), whereas the incompatible element-poor low-K tholeiitic suites on Western Epi and Merelava follow clinopyroxene-dominated trends (i.e. olivine:clinopyroxene = 0.3:0.7; Barsdell, 1988; Barsdell and Berry, in press).

Close examination of the liquid line of descent in the Ambae lavas, however, reveals a complex geochemical differentiation process involving considerable variation in the proportions of fractionating phases. The tight and linear whole-rock geochemical trends, which extend to very high MgO contents in this case, do not provide an accurate reflection of the liquid line of descent. Rather, they reflect the accumulation of phenocryst phases in evolved melt compositions in proportions representative of an extended interval of crystallisation, that is dominated initally by olivine and later by clinopyroxene fractionation. This example provides a clear demonstration of the need for caution when using crystal-rich whole rocks as analogues for melt compositions.

Detailed investigations of mineral chemistry are now complete for a large number of Vanuatu volcanic suites (Gaua; Barsdell, 1980: Merelava; Barsdell, 1988: Western Epi; Barsdell and Berry, in press: Anatom, Tanna, and Futuna; Barsdell, pers. comm., 1989: Ambae, Chapter 6: Ambrym, author's unpublished data). In each case, very primitive phenocryst populations dominated by highly magnesian olivine and clinopyroxene, and additional accessory Cr-rich spinel, have been identified (Table 8.1). The magnesian nature of the melts necessary to crystallise the most primitive phenocrysts can be gauged from application of the well established Fe/Mg partitioning relationship between olivine and basaltic liquids (i.e. $K_D^{Fe/Mg_{Ol-Liq}} = 0.30$; Roeder and Emslie, 1970; Ulmer, 1989). In this way, a majority of magmatic suites can be related to the crystallisation of parent melts with Mg# between 75 and 82 (see Table 8.1).

8.4 VANUATU ARC PARENT MAGMA GEOCHEMISTRY

Estimates for the composition of parent melts of individual Vanuatu volcanic suites may be obtained by backcalculating the effects of fractional crystallisation until compositions in equilibrium with the most primitive phenocrysts are attained, or alternatively, by selecting equally primitive whole-rock compositions. A fractionation-correction-procedure is employed here, entailing addition of multiple small increments (1%) of equilibrium olivine to primitive whole-rock compositions, observing at each step equilibrium between olivine and the adjusted bulk composition, by constraining Fe^{3+}/Fe^{2+} in the bulk composition using the method of Kilinc et al. (1983). This is enabled by approximating the liquidus temperature at each step using the method of Ramsay et al. (1984; see also Chapter 7 for details). In order to apply this technique it is necessary to restrict starting compositions to samples with Mg# >65, as these fall within the established compositional range where liquidus olivine is first joined by clinopyroxene, the second major liquidus phase to crystallise in Vanuatu magma suites (see Table 8.1; Barsdell, 1988; Barsdell and Berry, in press; and Chapter 6). This fractionation-correction-procedure also enables calculation of incompatible element abundances for the parent melts, by correcting trace elements that are highly incompatible in olivine, for dilution by the total mass of olivine added. Over thirty suitable samples, for which a complete range of trace

Table 8.1 A compilation of the most primtive olivine, clinopyroxene, plagioclase and Cr-spinel phenocryst compositions occurring in Vanuatu Arc volcanic suites.

Volcanic Suite	Olivine Mg#	Cpx MG#	Cr-spinel Cr#	Plag Ca#	Melt Mg#
Merelava	91.7	94.0	81	91	77.8
Gaua	93.3	90.7	79	?	80.7
Ambae LTS	93.4	92.4	83	90	80.7
Ambae HTS	90.9	91.5	70	95	75.0
Ambrym	93.7	93.5	88	?	81.7
Western Epi	92.1	94.4	86	95	79.2
Epi & Karua (submarine)	86	86	--	95	64.8
Erromango	88.4	89.7	--	95	70
Tanna	92.5	94.8	87.8	?	80.7
Futuna	90.9	81	61.8	88	75.0
Anatom	93.4	93.6	79	?	80.9
Mathew & Hunter	92.7	88.2	--	61	79.2

$Mg^{\#} = 100Mg/(Mg+Fe^{2+})$, $MG^{\#} = 100Mg/(Mg+Fe^{tot})$, $Cr^{\#} = 100Cr/(Cr+Al)$, $Ca^{\#} = 100Ca/(Ca+Na)$.
Data sources: Merelava (Barsdell, 1988); Western Epi (Barsdell and Berry, in press): Gaua, Tanna, Futuna, and Anatom (Barsdell, pers. comm., 1988); Erromango (Marcelot et al., 1983); Mathew and Hunter (Maillet et al., 1986); submarine Epi and Karua (Crawford et al., 1988); and Ambrym (author's unpublished data). Melt $Mg^{\#}$ is based on Fe/Mg partitioning relationships between either olivine or clinopyroxene and basaltic liquids (Roeder and Emslie, 1970; Barsdell, 1988).

elements are available, were processed by this method (see Appendix 5). In each case they have been equilibrated with olivine of $Mg^{\#}$ = 93, a singular value chosen as a best estimate for the most magnesian olivine phenocrysts occurring in the majority of suites (see Table 8.1). The only exceptions to this methodology have been made for Futuna and Ambae HTS compositions,which have been similarly corrected for fractionation but only until in equilibrium with olivine of $Mg^{\#}$ = 91, an approximation of the most Mg-rich olivine phenocrysts found in these suites (Chapter 6; Barsdell, pers. comm., 1989).

Representative examples of fractionation-corrected parental compositions for each of the major volcanic suites in the Vanuatu Arc are listed in Table 8.2. The extremely magnesian nature of these parent compositions, which is necessary to crystallise the very forsteritic olivine phenocrysts present in the Vanuatu lava suites, constitute compelling evidence for their near-primary or primary derivation from peridotite sources. This feature of the Vanuatu parents provides an intriguing comparison with those of primitive MORB and OIB, which crystallise olivine usually less magnesian than $Mg^{\#}$ = 91 (e.g. Chapter 4, le Roex et al., 1981; van Heerden and le Roex, 1988). In terms of major elements, the Vanuatu parents are similar to picritic Hawaiian parent compositions (see comparison in Table 8.2), except for the minor components TiO_2 and K_2O, which are considerably lower and higher respectively than in their Hawaiian counterparts. In contrast to primitive MORB, on the other hand, the Vanuatu parents are depleted in Al_2O_3 and TiO_2, and much richer in MgO, K_2O, and P_2O_5.

8.4.1 Pressure and Temperature of Primary Melt Generation

The low water contents of Vanuatu Arc magmas, as evidenced by the virtual absence of amphibole in all but a few evolved andesites/dacites found on Merig, Futuna, and Anatom (see Chapter 6), allow comparison of the Vanuatu parent (primary?) compositions with experimental volatile-free peridotite melting studies to ascertain their pressure and temperature of origin, and residual source mineralogy. Projection of representative parent compositions from each of the major Vanuatu volcanic suites onto the cotectic grids for melting of Tinaquillo lherzolite and MORB pyrolite (after Falloon et al., 1988), indicates equilibrium with lherzolite residues in the majority of cases at pressures between 2.5 and ~4GPa (Fig. 8.3). It is noted, however, that some Merelava and

Table 8.2 Selected fractionation-corrected Vanuatu Arc parent magma compositions.

	Merelava	Eastern Epi	Western Epi	Epi (submarine)	Tongoa	Anatom	Gaua	Ambae LTS	Ambrym	Ambae HKS	Futuna	Ambae HTS	Hawaii[b]
number	31541	670	71065	4DI-E	698	AYC55	G20	68638	1567	68567	FMAC18	68578	KILIKI
SiO2	49.03	46.02	47.33	47.67	48.48	48.41	46.34	47.71	47.53	47.02	51.39	47.13	48.18
TiO2	0.52	0.40	0.38	0.40	0.53	0.46	0.66	0.53	0.52	0.54	0.98	0.92	2.05
Al2O3	11.11	12.35	11.75	12.76	10.49	10.45	10.19	10.74	11.08	10.19	14.57	11.93	10.19
Fe2O3	1.71	1.82	1.75	1.66	1.84	1.82	2.01	2.18	2.17	2.20	1.78	2.43	2.51
FeO	7.62	8.48	7.78	7.62	8.30	8.06	8.44	7.84	7.82	7.91	6.39	8.76	9.03
MnO	0.21	0.19	0.17	0.17	0.19	0.17	0.25	0.17	0.19	0.19	0.15	0.21	0.16
MgO	17.34	19.06	17.72	17.27	18.76	18.22	18.99	18.27	18.16	18.50	10.46	15.44	16.05
CaO	10.48	9.91	11.42	10.53	9.02	10.25	10.57	9.84	9.89	10.41	10.87	10.63	9.39
Na2O	1.54	1.33	1.31	1.26	1.53	1.32	1.83	1.77	1.64	1.29	2.52	1.73	1.83
K2O	0.31	0.28	0.29	0.55	0.65	0.66	0.54	0.81	0.85	1.42	0.69	0.65	0.43
P2O5	0.10	0.07	0.04	0.06	0.15	0.13	0.13	0.14	0.14	0.32	0.21	0.17	0.20
L.O.I.													
H2O-													
rest													
total	99.97	99.91	99.94	99.95	99.94	99.95	99.95	100.00	99.99	99.99	100.01	100.00	100.02
Pb													
Rb	4.40	4.70	4.80	10.80	10.30	7.40	18.00	12.10	15.10	48.60	14.59	9.42	
Ba	100.00	90.00	136.00	112.00	105.00	99.30	174.00	295.00	199.00	405.00	109.95	252.60	
Sr	195.00	284.00	273.00	331.00	300.00	319.00	451.00	472.00	398.00	596.00	433.62	417.00	
La	1.52	2.08	2.57	3.88	4.77	5.02	6.38	7.06	7.86	15.05	10.69	8.13	
Ce	4.01	5.28	6.52	7.92	11.71	11.32	14.80	17.04		31.03	24.35	20.40	
Pr	0.66	0.70	0.80	1.09		1.70	1.98		2.44	4.15	3.05		
Nd	3.55	3.64	4.87	5.31	7.49	8.37	9.64	10.42	10.93	20.10	14.59	13.03	
Sm	1.21	0.98	1.19	1.43	1.81	2.24	2.46	2.47	2.18	4.24	2.00	3.33	
Eu	0.41	0.39	0.40	0.49	0.60	0.88	0.77	0.87	0.69	1.37	1.44	1.10	
Gd	1.47	1.24	1.49	1.57		2.47	2.09	2.46	2.18	3.89	3.87	3.56	
Tb	0.27	0.21			0.32		0.35		0.34				
Dy	1.70	1.41	1.78	1.72	1.96	2.28	1.93	2.40	2.02	3.46	3.59	3.81	
Ho													
Er	1.15	0.91	0.97	0.83		1.44	1.22	1.57	1.09	1.97	2.13	2.21	
Yb	1.14	0.80	0.90	0.85	1.21	1.16	1.12	1.39	1.04	1.79	1.87	2.02	
Lu													
Y	14.50	10.80	10.50	9.20	13.10	13.90	11.80	12.90	12.50	15.90	20.55	20.55	
Th		0.19			0.84				1.14				
U		0.08			0.28				0.29				
Zr	24.40	14.30	15.30	24.50	34.50	31.10	43.10	33.00	37.30	56.10	99.67	60.05	
Hf	0.71	0.33					1.06		1.13				
Sn													
Nb	0.50	0.40	0.80	0.80	0.84		0.90	0.80	1.20	1.90	5.40	3.40	
Ol. added[a]	23.24	33.50	19.61	29.53	33.50	24.50	12.68	24.50	20.81	7.21		17.30	

a. Ol-added is the percentage mass of olivine added to generate the bulk compositions listed.

b. Kilauea Iki parent melt estimate (Chapter 2).

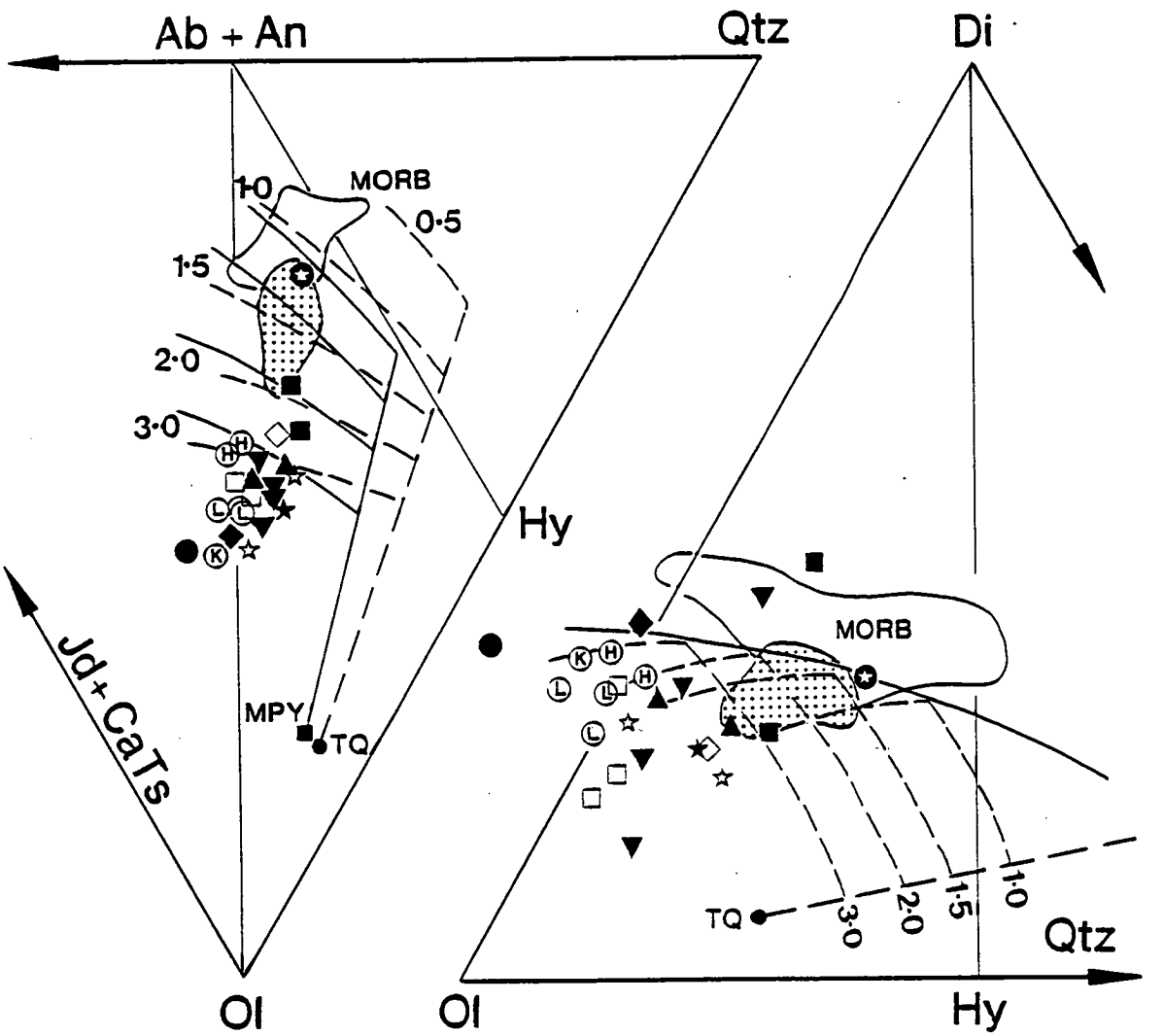

Figure 8.3 Selected Vanuatu Arc parent compositions plotted on Ol-Jd+CaTs-Qtz and Ol-Di-Qtz molecular normative projections following the methods of Green (1970) and Falloon and Green (1988). Dashed lines are cotectic grids for the melting of Tinaquillo Lherzolite (TQ), and solid lines are grids for the melting of MORB pyrolite (MPY), after Falloon and Green (1988) and Falloon et al. (1988). Numerals indicate the cotectic pressures in GPa. Plotted parent compositions include Western Epi (inverted triangles), Eastern Epi (unfilled squares), Ambrym (filled diamonds), Ambae (circled upper case letters, with H, K, and L indicating HTS, HKS, and LTS parents respectively), Anatom (filled triangles), Tanna (filled 5-point star), Merelava (filled square), Gaua (filled circle), Tongoa (5-point stars), and Futuna (circled star). Shown for comparison are the fields for primitive MORB glass compositions (after Falloon and Green, 1988), and the North Fiji Basin parent melt estimates (stippled).

Western Epi parent melts lie outside the field of melt compositions capable of being generated from Tinaquillo or MORB pyrolite-like peridotite. This observation has prompted Barsdell and Berry (1989) to propose that Merelava and Western Epi magmas result, instead, from melting of wehrlitic source mineralogies. These authors favour a model whereby melting of lower crustal cumulates occurs in response to ponding of hot, picritic, Ambae-like parent magmas at the crust-mantle interface. The Merelava and Western Epi primary magmas, however, may be consistent with a derivation by lherzolite melting if they have evolved from more olivine-rich compositions. This requires either differentiation from even more primitive compositions than current parent estimates calculated here, or that the assembled parent compositions (see Table 8.2) contain an excess component of accumulated clinopyroxene. The latter alternative is favoured given the nature of compositional variation resulting from phenocryst accumulation in the Ambae lavas (Chapter 7), and noting that the lava composition on which the Western Epi and Merelava parent estimates are based are very clinopyroxene phenocryst-rich (Barsdell, 1988; Barsdell and Berry, in press). In short, all Vanuatu primary magmas may be consistent with a derivation by partial melting of peridotite.

8.4.2 Incompatible Element Geochemistry of Vanuatu Arc Parent Magmas

The incompatible minor and trace element geochemical characteristics of the Vanuatu parent magmas is summarised in a series of multi-element diagrams in Figure 8.4. Again, samples are compiled into the main segments of the arc (cf. Figs. 8.1 and 8.2), along with an additional grouping of distinctive compositions from Futuna and the Ambae HTS, with which Merelava samples (the only Northern Islands parent melt compositions calculated) have been plotted for convenience.

8.5 A GEOCHEMICAL COMPARISON WITH N-MORB

Advocates of peridotite melting origins for IAB have repeatedly invoked depleted source compositions, in particular a MORB source, to account for geochemical and isotopic similarities existing between island arc volcanics (IAV) and MORB (e.g. Perfit et al., 1980). This proposal finds general support from geodynamic models of mantle flow within the mantle wedge, which predict entrainment of asthenosphere from the shallow

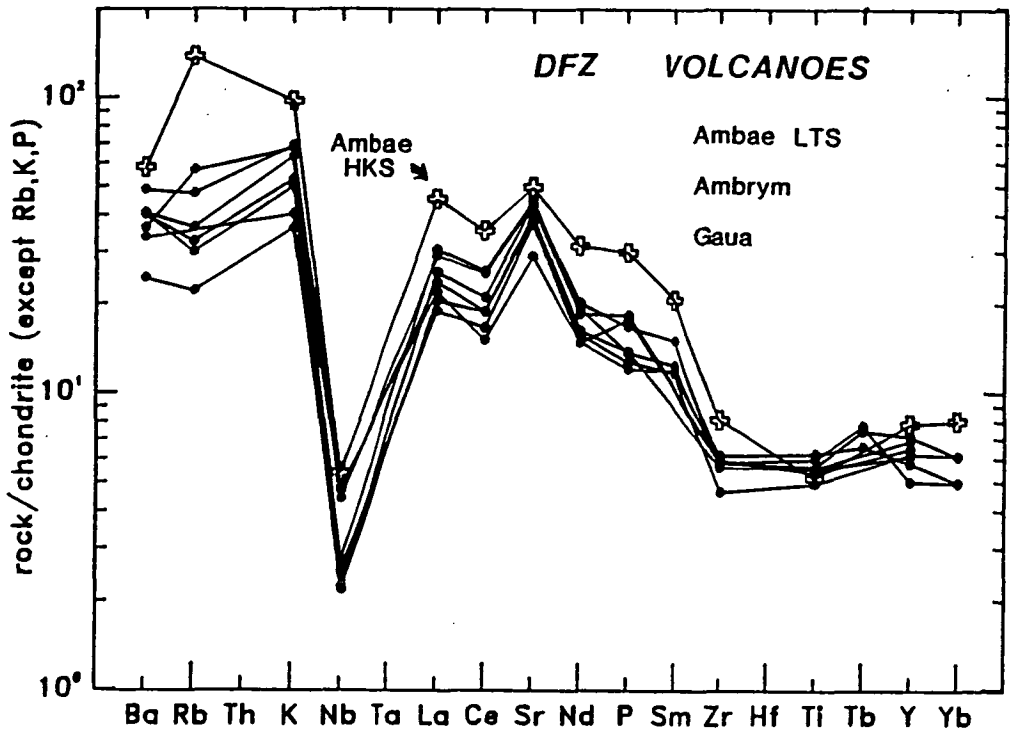
DFZ VOLCANOES
Ambae HKS
Ambae LTS
Ambrym
Gaua
rock/chondrite (except Rb,K,P)
10²
10¹
10⁰
Ba Rb Th K Nb Ta La Ce Sr Nd P Sm Zr Hf Ti Tb Y Yb

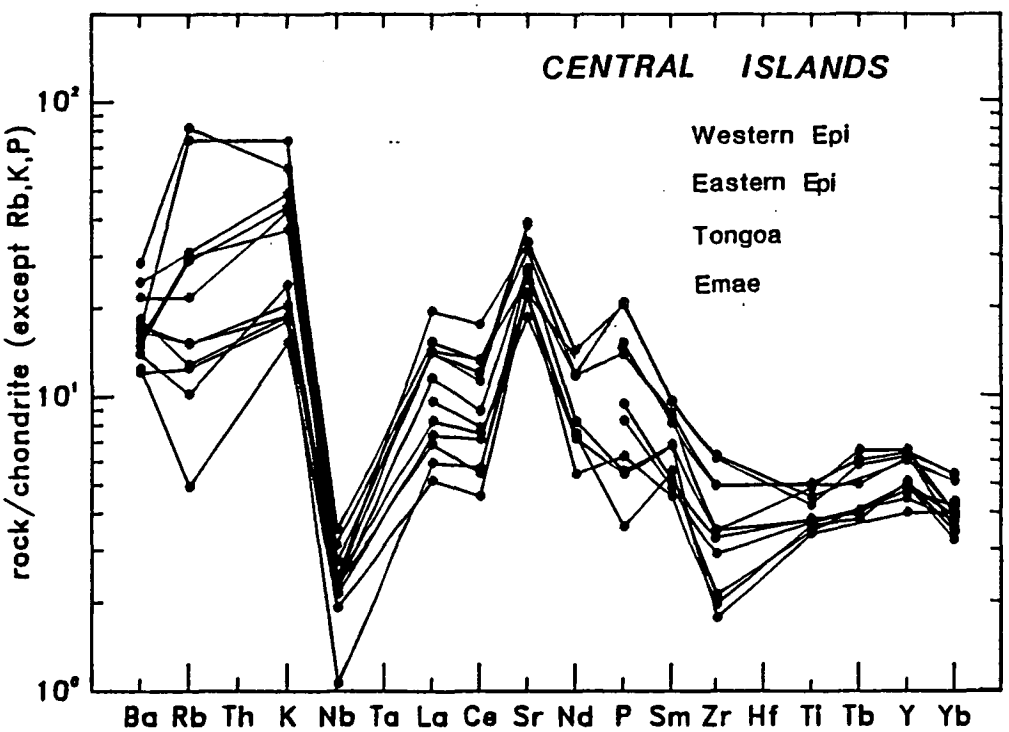
CENTRAL ISLANDS
Western Epi
Eastern Epi
Tongoa
Emae
rock/chondrite (except Rb,K,P)
10²
10¹
10⁰
Ba Rb Th K Nb Ta La Ce Sr Nd P Sm Zr Hf Ti Tb Y Yb

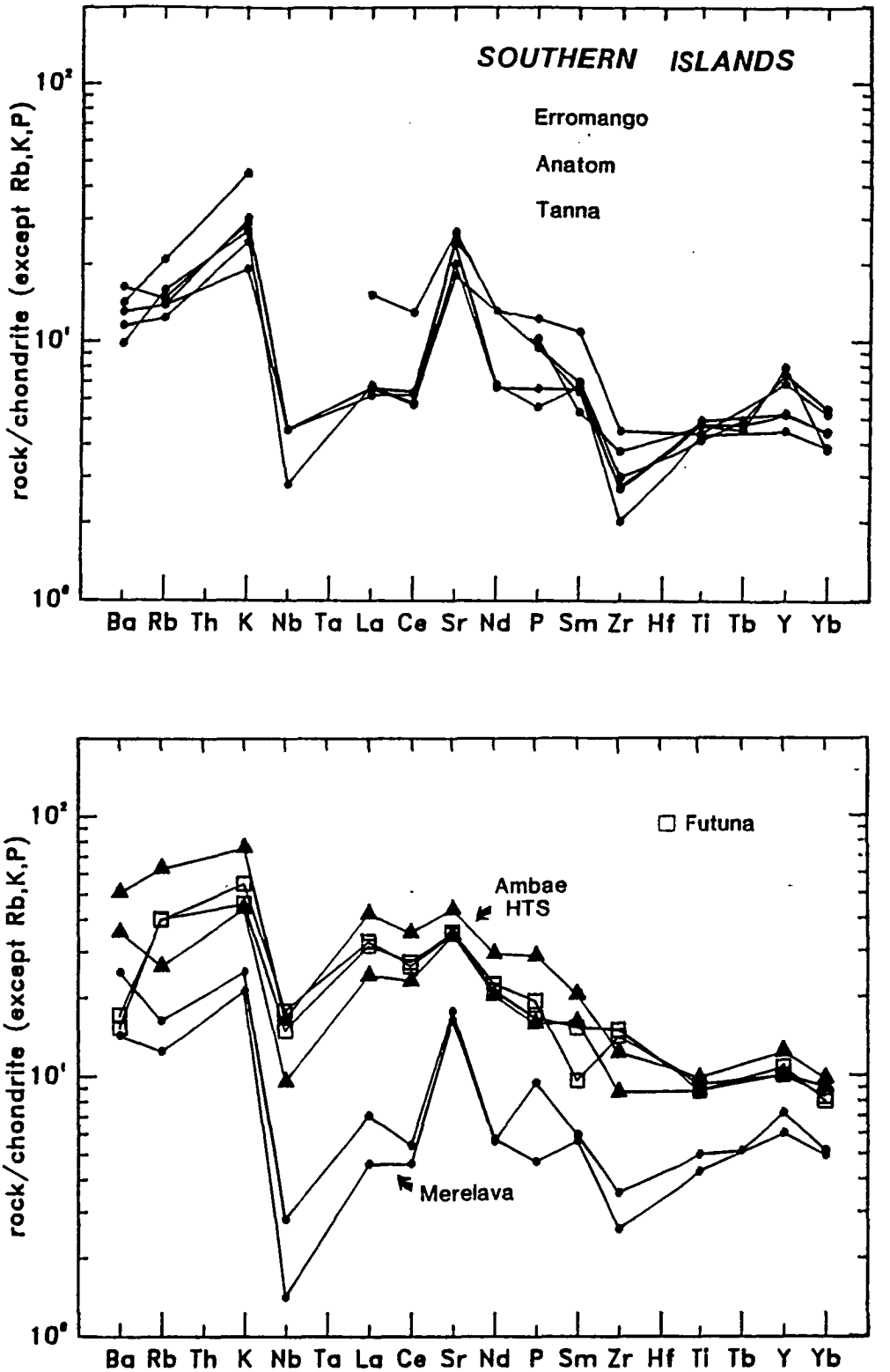

Figure 8.4 Multi-element diagrams for Vanuatu Arc parent magma compositions, compiled into the principal arc segments (see Figure 8.2). An additional grouping is made for the geochemically anomalous Futuna and Ambae HTS parent compositions, with which the Merelava parent estimates (the only Northern Islands parent compositions estimated) are plotted for convenience. Normalising values are those of Thompson (1982).

back-arc regions to occur due to the subducting slab-induced mantle counterflow. This material should be representative of the shallow convecting mantle behind the arc, which in the Vanuatu region is confirmed to be MORB source peridotite by the eruption of N-MORB type basalts in the North Fiji Basin (Price et al., submt.; Boespflug et al., 1989).

A comparison of the Vanuatu parents with magma compositions normally resulting from melting of N-MORB sources is enabled by normalisation to N-MORB abundance values (Fig. 8.5). This reveals some prominent compositional differences between the Vanuatu parents and N-MORB, including:

(1) much greater LILE abundances in the arc lavas;

(2) LRE elements varying markedly between values considerably below and above those of N-MORB, and

(3) HFSE and HREE abundances being consistently well below those of N-MORB, at levels between 0.2 and 0.5x N-MORB.

The only exceptions to these observations occur for the Ambae HTS and Futuna parents which have HREE and HFSE abundance levels more closely matching N-MORB compositions. A first conclusion might be that the peridotite source for Vanuatu Arc basalts is more refractory (depleted) than N-MORB source in HREE and HFSE.

If an N-MORB source is the protolith to Vanuatu Arc volcanism, then the high LIL and LRE element abundances need to be accounted for either by source enrichment processes, or degrees of melting considerably less than those generating N-MORB. The lower HREE and HFSE abundances, however, require either:

(1) residual phases capable of retaining the HREE and HFSE in the solid residue, and in some cases also the LREE (e.g. Merelava, Western Epi), or

(2) exceptionally large degrees of partial melting, over and above the 10 to 20% melting believed to generate N-MORB (Klein and Langmuir, 1987; Hofmann, 1988).

8.5.1 Residual Phases?

The possibility that residual titanates are responsible for the low abundances of HFSE and the negative abundance anomalies of these elements in island arc volcanics has received considerable attention recently (e.g. Morris and Hart, 1983, 1986; Perfit and Kay, 1986; Varne, 1985). Experimental studies by Green and Pearson (1987) and Ryerson and

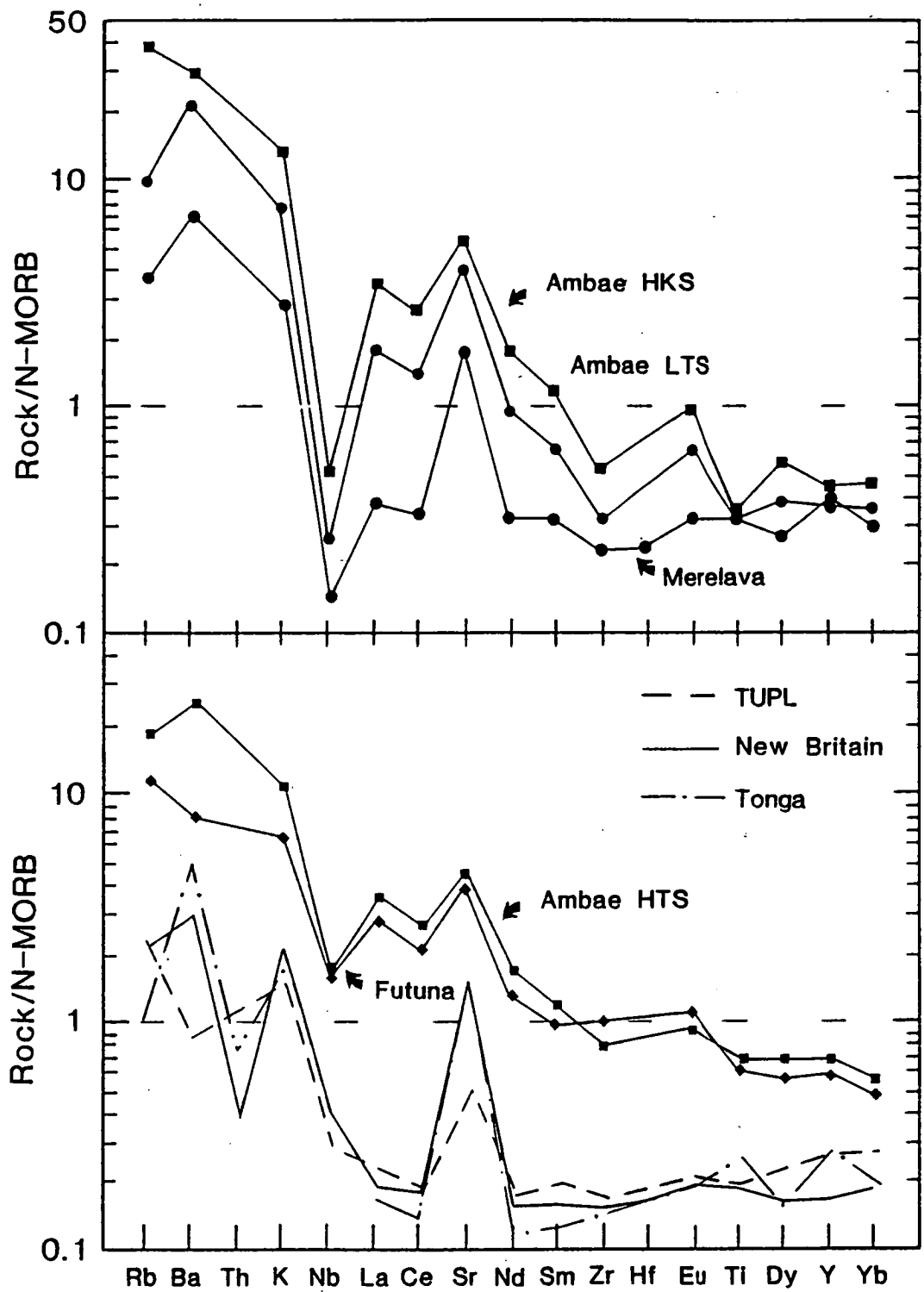

Figure 8.5 N-MORB-normalised multi-element diagrams for selected parent compositions representative of the compositional range occurring in the Vanuatu Arc. For comparison are shown primitive island arc tholeiites from Manam Island (Johnson et al., 1985) and Tonga (Ewart and Hawkesworth, 1987), and also a Troodos Upper Pillow Lava composition from Cameron (1985). Note the low abundances levels of HREE and HFSE relative to N-MORB, and the similarity between incompatible element-poor Vanuatu Arc parent compositions and the examples of primitive island arc tholeiites. Normalising values are the N-MORB values of Hofmann (1988).

Watson (1987) show, however, that low-Ti basalts of the type found in island arcs are unlikely to be saturated with titanate phases in their source regions. These studies indicate that the stabilisation of titanate phases is promoted by high pressure and low temperature conditions, and also by SiO_2-rich melt compositions. In this light, both groups of authors have suggested that relative HFSE depletion in arc magmas is a source feature, resulting from LILE and LREE enrichment by melt and/or fluid phases generated under high P and low T conditions in the presence of residual titanates, possibly within the subducting slab. If, contrary to these experimental findings, titanate phases do withold HFSE in the peridotite residues of the Vanuatu magmas, then an explanation for an equivalent level of depletion of HREE is also needed. Garnet is an obvious phase capable of preferentially retaining the HREE elements, particularly given the evidence for high pressure generation of Vanuatu primary magmas (Fig. 8.3). In view of the arguments against residual titanate phases (see also Arculus and Powell, 1986), however, this hypothesis deserves to be treated cautiously.

8.5.2 Large Degrees of Melting ?

The large degree of melting option is perhaps even more difficult to rationalise, as between 20 and 100% melting of an N-MORB source compositions is needed to produce the range of HFSE and HREE abundances in the Vanuatu parent compositions. The probable origin of Vanuatu primary melts from lherzolitic residues is likely to limit the maximum degree of melting to between 25 and 35% melting, the range in which clinopyroxene ceases to be a residual phase during melting of peridotite bulk compositions (e.g. Falloon and Green, 1988; McKenzie and Bickle, 1988). The role of water in enhancing melting in arc source regions is well established, however, the relatively low water contents present in primitive arc magmas (generally <1 to 3% H_2O;e.g. Tatsumi et al., 1986; Gill, 1981), as is confirmed for the Vanuatu Arc by the rareity of crystallising hydrous phases, argues against this method of producing the extreme degrees of melting required.

8.5.3 The Option of a Geochemically Highly Depleted Source ?

The simple alternative to both possibilities explored above, is for the Vanuatu Arc source to be depleted in HFSE and HREE relative to the source of N-MORB. The melting

products of sources which have previously lost a melt fraction may be called second-stage melts. In such second-stage melts incompatible element concentrations are greatly reduced compared to concentrations in the prior melting event i.e.

$$C_{i_2} = C_{i_1}/[1+f_2(D^{-1}-1)]^{-1} \quad (8.1)$$

where f_2 = degree of partial melting in second stage

D = bulk partition coefficient for element i

C_{i_1} and C_{i_2} = abundances of element i in initial and second stage melts

For highly incompatible elements, C_{i_2}/C_{i_1} will rapidly approach zero as f_2 increases, demonstrating the effectiveness of this means of depleting incompatible element abundances. It may be shown that ~10 to 20% melting of a source previously depleted by MORB extraction is necessary to attain the low abundances of the moderately incompatible HREE and HFSE observed in the Vanuatu parents (Fig. 8.6). Compelling evidence in support of very refractory (geochemically-depleted) source compositions comes from the highly magnesian olivine and clinopyroxene phenocrysts, and high $Cr^{\#}$ spinels, present in the Vanuatu lavas. These phenocryst compositions (Table 8.1) are amongst the most extreme known, and it is of particular note, that the olivine and spinel compositions overlap with those occurring in boninitic magmas, which are now well established as originating from very refractory mantle sources (Crawford et al., 1989).

8.6 GEOCHEMICAL VARIATION IN THE VANUATU PARENT MAGMAS

A wide range of incompatible element abundances occurs within the Vanuatu parent compositions, although there is little relative variation away from a typical pattern of arc geochemical characteristics, which include strong depletion of HFSE and enrichment of LILE relative to similarly incompatible LREE (Fig. 8.4). The range of element abundances within the Vanuatu parents encompasses large increases of most highly incompatible elements (e.g. LREE ~6-8 fold, K ~8 fold, Rb ~12 fold, and Ba ~6 fold) and lesser variation of the moderately incompatible elements (e.g. Ti-Yb ~2-3 fold). Considerable variability exists within each of the arc segments, with the exception of the dominant lava suites erupted from the DFZ volcanoes, which are virtually indistinguishable (Fig. 8.4). Among the trace element variation patterns observed, the

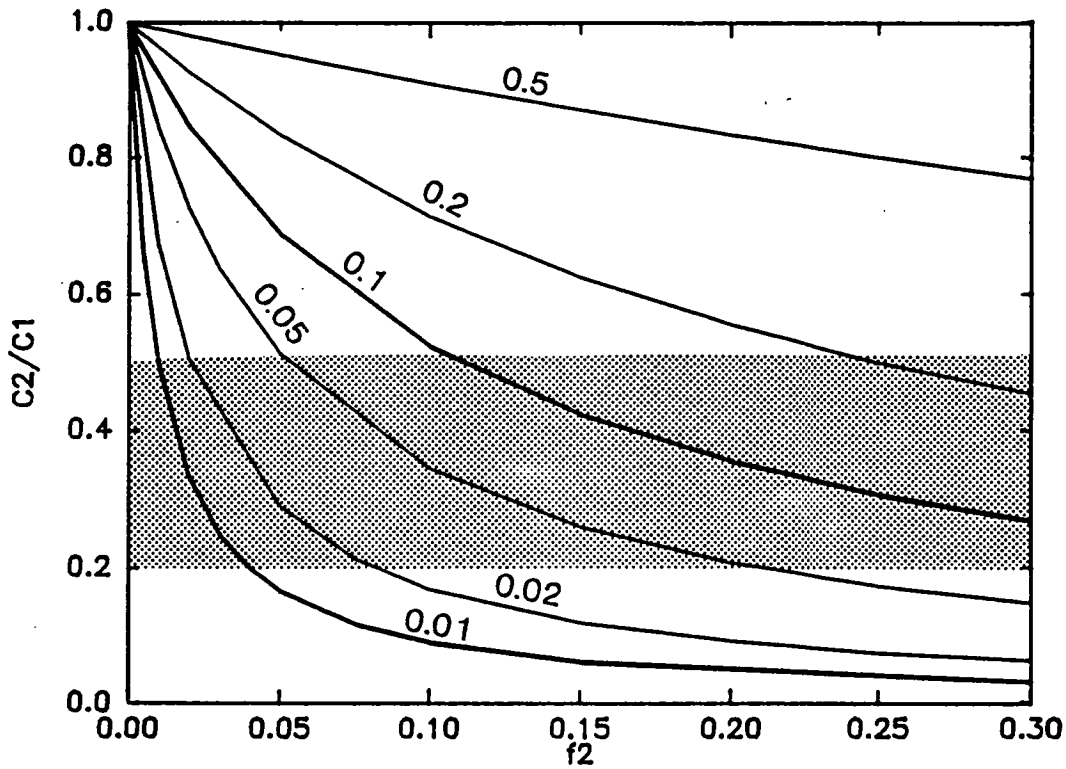

Figure 8.6 An illustration of the abundances of incompatible elements ($0.01<D^i_s<0.5$) occurring in a second stage melting (C_2) relative to a previous melting event (C_1), plotted as a function of the degree of second stage melting (f_2). The stippled pattern outlines the level of HFSE and HREE abundances occurring in the Vanuatu parent compositions relative to abundance levels in N-MORB.

Ambae HTS and Futuna parents are distinctive, due to their higher absolute and relative abundances of HFSE and HREE.

A number of coherent patterns of geochemical variation accompany trends occurring as incompatible element abundance levels increase in the Vanuatu parent magmas including:

1. a diminishing positive Sr spike (i.e. decreasing Sr/LREE values);

2. strong increases of Rb and possibly also K relative to other highly incompatible elements, with that relative to Ba being most pronounced;

3. increasing Zr relative to Ti and also HREE;

4. increasing LREE enrichment (i.e. increasing La/Yb), and

5. deepening of the Nb trough (i.e. increasing La/Nb values)

The multi-element diagrams serve as a qualitative guide to these incompatible element systematics, however, a more fruitful assessment may be achieved by plotting ratios of appropriate elements against element abundances. Such plots show that many of the relationships noted above are well correlated with increasing incompatible element abundances (Fig. 8.7), and demonstrate considerable variation in the behaviour of incompatible elements from different element groups. Of particular note is the systematic enrichment of LREE relative to HFSE, and the depletion of LILE relative to LREE, as incompatible element abundances increase. Shown for comparative purposes are a suite of (MORB-like) parent basalt compositions from the North Fiji Basin (Price et al., submt.), which have been olivine-fractionation-corrected (along the QFM oxygen buffer) until in equilibrium with olivine of Mg#90 olivine. These vary over a similar range of incompatible element abundances, however, the pattern of geochemical variation in these basalts bears little resemblance to the Vanuatu trends, being often subhorizontal and crosscutting to the Vanuatu Arc data.

Additional ratio-ratio plots are displayed in Figure 8.8 to emphasise the relationships existing between incompatible element groups in both the North Fiji Basin and Vanuatu parents. These plots clearly illustrate that the two features most commonly ascribed as being diagnostic of arc geochemistry (i.e. depletion of HFSE and enrichment of LILE relative to LREE), occur as separate and opposing geochemical end-members.

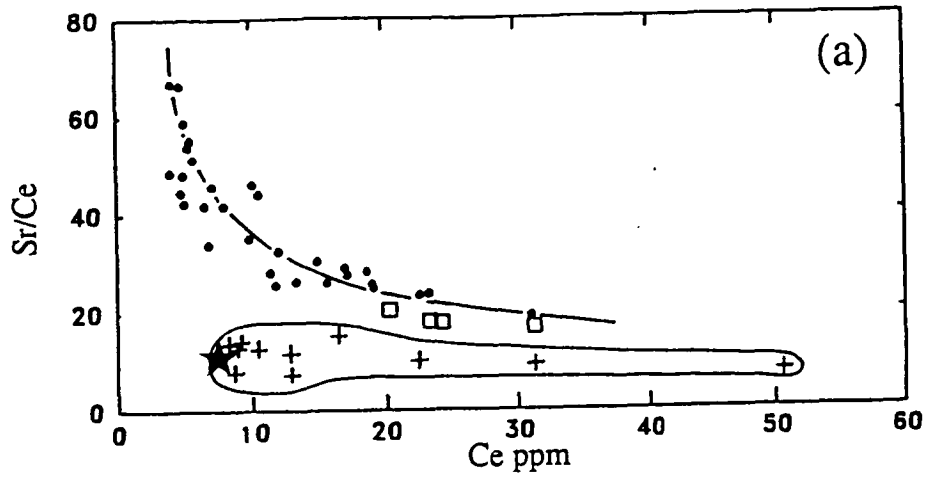
(a)
Sr/Ce
Ce ppm
0
20
40
60
80
0
10
20
30
40
50
60

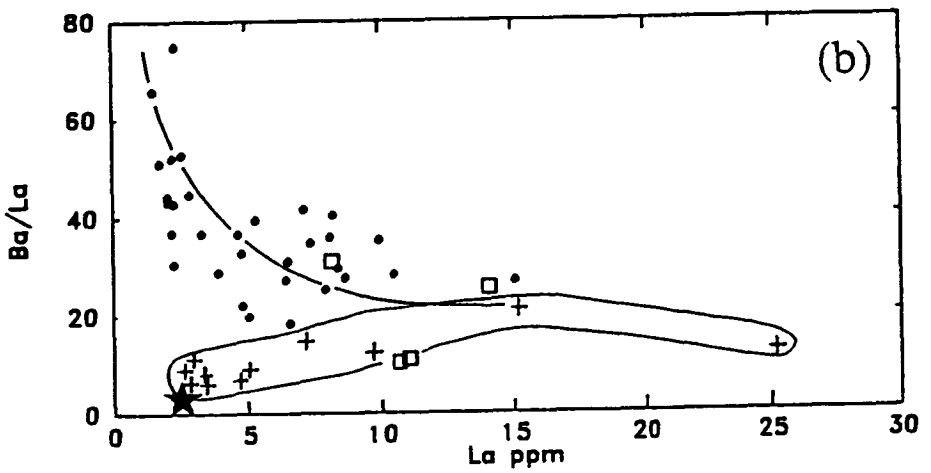
(b)
Ba/La
La ppm
0
20
40
60
80
0
5
10
15
20
25
30

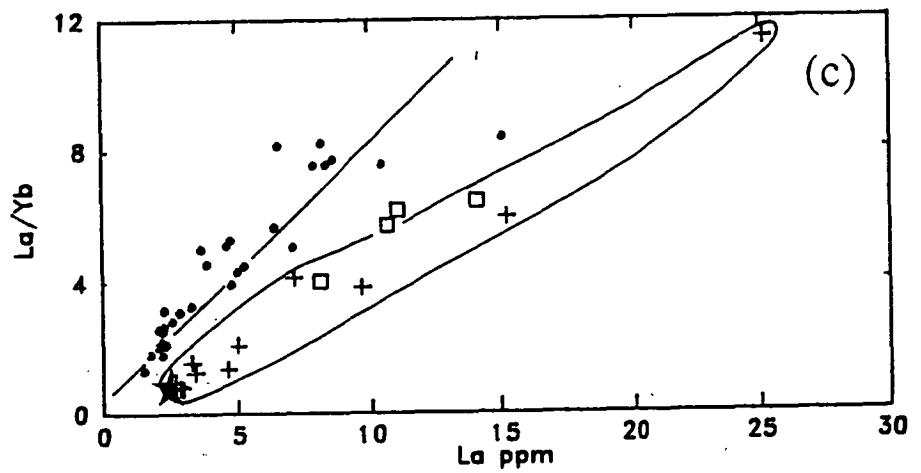
(c)
La/Yb
La ppm
0
4
8
12
0
5
10
15
20
25
30

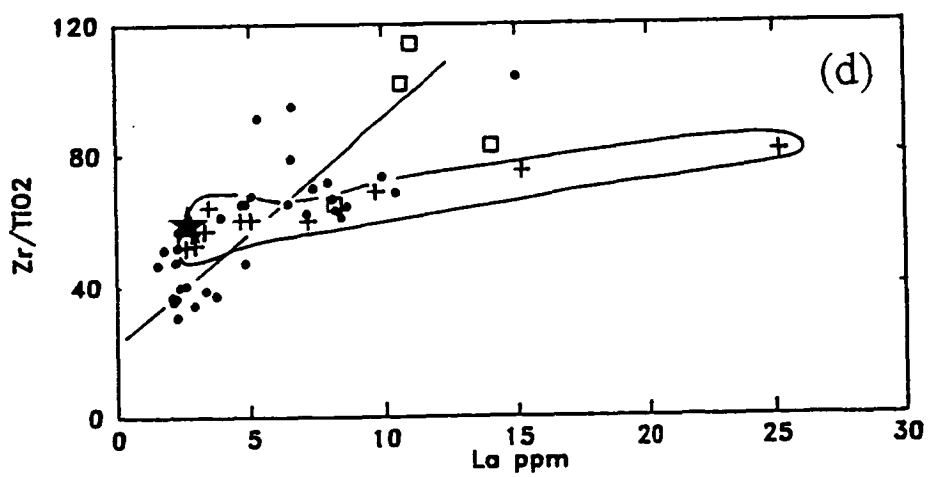
(d)
Zr/TiO2
La ppm
0
40
80
120
0
5
10
15
20
25
30

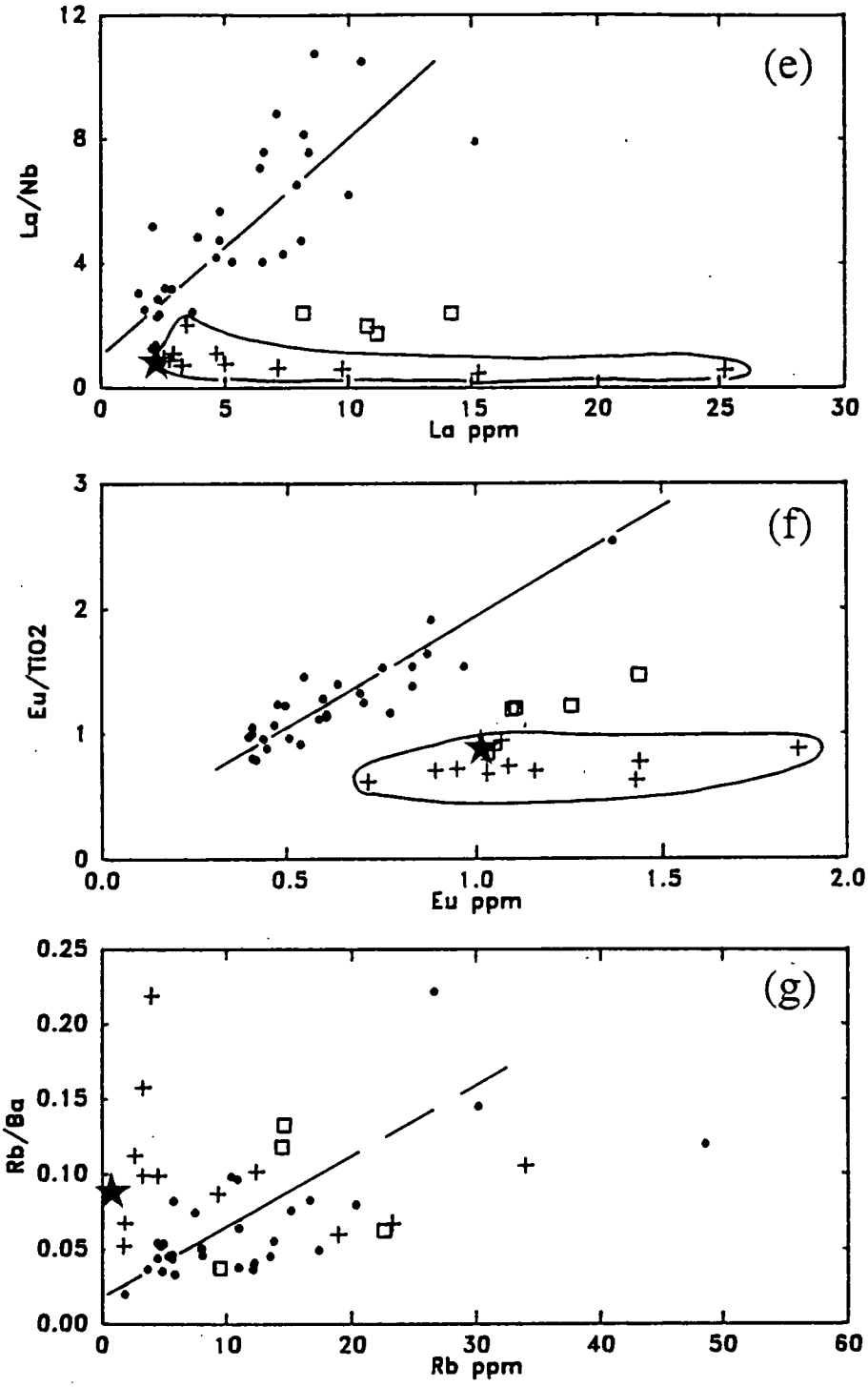

Figure 8.7 Incompatible element ratios versus incompatible element abundance plots for the Vanuatu Arc parent magmas (Futuna and Ambae HTS shown as squares, and others as solid circles) and the North Fiji Basin parent magmas (crosses). Note the systematic variation of most incompatible element pairs with increasing incompatible element abundances in the Vanuatu Arc parents, particularly for those pairs comprising elements from different chemical groups (i.e. LILE, HFSE, REE). This contrasts with the North Fiji Basin parent compositions which exhibit comparatively little or no variation of many of these element pairs (e.g. Sr/Ce, La/Nb, Eu/TiO_2, and Ba/La). Also note the similarity between most North Fiji Basin parents and the average composition of N-MORB (5-point star; from Hofmann, 1988).

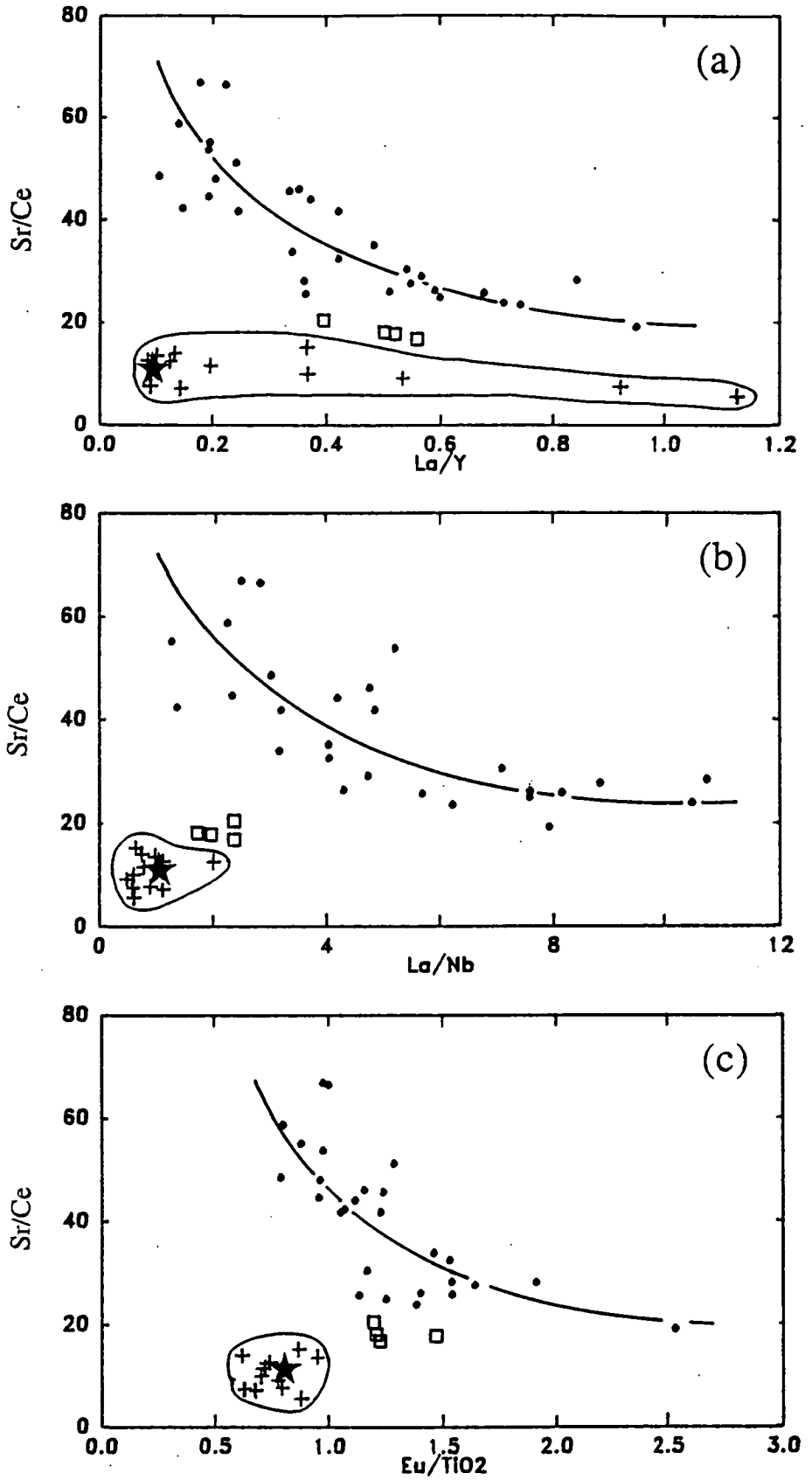

Figure 8.8 Selected incompatible element ratio-ratio plots for Vanuatu Arc and North Fiji Basin parent magma compositions. These plots clearly illustrate the separation of Vanuatu Arc parent magmas into two geochemically distinct end-members; one enriched in LILE over LREE, and the other depleted in HFSE relative to REE. Note the invariance among the North Fiji Basin parents of ratios comprising similarly incompatible trace elements (e.g. Sr/Ce, La/Nb, and Eu/Ti), and also the tendency for Futuna and Ambae HTS parents to plot between the Vanuatu Arc and the North Fiji Basin parent compositions. Symbols as for Figure 8.7.

Moreover, the systematic variation occurring between these widely separated endmembers contrasts markedly with the invariance of ratios comprising the same incompatible elements in the North Fiji Basin parents (see Fig. 8.8b and c). The Futuna and Ambae HTS basalts, which occupy an intermediate position between the North Fiji Basin and Vanuatu parent compositions, provide the only evidence for a link between the arc (Vanuatu) and back-arc (North Fiji Basin) geochemistry.

The patterns of element behaviour associated with increasing abundances of incompatible elements in the Vanuatu parent compositions, are broadly consistent with either progressively smaller degrees of melting and/or melting of mantle sources bearing systematic enrichments of these incompatible elements. The origin of this geochemical variability shall be assessed herein, beginning with the ability of partial melting to explain the data.

8.6.1 Non-Modal Melting of an Homogeneous Source

Relatively tight linear trends exist between highly incompatible/incompatible element ratio values and highly incompatible element abundances among the Vanuatu Arc parent compositions, to the exclusion only of Futuna and Ambae HTS lavas (e.g. Fig. 8.7c and d). Given the probable primary/near-primary nature of the Vanuatu parents, it is possible that these trends reflect progressive non-modal melting of a uniform source composition, as demonstrated using equation (8.1), following Minster and Allegre (1978) and Hofmann and Feigenson (1983), i.e.

$$C^h/C^i = (D^i_0/C^i_0).C^h + (C^h_0/C^i_0)(1-P^i) \qquad (8.2)$$

where C^h, C^i = concentrations of highly incompatible (*h*) and incompatible (*i*) elements in the primary melts,

C^h_0, C^i_0 = " " " in the source,

D^i_0 = bulk partition coefficient of element *i* with respect to the source,

P^i = " " " to phases entering the melt.

Regression of C^h/C^i values against C^h abundances facilitates the acquisition of slope (S^i) and intercept (I^i) values for individual elements *i*, which then allows estimation of the source concentration of these elements relative to the source concentration of element *h*, i.e.

$$C^i_0/Ch_0 = (1-P^i)/I^i \quad (8.3)$$

and also the source bulk partition coefficients (D^i_0) relative to the source concentration of element *h* i.e.

$$D^i_0/Ch_0 = S^i(1-P^i)/I^i \quad (8.4)$$

The evaluation of these expressions using linear regression analysis on the Vanuatu Arc parents, is enabled by calculating P^i from least squares estimates (using the GENMIX program of LeMaitre, 1980) of the proportions of peridotite phases forming the parent melt compositions (see Table 8.3). In this way, two sets of P^i values have been calculated for hypothetical garnet peridotite and spinel peridotite source mineralogies, using peridotite phase compositions from Takahashi (1986) and partition coefficients listed by Feigenson et al.(1983). In addition, it has been assumed that $P^{Nb} = P^{Th} = 0$, $P^{Zr} = P^{Sm} = P^{Hf}$, $P^{Ti} = P^{Eu}$, and $P^{Tb} = P^{Dy}$. La has been employed as the highly incompatible element after ruling out possible LILE which, as a group, behave anomalously and less incompatibly than La (see below). Selected regression data are plotted in Figure 8.9, and a full list of results is supplied in Table 8.3. La_0-normalised concentrations and bulk partition coefficient estimates for the Vanuatu source are illustrated on multi-element diagrams in Figure 8.10, where the element concentrations are further normalised using the relative values of Thompson (1982). For comparison are plotted results for the North Fiji Basin source, which has been analysed using an identical procedure to that employed with the Vanuatu parents. These results, in turn, are normalised to the Vanuatu source by assuming that the maximum degree of melting producing both the arc and back-arc magma suites is equal. This results in a North Fiji Basin source abundance estimate for La, which is 1.69x that of the Vanuatu Arc source. Note that results for melting of a spinel lherzolite source mineralogy are illustrated only, as little difference occurs between the spinel and garnet peridotite source models within error limits (2σ) obtained for slope and intercept values.

The characteristics of the modelled Vanuatu and North Fiji Basin sources are strikingly different. The North Fiji Basin source exhibits a smooth depletion in concentrations of the more incompatible elements, whereas the Vanuatu Arc source geochemistry is irregular with large positive anomalies for LILE, slight enrichment in

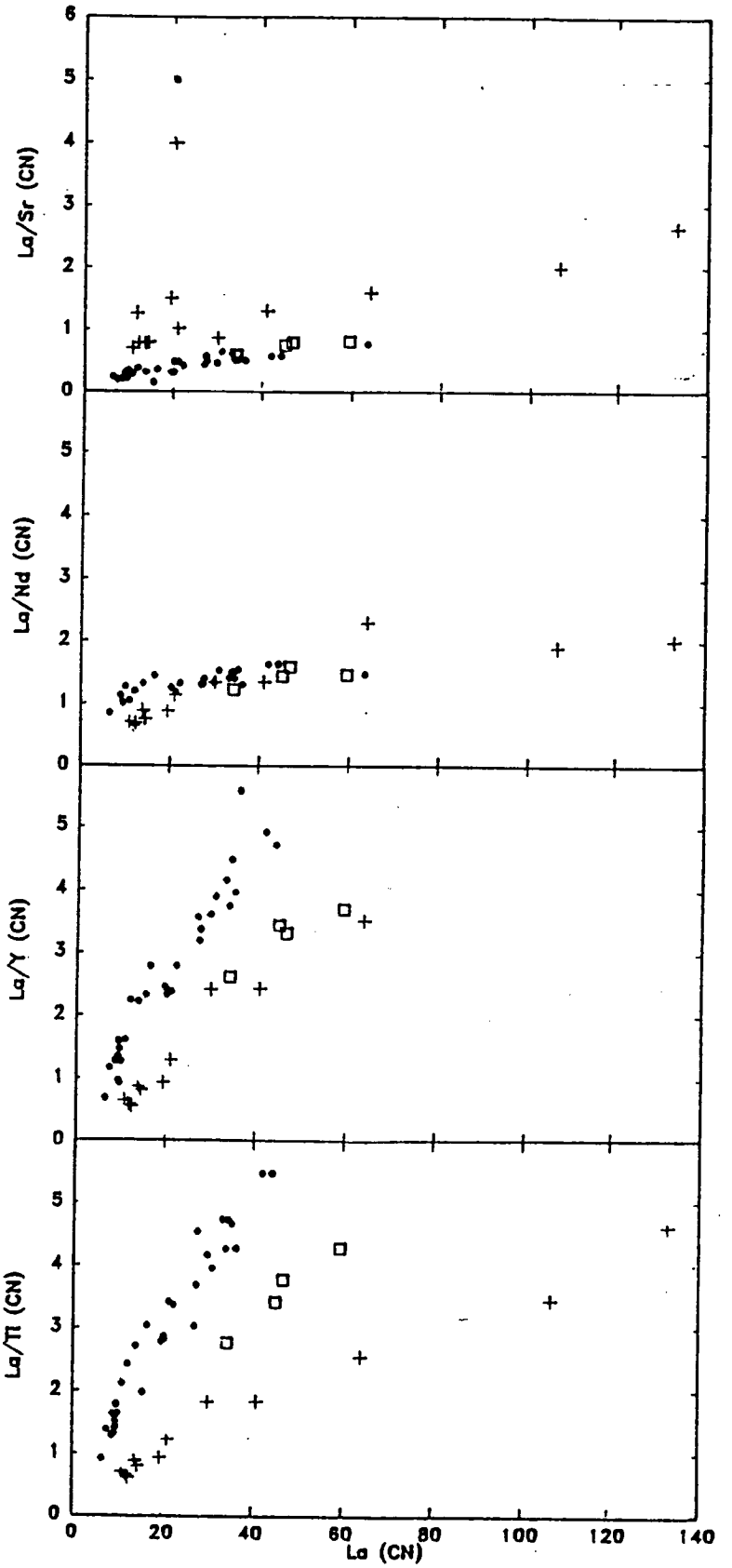

Figure 8.9 Selected examples of variation occurring between highly incompatible element/incompatible element ratios and La (a highly incompatible element) in the Vanuatu Arc and North Fiji Basin parent magmas. Note the rectilinear variation trends which occur in both cases. Ratios and abundances are normalised to the "chondritic" values of Thompson (1982). Symbols as for Figure 8.5.

Table 8.3 Regression data for Vanuatu Arc and North Fiji Basin source inversion models.

	Vanautu Arc (excluding Ambae HTS and Futuna)			North Fiji Basin		
	Slope(S^i)	Intercept (I^i)	R	Slope(S^i)	Intercept(I^i)	R
Ce	0.005±0.002	1.11±0.13	0.277	0.012±0.002	0.791±0.076	0.937
Nd	0.020±0.002	0.94±0.11	0.850	0.030±0.003	0.68±0.25	0.960
Sm	0.050±0.005	0.84±0.15	0.894	0.043±0.005	0.43±0.28	0.956
Eu	0.072±0.006	0.77±0.20	0.921	0.052±0.006	0.073±0.097	0.964
Gd	0.092±0.022	0.71±0.48	0.951	0.060±0.006	0.259±0.342	0.966
Tb	0.117±0.008	0.69±0.33	0.970			
Dy	0.074±0.009	0.48±0.38	0.966	0.038±0.004	0.09±0.38	0.973
Er	0.172±0.014	0.36±0.59	0.949			
Yb	0.178±0.012	0.47±0.46	0.942	0.092±0.010	-0.06±0.56	0.961
Y	0.144±0.008	0.28±0.28	0.964	0.074±0.008	0.02±0.43	0.965
Rb	0.005±0.004	0.48±0.16	0.241	-0.021±0.010	1.46±0.53	0.647
Ba	0.011±0.004	0.442±0.084	0.470	-0.049±0.017	3.14±0.93	0.747
Sr	0.017±0.002	0.203±0.063	0.898	0.021±0.009	0.90±0.50	0.663
K	0.007±0.002	0.241±0.068	0.629	-0.011±0.007	1.07±0.37	0.535
Th	-0.015±0.009	1.34±0.42	0.475			
Nb	0.266±0.035	1.20±1.53	0.819	-0.019±0.012	1.38±0.65	0.534
Zr	0.100±0.016	1.90±0.58	0.754	0.041±0.007	0.58±0.40	0.908
Hf	0.088±0.021	2.00±1.00	0.811			
Ti	0.160±0.007	0.61±0.29	0.971	0.051±0.003	0.34±0.29	0.966

Note that all S^i and I^i values are normalised to the values of Thompson (1982), except Eu, Gd, Dy, and Er which are normalised to 1.39x the C1-chondrite values of Sun and McDonough (1988). R is a correlation coefficient for La_0/i regressed against i. Quoted errors are 2σ deviations about the mean slope and intercept values. P^i values, used to evaluate C^i_0/La_0 and D^i_0/La_0 from S^i and I^i, have been calculated from the partition coefficients of Feigenson et al. (1983), using the following estimates for phase proportions being consumed during melting:

Garnet peridotite melting

Vanuatu Arc Parents; 20% orthopyroxene, 50% clinopyroxene and 30% garnet

Spinel peridotite melting

Vanuatu Arc Parents; 40% orthopyroxene, 50% clinopyroxene and 10% spinel

North Fiji Basin Parents; 55% orthopyroxene and 45% clinopyroxene.

LREE, and depletion of Zr and Hf, and possibly also Nb. The source bulk partition coefficient estimates follow a similar pattern to the source geochemistry estimates, with large anomalies occurring for LILE partition coefficients (Fig. 8.10b). Note, however, that both the Vanuatu Arc and the North Fiji sources possess similar, smoothly increasing partition coefficient estimates from the LREE through to the HREE (Fig. 8.10c).

The modelled North Fiji Basin source's geochemistry and trace element bulk partition coefficients are consistent with a mantle source similar to that of MORB, which is characterised by depletion in the more incompatible elements (see Fig.8.10a). The Vanuatu source model, in contrast, is greatly enriched in LILE relative to LREE, and depleted in HFSE (particularly Zr, Hf, and possibly also Nb) relative to LREE. In addition, on the basis of distinctive LILE and HFSE bulk partition coefficient patterns, the Vanuatu source could be considered mineralogically distinct from the North Fiji Basin source.

The similarity between the Vanuatu source bulk partition coefficient estimates and the pattern of element partitioning between amphibole and basaltic melts (cf. Figs. 8.10b and d), prompts suggesting that amphibole may be an important residual phase during generation of the Vanuatu parent magmas. This opens an interesting possibility, for by taking into account the effect of amphibole melting on P^i values, it may be possible to reduce the LILE anomalies in the Vanuatu source model to a smooth abundance pattern. However, the existence of an LILE enriched source is supported strongly by the most incompatible element-poor Vanuatu Arc parents, which represent the maximum degree of melting, having the greatest relative enrichment of LILE over LREE (i.e highest LILE/LREE values), and incompatible element abundance patterns which are indistinguishable from the calculated source model (cf. Merelava in Fig. 8.4d and the Vanuatu source in Fig. 8.10a). Given that amphibole is preferentially consumed with progressive melting, these samples should provide the closest approach to the source's geochemical characteristics.

Regardless of the possible effects of residual amphibole, it must be considered doubtful whether amphibole is a residual phase during generation of all the Vanuatu primary magmas. Even if the liquidus temperatures of the magnesian parent compositions (15-20 wt% MgO) are depressed by 100-200°C below their anhydrous liquidus

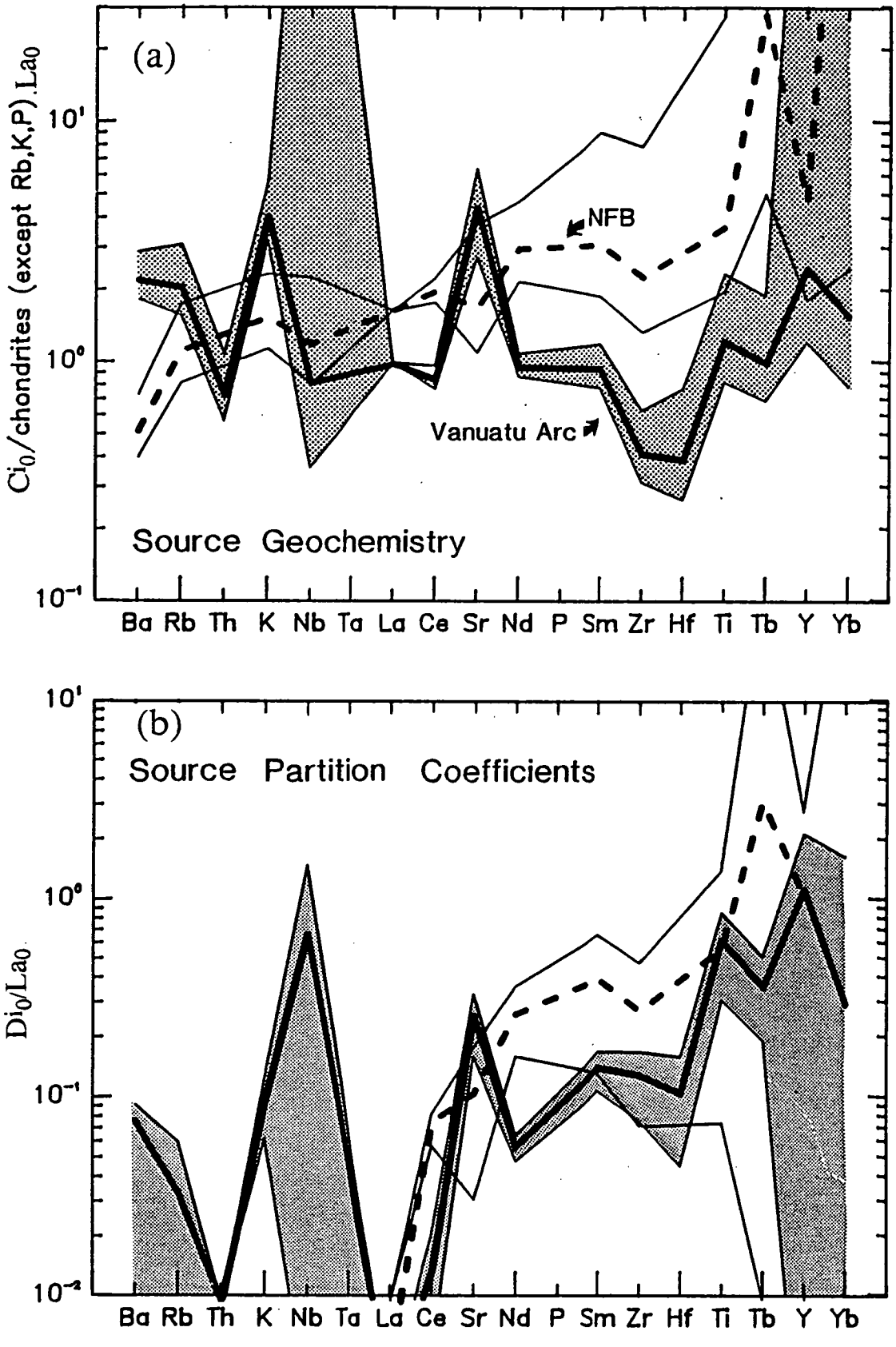

Figure 8.10 Vanuatu Arc and North Fiji Basin magma source characteristics calculated through inversion of non-modal melting equations (see text for details). (A) Trace element abundances in the Vanuatu Arc source (thick solid line) and North Fiji Basin source (thick dashed line) are normalised to the values of Thompson (1982), and additionally to a La_0 value of 1 for the Vanuatu Arc source. The stippled and plain regions outline 2σ error limits calculated from the regression statistics (see Table 8.3). (B) Relative bulk partition coefficients for incompatible elements in the magma sources

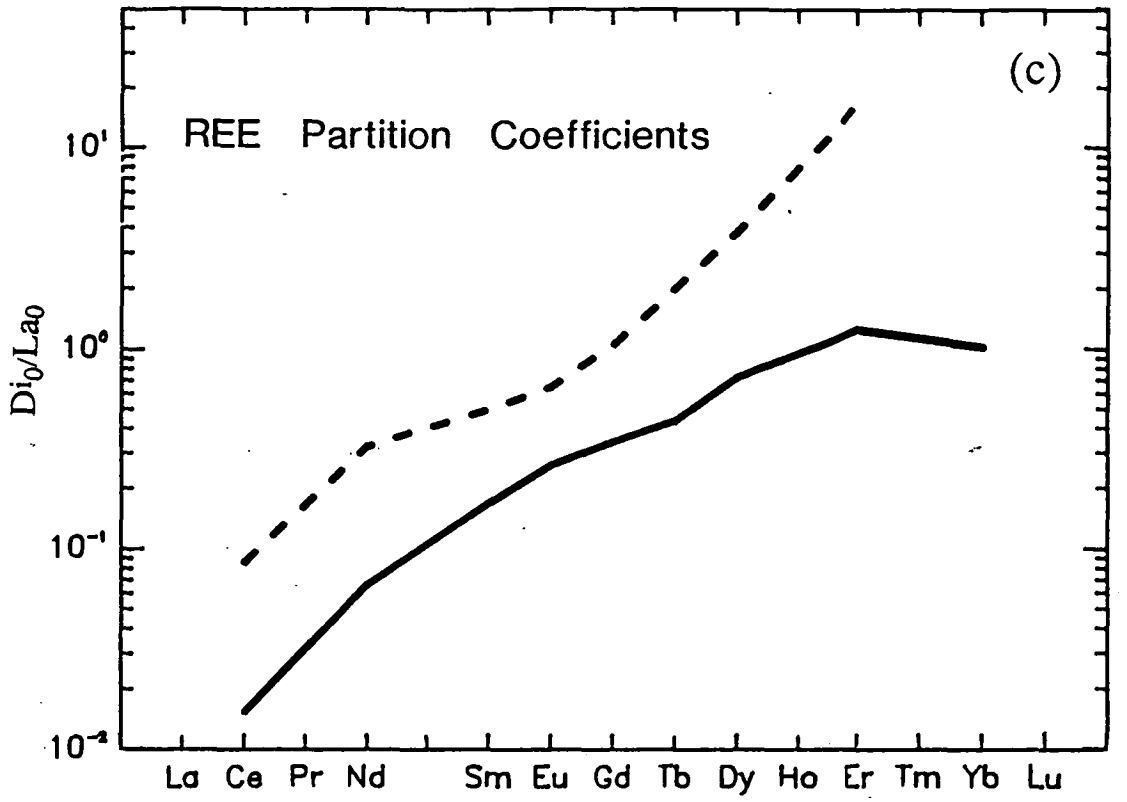

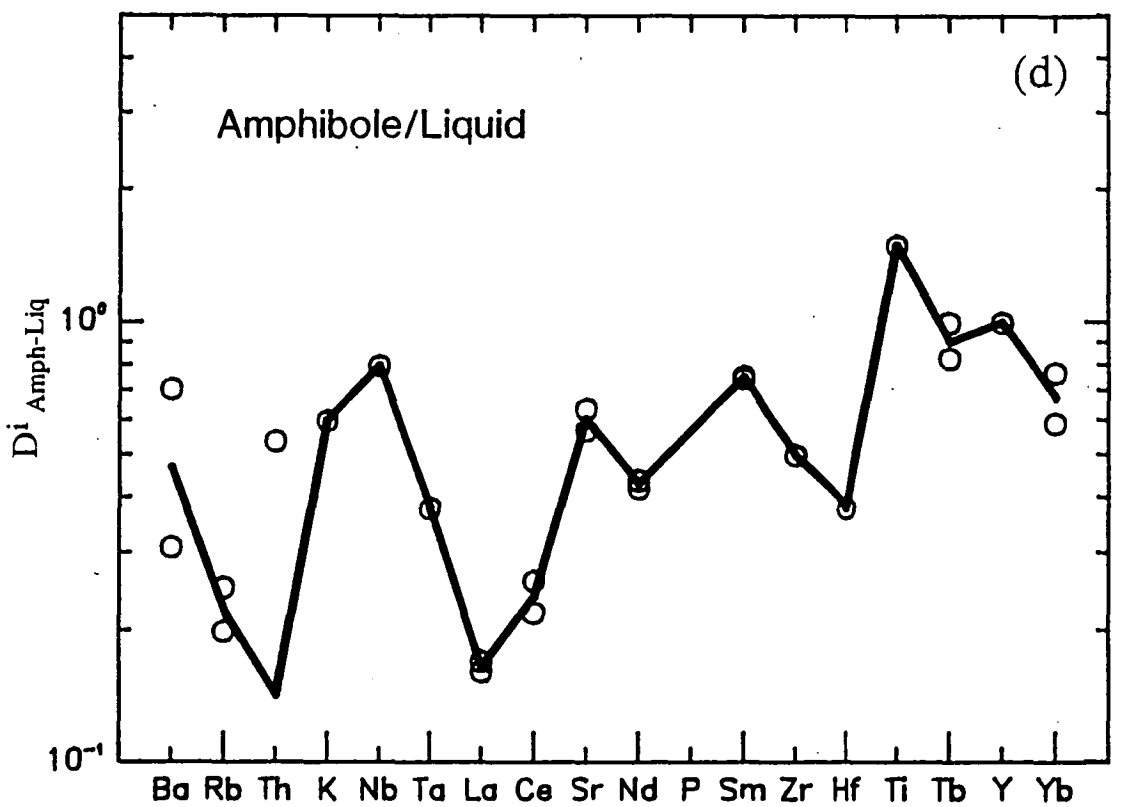

of the Vanautu Arc (thick solid lines) and North Fiji Basin (dashed line) prior to melting. (C) Relative bulk partition coeficients for REE in the Vanuatu Arc source (solid line) and North Fiji Basin source (dashed line). (D) Partition coefficients for the distribution of incompatible elements between amphibole and basaltic liquids (open circles), from Irving and Frey (1978) and G. Jenner (pers. comm., 1988). The average of these estimates is shown as a thick continuous line.

temperatures (Ramsay et al., 1984), by upwards of several wt% dissolved volatiles, their origin at pressures between 2 and ~4 GPa will, after allowing for adiabatic decompression, still require source temperatures between 1300 and 1500°C. These estimates are considerably in excess of the established stability limits for amphibole in mantle peridotite, which exists in favourable bulk compositions only at pressures <3.0GPa and temperatures <1200°C, but more often <1100°C or less, particularly in depleted peridotite compositions (Wallace, 1989).

In consideration of these shortcomings, and also the difficulty in rationalising the melting of a homogeneous LILE-enriched, amphibole-bearing, mantle source throughout the Vanuatu Arc (to the exclusion obviously of Ambae HTS and Futuna magma sources), it seems inappropriate to apply the quantitative inverse modelling to relate the Vanuatu Arc basalts to a common source. One possibility, which preserves a framework for producing the observed geochemical systematics by partial melting, is that addition of LILE-rich fluids may be responsible for increased degrees of melting and enrichment of LILE. This proposal, however, still does not account for the relative enrichment of LREE over HFSE occurring in the most incompatible element-rich samples (Figs. 8.7e&f and 8.9d), unless residual HFSE bearing phases are present at low degrees of melting. Preferably, in lieu of arguments provided earlier, the incompatible element-rich parents are more likely to arise from the addition to their source of LREE (and also LILE) without accompanying HFSE.

8.7 EVIDENCE FOR MANTLE SOURCE HETEROGENEITY

If arguments against the presence of incompatible element bearing residual phases (e.g. amphibole, titanates) during melting are accepted, then simple models relying on variable degrees of melting to explain the geochemical variation in the Vanuatu parent magmas can be ruled out. The geochemical systematics observed among the incompatible elements may instead be interpreted to reflect the interaction of two dominant and geochemically distinct source components. Neither component corresponds with the geochemical characteristics of non-island arc upper mantle source compositions, as illustrated by their distinction from North Fiji Basin basalts and average N-MORB in

Figures 8.7 and 8.8, yet a peridotite source is required by the primitive Mg-rich nature of the parent bulk compositions. This suggests that both components identified can be associated with enrichment processes affecting the Vanuatu Arc mantle source prior to, or during, melting. At least one additional geochemical component is needed to account for the Ambae HTS and Futuna parent compositions which lie off the main geochemical variation trends, and which usually fall between the Vanuatu Arc and North Fiji Basin compositional trends.

The linear variation in La/Nb and Eu/Ti values, increasing from near upper mantle values as La and Eu abundances increase (Figs. 8.7e&f), may be easily explained if LREE have been introduced into the Vanuatu mantle source without accompanying Nb and Ti. The geochemical systematics illustrated in Figure 8.7 show that LREE enrichment is also associated with increasing Rb/Ba, increasing LREE/HFSE (to values well in excess of N-MORB), decreasing LILE/LREE (to values near N-MORB), increasing Zr/TiO_2 (and also Zr/HREE), and also marked increases in all incompatible element abundances except HREE, Ti, and Nb. As may be gauged from the investigation of partial melting systematics above, this style of geochemical enrichment is consistent with the addition of a small, incompatible element-rich melt fractions deriving from a mafic or ultramafic source lithology. Furthermore, the fractionation of LREE from HFSE occurring with this geochemical enrichment, points to the derivation of responsible agents from within the presence of a residual HFSE retaining (titanate or other?) phase.

Although LILE abundances are highest in the incompatible element-rich end-member, the enrichment of LILE over LREE is most marked in the incompatible element-poor primitive magma compositions. Among the LILE, it is Ba and Sr which are most enriched over the LREE, with levels occurring up to 10x upper mantle values (i.e. Ba/La ~Sr/Ce ~100). K and particularly Rb, on the other hand, are enriched to a lesser extent (see Fig. 8.4) as demonstrated by the reduction in Rb/Ba values occurring with decreasing incompatible element abundances (see Fig. 8.7g).

A third geochemical component, necessary to account for the occurrence of Ambae HTS and Futuna parent compositions between those of the North Fiji Basin and the majority of Vanuatu Arc parents, is consistent with mixing of Vanuatu Arc and North Fiji

Basin (N-MORB) source components. This limited evidence for a simple upper mantle peridotite source component in the Vanuatu Arc is somewhat intriguing, for peridotite sources are implied by the primitive nature of all the Vanuatu parent compositions. The appearance of this upper mantle peridotite source component in the Ambae HTS and Futuna basalts, however, may reflect that the arc-source LILE and LREE enriching agents have been less effective in modifying the peridotite protoliths of these particular magma suites. This may arise if the Ambae HTS and Futuna mantle source protoliths are more fertile than elsewhere in the arc, and thus less susceptible to contamination (see also Chapter 7).

In short, geochemical systematics support the existence of two dominant and distinct styles of incompatible element enrichment within the Vanuatu Arc parent magmas. The continuum of compositions occurring between these two endmembers (e.g. Fig. 8.7), is consistent with their having competed to enrich the Vanuatu Arc mantle source. The geochemically anomalous Ambae HTS and Futuna parent compositions provide evidence for an additional upper mantle source component which matches the N-MORB mantle source of the nearby North Fiji Basin basalts.

8.8 A GEOCHEMICAL COMPARISON WITH GLOBAL PRIMITIVE IAB

A global compilation of primitive IAB has been assembled for the purpose of comparison with, and to aid the interpretation of, the geochemical systematics so far identified within the Vanuatu Arc. Analyses of primitive IAB have been selected from the literature on the basis of $Mg^{\#}$ (>55; $Fe^{2+}/Fe^{tot} = 0.8$) to avoid the possible disturbance of primary geochemical characteristic by protracted magmatic differentiation. In addition, magmas erupted in continental arcs have not been included in order to circumvent possible contamination by mature continental crust, and only sufficient samples to characterise the products of individual volcanic centres are collated. It should be noted that this selection process may exclude chemical groups of IAV which are less likely to retain primitive (Mg-rich) compositions, and also arc primary magmas that may not derive from mantle peridotite sources.

Several key plots, which have been used to discriminate between geochemical components in the Vanuatu Arc, are also employed to evaluate the global data set (Fig. 8.11). These illustrate a global pattern of incompatible trace element behaviour very similar to that documented in the Vanuatu Arc (see insets in Fig. 8.11 for comparisons). The most incompatible element-poor compositions are distinguished generally by enrichment of LILE over LREE (i.e. high Sr/Ce and Ba/La), and low Rb/Ba ratio values which are below most upper mantle source estimates (i.e. Rb/Ba~0.09). These grade into incompatible element-rich compositions possessing strong enrichments of LREE over HREE, and LREE (and LILE, not shown) over HFSE, and also high Rb/Ba values (>0.09).

At least one additional geochemical component is necessary to account for the diffuse nature of the global data variation. Judging from the mergence of compositions toward, and overlapping with N-MORB (see Fig. 8.11), it is suggested that this component is the global upper mantle peridotite source parental to N-MORB. However, it should be noted that OIB and MORB compositions are almost indistinguishable in most of the diagrams illustrated, and thus either the mantle sources of MORB or OIB, or both, may be present.

The comprehensive isotopic and trace element data available for the global data set provides further constraints on the nature of the incompatible element-rich and incompatible element-poor compositional end-members. For one, the incompatible element-poor IAB, which have low Eu/TiO_2 (LREE/HFSE) and high Sr/Ce (LILE/LREE) values, are characterised by unradiogenic Sr and radiogenic Nd isotope values, which are similar to those of MORB (see Fig. 8.12). This contrasts with the very radiogenic Sr and unradiogenic Nd isotopic ratios ($^{87}Sr/^{86}Sr$ ~0.705 to 0.706, εNd ~0 to -4) of the incompatible element-rich IAB, which have high Eu/TiO_2 and low Sr/Ce values in Fig. 8.12. The progressive enrichment of LILE over LREE in many of the incompatible element poor magmas is also found to correlate with increasing relative enrichment of Pb over LREE, resulting in Pb/Ce values up to 25x upper mantle estimates (i.e. referred to N-MORB and OIB values in Fig. 8.13). Despite this observation, no correlation was found between geochemical variables diagnostic of the geochemical end-members and Pb isotope

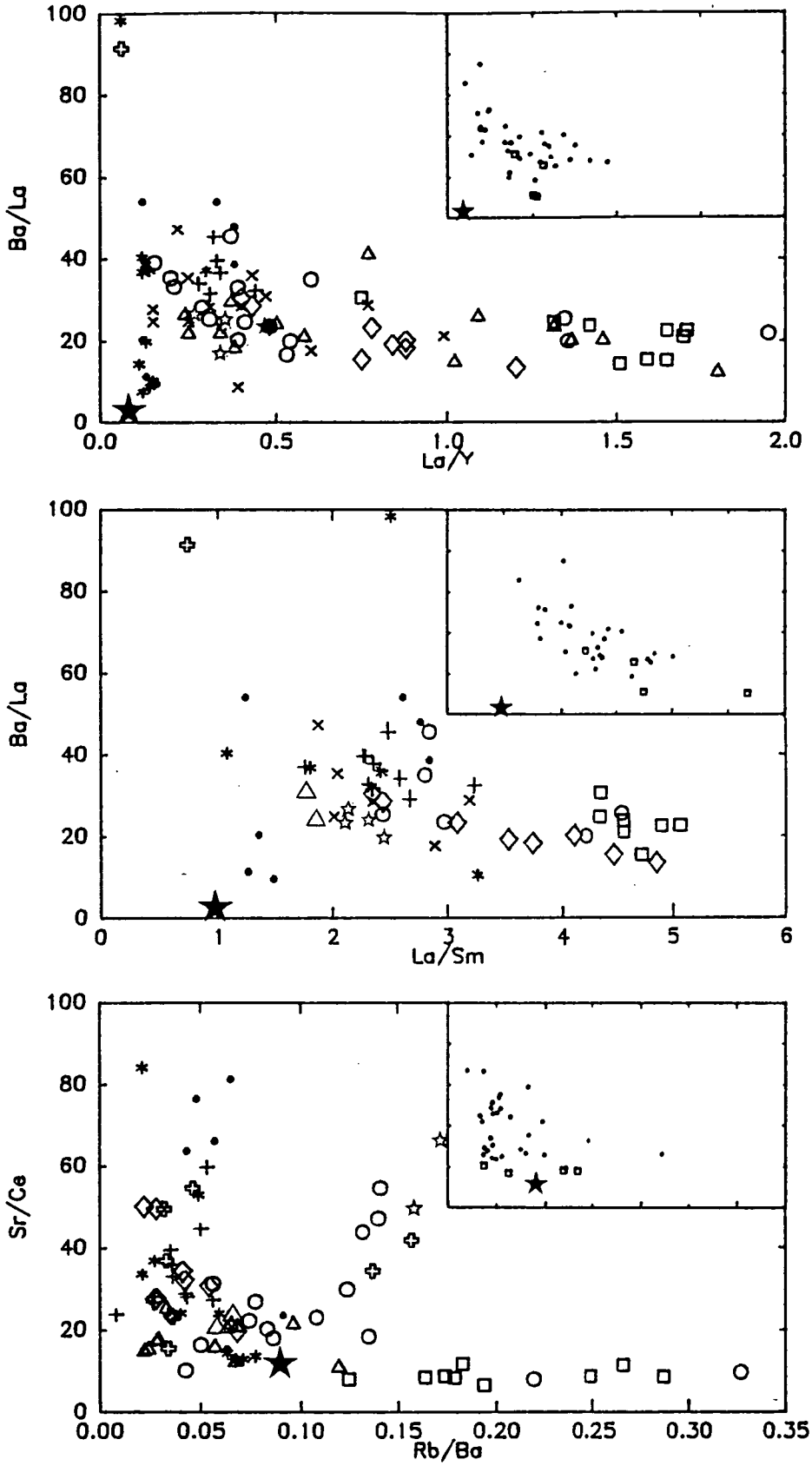

Figure 8.11 Incompatible element ratio-ratio and ratio-element abundance plots for primitive global IAB ($Mg^{\#}$>55, Fe^{2+}/Fe^{tot} = 0.80). Scaled comparisons of geochemical variation occurring among the Vanuatu Arc parent compositions are shown as insets in each plot. This geochemical variation is referenced to the average N-MORB composition of Hofmann (1988; 5-point star). The compilation includes samples from the New Britain Arc (solid circles: Johnson et al., 1985; the BVSP, 1981), the Aleutian Arc (crosses: McCulloch and Perfit, 1981; Nye and Reid, 1986), Japan (X's: Masuda et al., 1975 ;Katsui et al., 1978; Fujimaki, 1986; Sakuyama and Nesbitt, 1988), the Indonesian Arc (circles: Foden, 1983; Varne and Foden, 1986; Wheller et al., 1987;

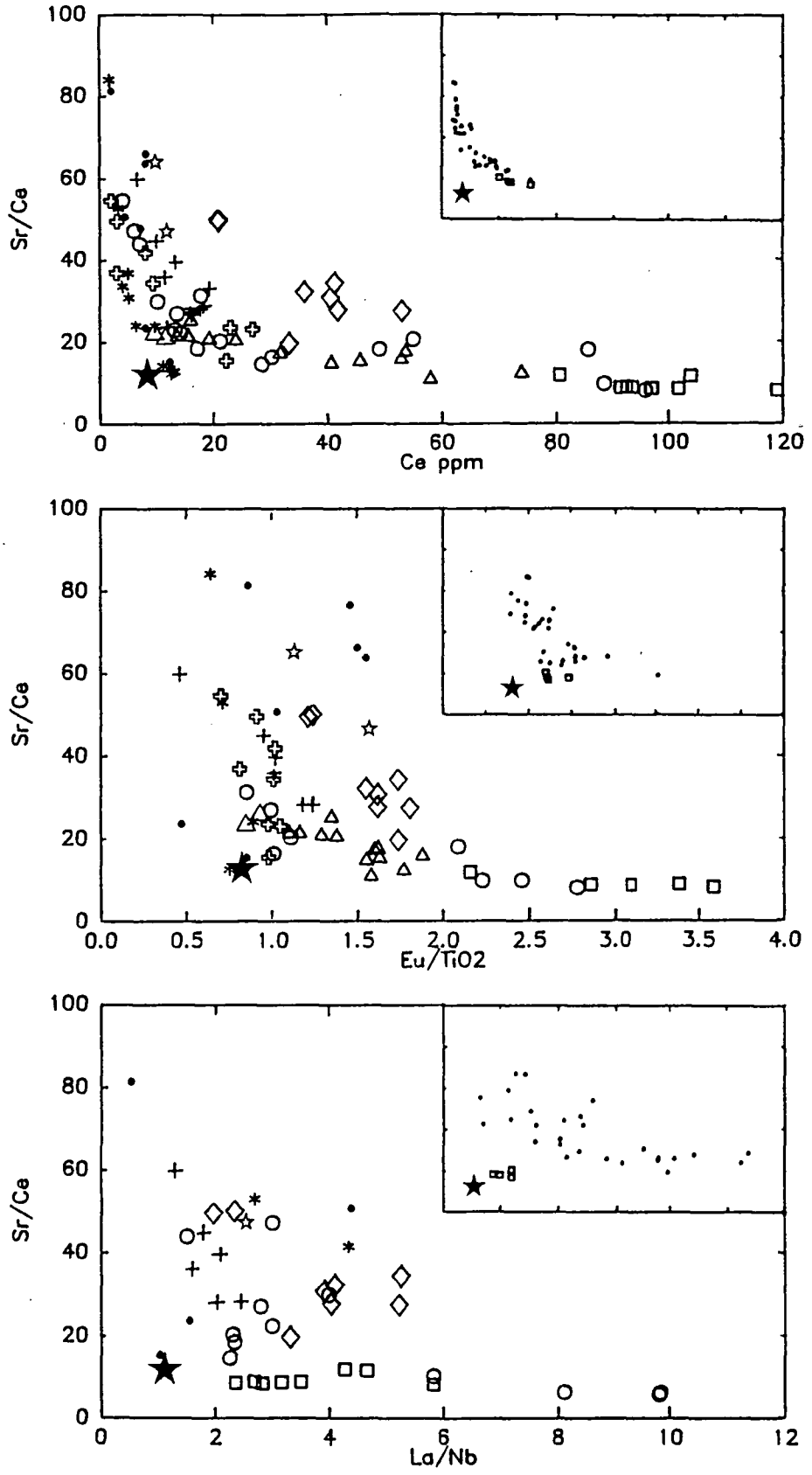

Wheller, 1987) including Batu Tara volcano (squares: Stolz et al., 1988; Varekamp et al., 1988), the Lesser Antilles (triangles: Arculus, 1978; Shimizu and Arculus, 1975; Hawkesworth et al., 1979; Dostal et al., 1983) including the Grenada C-series basalts (diamonds: Thirwall and Graham, 1984), the Tonga Arc (astericks: Ewart and Hawkesworth, 1987; Ewart et al., 1977), the South Sandwich Islands and Bransfield Strait (Swiss crosses: Weaver et al., 1979; Hawkesworth et al., 1977), and New Georgia in the Solomons Islands (unfilled 5-point stars; Ramsay et al., 1984). Symbols for the Vanuatu Arc parent compositions are as in Figure 8.10.

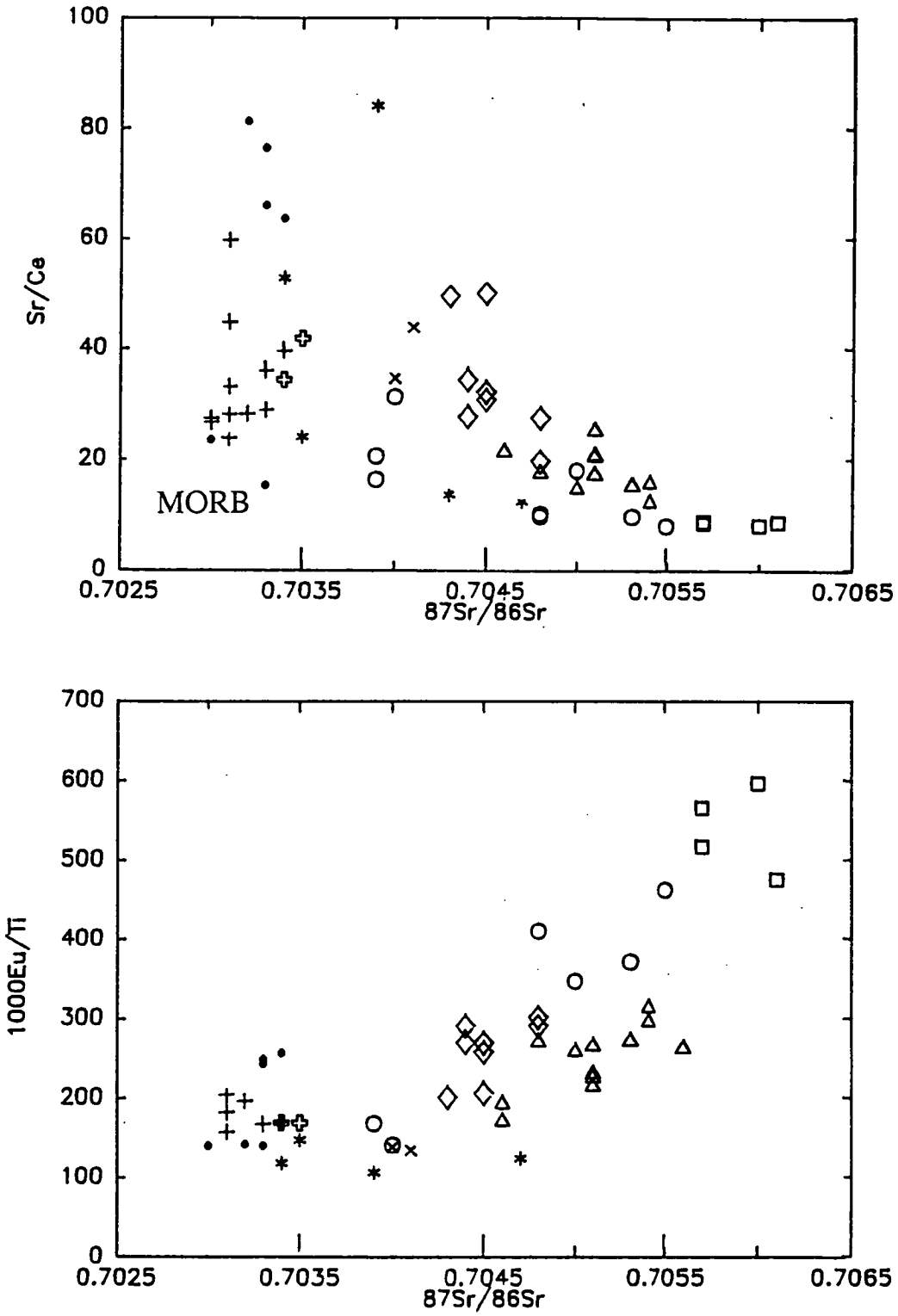

Figure 8.12 Covariation of $^{87}Sr/^{86}Sr$ isotope ratios with key incompatible element ratios which provide measures of the degree of LILE enrichment over LREE (i.e. Sr/Ce), and the depletion of HFSE relative to LREE. Symbols and data sources as in Figure 8.11.

values within the compiled set of primitive IAB (not shown). This clearly warrants further assessment using a more comprehensive IAV data set.

8.8.1 The Origin of Geochemical Components

LILE and Pb-rich, REE and HFSE-poor Component

The correlation between high Pb/LREE and high LILE/LREE values (Fig. 8.13) is consistent with the introduction of both LILE and Pb into arc magma sources by a single enriching agent. This coupled behaviour of Pb and LILE was first realised by Kay (1980), and later demonstrated in a larger data set by Arculus and Johnson (1981). Kay proposed a multicomponent mixing model to explain these correlations, in which the anomalous LILE and Pb enrichments were derived from pelagic sediment added to island arc source regions as a consequence of ocean crust subduction.

A major drawback for a sediment origin for these LILE and Pb enrichments, is that the high $^{87}Sr/^{86}Sr$ values of pelagic sediments (e.g. White and Dupre, 1986) are not observed in the most LILE and Pb enriched arc magmas. This is so despite being able to show, on the basis of Sr/Ce values exceeding ~40, that at least 75% of the Sr in such compositions derives from the LILE enriching agent (e.g. Hawkesworth and Ellam, 1989). Moreover, relatively few sea floor sediments, and then mostly pelagic carbonates, have the required enrichment in Sr, Ba, and Pb over LREE necessary to reproduce the LILE enrichment trend in IAB observed in Figure 8.13.

The presently accepted explanation for the anomalous enrichment of LILE over LREE occurring in IAB is the addition of LILE-rich fluids, possibly derived from the subducting ocean crust/lithosphere (e.g. Gill, 1981; Tatsumi et al., 1983; Ellam and Hawkesworth, 1988). This is founded on the observed mobility of LILE in hydrothermal fluids, and from experimental studies of element solubility in high pressure aqueous fluids (e.g. Tatsumi et al., 1986). The low $^{87}Sr/^{86}Sr$ values associated with this enriching agent dictate that the LILE are scavenged neither from sediments nor the seawater altered portion of the ocean crust but rather, from sources with depleted mantle reservoir characteristics (i.e. unaltered ocean crust or upper mantle peridotite). Clearly, Pb must also be an important dissolved component in these fluids.

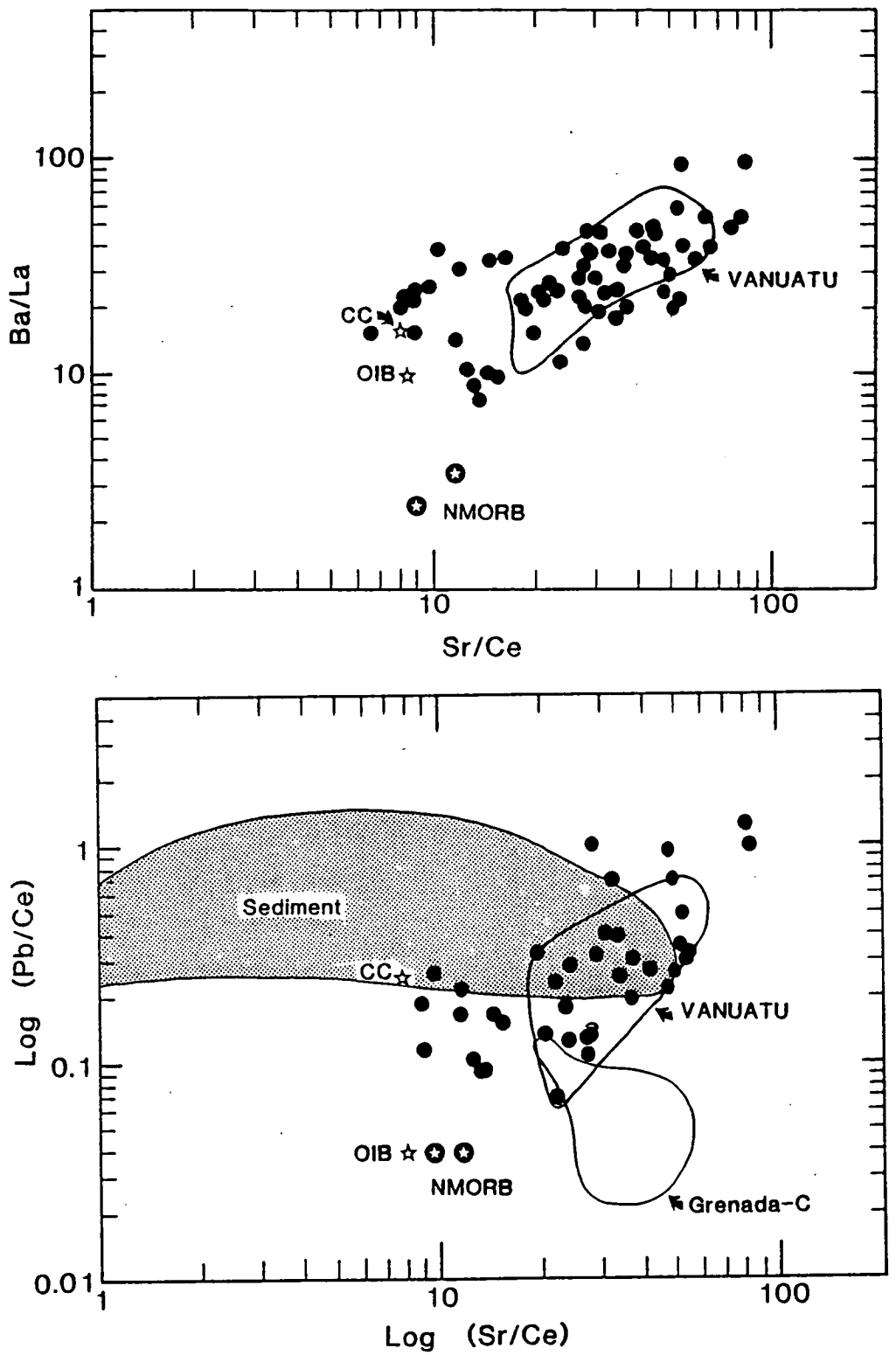

Figure 8.13 LILE/LREE and Pb/LREE systematics in primitive island arc basalts (solid circles), including the suite of Vanuatu Arc parental magmas (outlined field). Shown for comparison are the compositions of average N-MORB (circled stars: Hofmann, 1988; Sun and McDonough, 1988), average ocean island basalt (5-point star: Sun and McDonough, 1988), and average continental crust (filled 5-point star: Taylor and McLennan, 1985). Also shown is a field for pelagic sediment compositions compiled from Ben Othman and Hart (submt.), White et al. (1985), Kay and Kay (1988), and Glasby et al. (1987).

LILE and LREE-rich (HFSE depleted) Component

The changes toward high $^{87}Sr/^{86}Sr$ and low εNd values with increasing incompatible element abundance levels, and high LREE/HFSE and low LILE/LREE values in IAB, mark a profound change in the magma source to one characterised by long-lived enrichment in the more incompatible elements. It follows that these incompatible element-rich IAB derive from old incompatible element-rich components that are either pre-existing or introduced into the arc source region, as opposed to simply smaller degrees of partial melting as was entertained earlier for geochemical variation occurring in the Vanuatu Arc. The observed fractionation of REE/HFSE ratios, and also Rb/Ba ratios, to values exceeding accepted upper mantle values clearly requires special geochemical processes.

To date, detailed studies of incompatible element-rich, high-K IAB have failed to achieve consensus on the origin of their enriched source geochemical and isotopic characteristics. Nonetheless, proposals may be divided broadly into two groups; one arguing for source enrichment through addition of a subducted sediment component (e.g. Rogers et al., 1987; Ellam and Hawkesworth, 1988), and the other arguing for the involvement of OIB mantle sources (e.g. Morris and Hart, 1983, 1986; Varne and Foden, 1987; Wheller et al., 1987), although subcontinental mantle and crustal contamination have also been allocated roles in the formation of these trace element and isotopic enrichments (Varne, 1985; Davidson, 1987; Hawkesworth and Ellam, 1989). Arculus and Powell (1986) have pointed out that a degree of circularity may exist within these proposals, as the origin of enriched OIB mantle reservoirs, and also some subcontinental mantle geochemical signatures, have been attributed to the incorporation of subducted sedimentary components (e.g. Zindler and Hart, 1986). Several critical observations are worth mentioning in view of the application of either of these proposals.

(1) If an OIB mantle source is responsible for these characteristics then the presence of residual HFSE-bearing phase(s) is required to create the observed fractionation of REE from HFSE (e.g. Morris and Hart, 1986).

(2) Seafloor sediment trace element and isotope geochemistry is highly variable, a feature inconsistent with the well defined geochemical characteristics of the incompatible element-rich endmember observed in primitive IAB (Fig. 8.11).

Clearly, it is necessary to obtain better geochemical and isotopic characterisation of potential sediment and enriched mantle contributing to individual arcs, and to assess the mechanisms via which sediment may be incorporated into arc mantle sources, before this issue can be resolved.

Upper Mantle Peridotite Source Component

The geochemical and isotopic association occurring between MORB compositions and some primitive IAB, particularly low LILE/LREE Aleutian, New Britain, Ambae HTS, and Futuna compositions (see Figs. 8.11 & 8.12, and Chapter 7), provides evidence for the domination of some IAB magma sources by upper mantle peridotite protoliths.

8.9 TOWARD A FRAMEWORK FOR MAGMAGENESIS IN THE VANUATU ARC

A strong case has been made above for the origin of Vanuatu primary magmas by partial melting of peridotite at high pressure (probably within a range between 2.0 and 4.0 GPa) and high temperature (ranging from 1300 to 1500°C, depending on possible dissolved volatile contents up to several wt%). Models for the thermal structure of subduction zones show that these conditions exist only in the core of the mantle wedge, where warm mantle is entrained by the slab-drag-induced counterflow (Fig. 8.14). It is conceivable that partial melting may result from peridotite decompression in this flow regime. However, unless the subduction environment is characterised by very thin lithosphere or anomalously hot mantle is present (factors promoting melting in the case of MORB and OIB), the dry peridotite solidus is unlikely to be exceeded. On the other hand, the presence of small volatile fractions will promote melting at temperatures below the dry solidus of peridotite. This is in keeping with the recognition of elevated but generally small (<2-3 wt%) volatile contents in IAB (e.g. Gill, 1981; Tatsumi et al., 1983).

An obvious source for excess volatiles in IAV is dehydration reactions occurring in the subducted ocean crust, though oxidation of reduced mantle fluid species in and around subduction zones may also be an important source (Green et al., 1987). The diversity of potential hydrous phases present in the subducting slab, combined with their

widely varying stability limits and the geothermal gradient range likely to exist in subduction zones, means that fluid may be generated over a wide range of PT conditions within subduction environments. In a detailed consideration of possible reactions, Tatsumi (1989) has concluded that the pressure sensitive dehydration of amphibole within the subducting slab, and also the mantle wedge, is likely to be the principal source of fluids found in arc magmas, and that breakdown of phlogopite at even deeper levels may provide an additional source. There is, however, further need to consider the link between the evolution of fluids at subsolidus conditions (i.e. <1000°C) and their presence in high temperature magmas (>1300°) formed in the hot mantle wedge core.

The migration of volatile species within subduction zones will be controlled by the movement of hydrated materials through hydrous phase stability limits, and also by physical forces influencing the flow of evolved free fluid/melt phases. Considering the amphibole breakdown reaction in isolation, as an example, the slab and slab-drag motions in the mantle wedge will result in a front of amphibole dehydration/formation reactions as fluid is released, migrates, reforms amphibole, and is ultimately focused toward the volatile undersaturated/saturated solidus corresponding to the PT maximum of amphibole stability, as shown schematically in Figure 8.14. Available seismic evidence and thermal structure models for subduction zones indicate that incipient melting is most likely to occur in the mantle wedge (Tatsumi, 1989), however, if sufficiently warm conditions exist within the slab, it also may pass through the amphibole dehydration solidus.

The low temperature at which melt is generated by amphibole breakdown (~1100°C) still does not correspond to the higher temperatures at which the Vanuatu Arc primary melts have been derived from the mantle wedge peridotite. Diapiric ascent of cool, incipiently molten peridotite into the hotter overlying mantle wedge (e.g. Tatsumi, 1989) may satisfy this shortcoming if heat transfer constraints are met. In the Vanuatu case, however, diapir initiation at depths exceeding those of primary melt generation (i.e >2 to 4 GPa) is not a realistic option given that the maximum pressure limit for amphibole stability is ~3 GPa. Dynamic models accounting for non-hydrostatic forces exerted on fluid or melt present in subduction zones, reveal that more complex mechanisms of melt migration are likely to occur beneath island arcs (Spiegelman and McKenzie, 1986). These models

Figure 8.14 Schematic presentation of a cross-section through the mantle source region of the Vanuatu Arc, illustrating key elements in the generation of primary magmas. A hot mantle wedge core overlies a steeply inclined subducting slab; the possible source of both distinctive incompatible element enrichments observed in the Vanuatu Arc. One enriching agent is an LILE and Pb-rich fluid phase (marked F and f) released from dehydration reactions in the cool subducting slab (amphibole dehydration marked A). The other has characteristics consistent with a small melt fraction generated in the presence of a HFSE-bearing phase (titanate?). The latter enriching agent may be generated at deeper levels though the breakdown of phlogopite (marked P; e.g. Tatsumi, 1989). These fluid and melt phases are drawn toward the mantle wedge core (solid arrows) by non-hydrostatic pressure gradients related to the counterflow (hollow arrows) predicted to occur in the sub-arc mantle wedge (e.g. Spiegelman and McKenzie, 1987). The addition of these enriching agents to the mantle wedge is probably instrumental in lowering the peridotite solidus there. The wedge itself is variably depleted in basaltic components, due to either previous melt extraction in the arc environment (i.e. recycling of arc source diapirs by the mantle counterflow), or entrainment of refractory material, residual after MORB generation beneath the North Fiji Basin. Isotherms are drawn as solid lines, and mantle convection streamlines are marked by dotted lines.

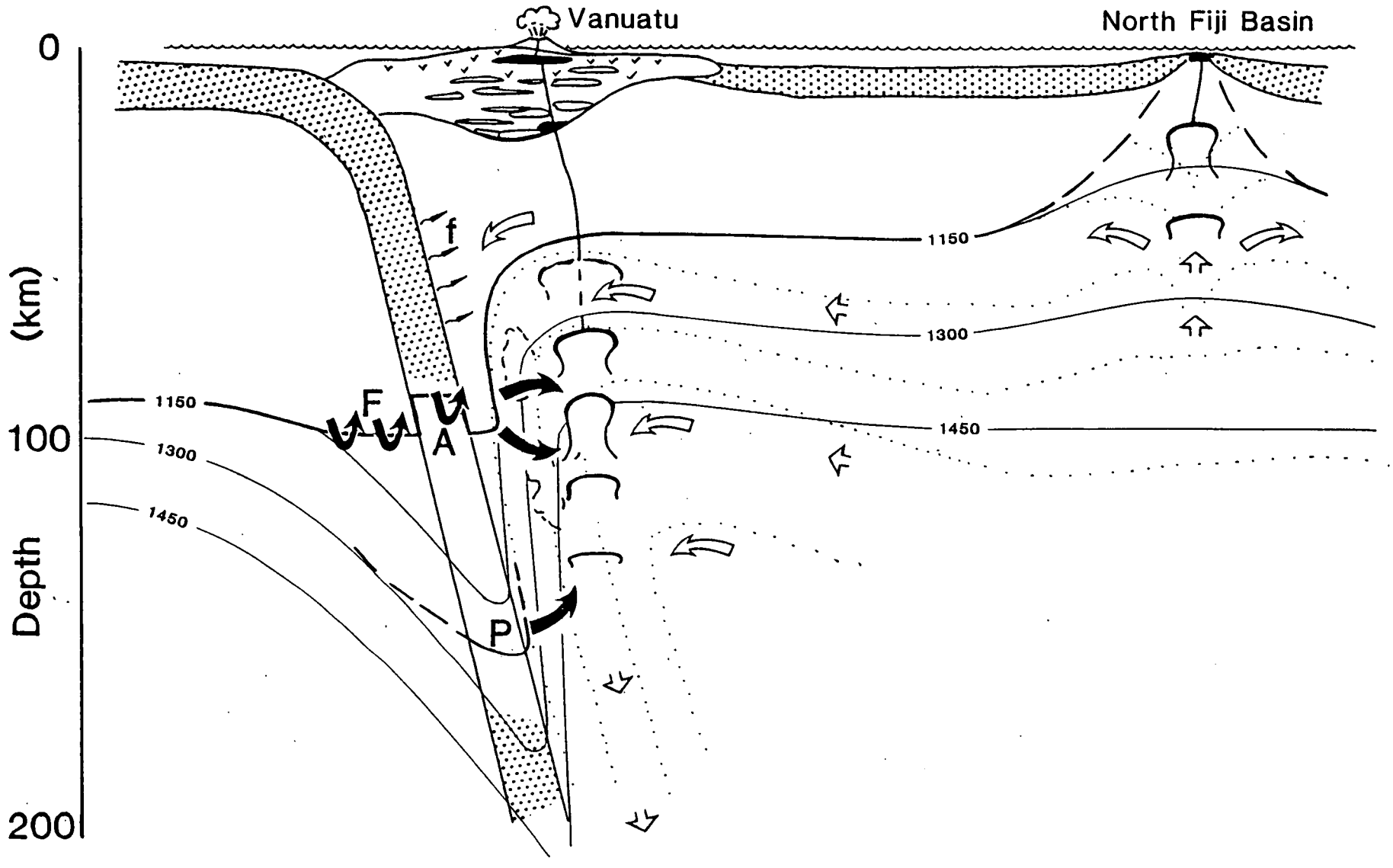
Vanuatu
North Fiji Basin
0
100
200
Depth
(km)
1150
1300
1450
f
F
A
P

demonstrate that free melt or fluid phases are not driven by buoyant percolation alone, but rather tend to be drawn toward the axis of the mantle counterflow, in a manner similar to that shown in Figure 8.14. Consequently, fluid or melt phases generated over a range of conditions within subduction zones are likely to be directed toward the hotter core of the mantle wedge. Diapiric ascent of destabilised partially molten regions of the mantle wedge could also play an important role in melt generation (e.g. Davies and Steyenson, 1988). Within this framework lies considerable scope for the interaction of fluid and/or melt components deriving from within the subduction environment. The sub-arc mantle wedge becomes, in effect, a staging (and mixing) point for these agents, which result in depression of the solidus and generation of high temperature primary arc magmas.

The geochemical systematics of the Vanuatu Arc magmas reveal the dominance of two geochemically distinct components, neither of which can be reconciled with a mantle wedge peridotite protolith. On the basis of dehydration reactions occurring in the subducting slab and element solubilites in supercritical fluids, the incompatible element-poor but LILE and Pb enriched source component is assigned to enrichments caused by aqueous fluids released from the subducting slab. From the similarity occurring between LILE ratios in the island arc tholeiites which are representative of this end-member (e.g. Merelava, Tongan tholeiites), and the element partitioning characteristics of amphibole (e.g. Ewart and Hawkesworth, 1988; this study), it is proposed that this fluid derives principally from the subsolidus breakdown of amphibole. The LILE and LREE-rich, HFSE-depleted end-member, on the other hand, may be interpreted to reflect enrichment by a small silicate melt fraction, possibly generated in the presence of a residual titanate phase. The enrichment in K and Rb over other LILE in IAB forming this end-member, may result from melting of a mica-bearing source, probably at higher pressures than the generation of LILE-enriched fluids. This proposal receives some support from the observation that the most incompatible element-rich (high-K) Vanuatu parent compositions appear to originate at higher pressures (~3-4 GPa) than the low K, LILE-enriched, parent compositions (~2-3GPa; see Fig. 8.3). Finally, given that conditions conducive to the formation of a carbonatite melt phase (high fO_2, low T; Wallace and Green, 1988) probably exist in subduction environments, the possibility that such a melt

phase may be responsible for the incompatible element enrichments observed in some IAB warrants future consideration.

8.9.1 The Role of Refractory Source Peridotite

The requirement for a refractory, incompatible element-depleted source, appears necessary to account for the low abundances of REE and HFSE in the Vanuatu parent compositions and other primitive IAB magmas (Figs. 8.5a&b). Several possibilities within the framework for magmagenesis outlined above may account for such source material. A simple explanation, using Figure 8.14 as a guide, is that (1) mantle, geochemically-depleted after melt extraction beneath back-arc spreading centres, is entrained into the arc source region by the mantle counterflow. Alternatively, and possibly in conjunction with (1), is that (2) the residues from partially molten diapirs rising beneath the arc, are also recycled back into the unstable diapir source regions as a result of the counterflow. On the other hand, if relatively undepleted mantle (i.e. MORB or even OIB source peridotite) is entrained into the arc magma source region, it will be less susceptible to geochemical modification by introduced incompatible element-rich agents. In the Vanuatu case, for example, it is proposed that relatively fertile MORB source material, equivalent to that from which the North Fiji Basin basalts are generated, provides the protolith for the Ambae HTS and Futuna magmas.

8.10 CONCLUSIONS

1. Vanuatu Arc magmas can be traced to highly magnesian parent compositions ($Mg^{\#}$ 75-82) from the primitive olivine and clinopyroxene phenocryst assemblages present in many lava suites. If primary, these melt compositions are likely to be generated by melting of peridotite in the mantle wedge at pressures between ~2 and ~4 GPa.

2. Two distinct geochemical components account for much of the incompatible element geochemical variation occurring in Vanuatu Arc parent compositions. These two components separately provide the diagnostic enrichments of LILE over LREE, and depletion of HFSE relative to LREE, which are characteristic of Vanuatu Arc and other island arc magmas. These enrichments may be assigned to (1) an LILE and Pb-rich fluid phase deriving mainly from subsolidus breakdown of amphibole in

the subducting oceanic lithosphere, and (2) an incompatible element- (LREE and LILE) rich, but HFSE-poor component, possibly a small melt fraction (carbonatitic?) generated in the presence of a residual HFSE bearing phase.

3. A third source component, consistent with the geochemical character of the upper mantle peridotite (N-MORB) source of the North Fiji Basin basalts, can be recognised in the Ambae HTS and Futuna parent compositions which are geochemically intermediate between the Vanuatu Arc and North Fiji Basin basalts. The fertile nature of this source component relative to peridotite protoliths elsewhere in the Vanuatu Arc, may make it less susceptible to the LILE and LREE enrichments affecting the Vanuatu Arc source region.

4. The very low HFSE and HREE, and sometimes also LREE, abundances (0.2-0.5x N-MORB) in many Vanuatu Arc parent compositions (Ambae HTS and Futuna excluded) are explained if melting involves a refractory incompatible element-poor source depleted by previous episodes of melt extraction. The presence of this refractory source material is also consistent with the highly magnesian olivine and clinopyroxene, and accessory Cr-rich (high $Cr^{\#}$) spinels, that are present in virtually all Vanuatu Arc basalt suites. The incorporation into the Vanuatu Arc source of peridotite residual after MORB extraction beneath the North Fiji Basin, and/or residual mantle recycled within the mantle wedge as part of the sub-arc mantle counterflow, may provide this depleted protolith.

5. Incompatible element systematics occurring in the Vanuatu Arc are mimicked by geochemical variation occurring in the global population of primitive IAB. These systematics may be largely accounted for by the addition of two enriched components (an LILE- and Pb-rich fluid phase, and an incompatible element-rich but HFSE depleted melt phase?) to peridotitic upper mantle sources and residues. The association between the melt phase enrichment characteristics and radiogenic Sr and unradiogenic Nd isotopes, indicates sampling of a long-lived incompatible element enriched reservoir, either pre-existing in the sub-arc mantle (OIB source?), or added as part of the subduction process (sediment?). In contrast, the fluid phase enrichments are associated with a long-term depleted mantle

isotopic signature, indicating this enriching agent is not derived from subducted sediment or the seawater altered part of the ocean crust.

References

Aggrey, K.E., Muenow, D.W., and Sinton, J.M., 1988. Volatile abundances in submarine glasses from the North Fiji and Lau back-arc basins. *Geochim. Cosmochim. Acta*, **52**, 2501-2506.

Albarede, F., 1983. Inversion of batch melting equations and the trace element pattern of the mantle. *J. Geophys. Res.*, **88**, 10573-10583.

Albarede, F., and Tamagnan, V., 1988. Modelling the recent geochemical evolution of the Piton de la Fournaise volcano, Reunion Island, 1931-1986. *J. Petrology*, **29**, 997-1030.

Anderson, A.T., 1974. Evidence for picritic, volatile-rich magma beneath Mt.Shasta, California. *J. Petrology*, **15**, 243-267.

Arculus, R.A., 1978. Mineralogy and petrology of Grenada, Lesser Antilles island arc. *Contrib. Mineral. Petrol.*, **65**, 413-424.

Arculus, R.J., and Johnson, R.W., 1981. Island arc magma sources: A geochemical assessment of the roles of slab-derived components and crustal contamination. *Geochem. Journal*, **15**, 109-133.

Arculus, R.J., and Wills, K.J.A., 1980. The Petrology of plutonic blocks and inclusions from the Lesser Antilles island arc. *J. Petrology*, **21**, 743-799.

Arculus, R.J., and Powell, R., 1986. Source component mixing in the regions of arc magma generation. *J. Geophys. Res.*, **91**, 5913-5926.

Ash, R.P., Carney, J.N., and MacFarlane, A., 1978. Geology of Efate and offshore islands. *Regional Report of the New Hebrides Govt. Geol. Survey*, 49pp.

Ash, R.P., Carney, J.N., and MacFarlane, A., 1980. Geology of the northern Banks Islands. *Regional Report of the New Hebrides Govt. Geol. Survey*, 52pp.

Auzende, J-M., Lafoy, Y., and Marsset, B., 1988. Recent geodynamic evolution of the North Fiji Basin (southwest Pacific). *Geology*, **16**, 925-929.

Barsdell, M., 1980. Petrological variation in the Banks Islands New Hebrides. Unpublished PhD Thesis, University of Auckland.

Barsdell, M., 1988. Petrology and petrogenesis of clinopyroxene-rich tholeiitic lavas, Merelava Volcano, Vanuatu. *J. Petrology*, **29**, 927-964.

Barsdell, M., Smith, I.E.M., and Sporli, K.B., 1982. The origin of reversed geochemical zoning in the northern New Hebrides volcanic arc. *Contrib. Mineral. Petrol.*, **81**, 148-155.

Barsdell, M., and Berry, R., (in press). The petrology and geochemistry of Western Epi. *J. Petrology*.

Basaltic Volcanism Study Project, 1981. Basaltic volcanism on the terrestrial planets. Pergamon Press, New York, 1286pp.

Ben Othman, D., White, W.M., and Patchett, J., (submt.). The geochemistry of marine sediments, island arc magmagenesis, and crust-mantle recycling. *Earth Planet. Sci. Lett.*

Bickle, M.J., Ford, C.E., and Nisbet, E.G., 1977. The petrogenesis of peridotitic komatiites: evidence from high-pressure melting experiments. *Earth Planet. Sci. Lett.*, **37**, 97-106.

Boespflug, X., Dosso, L., Bougault, H., Joron, J.L., and Calvez, J.Y., 1989. Back-arc basin evolution: a geochemical approach (trace elements and Sr-Nd-Pb isotopes). *Abstracts European Union of Geosciences*, **EUGV**, 335.

Brady, J.B., and McCallister, R.H., 1980. *Geol. Soc. Am. Abstr. Prog.*, (Atlanta), 391.

Brocher. T.M., 1985. On the formation of the Vitiaz trench lineament and the North Fiji Basin. In: Brocher, T.M. (Ed.), *Geological investigations of the Northern Melanesian Borderland, Circum Pacific Council for Energy and Mineral Resources*, Earth Science Series, **3**, 13-33.

Brophy, J.G., 1986. The Cold Bay volcanic center, Aleutian volcanic arc. I. Implications for the origin of hi-alumina arc basalts. *Contrib. Mineral. Petrol.*, **93**, 368-380.

Brophy, J.G., and Marsh, B.D., 1986. On the origin of high-alumina arc basalts and the mechanics of melt extraction. *J. Petrology*, **27**, 763-789.

Budahn, J.R., and Schmitt, R.A., 1985. Petrogenetic modeling of Hawaiian tholeiitic basalts: A geochemical approach. *Geochim. Cosmochim. Acta*, **49**, 67-87.

Buening, D.K., and Buseck, P.R., 1973. Fe-Mg lattice diffusion in olivine. *J. Geophys. Res.*, **78**, 6852-6862.

Cameron, W.E., 1985. Petrology and origin of primitive lavas from the Troodos ophiolite, Cyprus. *Contrib. Mineral. Petrol.*, **89**, 239-255.

Carlson, W.D., and Lindsley, D.H., 1988. Thermochemistry of pyroxenes on the join $Mg_2Si_2O_6$-$CaMgSi_2O_6$. *Amer. Mineral.*, **73**, 242-252.

Carmichael, I.S.E., 1989. Oxygen fugacities and redox states of magmas. *Abstr. IGU*, Washington, 1-240.

Carney, J.N., MacFarlane, A., and Mallick, D.I.J., 1985. The Vanuatu island arc: an outline of the stratigraphy, structure, and petrology. In: Nairn, A.E.M., Stehli, F.G., and Uyeda, S., (Eds.), *The Ocean Basins and Margins, Vol 7A.*, Plenum Publishing Corporation, 683-718.

Carney, J.N., and MacFarlane, A., 1979. Geology of Tanna, Aneityum, Futuna and Aniwa. *Regional Report of the New Hebrides Govt. Geol. Survey*, 71pp.

Carney, J.N., and MacFarlane, A., 1982. Geological evidence bearing on the Miocene to Recent structural evolution of the New Hebrides Arc, *Tectonophysics*, **87**, 147-175.

Casadevall, T.J., and Dzurisin, D., 1987. Stratigraphy and petrology of the Uwekahuna Bluff section, Kilauea Caldera. *USGS Prof. Paper*, **1350**, 351-376.

Chen, C-Y., and Frey, F.A., 1983. Origin of Hawaiian tholeiite and alkalic basalt. *Nature*, **302**, 785-789.

Chen, C-Y., and Frey, F.A., 1985. Trace element and isotopic geochemistry of lavas from Haleakala Volcano, East Maui, Hawaii: implications for the origin of Hawaiian basalts. *J. Geophys. Res.*, **90**, 8743-8768.

Clague, D.A., 1987. Hawaiian alkaline volcanism. In Fitton, J.G., and Upton, B.G.J., (Eds.), *Alkaline Igneous Rocks*, Geol. Soc. Spec. Pub., **30**, 227-252.

Clague, D.A., and Frey, F.A., 1982. Petrology and trace element geochemistry of the Honolulu Volcanics, Oahu: implications for the oceanic mantle below Hawaii. *J. Petrology*, **23**, 447-503.

Colley, H., and Ash, R.P., 1971. The geology of Erromango. *Regional Report of the New Hebrides Govt. Geol. Survey*, 112pp.

Collot, J.Y., Daniel, J., and Burne, R.V., 1985. Recent tectonics associated with the subduction/collision of the d'Entrecasteaux Zone in the central New Hebrides. *Tectonophysics*, **112**, 325-356.

Conrad, W.K., and Kay, R.W., 1984. Ultramafic and mafic inclusions from Adak Island: crystallization history, and implications for the nature of primary magmas and crustal evolution in the Aleutian Arc. *J. Petrology*, **25**, 88-125.

Crank, J., 1975. The mathematics of diffusion. Oxford University Press, 414pp.

Crawford, A.J., Greene, H.G., and Exon, N.F., 1988. Geology, petrology and geochemistry of submarine volcanoes around Epi island, New Hebrides island arc. In: Greene, H.G., and Wong, F.L., (Eds.), *Geology and offshore resources of Pacific islands arcs- Vanuatu region, Circum-Pacific Council for Energy and Mineral Resources, Earth Science Series*, **8**, 301-327

Crawford, A.J., Falloon, T.J., and Eggins, S., 1987. The origin of island arc high-alumina basalts. *Contrib. Mineral. Petrol.*, **97**, 417-430.

Crawford, A.J., Falloon, T.J., and Green, D.H., 1989. Classification, petrogenesis and tectonic setting of boninites. *In Boninites and related rocks*, Ed. A.J. Crawford, Unwin Hyman, London, 465pp.

Dalrymple, G.B., Lanphere, M.A., and Clague, D.A., 1980. Conventional and $^{40}Ar/^{39}Ar$ K-Ar ages of volcanic rocks from Ojin (site 430), Nintoku (site 432), and Suiko (site 433) seamounts and the chronology of volcanic propogation along the Hawaiian-Emperor chain. *Inital Rep. Deep Sea Drill. Proj.*, **55**, 659-676.

Daniel, J., Jouannic, C., Larue, B., and Recy, J., 1977. Interpretation of the d'Entrecasteaux Zone (North of New Caledonia). *Int. Symp. on Geodynamics in the South-West Pacific*, Noumea 1976, Technip, Paris, 117-124.

Davidson, J.P., 1987. Crustal contamination versus subduction zone enrichment: examples from the Lesser Antilles and implications for mantle source compositions of island arc volcanic rocks. *Geochim. Cosmochim. Acta*, **51**, 2185-2198.

Davies, J.H., and Stevenson, D.J., 1988. Flow direction of mantle in subduction zone wedge. *Abstr. Am. Geophys. Union*, **69**, No. 44, 1439.

Debari, S.M., Kay, S.M., and Kay, R.W., 1987. Ultramafic xenoliths from Adagdak Volcano, Adak, Aleutian Islands, Alaska: deformed igneous cumulates from the Moho of an island arc, *J. Geology*, **95**, 329-341.

Debari, S.M, and Coleman, R.G., 1989. Examination of the deep levels of an island arc: evidence from the Tonsina ultramafic-mafic assemblage, Tonsina, Alaska. *J. Geophys. Res.*, **94**, 4373-4391.

Detrick, R.S., and Crough, S.T., 1978. Island subsidence, hot spots, and lithospheric thinning. *J. Geophys Res.*, **83**, 1236-1246.

Dick, H.J.B., and Bullen, T., 1984. Chromian spinel as petrogenetic inidicator in abyssal and alpine-type peridotites and spatially associated lavas. *Contrib. Mineral. Petrol.*, **86**, 54-76.

Dodson, M.H., 1973. Closure temperature on cooling geochronological and petrological systems. *Contrib. Mineral. Petrol.*, **40**, 259-274.

Dostal, J., Dupuy, C., Carron, J.P., Le Guen De Kerneizon, M., and Maury, R.C., 1983. Partition coefficients of trace elements: application to volcanic rocks of St. Vincent, West Indies. *Geochim. Cosmochim. Acta*, **47**, 525-533.

Dubois, J., Lauray, J., Recy, J., and Marshall, J., 1977. New Hebrides Trench: subduction rate from associated lithosphere bulge. *Can. J. Earth Sci.*, **14**, 250-255.

Dubois, J., Dugas, F., Lapouille, A., and Louat, R., 1978. The troughs at the rear of the New Hebrides island arc: possible mechanisms of formation. *Can. J. Earth Sci.*, **15**, 351-360.

Duke, J.M., 1976. Distribution of the period four transition elements among olivine, calcic clinopyroxene and mafic silicate liquid: experimental results. *J. Petrology*, **17**, 499-521.

Duncan, A.R., Erlank, A.J., and Marsh, J.S., 1984. Regional geochemistry of the Karoo igneous province. *Spec. Publ. Geol. Soc. S. Afr.*, **13**, 355-388.

Duncan. R.A., and Green, D.H., 1987. The genesis of refractory melts in the formation of oceanic crust. *Contrib. Mineral. Petrol.*, **96**, 326-342.

Dupuy, C., Dostal, J., Marcelot, G., Bougault, H., Joron, J.L., and Treuil, M., 1982. Geochemistry of basalts from central and southern New Hebrides arc: implication for their source rock composition. *Earth Planet. Sci. Lett.*, **60**, 207-225.

Eaton, J.P., 1962. Crustal structure and volcanism in Hawaii. In: MacDonald, G.A., and Kuno, H., (Eds.), *The crust of the Pacific Basin., Geophys. Monogr.* Ser. 6., AGU Washington DC, pp13-29.

Ellam, R.M., and Hawkesworth, C.J., 1988. Elemental and isotopic variation in subduction related basalts: evidence for a three component model. *Contrib. Mineral. Petrol.*, **98**, 72-80.

Ewart, A., Brothers, R.N., and Mateen, A., 1977. An outline of the geology and geochemistry, and the possible petrogenetic evolution of the volcanic rocks of the Tonga-Kermadec-New Zealand island arc. *J. Volc. Geotherm. Res.*, **2**, 205-250.

Ewart, A., and Hawkesworth, C.J., 1987. The Pleistocene-Recent Tonga-Kermadec Arc lavas: interpretation of new isotopic and rare earth data in terms of a depleted mantle source. *J. Petrology*, **28**, 495-530.

Ewart, A.E., Chappell, B.W., and Menzies, M.A., 1988. An overview of the geochemical and isotopic characteristics of the eastern Australian Cainozoic volcanic provinces. *J. Petrology*, Special Lithosphere Issue, 225-273.

Falloon, T.J., and Green, D.H., 1988. Glass inclusions in magnesian olivine phenocrysts from Tonga: evidence for highly refractory parental magmas in the Tongan Arc. *Earth Planet. Sci. Lett.*, **81**, 95-103.

Falloon, T.J., and Green, D.H., 1988. Anhydrous partial melting of peridotite from 8 to 35 kbars and the Petrogenesis of MORB. *J. Petrology*, Special Lithosphere Issue, 379-414.

Falloon, T.J., Green, D.H., Hatton, C.J., and Harris, K.L., 1988. Anhydrous partial melting of a fertile and depleted peridotite from 2 to 30 kbars and application to basalt petrogenesis. *J. Petrology*, **29**, 1257-1282.

Falvey, D.A., 1978. Analysis of palaeomagnetic data from the New Hebrides: *Aust. Soc. Expl. Geophys. Bull.*, **9**, 117-123.

Feigenson, M.D., 1984. Geochemistry of Kauai volcanics and a mixing model for the origin of Hawaiian alkali basalts. *Contrib. Mineral. Petrol.*, **87**, 109-119.

Feigenson, M.D., 1986. Constraints on the origin of Hawaiian lavas. *J. Geophys. Res.*, **91**, 9383-9393.

Feigenson, M.D., Hofmann, A.W., and Spera, F.J., 1983. Case studies on the origin of basalt II. The transition from tholeiitic to alkalic volcanism on Kohala volcano Hawaii. *Contrib. Mineral. Petrol.*, **84**, 390-405.

Fiske, M.R., Upton, B.G.J., Ford, C.E., and White, W.M., 1988. Geochemical and experimental study of the genesis of magmas of Reunion Island, Indian ocean. *J. Geophys. Res.*, **93**, 4933-4950.

Foden, J.D., 1983. The petrology of the calc-alkaline lavas of Rindjani Volcano, East sunda Arc: a model for island arc petrogenesis. *J. Petrology*, **24**, 98-130.

Fodor, R.V., Keil, K., and Bunch, T.E., 1977. Contributions to the mineral chemistry of Hawaiian rocks. VI. Olivines in rocks from the Haleakala and West Maui Volcanoes, Maui, Hawaii. *Pacific Science*, **31**, 299-308.

Freer, R., 1981. Diffusion in silicate minerals and glasses: a data digest and guide to the literature. *Contrib. Mineral. Petrol.*, **76**, 440-454.

Freer, R., and O'Reilly, W., 1980. The diffusion of Fe^{2+} ions in spinels with relevance to the process of maghemization. *Mineral. Mag.*, **43**, 889-899.

Frey, F.A., and Clague, D.A., 1983. Geochemistry of diverse basalt types from Loihi Seamount Hawaii: petrogenetic implications. *Earth Planet. Sci. Lett.* **66**, 337-355.

Frey, F.A., Green, D.H., and Roy, S.D., 1978. Integrated models of basalt petrogenesis: A study of quartz tholeiites to olivine melilitites from south eastern Australia utilizing geochemical and experimental petrological data. *J. Petrology*, **19**, 463-513.

Frey, F.A., and Roden, M.F., 1987. The mantle source for the Hawaiian islands: constraints from the lavas and ultramaafic inclusions. In: Menzies, M.A., and

Hawkesworth, C.J., (Eds.), *Mantle Metasomatism*, Academic, London, pp423-463.

Fujimaki, H., 1986. Fractional crystallization of the basaltic suite of Usu volcano, southwest Hokkaido, Japan, and its relationships with the associated felsic suite. *Lithos*, **19**, 129-140.

Fujimaki, H., Tatsumoto, M., and Aoki, K., 1984. Partition coefficients of Hf, Zr, and REE between phenocrysts and groundmasses. *J. Geophys. Res.*, **89**, 662-672.

Galer, S.J.G., and O'Nions, R.K., 1986. Magmagenesis and the mapping of chemical and isotopic variations in the mantle. *Chem. Geol.*, **56**, 45-61.

Gill, J.B., 1978. Role of trace element partition coefficients in models of andesite genesis. *Geochim. Cosmochim. Acta*, **42**, 709-724.

Gill, J.B., 1981. Orogenic Andesites and Plate Tectonics. Springer, Berlin Heidelberg New York, 390pp.

Glasby, G.P., Gwozdz, R., Kunzendorf, H., Friedrich, G., and Thijssen, T., 1987. The distribution of rare earth and minor elements in manganese nodules and sediments from the equatorial and S.W. Pacific. *Lithos*, **20**, 97-113.

Ghiorso, M.S., and Carmichael, I.S.E., 1987. Modeling magmatic systems: petrologic application. *Reviews in Mineralogy*, **17**, 467-499.

Gorton, M.P., 1974. The geochemistry and geochronology of the New Hebrides. Unpublished PhD Thesis, Australian National University.

Gorton., M.P., 1977. The geochemistry and origin of Quaternary volcanism in the New Hebrides. *Geochim. Cosmochim. Acta*, **41**, 1257-1270.

Graham, I.J., and Hackett, W.R., 1987. Petrology of calc-alkaline lavas from Ruapehu volcano and related vents, Taupo Volcanic Zone, New Zealand. *J. Petrology*, **28**, 531-567.

Green, D.H., 1970. The origin of basaltic and nephelinitic magmas. *Trans. Leicester Lit. Philos. Soc.*, **64**, 28-59.

Green, D.H., 1971. Compositions of basaltic magmas as indicators of their conditions of origin: application to oceanic volcanism. *Phil. Trans. Roy. Soc. Lond.*, **268**, 707-725.

Green, D.H., 1974. Conditions of melting of basanite magma from garnet peridotite. *Earth Planet. Sci. Lett.*, **17**, 456-465.

Green, D.H., and Ringwood, A.E., 1967a. The genesis of basaltic magmas. *Contrib. Mineral. Petrol.*, **15**, 103-190.

Green, D.H., and Ringwood, A.E., 1967b. The stability fields of aluminous pyroxene peridotite and garnet peridotite and their relevance in upper mantle structure. *Earth Planet. Sci. Lett.*, **3**, 151-160.

Green, D.H., and Liebermann, R.C., 1976. Phase equilibria and elastic properties of a pyrolite model for the oceanic upper mantle. *Tectonophysics*, **32**, 61-92.

Green, D.H., Hibberson, W.O., and Jacques, A.L., 1979. Petrogenesis of mid-ocean ridge basalts. In: McElhinny, M.W. (Ed.), *The Earth: Its Origin, Structure and Evolution*, Academic, New York, 265-299.

Green, D.H., Falloon, T.J., and Taylor, W.R., 1987. Mantle-derived magmas-roles of variable source peridotite and variable C-H-O fluid compositions. In: Mysen, B.O., (Ed.), *Magmatic processes: physiochemical principles*, The geochemical Society, Special Publication No. 1, 139-154.

Green, D.H., and Wallace, M.E., 1988. Mantle metasomatism by ephemeral carbonatite melts. *Nature*, **336**, 459-462.

Green, T.H., and Pearson, N.J., 1985. Rare earth element partitioning between clinopyroxene and silicate liquid at moderate to high pressure. *Contrib. Mineral. Petrol.* **91**, 24-36.

Green, T.H., and Pearson, N.J., 1986. Ti-rich accessory phase saturation in hydrous mafic-felsic compositions at high P,T. *Chem. Geol.*, **54**, 185-201.

Greenland, L.P., 1988. Gases from the 1983-84 East-rift eruption. *USGS Prof. Paper*, **1463**, 145-153.

Griffiths, R.W., 1986. The differing effects of compositional and thermal buoyancies on the evolution of mantle diapirs. *Phys. Earth Planet. Int.*, **43**, 261-273.

Grove, T.L., and Bryan, W.B., 1983. Fractionation of pyroxene-phyric MORB at low pressure: an experimental study. *Contrib. Mineral. Petrol.*, **84**, 293-309.

Gunn, B.M., 1971. Trace element partitiong during olivine fractionation of Hawaiian basalts. *Chem. Geol.*, **8**, 1-13.

Gust, D.A., and Perfit, M.R., 1987. Phase relations of a high-Mg basalt from the Aleutian Island Arc: implications for primary island arc basalts and high-Al basalts. *Contrib. Mineral. Petrol.*, **97**, 7-18.

Hart, S.R., 1984. A large scale isotopic anomaly in the Southern Hemisphere mantle. *Nature*, **309**, 753-757.

Hart, S.R., 1988. Heterogeneous mantle domains: signatures, genesis and mixing chronologies. *Earth Planet. Sci Lett.*, **90**, 273-296.

Hart, S.R., and Davis, K.E., 1978. Nickel partitioning between olivine and silicate melt. *Earth Planet. Sci. Lett.*, **40**, 203-219.

Hart, S.R., Gerlach, D.C., and White, W.M., 1986. A possible new Sr-Nd-Pb mantle array and consequences for mantle mixing. *Geochim. Cosmochim. Acta*, **50**, 1551-1557.

Hawkesworth.,C.J., O'nions, R.K., Pankhurst, R.J., Hamilton, P.J., and Evensen, N.M., 1977. A geochemical study of island-arc and back-arc tholeiites from the Scotia sea. *Earth Planet. Sci. Lett.*, **36**, 253-262.

Hawkesworth, C.J., O'nions, R.K., and Arculus, R.J., 1979. Nd and Sr isotope geochemistry of island arc volcanics, Grenada, Lesser Antilles. *Earth Planet. Sci Lett.*, **45**, 237-248.

Hawkesworth, C.J., Mantovani, M.S.M., Taylor, P.N., and Palacz, Z., 1986. Evidence from the Parana of south Brazil for a continental contribution to Dupal basalts. *Nature*, **322**, 356-359.

Hawkesworth, C.J., Van Calsteren, P., Rogers, N.W., and Menzies, M.A., 1987. Isotope variations in recent volcanics: a trace-element perspective. In: Menzies, M.A., and Hawkesworth, C.J. (Eds.) *Mantle Metasomatism.* London: Academic Press, 365-388.

Hawkesworth, C., and Ellam, R., 1989. Chemical fluxes and wedge replenishment rates along recent destructive plate margins. *Geology*, **17**, 46-49.

Hawkins, J., and Melchior, J., 1983. Petrology of basalts from Loihi Seamount, Hawaii. *Earth Planet. Sci. Lett.*, **66**, 356-368.

Helz, R.T., 1987. Diverse olivine types in lava of the 1959 eruption of Kilauea volcano and their bearing on eruption dynamics. *USGS Prof. Paper*, **1350**, 691-722.

van Heerden, L.A., and le Roex, A.P., 1988. Petrogenesis of picrite and associated basalts from the southern mid-Atlantic ridge. *Contrib. Mineral. Petrol.*, **100**, 47-60.

Ho, R.A., and Garcia, M.O., 1988. Origin of differentiated lavas at Kilauea Volcano, Hawaii: implications from the 1955 eruption. *Bull. Volc.*, **50**, 35-46.

Hofmann, A.W., 1988. Chemical differentiation of the Earth: the relationship between mantle, continental crust, and oceanic crust. *Earth Planet. Sci. Lett.*, **90**, 297-314.

Hofmann, A.W., and Feigenson, M.D., 1983. Case studies on the origin of basalt. I. Theory and reassessment of Grenada basalts. *Contrib. Mineral. Petrol.*, **84**, 382-389.

Hofmann, A.W., Feigenson, M.D., and Raczek, I., 1984. Case studies of the origin of basalt: III. The petrogenesis of the Mauna Ulu eruption, Kilauea, 1969-1971. *Contrib. Mineral. Petrol.*, **88**, 24-35.

Hofmann, A.W., Feigenson, M.D., and Raczek, I., 1987. Kohala revisited. *Contrib. Mineral. Petrol.*, **95**, 114-122.

Hole, M.J., Saunders, A.D., Marriner, G.F., and Tarney, J., 1984. Subduction of pelagic sediments: implications for the origin of Ce-anomalous basalts from the Mariana Islands. *J. Geol. Soc. London*, **141**, 453-472.

Holness, M.B., and Richter, F.M., 1989. Possible effects of spreading rate on MORB isotopic and rare earth composition arising from melting of a heterogeneous source. *J. Geology*, **97**, 247-260.

Hunter, R.H., and McKenzie, D., 1989. The equilibrium geometry of carbonate melts in rocks of mantle composition. *Earth Planet. Sci. Lett.*, **92**, 347-356.

Irvine, T.N., 1979. Rocks whose composition is determined by crystal accumulation and sorting. In HS Yoder Jnr. (Ed.) *The evolution of the igneous rocks: fiftieth anniversary perspectives*. Princeton Univ Press, Princeton. pp245-306.

Irvine, T.N., and Kushiro, I., 1976. Partitioning of Ni and Mg between olivine and silicate liquids. *Carnegie Inst. Washington Yrbk.*, **75**, 668-674.

Irving, A.J., and Frey, F.A., 1984. Trace element abundances in megacrysts and their host basalts: constraints on partition coefficients and megacryst genesis. *Geochim. Cosmochim. Acta*, **48**, 1201-1221.

Ito, K., and Kennedy, G.C., 1968. Melting and phase relations in the plane tholeiite-lherzolite-nepheline basanite to 40 kilobars with geological implications. *Contrib. Mineral. Petrol.*, **19**, 177-211.

Jacques, A.L., and Green, D.H., 1980. Anhydrous melting of peridotite at 0-15kb pressure and the genesis of tholeiite basalts. *Contrib. Mineral. Petrol.*, **73**, 287-310

Jagoutz, E., Palme, H., Buddenhausen, H., Blum, K., Cendales, M., Dreibus, G., Spettel, B., Lorenz, V., and Wanke, H., 1979. The abundance of the major and trace elements in the earth's mantle as derived from primitive ultramafic nodules. *Proc. 10th Lunar Planet. Sci. Conf.*, **2**, 2031-2050.

Johnson, R.W., Jaques, A.L., Hickey, R.L., McKee, C.O., and Chappell, B.W., 1985. Manam Island, Papua New Guinea: petrology and geochemistry of a low-TiO_2 basaltic island-arc volcano. *J. Petrology*, **26**, 283-323.

Jurewicz, A.J.G., and Watson, E.B., 1988. Cations in olivine, Part 2: diffusion in olivine xenocrysts, with applications to petrology and mineral physics. *Contrib. Mineral. Petrol.*, **99**, 186-201.

Katsui, Y., Oba, Y., Ando, S., Nishimura, S., Masuda, Y., Kurasawa, H., and Fujimaki, H., 1978. Petrochemistry of the Quarternary volcanic rocks of Hokkaido, North Japan. *J. Fac. Sci. Hokkaido Univ.*, Series IV, **18**, 449-484.

Kay, R.W., 1980. Volcanic arc magmas: implications of a melting-mixing model for element recycling in the crust-upper mantle system. *J. Geology*, **88**, 497-522.

Kay, R.W., and Kay, S.M., 1988. Crystal recycling and the Aleutian arc. *Geochim. Cosmochim. Acta*, **52**, 1351-1359.

Kilinc, A., Carmichael, I.S.E., Rivers, M.L., and Sack, R.O., 1983. The ferric-ferrous ratio of natural silicate liquids equilibrated in air. *Contrib. Mineral. Petrol.*, **83**, 136-140.

Klein, E.M., and Langmuir, C.H., 1987. Ocean ridge basalt chemistry, axial depth, crustal thickness and temperature variations in the mantle. *J. Geophys. Res.*, **92**, 8089-8115.

Klein, F.W., Earthquakes at Loihi submarine volcano and the Hawaiian hot spot. *J. Geophys. Res.*, **87**, 7719-7726.

Klein, F.W., Koyanagi, R.Y., Nakata, J.S., and Tanigawa, W.R., 1987. The seismicity of Kilauea's magma system. *USGS Prof. Paper*, **1350**, 1019-1186.

Kroenke, L.W., 1972. Geology of the Ontong Java Plateau. Unpublished PhD thesis, University of Hawaii, Honolulu.

Kroenke, L.W., 1984. Formation of the New Hebrides-Vitiaz arcs and the development of the North Fiji Basin. In: Kroenke L.W., Cenozoic development of the southwest Pacific. *U.N. ESCAP, CCOP/SOPAC*, **Tech. Bull. 6**, 63-75.

Kuno, H., and Aoki, K., 1970. Chemistry of ultramafic nodules and their bearing on the origin of basaltic magmas. *Phys. Earth Planet. Int.* **3**, 273-301.

Lanphere, M.A., and Frey, F.A., 1987. Geochemical evolution of Kohala Volcano, Hawaii. *Contrib. Mineral. Petrol.*, **95**, 100-113.

Leeman, W.P., and Scheidegger, K.F., 1977. Olivine/liquid distribution coefficients and a test for crystal-liquid equilibrium. *Earth Planet. Sci. Lett.*, **35**, 247-257.

LeMaitre, R.W., 1980. GENMIX - a generalized petrological mixing model program. *Comput. Geosci.* **7**, 229-247.

Liotard, J.M., Barsczus, H.G., Dupuy, C., and Dostal, J., 1986. Geochemistry and origin of basaltic lavas from Marquesas Archipelago, French Polynesia. *Contrib. Mineral. Petrol.*, **92**, 260-268.

Liu, M., and Chase, C.G., 1989. Evolution of midplate hotspot swells: numerical solutions. *J. Geophys. Res.*, **94**, 5571-5584.

Ludden, J.N., 1978. Magmatic evolution of the basaltic shield volcanoes of Reunion Island. *J. Volc. Geotherm. Res.*, **4**, 171-198.

Luhr, J.F., and Carmichael, I.S.E., 1985. Jorullo Volcano, Michoacan, Mexico (1759-1774): the earliest stages of fractionation in calc-alkaline magmas. *Contrib. Mineral. Petrol.*, **90**, 142-161.

Maaloe, S., 1979. Compositional range of primary tholeiite magmas evaluated from major-element trends. *Lithos* **12**, 59-72.

Maaloe, S., 1985. Principles of igneous petrology. Springer, Berlin Heidelberg New York Tokyo, 374pp.

Maaloe, S., and Aoki, K., 1977. The major element composition of the upper mantle estimated from the composition of lherzolites. *Contrib. Mineral. Petrol.*, **63**, 161-173.

Maaloe, S., and Hansen, B., 1982. Olivine phenocrysts of Hawaiian olivine tholeiite and oceanite. *Contrib. Mineral. Petrol.*, **81**, 203-211.

MacDonald, G.A., and Katsura, T., 1961. Variations in the lava of the 1959 eruption of Kilauea Iki, *J. Petrology*, **5**, 82-133.

MacGregor, I.D., 1964. The reaction 4 enstatite + spinel = forsterite + pyrope, *Carnegie Inst. Washington Yrbk.* **63**, 157.

Maillet, P., Monzier, M., Selo, M., and Storzer, D., 1983. The D'Entrecasteasux Zone (southwest Pacific). A petrological and geochronological reappraisal. *Marine Geol.*, **53**, 179-197.

Maillet, P., Monzier, M., and Lefevre, C., 1986. Petrology of Mathew and Hunter volcanoes, south New Hebrides island arc (southwest Pacific). *J. Volc. Geotherm. Res.*, **30**, 1-27.

Mallick, D.I.J., 1973. Some petrological and structural variations in the New Hebrides. In: Coleman, P.J., (Ed.), *The western Pacific: island arcs, marginal seas, and geochemistry,* University of Western Australia Press, 193-212.

Mallick, D.I.J., and Ash, R.P., 1975. Geology of the southern Banks Islands. *Regional Report New Hebrides Govt. Geol. Survey*, 33pp.

Marcelot, G., 1981. Geochimie des lavas de l'ile d'Erromango (Nouvelles-Hebrides): implications petrogenetiques. *Bull. Soc. geol. France*, **23**, 367-376.

Marcelot, G., Dupuy, C., Girod, M., and Maury, R.C., 1983. Petrology of Futuna island lavas (New Hebrides): an example of calc-akaline magmatism associated with the initial stages of back-arc spreading. *Chem. Geol.*, **38**, 23-37.

Marcelot, G., Maury, R.C., and Lefevre, C., 1983. Mineralogy of Erromango lavas (New Hebrides): evidence of an early stage of fractionation in island arc basalts. *Lithos*, **16**, 135-161.

Marsh, B.D., 1988. Crystal size distribution (CSD) in rocks and the kinetics and dynamics of crystallization. I. Theory. *Contrib. Mineral. Petrol.*, **99**, 277-291.

Masuda, Y., Nishimura, S., Ikeda, T., Katsui, Y., 1975. Rare -earth and trace elements in Quarternary volcanic rocks of Hokkaido, Japan. *Chem. Geol.*, **15**, 251-271.

Maurel, C., and Maurel, P., 1984. Etude experimentale de la distribution du fer ferrique entre spinelle chromifere et bain silicate basique. *Bull. Mineral.*, **107**, 25-33.

McCulloch, M.T., 1988. Nd-Sr isotope geochemistry of the Tasmantid Seamounts - evolution of a hotspot trace. *Geol. Soc. Aust. Abstr.*, **21**, 260-261.

McCulloch, M.T., and Perfit, M.R., 1981. $^{143}Nd/^{144}Nd$, $^{87}Sr/^{86}Sr$ and trace element constraints on the petrogenesis of Aleutian island arc magmas. *Earth Planet. Sci. Lett.*, **56**, 167-179.

McDonough, W.F., McCulloch, M.T., Sun, S.S., 1985. Isotopic and geochemical systematics in Tertiary-Recent basalts from southeastern Australia and implications for the evolution of the sub-continental lithosphere. *Geochim. Cosmochim. Acta*, **49**, 2051-2067.

McDougall, I., Embleton, B.J.J., and Stone, D.B., 1981. Origin and evolution of Lord Howe Island. *J. Geol. Soc. Aust.*, **28**, 155-176.

McDougall, I., and Duncan, R.A., 1988. Age progressive volcanism in the Tasmantid Seamounts. *Earth Planet. Sci. Lett.*, **89**, 207-220.

McKenzie, D., 1984. The generation and compaction of partially molten rock. *J. Petrology*, **25**, 713-765.

McKenzie, D., 1985a. ^{230}Th-^{238}U disequilibrium and the melting process beneath ridge axes. *Earth planet. Sci. Lett.* **72**, 149-157.

McKenzie, D., 1985b. The extraction of magma from the crust and mantle. *Earth Planet. Sci. Lett.*, **74**, 81-91.

McKenzie, D., and Bickle, M.J., 1988. The volume and composition of melt generated by extension of the lithosphere. *J. Petrology*, **29**, 625-679.

Melson, W.G., Jurosewick, E., and Lundquist, C.A., 1970. Volcanic eruption at Metis Shoal, Tonga, 1967-1958: description and petrology. *Smithsonian Contrib. Earth Sci.*, **No. 4.**

Michael, P.J., 1988. The concentration, behaviour and storage of H_2O in the suboceanic upper mantle: Implications for mantle metasomatism. *Geochim. Cosmochim. Acta*, **52**, 555-566.

Michael, P.J., and Chase, R.L., 1987. The influence of primary magma composition, H_2O and pressure on Mid-Ocean Ridge basalt differentiation. *Contrib. Mineral. Petrol.*, **96**, 245-263.

Minster, J.F., and Allegre, C.J., 1978. Systematic use of trace elements in igneous petrology. *Contrib. Mineral. Petrol.*, **68**, 37-52.

Miyashiro, A., 1974. Volcanic rock series in island arcs and active continental margins. *Am. J. Sci.*, **274**, 321-325.

Monjaret, M-C., 1989. Le magmatisme des fosse a l'arriere de l'arc Nouvelles Hebrides. Unpublished PhD Thesis, L'Universite de Bretagne Occidentale, pp273.

Morris, J.D., and Hart, S.R., 1983. Isotopic and incompatible element constraints on the genesis of island arc volcanics from Cold Bay and Amak Island, Aleutians, and implications for mantle structure. *Geochem. Cosmochim. Acta*, **47**, 2015-2030.

Morris, J.D., and Hart, S.R., 1986. Isotopic and incompatible element constraints on the genesis of island arc volcanics from Cold Bay and Amak Island, Aleutians, and implications for mantle structure: Reply to a critical comment by M.R. Perfit and R.W. Kay. *Geochim. Cosmochim. Acta*, **50**, 483-487.

Murata, K.J., and Richter, D.H., 1966. The settling of olivine in Kilauean magma as shown by lavas of the 1959 eruption. *Am. J. Science*, **264**, 194-203.

Murck, B.W., and Campbell, I.H., 1986. The effects of temperature, oxygen fugacity and melt composition on the behaviour of chromium in basic and ultrabasic melts. *Geochim. Cosmochim. Acta*, **50**, 1871-1887.

Mysen, B.O., and Kushiro, I., 1977. Compositional variations of coexisting phases with degree of melting of peridotite in the upper mantle. *Am. Mineral.*, **62**, 843-865.

Nicholls, I.A., and Ringwood, A.E., 1973. Effect of water on olivine stability in tholeiites and the production of silica-saturated magmas in the island-arc environment. *J. Geology*, **81**, 285-300.

Nicholls, I.A., and Harris, K.L., 1980. Experimental rare earth element partition coefficients for garnet, clinopyroxene and amphibole coexisting with andesitic and basaltic liquids. *Geochim. Cosmochim. Acta*, **44**, 287-308.

Nicholls, J., and Stout, M.Z., 1988. Picritic melts in Kilauea- evidence from the 1967-1968 Halemaumau and Hiiaka eruptions. *J. Petrology*, **29**, 1031-1057.

Norrish, K., and Hutton, J.T., 1969. An accurate X-ray spectrographic method for analysis of a wide range of geological samples. *Geochim. Cosmochim. Acta*, 33, 431-453.

Norrish, K., and Chappell, B.W., 1977. X-ray flourescence spectrometry. In: Zussman, J., (Ed.), *Physical Methods in Determinative Mineralogy*, 2nd Ed., Academic Press, London, 254-272.

Nye, C.J., and Reid, M.R., 1986. Geochemistry of primary and least fractionated lavas from Okmok Volcano, Central Aleutians: implications for arc magmagenesis. *J. Geophys. Res.*, **91**, 10271-10287.

Obata, M., 1976. The solubility of Al_2O_3 in orthopyroxenes in spinel and plagioclase peridotites and spinel pyroxenite. *Am. Mineral.*, **61**, 804-816.

O'Hara, M.J., 1968. The bearing of phase equilibrium studies in synthetic and natural systems on the origin of basic and ultrabasic rocks. *Earth Sci. Rev.*, **4**, 69-133.

O'Hara, M.J., 1977. Geochemical evolution during fractional crystallisation of a periodically refilled magma chamber. *Nature*, **266**, 503-507.

O'Hara, M.J., 1985. Importance of the "shape" of the melting regime during partial melting of the mantle. *Nature*, **314**, 58-62.

O'Hara, M.J., Richardson, S.W., and Wilson, G., 1971. Garnet-peridotite stability and occurrence in crust and mantle. *Contrib. Mineral. Petrol.*, **32**, 46-68.

O'Hara, M.J., and Mathews, R.E., 1981. Geochemical evolution in an advancing, periodically replenished, periodically tapped, continuously fractionated magma chamber. *J. Geol. Soc. London*, **138**, 237-277.

O'Neill, H.St-C., 1981. The transition between spinel lherzolite and garnet lherzolite, and its use as a geobarometer. *Contrib. Mineral. Petrol.*, **77**, 185-194.

O'Neill, H.St.C., and Wall, V.J., 1987. The olivine-orthopyroxene-spinel oxygen geobarometer, the nickel precipitation curve, and the oxygen fugacity of the Earth's upper mantle. *J. Petrology*, **28**, 1169-1191.

O'Reilly, S.Y., and Griffin, W.L., 1988. Mantle matasomatism beneath western Victoria, Australia: I. Metasomatic processes in Cr-diopside lherzolites. *Geochim. Cosmochim. Acta*, **52**, 433-447.

Ozawa, K., 1983. Evaluation of olivine-spinel geothermometry as an indicator of thermal history of peridotites. *Contrib. Mineral. Petrol.*, **82**, 52-65.

Ozawa, K., 1984. Olivine-spinel geospeedometry: analysis of diffusion-controlled Mg-Fe^{2+} exchange. *Geochim. Cosmochim. Acta*, **48**, 2597-2611.

Palacz, Z.A., and Saunders, A.D., 1986. Coupled trace element and isotope enrichment in the Cook-Austral-Samoa islands, southwest Pacific. *Earth Planet. Sci. Lett.*, **79**, 270-280.

Parrot, J.F., and Dugas, F., 1980. The disrupted ophiolitic belt of the southwestern Pacific: evidence of an Eocene subduction zone. *Tectonophysics*, **66**, 349-372.

Pascal, G., Isacks, B.L., Barazangi, M., and Dubois, J., 1978. Precise relocations of earthquakes and seismotectonics of the New Hebrides island arc. *J. Geophys. Res.*, **83**, 4957-4973.

Peccerillo, A., and Taylor, S.R., 1976. Geochemistry of Eocene calc-alkaline volcanic rocks from the Kastamanu area, northern Turkey. *Contrib. Mineral. petrol.*, **58**, 63-81.

Perfit, M.R., and Kay, R.W., 1986. Comment on "Isotopic and incompatible element constraints on the genesis of island arc volcanics from Cold Bay and Amak island, Aleutians, and implications for mantle structure" by J.D. Morris and S.R. Hart. *Geochim. Cosmochim. Acta*, **50**, 477-481.

Perfit, M.R., Gust, D.A., Bence, A.E., Arculus, R.J., and Taylor, S.R., 1980. Chemical characteristics of island-arc basalts: implications for mantle sources. *Chem. Geol.*, **30**, 227-256.

Price, R.C., Johnson, L.E., and Crawford, A.J.C., (in prep.). Petrology and geochemistry of North Fiji Basin basalts: the relationship between tectonic setting and rock chemistry and implications for the origin of back-arc basin magmas.

Ramsay, W.R.H., Crawford, A.J., and Foden, A.J., 1984. Field setting, mineralogy, chemistry, and genesis of arc picrites, New Georgia, Solomon Islands. *Contrib. Mineral. Petrol.*, **88**, 386-402.

Ribe, N.M., 1985. The deformation and compaction of partial molten zones. *Geophys. J. R. Astr. Soc.* **83**, 487-501.

Ribe, N.M., 1987. On the dynamics of mid-ocean ridges. *J. Geophys. Res.*, **93**, 429-436.

Ribe, N.M., 1987. Theory of melt segregation - A review. *J. Volc. Geotherm. Res.*, **33**, 241-253.

Ribe, N.M., 1988. Dynamical geochemistry of the Hawaiian plume. *Earth Planet. Sci. Lett.*, **88**, 37-46.

Ribe, N.M., and Smooke, M.D., 1987. A stagnation point flow model for melt extraction from a mantle plume. *J. Geophys. Res.*, **92**, 6437-6443.

Richardson, S.H., Erlank, A.J., Duncan, A.R., and Reid, D.L., 1982. Correlated Nd, Sr and Pb isotope variation in Walvis Ridge basalts and implications for the evolution of their mantle source. *Earth planet. Sci. Lett.*, **59**, 327-342.

Richter, F.M., 1986. Simple models for trace element fractionation during melt segregation. *Earth Planet. Sci. Lett.*, **77**, 333-344.

Richter, F.M., and McKenzie, D., 1984. Dynamical models for melt segregation from a deformable matrix. *J. Geology*, **92**, 729-740.

Robinson, P., Higgins, N.C., and Jenner, G.A., 1986. Determination of rare-earth elements, yttrium and scandium in rocks by an ion exchange-X-ray flourescence technique. *Chem. Geol.*, **55**, 121-137.

Roca, J.L., 1978. Contribution a l'etude petrologique et structurale des Nouvelles Hebrides. Unpublished PhD Thesis. University of Montpellier, 147pp.

Roden, M.F., Frey, F.A., and Clague, D.A., 1984. Geochemistry of tholeiitic and alkalic lavas from the Koolau Range, Oahu, Hawaii: implications for Hawaiian volcanism. *Earth Planet. Sci. Lett.*, **87**, 109-119.

Roeder, P.L., and Emslie, R.F., 1970. Olivine-liquid equilibrium. *Contrib. Mineral. Petrol.*, **29**, 275-289.

le Roex, A.P., Erlank, A.J., and Needham, H.D., 1981. Geochemical and mineralogical evidence for the occurrence of at least three distinct magma types in the "Famous" Region. *Contrib. Mineral. Petrol.*, **77**, 24-37.

Rogers, N.W., Hawkesworth, C.J., Mattey, D.P., and Harmon, R.S., 1987. Sediment subduction and the source of potassium in orogenic leucitites. *Geology*, **15**, 451-453.

Ryan, M.P., 1987. Elasticity and contractancy of Hawaiian olivine tholeiite and its role in the stability and structural evolution of subcaldera magma reservoirs and rift systems. *USGS Prof. Paper*, **1350**, 1395-1447.

Ryerson, F.J., and Watson, E.B., 1987. Rutile saturation in magmas: implications for Ti-Nb-Ta depletion in island arc basalts. *Earth Planet. Sci. Lett.*, **86**, 225-239.

Sack, R.O., Carmichael, I.S.E., Rivers, M., and Ghiorso, M.S., 1980. Ferric-ferrous equilibria in natural silicate liquids at 1 Bar. *Contrib. Mineral Petrol.*, **75**, 369-376.

Sack, R.O., Walker, D., and Carmichael, I.S.E., 1987. Experimental petrology of alkalic lavas: constraints on cotectics of multiple saturation in natural basic liquids. *Contrib. Mineral. Petrol.*, **96**, 1-23.

Sakuyama, M., and Nesbitt, R.W., 1986. Geochemistry of the Quarternary volcanic rocks of the northest Japan arc. *J. Volc. Geotherm. Res.*, **29**, 413-450.

Scott, D.R., and Stevenson, D.J., 1986. Magma ascent by porous flow. *J. Geophys. Res.*, **91**, 9283-9296.

Seitz, M.G., 1973. Uranium and thorium diffusion in diopside and flourapatite, *Carn. Inst. Wash. Yrbk.*, **72**, 586-588.

Sen., G, and Presnall, D.C., 1986. Petrogenesis of dunite xenoliths from Koolau volcano, Oahu, Hawaii: implications for Hawaiian volcanism. *J. Petrology*, **27**, 197-217.

Shaw, D.M., 1970. Trace element fractionation during anatexis. *Geochim. Cosmochim. Acta*, **34**, 237-243.

Shimizu, N., and Arculus, R.J., 1975. Rare earth element concentrations in a suite of basanitoids and alkali olivine basalts from Grenada, Lesser Antilles. *Contrib. Mineral. Petrol.*, **50**, 231-240.

Slater, R.A., and Goodwin, R.H., 1973. Tasman Sea guyots. *Mar. Geology*, **14**, 81-99.

Sleep, N.H., 1988. Tapping of melt by veins and dykes. *J. Geophys. Res.*, **93**, 10225-10272.

Spiegelman, M., and McKenzie, D., 1987. Simple 2-D models for melt extraction at mid-ocean ridges and island arcs. *Earth Planet. Sci. Lett.*, **83**, 137-152.

Stille, P., Unruth, D.M., and Tatsumoto, M., 1986. Pb, Sr, Nd, and Hf isotopic constraints on the origin of Hawaiian basalts and the evidence for a unique mantle source. *Geochim. Cosmochim. Acta.* **50**, 2303-2319.

Stolz. A.J., Varne, R., Wheller, G.E., Foden, J.D., and Abbott, M.J., 1988. The geochemistry and petrogenesis of K-rich alkaline volcanics from the Batu Tara volcano, eastern Sunda arc. *Contrib. Mineral. Petrol.*, **98**, 374-389.

Sun, S-s., 1980. Lead isotopic study of young volcanic rocks from mid-ocean ridges, ocean islands and island arcs. *Phil. Trans. R. Soc. Lond.*, **297**, 409-445.

Sun, S-s., and McDonough, W.F. 1988. Chemical and isotopic systematics of oceanic basalts: implications for mantle composition and processes. In: Saunders, A.D., and Norry, M.J., (Eds.), *Magmatism in Ocean Basins*, Spec. Publ. 42, 315-345. London: Geological Society.

Takahashi, E., 1986. Melting of dry peridotite KLB-1 up to 14 GPa: implications on the origin of peridotitic upper mantle. *J. Geophys. Res.*, **91**, 9367-9382.

Takahashi, E., Uto, K., and Schilling, J.-G., 1987. Primary magma composition and Mg/Fe ratios of their mantle residues along the Mid Atlantic Ridge, 29°N to 73°N. *Tech. Rpt. Inst. Study Earth's Int., Okayama University.* **Ser.A, 9**, 1-14.

Tatsumi, Y., Sakuyama, M., Fukuyama, H., and Kushiro, I., 1983. Generation of arc basalt magmas and thermal structure of the mantle wedge in subduction zones. *J. Geophys. Res.*, **88**, 5815-5825.

Tatsumi, Y., Hamilton, D.L., and Nesbitt, R.W., 1986. Chemical characteristics of fluid phase released from a subducted lithosphere and origin of arc magmas:

evidence from high-pressure experiments and natural rocks. *J. Volc. Geotherm. Res.*, **29**, 293-309.

Tatsumi, Y., 1989. Migration of fluid phases and genesis of basaltic magmas in subduction Zones. *J. Geophys. Res.*, **94**, 4697-4707.

Taylor, S.R., and McClennan, S.M., 1985. The continental crust: its composition and evolution. Blackwell Sci. Publications.

Thirwall, M.F., and Graham, A.M., 1984. Evolution of high Ca, high Sr C-series basalt from Grenada, Lesser Antilles: the effects of intracrustal contamination. *J. Geol. Soc. London*, **141**, 427-445.

Thompson, R.N., 1974. Primary basalts and magma genesis. I. Skye, north-west Scotland. *Contrib. Mineral. Petrol.* **45**, 317-341.

Thompson, R.N., 1982. Magmatism of the British Tertiary volcanic province. *Scott. J. Geol.* **18**, 49-107.

Thompson, R.N., 1987. Phase-equilibria constraints on the genesis and evolution of oceanic basalts. *Earth Sci. Rev.*, **24**, 161-210.

Tilling, R.I., Wright, T.L., and Millard, H.T. Jr., 1987. Trace element chemistry of Kilauea and Mauna Loa lava in space and time; a reconnaissance. *USGS Prof. Paper*, **1350**, 641-680.

Turcotte, D.L., and Ahern, J.L., A porous flow model for migration in the asthenosphere. *J. Geophys. Res.*, **83**, 767-772.

Ulmer, P., 1989. The dependence of the Fe^{2+}-Mg cation-partitioning between olivine and basaltic liquid on pressure, temperature and composition. An experimental study to 30 kbars. *Contrib. Mineral. Petrol.*, **101**, 261-273.

Varekamp, J.C., Vanbergen, M.J., Vroon, P.Z., Poorter, R.P.E., Wirakusuma, A.D., Erfan, R., Sriwana, T., and Suharyono, K., 1987. The nature of potassic volcanism in the Sunda Arc, (unpubl. manuscript).

Varne, R., 1985. Ancient subcontinental mantle: a source for K-rich orogenic volcanics. *Geology*, **13**, 405-408.

Varne, R., and Foden, J.D., 1986. Geochemical and isotopic systematics of eastern Sunda Arc volcanics: implications for mantle sources and mantle mixing processes. In: Wezel, F.-C., (Ed.), *The Origin of Arcs.*, Elsevier, Amsterdam, 159-189.

Vogt, P.R., and Conolly, J.R., 1971. Tasmantid Guyots, the age of the Tasman Basin, and motion between the Australian plate and the mantle. *Geol. Soc. Am. Bull.*, **82**, 2577-2584.

Waff, H.S., and Balau, J.R., 1979. Equilibrium fluid distribution in an ultramafic partial melt under hydrostaic stress condition. *J. Geophys. Res.*, **84**, 6109-6114.

Wallace, M.E., 1989. Stability of amphibole and carbonate in an oxidized mantle and the genesis of carbonatite. Unpubl. phD Thesis, University of Tasmania, 171pp.

Wallace, M.E., and Green, D.H., 1988. An experimental determination of primary carbonatite magma composition. *Nature*, **335**, 343-345.

Warden, A.J., 1970. Evolution of Aoba caldera volcano, New Hebrides. *Bull. Volc.*, **34**, 107-140.

Warden, A.J., 1967. The geology of Central Islands. *Regional Report of the New Hebrides Govt. Geol. Survey*, 108pp.

Weaver, S.D., Saunders, A.D., Pankhurst, R.J., and Tarney, J., 1979. A geochemical study of magmatism associated with the initial stages of back-arc spreading. *Contrib. Mineral. Petrol.*, **68**, 151-169.

Weaver, B.L., Wood, D.A., Tarney, J., and Loron, J.A., 1986. Role of subducted sediment in the genesis of acean-island basalts: geochemical evidence from South Atlantic Ocean islands. *Geology*, **14**, 275-278.

Wedepohl, K.H., 1985. Origin of the Tertiary basaltic volcanism in the northern Hessian Depression. *Contrib. Mineral. Petrol.* **89**, 122-143.

Weissel, J.K., and Hayes, D.E., 1977. Evolution of the Tasman Sea reappraised. *Earth Planet. Sci. Lett.*, **36**, 77-84.

Wellman, P., and McDougall, I., 1974. Cainozoic igneous activity in eastern Australia. *Tectonophysics*, **23**, 49-65.

West, H.B., and Leeman, W.P., 1987. Isotopic evolution of lavas from Haleakala Crater, Hawaii. *Earth Planet. Sci. Lett.*, **84**, 211-225.

Westercamp, D., 1988. Magma generation in the Lesser Antilles: geological constraints. *Tectonophysics*, **149**, 145-163.

Wheller, G.E. 1986. Petrogenesis of Batur Caldera, Bali, and the geochemistry of Sunda-banda arc basalts. Unpublished PhD thesis, University of Tasmania, 156pp.

Wheller, G.E., Varne, R., Foden, J.D., and Abbott, M.J., 1987. Geochemistry of Quarternary volcanism in the Sunda-Banda arc, Indonesia, and three-component genesis of island-arc basaltic magmas. *J. Volc. Geotherm. Res.*, **32**, 137-160.

White, W.M., Dupre, B., and Vidal, P., 1985. Isotope and trace element geochemistry of sediments from the Barbados Ridge-Demerara Plain region, Atlantic Ocean. *Geochim. Cosmochim. Acta*, **49**, 1985.

White, W.M., and Dupre, B., 1986. Sediment subduction and magma genesis in the Lesser Antilles: isotopic and trace element constraints. *J. Geophys. Res.*, **91**, 5927-5941.

Wilkinson, J.F.G., and Hensel, H.D., 1988. The petrology of some picrites from Mauna Loa and Kilauea volcanoes, Hawaii. *Contrib. Mineral. Petrol.*, **98**, 326-345.

Williams, R.W., and Gill, J.B., 1989. Effects of partial melting on the uranium decay series. *Geochim Cosmochim Acta.*, **53**, 1607-1619.

Wilson, J.T., 1963. Continental drift. *Sci. American*, **208**, 86-100.

Wood, D.A., 1979. Variably veined suboceanic upper mantle- genetic significance for mid-ocean ridge basalts from geochemical evidence. *Geology*, **7**, 499-503.

Wright, T.L., 1971. Chemistry of Kilauea and Mauna Loa lava in space and time. *USGS Prof. Paper.*, **735**, 40pp.

Wright, T.L., 1984. Origin of Hawaiian Tholeiite: a metasomatic model. *J. Geophys. Res.* **89**, 3233-3252.

Wright, T.L., and Helz, R.T., 1987. Recent advances in Hawaiian petrology and geochemistry. *USGS Prof. Paper*, **1350**, 625-639.

Wyllie, P.J., 1988. Solidus curves, mantle plumes, and magma generation beneath Hawaii. *J. Geophys. Res.*, **93**, 4171-4181.

Yamamoto, M., 1984. Origin of calc-alkaline andesite from Oshima-Oshima volcano, north Japan. *J. Fac. Sci. Hokkaido University*, **21**, 77-131.

Yamamoto, M., 1988. Picritic primary magma and its source mantle for Oshima-oshima and back-arc side volcanoes, northeast Japan arc. *Contrib. Mineral. Petrol.*, **99**, 352-259.

Zindler, A., and Hart, S., 1986. Chemical geodynamics. *Ann. Rev. Earth Planet. Sci.*, **14**, 493-571.

Additional References for Chapter 6 and Chapter 7

Ballhaus C.G. and Glikson A.Y., 1989. Magma mixing and intraplutonic quenching in the Wingellina Hills intrusion, Giles Complex, central Australia. *J. Petrology*, 30, 1443-1449.

Ballhaus C.G, Berry R.F., Green D.H., in press. Oxygen fugacity controls in the Earth's upper mantle. *Contrib Mineral Petrol.*

Brophy J.G., 1989. Basalt convection and plagioclase retention: a model for the generation of high-alumina basalt. *J. Geology*, 97, 319-329.

Cox K.G. and Bell J.D., 1972. A crystal fractionation model for the basaltic rocks of the New Georgia Group, Britich Solomons Islands. *Contrib. Mineral. Petrol.*, 37, 1-13.

Huppert H.E. and Sparks R.J.S., 1980. The fluid dynamics of basaltic magma chamber replenished by influx of hot, dense ultrbasic magma. *Contrib. Mineral. Petrol.*, 75, 279-289.

Huppert H.E. and Sparks R.J.S., 1985. Cooling and contamination of mafic and ultramafic magmas during ascent through continental crust. *Earth Planet. Sci. Lett.*, 74, 371-386.

Jakes, P. and Gill, J., 1970. Rare earth elements and the island arc tholeiite series. *Earth Planet. Sci. Lett.*, 9, 17-28.

Krishnamurthy P. and Cox K.G., 1977. Picrite basalt and related lavas from the Deccan Traps of western India. *Contrib. Mineral. Petrol.*, 62, 53-75.

Martin D. and Nokes R., 1988. Crystal settling in a vigorously convecting magma chamber. *Nature*, 332, 535-537.

Marsh B.D. and Maxey M.R., 1985. On the distribution and separation of crystals in convecting magma. *J. Volc. Geotherm. Res.*, 24, 95-150.

Maaloe S., Sorenson I., and Hertogen J., 1986. The trachybasaltic suite of Jan Mayen, *J. Petrology*, 27, 439-466.

Maaloe S., Pedersen R.B., and James, D., 1988. Delayed fractionation of basaltic lavas. *Contrib. Mineral. Petrol.*, 98, 401-407.

Mattioli G.S., and Wood B.J., 1986. Upper mantle oxygen fugacity recorded by spinel lherzolites. *Nature*, 322, 626-628.

Shaw H.R., 1973. Viscosities of magmatic silicate liquids: an empirical method of prediction. *Am. J. Sci.*, 272, 870-893.

Appendix 1

Whole-rock Chemical Analysis

Sample Preparation

Hand specimens were trimmed of weathered portions and crushed to ~5mm diameter fractions in a Sturtevart steel jaw crusher. Approximately 100g was then ground for 2 minutes in a tungsten carbide swing mill.

X-ray Flourescence Spectrometry

Major and trace elements have been determined by XRF spectrometry using an automated Phillips 1410 spectrometer. For major elements, fused glass discs were prepared following the methods of Norrish and Hutton (1969), and LOI (loss on ignition) values were obtained by calculating the percentage loss in weight after heating ~1-2g of each sample for 8-12 hours at 1000°C.

Trace element analyses were made on 4-5g pressed powder pellets following the methods of Norrish and Chappell (1977), with concentrations being determined using mass absorption coefficients calculated from major element analyses. REE concentrations have also been determined by an ion-exchange-XRF spectrometry technique developed by Robinson et al. (1986). Note, however, that where La, Ce, and Nd analyses are reported they have been determined using the methods of Norrish and Chappell (1977).

International standards have been used for calibration, and precision has been monitored using "in house" standards. Precision estimates based on multiple analyses of standards run during the course of this study, and also Ambae sample #68611, are compiled below.

Table 1.A Precision estimates determined for multiple analyses (n) of Tasmania University standard rocks (TasBas, TasDol, 47805) and Ambae sample #68611.

	TasBas			47805 or TasDol			68611		
	(+1σ)	n	σ%	(+1σ)	n	σ%	(+1σ)	n	σ%
Major Elements									
SiO_2	45.98±0.23	46	0.5						
TiO_2	2.40±0.04	46	1.7						
Al_2O_3	14.60±0.10	46	0.7						
Fe_2O_3	11.75±0.09	46	0.8						
MnO	0.18±0.01	46	5.1						
MgO	8.46±0.11	46	1.3						
CaO	8.08±0.06	46	0.8						
Na_2O	5.63±0.12	46	2.1						
K_2O	1.94±0.03	46	1.6						
P_2O_5	1.00±0.03	46	2.6						
Trace Elements									
Rb	16.5±0.7	27	4.2	3.9±0.6[a]	12	15.4	11.3±0.6	9	5.4
Ba	204±3.0	8	1.5	388±4.7[b]	10	1.2			
Sr	1025±11.2	25	1.1	64.9±1.0[a]	12	1.5	591±3.1	10	0.5
La	43.4±1.4	30	3.2				9.6±1.3	6	14
Ce	89.0±3.4	30	3.8				20.1±2.0	6	10
Nd	41.2±2.4	30	5.8				12.6±0.6	6	4.4
Y	23.1±0.6	27	2.6	3.4±0.4[a]	12	11.8	17.7±0.5	10	3.0
Zr	260±4.3	27	1.7	34.6±0.9[a]	12	2.6	44.7±1.0	10	2.2
Sc	13.1±0.5	8	3.8	25.0±0.8[b]	10	3.2			
Nb	61.4±1.2	27	2.0	2.7±0.5[a]	12	18.5	1.4±0.5	10	38
V	163±2.3	26	1.4						
Cr	198±4.1	26	2.1						
Ni	154±2.0	26	1.3						
REE (analysed by ion exchange technique[c])									
La	43.2±1.25	3	2.9						
Ce	89.1±2.58	3	2.9						
Pr	10.34±0.28	3	2.7						
Nd	41.8±0.79	3	1.9						
Sm	8.15±0.10	3	1.2						
Eu	2.61±0.11	3	4.3						
Gd	7.01±0.10	3	1.5						
Dy	4.89±0.10	3	2.0						
Er	2.05±0.15	3	7.2						
Yb	1.26±0.06	3	4.6						

a. Analyses of standard 47805.
b. Analyses of standard TasDol.
c. Precision estimates after Robinson et al. (1986).

Appendix 2

Tasmantid Seamount Database

A compilation of whole-rock major and trace element analyses for dredged samples from the Tasmantid Seamounts. Analyses are grouped on the basis of seamount of derivation (see Fig. 1.1, Chapter 1, for locations). Details of sample preparation and analytical techniques, including precision estimates, are listed in Appendix 1.

GASCOYNE

number	65821	65818	65810	65812	65809	65820	65808	65811	65813	85-169
SiO2	48.85	47.84	46.17	49.26	48.67	50.63	49.67	50.25	49.80	49.40
TiO2	1.84	1.84	1.87	1.79	2.48	2.34	1.89	1.72	1.75	2.46
Al2O3	13.79	13.76	13.91	13.54	14.51	13.92	13.66	13.46	13.35	13.14
Fe2O3	11.57	11.61	11.91	11.52	11.16	10.91	11.13	10.87	11.04	11.47
FeO										
MnO	0.16	0.16	0.16	0.16	0.14	0.14	0.15	0.15	0.16	0.14
MgO	11.37	11.32	11.04	10.86	8.15	8.47	10.12	10.08	10.31	9.73
CaO	8.70	8.93	9.41	8.42	8.11	7.94	8.44	8.26	8.41	8.15
Na2O	2.89	3.86	3.12	2.77	3.52	3.55	2.92	2.77	2.70	2.94
K2O	0.54	0.50	0.33	0.69	1.19	1.22	0.85	0.75	0.75	1.15
P2O5	0.37	0.42	0.77	0.38	0.73	0.50	0.53	0.30	0.31	0.49
L.O.I.	0.56	0.77	1.34	0.49	0.59	0.38	0.50	0.77	0.48	0.57
H2O-										
rest										
total	100.64	101.01	100.03	99.88	99.25	100.00	99.86	99.38	99.06	99.64
Cs										
Pb										
Rb	6.60	12.00	2.00	11.00	19.00	19.00	13.00	12.00	5.30	18.00
Ba	160.00	167.00	119.00	154.00	296.00	261.00	207.00	143.00	134.00	287.00
Sr	446.00	458.00	514.00	432.00	626.00	583.00	551.00	442.00	440.00	611.00
La	15.40			13.00	28.00	24.00	16.20	11.00	12.00	25.00
Ce	29.80			26.00	62.00	48.00	36.60	25.70	21.00	56.00
Pr	3.75				7.62		4.55	3.40		
Nd	18.70			20.00	34.00	33.00	22.00	16.40	19.00	29.00
Sm	4.64				7.36		5.01	3.88		
Eu	1.75				2.53		1.92	1.84		
Gd	4.96				6.94		5.19	3.99		
Tb										
Dy	4.07				5.10		4.08	3.67		
Ho										
Er	1.88				2.11		1.85	1.93		
Yb	1.47				1.58		1.38	1.42		
Lu										
Y	18.00	21.00	21.00	18.00	25.00	23.00	20.00	19.00	19.00	23.00
Th										
U										
Zr	121.00	125.00	120.00	120.00	242.00	207.00	149.00	119.00	119.00	204.00
Hf										
Sn										
Nb	15.00	15.00	15.00	14.00	36.00	28.00	17.00	12.00	13.00	33.00
Cu										
Co										
Sc	25.00	21.00	24.00	21.00	18.00	17.00	22.00	21.00	23.00	22.00
V	185.00	176.00	180.00	180.00	177.00	166.00	174.00	167.00	187.00	201.00
Cr	553.00	528.00	535.00	535.00	317.00	367.00	484.00	503.00	555.00	442.00
Ni	314.00	297.00	306.00	307.00	254.00	252.00	301.00	274.00	307.00	307.00

GASCOYNE

number	85-170	65817
SiO2	51.39	49.13
TiO2	2.27	1.79
Al2O3	13.74	13.58
Fe2O3	11.02	11.43
FeO		
MnO	0.13	0.15
MgO	7.47	11.02
CaO	7.89	8.84
Na2O	3.16	3.35
K2O	1.18	0.63
P2O5	0.53	0.31
L.O.I.	0.68	0.46
H2O-		
rest		
total	99.46	100.69
Cs		
Pb		
Rb	18.00	8.70
Ba	255.00	156.00
Sr	585.00	455.00
La	21.80	14.00
Ce	47.00	23.00
Pr	6.30	
Nd	28.40	19.00
Sm	6.34	
Eu	2.33	
Gd	5.97	
Tb		
Dy	4.70	
Ho		
Er	2.01	
Yb	1.20	
Lu		
Y	24.00	19.00
Th		
U		
Zr	201.00	124.00
Hf		
Sn		
Nb	29.00	15.00
Cu	42.00	
Co		
Sc	20.00	23.00
V	179.00	183.00
Cr	361.00	529.00
Ni	247.00	313.00

DERWENT HUNTER

number	65828	65835	65838	65832	65840	65836	65833	85-177	85-179	85-181
SiO2	50.32	47.73	48.57	48.26	48.91	49.56	44.87	45.09	50.21	50.57
TiO2	1.80	3.46	3.23	3.09	2.85	3.67	3.27	3.10	2.51	2.57
Al2O3	13.30	15.15	15.52	16.93	16.28	16.00	15.58	13.71	15.27	15.52
Fe2O3	10.51	11.26	11.14	10.78	9.77	10.03	11.24	12.84	10.98	10.66
FeO										
MnO	0.15	0.13	0.12	0.12	0.12	0.12	0.21	0.16	0.11	0.12
MgO	8.99	4.87	4.69	4.36	4.22	3.61	3.18	6.30	5.33	4.56
CaO	9.27	9.35	8.82	9.28	10.39	8.13	9.46	8.38	8.61	8.79
Na2O	2.84	3.28	3.38	3.48	3.08	4.17	4.02	2.93	3.43	3.29
K2O	0.57	1.15	1.32	0.92	1.61	2.30	1.50	1.51	1.14	1.55
P2O5	0.28	1.64	0.74	0.76	1.11	0.87	2.13	0.60	0.50	0.58
L.O.I.	2.21	1.84	1.83	1.92	2.03	1.87	4.10	4.74	1.78	1.40
H2O-										
rest										
total	100.24	99.86	99.36	99.90	100.37	100.33	99.56	99.36	99.87	99.61
Cs										
Pb										
Rb	9.50	33.00	18.00	12.00	19.00	20.00	21.00	27.00	26.00	21.00
Ba	103.00	340.00	342.00	283.00	397.00	602.00	333.00	336.00	277.00	337.00
Sr	416.00	609.00	632.00	679.00	733.00	711.00	666.00	566.00	549.00	608.00
La	11.10	32.60	29.00	27.00	28.00	38.00	29.00	28.00	21.00	25.00
Ce	26.30	71.80	68.00	63.00	60.00	91.80	61.00	67.00	51.00	56.00
Pr	3.45	9.32				11.60				
Nd	17.20	41.80	40.00	38.00	38.00	50.70	40.00	38.00	28.00	35.00
Sm	4.62	9.64				10.50				
Eu	1.69	3.41				3.40				
Gd	5.22	9.65				9.77				
Tb										
Dy	4.31	7.46				7.56				
Ho										
Er	2.01	3.75				3.74				
Yb	1.59	2.73				2.73				
Lu										
Y	22.00	37.00	34.00	33.00	27.00	38.00	42.00	26.00	29.00	28.00
Th										
U										
Zr	125.00	282.00	235.00	241.00	243.00	346.00	242.00	235.00	194.00	226.00
Hf										
Sn										
Nb	13.00	39.00	34.00	32.00	28.00	41.00	35.00	39.00	27.00	28.00
Cu								79.00	38.00	40.00
Co										
Sc	20.00	22.00	22.00	22.00	21.00	21.00	25.00	20.00	21.00	23.00
V	179.00	266.00	251.00	248.00	222.00	249.00	268.00	299.00	200.00	234.00
Cr	559.00	49.00	33.00	76.00	88.00	20.00	52.00	465.00	83.00	175.00
Ni	322.00	59.00	55.00	51.00	53.00	34.00	79.00	317.00	101.00	43.00

DERWENT HUNTER

number	85-182	85-183
SiO2	48.13	49.09
TiO2	3.05	2.33
Al2O3	15.41	16.50
Fe2O3	11.01	8.58
FeO		
MnO	0.12	0.10
MgO	4.46	4.54
CaO	8.84	10.24
Na2O	3.47	3.55
K2O	1.40	1.08
P2O5	1.05	0.69
L.O.I.	2.83	3.30
H2O-		
rest		
total	99.77	100.00
Cs		
Pb		
Rb	25.00	11.00
Ba	443.00	349.00
Sr	748.00	705.00
La	32.00	21.00
Ce	68.00	50.00
Pr		
Nd	44.00	33.00
Sm		
Eu		
Gd		
Tb		
Dy		
Ho		
Er		
Yb		
Lu		
Y	33.00	24.00
Th		
U		
Zr	264.00	189.00
Hf		
Sn		
Nb	36.00	23.00
Cu	27.00	37.00
Co		
Sc	23.00	22.00
V	257.00	202.00
Cr	67.00	166.00
Ni	53.00	79.00

				TAUPO		
number	65803	65839	65805	85-174A	85-175	85-176
SiO2	50.41	50.08	49.90	51.01	45.86	46.39
TiO2	3.13	3.04	3.04	2.94	2.81	2.70
Al2O3	15.42	14.98	15.21	14.76	15.14	14.62
Fe2O3	11.74	11.97	11.75	11.78	11.93	11.48
FeO						
MnO	0.13	0.15	0.13	0.13	0.14	0.13
MgO	4.70	4.84	5.28	4.80	6.76	8.19
CaO	7.85	7.61	7.69	7.05	8.17	8.01
Na2O	4.07	3.93	4.38	3.50	3.36	3.30
K2O	1.16	1.23	1.24	1.27	1.17	1.07
P2O5	0.60	0.59	0.59	0.59	0.78	0.73
L.O.I.	1.42	1.22	1.21	1.98	3.68	3.79
H2O-						
rest						
total	100.63	99.64	100.42	99.81	99.80	100.41
Cs						
Pb						
Rb	20.00	20.00	21.00	21.00	10.00	10.00
Ba	217.00	249.00	261.00	254.00	417.00	399.00
Sr	565.00	538.00	535.00	531.00	920.00	826.00
La		26.30			36.60	37.00
Ce		51.10			77.20	80.00
Pr		7.36			9.82	
Nd		32.30			41.90	43.00
Sm		8.20			8.55	
Eu		2.84			3.00	
Gd		8.66			7.77	
Tb						
Dy		6.45			5.99	
Ho						
Er		2.71			3.09	
Yb		1.89			1.83	
Lu						
Y	31.00	30.00	29.00	31.00	28.00	26.00
Th						
U						
Zr	236.00	238.00	230.00	236.00	279.00	275.00
Hf						
Sn						
Nb	30.00	31.00	29.00	29.00	51.00	50.00
Cu				28.00	41.00	39.00
Co						
Sc	16.00	17.00	15.00	17.00	17.00	16.00
V	176.00	168.00	167.00	166.00	199.00	188.00
Cr	86.00	83.00	81.00	83.00	273.00	286.00
Ni	78.00	76.00	74.00	78.00	238.00	253.00

BRITANNIA

number	68644
SiO2	51.48
TiO2	1.31
Al2O3	13.90
Fe2O3	11.44
FeO	
MnO	0.14
MgO	9.26
CaO	8.25
Na2O	2.80
K2O	0.44
P2O5	0.31
L.O.I.	0.39
H2O-	
rest	
total	99.72
Cs	
Pb	
Rb	8.00
Ba	122.00
Sr	293.00
La	8.22
Ce	20.00
Pr	2.71
Nd	12.40
Sm	3.54
Eu	1.48
Gd	4.03
Tb	
Dy	3.83
Ho	
Er	2.21
Yb	1.72
Lu	
Y	19.00
Th	
U	
Zr	97.00
Hf	
Sn	
Nb	8.00
Cu	
Co	
Sc	23.00
V	172.00
Cr	499.00
Ni	302.00

Appendix 3

Experimental Phase Chemistry of Kilauea Iki Parent Melt

A compilation of the high PT phase chemistry of a new parent melt composition for Kilauea Iki (see Table 2.2, in Chapter 2, for bulk composition). All analyses have been obtained using a Jeol-JXA-50A electron microprobe with EDAX attachment, housed in the Central Science Laboratory at the University of Tasmania. Typical precision for single analyses are +3% for most elements, with minimum errors (2σ) being +0.3wt% for Na_2O and +0.2wt% for other oxides.

Table 3.A Experimental phase compositions.

P(GPa)	1.0	1.0	1.0	1.0	1.5	1.5	1.5	1.5	1.5	1.5
T(°C)	1400	1320	1280	1240	1440	1400	1380	1360	1340	1320
Olivine										
SiO_2	40.75	40.45	39.60	39.74	40.69	40.51	40.00	40.46	39.85	39.19
FeO	11.25	13.74	14.50	16.58	11.10	12.29	12.84	13.47	14.19	15.41
MgO	47.76	45.50	45.07	43.39	47.44	46.64	46.44	45.81	45.17	44.56
CaO	0.23	0.30	0.35	0.29	0.30	0.22	0.25	0.27	0.39	0.32
Total	99.99	99.99	99.52	100.00	99.53	99.66	99.53	100.01	99.60	99.48
Mg#	88.3	85.5	84.7	82.3	88.4	87.1	86.6	85.8	85.0	83.8
Orthopyxroxene										
SiO_2						55.82		55.62	55.73	
TiO_2						0.25		0.18	0.23	
Al_2O_3						2.31		1.48	1.63	
FeOtot						7.80		8.54	8.67	
MgO						31.30		31.66	28.19	
CaO						2.18		2.20	5.18	
Cr_2O_3						0.33		0.32	0.36	
Total						99.99		100.00	99.99	
Mg#						87.7		86.9	85.3	
Clinopyroxene										
SiO_2								54.92	52.97	53.26
TiO_2								0.38	0.77	0.59
Al_2O_3								2.49	4.80	4.42
FeOtot								8.95	8.08	8.29
MgO								27.53	24.20	23.23
CaO								5.25	8.60	9.48
Na_2O								0.00	0.00	0.25
Total								99.52	99.42	99.52
Mg#								84.6	84.2	83.3
Liquid										
SiO_2	48.05	49.51	49.73	49.49	48.23	48.55	48.84	48.30	47.67	48.00
TiO_2	1.95	2.39	2.51	2.76	2.06	2.23	2.27	2.43	2.49	2.79
Al_2O_3	10.70	12.13	12.95	14.50	10.51	11.48	11.50	12.28	12.89	13.67
FeOtot	11.51	10.88	10.46	10.65	11.35	11.49	11.32	11.51	11.73	12.17
MgO	15.54	11.51	9.94	8.41	16.06	13.53	13.23	12.23	10.95	9.28
CaO	9.54	10.81	11.09	10.76	9.44	10.22	10.22	10.46	10.58	10.44
Na_2O	1.92	1.96	2.34	2.58	1.70	1.88	1.90	2.08	2.61	2.95
K_2O	0.37	0.41	0.46	0.50	0.40	0.36	0.40	0.46	0.47	0.48
P_2O_5	0.21	0.32	0.33	0.32	0.27	0.26	0.27	0.27	0.36	0.23
Total	99.79	99.92	99.81	99.97	100.02	100.00	99.95	100.02	99.75	100.01
$Mg^{\#}$	70.6	65.3	62.8	58.3	71.6	67.7	65.7	65.4	65.2	62.2

P(GPa)	2.0	2.0	2.0	2.0	2.2	2.2	2.15	2.5
T(°C)	1460	1440	1420	1400	1450	1460	1465	1490
Olivine								
SiO_2		40.21	39.95	39.77				
FeOtot		12.50	12.78	13.88				
MgO		46.47	46.39	45.65				
CaO		0.24	0.29	0.27				
Total		99.42	99.41	99.57				
Mg#		86.9	86.6	85.4				
Orthopyroxene								
SiO_2	55.65	55.93	54.43			56.14	55.89	55.53
TiO_2	0.00	0.25	0.32			0.17	0.28	0.18
Al_2O_3	3.41	2.28	4.40			2.35	3.12	3.28
FeOtot	7.04	7.78	7.97			7.22	6.54	7.44
MgO	31.40	31.20	29.89			31.53	31.85	30.83
CaO	2.27	2.27	2.55			2.34	1.99	2.39
Cr_2O_3	0.24	0.29	0.43			0.26	0.33	0.35
Total	100.01	100.00	99.99			100.01	100.00	100.00
Mg#	88.88	87.7	87.0			88.6	89.7	88.1
Clinopyroxene								
SiO_2			54.18	53.27	54.10	56.01		
TiO_2			0.29	0.49	0.39	0.00		
Al_2O_3			4.01	5.34	4.66	2.75		
FeOtot			7.99	8.18	7.72	7.29		
MgO			26.30	24.07	25.67	28.48		
CaO			6.56	7.80	6.82	5.20		
Na_2O			0.28	0.54	0.35	0.00		
Cr_2O_3			0.40	0.30	0.29	0.27		
Total			100.01	99.99	100.00	100.00		
Mg#			85.4	84.0	85.6	87.4		
Liquid								
SiO_2	47.68	47.35	48.56	45.42	45.30	47.23	47.99	47.12
TiO_2	2.02	2.29	2.30	2.72	2.95	2.25	2.09	2.35
Al_2O_3	10.51	11.15	11.49	13.53	13.30	11.21	10.36	11.04
FeOtot	11.46	11.97	11.43	13.60	12.00	12.37	11.04	12.18
MgO	16.00	14.89	13.20	11.68	12.20	14.68	16.57	15.12
CaO	9.71	10.10	10.25	8.84	10.90	9.87	9.73	9.71
Na_2O	1.85	1.61	2.03	3.06	2.45	1.82	1.75	1.74
K_2O	0.31	0.40	0.40	0.76	0.61	0.36	0.24	0.42
P_2O_5	0.22	0.24	0.32	0.40	0.38	0.20	0.26	-
Total	99.76	100.00	99.98	100.01	100.09	99.99	100.03	99.68
Mg#	71.3	68.9	67.3	65.2	65.2	70.7	72.8	68.9

P(GPa)	2.5	2.5	2.5	2.8	3.0	3.0	3.5
T(°C)	1480	1460	1440	1505	1520	1490	1540
Clinopyroxene							
SiO_2	54.43	52.96	52.68	54.19	53.13	52.66	52.53
TiO_2	0.34	0.51	0.55	0.31	0.36	0.50	0.39
Al_2O_3	4.75	6.24	6.86	4.85	6.60	7.29	7.39
FeOtot	7.46	7.87	8.11	7.27	7.65	7.68	7.53
MgO	25.28	23.44	21.61	25.16	22.14	21.11	21.38
CaO	7.12	8.20	9.17	7.36	9.06	9.46	9.47
Na_2O	0.38	0.50	0.79	0.54	0.78	1.05	1.09
Cr_2O_3	0.24	0.28	0.24	0.31	0.28	0.25	0.22
Total	100.00	100.00	100.01	99.99	100.00	100.00	100.00
Mg#	85.8	84.2	82.6	86.0	83.8	83.0	83.5
Garnet							
SiO_2							42.00
TiO_2							0.70
Al_2O_3							23.22
FeOtot							8.87
MgO							19.75
CaO							5.05
Total							99.59
Mg#							79.9

Appendix 4

Vanuatu Arc Database

A compilation of volcanic rock samples from the Vanuatu Arc which have been analysed for major and/or trace elements. Sample order within the database follows the sequence of volcanoes/islands from north to south through the Vanuatu Arc (see Fig. 5.2). Data sources include;

a. Ash et al. (1978),
b. Ash et al. (1980),
c. Barsdell (1980),
d. Barsdell et al. (1982),
e. Barsdell (1988),
f. Barsdell and Berry (in press),
g. M. Barsdell (unpublished data),
h. Carney and Macfarlane (1979),
i. Colley and Ash (1971),
j. Crawford et al (1988),
k. Gorton (1974),
l. Gorton (1977),
m. Maillet et al. (1986),
n. Mallick and Ash (1975),
o. Marcelot (1981),
p. Marcelot et al (1983),
q. Roca (1978),
r. P.J. Stephenson (unpublished data),
s. Warden (1967),
t. Warden (1970),

	Ureparapara									
number	URE4	URE5	URE6A	URE6B	URE8	URE10	URE11	UA10	UMAC4	UA1
SiO2	55.36	49.97	52.18	49.64	51.95	50.59	49.92	49.80	50.56	51.80
TiO2	0.82	0.88	1.18	0.82	0.81	0.82	0.88	0.75	0.80	0.75
Al2O3	17.73	17.25	17.96	16.25	17.32	16.34	15.92	16.50	19.88	18.00
Fe2O3	3.74	4.25	4.87	4.86	4.19	5.29	4.65	3.65	4.20	3.70
FeO	4.32	5.18	4.21	5.05	5.15	4.98	5.43	6.00	4.70	5.50
MnO	0.15	0.19	0.28	0.21	0.19	0.20	0.22	0.20	0.16	0.20
MgO	3.19	4.09	3.57	6.06	4.90	5.90	6.09	6.80	3.37	5.70
CaO	7.49	9.89	8.92	10.76	9.39	10.57	10.92	11.30	9.70	10.00
Na2O	3.71	3.20	3.47	2.77	3.06	2.75	2.77	2.30	3.28	2.10
K2O	1.58	1.29	1.21	1.00	1.23	1.04	0.96	0.50	1.16	0.70
P2O5	0.26	0.28	0.38	0.20	0.22	0.21	0.21	0.25	0.23	0.20
L.O.I.	1.63	3.44	1.70	2.11	1.59	1.18	1.51	0.23	0.69	0.50
H2O-								0.53	0.87	0.78
rest										
total	99.98	99.91	99.93	99.73	100.00	99.87	99.48	98.81	99.60	99.93
Cs										
Pb										
Rb				12.00			13.00	10.00	9.00	5.00
Ba									270.00	
Sr				509.00			520.00		680.00	
La										
Ce										
Pr										
Nd										
Sm										
Eu										
Gd										
Tb										
Dy										
Ho										
Er										
Yb										
Lu										
Y										
Th										
U										
Zr				61.00			65.00			
Hf										
Sn										
Nb										
Cu								150.00		100.00
Co								15.00		25.00
Sc										
V									325.00	
Cr				119.00			102.00			
Ni				32.00			21.00	20.00		25.00

Barsdell (1980) Ash et al. (1980)

			Ureparapara		
number	UA3	UA2	UA10	UMAC10	UMAC14
SiO2	55.22	53.77	50.58	52.23	49.94
TiO2	0.83	0.76	0.79	0.79	0.82
Al2O3	17.73	17.08	16.40	18.22	17.04
Fe2O3	4.50	8.89	10.66	9.68	10.82
FeO	3.70				
MnO	0.19	0.16	0.18	0.18	0.18
MgO	3.52	4.43	6.10	4.26	5.53
CaO	8.30	8.70	10.58	8.91	10.68
Na2O	3.65	3.63	3.05	3.42	2.96
K2O	1.36	1.29	1.13	1.28	1.12
P2O5	0.22	0.23	0.27	0.22	0.22
L.O.I.	0.35	0.67	0.45	0.71	0.53
H2O-	0.21				
rest					
total	99.78	99.61	100.19	99.90	99.84
Cs					
Pb					
Rb	20.00				
Ba	320.00				
Sr	490.00				
La					
Ce					
Pr					
Nd					
Sm					
Eu					
Gd					
Tb					
Dy					
Ho					
Er					
Yb					
Lu					
Y					
Th					
U					
Zr					
Hf					
Sn					
Nb					
Cu					
Co					
Sc					
V	300.00				
Cr					
Ni					

Ash et al. (1980) Barsdell (unpubl. data)

	Motalava									
number	RA1	MOL5	MOL7	MOL10	MOL13	MOL15	MOL17	MOL19	MOL22	MVB1
SiO2	48.88	49.37	51.21	50.20	51.35	49.87	48.11	50.00	53.21	47.80
TiO2	0.73	0.78	1.02	0.75	0.79	0.73	0.83	0.66	0.77	0.55
Al2O3	18.32	17.59	17.75	15.82	16.80	15.82	16.94	14.45	19.39	14.20
Fe2O3	5.39	5.08	6.65	5.88	3.45	3.97	5.17	3.34	4.00	2.65
FeO	5.30	6.40	3.45	4.23	6.17	6.92	5.78	5.86	4.63	6.45
MnO	0.21	0.27	0.22	0.21	0.21	0.22	0.20	0.20	0.20	0.20
MgO	7.31	6.20	4.87	7.50	5.93	7.30	6.78	10.89	3.31	13.50
CaO	10.49	10.05	10.10	11.79	10.62	11.67	11.31	11.40	8.73	12.40
Na2O	2.38	2.37	2.90	2.01	2.54	2.11	2.28	1.91	3.52	1.30
K2O	0.37	0.43	0.74	0.39	0.74	0.40	0.52	0.31	0.86	0.25
P2O5	0.18	0.19	0.25	0.15	0.21	0.15	0.17	0.11	0.25	0.10
L.O.I.	1.04	1.06	1.18	0.89	1.03	0.98	1.90	0.95	1.08	0.17
H2O-										0.13
rest										
total	100.60	99.79	100.34	99.82	99.84	100.14	99.99	100.08	99.95	99.70
Cs										
Pb										
Rb	5.30			6.00	11.00				11.00	10.00
Ba										
Sr	568.00			384.00	515.00				578.00	
La										
Ce										
Pr										
Nd										
Sm										
Eu										
Gd										
Tb										
Dy										
Ho										
Er										
Yb										
Lu										
Y										
Th										
U										
Zr	38.00			50.00	63.00				73.00	
Hf										
Sn										
Nb										
Cu										65.00
Co										30.00
Sc										
V										
Cr	122.00			248.00	127.00				12.00	
Ni	46.00			51.00	39.00				2.40	180.00

Barsdell (1980)

				Motalava			
number	MVA1	MLM43	MLM23	MLM13	MLM26	MVA11	MVA15
SiO2	48.10	48.35	48.53	49.16	51.33	49.40	49.63
TiO2	0.75	0.82	0.74	0.58	0.77	1.51	0.66
Al2O3	18.20	17.92	17.56	14.18	17.02	16.24	13.82
Fe2O3	4.15	5.57	5.17	3.67	3.93	11.16	10.56
FeO	6.70	5.85	6.45	5.20	5.85		
MnO	0.25	0.21	0.22	0.17	0.19	0.19	0.17
MgO	7.00	6.05	5.99	12.10	5.79	5.94	9.61
CaO	11.20	11.09	10.57	12.43	10.63	11.26	12.06
Na2O	2.00	2.58	2.38	1.59	2.53	3.79	1.94
K2O	0.50	0.62	0.47	0.17	0.84	0.32	0.57
P2O5	0.20	0.18	0.18	0.07	0.19	0.18	0.17
L.O.I.	0.35	0.40	0.91	0.38	0.58	0.20	0.97
H2O-	0.40	0.12	0.23	0.18	0.30		
rest							
total	99.80	99.76	99.40	99.88	99.95	100.19	100.16
Cs							
Pb							
Rb	15.00	8.00	2.00	2.00	10.00		
Ba		230.00	250.00	70.00	220.00		
Sr		540.00	540.00	240.00	500.00		
La							
Ce							
Pr							
Nd							
Sm							
Eu							
Gd							
Tb							
Dy							
Ho							
Er							
Yb							
Lu							
Y							
Th							
U							
Zr							
Hf							
Sn							
Nb							
Cu	100.00						
Co	25.00						
Sc							
V		380.00	445.00	310.00	370.00		
Cr							
Ni	20.00						

Ash et al. (1980) Barsdell (unpubl. data)

Vat Ganai

number	VAT1	VAT2	31592	VGA1
SiO2	53.51	52.39	52.89	52.31
TiO2	0.75	0.75	0.73	0.69
Al2O3	18.60	17.34	17.30	16.78
Fe2O3	3.31	4.76	10.24	9.97
FeO	4.79	4.54		
MnO	0.19	0.17	0.16	0.17
MgO	3.88	4.99	5.16	5.30
CaO	9.22	9.44	9.67	9.84
Na2O	2.67	2.50	2.41	2.24
K2O	1.04	1.07	1.07	0.84
P2O5	0.26	0.24	0.21	0.19
L.O.I.	1.72	1.37	0.61	0.82
H2O-				
rest				
total	99.94	99.56	100.45	99.15
Cs				
Pb				
Rb		15.00		
Ba				
Sr		509.00		
La				
Ce				
Pr				
Nd				
Sm				
Eu				
Gd				
Tb				
Dy				
Ho				
Er				
Yb				
Lu				
Y				
Th				
U				
Zr		67.00		
Hf				
Sn				
Nb				
Cu				
Co				
Sc				
V				
Cr		29.00		
Ni		11.00		

Barsdell (1980)

Vot Tande

number	VGA1	VGA3	VGA7	VGM2
SiO2	52.00	52.64	52.79	53.45
TiO2	0.65	0.71	0.69	0.71
Al2O3	17.30	16.57	16.50	18.26
Fe2O3	2.65	3.94	5.04	4.07
FeO	6.25	5.35	4.40	4.45
MnO	0.20	0.17	0.15	0.16
MgO	6.30	5.41	5.21	3.85
CaO	10.30	9.99	10.24	9.17
Na2O	1.90	2.35	2.46	2.60
K2O	0.50	0.84	0.99	1.10
P2O5	0.25	0.24	0.25	0.25
L.O.I.	0.70	1.09	0.41	1.05
H2O-	0.54	0.37	0.57	0.21
rest				
total	99.54	99.67	99.70	99.33
Cs				
Pb				
Rb	50.00	15.00	13.00	18.00
Ba		170.00	160.00	180.00
Sr		550.00	540.00	560.00
La				
Ce				
Pr				
Nd				
Sm				
Eu				
Gd				
Tb				
Dy				
Ho				
Er				
Yb				
Lu				
Y				
Th				
U				
Zr				
Hf				
Sn				
Nb				
Cu	70.00			
Co	10.00			
Sc				
V		380.00	370.00	350.00
Cr				
Ni	5.00			

Ash et al. (1980)

					Moto					
number	MO1	MO2	MO3	MO4	MO5	MO6	MO7	MO8	MOA5	MOM4
SiO2	48.81	48.80	48.78	48.81	48.86	48.70	48.66	48.68	48.30	48.47
TiO2	0.82	0.74	0.77	0.82	0.82	0.82	0.80	0.80	0.65	0.74
Al2O3	16.85	15.52	15.89	16.60	16.78	16.38	16.80	16.62	16.20	16.47
Fe2O3	6.25	3.58	5.39	6.22	6.81	5.52	5.06	6.23	5.10	5.79
FeO	5.21	6.84	5.52	4.96	4.31	5.82	6.40	4.96	5.75	5.50
MnO	0.30	0.29	0.29	0.29	0.27	0.28	0.27	0.30	0.20	0.20
MgO	6.45	8.47	7.80	6.66	6.62	6.64	6.28	7.21	9.10	7.42
CaO	10.46	11.29	10.83	10.54	10.53	10.76	10.66	11.15	11.80	11.47
Na2O	2.46	2.22	2.38	2.44	2.55	2.46	2.30	2.36	1.70	2.35
K2O	0.77	0.66	0.65	0.78	0.86	0.70	0.64	0.62	0.35	0.74
P2O5	0.21	0.19	0.20	0.24	0.24	0.20	0.19	0.20	0.20	0.16
L.O.I.	0.93	1.30	1.13	1.10	0.92	1.22	1.41	0.93	0.18	0.31
H2O-									0.21	0.15
rest										
total	99.52	99.90	99.63	99.46	99.57	99.50	99.47	100.06	99.74	99.77
Cs										
Pb										
Rb				11.00					10.00	7.00
Ba										140.00
Sr				586.00						540.00
La										
Ce										
Pr										
Nd										
Sm										
Eu										
Gd										
Tb										
Dy										
Ho										
Er										
Yb										
Lu										
Y										
Th										
U										
Zr				54.00						
Hf										
Sn										
Nb										
Cu									120.00	
Co									25.00	
Sc										
V										395.00
Cr				93.00						
Ni				40.00					55.00	

Barsdell (1980) Ash et al. (1980)

Moto

number	MOM3	MO3
SiO2	48.83	48.67
TiO2	0.78	0.73
Al2O3	16.77	17.14
Fe2O3	7.50	12.03
FeO	4.45	
MnO	0.21	0.21
MgO	6.34	6.76
CaO	10.46	10.47
Na2O	2.35	2.44
K2O	0.78	0.73
P2O5	0.21	0.18
L.O.I.	0.61	0.26
H2O-	0.23	
rest		
total	99.52	99.62
Cs		
Pb		
Rb	10.00	
Ba	200.00	
Sr	580.00	
La		
Ce		
Pr		
Nd		
Sm		
Eu		
Gd		
Tb		
Dy		
Ho		
Er		
Yb		
Lu		
Y		
Th		
U		
Zr		
Hf		
Sn		
Nb		
Cu		
Co		
Sc		
V	395.00	
Cr		
Ni		

Ash et al. (1980)

					Merig					
number	MIG1A	MIG1B	MERM14	MIG3	MIG4A	MIG1	MIG2	MIG4	MIG5	MIG6
SiO2	53.47	49.76	55.71	46.72	46.50	61.35	60.34	62.79	59.82	54.42
TiO2	1.00	0.67	0.64	1.14	1.32	0.56	0.59	0.52	0.64	1.00
Al2O3	15.46	9.37	9.62	9.68	14.17	16.74	16.78	17.17	16.74	16.82
Fe2O3	3.80	4.68	1.99	3.92	4.70	2.63	2.56	2.15	2.93	2.76
FeO	4.87	5.53	5.02	6.19	5.14	2.51	2.77	2.36	2.79	5.40
MnO	0.29	0.26	0.30	0.30	0.26	0.23	0.22	0.21	0.20	0.28
MgO	7.62	12.67	11.47	17.30	12.18	3.29	3.80	2.04	3.46	5.26
CaO	9.58	14.55	12.45	11.05	11.13	6.60	6.78	6.08	6.86	8.62
Na2O	2.15	1.20	1.75	1.74	2.35	3.23	3.08	3.66	3.63	2.82
K2O	0.67	0.17	0.45	0.28	0.43	1.30	1.26	1.37	1.29	1.03
P2O5	0.18	0.10	0.12	0.06	0.08	0.20	0.22	0.26	0.21	0.27
L.O.I.	1.00	1.13	1.10	1.12	1.10	1.40	1.20	0.94	1.57	1.02
H2O-										
rest										
total	100.09	100.09	100.62	99.50	99.36	100.04	99.60	99.55	100.14	99.70
Cs						0.21		0.24		0.32
Pb						6.16		6.05		6.09
Rb						31.00		34.00	29.00	25.00
Ba						464.00		385.00		353.00
Sr						565.00		525.00	543.00	524.00
La						16.28		18.33		13.55
Ce						30.82		38.50		31.69
Pr						3.76		4.97		4.00
Nd						14.05		18.29		16.91
Sm						2.93		3.75		3.86
Eu						0.94		1.11		1.21
Gd						2.67		3.44		3.77
Tb						0.41		0.53		0.61
Dy						2.66		3.34		3.86
Ho						0.56		0.72		0.86
Er						1.70		2.22		2.50
Yb						1.90		2.37		2.55
Lu										
Y						17.68		20.81		25.44
Th						1.98		2.30		1.48
U						0.82		0.82		0.55
Zr						117.00		156.00	117.00	108.00
Hf						2.53		3.69		2.30
Sn										
Nb						4.75		9.08		4.84
Cu										
Co										
Sc										
V						137.00		85.00	150.00	244.00
Cr						75.00		43.00	40.00	101.00
Ni						29.00		16.00	22.00	37.00

Barsdell (1980) Barsdell et al. (1982)

					Merig			
number	MIG7	MIG8	MIG3X	MERM1	MERM10	BC20	MERM7	MERM11
SiO2	56.76	56.66	61.28	57.70	61.60	62.00	49.15	49.79
TiO2	0.88	0.91	0.54	0.80	0.45	0.46	0.90	0.93
Al2O3	17.17	17.44	16.45	16.80	16.50	17.70	13.44	13.33
Fe2O3	3.08	4.22	2.61	3.15	2.50	4.04	10.29	10.48
FeO	4.26	3.32	2.63	3.90	2.80	0.86		
MnO	0.29	0.29	0.22	0.21	0.15	0.15	0.16	0.18
MgO	3.83	3.72	3.60	4.50	4.30	2.32	11.04	11.33
CaO	7.75	7.81	6.45	7.95	6.85	6.03	10.30	10.40
Na2O	2.93	3.04	3.70	2.95	3.20	3.89	2.38	2.31
K2O	1.22	1.19	1.24	1.35	1.65	1.52	0.60	0.54
P2O5	0.32	0.32	0.21	0.32	0.21	0.22	0.17	0.16
L.O.I.	1.30	0.91	0.79			0.77	1.18	0.58
H2O-						0.07		
rest					0.29			
total	99.79	99.83	99.72	99.63	100.50	100.03	99.61	100.03
Cs								
Pb								
Rb		28.00					6.50	5.60
Ba							217.00	194.00
Sr		549.00					355.00	332.00
La							6.53	6.56
Ce							15.60	16.30
Pr							2.10	2.35
Nd							10.50	10.80
Sm							2.81	2.71
Eu							1.20	0.90
Gd							3.26	3.39
Tb								
Dy							3.67	3.99
Ho								2.00
Er							2.64	2.74
Yb							2.21	2.37
Lu								
Y							23.00	24.00
Th								
U								
Zr		127.00					63.70	66.00
Hf								
Sn								
Nb							2.40	2.70
Cu								
Co								
Sc							34.00	14.70
V		185.00					245.00	306.00
Cr		31.00					524.00	666.00
Ni		25.00					183.00	214.00

Barsdell (1980) Barsdell (unpubl. data) Mallick and Ash (1975)

Vanua Lava

number	VMAC6	VL6	VL13	VL5	VL14	VMAC5	VL19	VL10	VL1	VL24
SiO2	47.21	47.95	48.42	49.01	49.16	49.32	51.31	53.79	61.69	47.70
TiO2	0.85	0.65	0.72	0.71	0.69	0.84	0.80	0.75	0.77	0.65
Al2O3	17.86	19.47	16.64	19.16	16.90	15.70	19.54	17.25	15.75	19.83
Fe2O3	4.61	4.20	5.01	4.98	4.42	4.49	3.57	2.97	3.28	4.37
FeO	7.23	5.52	5.88	5.57	5.09	6.82	6.07	6.32	4.06	5.81
MnO	0.20	0.18	0.39	0.18	0.12	0.20	0.22	0.11	0.24	0.19
MgO	6.44	5.79	7.17	4.36	7.25	6.82	3.54	4.49	1.45	5.58
CaO	11.69	11.95	11.98	10.46	12.72	11.27	9.97	8.87	3.44	11.26
Na2O	2.52	2.75	2.57	2.83	2.44	2.53	3.15	3.12	4.35	2.58
K2O	0.91	0.37	0.81	0.43	0.59	0.93	0.78	1.13	2.48	0.59
P2O5	0.21	0.08	0.12	0.09	0.12	0.20	0.17	0.13	0.45	0.10
L.O.I.	0.38	0.74	0.40		0.40	0.76	0.62	0.72	1.58	1.05
H2O-										
rest				1.83						
total	100.11	99.65	100.11	99.61	99.90	99.88	99.74	99.65	99.54	99.71
Cs										
Pb										
Rb	13.00	2.20	10.00				10.00	17.00	39.00	
Ba										
Sr	696.00	584.00	666.00				666.00	462.00	376.00	
La		3.18				7.77				
Ce		7.25				18.70				
Pr		1.10				2.92				
Nd		5.75				12.80				
Sm		1.68				3.01				
Eu		0.84				0.97				
Gd		1.94				3.36				
Tb										
Dy		2.30				3.51				
Ho										
Er		1.33				2.22				
Yb		1.25				1.86				
Lu										
Y										
Th										
U										
Zr	48.00	36.00	45.00				48.00	73.00	133.00	
Hf										
Sn										
Nb										
Cu										
Co										
Sc										
V	451.00	363.00	388.00				348.00	327.00	98.00	
Cr	35.00	23.00	69.00				1.20	10.00		
Ni	20.00	20.00	40.00				3.20	7.00		

Barsdell (1980)

Vanua Lava

number	VL17	VL16	VL15	VL20	VL21	VL3	VLL39	VLL36	VLA18	VLA59
SiO2	47.85	48.34	49.01	51.42	53.18	53.72	61.82	62.00	44.00	46.00
TiO2	0.76	0.80	0.78	0.74	0.73	0.75	0.70	0.74	0.77	0.65
Al2O3	18.17	17.96	17.76	20.05	16.18	17.03	16.15	15.77	17.90	15.10
Fe2O3	6.31	5.64	5.55	4.19	4.63	3.17	2.75	3.03	7.80	9.50
FeO	5.23	6.16	5.65	4.82	5.83	6.19	4.27	3.60	4.30	3.65
MnO	0.22	0.44	0.13	0.21	0.21	0.21	0.20	0.21	0.20	0.22
MgO	5.30	5.27	5.28	3.35	4.83	4.40	1.50	1.66	6.30	8.80
CaO	11.11	10.91	11.37	9.56	8.92	8.74	3.94	4.12	11.80	13.00
Na2O	2.52	2.67	2.79	3.43	3.50	3.25	4.37	4.70	2.10	1.40
K2O	0.75	0.60	0.87	0.95	1.31	1.26	2.38	2.58	1.00	0.80
P2O5	0.18	0.11	0.19	0.23	0.17	0.13	0.36	0.38	0.15	0.14
L.O.I.	1.19	1.23	0.51	0.74	0.52	0.55	1.29	1.04	1.95	0.44
H2O-									0.80	0.02
rest										
total	99.59	100.13	99.89	99.69	100.01	99.40	99.73	99.83	99.07	99.72
Cs										
Pb										30.00
Rb										
Ba										
Sr										
La										
Ce										
Pr										
Nd										
Sm										
Eu										
Gd										
Tb										
Dy										
Ho										
Er										
Yb										
Lu										
Y										
Th										
U										
Zr										
Hf										
Sn										
Nb										
Cu										80.00
Co										100.00
Sc										
V										
Cr										250.00
Ni										90.00

Barsdell (1980) Ash et al. (1980)

	Vanua Lava									
number	VLA39	VLA47	VLB13	VLB15	VLA28	VLA17	VLC101	VLC40	VLC60	VLA81A
SiO2	47.00	47.00	48.42	49.01	50.00	50.50	53.66	53.57	56.23	58.50
TiO2	0.65	0.70	0.72	0.78	0.74	0.80	0.72	0.70	0.80	0.85
Al2O3	13.80	16.20	16.64	17.76	19.40	18.10	17.29	16.52	16.80	16.60
Fe2O3	7.20	10.60	2.22	2.28	6.70	5.20	3.52	5.61	4.91	3.40
FeO	3.85	2.55	8.67	8.92	3.90	4.85	5.90	4.15	4.20	5.75
MnO	0.19	0.21	0.39	0.13	0.20	0.21	0.19	0.17	0.21	0.20
MgO	10.00	7.30	7.17	5.28	4.10	4.90	4.36	3.53	2.82	2.20
CaO	12.70	11.90	11.98	11.37	9.90	9.50	8.84	8.49	6.95	6.10
Na2O	1.75	2.00	2.57	2.79	3.70	3.50	3.13	3.35	3.97	3.50
K2O	1.00	0.60	0.81	0.87	0.80	1.00	1.18	1.50	2.03	1.80
P2O5	0.13	0.15	0.12	0.19	0.19	0.18	0.14	0.17	0.26	0.40
L.O.I.	0.76	0.57	0.41	0.51	0.41	0.64	0.64	0.51	0.31	0.49
H2O-	0.19	0.08			0.07	0.51	0.10	0.59	0.29	1.07
rest										
total	99.22	99.86	100.12	99.89	100.11	99.89	99.67	98.86	99.78	100.86
Cs										
Pb	30.00	40.00			30.00	150.00				10.00
Rb							16.00	22.00	30.00	
Ba							290.00	380.00	520.00	
Sr							480.00	520.00	560.00	
La										
Ce										
Pr										
Nd										
Sm										
Eu										
Gd										
Tb										
Dy										
Ho										
Er										
Yb										
Lu										
Y										
Th										
U										
Zr										
Hf										
Sn										
Nb										
Cu	80.00	100.00			80.00	100.00				270.00
Co	100.00	100.00			80.00	100.00				90.00
Sc										
V							350.00	350.00	300.00	
Cr	1000.00	100.00			30.00	60.00				
Ni	120.00	90.00			20.00	40.00				5.00

Ash et al. (1980)

Vanua Lava

number	VLA14	VLC111	VLC54	VLA8	VLC70	VLC7	VLC19	VLA27	VLA35	VLA49
SiO2	61.50	52.26	52.80	54.00	55.09	55.20	59.43	61.00	55.89	47.52
TiO2	0.75	0.78	0.71	0.69	0.70	0.70	0.65	0.74	0.92	0.77
Al2O3	15.50	17.32	17.42	16.50	16.60	16.86	17.03	15.70	21.57	18.61
Fe2O3	4.90	5.06	4.67	8.60	3.62	4.01	3.76	6.80	13.19	12.34
FeO	2.00	5.30	4.60	0.99	5.40	5.20	3.45	1.10		
MnO	0.21	0.20	0.20	0.19	0.18	0.19	0.16	0.22	0.06	0.21
MgO	1.70	4.23	4.23	4.10	3.90	4.00	2.16	2.00	3.54	5.20
CaO	4.10	8.60	7.85	8.20	7.76	8.24	5.79	4.10	2.08	10.52
Na2O	5.90	3.00	3.10	3.80	3.13	3.25	4.02	5.60	0.97	2.44
K2O	2.90	1.27	1.17	1.60	1.63	1.48	2.45	2.60	0.84	0.71
P2O5	0.43	0.18	0.16	0.18	0.16	0.16	0.26	0.48	0.09	0.16
L.O.I.	0.49	1.04	1.88	0.40	1.18	0.44	0.34	0.28	0.18	1.13
H2O-	0.34	0.56	0.80	0.27	0.36	0.16	0.32	0.01		
rest										
total	100.72	99.80	99.59	99.52	99.71	99.89	99.82	100.63	99.33	99.61
Cs										
Pb	80.00			10.00				30.00		
Rb		12.00	18.00		24.00	22.00	38.00			
Ba		360.00	310.00		400.00	370.00	560.00			
Sr		500.00	430.00		430.00	460.00	440.00			
La									7.95	
Ce									20.40	
Pr									3.01	
Nd									14.10	
Sm									3.22	
Eu									0.96	
Gd									3.57	
Tb										
Dy									4.30	
Ho										
Er									2.87	
Yb									2.57	
Lu										
Y										
Th										
U										
Zr										
Hf										
Sn										
Nb										
Cu	20.00			150.00				20.00		
Co	20.00			80.00				60.00		
Sc										
V		370.00	320.00		330.00	320.00	185.00			
Cr	20.00			40.00				60.00		
Ni				30.00				20.00		

Ash et al. (1980) Barsdell (unpubl. data)

Vanua Lava

number	VLA69	VMAC006
SiO2	55.30	48.90
TiO2	0.68	0.80
Al2O3	16.97	16.07
Fe2O3	9.48	12.04
FeO		
MnO	0.19	0.20
MgO	3.81	6.30
CaO	7.65	11.13
Na2O	3.50	2.54
K2O	1.51	0.89
P2O5	0.15	0.17
L.O.I.	0.33	0.22
H2O-		
rest		
total	99.57	99.26
Cs		
Pb		
Rb		
Ba		
Sr		
La		9.38
Ce		21.20
Pr		2.77
Nd		13.50
Sm		2.74
Eu		0.97
Gd		3.02
Tb		
Dy		3.50
Ho		
Er		2.21
Yb		2.00
Lu		
Y		
Th		
U		
Zr		
Hf		
Sn		
Nb		
Cu		
Co		
Sc		
V		
Cr		
Ni		

Barsdell (unpubl. data)

			Merelava							
number	BC13G	MLM7G	31541	31542	31543	31544	31545	31546	31547	31548
SiO2	50.80	53.10	50.82	51.77	51.48	50.81	51.04	52.00	52.03	51.90
TiO2	0.71	0.73	0.64	0.72	0.72	0.64	0.74	0.74	0.63	0.74
Al2O3	15.20	17.00	13.67	14.71	17.64	14.05	16.72	19.05	15.70	18.14
Fe2O3	10.00	10.10	2.73	2.53	3.57	3.40	3.20	3.47	4.35	2.59
FeO			6.79	6.55	6.32	6.37	6.76	5.75	5.46	6.65
MnO	0.16	0.17	0.21	0.17	0.18	0.18	0.19	0.22	0.18	0.17
MgO	8.82	5.28	9.74	8.86	5.40	9.20	6.23	4.32	7.36	4.95
CaO	11.80	10.50	12.90	12.00	11.25	12.36	11.39	11.20	11.23	11.54
Na2O	2.09	2.45	1.89	2.10	2.34	2.00	2.42	2.51	2.07	2.50
K2O	0.48	0.58	0.38	0.44	0.62	0.46	0.52	0.53	0.43	0.55
P2O5	0.07	0.07	0.12	0.11	0.12	0.08	0.12	0.12	0.08	0.12
L.O.I.	0.20	-0.04	0.20	0.15	0.33	0.25	0.32	0.15	0.16	0.41
H2O-										
rest										
total	100.33	99.94	100.09	100.11	99.97	99.80	99.65	100.06	99.68	100.26
Cs			0.15					0.09	0.11	
Pb			3.27					7.38	2.90	
Rb		9.00	5.40	6.70			8.30	7.40	6.70	7.00
Ba		210.00	123.00					224.00	162.00	
Sr		289.00	240.00	258.00			337.00	353.00	255.00	316.00
La			1.86					2.60	2.34	
Ce			4.92					6.80	5.55	
Pr			0.81					1.03	0.88	
Nd			4.36					5.33	4.69	
Sm			1.48					1.60	1.59	
Eu			0.51					1.60	0.59	
Gd			1.80					2.02	1.97	
Tb			0.33					0.37	0.36	
Dy			2.08					2.38	2.38	
Ho			0.48					0.52	0.51	
Er			1.41					1.47	1.52	
Yb			1.39					1.56	1.70	
Lu										
Y		23.30	17.81					17.37		
Th			0.17					0.18	0.22	
U			0.10					0.13	0.16	
Zr		43.00	47.00	53.00			49.00	50.00	49.00	50.00
Hf			0.87					0.96	0.99	
Sn										
Nb			0.61					0.75		
Cu										
Co										
Sc		40.00								
V		380.00								
Cr		88.00	372.00	319.00			94.00	21.00	179.00	32.00
Ni		31.00	75.00	74.00			27.00	16.00	47.00	22.00

Barsdell (1988) Barsdell et al. (1982)

Merelava

number	31549	31550	31551	31552	31553	31554	31555	31556	31557	BC13
SiO2	51.41	51.87	51.33	51.43	51.54	50.58	51.11	51.14	52.35	50.20
TiO2	0.69	0.68	0.59	0.69	0.75	0.58	0.58	0.71	0.70	0.46
Al2O3	14.73	15.38	13.10	14.85	16.74	12.75	12.75	16.38	17.58	10.30
Fe2O3	3.04	3.32	2.40	3.04	3.49	3.58	2.66	3.26	2.42	2.43
FeO	6.37	5.60	6.04	6.07	6.24	5.68	6.37	5.96	5.91	5.90
MnO	0.20	0.23	0.22	0.16	0.22	0.20	0.16	0.23	0.23	0.17
MgO	8.21	7.80	10.67	8.88	6.14	11.00	11.00	7.06	6.00	13.71
CaO	12.19	11.65	12.45	12.20	11.02	12.94	12.80	11.75	11.33	13.69
Na2O	2.20	2.38	1.78	2.00	2.50	1.81	1.83	2.24	2.20	1.60
K2O	0.49	0.42	0.35	0.43	0.45	0.38	0.40	0.50	0.48	0.38
P2O5	0.10	0.09	0.07	0.11	0.14	0.10	0.09	0.10	0.09	0.06
L.O.I.	0.16	0.39	0.62	0.26	0.27	0.29	0.30	0.33	0.35	0.52
H2O-										0.38
rest										
total	99.79	99.81	99.62	100.12	99.50	99.89	100.05	99.66	99.64	99.80
Cs										
Pb										
Rb	6.60									6.00
Ba										181.00
Sr	277.00									218.00
La										2.42
Ce										4.87
Pr										0.67
Nd										3.76
Sm										1.19
Eu										0.44
Gd										1.45
Tb										
Dy										1.81
Ho										
Er										1.16
Yb										1.12
Lu										
Y										12.50
Th										
U										
Zr	47.00									18.30
Hf										
Sn										
Nb										
Cu										
Co										
Sc										52.00
V										262.00
Cr	304.00									695.00
Ni	63.00									137.00

Barsdell (1988) Barsdell et al. (1982)

				Merelava	
number	MLM7	BC14	BC12	MLM6	MLM10A
SiO2	51.30	51.27	51.69	52.00	52.00
TiO2	0.50	0.56	0.54	0.59	0.54
Al2O3	13.40	14.72	14.85	17.60	17.70
Fe2O3	9.08	2.51	1.95	1.75	1.25
FeO		6.34	6.60	6.75	6.05
MnO	0.16	0.18	0.17	0.19	0.17
MgO	11.00	9.38	9.06	5.20	6.40
CaO	12.70	12.18	12.14	11.60	11.70
Na2O	1.74	2.13	2.08	2.20	2.15
K2O	0.38	0.42	0.42	0.45	0.65
P2O5	0.07	0.07	0.04	0.09	0.09
L.O.I.	-0.05	0.30	0.40		
H2O-		0.10	0.16		
rest				0.51	0.14
total	100.28	100.16	100.10	98.93	98.84
Cs					
Pb					
Rb	6.00				
Ba	144.00				
Sr	206.00				
La					
Ce					
Pr					
Nd					
Sm					
Eu					
Gd					
Tb					
Dy					
Ho					
Er					
Yb					
Lu					
Y	14.40				
Th					
U					
Zr	24.60				
Hf					
Sn					
Nb					
Cu					
Co					
Sc	54.00				
V	284.00				
Cr	633.00				
Ni	126.00				

Mallick and Ash (1975)

Gaua

number	G1	G2	G6	G14	G10	G20	G21	G22	G24	G4
SiO2	57.04	64.15	51.92	50.80	55.40	46.50	49.33	46.44	48.22	56.43
TiO2	0.81	0.52	0.82	0.82	0.93	0.74	0.96	0.81	0.91	0.92
Al2O3	16.88	16.53	18.84	18.26	17.01	11.36	15.21	11.69	14.74	16.42
Fe2O3	2.76	0.98	7.15	4.68	4.85	5.52	6.04	6.06	5.65	3.51
FeO	4.74	2.65	1.97	4.93	4.07	5.48	6.08	5.99	6.28	4.91
MnO	0.27	0.23	0.21	0.31	0.33	0.26	0.30	0.30	0.29	0.33
MgO	2.53	0.60	2.56	3.99	2.36	14.81	6.33	11.00	6.22	2.31
CaO	5.31	1.41	7.48	9.96	5.58	11.78	10.66	13.01	11.59	4.86
Na2O	4.51	5.45	3.82	3.52	4.35	2.04	2.90	2.22	2.94	4.58
K2O	3.48	6.01	2.56	1.57	3.49	0.60	0.79	0.78	1.48	3.90
P2O5	0.42	0.65	0.44	0.29	0.56	0.15	0.22	0.23	0.35	0.64
L.O.I.	0.79	0.66	2.04	0.99	0.94	1.09	1.19	1.33	1.43	0.86
H2O-										
rest										
total	99.54	99.84	99.81	100.12	99.87	100.33	100.01	99.86	100.10	99.67
Cs	0.48	1.38				0.05	0.10	0.10	0.44	
Pb	12.08	20.91				2.05	2.02	5.25	6.96	
Rb	56.00	96.00	43.00	25.00	52.00	8.90	12.00		28.00	
Ba	642.00	991.00				193.00	237.00	310.00	516.00	
Sr	671.00	203.00	887.00	1014.00	813.00	502.00	529.00	687.00	998.00	
La	22.21	27.88				8.33	9.83	11.21	17.36	
Ce	47.56	57.70				17.00	22.96	24.28	39.88	
Pr	6.58	6.57				2.45	2.89	3.46	4.80	
Nd	29.94	25.35				11.30	14.01	16.95	21.04	
Sm	7.10	5.34				2.37	3.81	4.06	4.83	
Eu	2.05	1.20				0.79	1.25	1.27	1.40	
Gd	5.27	3.98				2.42	3.19	3.63	3.75	
Tb	0.81	0.63					0.51	0.53	0.50	
Dy	4.86	4.06				2.45	3.16	3.16	3.02	
Ho	0.91	0.84					0.71	0.55	0.63	
Er	2.65	2.71				1.57	2.11	1.36	1.64	
Yb	3.08	2.95				1.15	2.19	1.45	1.55	
Lu										
Y	22.06	29.32				13.09	27.40	13.33	18.99	
Th	4.08	6.15				0.60	0.86	1.21	1.91	
U	1.67	2.53				0.26	0.34	0.45	0.68	
Zr	128.00	213.00	98.00	64.00	126.00	48.00	61.00	53.00	63.00	
Hf	3.60	4.71				1.18	1.74	1.60	1.78	
Sn										
Nb	2.99	5.71				0.94	1.11	1.02	1.90	
Cu										
Co										
Sc										
V	218.00	36.00	277.00			328.00	390.00	407.00	381.00	
Cr	4.40	1.60	16.00			854.00	41.00	398.00	53.00	
Ni	4.10		16.00			265.00	29.00	120.00	19.00	

Barsdell (1980) Barsdell et al. (1982)

Gaua

number	G9	G13	G15	G17	G18	G23	G25	GM17	GM32	GM2
SiO2	51.98	54.92	47.29	53.30	53.45	51.41	52.79	46.71	50.56	51.20
TiO2	0.97	0.87	0.69	0.84	0.83	0.86	0.81	0.74	0.89	0.82
Al2O3	16.16	17.34	11.07	16.06	17.22	15.96	18.61	11.13	16.59	18.40
Fe2O3	3.97	3.13	4.51	4.24	4.46	4.94	5.93	5.46	5.43	5.97
FeO	6.35	5.30	5.97	5.20	4.42	5.36	2.93	6.34	5.44	4.43
MnO	0.31	0.33	0.28	0.30	0.27	0.30	0.29	0.19	0.21	0.20
MgO	3.86	2.53	15.64	4.13	3.68	5.19	3.08	12.94	4.84	3.79
CaO	7.93	6.51	10.67	8.04	7.65	9.61	8.36	13.51	9.98	10.30
Na2O	3.72	4.30	2.18	3.75	4.07	3.37	3.90	1.63	3.51	3.22
K2O	2.38	3.32	0.83	2.55	2.55	2.08	2.34	0.60	2.16	1.07
P2O5	0.44	0.56	0.17	0.40	0.39	0.36	0.44	0.22	0.45	0.22
L.O.I.	1.52	0.72	1.08	0.93	0.88	1.04	0.45	0.58	0.48	0.65
H2O-								0.60	0.21	0.47
rest										
total	99.59	99.83	100.38	99.74	99.87	100.48	99.93	100.65	100.75	100.74
Cs										
Pb										
Rb										
Ba										
Sr										
La			9.49							
Ce			19.20							
Pr			2.58							
Nd			11.80							
Sm			2.76							
Eu			0.74							
Gd			2.64							
Tb										
Dy			2.53							
Ho										
Er			1.46							
Yb			1.20							
Lu										
Y										
Th										
U										
Zr										
Hf										
Sn										
Nb										
Cu										
Co										
Sc										
V										
Cr										
Ni										

Barsdell (1980) Mallick and Ash (1975)

Gaua

number	GM22	GA1	GA33
SiO2	52.05	55.82	56.18
TiO2	0.89	0.98	0.80
Al2O3	16.91	16.99	18.03
Fe2O3	4.51	4.50	4.41
FeO	5.58	4.25	3.72
MnO	0.21	0.25	0.24
MgO	4.07	2.32	1.48
CaO	8.95	5.08	3.90
Na2O	3.72	5.02	5.48
K2O	2.42	3.64	3.66
P2O5	0.46	0.75	0.74
L.O.I.	0.71	0.71	0.98
H2O-	0.37	0.39	1.13
rest			
total	100.85	100.70	100.75
Cs			
Pb			
Rb			
Ba			
Sr			
La			
Ce			
Pr			
Nd			
Sm			
Eu			
Gd			
Tb			
Dy			
Ho			
Er			
Yb			
Lu			
Y			
Th			
U			
Zr			
Hf			
Sn			
Nb			
Cu			
Co			
Sc			
V			
Cr			
Ni			

Mallick and Ash (1975)

	Ambae									
number	491	566	531	574	535	580	521	567	553	481
SiO2	45.31	46.13	46.18	46.55	46.93	46.58	47.32	46.68	47.33	46.96
TiO2	0.46	0.53	0.58	0.59	0.57	0.62	0.63	0.64	0.63	0.66
Al2O3	8.64	9.51	10.46	10.68	10.88	11.02	11.73	11.85	11.98	12.23
Fe2O3	4.49	4.39	4.45	4.49	4.33	4.40	4.19	4.51	4.35	4.40
FeO	8.08	7.91	8.01	8.09	7.80	7.92	7.54	8.11	7.83	7.92
MnO	0.21	0.20	0.21	0.20	0.20	0.21	0.21	0.20	0.19	0.20
MgO	22.09	18.40	15.82	15.94	15.37	15.38	13.45	13.78	13.07	13.18
CaO	8.33	10.26	11.67	10.44	10.87	10.60	11.88	10.93	11.50	10.91
Na2O	1.40	1.53	1.63	1.83	1.85	1.89	1.98	1.95	1.90	2.09
K2O	0.79	0.95	0.83	1.02	1.00	1.15	0.91	1.12	1.04	1.22
P2O5	0.21	0.20	0.17	0.20	0.20	0.23	0.18	0.23	0.21	0.23
L.O.I.										
H2O-										
rest										
total	100.01	100.01	100.01	100.03	100.00	100.00	100.02	100.00	100.03	100.00
Cs										
Pb	1.45									
Rb	13.90	17.30	14.20	15.20	17.20	20.30	13.60	21.50	16.50	21.80
Ba	230.00	250.00	250.00	370.00	320.00	350.00	280.00	360.00	390.00	350.00
Sr	422.00	498.00	476.00	572.00	523.00	621.00	595.00	607.00	609.00	679.00
La	6.00									
Ce	12.80									
Pr	1.63									
Nd	7.10									
Sm	1.76									
Eu	0.56									
Gd	1.83									
Tb	0.27									
Dy	1.65									
Ho	0.33									
Er	0.90									
Yb	0.93									
Lu										
Y	12.10	13.50	15.80	15.40	15.20	14.80	15.40	17.90	17.90	17.20
Th	0.86									
U	0.24									
Zr	33.00	41.00	40.00	44.00	39.00	46.00	44.00	50.00	46.00	48.00
Hf	0.90									
Sn										
Nb	0.70									
Cu	75.00	96.00	80.00	60.00		140.00	58.00	34.00	40.00	90.00
Co	80.00	73.00	64.00	67.00	62.00	60.00	46.00	63.00	60.00	61.00
Sc	29.00	36.00	44.00	42.00	37.00	36.00	42.00	42.00	44.00	36.00
V	230.00	290.00	330.00	350.00	330.00	320.00	350.00	390.00	390.00	360.00
Cr	1650.00	2900.00	1250.00	1130.00	1200.00	900.00	760.00	1100.00	2400.00	830.00
Ni	480.00	350.00	260.00	290.00	260.00	280.00	210.00	230.00	210.00	210.00

Gorton (1974) (Gorton, 1977)

	Ambae									
number	498	506	502	576	484	505	522	495	561	512
SiO2	47.06	47.50	47.50	47.84	47.99	48.29	49.67	47.87	46.85	48.57
TiO2	0.68	0.67	0.67	0.72	0.73	0.68	0.82	0.77	1.23	0.79
Al2O3	12.15	12.44	13.01	13.19	13.87	12.99	15.61	13.83	13.70	15.07
Fe2O3	4.51	4.34	4.31	4.34	4.36	4.41	3.96	4.63	4.55	4.36
FeO	8.12	7.82	7.76	7.81	7.84	7.94	7.13	8.34	8.19	7.85
MnO	0.21	0.20	0.20	0.21	0.21	0.20	0.18	0.21	0.21	0.20
MgO	13.22	12.39	12.28	10.83	10.28	10.21	8.10	9.25	8.85	8.12
CaO	10.58	11.16	10.53	11.38	10.68	11.95	10.56	11.31	12.48	10.63
Na2O	2.08	2.14	2.28	2.29	2.54	2.11	2.74	2.35	2.35	2.67
K2O	1.16	1.12	1.22	1.15	1.25	1.04	1.00	1.20	1.23	1.49
P2O5	0.22	0.22	0.22	0.23	0.24	0.20	0.22	0.24	0.35	0.25
L.O.I.										
H2O-										
rest										
total	99.99	100.00	99.98	99.99	99.99	100.02	99.99	100.00	99.99	100.00
Cs										
Pb				4.60		1.80				
Rb	19.40	17.80	20.00	18.70	18.80	17.20	18.50	19.50	24.50	24.50
Ba	360.00	410.00	330.00	360.00	360.00	310.00	420.00	340.00	410.00	510.00
Sr	625.00	608.00	628.00	677.00	688.00	601.00	493.00	681.00	616.00	761.00
La				12.76		10.46				
Ce				28.40		24.10				
Pr				3.38		2.99				
Nd				15.38		13.38				
Sm				3.17		2.84				
Eu				1.01		0.88				
Gd				3.15		2.52				
Tb				0.49		0.42				
Dy				2.94		2.51				
Ho				0.59		0.56				
Er				1.70		1.48				
Yb				1.68		1.38				
Lu										
Y	18.20	16.50	17.20	17.90	19.00	17.40	24.10	20.90	29.10	20.30
Th				1.38		0.94				
U				0.46		0.31				
Zr	51.00	48.00	47.00	50.00	50.00	43.00	76.00	53.00	100.00	59.00
Hf				1.50		1.20				
Sn										
Nb				1.16		1.35				
Cu	130.00	90.00	125.00	130.00	40.00	130.00	95.00	95.00	100.00	120.00
Co	51.00	55.00	54.00	49.00	41.00	54.00	31.00	42.00	51.00	47.00
Sc	33.00	37.00	30.00	36.00	30.00	39.00	34.00	36.00	45.00	33.00
V	360.00	360.00	310.00	380.00	350.00	350.00	370.00	400.00	450.00	480.00
Cr	900.00	600.00	620.00	590.00	570.00	490.00	320.00	480.00	300.00	270.00
Ni	230.00	200.00	200.00	165.00	165.00	150.00	88.00	115.00	88.00	115.00

Gorton (1974) Gorton (1977)

	Ambae									
number	576A	552	524	512	541	482	572	548	573	515
SiO2	48.31	46.65	48.45	48.62	48.71	48.96	48.70	48.83	48.36	48.39
TiO2	0.79	1.24	0.80	0.80	0.79	0.84	0.84	1.07	0.87	0.82
Al2O3	14.73	14.38	15.57	15.04	15.69	16.18	15.77	16.41	15.62	15.99
Fe2O3	4.31	4.58	4.29	4.28	4.37	4.33	4.32	4.37	4.59	4.43
FeO	7.75	8.25	7.72	7.70	7.86	7.80	7.77	7.87	8.27	7.98
MnO	0.22	0.21	0.21	0.19	0.19	0.18	0.18	0.20	0.20	0.21
MgO	8.01	8.32	7.34	7.15	6.65	6.33	6.25	6.22	6.48	6.24
CaO	11.75	12.26	11.29	11.79	11.34	10.51	11.62	10.81	10.59	11.43
Na2O	2.57	2.38	2.58	2.63	2.74	3.07	2.86	2.78	2.91	2.74
K2O	1.30	1.38	1.47	1.53	1.43	1.54	1.42	1.16	1.79	1.50
P2O5	0.26	0.35	0.29	0.27	0.24	0.26	0.28	0.28	0.33	0.27
L.O.I.										
H2O-										
rest										
total	100.00	100.00	100.01	100.00	100.01	100.00	100.01	100.00	100.01	100.00
Cs										
Pb								3.80		
Rb	21.10	25.10	25.30	24.70	23.80	23.30	23.60	16.70	29.60	24.30
Ba	410.00	420.00	470.00	540.00	570.00	460.00	410.00	420.00	660.00	450.00
Sr	860.00	637.00	752.00	802.00	763.00	798.00	811.00	620.00	874.00	785.00
La								11.70		
Ce								26.10		
Pr								3.37		
Nd								13.70		
Sm								3.43		
Eu								1.15		
Gd								3.90		
Tb								0.58		
Dy								3.51		
Ho								0.79		
Er								2.30		
Yb								2.25		
Lu										
Y	20.20	32.10	21.10	20.50	20.00	21.40	20.90	29.40	23.30	21.60
Th								1.39		
U								0.41		
Zr	56.00	105.00	62.00	61.00	58.00	60.00	59.00	91.00	67.00	61.00
Hf								2.10		
Sn										
Nb								4.10		
Cu	150.00	105.00	120.00	71.00	67.00	80.00	150.00	115.00	190.00	170.00
Co	50.00	47.00	34.00	48.00	36.00	33.00	42.00	31.00	47.00	42.00
Sc	40.00	42.00	35.00	40.00	41.00	29.00	32.00	38.00	34.00	35.00
V	430.00	460.00	510.00	550.00	580.00	440.00	430.00	490.00	570.00	530.00
Cr	380.00	240.00	240.00	240.00	140.00	112.00	70.00	160.00	180.00	130.00
Ni	160.00	77.00	90.00	87.00	71.00	63.00	62.00	63.00	86.00	46.00

Gorton (1974) Gorton (1977)

Ambae

number	494	577	516	527	534	538	532	525	570	478
SiO2	49.78	49.35	49.66	49.71	47.62	48.81	47.57	49.42	49.32	48.87
TiO2	0.94	0.87	0.87	0.79	0.86	0.88	0.88	0.80	1.06	0.93
Al2O3	15.85	16.28	16.01	17.31	16.04	16.21	16.04	17.77	17.27	15.98
Fe2O3	4.38	4.31	4.50	4.19	4.84	4.56	4.88	4.16	4.27	4.76
FeO	7.89	7.75	8.11	7.55	8.71	8.20	8.77	7.48	7.68	8.56
MnO	0.22	0.20	0.21	0.18	0.20	0.20	0.21	0.19	0.20	0.21
MgO	5.88	5.70	5.80	5.29	5.92	5.49	5.82	4.90	5.03	5.20
CaO	10.16	10.81	10.47	10.48	11.59	10.62	11.65	10.86	10.67	10.37
Na2O	3.13	2.89	2.96	2.91	2.71	2.93	2.63	2.92	2.91	3.01
K2O	1.51	1.54	1.15	1.36	1.28	1.79	1.29	1.29	1.31	1.76
P2O5	0.28	0.28	0.25	0.23	0.22	0.32	0.25	0.21	0.28	0.34
L.O.I.										
H2O-										
rest										
total	100.02	99.98	99.99	100.00	99.99	100.01	99.99	100.00	100.00	99.99
Cs										
Pb			4.40			7.60				
Rb	24.00	25.90	20.20	23.60	18.20	28.20	19.80	19.40	22.00	28.40
Ba	430.00	500.00	430.00	490.00		510.00	430.00		400.00	480.00
Sr	680.00	721.00	538.00	735.00	743.00	935.00	761.00	714.00	676.00	851.00
La			7.10			12.40				
Ce			15.70			29.20				
Pr			2.20			3.80				
Nd			9.00			15.00				
Sm			2.52			3.78				
Eu			0.85			1.15				
Gd			2.88			3.20				
Tb			0.47			0.58				
Dy			2.90			3.30				
Ho			0.63			0.61				
Er			1.85			1.70				
Yb			1.80			1.70				
Lu										
Y	27.30	22.30	26.50	21.60	21.90	21.30	22.60	21.40	28.30	23.40
Th			0.95			2.00				
U			0.32			0.65				
Zr	74.00	61.00	63.00	63.00	59.00	67.00	58.00	60.00	85.00	68.00
Hf			1.50			1.90				
Sn										
Nb			1.70			1.50				
Cu	180.00	140.00	135.00	220.00		155.00	55.00		130.00	1.00
Co	40.00	40.00	32.00	39.00		32.00	47.00		39.00	35.00
Sc	30.00	32.00	35.00	33.00		27.00	36.00		32.00	29.00
V	380.00	490.00	460.00	52.00		450.00	530.00		490.00	440.00
Cr	140.00	95.00	91.00	55.00		29.00	12.00		88.00	9.00
Ni	52.00	59.00	32.00	29.00		35.00	30.00		38.00	30.00

Gorton (1974) Gorton (1977)

Ambae Low Ti Suite

number	68564	68611	68613	68615	68622	68623	68626	68627	68634	68576
SiO2	48.01	47.81	47.66	49.03	46.90	47.43	48.17	49.09	49.87	49.65
TiO2	0.64	0.70	0.61	0.75	0.54	0.59	0.60	0.79	0.83	1.00
Al2O3	12.19	12.59	11.26	14.48	9.35	11.18	11.67	16.23	16.11	16.98
Fe2O3	11.07	11.29	11.38	11.16	11.61	11.20	11.11	11.52	11.00	12.17
FeO										
MnO	0.19	0.19	0.19	0.18	0.20	0.19	0.19	0.20	0.18	0.21
MgO	13.49	12.08	16.16	8.62	19.35	14.85	14.27	5.91	6.38	4.58
CaO	11.20	11.86	9.74	12.14	9.97	10.94	10.63	11.54	10.87	10.12
Na2O	1.78	1.85	1.70	2.34	1.27	1.84	1.99	2.76	3.13	3.01
K2O	1.19	0.89	0.85	1.17	0.84	1.18	1.23	1.45	1.54	1.45
P2O5	0.23	0.18	0.17	0.25	0.17	0.23	0.23	0.27	0.29	0.29
L.O.I.	-0.10	0.15	-0.09	0.16	-0.21	-0.32	-0.19	-0.11	-0.04	0.25
H2O-										
rest										
total	99.89	99.59	99.63	100.28	99.99	99.31	99.90	99.65	100.16	99.71
Cs										
Pb										
Rb	20.00	13.00	13.00	17.00	12.00	21.00	19.00	22.00	23.00	27.00
Ba	417.00	345.00	347.00	430.00	329.00	470.00	415.00	508.00	543.00	467.00
Sr	683.00	583.00	493.00	710.00	490.00	641.00	643.00	774.00	790.00	654.00
La	11.20	9.60	9.00	12.90	8.13	12.80	12.40	15.00	15.50	14.70
Ce	25.90	22.60	15.90	22.70	19.00	29.30	26.00	29.10	34.10	29.90
Pr					2.49					
Nd	16.60	12.60	11.60	15.70	11.40	16.50	15.80	18.30	18.50	17.40
Sm					2.62					
Eu					0.83					
Gd					2.44					
Tb										
Dy					2.10					
Ho										
Er					1.24					
Yb					0.99					
Lu										
Y	16.00	17.00	16.00	19.00	12.00	16.00	17.00	21.00	20.00	26.00
Th										
U										
Zr	48.00	47.00	38.00	50.00	34.00	45.00	45.00	56.00	60.00	76.00
Hf										
Sn										
Nb	2.00	2.00	2.00	2.00	1.00	2.00	1.00	1.00	2.00	2.00
Cu										
Co										
Sc	38.00	41.00	35.00	41.00	38.00	35.00	38.00	34.00	31.00	33.00
V	328.00	385.00	306.00	381.00	257.00	298.00	299.00	403.00	398.00	443.00
Cr	741.00	552.00	949.00	296.00	1221.00	732.00	735.00	30.00	131.00	23.00
Ni	268.00	190.00	378.00	113.00	457.00	306.00	301.00	46.00	68.00	25.00

This study

Ambae Low Ti Suite

number	68583	68584	68588	68591	68599	68605	68606	68610	68562	68635
SiO2	47.68	49.59	49.37	47.33	48.70	48.10	49.49	49.30	48.96	48.92
TiO2	0.59	0.75	0.85	0.55	0.72	0.64	0.85	0.86	0.72	0.70
Al2O3	11.34	14.93	16.46	10.06	15.87	12.66	16.46	15.97	13.90	13.76
Fe2O3	11.39	11.01	11.58	11.14	10.93	11.39	11.15	11.85	11.13	11.19
FeO										
MnO	0.19	0.19	0.20	0.18	0.19	0.19	0.19	0.20	0.20	0.20
MgO	14.83	7.67	5.39	17.75	7.53	13.02	6.28	6.51	9.95	10.77
CaO	11.15	12.39	10.83	10.54	12.04	11.04	10.74	11.17	11.50	11.21
Na2O	1.66	2.23	2.93	1.62	2.43	1.84	2.93	2.91	2.22	2.14
K2O	1.04	1.26	1.75	0.92	0.91	1.10	1.63	1.38	1.31	1.28
P2O5	0.22	0.23	0.30	0.22	0.20	0.23	0.32	0.27	0.26	0.26
L.O.I.	-0.18	0.03	0.22	-0.17	0.54	-0.19	0.33	-0.03	-0.23	-0.23
H2O-										
rest										
total	99.91	100.28	99.88	100.14	100.06	100.02	100.37	100.39	99.92	100.20
Cs										
Pb										
Rb	20.00	18.00	28.00	17.00	14.00	16.00	32.00	18.00	22.00	23.00
Ba	347.00	485.00	597.00	258.00	359.00	375.00	488.00	513.00	445.00	446.00
Sr	557.00	732.00	938.00	488.00	578.00	632.00	773.00	727.00	673.00	763.00
La	12.70	12.10	14.30	10.10	10.00	12.40	15.70	12.90	12.60	15.40
Ce	24.00	25.90	33.90	23.50	17.50	24.30	32.00	29.70	28.70	29.30
Pr			4.37							
Nd	15.90	18.30	19.40	12.40	11.70	15.80	20.90	17.90	15.30	18.80
Sm			4.50							
Eu			1.52							
Gd			4.09							
Tb										
Dy			3.26							
Ho										
Er			1.73							
Yb			1.48							
Lu										
Y	15.00	19.00	21.00	13.00	18.00	16.00	21.00	20.00	17.00	19.00
Th										
U										
Zr	46.00	52.00	65.00	39.00	47.00	45.00	68.00	57.00	53.00	52.00
Hf										
Sn										
Nb	2.00	1.00	2.00	1.00	2.00	2.00	3.00	3.00	2.00	2.00
Cu										
Co										
Sc	40.00	37.00	29.00	40.00	42.00	39.00	33.00	34.00	36.00	35.00
V	288.00	370.00	428.00	270.00	369.00	320.00	393.00	408.00	359.00	354.00
Cr	789.00	211.00	20.00	1177.00	199.00	652.00	166.00	106.00	343.00	467.00
Ni	281.00	79.00	40.00	418.00	75.00	253.00	72.00	55.00	146.00	187.00

This study

Ambae Low Ti Suite

number	68637	68638	68639	68642	68565
SiO2	50.02	48.79	47.76	48.01	50.38
TiO2	0.84	0.65	0.54	0.56	0.79
Al2O3	16.53	13.21	11.18	11.44	15.83
Fe2O3	10.97	11.06	11.19	11.14	10.52
FeO					
MnO	0.19	0.18	0.19	0.20	0.18
MgO	5.90	10.41	15.61	14.74	6.58
CaO	10.78	12.10	11.15	11.53	11.68
Na2O	3.20	2.19	1.64	1.77	2.60
K2O	1.53	1.00	0.89	0.90	1.46
P2O5	0.27	0.18	0.18	0.17	0.26
L.O.I.	0.04	-0.51	-0.42	-0.49	-0.09
H2O-					
rest					
total	100.27	99.26	99.91	99.97	100.19
Cs					
Pb					
Rb	24.00	15.00	15.00	15.00	23.00
Ba	546.00	366.00	330.00	363.00	500.00
Sr	819.00	585.00	526.00	542.00	748.00
La	13.70	8.74	10.70	7.90	12.80
Ce	27.00	21.10	16.50	18.90	26.40
Pr		2.83			
Nd	17.50	12.90	13.50	13.30	16.70
Sm		3.05			
Eu		1.08			
Gd		3.04			
Tb					
Dy		2.96			
Ho					
Er		1.96			
Yb		1.73			
Lu					
Y	20.00	16.00	14.00	17.00	22.00
Th					
U					
Zr	60.00	41.00	36.00	37.00	56.00
Hf					
Sn					
Nb	2.00	1.00	2.00	2.00	1.00
Cu					
Co					
Sc	29.00	44.00	42.00	40.00	37.00
V	429.00	343.00	302.00	280.00	
Cr	96.00	465.00	858.00	773.00	
Ni	55.00	163.00	330.00	302.00	

This study

Ambae High Ti Suite

number	68577	68573	68574	68586	68587	68595	68596	68603	68569	68570
SiO2	55.95	47.31	48.75	49.03	49.94	47.66	48.11	49.67	47.79	48.50
TiO2	1.30	1.36	1.24	1.19	1.16	1.27	1.58	1.31	1.22	1.61
Al2O3	15.96	14.81	16.06	16.03	15.85	15.22	16.78	17.09	14.27	16.85
Fe2O3	9.35	12.16	13.16	11.39	10.88	11.60	12.54	10.90	11.65	12.48
FeO										
MnO	0.21	0.22	0.23	0.22	0.21	0.21	0.23	0.18	0.21	0.21
MgO	2.47	8.05	5.26	6.90	6.12	7.35	4.99	5.28	8.56	4.88
CaO	5.85	12.67	10.95	10.91	10.40	12.19	10.93	10.86	12.58	10.76
Na2O	4.92	2.40	2.91	2.83	3.07	2.48	3.15	2.96	1.97	2.84
K2O	2.40	0.86	1.29	0.92	1.21	1.50	1.51	1.36	1.33	1.54
P2O5	0.66	0.28	0.31	0.30	0.32	0.37	0.45	0.35	0.37	0.45
L.O.I.	0.45	-0.02	-0.02	0.32	0.15			0.23	-0.22	0.13
H2O-										
rest										
total	99.52	100.10	100.14	100.04	99.31	99.85	100.27	100.19	99.73	100.25
Cs										
Pb										
Rb	38.00	13.00	18.00	12.00	22.00	31.00	30.00	21.00	27.00	32.00
Ba	713.00	292.00	401.00	398.00	407.00	452.00	383.00	427.00	431.00	394.00
Sr	438.00	536.00	676.00	579.00	586.00	674.00	630.00	687.00	627.00	658.00
La	26.60	13.20	14.80	15.50	15.90	20.20	20.90	18.00	16.80	20.30
Ce	65.50	30.20	36.00	33.90	34.20	42.90	43.30	36.30	37.40	44.30
Pr	8.32		4.55						4.74	5.99
Nd	36.30	18.80	21.70	19.60	20.60	25.70	28.90	22.10	22.60	27.70
Sm	7.74		5.00						5.06	6.36
Eu	2.20		1.63						1.51	2.07
Gd	7.95		5.18						5.05	6.38
Tb										
Dy	8.56		5.27						5.02	6.62
Ho										
Er	5.47		3.13						2.82	3.96
Yb	5.14		2.77						2.60	3.47
Lu										
Y	49.00	32.00	31.00	32.00	32.00	32.00	37.00	33.00	30.00	38.00
Th										
U										
Zr	194.00	107.00	94.00	117.00	123.00	108.00	141.00	118.00	102.00	146.00
Hf										
Sn										
Nb	10.00	9.00	5.00	8.00	7.00	8.00	12.00	8.00	7.00	12.00
Cu										
Co										
Sc	21.00	40.00	36.00	35.00	34.00	38.00	30.00	33.00	42.00	33.00
V	222.00	387.00	454.00	356.00	347.00	347.00	421.00	379.00	343.00	428.00
Cr	3.00	187.00	13.00	130.00	167.00	167.00	18.00	80.00	241.00	11.00
Ni	3.00	69.00	28.00	58.00	53.00	58.00	24.00	34.00	78.00	22.00

This study

Ambae High Ti Suite

number	68578	68593	68571
SiO2	47.74	49.99	47.76
TiO2	1.07	1.17	1.24
Al2O3	13.84	15.83	14.28
Fe2O3	12.10	10.96	11.70
FeO			
MnO	0.21	0.20	0.21
MgO	9.65	6.34	8.60
CaO	12.34	10.45	12.72
Na2O	2.01	2.99	2.16
K2O	0.75	1.20	1.37
P2O5	0.20	0.31	0.33
L.O.I.	-0.21	0.11	-0.07
H2O-			
rest			
total	99.70	99.55	100.30
Cs			
Pb			
Rb	11.00	19.00	26.00
Ba	294.00	411.00	431.00
Sr	487.00	579.00	634.00
La	9.49	14.20	17.90
Ce	23.80	31.90	38.20
Pr	3.14		
Nd	15.20	21.50	23.40
Sm	3.88		
Eu	1.29		
Gd	4.15		
Tb			
Dy	4.45		
Ho			
Er	2.58		
Yb	2.35		
Lu			
Y	24.00	32.00	30.00
Th			
U			
Zr	70.00	122.00	101.00
Hf			
Sn			
Nb	4.00	7.00	7.00
Cu			
Co			
Sc	44.00	36.00	43.00
V	370.00	365.00	374.00
Cr	308.00	136.00	250.00
Ni	101.00	54.00	75.00

This study

Ambae High K Suite

number	68566	68567
SiO2	47.11	47.18
TiO2	0.58	0.58
Al2O3	10.70	10.87
Fe2O3	11.24	11.14
FeO		
MnO	0.19	0.19
MgO	15.60	16.05
CaO	11.29	11.11
Na2O	1.40	1.38
K2O	1.40	1.52
P2O5	0.31	0.34
L.O.I.	0.06	-0.22
H2O-		
rest		
total	99.88	100.14
Cs		
Pb		
Rb	42.00	52.00
Ba	409.00	433.00
Sr	645.00	638.00
La	15.00	16.10
Ce	32.00	33.20
Pr		4.44
Nd	18.70	21.50
Sm		4.54
Eu		1.47
Gd		4.16
Tb		
Dy		3.70
Ho		
Er		2.11
Yb		1.92
Lu		
Y	17.00	17.00
Th		
U		
Zr	57.00	60.00
Hf		
Sn		
Nb	1.00	2.00
Cu		
Co		
Sc	40.00	39.00
V		280.00
Cr		896.00
Ni		330.00

This study

					Ambrym					
number	1566	1567	1568	1569	2	3	5	6	8	9
SiO2	51.23	48.92	52.57	52.43	49.26	49.60	50.66	50.82	49.90	51.08
TiO2	0.87	0.63	0.99	1.07	0.89	1.00	0.95	0.88	0.72	0.90
Al2O3	17.47	13.40	16.70	16.74	17.18	17.20	15.84	13.87	12.74	16.66
Fe2O3	1.64	1.71	1.65	1.98	5.47	3.97	12.62	11.50	11.00	11.31
FeO	8.20	8.51	8.25	9.91	6.10	7.85				
MnO	0.19	0.20	0.19	0.23		0.37	0.23	0.20	0.19	0.20
MgO	5.14	11.50	4.65	4.13	4.28	4.98	4.75	7.71	10.96	4.76
CaO	10.31	11.96	8.83	9.13	10.78	10.12	9.48	10.33	11.22	9.75
Na2O	2.81	1.99	3.27	3.24	3.20	2.24	3.12	2.55	2.26	3.00
K2O	1.87	1.03	2.55	0.97	1.76	1.66	1.86	1.74	1.28	1.87
P2O5	0.26	0.17	0.35	0.17	0.37	0.40	0.34	0.34	0.22	0.33
L.O.I.	0.81	0.43	0.49	0.93	0.90		-0.03	-0.42	-0.21	-0.21
H2O-					0.12					
rest										
total	100.80	100.45	100.49	100.93	100.31	99.39	99.82	99.52	100.28	99.65
Cs										
Pb	8.00	8.00	11.00	5.60						
Rb	34.20	18.20	50.10	15.80			36.00	37.00	23.00	36.00
Ba		240.00	400.00	310.00			395.00	415.00	307.00	406.00
Sr	672.00	480.00	690.00	416.00			639.00	542.00	483.00	666.00
La		9.49	10.50	6.46			10.90	11.50	9.10	11.50
Ce			22.40	16.20			20.70	25.90	15.70	24.50
Pr		2.95	3.10	2.20						
Nd		13.17	13.20	9.20			16.00	15.10	11.40	16.20
Sm		2.63	3.38	2.72						
Eu		0.83	1.11	0.95						
Gd		2.63	3.70	3.40						
Tb		0.41	0.55	0.51						
Dy		2.44	3.20	3.37						
Ho		0.48	0.73	0.83						
Er		1.32	2.06	2.42						
Yb		1.26	2.03	2.35						
Lu										
Y	20.80	15.10	22.90	29.00			23.00	18.00	16.00	20.00
Th		1.18	1.94	0.83						
U		0.31	0.70	0.28						
Zr	74.00	45.00	92.10	73.40			73.00	71.00	54.00	79.00
Hf		1.30	2.60	2.00						
Sn										
Nb		1.48	3.30	1.95			2.00	3.00	2.00	3.00
Cu										
Co										
Sc							37.00	37.00	44.00	37.00
V							398.00	357.00	325.00	383.00
Cr							12.00	279.00	579.00	25.00
Ni							26.00	88.00	216.00	31.00

Gorton (1977) This study

	Ambrym									
number	14	17	16	20	21	26	27	37	40	47
SiO2	51.54	48.97	49.54	50.62	51.26	51.45	51.24	49.09	54.42	51.59
TiO2	0.96	0.81	0.63	0.92	0.87	0.70	0.81	0.51	0.86	0.93
Al2O3	16.52	16.11	10.00	16.30	17.85	14.71	17.90	21.10	16.15	16.46
Fe2O3	11.55	11.95	10.92	12.32	10.56	10.68	10.17	8.82	11.28	10.98
FeO										
MnO	0.20	0.21	0.19	0.22	0.19	0.18	0.17	0.14	0.23	0.18
MgO	4.54	6.36	13.56	4.61	4.28	9.16	4.60	3.70	3.79	4.76
CaO	9.06	11.76	12.36	9.62	9.87	10.08	10.06	12.20	8.21	9.02
Na2O	3.44	2.46	1.83	3.25	3.02	2.55	2.91	2.56	3.52	3.28
K2O	2.14	1.11	1.11	1.84	1.86	1.09	1.84	0.56	1.30	2.15
P2O5	0.39	0.21	0.20	0.35	0.35	0.21	0.33	0.09	0.27	0.39
L.O.I.	-0.29	-0.22	-0.27	-0.23	0.10	-0.41	-0.08	0.54	0.19	-0.07
H2O-										
rest										
total	100.05	99.73	100.07	99.82	100.21	100.40	99.95	99.31	100.22	99.67
Cs										
Pb										
Rb	41.00	19.00	24.00	37.00	37.00	21.00	34.00	9.00	25.00	42.00
Ba	466.00	258.00	272.00	405.00	437.00	254.00	420.00	215.00	394.00	450.00
Sr	676.00	554.00	390.00	670.00	698.00	436.00	695.00	501.00	423.00	651.00
La	13.80	8.90	6.80	9.80	11.50	8.20	10.70	3.00	10.20	11.50
Ce	27.50	14.70	14.60	24.40	21.30	12.40	22.70	10.20	18.60	25.80
Pr										
Nd	15.40	11.30	10.80	16.10	15.60	12.30	14.60	9.00	14.30	16.50
Sm										
Eu										
Gd										
Tb										
Dy										
Ho										
Er										
Yb										
Lu										
Y	21.00	16.00	13.00	22.00	19.00	17.00	18.00	13.00	26.00	18.00
Th										
U										
Zr	84.00	50.00	45.00	72.00	75.00	55.00	70.00	24.00	73.00	82.00
Hf										
Sn										
Nb	3.00	3.00	2.00	3.00	3.00	2.00	2.00	1.00	2.00	3.00
Cu										
Co										
Sc	33.00	45.00	51.00	35.00	32.00	35.00	30.00	30.00	37.00	30.00
V	379.00	399.00	299.00	383.00	366.00	304.00	331.00	270.00	185.00	376.00
Cr	11.00	54.00	899.00	13.00	25.00	541.00	67.00	23.00	16.00	53.00
Ni	25.00	35.00	226.00	27.00	26.00	174.00	39.00	16.00	15.00	39.00

This study

	Ambrym									
number	48	49	50	51	55	58	59	61	62	63
SiO2	50.71	50.35	50.25	50.47	50.81	48.58	64.25	49.21	50.80	48.53
TiO2	0.80	0.89	0.89	0.88	0.87	0.72	0.50	0.76	0.80	0.72
Al2O3	17.51	16.38	16.45	17.10	17.30	14.36	15.95	14.37	18.56	14.06
Fe2O3	9.96	12.00	12.43	10.74	11.19	10.22	5.97	10.36	9.69	10.44
FeO										
MnO	0.17	0.21	0.21	0.19	0.19	0.17	0.17	0.18	0.16	0.17
MgO	5.12	4.62	4.77	4.52	4.51	10.44	1.33	10.33	4.35	11.85
CaO	10.09	9.63	9.47	9.61	9.82	12.44	3.00	12.22	9.89	10.62
Na2O	2.89	3.31	3.46	3.39	2.79	2.02	5.06	2.17	3.08	2.14
K2O	1.73	1.85	1.77	1.91	1.87	0.62	3.76	0.78	1.79	0.83
P2O5	0.30	0.32	0.34	0.33	0.35	0.11	0.20	0.16	0.33	0.12
L.O.I.	0.08	-0.14	-0.26	0.49	-0.26	-0.36	0.01	-0.42	-0.03	-0.09
H2O-										
rest										
total	99.36	99.42	99.78	99.63	99.44	99.32	100.20	100.12	99.42	99.39
Cs										
Pb										
Rb	32.00	35.00	35.00	34.00	36.00	9.00	71.00	14.00	32.00	12.00
Ba	395.00	406.00	385.00	404.00	417.00	191.00	739.00	220.00	427.00	221.00
Sr	704.00	660.00	653.00	680.00	680.00	313.00	319.00	352.00	729.00	360.00
La	8.70	10.10	8.50	9.90	10.70	3.50	18.80	5.40	12.10	4.70
Ce	22.20	23.30	20.30	24.00	22.80	8.40	39.10	14.20	23.60	11.60
Pr										
Nd	15.60	15.10	15.70	15.20	16.60	6.00	21.40	9.40	15.20	8.00
Sm										
Eu										
Gd										
Tb										
Dy										
Ho										
Er										
Yb										
Lu										
Y	18.00	21.00	20.00	20.00	19.00	16.00	30.00	17.00	18.00	15.00
Th										
U										
Zr	69.00	69.00	71.00	77.00	75.00	36.00	181.00	44.00	69.00	42.00
Hf										
Sn										
Nb	3.00	2.00	2.00	2.00	2.00	1.00	6.00	2.00	3.00	1.00
Cu										
Co										
Sc	31.00	34.00	33.00	32.00	32.00	47.00	13.00	44.00	27.00	38.00
V	339.00	374.00	372.00	374.00	351.00	287.00	20.00	285.00	309.00	308.00
Cr	86.00	16.00	16.00	26.00	35.00	464.00	6.00	434.00	49.00	547.00
Ni	47.00	27.00	27.00	28.00	33.00	109.00	3.00	115.00	38.00	211.00

This study

	Ambrym									
number	66	71	74	87	89	96	97	101	102	109
SiO2	48.39	49.75	48.08	52.41	48.82	48.75	51.59	50.84	50.82	49.23
TiO2	0.68	0.57	0.77	0.85	0.80	0.66	0.85	0.91	0.93	0.65
Al2O3	13.33	8.77	15.12	19.07	16.22	10.28	18.22	16.04	16.47	18.55
Fe2O3	10.33	9.50	11.08	9.03	13.05	11.19	9.79	12.57	12.21	10.58
FeO										
MnO	0.17	0.18	0.18	0.14	0.21	0.18	0.15	0.22	0.22	0.18
MgO	12.60	13.10	9.77	3.90	4.44	13.28	4.37	4.35	4.53	4.89
CaO	11.23	16.75	11.64	9.07	10.44	12.10	9.28	9.30	9.60	11.78
Na2O	1.93	1.17	2.81	3.27	2.33	1.86	3.35	3.37	3.27	2.92
K2O	0.74	0.25	0.66	2.24	1.10	1.13	2.09	2.83	1.81	1.16
P2O5	0.15	0.03	0.14	0.40	0.20	0.22	0.39	0.33	0.32	0.17
L.O.I.	-0.16	0.06	-0.26	0.17	1.94	-0.30	-0.13	-0.43	-0.26	-0.27
H2O-										
rest										
total	99.39	100.13	99.99	100.55	99.55	99.35	99.95	100.33	99.92	99.84
Cs										
Pb										
Rb	13.00	4.00	11.00	44.00	24.00	23.00	43.00	36.00	37.00	21.00
Ba	210.00	111.00	187.00	466.00	302.00	289.00	467.00	417.00	414.00	305.00
Sr	334.00	163.00	332.00	774.00	530.00	395.00	760.00	649.00	678.00	618.00
La	5.70		6.10	12.70	9.90	8.30	12.40	9.30	12.90	8.30
Ce	10.20		11.70	29.80	20.70	15.00	24.30	26.40	21.40	19.90
Pr										
Nd	8.20	5.00	7.40	17.80	12.70	10.70	16.00	16.20	15.90	11.60
Sm										
Eu										
Gd										
Tb										
Dy										
Ho										
Er										
Yb										
Lu										
Y	15.00	14.00	16.00	17.00	17.00	14.00	18.00	21.00	21.00	16.00
Th										
U										
Zr	39.00	23.00	40.00	86.00	44.00	46.00	77.00	74.00	74.00	48.00
Hf										
Sn										
Nb	1.00	1.00	1.00	3.00	1.00	2.00	3.00	2.00	2.00	2.00
Cu										
Co										
Sc	44.00	88.00	44.00	22.00	32.00	52.00	24.00	35.00	33.00	38.00
V	289.00	297.00	280.00	317.00	411.00	281.00	323.00	395.00	366.00	320.00
Cr	801.00	1034.00	324.00	55.00	17.00	876.00	51.00	5.00	12.00	70.00
Ni	223.00	101.00	97.00	41.00	22.00	220.00	38.00	19.00	25.00	33.00

This study

Ambrym

number	110	113
SiO2	49.85	50.89
TiO2	0.73	0.80
Al2O3	17.41	18.45
Fe2O3	11.04	10.06
FeO		
MnO	0.18	0.17
MgO	4.89	4.34
CaO	10.96	10.29
Na2O	2.98	3.32
K2O	1.49	1.66
P2O5	0.24	0.27
L.O.I.	-0.14	0.03
H2O-		
rest		
total	99.63	100.28
Cs		
Pb		
Rb	21.00	31.00
Ba	324.00	392.00
Sr	618.00	702.00
La	9.20	9.30
Ce	19.50	21.20
Pr		
Nd	13.60	14.10
Sm		
Eu		
Gd		
Tb		
Dy		
Ho		
Er		
Yb		
Lu		
Y	16.00	18.00
Th		
U		
Zr	48.00	71.00
Hf		
Sn		
Nb	2.00	3.00
Cu		
Co		
Sc	38.00	29.00
V	337.00	323.00
Cr	16.00	32.00
Ni	28.00	30.00

This study

Ambrym

number	S4	S16	S19	S20	S28	S35	S38	S50	S51	S54
SiO2	51.44	51.73	48.93	50.89	51.81	53.36	52.04	50.78	51.27	50.27
TiO2	0.84	0.92	0.60	0.94	0.96	0.98	0.96	0.86	0.86	0.70
Al2O3	17.63	17.14	13.59	16.40	16.73	16.88	16.55	17.12	17.85	17.71
Fe2O3				12.29			10.64	11.25		
FeO	9.74	10.20	9.99		11.21	9.65			10.08	10.39
MnO	0.17	0.19	0.18	0.22	0.22	0.18	0.17	0.19	0.18	0.19
MgO	4.88	4.40	11.06	4.27	4.32	4.44	4.51	4.88	4.53	5.59
CaO	10.38	10.37	12.16	9.01	9.27	8.84	8.73	10.01	10.04	11.89
Na2O	2.79	2.58	2.02	3.12	3.17	2.70	3.28	2.84	2.96	1.99
K2O	1.83	2.11	1.27	1.94	1.97	2.53	2.32	1.84	1.89	1.08
P2O5	0.33	0.41	0.23	0.38	0.39	0.49	0.42	0.33	0.38	0.23
L.O.I.				0.41			0.22	0.35		
H2O-										
rest										
total	100.03	100.05	100.03	99.87	100.05	100.05	99.84	100.45	100.04	100.04
Cs										
Pb										
Rb	35.00	47.00	19.00	40.00		19.00	51.00	36.00	39.00	22.00
Ba										
Sr	683.00	645.00	491.00	679.00		508.00	703.00	678.00	714.00	571.00
La										
Ce										
Pr										
Nd										
Sm										
Eu										
Gd										
Tb										
Dy										
Ho										
Er										
Yb										
Lu										
Y	19.00	20.00	15.00	24.00		18.00	22.00	19.00	19.00	18.00
Th										
U										
Zr	74.00	82.00	46.00	81.00		52.00	96.00	76.00	78.00	52.00
Hf										
Sn										
Nb	2.80	2.50	0.70	1.90		1.00	2.80	2.00	3.00	0.60
Cu										
Co										
Sc										
V	333.00	349.00	303.00	365.00	344.00	386.00	453.00	328.00	355.00	340.00
Cr	55.00	29.00	528.00	7.00	6.00	12.00	22.00	44.00	37.00	46.00
Ni	35.00	32.00	175.00	17.00	14.00	16.00	30.00	31.00	29.00	31.00

Stephenson (unpubl. data) & this study

Ambrym

number	S55	S56	S61	S83	S87	S93	S110	S121	S126	S06
SiO2	50.26	52.20	49.92	52.09	50.24	51.20	51.34	53.03	50.87	51.15
TiO2	0.72	0.94	0.41	0.83	0.89	0.92	1.02	0.76	0.91	0.96
Al2O3	17.33	16.99	12.24	18.65	16.32	16.39	16.33	16.48	16.75	16.20
Fe2O3							12.62			
FeO	10.57	9.98	9.41	8.84	11.60	11.29		9.95	11.14	11.62
MnO	0.19	0.18	0.19	0.17	0.22	0.22	0.22	0.22	0.21	0.22
MgO	5.62	4.53	11.41	4.17	5.25	4.93	3.85	4.47	5.07	4.71
CaO	12.00	9.32	14.30	9.74	10.91	9.44	8.94	10.79	10.07	9.77
Na2O	2.04	3.01	1.63	3.07	2.75	3.38	3.20	2.72	2.84	3.06
K2O	1.11	2.53	0.43	2.07	1.49	1.93	0.95	1.10	1.84	1.96
P2O5	0.22	0.45	0.11	0.43	0.36	0.32	0.21	0.19	0.35	0.39
L.O.I.							0.49			
H2O-										
rest										
total	100.06	100.13	100.05	100.06	100.03	100.02	99.17	99.71	100.05	100.04
Cs										
Pb										
Rb	22.00	44.00	8.00	43.00	30.00	48.00	18.00	21.00		
Ba										
Sr	568.00	683.00	312.00	753.00	689.00	645.00	410.00	421.00		
La										
Ce										
Pr										
Nd										
Sm										
Eu										
Gd										
Tb										
Dy										
Ho										
Er										
Yb										
Lu										
Y	17.00	20.00	11.00	19.00	20.00	16.00	27.00	23.00		
Th										
U										
Zr	53.00	90.00	23.00	82.00	71.00	77.00	77.00	70.00		
Hf										
Sn										
Nb	1.10	3.20	0.80	2.50	2.40	3.10	1.60	1.30		
Cu										
Co										
Sc										
V	343.00	393.00	300.00	319.00	417.00	368.00	404.00	297.00		
Cr	46.00	23.00	615.00	42.00	37.00	20.00	9.00	23.00		
Ni	31.00	33.00	99.00	29.00	28.00	19.00	9.00	19.00		

Stephenson (unpubl. data) & this study

	Ambrym									
number	GR18	GR45	GR47	M78	M88	M102	M117	M119	M123	M133
SiO2	47.51	52.37	50.97	49.16	55.36	51.47	49.71	50.64	53.60	54.38
TiO2	0.44	0.92	1.05	0.62	0.96	0.88	0.92	0.92	0.85	0.86
Al2O3	11.93	17.81	17.80	14.06	16.19	17.25	16.05	17.17	15.91	16.01
Fe2O3	9.96						12.68		11.13	
FeO		9.43	9.92	9.03	11.10	10.11		11.21		11.43
MnO	0.18	0.17	0.17	0.17	0.24	0.18	0.21	0.21	0.20	0.21
MgO	13.05	4.21	6.07	12.24	3.36	4.77	4.83	4.57	3.46	3.95
CaO	12.38	9.28	10.58	11.91	7.49	10.20	9.95	10.20	7.99	8.35
Na2O	1.31	3.18	2.97	1.99	3.59	2.97	2.65	3.14	3.67	3.42
K2O	0.59	2.24	0.33	0.63	1.29	1.81	1.67	1.75	1.25	1.20
P2O5	0.10	0.39	0.17	0.18	0.33	0.40	0.31	0.34	0.25	0.23
L.O.I.	2.66						0.50		1.00	
H2O-										
rest										
total	100.11	100.00	100.03	99.99	99.91	100.04	99.48	100.15	99.31	100.04
Cs										
Pb										
Rb	12.00	43.00	9.00	10.00	27.00	35.00	33.00	34.00		23.00
Ba										
Sr	321.00	722.00	293.00	366.00	442.00	665.00	651.00	710.00		401.00
La										
Ce										
Pr										
Nd										
Sm										
Eu										
Gd										
Tb										
Dy										
Ho										
Er										
Yb										
Lu										
Y	12.00	22.00	28.00	13.00	26.00	19.00	21.00	20.00		27.00
Th										
U										
Zr	29.00	90.00	82.00	42.00	72.00	79.00	73.00	72.00		74.00
Hf										
Sn										
Nb	0.30	2.60	2.80	0.90	2.80	2.90	2.30	2.60		2.30
Cu										
Co										
Sc										
V	261.00	352.00	294.00	250.00	331.00	379.00	378.00	361.00		376.00
Cr	965.00	137.00	139.00	801.00	179.00	98.00	105.00	155.00		80.00
Ni	180.00	38.00	32.00	173.00	71.00	29.00	25.00	21.00		14.00

Stephenson (unpubl. data) & this study

	Ambrym									
number	M146C	A23	A28	A29	A35	A38	A40	A43	A44	A1
SiO2	50.78	49.13	50.68	51.97	51.71	46.87	52.31	49.16	47.50	50.63
TiO2	0.72	0.86	0.92	0.84	0.91	0.14	0.85	0.80	0.42	0.85
Al2O3	19.51	17.36	15.73	18.37	17.48	22.53	18.25	16.64	16.79	15.99
Fe2O3						5.78		12.93	10.99	
FeO	10.06	11.26	12.83	8.85	10.19		8.85			10.85
MnO	0.18	0.22	0.26	0.17	0.20	0.09	0.17	0.25	0.19	0.23
MgO	3.78	5.95	4.93	4.66	4.75	6.16	4.43	5.28	8.24	6.35
CaO	11.28	11.27	9.86	9.40	9.94	15.40	9.45	10.82	12.93	10.46
Na2O	2.62	2.56	3.05	3.27	2.53	1.46	3.20	2.84	1.72	2.72
K2O	0.78	1.12	1.45	2.08	1.91	0.13	2.11	0.65	0.41	1.63
P2O5	0.19	0.25	0.29	0.37	0.37	0.03	0.37	0.11	0.10	0.28
L.O.I.						1.00		0.58	0.22	
H2O-										
rest										
total	99.90	99.98	100.00	99.98	99.99	99.59	99.99	100.06	99.51	99.99
Cs										
Pb										
Rb	14.00	18.00	26.00	44.00	35.00		42.00	15.00	10.00	33.00
Ba										
Sr	483.00	584.00	559.00	770.00	690.00		741.00	553.00	470.00	628.00
La										
Ce										
Pr										
Nd										
Sm										
Eu										
Gd										
Tb										
Dy										
Ho										
Er										
Yb										
Lu										
Y	20.00	20.00	21.00	19.00	20.00		19.00	18.00	12.00	19.00
Th										
U										
Zr	47.00	56.00	67.00	85.00	84.00		81.00	25.00	22.00	65.00
Hf										
Sn										
Nb	0.80	1.90	2.30	3.20	2.20		3.00	0.20	0.60	1.50
Cu										
Co										
Sc										
V	360.00	381.00	427.00	259.00	349.00		317.00	438.00	218.00	342.00
Cr	109.00	34.00	10.00	69.00	28.00		69.00	27.00	73.00	154.00
Ni	18.00	37.00	21.00	49.00	31.00		53.00	31.00	69.00	70.00

Stephenson (unpubl. data) & this study

	Ambrym									
number	A3	A6	A7	A12	A16	A18	A19	L9	L12	1566
SiO2	48.62	49.97	51.75	50.99	50.55	48.90	52.51	51.29	50.12	51.23
TiO2	0.62	0.82	0.83	0.94	0.95	0.56	0.97	0.97	0.77	0.87
Al2O3	12.08	16.14	18.20	16.22	16.08	15.65	16.68	16.26	14.55	17.47
Fe2O3	11.17				12.68	11.17				1.64
FeO		11.28	9.33	11.71			9.79	11.77	9.81	8.20
MnO	0.19	0.22	0.19	0.24	0.22	0.19	0.19	0.24	0.19	0.19
MgO	12.00	6.04	4.24	4.78	4.83	7.63	4.51	4.83	9.30	5.14
CaO	12.64	11.02	9.91	9.72	9.63	12.13	8.81	9.71	11.55	10.31
Na2O	1.60	2.71	3.25	3.25	3.09	2.13	3.70	2.67	2.15	2.81
K2O	0.89	1.54	1.93	1.90	1.85	0.85	2.43	1.91	1.32	1.87
P2O5	0.16	0.26	0.36	0.33	0.34	0.15	0.42	0.36	0.25	0.26
L.O.I.	0.24				-0.64	0.18				0.81
H2O-										
rest										
total	100.21	100.00	99.99	100.08	99.58	99.54	100.01	100.01	100.01	100.80
Cs										
Pb										
Rb	21.00	28.00	42.00	38.00	37.00	16.00	50.00	39.00	26.00	34.20
Ba										
Sr	449.00	640.00	758.00	684.00	656.00	472.00	695.00	705.00	559.00	672.00
La										
Ce										
Pr										
Nd										
Sm										
Eu										
Gd										
Tb										
Dy										
Ho										
Er										
Yb										
Lu										
Y	13.00	20.00	20.00	22.00	22.00	13.00	23.00	24.00	17.00	20.80
Th										
U										
Zr	36.00	62.00	80.00	78.00	75.00	39.00	97.00	81.00	56.00	74.00
Hf										
Sn										
Nb	3.10	1.90	1.80	2.70	1.90	1.00	3.00	1.10	1.70	
Cu										
Co										
Sc										
V	280.00	338.00	314.00	371.00	366.00	264.00	387.00	330.00	289.00	
Cr	824.00	59.00	39.00	13.00	14.00	97.00	27.00	12.00	338.00	
Ni	247.00	42.00	28.00	29.00	28.00	62.00	42.00	28.00	146.00	

Stephenson (unpubl. data) & this study

					Ambrym					
number	L53	L144	M85	MA003	MA010	MA015	M77	MA001	MA004	MA018
SiO2	51.88	51.61	47.18	54.09	48.96	49.05	47.73	50.29	55.51	49.75
TiO2	0.83	0.92	0.78	0.84	0.83	0.75	0.66	0.85	0.82	0.83
Al2O3	19.06	17.15	14.02	15.46	16.57	18.51	12.49	16.61	16.29	16.30
Fe2O3			10.70	12.17	12.08	11.34	10.37	13.24	10.69	13.21
FeO	8.79	11.21								
MnO	0.17	0.23	0.18	0.23	0.20	0.20	0.17	0.24	0.22	0.23
MgO	3.81	4.56	11.56	3.81	6.00	4.01	13.66	4.81	3.40	4.76
CaO	9.87	9.87	12.17	8.22	11.44	10.87	11.64	10.51	7.76	10.30
Na2O	3.24	2.19	1.85	3.40	2.61	2.75	1.74	2.35	3.40	2.40
K2O	2.01	1.87	0.41	1.24	1.19	1.37	0.60	1.32	1.42	1.27
P2O5	0.37	0.36	0.11	0.17	0.26	0.28	0.14	0.24	0.31	0.23
L.O.I.			1.00	0.50		1.00	1.00	-0.45	0.01	0.27
H2O-										
rest										
total	100.03	99.97	99.96	100.13	100.14	100.13	100.20	100.01	99.83	99.55
Cs										
Pb										
Rb	42.00	37.00	5.00	23.00	22.00	27.00	10.00	24.00	26.00	23.00
Ba										
Sr	804.00	693.00	354.00	397.00	602.00	660.00	326.00	605.00	422.00	579.00
La										
Ce										
Pr										
Nd										
Sm										
Eu										
Gd										
Tb										
Dy										
Ho										
Er										
Yb										
Lu										
Y	20.00	21.00	15.00	27.00	18.00	19.00	14.00	22.00	23.00	19.00
Th										
U										
Zr	79.00	75.00	42.00	80.00	55.00	60.00	41.00	61.00	86.00	58.00
Hf										
Sn										
Nb	3.00	2.50	1.50	1.20	2.00	1.70	1.40	1.20	1.80	0.90
Cu										
Co										
Sc										
V	301.00	369.00	319.00	370.00	386.00	308.00	275.00	372.00	230.00	401.00
Cr	46.00	14.00	710.00	11.00	37.00	15.00	1156.00	14.00	16.00	17.00
Ni	39.00	28.00	147.00	11.00	26.00	15.00	260.00	19.00	10.00	19.00

Stephenson (unpubl. data) & this study

Lopevi

number	R2	R3	LW14	LW13	R1	LW17A	LW3C2	14	13
SiO2	49.60	49.60	50.62	50.88	50.90	51.80	55.60	58.82	59.88
TiO2	0.40	0.25	0.71	0.72	0.50	0.63	0.62	0.30	0.30
Al2O3	22.05	19.60	18.31	18.18	21.20	17.55	14.90	17.00	17.66
Fe2O3	4.20	3.85	2.32	2.10	4.75	9.33	8.80	7.31	6.96
FeO	4.75	5.40	6.67	6.94	4.45				
MnO	0.15	0.05	0.17	0.06	0.15	0.15	0.15	0.22	0.21
MgO	4.00	5.30	7.33	7.20	4.40	6.05	6.55	3.10	3.10
CaO	12.15	12.15	11.12	11.22	11.30	11.14	9.07	6.05	5.04
Na2O	2.40	2.25	2.35	2.36	2.25	2.46	2.78	5.08	5.09
K2O	0.65	0.75	0.57	0.54	0.65	0.71	1.26	1.63	1.64
P2O5	0.15	0.15	0.01	0.01	0.20	0.14	0.16	0.20	0.20
L.O.I.			0.04	0.54				0.29	0.37
H2O-	0.05	0.20	0.05	0.07	0.05				
rest								0.06	0.06
total	100.55	99.55	100.27	100.82	100.80	99.96	99.89	100.06	100.51
Cs									
Pb									
Rb									
Ba									
Sr									
La									
Ce									
Pr									
Nd									
Sm									
Eu									
Gd									
Tb									
Dy									
Ho									
Er									
Yb									
Lu									
Y									
Th									
U									
Zr									
Hf									
Sn									
Nb									
Cu									
Co									
Sc									
V									
Cr									
Ni									

Warden (1967)

Western Epi

number	666	667	672	673	674	675	676	677	678	679
SiO2	55.25	55.58	57.46	61.86	61.48	61.02	60.82	60.74	61.36	60.97
TiO2	0.67	0.66	0.69	0.80	0.80	0.79	0.85	0.86	0.86	0.83
Al2O3	15.94	16.16	16.00	15.75	15.85	16.01	15.35	15.24	15.27	15.39
Fe2O3	1.43	1.39	1.38	1.17	1.20	1.18	1.28	1.27	1.23	1.30
FeO	7.15	6.95	6.89	5.87	5.99	5.90	6.38	6.37	6.14	6.51
MnO	0.16	0.14	0.18	0.15	0.15	0.15	0.16	0.13	0.16	0.20
MgO	5.49	5.29	4.16	1.95	1.98	2.16	2.66	2.92	2.42	2.23
CaO	9.18	9.01	7.59	4.86	5.05	5.15	5.15	4.94	5.01	4.98
Na2O	2.49	2.65	3.13	3.49	3.60	3.53	3.31	3.59	3.54	3.38
K2O	2.00	2.00	2.25	3.76	3.58	3.65	3.71	3.48	3.67	3.85
P2O5	0.23	0.18	0.27	0.35	0.34	0.46	0.36	0.46	0.36	0.36
L.O.I.	1.52	1.39	1.73	1.77	1.45	1.57	1.67	1.28	1.58	1.58
H2O-										
rest										
total	101.51	101.40	101.73	101.78	101.47	101.57	101.70	101.28	101.60	101.58
Cs										
Pb	7.40							12.40		
Rb	44.70	46.70	48.00			84.10	89.30	81.50	83.40	82.70
Ba	600.00		410.00			800.00		730.00		
Sr	496.00	505.00	493.00			427.00	452.00	441.00	443.00	439.00
La	13.80							23.70		
Ce	30.50							55.60		
Pr	3.40							6.10		
Nd	12.90							21.10		
Sm	3.04							4.60		
Eu	0.88							1.21		
Gd	3.32							4.18		
Tb	0.50							0.73		
Dy	2.80							4.31		
Ho	0.60							0.88		
Er	1.75							2.50		
Yb	1.86							2.83		
Lu										
Y	23.50	22.40	29.10			38.50	34.20	34.10	34.40	33.30
Th	2.62							4.06		
U	0.83							1.54		
Zr	101.00	98.00	106.00			191.00	176.00	176.00	181.00	178.00
Hf	2.35							3.76		
Sn										
Nb	2.84							3.85		
Cu			100.00			60.00		80.00		
Co			24.00			16.00		18.00		
Sc			19.00			18.00		15.00		
V			200.00			160.00		150.00		
Cr			39.00			6.00		31.00		
Ni			16.00			2.50		9.00		

Gorton (1974) Gorton (1977)

	Western Epi									
number	680	681	682	662	663	664	665	668	EP16	EP25
SiO2	61.07	58.17	61.76	49.60	49.61	50.29	49.85	54.46	47.55	48.00
TiO2	0.87	0.73	0.79	0.84	0.69	0.85	0.83	0.92	0.67	0.51
Al2O3	15.25	16.98	15.89	18.61	17.52	18.36	17.43	16.02	16.96	12.84
Fe2O3	1.26	1.28	1.17	1.90	1.75	1.89	1.86	1.86	1.50	3.67
FeO	6.30	6.42	5.87	9.48	8.90	9.43	9.30	9.32	9.11	6.15
MnO	0.16	0.14	0.15	0.22	0.20	0.22	0.21	0.24	0.19	0.18
MgO	2.36	3.08	1.91	4.95	6.55	4.80	5.81	4.29	6.79	11.44
CaO	5.12	7.03	4.85	10.39	11.42	9.98	10.74	7.99	12.16	13.86
Na2O	3.41	3.45	3.53	2.89	2.36	2.91	2.61	3.40	2.63	1.44
K2O	3.70	2.47	3.73	0.87	0.79	1.02	1.13	1.33	0.73	0.32
P2O5	0.49	0.25	0.34	0.25	0.18	0.26	0.23	0.18	0.16	0.08
L.O.I.	1.81	1.11	1.83	0.90	0.59	0.59	0.63	2.49	0.09	0.20
H2O-									0.27	0.82
rest										
total	101.80	101.11	101.82	100.90	100.56	100.60	100.63	102.50	98.81	99.51
Cs										
Pb										
Rb	82.40	57.60	87.00	13.70	12.70	17.50	20.10	22.20	13.20	
Ba	720.00								276.00	
Sr	453.00	528.00	412.00	640.00	769.00	789.00	589.00	475.00	541.00	
La										
Ce										
Pr										
Nd										
Sm										
Eu										
Gd										
Tb										
Dy										
Ho										
Er										
Yb										
Lu										
Y	36.20	29.00	40.00	17.70	21.30	22.30	22.90	28.00	16.20	
Th									0.98	
U										
Zr	184.00	123.00	196.00	36.00	47.00	51.00	54.00	75.00	43.00	
Hf									1.11	
Sn										
Nb										
Cu	53.00									
Co	16.00								46.00	
Sc	13.00									
V	150.00								303.00	
Cr	23.00								78.00	
Ni	6.00								55.00	

Gorton (1974) Roca (1978)

Western Epi

number	EPI24	EP37	EP19	EP23	EP1	EP20	EP33	EP4	EP7	EP12
SiO2	48.17	49.11	49.75	50.07	59.70	59.80	59.92	60.29	60.40	60.42
TiO2	0.52	0.74	0.91	0.76	0.87	0.73	0.88	0.88	0.88	0.86
Al2O3	16.40	17.29	18.01	17.18	13.96	15.80	14.20	14.20	14.27	14.92
Fe2O3	1.50	1.50	1.50	1.50	2.13	1.50	2.00	1.85	2.07	1.50
FeO	8.45	8.65	9.02	8.90	5.46	5.54	5.43	5.60	5.29	6.36
MnO	0.19	0.18	0.19	0.19	0.15	0.15	0.16	0.16	0.15	0.16
MgO	8.59	5.85	5.35	5.73	2.78	3.21	2.62	2.24	2.23	3.03
CaO	13.43	11.13	10.47	10.75	5.05	6.08	5.15	4.85	4.78	5.21
Na2O	1.86	2.47	3.40	2.55	3.41	3.51	3.20	3.42	3.40	3.62
K2O	0.30	1.83	0.73	1.38	3.46	3.27	3.64	3.56	3.68	3.52
P2O5	0.12	0.44	0.18	0.33	0.52	0.27	0.49	0.51	0.49	0.46
L.O.I.	0.07	0.13	0.06	0.07	0.09	0.17	0.27	0.19	0.18	0.35
H2O-	0.36	0.01	0.37	0.38	1.56	0.89	1.60	1.50	1.48	0.09
rest										
total	99.96	99.33	99.94	99.79	99.14	100.92	99.56	99.25	99.30	100.50
Cs										
Pb										
Rb	2.50	81.00	10.00	46.70		66.00				76.00
Ba	122.00			266.00						
Sr	374.00	841.00	484.00	587.00		477.00				440.00
La	2.40			6.70						
Ce	5.60			15.20						
Pr										
Nd										
Sm	1.40			2.30						
Eu	0.54			0.87						
Gd										
Tb	0.30			0.49						
Dy										
Ho										
Er										
Yb	1.30			1.60						
Lu	0.22			0.28						
Y	13.40	21.00	24.00	19.40		30.00				37.00
Th	0.26			0.97						
U										
Zr	28.00	89.00	46.00	77.00		139.00				169.00
Hf	0.65									
Sn										
Nb	1.00	2.00	2.00	3.90		4.00				6.00
Cu										
Co	28.00	39.00	39.00	40.00						20.00
Sc	48.00									
V	279.00			323.00						
Cr	198.00			87.00						
Ni	58.00			30.00						

Roca (1978)

	Western Epi									
number	EP30	EP29	EP17	EP3	71047	71041	71048	71052	71065	71067
SiO2	60.88	60.88	60.88	62.99	47.80	47.80	47.90	47.90	48.00	48.00
TiO2	0.88	0.88	0.70	0.78	0.54	0.43	0.53	0.55	0.45	0.52
Al2O3	15.02	15.12	16.02	15.43	18.40	13.60	16.30	16.70	13.90	16.10
Fe2O3	1.50	1.50	1.50	1.50	11.50	10.60	11.50	11.40	10.50	11.50
FeO	6.21	6.26	5.19	5.25						
MnO	0.16	0.15	0.12	0.13	0.19	0.18	0.19	0.19	0.18	0.19
MgO	2.62	2.81	2.89	1.87	6.80	10.70	8.30	8.30	11.20	8.85
CaO	5.05	5.04	5.99	4.37	12.50	14.20	13.30	12.70	13.50	13.10
Na2O	3.51	3.39	3.63	3.30	1.80	1.29	1.44	1.70	1.55	1.68
K2O	3.62	3.66	3.02	4.11	0.45	0.35	0.41	0.38	0.35	0.36
P2O5	0.43	0.45	0.27	0.36	0.08	0.09	0.06	0.06	0.05	0.07
L.O.I.	0.26	0.32	0.46	0.32	0.07	0.31	-0.16	0.36	0.01	-0.12
H2O-	0.77	0.87	0.38	1.59						
rest										
total	100.91	101.33	101.05	102.00	100.13	99.55	99.77	100.24	99.69	100.25
Cs										
Pb										
Rb	80.00	81.00	70.00	96.00	8.00	6.00	8.00	6.00	5.70	5.20
Ba					173.00	160.00		186.00	161.00	152.00
Sr	436.00	442.00	471.00	373.00	461.00	357.00	395.00	390.00	322.00	380.00
La					4.70				3.03	
Ce					10.10				7.69	
Pr					1.42				0.95	
Nd					7.05				5.75	
Sm					1.68				1.40	
Eu					0.67				0.47	
Gd					2.21				1.76	
Tb										
Dy					2.47				2.10	
Ho										
Er					1.50				1.14	
Yb					1.43				1.07	
Lu										
Y	37.00	39.00	31.00	41.00	13.70	11.80	12.80	15.00	12.40	12.90
Th										
U										
Zr	174.00	178.00	143.00	202.00	20.80	15.50	19.20	20.30	18.00	17.10
Hf										
Sn										
Nb	5.00	6.00	4.00	7.00						
Cu										
Co	20.00	18.00	16.00	14.00						
Sc					45.00	58.00		49.00	57.00	53.00
V					371.00	322.00	351.00	343.00	321.00	350.00
Cr					39.50	448.00	185.00	175.00	533.00	205.00
Ni					37.00	97.00	59.00	64.00	124.00	71.00

Roca (1978) Barsdell and Berry (in press)

					Western Epi					
number	71043	71046	71042	71045	71068	71077	71059	71076	71074	71073
SiO2	48.10	48.20	48.20	48.40	48.50	48.90	49.00	49.00	49.30	49.80
TiO2	0.50	0.39	0.45	0.53	0.50	0.65	0.64	0.59	0.83	0.83
Al2O3	14.80	11.50	13.80	15.00	16.60	19.30	18.70	16.60	17.80	18.40
Fe2O3	11.10	9.90	10.80	11.30	10.80	10.70	10.70	10.90	12.20	11.10
FeO										
MnO	0.19	0.16	0.17	0.19	0.19	0.18	0.17	0.18	0.21	0.19
MgO	9.46	13.50	10.50	9.50	8.78	5.39	5.78	7.62	4.77	5.51
CaO	13.30	14.40	14.20	13.00	12.80	11.30	11.40	11.60	9.97	10.90
Na2O	1.49	1.05	1.26	1.49	1.87	2.55	2.36	2.67	3.27	2.68
K2O	0.40	0.31	0.37	0.46	0.28	0.77	0.58	0.54	0.99	0.55
P2O5	0.10	0.07	0.07	0.06	0.06	0.17	0.12	0.12	0.32	0.15
L.O.I.	0.59	0.10	0.10	-0.10	-0.36	0.05	0.08	-0.02	-0.10	-0.16
H2O-										
rest										
total	100.03	99.58	99.92	99.83	100.02	99.96	99.53	99.80	99.56	99.95
Cs										
Pb										
Rb	6.00	6.00	5.00	7.00	4.30	17.50	13.00	11.20	15.30	9.10
Ba	181.00	137.00	156.00	183.00	142.00	312.00	248.00	258.00	310.00	205.00
Sr	378.00	246.00	345.00	374.00	367.00	605.00	479.00	434.00	780.00	460.00
La		3.05							3.20	
Ce		7.26							11.00	
Pr		1.01							26.00	
Nd		5.04							3.75	
Sm		1.54							17.30	
Eu		0.57							1.30	
Gd		1.83							4.05	
Tb										
Dy		1.91							3.82	
Ho										
Er		1.06							2.15	
Yb		0.98							1.80	
Lu										
Y	13.10	8.70	12.70	14.50	12.00	16.00	21.00	14.50	21.00	19.40
Th										
U										
Zr	20.00	13.50	14.00	21.00	15.00	36.00	30.00	29.00	49.00	35.00
Hf										
Sn										
Nb								1.00		
Cu										
Co										
Sc	54.00	66.00	60.00	53.00	56.00	35.50	53.00	47.00	35.50	39.00
V	353.00	295.00	327.00	350.00	339.00	350.00	367.00	329.00	404.00	416.00
Cr	360.00	820.00	445.00	373.00	204.00	45.00	44.00	142.00	8.60	36.00
Ni	84.00	172.00	95.00	89.00	64.00	27.00	25.50	48.00	12.10	29.00

Barsdell and Berry (in press)

	Western Epi									
number	71075	71069	71073	71071	71064	71066	71061	71057	71040	71049
SiO2	49.90	50.30	50.90	50.90	53.90	54.90	56.40	56.60	57.00	57.30
TiO2	0.80	0.74	0.70	0.64	0.86	0.89	0.82	0.69	0.92	0.87
Al2O3	17.60	18.70	18.70	16.00	15.30	15.60	16.20	16.70	15.50	15.80
Fe2O3	11.60	11.20	11.60	10.80	10.80	11.40	10.50	8.32	11.10	10.50
FeO										
MnO	0.20	0.19	0.22	0.19	0.20	0.22	0.21	0.15	0.23	0.21
MgO	5.49	4.78	4.50	6.73	4.43	3.58	2.86	3.17	2.97	2.97
CaO	10.30	9.89	9.69	11.70	8.63	7.79	6.92	7.08	6.54	6.70
Na2O	2.90	2.67	2.98	2.31	3.12	3.56	3.63	3.07	3.81	3.97
K2O	0.96	1.37	0.91	0.77	1.70	1.48	1.79	2.31	1.60	1.63
P2O5	0.27	0.35	0.17	0.13	0.40	0.31	0.35	0.32	0.32	0.34
L.O.I.	-0.07	-0.16	-0.19	-0.08	0.51	-0.18	0.16	1.10	-0.06	-0.28
H2O-										
rest										
total	99.95	100.03	100.18	100.09	99.85	99.55	99.84	99.51	99.93	100.01
Cs										
Pb										
Rb	17.00	46.00	16.00	12.30	35.00	28.00	32.00	52.00	27.00	31.00
Ba	356.00	316.00	289.00	266.00	477.00	467.00	549.00	701.00	524.00	489.00
Sr	555.00	591.00	553.00	444.00	485.00	477.00	484.00	514.00	540.00	473.00
La		8.01	8.30	5.30	12.60					11.50
Ce		18.20	19.40	13.20	29.00					28.00
Pr		2.40	2.70	1.80	3.70					3.80
Nd		11.90	12.20	9.20	17.40					17.70
Sm		3.10	2.90	2.40	3.70					4.30
Eu		1.14	1.10	0.90	1.20					1.60
Gd		3.30	3.40	2.80	4.10					4.70
Tb										
Dy		3.50	3.90	3.20	4.70					5.30
Ho										
Er		2.23	2.60	2.20	3.20					3.50
Yb		1.77	2.20	1.80	2.80					3.30
Lu										
Y	22.50	18.60	21.60	18.30	29.00	28.00	31.00	30.00	34.50	32.00
Th										
U										
Zr	52.00	68.00	49.00	36.00	88.00	82.00	102.00	124.00	88.40	87.00
Hf										
Sn										
Nb	1.70	1.80	1.20		1.60	1.50	3.00	3.00	2.00	3.00
Cu										
Co										
Sc	40.00	35.00	31.40	49.00	34.00	35.00	31.40	26.20	30.00	31.00
V	372.00	373.00	318.00	335.00	288.00	320.00	235.00	224.00	230.00	244.00
Cr	43.00	25.00	6.80	156.00	57.00	10.00	5.20	27.00	3.50	10.90
Ni	27.00	19.00	5.40	38.00	20.40	9.50	3.50	11.70	1.80	2.50

Barsdell and Berry (in press)

	Eastern Epi									
number	670	671	683	684	685	688	689	690	691	EPI26
SiO2	47.79	56.04	48.86	48.95	49.66	49.00	53.96	51.26	49.41	47.70
TiO2	0.54	0.91	0.60	0.59	0.69	0.81	0.85	0.77	0.66	0.57
Al2O3	16.49	15.93	13.45	13.08	17.28	18.20	17.13	17.17	17.14	16.98
Fe2O3	1.76	1.76	1.66	1.67	1.77	1.99	1.69	1.76	1.63	1.50
FeO	8.80	8.82	8.32	8.37	8.83	9.94	8.43	8.78	8.13	9.23
MnO	0.20	0.21	0.18	0.21	0.20	0.24	0.19	0.19	0.18	0.20
MgO	8.94	3.39	12.47	12.68	7.18	5.61	3.85	5.81	8.19	7.46
CaO	13.24	7.57	11.53	11.54	10.88	10.66	8.83	10.36	11.21	13.03
Na2O	1.78	3.57	1.97	1.89	2.46	2.52	3.23	2.60	2.44	1.98
K2O	0.38	1.55	0.76	0.84	0.91	0.82	1.60	1.12	0.82	0.50
P2O5	0.09	0.24	0.19	0.19	0.15	0.20	0.24	0.16	0.18	0.14
L.O.I.	0.59	0.98	1.10	0.60	0.84	0.90	0.54	0.68	0.68	0.17
H2O-										0.21
rest										
total	100.60	100.97	101.09	100.61	100.85	100.89	100.54	100.66	100.67	99.67
Cs										
Pb	2.50									
Rb	6.20	25.10	12.70	14.90	14.70	11.20	29.60	21.20	12.20	5.10
Ba	120.00		180.00	170.00					240.00	138.00
Sr	378.00	456.00	520.00	516.00	669.00	765.00	480.00	625.00	648.00	445.00
La	2.78									3.20
Ce	7.03									6.70
Pr	0.94									
Nd	4.85									
Sm	1.31									1.50
Eu	0.52									0.57
Gd	1.65									
Tb	0.28									0.30
Dy	1.88									
Ho	0.39									
Er	1.21									
Yb	1.07									1.01
Lu										0.16
Y	14.40	39.90	14.10	14.40	18.10	21.10	25.60	19.60	16.60	14.40
Th	0.20									0.41
U	0.09									
Zr	19.00	87.00	34.00	32.00	36.00	45.00	79.00	55.00	36.00	32.00
Hf	0.44									
Sn										
Nb	0.46									1.10
Cu			97.00	84.00					120.00	
Co			48.00	51.00					39.00	38.00
Sc			35.00	34.00					27.00	39.00
V			320.00	330.00					350.00	335.00
Cr			940.00	970.00					280.00	86.00
Ni			190.00	210.00					99.00	38.00

Gorton (1974) Gorton (1977) Roca (1978)

Eastern Epi

number	EPI10	EPI10	EP11	EP9	EP14	EP13	EP26	EMW5	EMW2	EPW58
SiO2	48.39	48.80	49.10	49.55	49.74	53.85	55.44	45.28	47.78	48.20
TiO2	0.59	0.63	0.63	0.63	0.87	0.94	0.65	0.72	0.70	0.79
Al2O3	12.99	12.56	12.45	14.77	17.43	15.79	15.43	17.12	15.90	19.29
Fe2O3	1.50	2.97	3.13	1.50	1.50	1.50	1.50	7.06	5.15	3.73
FeO	8.30	6.75	6.81	8.59	9.68	9.68	6.98	6.40	6.11	7.62
MnO	0.18	0.18	0.18	0.19	0.21	0.22	0.15	0.16	0.20	0.19
MgO	12.35	12.30	12.66	9.21	4.69	3.88	4.93	7.61	9.20	5.25
CaO	11.63	11.21	11.12	11.87	10.22	8.42	9.03	13.01	12.32	11.94
Na2O	2.09	1.96	1.98	2.49	3.05	3.59	2.41	1.76	2.18	2.26
K2O	0.82	0.81	0.81	0.80	1.11	1.27	2.11	0.13	0.75	0.86
P2O5	0.19	0.20	0.19	0.17	0.33	0.23	0.19	0.04	0.02	0.02
L.O.I.	0.09	0.08	0.07	0.09	0.07	0.26	0.33	0.55	0.31	0.40
H2O-	0.30	0.57	0.68	0.11	0.24	0.03	1.07	0.55	0.18	0.04
rest										
total	99.42	99.02	99.81	99.97	99.14	99.66	100.22	100.39	100.80	100.59
Cs										
Pb										
Rb	12.50			11.00	16.00	20.50	58.00			
Ba	195.00					381.00				
Sr	530.00			566.00	785.00	497.00	498.00			
La	5.30						22.00			
Ce	12.00									
Pr										
Nd										
Sm	1.90									
Eu	0.66									
Gd										
Tb	0.30									
Dy										
Ho										
Er										
Yb	1.03									
Lu	0.18									
Y	14.20			15.00	24.00	27.30	22.00			
Th	0.82					1.20				
U										
Zr	39.00			44.00	66.00	85.00	110.00			
Hf	1.12					2.16				
Sn										
Nb	1.30			1.00	1.00	2.50	3.00			
Cu										
Co	53.00			45.00	41.00	35.00	31.00			
Sc	34.00					29.00				
V	270.00					318.00				
Cr	670.00					13.00				
Ni	200.00					3.00				

Roca (1978) Warden (1967)

Eastern Epi

number	EPW52	EPW75	EPW20
SiO2	50.00	55.01	56.43
TiO2	0.60	0.76	0.68
Al2O3	17.73	17.14	16.83
Fe2O3	7.70	5.64	4.16
FeO		2.98	3.04
MnO	0.20	0.14	0.15
MgO	7.50	1.93	2.94
CaO	11.30	4.92	6.06
Na2O	2.63	2.70	2.35
K2O	0.60	1.78	2.32
P2O5	0.20	0.32	0.25
L.O.I.		3.10	3.54
H2O-		2.38	1.63
rest			
total	98.46	98.80	100.38
Cs			
Pb			
Rb			
Ba			
Sr			
La			
Ce			
Pr			
Nd			
Sm			
Eu			
Gd			
Tb			
Dy			
Ho			
Er			
Yb			
Lu			
Y			
Th			
U			
Zr			
Hf			
Sn			
Nb			
Cu			
Co			
Sc			
V			
Cr			
Ni			

Warden (1967)

Epi A (submarine)

number	3D1-D	4D1-C	4D1-E	4D2-A	3D1-C	3D1-B	3D1-A	4D1-I	4D1-K	3D1-P
SiO2	48.00	50.60	49.90	49.20	64.90	64.50	63.40	63.30	63.10	63.80
TiO2	0.60	0.54	0.52	0.56	0.55	0.61	0.56	0.52	0.52	0.53
Al2O3	17.10	16.50	16.60	16.60	15.30	15.80	15.40	15.00	15.10	15.20
Fe2O3	11.30	9.95	10.10	10.80	5.86	6.41	6.53	6.44	6.21	5.91
FeO										
MnO	0.18	0.17	0.17	0.19	0.13	0.13	0.14	0.14	0.13	0.14
MgO	6.92	6.71	7.81	7.18	1.48	1.81	2.09	2.46	2.10	1.75
CaO	13.50	12.50	13.70	13.50	3.52	3.34	3.68	4.62	4.51	3.93
Na2O	1.78	2.04	1.63	1.68	4.28	4.21	4.32	3.94	3.95	4.96
K2O	0.60	1.04	0.72	0.67	3.75	3.56	3.56	3.38	3.48	3.53
P2O5	0.08	0.10	0.08	0.10	0.21	0.21	0.21	0.16	0.16	0.16
L.O.I.	0.46	0.23	0.17	0.28	1.38		2.64	0.78	0.79	5.15
H2O-										
rest										
total	100.52	100.38	101.40	100.76	101.36	100.58	102.53	100.74	100.05	105.06
Cs										
Pb										
Rb	11.00	20.00	14.00	13.00	78.00	70.00	68.00	72.00	72.00	71.00
Ba	120.00	204.00	145.00	149.00	630.00	572.00	602.00	592.00	601.00	558.00
Sr	460.00	420.00	430.00	471.00	246.00	219.00	242.00	261.00	256.00	240.00
La	4.54		5.03		21.32				18.67	
Ce	9.30		10.28		48.95				41.65	
Pr	1.42		1.41		6.05				5.40	
Nd	6.85		6.90		26.22				22.88	
Sm	1.84		1.85		5.76				4.87	
Eu	0.55		0.64		1.51				1.09	
Gd	2.08		2.03		5.70				4.82	
Tb										
Dy	2.15		2.23		5.76				4.85	
Ho										
Er	1.16		1.07		3.98				3.32	
Yb	1.10		1.10		4.66				3.06	
Lu										
Y	12.40	15.00	12.00	13.00	39.50	33.00	33.00	32.00	32.00	31.00
Th										
U										
Zr	30.00	54.00	37.00	33.00	192.00	188.00	192.00	184.00	187.00	182.00
Hf										
Sn										
Nb	1.00	1.00	1.00	1.00	5.20	6.00	5.10	4.60	5.10	5.40
Cu										
Co										
Sc	47.00	46.00	49.00	47.00	14.00	16.00	15.00	18.00	19.00	14.00
V	376.00	313.00	298.00	346.00	67.00	86.00	72.00	94.00	98.00	72.00
Cr	61.00	136.00	163.00	124.00	14.00	22.00	11.00	62.00	35.00	15.00
Ni	34.00	40.00	56.00	44.00	6.00	9.00	7.00	18.00	11.00	6.00

Crawford et al. (1988)

	Epi A (submarine)				
number	4D1-P	4D2-P	4D1-G	4D1-H	4D1-L
SiO2	62.30	63.30	47.20	47.00	47.60
TiO2	0.52	0.52	0.32	0.47	0.29
Al2O3	14.90	15.30	18.90	16.80	11.70
Fe2O3	6.49	6.32	7.84	10.20	7.57
FeO					
MnO	0.13	0.15	0.13	0.16	0.12
MgO	2.73	2.21	8.40	8.64	13.00
CaO	4.88	4.60	16.50	15.20	18.80
Na2O	4.38	4.04	1.02	1.29	0.62
K2O	3.27	3.50	0.18	0.28	0.11
P2O5	0.16	0.17	0.04	0.08	0.02
L.O.I.	6.94	3.53	0.22	0.14	0.17
H2O-					
rest					
total	106.70	103.64	100.75	100.26	100.00
Cs					
Pb					
Rb	64.00	72.00	4.00		
Ba	539.00	600.00	57.00		47.00
Sr	245.00	261.00	467.00		253.00
La					
Ce					
Pr					
Nd					
Sm					
Eu					
Gd					
Tb					
Dy					
Ho					
Er					
Yb					
Lu					
Y	28.00	32.00	6.00		6.00
Th					
U					
Zr	164.00	184.00	12.00		6.00
Hf					
Sn					
Nb	3.70	4.60	1.00		1.00
Cu					
Co					
Sc	18.00	19.00	95.00		139.00
V	101.00	96.00	212.00		186.00
Cr	52.00	28.00	197.00		956.00
Ni	17.00	10.00	65.00		110.00

Crawford et al. (1988)

					Karua					
number	12	K2D1-3	K2D1-9	K2D1-15	K2D1-16	KB19	KH13	KB7	KE1	KH4
SiO2	54.92	52.30	52.20	52.50	51.90	51.10	52.10	56.30	56.10	55.10
TiO2	0.30	0.78	0.72	0.72	0.73	0.66	0.64	0.63	0.63	0.56
Al2O3	19.60	19.00	17.20	17.20	17.00	17.10	17.70	18.50	18.20	18.70
Fe2O3	7.47	10.40	11.00	10.90	10.80	10.60	10.00	8.30	8.70	7.90
FeO										
MnO	0.20	0.19	0.18	0.21	0.18	0.12	0.16	0.11	0.16	0.09
MgO	3.00	3.24	4.53	4.22	4.96	6.96	4.95	3.03	2.86	2.83
CaO	6.72	10.10	10.30	10.30	10.80	10.30	9.81	8.20	8.59	7.74
Na2O	5.09	2.69	2.35	2.35	2.47	2.69	2.61	3.66	3.19	3.72
K2O	1.39	1.16	1.22	1.22	1.04	0.39	0.90	1.15	1.47	1.27
P2O5	0.20	0.23	0.22	0.22	0.23	0.14	0.16	0.20	0.19	0.20
L.O.I.	0.22	0.95	1.21	1.17	1.11	3.66	0.26	0.20	0.09	1.76
H2O-										
rest										
total	99.11	101.04	101.13	101.01	101.22	103.72	99.29	100.28	100.18	99.87
Cs										
Pb										
Rb		20.00	22.00	22.00	18.00	9.00	18.00	21.00	29.00	23.00
Ba		270.00	274.00	270.00	273.00	153.00	180.00	256.00	274.00	272.00
Sr		515.00	493.00	480.00	534.00	374.00	427.00	431.00	448.00	447.00
La					8.97		6.33			8.76
Ce					20.03		15.11			21.36
Pr					2.95		2.20			2.69
Nd					13.56		10.35			12.58
Sm					3.37		2.60			3.25
Eu					1.20		0.90			1.05
Gd					3.71		3.11			3.51
Tb										
Dy					3.45		3.14			3.78
Ho										
Er					2.00		1.79			2.39
Yb					1.98		1.79			2.49
Lu										
Y		21.00	22.00	21.00	21.00	18.00	16.00	21.00	22.00	21.00
Th										
U										
Zr		58.00	62.00	62.00	52.00	48.00	50.00	75.00	77.00	76.00
Hf										
Sn										
Nb		1.70	1.00	1.30	1.30	1.00	1.00	1.40	2.00	2.20
Cu										
Co										
Sc		33.00	40.00	41.00	42.00	44.00	41.00	26.00	25.00	23.00
V		338.00	321.00	320.00	340.00	376.00	330.00	192.00	204.00	163.00
Cr		24.00	55.00	52.00	85.00	63.00	87.00	13.00	15.00	10.00
Ni		12.00	20.00	18.00	24.00	24.00	32.00	7.00	7.00	5.00

Warden (1967) Crawford et al. (1988)

Laika

number	LA6	LA3	LA7
SiO2	64.00	64.77	65.26
TiO2	0.61	0.60	0.59
Al2O3	15.54	15.61	15.42
Fe2O3	1.50	1.50	1.50
FeO	4.79	4.60	4.21
MnO	0.15	0.15	0.14
MgO	1.90	1.71	1.56
CaO	4.79	4.61	4.25
Na2O	4.00	4.11	4.15
K2O	2.53	2.60	2.73
P2O5	0.22	0.23	0.22
L.O.I.	0.04	0.02	0.01
H2O-	0.15	0.05	0.07
rest			
total	100.22	100.56	100.11
Cs			
Pb			
Rb	47.00	49.00	52.00
Ba			
Sr	363.00	353.00	333.00
La			
Ce			
Pr			
Nd			
Sm			
Eu			
Gd			
Tb			
Dy			
Ho			
Er			
Yb			
Lu			
Y	31.00	32.00	31.00
Th			
U			
Zr	119.00	126.00	132.00
Hf			
Sn			
Nb	3.00	3.00	4.00
Cu			
Co	15.00	13.00	12.00
Sc			
V			
Cr			
Ni			

Roca (1978)

Namuka

number	NA2	NA3
SiO2	49.01	49.11
TiO2	0.69	0.73
Al2O3	19.03	18.36
Fe2O3	1.50	1.50
FeO	8.96	9.66
MnO	0.19	0.21
MgO	5.26	5.27
CaO	11.66	11.24
Na2O	2.20	2.13
K2O	0.59	0.86
P2O5	0.16	0.22
L.O.I.	0.14	0.07
H2O-	0.12	0.34
rest		
total	99.51	99.70
Cs		
Pb		
Rb	7.00	12.00
Ba		
Sr	582.00	633.00
La		
Ce		
Pr		
Nd		
Sm		
Eu		
Gd		
Tb		
Dy		
Ho		
Er		
Yb		
Lu		
Y	16.00	19.00
Th		
U		
Zr	34.00	50.00
Hf		
Sn		
Nb	1.00	2.00
Cu		
Co	38.00	40.00
Sc		
V		
Cr		
Ni		

Roca (1978)

				Mataso		
number	MTA4	MTA5	MTA9	MTA14	MTA3	MO3
SiO2	46.83	47.39	46.73	46.72	46.63	48.67
TiO2	0.84	0.99	0.85	0.83	0.81	0.73
Al2O3	17.13	16.84	17.09	16.43	18.56	17.14
Fe2O3	12.94	13.00	11.99	11.87	12.56	12.03
FeO						
MnO	0.22	0.23	0.20	0.20	0.20	0.21
MgO	6.77	4.93	6.46	7.11	5.82	6.76
CaO	12.93	11.14	12.40	12.45	12.65	10.47
Na2O	2.00	3.02	2.50	2.25	2.26	2.44
K2O	0.52	0.84	1.03	1.39	0.53	0.73
P2O5	0.16	0.28	0.48	0.49	0.16	0.18
L.O.I.	-0.16	0.75	-0.09	-0.08	-0.08	0.26
H2O-						
rest						
total	100.18	99.41	99.64	99.66	100.10	99.62
Cs						
Pb						
Rb						
Ba						
Sr						
La	6.00	8.42	14.50	15.60		
Ce	14.80	19.70	35.50	37.50		
Pr	2.24	2.90	4.98	5.10		
Nd	10.90	14.50	23.10	24.90		
Sm	2.89	3.44	5.47	5.70		
Eu	1.09	1.30	2.06	2.10		
Gd	2.98	3.66	5.18	5.46		
Tb						
Dy	3.10	3.65	4.11	3.95		
Ho						
Er	1.79	2.30	2.19	1.96		
Yb	1.41	1.67	1.65	1.40		
Lu						
Y						
Th						
U						
Zr						
Hf						
Sn						
Nb						
Cu						
Co						
Sc						
V						
Cr						
Ni						

Barsdell (unpubl. data)

Makura

number	MA1	MA3	MA6	MA5
SiO2	47.23	47.90	48.51	48.91
TiO2	1.03	0.98	0.94	0.97
Al2O3	16.14	18.09	17.88	17.04
Fe2O3	1.50	1.50	1.50	4.31
FeO	11.03	9.51	10.12	6.72
MnO	0.26	0.27	0.23	0.21
MgO	5.78	4.77	5.36	4.84
CaO	12.10	11.17	11.31	11.45
Na2O	3.30	2.98	2.91	2.98
K2O	0.52	0.78	0.74	0.73
P2O5	0.48	0.54	0.55	0.50
L.O.I.	0.11	0.45	0.07	0.13
H2O-	0.32	0.30	0.27	0.47
rest				
total	99.80	99.24	100.39	99.26
Cs				
Pb				
Rb	5.00	10.00	8.00	
Ba				
Sr	1022.00	1124.00	1067.00	
La				
Ce				
Pr				
Nd				
Sm				
Eu				
Gd				
Tb				
Dy				
Ho				
Er				
Yb				
Lu				
Y	23.00	22.00	22.00	
Th				
U				
Zr	33.00	36.00	44.00	
Hf				
Sn				
Nb	1.00	1.00	1.00	
Cu				
Co	41.00	37.00		
Sc				
V				
Cr				
Ni				

Roca (1978)

Ririna

number	R109	R110	R113	R118	R114	R15	R111	R14	R13	R17
SiO2	48.95	50.11	50.21	50.27	50.76	58.16	58.27	62.74	63.53	63.69
TiO2	0.91	0.96	0.83	0.91	0.84	0.66	0.66	0.64	0.64	0.62
Al2O3	16.48	18.65	16.13	15.84	16.36	15.45	15.23	14.73	15.64	15.58
Fe2O3	1.50	1.50	1.50	4.97	1.50	1.50	1.50	1.50	1.50	1.50
FeO	9.80	8.09	9.51	6.61	9.50	6.71	6.63	4.88	5.05	4.94
MnO	0.20	0.17	0.20	0.20	0.21	0.16	0.17	0.16	0.15	0.15
MgO	5.84	4.50	5.85	5.58	5.86	4.24	4.15	1.58	1.72	1.95
CaO	11.25	10.99	11.08	10.39	11.06	7.70	7.69	4.42	4.45	4.96
Na2O	2.98	2.84	2.47	2.58	2.71	3.47	3.72	4.12	4.07	4.20
K2O	0.90	1.31	1.03	0.99	1.03	1.90	1.89	3.04	3.06	2.48
P2O5	0.20	0.26	0.23	0.23	0.19	0.25	0.24	0.34	0.30	0.21
L.O.I.	0.09	0.05	0.08	0.11	0.07	0.06	0.08	0.02	0.08	0.04
H2O-	0.23	0.44	0.21	0.74	0.18	0.04	0.04	0.76	0.13	0.47
rest										
total	99.33	99.87	99.33	99.42	100.27	100.30	100.27	98.93	100.32	100.79
Cs										
Pb										
Rb	14.00	22.00	16.00		14.00	35.00	35.00		60.00	47.00
Ba										
Sr	459.00	634.00	560.00		562.00	404.00	399.00		359.00	368.00
La										
Ce										
Pr										
Nd										
Sm										
Eu										
Gd										
Tb										
Dy										
Ho										
Er										
Yb										
Lu										
Y	24.00	23.00	21.00		21.00	26.00	25.00		36.00	30.00
Th										
U										
Zr	59.00	57.00	57.00		65.00	93.00	92.00		144.00	116.00
Hf										
Sn										
Nb	2.00	3.00	2.00		2.00	4.00	3.00		5.00	4.00
Cu										
Co	44.00	32.00			41.00	25.00			13.00	15.00
Sc										
V										
Cr										
Ni										

Roca (1978)

Ririna

number	RI17	RI13
SiO2	64.21	50.21
TiO2	0.59	0.83
Al2O3	14.64	16.13
Fe2O3	1.61	12.06
FeO	4.31	
MnO	0.14	0.20
MgO	1.75	5.85
CaO	4.71	11.08
Na2O	3.93	2.47
K2O	2.63	1.03
P2O5	0.22	0.23
L.O.I.	0.02	0.08
H2O-	0.41	0.21
rest		
total	99.17	100.38
Cs		
Pb		
Rb		16.20
Ba		180.00
Sr		560.00
La		7.10
Ce		15.80
Pr		
Nd		
Sm		3.00
Eu		0.96
Gd		
Tb		0.56
Dy		
Ho		
Er		
Yb		1.80
Lu		0.28
Y		20.90
Th		0.90
U		
Zr		57.00
Hf		
Sn		
Nb		1.90
Cu		
Co		42.00
Sc		38.00
V		323.00
Cr		46.00
Ni		33.00

Roca (1978) Dupuy et al. (1982)

					Emae					
number	EM4	EM9	EM11	EM10	EM1	EM5	EM6	EM17	EM7	EM16
SiO2	46.61	47.29	47.91	48.40	48.64	48.90	49.76	50.30	51.23	52.48
TiO2	0.70	0.77	0.65	0.72	0.73	0.84	0.84	0.73	0.79	0.65
Al2O3	14.61	15.74	13.72	15.66	16.32	17.71	18.63	18.60	19.12	18.81
Fe2O3	11.94	1.50	6.03	6.10	1.50	4.38	10.93	1.50	1.50	1.50
FeO		9.35	4.74	4.71	9.53	6.26		8.90	7.49	7.81
MnO	0.20	0.22	0.20	0.20	0.21	0.20	0.19	0.20	0.17	0.19
MgO	8.47	7.99	10.60	8.47	6.53	5.68	4.02	4.49	4.07	4.05
CaO	13.07	11.70	12.46	12.08	12.09	10.80	10.69	9.85	9.44	9.41
Na2O	2.32	2.57	2.15	2.39	3.04	2.40	3.51	2.71	3.70	3.15
K2O	0.86	1.05	0.70	0.91	0.59	1.08	1.29	1.27	1.44	1.24
P2O5	0.20	0.23	0.19	0.24	0.19	0.27	0.31	0.31	0.34	0.31
L.O.I.	0.16	0.09	0.10	0.05	0.10	0.21	0.18	0.15	0.54	0.15
H2O-	0.86	0.09	0.48	0.35	0.22	0.70	0.36	0.12	0.24	0.20
rest										
total	100.00	98.59	99.93	100.28	99.69	99.43	100.71	99.13	100.07	99.95
Cs										
Pb										
Rb	10.70	17.00			7.00		19.10	23.00	23.00	26.00
Ba	209.00									
Sr	623.00	725.00			504.00		841.00	712.00	891.00	720.00
La	6.40									
Ce	13.50									
Pr										
Nd										
Sm	2.40									
Eu	0.80									
Gd										
Tb	0.47									
Dy										
Ho										
Er										
Yb	1.21									
Lu	0.19									
Y	18.20	16.00			21.00		21.50	23.00	22.00	22.00
Th	0.86									
U										
Zr	33.00	45.00			42.00		54.00	66.00	60.00	61.00
Hf	1.00									
Sn										
Nb	1.40	3.00			1.00		2.30	2.00	2.00	1.00
Cu										
Co	50.00	48.00			45.00		34.00	37.00	28.00	30.00
Sc	34.00									
V	309.00						351.00			
Cr	227.00						30.00			
Ni	75.00						25.00			

Roca (1978)

Emae

number	EM13	EM14
SiO2	54.20	56.68
TiO2	0.82	0.67
Al2O3	17.82	17.86
Fe2O3	3.23	1.50
FeO	5.69	6.57
MnO	0.18	0.19
MgO	3.60	3.47
CaO	8.30	7.30
Na2O	3.78	3.93
K2O	1.00	1.11
P2O5	0.30	0.27
L.O.I.	0.07	0.22
H2O-	0.35	0.29
rest		
total	99.34	100.06
Cs		
Pb		
Rb		12.00
Ba		
Sr		627.00
La		
Ce		
Pr		
Nd		
Sm		
Eu		
Gd		
Tb		
Dy		
Ho		
Er		
Yb		
Lu		
Y		26.00
Th		
U		
Zr		64.00
Hf		
Sn		
Nb		3.00
Cu		
Co		20.00
Sc		
V		
Cr		
Ni		

Roca (1978)

Tongoa

number	694	695	698	699	702	704	705	706	707	709
SiO2	48.41	48.51	51.14	48.95	50.82	48.81	48.79	51.81	52.65	48.94
TiO2	0.77	0.67	0.71	0.87	0.66	0.64	0.76	0.73	0.86	0.62
Al2O3	17.40	19.66	14.03	17.18	16.32	19.15	17.59	19.39	17.72	12.90
Fe2O3	1.98	1.72	1.70	2.00	1.76	1.79	2.05	1.56	1.73	1.85
FeO	9.88	8.58	8.51	9.99	8.79	8.95	10.25	7.80	8.67	9.24
MnO	0.22	0.19	0.20	0.23	0.19	0.19	0.23	0.17	0.20	0.21
MgO	6.07	5.09	8.54	5.64	6.58	5.80	4.58	3.58	3.95	9.71
CaO	11.82	12.35	12.06	11.15	11.44	12.10	12.33	10.54	9.48	14.14
Na2O	2.25	2.20	2.05	2.88	2.35	2.11	2.19	3.01	3.02	1.72
K2O	1.03	0.86	0.87	0.90	0.96	0.39	1.00	1.22	1.49	0.53
P2O5	0.18	0.19	0.20	0.22	0.13	0.08	0.22	0.19	0.24	0.14
L.O.I.	0.37	0.44	0.57	0.56	0.84	0.61	0.50	0.63	1.53	0.57
H2O-										
rest										
total	100.38	100.46	100.58	100.57	100.84	100.62	100.49	100.63	101.54	100.57
Cs										
Pb			4.50							
Rb	18.60	18.60	13.80	12.90	17.50	6.00	18.50	21.30	26.40	9.40
Ba		140.00	140.00				200.00			105.00
Sr	607.00	607.00	400.00	695.00	432.00	426.00	542.00	618.00	564.00	356.00
La			6.37							
Ce			15.63							
Pr			2.06							
Nd			10.00							
Sm			2.41							
Eu			0.80							
Gd										
Tb			0.43							
Dy			2.62							
Ho			0.59							
Er			1.76							
Yb			1.62							
Lu										
Y	17.40	17.40	17.50	22.50	18.40	15.80	18.60	20.00	23.80	13.90
Th			0.90	45.00						
U			0.30							
Zr	42.00	42.00	46.00	45.00	52.00	26.90	40.10	56.00	69.00	27.00
Hf			1.44							
Sn										
Nb			1.12							
Cu		132.00	140.00				120.00			105.00
Co		36.00	39.00				43.00			50.00
Sc		19.00	28.00				33.00			44.00
V		270.00	240.00				420.00			310.00
Cr		32.00	200.00				31.00			530.00
Ni		20.00	58.00				30.00			76.00

Gorton (1974) Gorton (1977)

Tongoa

number	711	712	713	697	701	703	716	717	700	710
SiO2	49.86	49.44	51.09	49.42	49.62	49.31	49.61	49.92	63.99	63.83
TiO2	0.70	0.61	0.75	0.60	0.71	0.68	0.75	0.75	0.60	0.60
Al2O3	17.95	16.35	16.69	13.14	15.33	18.42	16.82	16.88	15.69	15.85
Fe2O3	1.89	1.81	1.94	1.83	1.85	1.74	1.93	1.93	1.04	1.06
FeO	9.44	9.05	9.71	9.16	9.25	8.72	9.63	9.65	5.19	5.32
MnO	0.19	0.19	0.22	0.20	0.20	0.19	0.21	0.21	0.15	0.15
MgO	5.53	7.46	5.15	9.37	7.23	5.36	5.95	5.95	1.83	1.77
CaO	10.96	12.28	10.93	12.77	11.82	11.80	11.00	10.51	4.80	4.88
Na2O	2.25	1.86	2.39	1.76	2.38	2.17	2.27	2.31	4.08	3.97
K2O	1.05	0.80	0.97	1.45	1.32	1.39	1.57	1.62	2.50	2.43
P2O5	0.19	0.14	0.16	0.30	0.28	0.22	0.26	0.27	0.13	0.13
L.O.I.	0.48	0.54	0.67	0.64	0.75	0.43	0.58	0.67	1.02	0.50
H2O-										
rest										
total	100.49	100.53	100.67	100.64	100.74	100.43	100.58	100.67	101.02	100.49
Cs										
Pb				4.00						
Rb	18.00	15.90	14.30	35.50	25.40	30.60	36.30	36.60	48.80	46.70
Ba	170.00			160.00						
Sr	508.00	462.00	482.00	539.00	606.00	530.00	727.00	733.00	365.00	363.00
La				8.71						
Ce				20.70						
Pr				2.71						
Nd				12.29						
Sm				2.65						
Eu				0.84						
Gd										
Tb				0.42						
Dy				2.26						
Ho				0.46						
Er				1.21						
Yb				1.07						
Lu										
Y	16.10	13.80	18.90	17.10	21.50	18.80	19.30	19.70	29.80	28.90
Th				1.33						
U				0.48						
Zr	44.00	40.00	43.00	57.00	64.00	52.00	66.00	67.00	126.00	126.00
Hf				1.20						
Sn										
Nb				1.15						
Cu	165.00			90.00						
Co	38.00			44.00						
Sc	27.00			31.00						
V	320.00			250.00						
Cr	38.00			260.00						
Ni	27.00			46.00						

Gorton (1974) Gorton (1977)

	Tongoa									
number	714	715	T2A	T11	TG15	TG6	TG6	TG30	TG16	TG14
SiO2	63.62	63.64	47.33	47.71	48.21	48.47	48.65	49.00	49.09	49.30
TiO2	0.60	0.62	0.74	0.72	0.66	0.77	0.64	0.65	0.68	0.76
Al2O3	15.72	15.77	17.33	18.00	19.40	17.29	18.10	13.60	15.00	16.35
Fe2O3	1.07	1.06	1.50	1.50	1.50	1.50	1.50	1.50	1.50	1.50
FeO	5.36	5.29	10.35	9.54	8.83	10.45	8.71	9.73	9.86	10.22
MnO	0.15	0.16	0.21	0.20	0.16	0.22	0.17	0.19	0.20	0.20
MgO	2.07	1.79	6.81	5.62	4.94	5.35	5.92	8.80	6.59	5.77
CaO	4.87	4.97	12.13	11.86	12.38	11.81	11.80	13.92	11.46	11.01
Na2O	3.98	4.00	1.46	2.05	2.19	2.17	2.30	1.70	2.29	2.09
K2O	2.43	2.45	0.87	0.91	0.88	0.75	1.15	0.40	1.85	1.65
P2O5	0.13	0.24	0.20	0.21	0.20	0.25	0.24	0.16	0.36	0.33
L.O.I.	0.29	0.56	0.34	0.19	0.04	0.03	0.08	0.65	0.05	0.05
H2O-			0.12	0.19	0.25	0.19	0.12	0.71	0.28	0.37
rest										
total	100.29	100.55	99.39	98.70	99.64	99.25	99.38	101.01	99.21	99.60
Cs										
Pb		7.00								
Rb	48.10	47.70	16.00	14.00	12.00	15.00	20.00	2.80	44.10	34.00
Ba		330.00						96.00	232.00	
Sr	371.00	368.00	560.00	592.00	691.00	582.00	519.00	399.00	664.00	735.00
La		10.40								
Ce		24.00								
Pr		3.10								
Nd		11.60								
Sm		3.00								
Eu		0.88								
Gd		3.27								
Tb		0.49								
Dy		3.14								
Ho		0.76								
Er		2.15								
Yb		2.34								
Lu										
Y	29.30	31.40	21.00	22.00	16.00	18.00	17.00	15.70	20.00	19.00
Th		2.12						0.44	1.96	
U		0.88								
Zr	124.00	121.00	51.00	50.00	41.00	50.00	54.00	41.00	77.00	74.00
Hf		2.82						1.00	1.85	
Sn										
Nb		2.56	4.00	5.00	2.00	2.00	2.00	1.90	2.20	3.00
Cu		44.00								
Co		15.00	49.00	40.00	40.00	46.00	44.00	54.00	47.00	44.00
Sc		13.00						44.00	34.00	
V		110.00	360.00	329.00				306.00	318.00	
Cr		4.00	21.00	23.00				329.00	119.00	
Ni		0.50	27.00	20.00				55.00	34.00	

Gorton (1974) Gorton (1977) Roca (1978)

	Tongoa									
number	TG5	TG22	T4	TG31	T148	T18	T5	T14A	TG4	T7A
SiO2	49.41	50.39	50.69	52.22	58.09	58.76	59.37	60.05	62.41	63.54
TiO2	0.69	0.70	0.71	0.82	0.60	0.63	0.59	0.61	0.64	0.63
Al2O3	14.63	13.64	14.37	18.01	15.22	16.07	15.90	15.89	15.97	15.46
Fe2O3	1.50	1.50	1.50	1.50	1.50	1.50	1.50	1.50	1.50	1.50
FeO	9.73	8.69	8.93	8.70	6.54	6.35	6.96	6.36	5.42	4.96
MnO	0.20	0.18	0.18	0.18	0.16	0.16	0.15	0.15	0.15	0.15
MgO	7.39	8.11	7.38	3.86	3.48	3.96	3.64	3.33	2.51	1.80
CaO	12.29	12.25	11.33	10.05	7.28	7.27	7.15	7.18	5.51	5.14
Na2O	2.67	2.09	1.79	2.96	3.11	2.98	3.06	2.96	3.77	3.98
K2O	0.88	0.93	1.88	1.43	1.77	1.63	1.88	1.88	2.41	1.74
P2O5	0.22	0.19	0.38	0.25	0.18	0.23	0.16	0.18	0.21	0.24
L.O.I.	0.09	0.12	0.07	0.12	0.15	0.07	0.03	0.03	0.04	0.09
H2O-	0.35	0.26	0.10	0.39	0.78	0.01	0.28	0.23		
rest										
total	100.05	99.05	99.31	100.49	98.86	99.62	100.67	100.35	100.54	99.23
Cs										
Pb										
Rb	12.00	15.30	39.00	21.00	43.00	35.00	37.00	36.00	45.00	45.00
Ba	157.00									
Sr	432.00	407.00	582.00	586.00	395.00	377.00	368.00	371.00	381.00	365.00
La										
Ce										
Pr										
Nd										
Sm										
Eu										
Gd										
Tb										
Dy										
Ho										
Er										
Yb										
Lu										
Y	18.60	16.60	36.00	21.00	39.00	35.00	37.00	37.00	30.00	44.00
Th	0.83	0.94								
U										
Zr	50.00	54.00	90.00	69.00	106.00	102.00	104.00	98.00	113.00	121.00
Hf	1.28	1.48								
Sn										
Nb	1.20	2.10	4.00	2.00	5.00	4.00	4.00	5.00	3.00	5.00
Cu										
Co	51.00	42.00	44.00	35.00	25.00	41.00	22.00	23.00	18.00	14.00
Sc	36.00	38.00								
V	361.00	274.00	329.00		181.00	203.00	193.00	189.00		115.00
Cr	138.00	244.00	131.00		41.00	41.00	36.00	43.00		5.00
Ni	47.00	64.00	37.00		21.00	17.00	16.00	17.00		3.00

Roca (1978)

	Tongoa							
number	TG12	TG13	TG33	T1A	T12	TOW24B	TOW24A	TOW2
SiO2	63.58	63.60	63.79	63.93	64.70	62.42	62.95	63.23
TiO2	0.62	0.63	0.62	0.65	0.64	0.64	0.67	0.37
Al2O3	15.73	15.88	15.73	14.92	15.23	16.05	16.15	15.91
Fe2O3	1.50	1.50	1.50	1.50	1.50	1.74	0.78	2.28
FeO	4.92	5.03	4.93	5.04	5.02	4.86	5.41	4.52
MnO	0.15	0.16	0.15	0.15	0.16	0.09	0.15	0.14
MgO	2.22	1.91	1.84	2.07	1.64	1.98	1.94	1.69
CaO	4.98	4.95	4.83	5.47	5.02	5.38	4.88	4.80
Na2O	3.80	4.23	3.95	3.71	3.88	3.98	4.00	3.87
K2O	2.46	2.54	2.51	2.31	2.35	2.40	2.58	2.19
P2O5	0.20	0.20	0.22	0.21		0.20	0.22	0.17
L.O.I.	0.04	0.05	0.05	0.07		0.17	0.42	0.54
H2O-	0.05	0.04	0.02	0.14	0.06	0.01	0.06	0.41
rest								
total	100.25	100.72	100.14	100.17	100.20	99.92	100.21	100.12
Cs								
Pb								
Rb	46.00	48.00	47.00	44.00	49.00			
Ba								
Sr	368.00	371.00	366.00	373.00	366.00			
La								
Ce								
Pr								
Nd								
Sm								
Eu								
Gd								
Tb								
Dy								
Ho								
Er								
Yb								
Lu								
Y	30.00	31.00	30.00	46.00	48.00			
Th								
U								
Zr	121.00	123.00	119.00	117.00	134.00			
Hf								
Sn								
Nb	4.00	4.00	3.00	5.00	5.00			
Cu								
Co	15.00	160.00	15.00	16.00	14.00			
Sc								
V				124.00	99.00			
Cr				11.00	10.00			
Ni				9.00	8.00			

Roca (1978) Warden (1967)

				EFATE						
number	VA76	EA229	NGA7	EFC1	PEA8	VA164	MTA13	MTA19	NGA23	EA200
SiO2	44.76	45.72	45.78	46.37	46.64	47.07	47.30	47.50	48.34	61.78
TiO2	0.85	0.92	0.72	0.92	0.80	0.80	0.84	1.05	1.05	0.73
Al2O3	19.99	18.47	18.75	17.25	18.94	18.00	16.60	15.50	17.96	18.02
Fe2O3	4.83	6.16	4.63	7.31	4.13	5.67	7.85	4.30	4.40	3.48
FeO	6.10	5.52	6.18	4.73	6.05	5.88	3.20	8.30	7.90	0.58
MnO	0.16	0.20	0.17	0.16	0.17	0.19	0.21	0.26	0.24	0.09
MgO	6.13	6.70	7.46	5.66	7.01	5.57	6.50	6.00	5.33	0.77
CaO	12.22	13.08	12.97	11.50	12.11	12.03	12.40	12.00	10.31	1.61
Na2O	1.20	2.34	1.95	2.78	2.41	1.66	2.00	2.25	3.02	5.65
K2O	0.43	0.58	0.40	0.64	0.60	0.43	1.55	0.45	0.39	5.92
P2O5	0.47	0.38	0.10	0.42	0.24	0.40	0.34	0.23	0.36	0.15
L.O.I.	1.49	0.22	0.39	1.14	0.44	1.18		0.40	0.23	0.56
H2O-	0.79	0.14	0.61	0.92	0.48	0.98			0.41	0.63
rest							0.37	0.46		
total	99.42	100.43	100.11	99.80	100.02	99.86	99.16	98.70	99.94	99.97
Cs										
Pb										
Rb										
Ba										
Sr										
La										
Ce										
Pr										
Nd										
Sm										
Eu										
Gd										
Tb										
Dy										
Ho										
Er										
Yb										
Lu										
Y										
Th										
U										
Zr										
Hf										
Sn										
Nb										
Cu										
Co										
Sc										
V										
Cr										
Ni										

Ash et al (1978).

					EFATE		
number	VA35	L51	EFC45	EA310	V36	V20	V60
SiO2	64.36	66.26	66.52	68.40	46.32	47.28	47.70
TiO2	0.60	0.76	0.51	0.42	0.78	1.11	0.97
Al2O3	16.05	15.40	14.68	15.60	18.50	17.55	18.94
Fe2O3	1.02	2.02	1.66	0.55	4.61	5.97	4.49
FeO	2.37	1.84	1.60	2.15	5.50	6.40	6.36
MnO	0.11	0.08	0.70	0.10	0.17	0.22	0.20
MgO	0.65	0.72	0.61	0.64	7.45	5.26	4.68
CaO	3.18	2.02	1.25	1.89	12.59	11.18	11.08
Na2O	3.58	4.52	5.19	4.45	2.24	2.84	2.71
K2O	4.40	4.78	5.54	6.10	0.53	0.63	1.14
P2O5	0.22	0.09	0.10	0.10	0.26	0.39	0.45
L.O.I.	0.13	0.91	1.72	1.60	0.06	0.16	0.09
H2O-	2.71	0.83	0.08		0.36	0.60	0.33
rest				0.27			
total	99.38	100.23	100.16	102.27	99.37	99.59	99.14
Cs							
Pb							
Rb					6.60	6.50	22.00
Ba							235.00
Sr					987.00	972.00	989.00
La					4.90	6.70	7.80
Ce					11.00	14.80	18.00
Pr							
Nd							
Sm					2.10	2.90	3.30
Eu					0.71	1.00	1.10
Gd							
Tb					0.33	0.46	0.55
Dy							
Ho							
Er							
Yb					0.98	1.42	1.54
Lu					0.16	0.23	0.26
Y					14.00	23.10	22.00
Th					0.42	0.78	0.84
U							
Zr					29.00	37.00	47.00
Hf							1.21
Sn							
Nb					2.00	2.10	2.10
Cu							
Co					43.00	43.00	38.00
Sc					26.00	28.00	26.50
V					347.00	474.00	388.00
Cr					204.00	31.00	18.00
Ni					88.00	17.00	21.00

Ash et al (1978). Dupuy et al. (1982)

Erromango

number	PERC12	PERC234	PERC97	PERC620	PERC624	PERC715	PERC21	PERC731	PERC602	PERC643
SiO2	48.22	49.95	50.20	49.82	49.06	49.23	46.79	51.92	56.64	49.37
TiO2	0.74	0.75	0.57	0.72	0.58	0.66	0.69	0.57	0.47	0.54
Al2O3	16.39	13.19	13.26	18.94	13.12	17.54	17.77	19.07	18.25	14.51
Fe2O3	4.73	5.16	5.76	6.14	4.06	6.86	4.50	5.72	5.56	3.95
FeO	6.10	5.61	5.63	4.88	6.56	4.83	7.92	3.61	2.04	5.84
MnO	0.19	0.14	0.15	0.13	0.15	0.22	0.16	0.13	0.11	0.14
MgO	7.14	9.72	10.16	3.18	8.88	3.51	5.77	3.93	2.35	8.70
CaO	9.77	10.24	11.54	9.46	12.15	9.91	11.92	9.60	7.68	13.83
Na2O	2.62	3.05	2.17	3.19	2.28	3.64	1.91	2.53	2.88	2.03
K2O	1.53	1.22	0.48	1.61	1.10	2.13	0.43	0.87	1.07	0.68
P2O5	0.15	0.22	0.10	0.20	0.15	0.27	0.09	0.15	0.15	0.08
L.O.I.	1.90	0.58	0.33	1.72	1.92	1.19	1.13	0.83	1.48	0.45
H2O-	0.39	0.30	0.14	0.60	0.43	0.58	0.54	0.76	0.92	0.38
rest										
total	99.87	100.13	100.49	100.59	100.44	100.57	99.62	99.69	99.60	100.50
Cs										
Pb										
Rb									13.00	
Ba										
Sr		291.00					109.00		315.00	181.00
La										
Ce										
Pr										
Nd										
Sm										
Eu										
Gd										
Tb										
Dy										
Ho										
Er										
Yb										
Lu										
Y										
Th										
U										
Zr		83.00					37.00		78.00	33.00
Hf										
Sn										
Nb										
Cu										
Co										
Sc										
V		213.00					241.00		95.00	177.00
Cr		258.00					26.00			225.00
Ni		563.00					89.00		5.00	256.00

Colley and Ash (1971)

Erromango

number	PERC704	PERW1	RTERC86	RTERC96	RT745	RT825	RT825	RT846	RT862	RT860
SiO2	54.06	53.75	47.59	48.32	48.27	48.84	48.84	52.00	52.72	56.48
TiO2	0.65	0.50	0.65	0.60	0.42	0.50	0.50	0.77	0.86	0.89
Al2O3	16.58	18.54	19.10	15.15	9.72	11.31	11.31	18.34	18.65	15.99
Fe2O3	4.49	5.29	4.64	4.27	5.24	5.57	5.57	4.26	5.77	3.43
FeO	5.43	2.94	5.81	6.13	4.12	4.20	4.20	4.60	3.29	5.77
MnO	0.14	0.14	0.17	0.14	0.14	0.13	0.13	0.13	0.12	0.19
MgO	4.53	3.31	6.75	8.51	13.99	10.90	10.90	2.85	2.14	1.81
CaO	8.87	8.75	11.15	13.29	14.76	14.52	14.52	8.88	7.58	6.17
Na2O	3.23	2.73	1.97	2.09	1.19	1.51	1.51	3.46	3.99	3.66
K2O	1.20	0.81	0.61	0.74	0.51	0.06	0.51	2.20	2.73	3.42
P2O5	0.15	0.07	0.07	0.09	0.10	0.99	0.06	0.31	0.33	0.51
L.O.I.	0.67	2.62	1.03	0.44	1.36	0.38	0.99	1.05	1.60	0.98
H2O-	0.34	0.57	0.35	0.26	0.79		0.38	0.59	0.70	0.55
rest										
total	100.34	100.02	99.89	100.03	100.61	98.91	99.42	99.44	100.48	99.85
Cs										
Pb										
Rb	3.00	5.00						18.00		50.00
Ba										
Sr	331.00	289.00		163.00	208.00			491.00		313.00
La										
Ce										
Pr										
Nd										
Sm										
Eu										
Gd										
Tb										
Dy										
Ho										
Er										
Yb										
Lu										
Y										
Th										
U										
Zr	75.00	75.00		31.00	39.00			132.00		180.00
Hf										
Sn										
Nb										
Cu										
Co										
Sc										
V	188.00	112.00		154.00	193.00			149.00		149.00
Cr	28.00			573.00	186.00			6.00		
Ni	50.00	21.00		606.00	158.00			41.00		9.00

Colley and Ash (1971)

Erromango

number	RT765	RT795	RT764	RT814	RT826	MW394	MW397	MW413	MW404	MW504
SiO2	47.38	47.84	52.08	47.06	46.56	47.53	46.93	48.02	50.45	49.40
TiO2	1.03	0.68	0.25	0.76	0.59	0.76	0.76	0.82	0.73	0.61
Al2O3	15.68	19.28	2.93	19.13	13.77	18.26	14.86	19.14	18.26	17.48
Fe2O3	5.67	5.44		8.37	9.09	4.72	5.83	4.51	5.79	4.71
FeO	8.78	6.09	6.92	2.84	3.07	7.26	6.30	6.54	5.84	5.97
MnO	0.20	0.16	0.11	0.11	0.13	0.15	0.16	0.16	0.12	0.16
MgO	4.74	4.76	16.00	3.77	7.29	4.30	7.79	4.46	3.79	5.54
CaO	10.51	10.30	20.32	9.49	11.29	11.13	13.13	10.60	10.03	10.74
Na2O	2.62	2.39	0.45	1.93	1.35	2.48	1.77	2.38	2.34	2.93
K2O	0.90	0.96	0.08	0.45	0.39	0.86	0.57	0.90	0.66	1.33
P2O5	0.21	0.16	0.01	0.12	0.07	0.15	0.11	0.18	0.10	0.16
L.O.I.	1.25	0.54		4.19	5.41	1.09	0.85	0.85	0.66	0.98
H2O-	1.06	0.98		1.44	1.14	0.77	0.68	0.97	0.92	0.27
rest										
total	100.03	99.58	99.15	99.66	100.15	99.46	99.74	99.53	99.69	100.28
Cs										
Pb										
Rb										
Ba										
Sr	238.00					285.00	185.00	298.00		452.00
La										
Ce										
Pr										
Nd										
Sm										
Eu										
Gd										
Tb										
Dy										
Ho										
Er										
Yb										
Lu										
Y										
Th										
U										
Zr	55.00					58.00	33.00	66.00		72.00
Hf										
Sn										
Nb										
Cu										
Co										
Sc										
V	300.00					222.00	257.00	193.00		253.00
Cr							117.00			33.00
Ni						34.00	183.00	31.00		72.00

Colley and Ash (1971)

Erromango

number	MW692	MW163	MW256	MW463	MW519	MW58	MW67	MW72	MW556	MW171
SiO2	46.00	51.33	56.37	57.87	54.46	51.90	48.10	47.11	50.49	47.82
TiO2	0.70	0.65	0.72	0.46	0.61	0.68	0.69	0.73	0.65	0.70
Al2O3	18.06	13.53	15.90	18.43	18.67	16.76	20.69	18.65	18.19	18.35
Fe2O3	4.66	4.37	5.22	4.01	4.20	4.70	5.16	6.07	4.81	6.17
FeO	7.65	6.08	4.85	4.01	4.95	5.75	6.11	6.82	5.39	5.45
MnO	0.20	0.15	0.13	0.20	0.18	0.16	0.15	0.17	0.14	0.17
MgO	6.79	8.08	3.71	3.55	4.12	4.49	3.85	5.65	4.54	5.30
CaO	11.91	11.38	7.50	7.00	8.54	9.88	10.80	11.34	10.07	10.84
Na2O	1.85	2.39	3.50	2.49	2.52	2.98	2.04	2.06	3.13	2.12
K2O	0.64	0.83	1.14	0.80	1.03	1.00	0.35	0.54	1.39	0.93
P2O5	0.11	0.13	0.16	0.16	0.19	0.17	0.09	0.10	0.17	0.14
L.O.I.	0.96	0.98	0.71	0.23	0.73	0.55	1.13	0.50	0.84	1.53
H2O-	0.82	0.31	0.25	0.93	0.35	0.74	0.60	0.73	0.46	0.32
rest										
total	100.35	100.21	100.16	100.14	100.55	99.76	99.76	100.47	100.27	99.84
Cs										
Pb										
Rb			1.00	6.00	3.00					
Ba										
Sr			271.00	249.00	271.00	328.00			391.00	
La										
Ce										
Pr										
Nd										
Sm										
Eu										
Gd										
Tb										
Dy										
Ho										
Er										
Yb										
Lu										
Y										
Th										
U										
Zr			145.00	57.00	64.00	75.00			79.00	
Hf										
Sn										
Nb										
Cu										
Co										
Sc										
V			196.00	71.00	157.00	227.00			234.00	
Cr					17.00	22.00			38.00	
Ni			34.00	13.00	39.00	71.00			65.00	

Colley and Ash (1971)

Erromango

number	MW171	MW224	ERC120	ERC145	ERC140	ERC131	ERC111	ERC118	ERC100	ERC107
SiO2	46.61	46.61	50.97	49.01	48.23	49.40	50.78	53.78	50.75	50.22
TiO2	0.65	0.65	0.70	0.63	0.59	0.60	0.65	0.58	0.68	0.57
Al2O3	17.04	17.04	18.44	17.09	17.26	18.15	16.82	17.93	17.07	19.66
Fe2O3	5.23	5.23	4.83	5.13	4.44	4.68	4.68	3.67	3.58	7.36
FeO	7.01	7.01	5.96	6.66	6.70	6.01	6.40	5.59	7.79	2.45
MnO	0.18	0.18	0.15	0.16	0.16	0.15	0.15	0.14	0.16	0.17
MgO	5.77	5.77	4.74	6.81	7.16	6.22	5.62	4.31	5.62	4.90
CaO	12.33	12.33	10.95	11.15	11.94	11.60	11.05	9.21	11.28	11.32
Na2O	1.70	1.70	2.47	2.11	2.05	2.24	2.32	3.03	2.58	2.28
K2O	0.44	0.44	0.51	0.39	0.42	0.43	0.55	0.85	0.47	0.55
P2O5	0.11	0.11	0.09	0.08	0.08	0.08	0.09	0.13	0.10	0.11
L.O.I.	1.75	1.75	0.36	0.88	0.46	0.68	0.50	0.38	0.36	0.59
H2O-	0.66	0.66	0.22	0.28	0.44	0.19	0.25	0.27	0.28	0.23
rest										
total	99.48	99.48	100.39	100.38	99.93	100.43	99.86	99.87	100.72	100.41
Cs										
Pb										
Rb										
Ba										
Sr		228.00	144.00					189.00	181.00	
La										
Ce										
Pr										
Nd										
Sm										
Eu										
Gd										
Tb										
Dy										
Ho										
Er										
Yb										
Lu										
Y										
Th										
U										
Zr		39.00	44.00					55.00	37.00	
Hf										
Sn										
Nb										
Cu										
Co										
Sc										
V		236.00	185.00					163.00	235.00	
Cr		41.00	42.00					16.00	26.00	
Ni		86.00	47.00					45.00	106.00	

Colley and Ash (1971)

	Erromango					
number	E14	E11	E16	E40	E46	E53
SiO2	48.41	46.97	48.72	53.96	49.46	51.25
TiO2	0.65	0.73	0.64	0.56	0.61	0.72
Al2O3	15.57	17.76	18.70	19.60	17.40	18.00
Fe2O3	7.15	3.34	5.95	3.52	3.48	3.51
FeO	3.30	8.02	4.68	4.42	7.04	6.90
MnO	0.20	0.22	0.19	0.17	0.19	0.18
MgO	7.65	6.84	4.95	2.87	6.92	4.49
CaO	12.98	11.24	10.95	8.27	12.13	9.66
Na2O	1.77	1.85	2.24	3.02	2.02	2.97
K2O	0.88	0.41	0.85	1.29	0.62	0.61
P2O5	0.16	0.15	0.17	0.24	0.14	0.18
L.O.I.	0.65	0.42	0.37	0.50	0.03	0.10
H2O-	0.93	1.37	1.01	1.33	0.39	0.48
rest						
total	100.30	99.32	99.42	99.75	100.43	99.05
Cs						
Pb						
Rb	12.20	7.10	9.60	19.80	6.90	7.10
Ba	123.00	133.00	153.00	213.00		138.00
Sr	400.00	441.00	500.00	445.00	301.00	352.00
La		3.00	3.80	5.00	3.10	4.60
Ce		8.00	8.80	12.30	7.10	9.90
Pr						
Nd						
Sm		1.90	2.00	2.50	2.00	2.40
Eu		0.64	0.69	0.85	0.65	0.81
Gd						
Tb		0.36	0.38	0.45	0.37	0.45
Dy						
Ho						
Er						
Yb		1.45	1.51	1.92	1.70	2.10
Lu		0.28	0.28	0.38	0.32	0.37
Y	17.40	15.30	16.10	21.10	15.70	21.20
Th			0.29	0.50	0.26	0.35
U						
Zr	37.00	27.00	32.00	52.00	29.00	36.00
Hf	0.99		0.98	1.48		
Sn						
Nb	2.20				2.30	2.20
Cu		123.00	50.00	70.00	120.00	177.00
Co	42.00	42.00	37.00	19.00	40.00	30.00
Sc		39.00	32.00	17.00	48.00	35.00
V	312.00	379.00	330.00	160.00	314.00	325.00
Cr	219.00	67.00	57.00	10.00	67.00	13.00
Ni	56.00	34.00	28.00	19.00	30.00	17.00

Dupuy et al. (1982) Marcelot (1981)

TANNA

number	TAC75	TAC56	TAC55	TAC39	TAC51	TAC67	TAC111	TAC152	TAC100	TAC129
SiO2	48.87	49.47	49.63	49.99	50.72	55.99	46.02	47.34	48.00	48.92
TiO2	0.79	0.85	0.83	0.68	0.68	0.76	0.85	0.70	0.75	0.34
Al2O3	19.97	15.23	15.48	16.43	16.19	16.13	16.22	16.69	18.24	7.32
Fe2O3	4.10	6.41	7.30	5.27	4.20	2.92	3.55	3.15	2.44	1.72
FeO	6.45	6.65	5.45	5.55	6.55	5.75	8.25	8.25	8.10	6.30
MnO	0.21	0.20	0.18	0.17	0.19	0.17	0.20	0.21	0.19	0.16
MgO	4.34	4.78	4.58	4.91	5.21	3.32	7.16	7.43	6.76	16.70
CaO	10.47	10.04	10.06	10.88	11.90	6.90	11.87	12.55	12.50	15.60
Na2O	2.60	2.42	2.50	2.45	2.48	3.74	1.57	1.70	1.73	0.83
K2O	0.92	0.69	0.89	0.76	0.80	2.29	1.26	0.43	0.34	0.32
P2O5	0.19	0.17	0.20	0.16	0.16	0.35	0.28	0.12	0.09	0.08
L.O.I.	0.73	1.65	1.71	1.34	0.71	0.49	1.55	0.70	0.50	0.48
H2O-	0.13	0.97	0.95	0.68	0.25	0.07	0.31	0.23	0.06	0.10
rest										
total	99.77	99.53	99.76	99.27	100.04	98.88	99.09	99.50	99.70	98.87
Cs										
Pb										
Rb	12.00	8.00	12.00	9.00	10.00	34.00	22.00	3.00	5.00	5.00
Ba	300.00	150.00	200.00	180.00	170.00	640.00	170.00	140.00	120.00	70.00
Sr	1100.00	450.00	560.00	460.00	460.00	620.00	560.00	400.00	310.00	230.00
La										
Ce										
Pr										
Nd										
Sm										
Eu										
Gd										
Tb										
Dy										
Ho										
Er										
Yb										
Lu										
Y										
Th										
U										
Zr										
Hf										
Sn										
Nb										
Cu										
Co										
Sc										
V	350.00	450.00	480.00	360.00	400.00	280.00	480.00	420.00	420.00	280.00
Cr										
Ni										

Carney and Macfarlane (1979)

TANNA

number	TAC10	TAC82	TAC136	TY1	TAC156	TY2	TAC133	720A	720B	5
SiO2	56.10	51.53	54.82	55.32	55.41	56.01	56.22	56.80	57.44	61.10
TiO2	0.76	0.69	0.78	0.74	0.74	0.71	0.84	0.77	0.73	1.00
Al2O3	16.08	18.50	16.67	17.06	17.75	17.66	16.58	17.73	18.82	19.00
Fe2O3	3.53	3.56	4.15	2.11	2.44	2.01	2.39	1.29	1.21	1.30
FeO	5.20	5.55	4.00	5.82	5.60	5.70	6.55	6.45	6.07	1.80
MnO	0.17	0.16	0.17	0.17	0.15	0.16	0.18	0.15	0.12	0.10
MgO	3.32	3.32	2.88	3.78	2.86	3.26	3.15	2.77	2.34	0.50
CaO	6.81	9.73	7.06	7.75	7.66	7.17	6.93	6.90	7.57	2.10
Na2O	4.09	3.25	3.15	3.73	3.70	3.75	3.70	3.93	3.27	6.20
K2O	2.42	1.26	2.58	2.46	2.53	2.40	2.59	2.86	2.09	5.20
P2O5	0.35	0.20	0.43	0.38	0.38	0.42	0.45	0.35	0.34	0.10
L.O.I.	0.19	0.36	1.50	0.14	0.34	0.11	0.26			1.10
H2O-	0.03	0.70	1.12	0.99	0.05	0.15	0.02			0.50
rest										
total	99.05	98.81	99.31	100.45	99.61	99.51	99.86	100.00	100.00	100.00
Cs										
Pb										
Rb	36.00	12.00	34.00		36.00		38.00	43.00	34.00	
Ba	660.00	390.00	700.00		620.00		680.00			
Sr	620.00	740.00	660.00		660.00		660.00	639.00	692.00	
La										
Ce										
Pr										
Nd										
Sm										
Eu										
Gd										
Tb										
Dy										
Ho										
Er										
Yb										
Lu										
Y										
Th										
U										
Zr										
Hf										
Sn										
Nb										
Cu		200.00								
Co										
Sc										
V	290.00	400.00	280.00		310.00		330.00		500.00	
Cr										
Ni										

Carney and Macfarlane (1979)

				TANNA					
number	7	T153	TA93	TA72	T24	TAC9	TAC53	TAC64	TAC73	TAC76
SiO2	68.30	45.10	47.70	47.33	48.21	48.38	51.58	53.51	47.78	51.74
TiO2	0.60	0.91	0.72	0.82	0.61	0.72	0.66	0.88	0.79	0.65
Al2O3	15.10	19.14	16.14	18.60	13.41	16.43	17.24	15.64	18.35	16.44
Fe2O3	1.20	3.86	3.41	4.38	12.07	12.45	10.75	12.92	12.38	10.85
FeO	2.40	8.39	8.28	6.78						
MnO	0.10	0.22	0.22	0.22	0.22	0.20	0.17	0.22	0.20	0.18
MgO	0.80	6.55	7.80	6.02	9.58	7.50	4.55	3.60	5.59	6.50
CaO	2.00	11.58	12.51	11.76	13.45	11.78	10.32	8.39	11.32	10.63
Na2O	3.50	1.70	1.84	2.35	1.28	1.79	2.59	2.98	2.12	2.32
K2O	5.40	0.14	0.59	0.60	0.56	0.74	0.41	1.18	0.61	0.41
P2O5	0.10	0.11	0.16	0.18	0.08	0.13	0.18	0.26	0.13	0.12
L.O.I.	0.80	0.69	0.26	0.20	0.40	-0.47	0.43	0.14	0.05	-0.05
H2O-	0.10	0.99	0.54	0.54						
rest										
total	100.40	99.38	100.17	99.78	99.87	99.65	98.88	99.72	99.32	99.79
Cs										
Pb										
Rb		2.10	8.30	6.40	7.00	10.00	11.00	16.00	8.00	11.00
Ba		96.00	101.00	159.00	155.00	193.00	159.00	168.00	156.00	254.00
Sr		365.00	430.00	955.00	387.00	505.00	468.00	474.00	641.00	742.00
La			3.30	5.70	2.95					4.58
Ce			7.30	11.80	7.56					12.10
Pr					1.13					1.65
Nd					5.84					8.19
Sm			1.60	2.60	1.86					2.34
Eu			0.59	0.84	0.79					0.72
Gd					1.96					2.43
Tb			0.35	0.38						
Dy					2.20					2.51
Ho										
Er					1.37					1.56
Yb			1.24	1.41	1.16					1.72
Lu			0.18	0.19						
Y		23.50	23.50	22.80	12.30	13.80	22.50	27.00	16.10	15.00
Th		0.25	0.29	0.61						
U										
Zr		21.00	38.00	38.00	18.80	22.00	46.00	57.00	25.10	28.40
Hf		0.64	0.80	1.29						
Sn										
Nb		2.60	1.40	2.20						
Cu										
Co		44.00	43.00	34.00						
Sc			26.00	24.00	64.00	45.30	39.70	38.00	45.00	43.00
V		422.00	349.00	312.00	377.00	383.00	337.00	365.00	386.00	333.00
Cr		21.00	81.00	28.00	388.00	164.00	63.00	4.60	51.00	184.00
Ni		14.00	29.00	29.00	84.00	54.00	32.00	8.20	28.00	36.00

Carney and MacFarlane (1979) Dupuy et al. (1982) Barsdell (unpubl. data)

TANNA

number	TAC82	TAC133	TAC85	TAC84	TAC86	TAC90	T108	T111	T114	T115
SiO2	51.88	55.95	50.93	53.14	53.33	46.11	46.24	46.43	56.46	47.33
TiO2	0.68	0.83	0.69	0.78	0.72	0.84	0.85	0.85	0.80	0.79
Al2O3	18.88	16.11	18.03	14.72	14.95	17.79	16.43	16.42	16.70	19.14
Fe2O3	9.95	9.88	9.91	10.91	10.25	13.70	13.27	13.20	9.80	12.52
FeO										
MnO	0.17	0.18	0.16	0.18	0.18	0.21	0.19	0.20	0.18	0.20
MgO	3.52	3.11	3.61	5.81	5.12	7.19	6.89	7.25	2.56	5.67
CaO	9.66	6.67	9.27	8.21	8.20	12.16	11.65	11.70	6.02	11.75
Na2O	3.23	3.96	3.04	3.05	3.14	1.43	1.47	1.49	4.05	1.77
K2O	1.18	2.59	0.87	2.08	2.13	0.49	1.29	1.25	2.56	0.41
P2O5	0.21	0.46	0.18	0.34	0.37	0.22	0.31	0.30	0.45	0.10
L.O.I.	0.92	-0.34	2.80	0.21	1.22	0.07	1.03	1.10	0.43	0.03
H2O-										
rest										
total	100.28	99.40	99.49	99.43	99.61	100.21	99.62	100.19	100.01	99.71
Cs										
Pb										
Rb	13.00	40.00	5.00	31.00	34.00	3.00	19.00	21.00	29.00	5.00
Ba	315.00	530.00	333.00	447.00	475.00	142.00	152.00	144.00	537.00	130.00
Sr	757.00	607.00	739.00	516.00	547.00	523.00	546.00	530.00	599.00	339.00
La	6.80	13.00		10.30		3.25	4.67			
Ce	17.30	32.10		24.80		9.27	12.10			
Pr	2.42	4.66		3.69		1.36	1.73			
Nd	12.20	20.60		16.30		7.35	9.19			
Sm	3.38	5.12		4.13		2.46	2.78			
Eu	1.09	1.51		1.02		0.91	0.93			
Gd	3.40	4.83		3.91		2.69	2.79			
Tb										
Dy	3.43	4.82		4.00		2.89	2.62			
Ho										
Er	2.21	3.30		2.49		1.60	1.77			
Yb	2.24	3.30		2.42		1.45	1.51			
Lu										
Y	20.00	27.00	19.00	24.00	25.00	15.30	14.60	16.10	30.00	10.80
Th										
U										
Zr	43.00	101.00	43.00	81.00	88.90	24.00	31.60	32.00	109.00	16.50
Hf										
Sn										
Nb									1.00	
Cu										
Co										
Sc	30.60	27.00	28.00	33.00	30.00	58.00	52.00	54.80	25.40	51.00
V	320.00	311.00	327.00	309.00	273.00	416.00	441.00	437.00	239.00	407.00
Cr	9.30	8.40	4.40	171.00	151.00	95.00	115.00	129.00	7.60	21.00
Ni	12.90	13.10	11.60	64.00	58.00	37.00	44.00	47.00	10.70	22.00

Barsdell (unpubl. data)

number	T129B
SiO2	49.50
TiO2	0.31
Al2O3	7.59
Fe2O3	8.82
FeO	
MnO	0.15
MgO	16.79
CaO	15.31
Na2O	0.69
K2O	0.31
P2O5	0.06
L.O.I.	-0.08
H2O-	
rest	
total	99.45
Cs	
Pb	
Rb	3.20
Ba	86.00
Sr	220.00
La	2.16
Ce	4.85
Pr	0.82
Nd	3.93
Sm	1.16
Eu	0.43
Gd	1.22
Tb	
Dy	1.40
Ho	
Er	0.96
Yb	0.92
Lu	
Y	7.00
Th	
U	
Zr	11.00
Hf	
Sn	
Nb	
Cu	
Co	
Sc	67.00
V	234.00
Cr	1404.00
Ni	237.00

Barsdell (unpubl. data)

FUTUNA

number	FMA66A	FMA18	FMA23	FMA64	FMA55	FMA59	FMA2	FM65	FM55	FMAC18
SiO2	48.78	50.13	52.66	52.41	54.44	54.59	51.38	53.72	55.10	50.10
TiO2	0.10	0.96	0.92	0.82	0.82	0.89	1.06	0.95	0.89	0.95
Al2O3	18.92	14.01	14.30	16.40	17.66	18.03	17.54	17.59	17.58	14.20
Fe2O3	0.98	1.62	2.15	3.82	3.03	3.35	3.63	3.94	3.26	8.66
FeO	3.75	6.25	5.35	5.15	4.45	4.55	4.88	3.96	4.20	
MnO	0.15	0.15	0.14	0.16	0.16	0.17	0.16	0.16	0.16	0.15
MgO	9.28	10.00	9.09	5.16	4.01	3.81	4.84	4.34	4.08	10.20
CaO	15.60	10.40	9.05	10.53	8.72	8.64	10.22	8.76	8.53	10.60
Na2O	0.83	2.29	2.38	2.52	2.60	2.78	2.60	2.98	2.78	2.45
K2O	0.13	0.71	0.84	1.40	1.59	1.48	1.48	1.43	1.64	0.67
P2O5	0.04	0.19	0.18	0.23	0.29	0.28	0.31	0.30	0.32	0.21
L.O.I.	0.45	1.55	1.83	0.36	0.85	0.83	0.10	0.16	0.11	1.93
H2O-	0.12	0.23	0.65	0.62	0.11	0.11	1.84	0.89	1.24	
rest										
total	99.13	98.49	99.54	99.58	98.73	99.51	100.04	99.18	99.89	100.12
Cs										
Pb										
Rb	1.00	13.00	17.00	20.00	22.00	19.00	18.30	17.80	22.50	14.20
Ba	60.00	100.00	130.00	120.00	280.00	330.00	211.00	240.00	292.00	107.00
Sr	140.00	440.00	450.00	600.00	780.00	800.00	899.00	833.00	790.00	422.00
La							15.40	17.30	17.00	10.40
Ce							30.90	35.70	34.30	23.70
Pr										2.97
Nd										14.20
Sm							3.40	3.80	3.80	3.49
Eu							1.10	1.30	1.20	1.40
Gd										3.77
Tb							0.47	0.58	0.50	
Dy										3.49
Ho										
Er										2.07
Yb							1.74	2.10	1.81	1.82
Lu							0.25	0.31	0.25	
Y							24.20	24.30	22.90	20.00
Th							2.10	2.20	2.10	
U										
Zr							90.00	98.00	102.00	97.00
Hf							2.21	2.74	2.71	
Sn										
Nb							6.60	6.60	6.20	5.30
Cu				80.00						
Co							26.00	25.00	22.00	
Sc							27.00	22.00	16.00	32.90
V	110.00	220.00	200.00	390.00	300.00	300.00	305.00	250.00	245.00	217.00
Cr							31.00	23.00	17.00	599.00
Ni							21.00	17.00	13.00	253.00

Barsdell (unpubl. data) Dupuy et al.(1982) Marcelot et al. (1983)

FUTUNA

number	FMAC19	FMAC22	FMAC44	FMAC48	FMAC50	FMAC54	FMAC61	FMAC93
SiO2	49.90	52.40	55.20	56.40	55.80	55.10	51.80	52.80
TiO2	0.93	0.91	0.81	0.72	0.71	0.83	0.79	0.92
Al2O3	13.90	14.40	17.90	17.10	16.90	18.10	16.50	18.10
Fe2O3	8.53	8.27	7.71	7.21	7.20	8.06	9.56	8.74
FeO								
MnO	0.15	0.14	0.15	0.14	0.14	0.15	0.17	0.16
MgO	10.00	9.33	3.73	4.90	5.01	3.88	5.88	4.49
CaO	10.80	8.97	8.42	8.81	8.64	8.68	10.30	9.14
Na2O	2.32	2.49	2.68	2.48	2.46	2.72	2.37	2.72
K2O	0.73	0.82	1.57	1.30	1.30	1.56	0.99	1.32
P2O5	0.17	0.18	0.33	0.19	0.20	0.31	0.25	0.28
L.O.I.	2.23	1.94	1.55	1.01	1.12	0.92	1.00	0.82
H2O-								
rest								
total	99.66	99.85	100.05	100.26	99.48	100.31	99.61	99.49
Cs								
Pb								
Rb	15.60	14.30	18.20	17.80	17.20	21.40	18.40	18.00
Ba	104.00	121.00	279.00	248.00	256.00	272.00	120.00	270.00
Sr	425.00	420.00	673.00	607.00	598.00	768.90	597.00	754.00
La		11.00						
Ce		23.20						
Pr		2.83						
Nd		13.60						
Sm		3.15						
Eu		1.10						
Gd		3.29						
Tb								
Dy		3.30						
Ho								
Er		2.02						
Yb		1.78						
Lu								
Y	21.00	21.90	20.40	19.60	18.40	22.90	22.00	33.00
Th								
U								
Zr	95.00	103.60	94.20	78.00	77.20	101.20	72.00	85.00
Hf								
Sn								
Nb	5.80	6.30	5.10	3.60	3.80	4.90	2.30	4.10
Cu								
Co								
Sc	29.80	31.00	22.20	31.00	31.00	23.60	38.90	31.50
V	208.00	204.00	244.00	229.00	253.00	275.00	304.00	316.00
Cr	568.00	532.00	14.20	98.00	103.00	15.00	148.00	30.00
Ni	238.00	217.00	14.70	37.90	45.60	17.20	50.00	26.00

Barsdell (unpubl. data)

Anatom

number	AYM38	AYM20	AYM1	AYM17	AYM22	AYC28	AYC22	AYC63	AY42	AY49
SiO2	47.92	48.34	51.01	57.30	58.23	46.47	46.57	48.16	48.84	50.00
TiO2	0.74	0.85	0.74	0.48	0.41	0.84	0.77	0.54	0.85	0.83
Al2O3	14.22	20.63	19.11	18.47	17.90	17.14	16.25	15.23	15.54	17.32
Fe2O3	3.68	5.11	3.11	3.04	3.63	3.34	4.20	3.33	4.82	5.04
FeO	6.85	4.95	5.90	3.55	2.65	8.05	5.85	5.50	5.98	5.34
MnO	0.19	0.19	0.17	0.17	0.17	0.20	0.21	0.17	0.20	0.19
MgO	8.02	3.50	4.30	2.69	2.25	5.50	6.63	9.65	7.16	4.57
CaO	13.02	11.36	10.31	8.30	7.70	12.28	13.45	13.00	11.90	10.32
Na2O	1.85	2.52	2.67	3.10	2.93	2.10	1.76	1.66	2.30	2.70
K2O	0.86	0.61	0.82	1.37	1.27	0.71	0.42	0.27	0.67	0.76
P2O5	0.20	0.14	0.18	0.19	0.17	0.15	0.13	0.08	0.17	0.20
L.O.I.	1.16	0.98	0.95	0.11	1.93	1.18	2.59	1.60	0.36	0.64
H2O-	0.92	0.60	0.71	0.15	0.12	0.85	0.18	0.15	0.70	1.30
rest										
total	99.63	99.78	99.98	98.92	99.36	98.81	99.01	99.34	99.49	99.21
Cs										
Pb										
Rb	13.00	9.00	13.00	19.00	22.00	8.00	5.00	1.00	4.70	3.20
Ba	90.00	120.00	150.00	230.00	240.00	70.00	90.00	90.00	120.00	149.00
Sr	560.00	520.00	520.00	580.00	620.00	540.00	350.00	280.00	450.00	544.00
La									4.00	5.40
Ce									9.20	11.40
Pr										
Nd										
Sm									2.20	2.30
Eu									0.67	0.79
Gd										
Tb									0.42	0.46
Dy										
Ho										
Er										
Yb									1.62	1.81
Lu									0.29	0.31
Y									21.20	22.00
Th									0.44	0.47
U										
Zr									40.00	50.00
Hf									1.24	1.43
Sn										
Nb										1.90
Cu	118.00	142.00	120.00	82.00	42.00	172.00	118.00	110.00		
Co									47.00	33.00
Sc									34.00	30.00
V	380.00	440.00	390.00	260.00	180.00	510.00	440.00	380.00	324.00	328.00
Cr									144.00	39.00
Ni									39.00	31.00

Carney and MacFarlane (1979) Dupuy et al (1982)

Anatom

number	AYC2	AYC10	AYC47	AYC49	AYC55	AYC62	AYMAC6	AYMAC9	AYMAC15	AYMAC18
SiO2	49.81	47.79	51.48	50.03	49.30	48.10	46.82	46.64	48.21	47.58
TiO2	0.80	0.82	0.64	0.75	0.57	0.79	0.85	0.77	0.80	0.77
Al2O3	20.39	17.84	17.51	18.38	12.77	17.25	20.64	20.37	19.51	19.36
Fe2O3	10.43	11.26	9.56	11.48	10.84	11.43	12.00	12.28	11.16	11.82
FeO										
MnO	0.18	0.19	0.18	0.19	0.18	0.19	0.21	0.19	0.18	0.18
MgO	4.31	6.56	5.92	4.35	10.25	6.52	4.43	4.94	4.90	5.21
CaO	9.83	11.62	10.49	10.23	12.53	11.22	11.09	11.61	11.64	11.38
Na2O	2.58	1.74	2.45	2.60	1.62	1.86	2.20	2.18	1.94	2.08
K2O	0.62	0.71	0.94	0.77	0.80	1.64	0.44	0.56	0.83	0.67
P2O5	0.15	0.13	0.16	0.20	0.16	0.37	0.16	0.16	0.16	0.20
L.O.I.	0.86	1.13	0.60	1.35	1.15	0.12	0.68	0.21	0.28	0.86
H2O-										
rest										
total	99.96	99.79	99.93	100.33	100.17	99.49	99.52	99.91	99.61	100.11
Cs										
Pb										
Rb	5.00	6.00	11.00	4.00	9.00	25.00	2.00	3.00	10.00	5.00
Ba	98.00	109.00	166.00	170.00	121.00	207.00	114.00	115.00	107.00	139.00
Sr	410.00	407.00	522.00	546.00	389.00	806.00	548.00	524.00	468.00	598.00
La					6.12	12.60				
Ce					13.80	28.90				
Pr					2.08	3.87				
Nd					10.20	18.90				
Sm					2.73	4.79				
Eu					1.07	1.64				
Gd					3.02	5.05				
Tb										
Dy					2.78	4.03				
Ho										
Er					1.75	2.23				
Yb					1.41	1.86				
Lu										
Y	21.00	20.00	21.00	19.50	17.00	23.00	20.30	17.00	16.70	23.50
Th										
U										
Zr	42.80	42.00	39.00	40.00	38.00	61.00	32.40	27.00	30.00	35.40
Hf										
Sn										
Nb										
Cu										
Co										
Sc	32.50	46.00	45.00	41.00	56.00	46.00	41.00	37.00	43.00	41.00
V	328.00	349.00	336.00	408.00	310.00	386.00	369.00	392.00	401.00	
Cr	17.10	106.00	102.00	31.00	456.00	115.00	15.70	31.50	48.00	
Ni	14.60	44.20	31.80	22.70	93.30	50.00	18.40	24.90	23.60	

Barsdell (unpubl. data)

Anatom

number	AYMAC34	AYMAC36	AYMAC68
SiO2	46.60	49.60	46.50
TiO2	0.69	0.62	0.59
Al2O3	15.81	18.10	13.20
Fe2O3	12.28	10.80	10.80
FeO			
MnO	0.20	0.19	0.15
MgO	7.17	6.00	12.90
CaO	11.82	11.30	12.60
Na2O	1.75	1.89	1.39
K2O	0.72	0.85	0.40
P2O5	0.23	0.17	0.08
L.O.I.	2.43	0.39	0.94
H2O-			
rest			
total	99.70	99.91	99.55
Cs			
Pb			
Rb	5.00	12.00	5.00
Ba	105.00	131.00	91.00
Sr	732.00	554.00	269.00
La		6.88	2.46
Ce		15.40	5.60
Pr		2.14	0.91
Nd		9.68	4.74
Sm		2.58	1.51
Eu		0.87	0.57
Gd		2.82	2.00
Tb			
Dy		2.64	2.20
Ho			
Er		2.03	1.42
Yb		1.68	1.11
Lu			
Y	16.50	15.30	12.00
Th			
U			
Zr	33.20	34.00	21.30
Hf			
Sn			
Nb			
Cu			
Co			
Sc	47.00	39.00	54.00
V	370.00	302.00	358.00
Cr	122.00	98.80	860.00
Ni	57.00	33.10	244.00

Barsdell (unpubl. data)

				MATHEW	
number	M8	M7	M15	MT1B	MT14A
SiO2	60.46	61.53	60.96	58.47	57.88
TiO2	0.43	0.40	0.42	0.47	0.44
Al2O3	16.15	16.03	16.09	15.64	15.89
Fe2O3	6.43	6.09	6.27	7.20	7.60
FeO					
MnO	0.11	0.13	0.12	0.12	0.12
MgO	3.89	3.48	3.70	4.98	5.52
CaO	7.36	6.96	7.17	8.74	8.93
Na2O	3.93	4.07	3.99	3.57	3.45
K2O	0.99	0.88	0.94	0.86	0.89
P2O5	0.18	0.13	0.15	0.23	0.20
L.O.I.	0.08	0.22	0.15	0.06	
H2O-					
rest					
total	100.01	99.92	99.96	100.34	100.92
Cs					
Pb					
Rb					
Ba					
Sr					
La					
Ce					
Pr					
Nd					
Sm					
Eu					
Gd					
Tb					
Dy					
Ho					
Er					
Yb					
Lu					
Y					
Th					
U					
Zr					
Hf					
Sn					
Nb					
Cu					
Co					
Sc					
V					
Cr					
Ni					

Maillet et al. (1986)

			HUNTER				
number	HR4H	M6	HR4N	HR8G	HR4I	HR8B	HR4L
SiO2	55.76	60.72	55.61	55.98	56.14	54.92	54.09
TiO2	0.35	0.36	0.34	0.30	0.36	0.29	0.25
Al2O3	16.77	15.45	14.24	14.24	16.46	15.81	7.27
Fe2O3	7.60	6.11	7.89	7.34	7.60	8.18	8.28
FeO							
MnO	0.12	0.10	0.13	0.12	0.12	0.14	0.16
MgO	5.60	5.03	9.05	9.79	6.04	7.95	14.47
CaO	8.98	6.95	8.09	8.23	8.80	9.18	13.54
Na2O	3.14	3.70	3.04	3.10	3.27	3.03	1.21
K2O	0.50	0.94	0.65	0.55	0.46	0.30	0.21
P2O5	0.12	0.13	0.10	0.11	0.12	0.12	0.09
L.O.I.	0.30	0.11	0.05	0.70	0.38	0.10	0.30
H2O-							
rest							
total	99.24	99.60	99.19	100.46	99.75	100.02	99.87
Cs							
Pb							
Rb							
Ba							
Sr							
La							
Ce							
Pr							
Nd							
Sm							
Eu							
Gd							
Tb							
Dy							
Ho							
Er							
Yb							
Lu							
Y							
Th							
U							
Zr							
Hf							
Sn							
Nb							
Cu							
Co							
Sc							
V							
Cr							
Ni							

Maillet et al. (1986)

Appendix 5

Vanuatu Arc and North Fiji Basin Parent Magma Composition Estimates

A compilation of olivine-fractionation-corrected major and trace element compositions of primitive Vanuatu Arc and North Fiji Basin parent melt estimates (see chapter 8 for details). Note that "%Ol" denotes the mass fraction of olivine added in the fractionation-correction procedure.

	Ambae	Ambae	Western Epi	Western Epi	Ambrym	Eastern Epi	Western Epi	Erromango	Gaua
number	68638	68567	71065	71046	96	E10	24	E11	G20
SiO2	47.71	47.02	47.34	48.25	48.30	47.77	46.61	45.67	46.35
TiO2	0.53	0.54	0.38	0.37	0.58	0.52	0.40	0.50	0.66
Al2O3	10.74	10.19	11.75	10.76	9.05	11.29	12.58	12.12	10.19
Fe2O3	2.18	2.20	2.08	1.98	2.20	2.11	2.16	2.45	2.28
FeO	7.84	7.91	7.49	7.13	7.92	7.61	7.78	8.82	8.20
MnO	0.17	0.19	0.17	0.16	0.17	0.17	0.18	0.22	0.25
MgO	18.27	18.50	17.72	16.53	18.28	17.73	18.24	20.92	18.99
CaO	9.84	10.41	11.42	13.47	10.66	10.11	10.30	7.67	10.57
Na2O	1.77	1.29	1.31	0.99	1.64	1.81	1.43	1.26	1.83
K2O	0.81	1.42	0.29	0.29	1.00	0.71	0.23	0.28	0.54
P2O5	0.14	0.32	0.04	0.06	0.19	0.16	0.09	0.10	0.13
L.O.I.									
H2O-									
rest									
total	100.00	99.99	99.99	99.99	99.99	99.99	100.00	100.01	99.99
Cs									
Pb									
Rb	12.10	48.60	4.80	5.60	20.30	10.90	1.80	4.90	8.00
Ba	295.00	405.00	136.00	128.00	255.00	170.00	90.00	91.00	174.00
Sr	472.00	596.00	273.00	231.00	349.00	462.00	275.00	302.00	451.00
La	7.06	15.05	2.57	2.86	7.32	4.62	1.76	2.05	6.38
Ce	17.04	31.03	6.52	6.81	13.24	10.46	4.11	5.47	14.80
Pr		4.15	0.80	0.95					1.98
Nd	10.42	20.10	4.87	4.73	9.45				9.64
Sm	2.47	4.24	1.19	1.44		1.65	1.03	1.30	2.46
Eu	0.87	1.37	0.40	0.54		0.58	0.39	0.44	0.77
Gd	2.46	3.89	1.49	1.72					2.09
Tb						0.26	0.22	0.25	0.35
Dy	2.40	3.46	1.78	1.79					1.93
Ho									
Er	1.57	1.97	0.97	1.07					1.22
Yb	1.39	1.79	0.90	0.92		0.90	0.96	0.99	1.12
Lu						0.16	0.16	0.19	
Y	12.90	15.90	10.50	8.40	12.40	12.40	9.90	10.50	11.80
Th									
U									
Zr	33.00	56.10	15.30	12.70	40.60	33.90	20.60	18.50	43.10
Hf									
Sn									
Nb	0.80	1.90	0.80	0.90	1.70	1.10	0.70	1.60	0.90
Cu									
Co									
Sc									
V									
Cr									
Ni									
%ol. added	24.50	7.21	19.61	8.29	14.95	16.10	36.82	50.38	12.68

	Merelava	Ambrym	Ambae	Ambae	Efate	Emae	Epi (submarine)	Eastern Epi	Eastern Epi	Erromango
number	31541	1567	505	576	V36	EM4	4D1-E	670	E26	E46
SiO2	49.03	47.53	47.67	47.52	45.32	45.72	47.68	46.04	45.86	46.93
TiO2	0.52	0.52	0.56	0.60	0.58	0.52	0.40	0.40	0.40	0.43
Al2O3	11.11	11.08	10.57	11.06	13.77	10.84	12.76	12.36	12.06	12.29
Fe2O3	2.04	2.17	2.19	2.16	2.17	2.35	2.03	2.25	2.33	2.26
FeO	7.33	7.82	7.88	7.78	7.80	8.46	7.29	8.10	8.37	8.13
MnO	0.21	0.19	0.19	0.20	0.17	0.19	0.17	0.19	0.19	0.19
MgO	17.34	18.16	18.51	18.11	18.57	19.70	17.27	19.07	19.68	19.24
CaO	10.48	9.89	9.71	9.55	9.38	9.70	10.53	9.91	9.25	8.57
Na2O	1.54	1.64	1.71	1.92	1.66	1.72	1.26	1.33	1.41	1.43
K2O	0.31	0.85	0.84	0.96	0.40	0.64	0.55	0.28	0.35	0.44
P2O5	0.10	0.14	0.16	0.15	0.19	0.15	0.06	0.07	0.10	0.10
L.O.I.										
H2O-										
rest										
total	100.01	99.99	99.99	100.01	100.01	99.99	100.00	100.00	100.00	100.01
Cs										
Pb										
Rb	4.40	15.10	13.70	13.40	4.90	7.90	10.80	4.70	3.60	4.90
Ba	100.00	199.00	247.00	296.00		156.00	112.00	90.00	98.00	
Sr	195.00	398.00	479.00	556.00	736.00	463.00	331.00	284.00	317.00	213.00
La	1.52	7.86	8.34	10.48	3.66	4.76	3.88	2.08	2.28	2.20
Ce	4.01		19.20	23.32	8.21	10.04	7.92	5.28	4.77	5.03
Pr	0.66	2.44	2.39	2.78			1.09	0.70		
Nd	3.55	10.93	10.66	12.63			5.31	3.64		
Sm	1.21	2.18	2.27	2.61	1.56	1.78	1.43	0.98	1.07	1.42
Eu	0.41	0.69	0.70	0.83	0.53	0.60	0.49	0.39	0.40	0.46
Gd	1.47	2.18	2.00	2.59			1.57	1.24		
Tb	0.27	0.34	0.33	0.40	0.25	0.35		0.21	0.21	0.26
Dy	1.70	2.02	2.00	2.42			1.72	1.41		
Ho										
Er	1.15	1.09	1.18	1.39			0.83	0.91		
Yb	1.14	1.04	1.10	1.38	0.73	0.90	0.85	0.80	0.72	1.21
Lu										
Y	14.50	12.50	13.90	14.70	10.40	13.50	9.20	10.80	10.20	15.00
Th										
U										
Zr	24.40	37.30	34.30	41.10	21.60	24.60	24.50	14.30	22.80	20.50
Hf										
Sn										
Nb	0.50	1.20	1.10	1.00	1.50	1.00	0.80	0.40	0.80	1.60
Cu										
Co										
Sc										
V										
Cr										
Ni										
% Ol-added	23.24	20.81	25.72	22.02	36.13	37.49	29.53	33.50	41.70	41.70

	Anatom	Anatom	Gaua	Tanna	Tanna	Ambae	Ambrym	Ambae	Merelava	Western Epi
number	AYC55	68	G22	T24	T93	68622	26	68611	BC13	71047
SiO2	48.42	46.74	45.80	46.92	45.73	47.26	49.24	47.30	50.47	45.90
TiO2	0.46	0.52	0.63	0.46	0.50	0.54	0.55	0.59	0.45	0.38
Al2O3	10.45	11.74	9.10	10.20	11.14	9.42	11.60	10.68	10.00	12.84
Fe2O3	2.16	2.16	2.45	2.36	2.45	2.34	2.11	2.22	1.81	2.31
FeO	7.76	7.76	8.81	8.48	8.81	8.42	7.60	7.99	6.51	8.30
MnO	0.17	0.15	0.29	0.21	0.21	0.20	0.18	0.18	0.17	0.18
MgO	18.22	18.04	20.27	19.68	20.77	19.49	17.74	18.49	15.32	19.74
CaO	10.25	11.21	10.13	10.23	8.63	10.04	7.95	10.07	13.30	8.72
Na2O	1.32	1.24	1.73	0.97	1.26	1.28	2.01	1.57	1.55	1.26
K2O	0.66	0.36	0.60	0.43	0.40	0.85	0.86	0.75	0.37	0.31
P2O5	0.13	0.07	0.18	0.06	0.11	0.17	0.16	0.15	0,05	0.06
L.O.I.										
H2O-										
rest										
total	100.00	99.99	99.99	100.00	100.01	100.01	100.00	99.99	100.00	100.00
Cs										
Pb										
Rb	7.40	4.40		5.30	5.70	12.03	16.60	10.90	5.80	5.60
Ba	99.30	81.10	238.00	116.00	69.40	330.00	201.00	289.00	176.00	121.00
Sr	319.00	240.00	527.00	291.00	295.00	491.00	344.00	489.00	212.00	323.00
La	5.02	2.19	8.59	2.22	2.27	8.15	6.47	8.04	2.35	3.29
Ce	11.32	4.99	18.61	5.68	5.02	19.04	9.79	16.84	4.75	7.07
Pr	1.70	0.81	2.65	0.85		2.50			0.65	1.00
Nd	8.37	4.23	12.99	4.39		11.43	9.71	10.56	3.66	4.93
Sm	2.24	1.35	3.11	1.39	1.10	2.63			1.16	1.18
Eu	0.88	0.50	0.97	0.59	0.40	0.83			0.43	0.47
Gd	2.47	1.78	2.78	1.48		2.45			1.41	1.54
Tb			0.41		0.24					
Dy	2.28	1.97	2.42	1.66		2.10			1.76	1.73
Ho										
Er	1.44	1.27	1.04	1.03		1.24			1.13	1.05
Yb	1.16	0.99	1.11	0.87	0.85	0.99			1.10	1.00
Lu										
Y	13.90	10.70	10.20	9.20	16.20	12.03	13.40	14.20	12.20	9.80
Th										
U										
Zr	31.10	19.00	40.60	14.10	26.10	34.08	43.40	39.40	17.90	14.70
Hf										
Sn										
Nb			0.80		1.00	1.00	1.60	1.70	1.00	
Cu										
Co										
Sc										
V										
Cr										
Ni										
% Ol. added	24.50	15.00	30.80	33.50	46.00		27.00	19.60	4.00	44.50

	Western Epi	Ambae	Tongoa	Tongoa
number	71069	68562	697	698
SiO2	47.11	47.57	47.24	48.49
TiO2	0.49	0.57	0.45	0.53
Al2O3	12.27	11.03	9.84	10.49
Fe2O3	2.34	2.18	2.32	2.21
FeO	8.43	7.85	8.34	7.97
MnO	0.19	0.19	0.19	0.19
MgO	19.78	18.47	19.43	18.76
CaO	6.49	9.14	9.56	9.02
Na2O	1.76	1.76	1.32	1.53
K2O	0.90	1.04	1.09	0.65
P2O5	0.23	0.20	0.22	0.15
L.O.I.				
H2O-				
rest				
total	99.99	100.00	100.00	99.99
Cs				
Pb				
Rb	30.20	17.30	26.60	10.30
Ba	208.00	351.00	120.00	105.00
Sr	389.00	531.00	404.00	300.00
La	5.27	9.95	6.53	4.77
Ce	11.98	22.65	15.51	11.71
Pr	1.58			
Nd	7.83	12.07	9.21	7.49
Sm	2.04		1.99	1.81
Eu	0.75		0.63	0.60
Gd	2.17			
Tb			0.31	0.32
Dy	2.30		1.69	1.96
Ho				
Er	1.47			
Yb	1.17		0.80	1.21
Lu				
Y	12.50	13.40	12.80	13.10
Th				
U				
Zr	44.70	41.80	42.70	34.50
Hf				
Sn				
Nb	1.30	1.60	0.86	0.84
Cu				
Co				
Sc				
V				
Cr				
Ni				
% Ol. added	53.40	27.00	33.50	33.50

	Ambae	Ambae	Futuna	Futuna
number	68578	68569	FMAC22	FMAC18
SiO2	47.13	47.00	53.64	51.39
TiO2	0.92	1.03	0.92	0.98
Al2O3	11.93	12.05	14.51	14.57
Fe2O3	2.43	2.36	1.71	1.78
FeO	8.76	8.50	6.16	6.39
MnO	0.21	0.21	0.14	0.15
MgO	15.44	15.13	10.37	10.46
CaO	10.63	10.62	9.05	10.87
Na2O	1.73	1.66	2.51	2.52
K2O	0.65	1.12	0.82	0.69
P2O5	0.17	0.31	0.18	0.21
L.O.I.				
H2O-				
rest				
total	100.00	99.99	100.01	100.01
Cs				
Pb				
Rb	9.42	22.60	14.40	14.59
Ba	252.60	361.00	122.00	109.95
Sr	417.00	526.00	424.00	433.62
La	8.13	14.10	11.08	10.69
Ce	20.40	31.30	23.40	24.35
Pr		3.97	2.86	3.05
Nd	13.03	18.90	13.73	14.59
Sm	3.33	4.24	3.18	2.00
Eu	1.10	1.26	1.11	1.44
Gd	3.56	4.23	3.32	3.87
Tb				
Dy	3.81	4.21	3.33	3.59
Ho				
Er	2.21	2.37	2.04	2.13
Yb	2.02	2.18	1.79	1.87
Lu				
Y	20.55	25.20	22.10	20.55
Th				
U				
Zr	60.05	85.50	105.00	99.67
Hf				
Sn				
Nb	3.40	5.90	6.40	5.40
Cu				
Co				
Sc				
V				
Cr				
Ni				
% Ol. added	17.30	19.61	2.00	

North Fiji Basin

number	13	2A	2B	4A	4B	4C	5	6A	6B	7
SiO2	49.57	47.55	47.85	49.74	50.07	49.05	49.33	49.38	48.69	50.07
TiO2	1.86	1.30	1.52	1.65	1.21	2.28	1.13	1.15	1.32	1.47
Al2O3	15.77	11.09	11.84	14.92	15.11	15.51	12.49	13.51	12.22	12.50
Fe2O3	1.75	2.69	2.53	1.88	1.81	1.79	2.26	2.09	2.37	2.14
FeO	6.28	9.67	9.10	6.77	6.51	6.46	8.13	7.51	8.54	7.70
MnO	0.21	0.23	0.22	0.18	0.16	0.16	0.21	0.20	0.22	0.23
MgO	10.81	16.15	15.27	11.32	10.86	10.77	13.56	12.48	14.10	12.88
CaO	9.08	9.08	9.29	9.84	11.26	9.18	10.39	11.01	9.83	10.44
Na2O	3.28	1.88	1.99	2.83	2.44	3.16	2.31	2.43	2.40	2.32
K2O	1.08	0.23	0.23	0.62	0.42	1.16	0.09	0.12	0.19	0.11
P2O5	0.33	0.14	0.17	0.25	0.16	0.48	0.10	0.12	0.13	0.14
L.O.I.										
H2O-										
rest										
total	100.02	100.01	100.01	100.00	100.01	100.00	100.00	100.00	100.01	100.00
Cs										
Pb										
Rb	34.00	3.90	3.20	12.30	9.20	18.90	2.60	1.80	3.30	1.70
Ba	321.00	17.80	32.20	121.00	106.00	315.00	23.10	26.70	20.90	32.50
Sr	290.00	67.30	93.50	228.00	249.00	384.00	111.00	128.00	130.00	112.00
La	15.18	2.78	4.60	9.72	7.10	25.20	2.57	3.29	3.42	2.91
Ce	31.29	8.67	12.82	22.56	16.30	50.60	8.14	9.08	10.35	8.82
Pr	3.84	1.37	1.85	2.98	2.19	6.17	1.40	1.23	1.63	1.24
Nd	13.00	8.43	10.24	14.16	10.42	26.01	7.20	7.30	8.93	8.31
Sm	4.14	2.55	3.00	3.27	2.90	5.02	2.46	1.87	2.34	3.06
Eu	1.44	1.03	1.03	1.16	1.05	1.43	1.07	0.71	0.95	1.09
Gd	4.61	3.95	4.19	4.11	3.15	5.31	3.48	2.83	3.49	4.20
Tb										
Dy	4.86	5.09	5.57	4.73	3.47	5.35	4.22	3.68	4.43	5.56
Ho										
Er	2.93	3.40	3.67	2.90	2.02	2.80	2.73	2.33	2.84	3.92
Yb	2.53	3.25	3.30	2.52	1.71	2.21	2.65	2.11	2.69	3.56
Lu										
Y	28.50	31.00	32.20	26.40	19.40	27.40	25.70	24.90	27.60	34.30
Th										
U										
Zr	140.00	73.50	92.00	114.00	72.90	185.00	59.10	65.90	85.10	77.90
Hf										
Sn										
Nb	31.30	3.10	4.10	16.00	11.10	43.60	2.60	4.40	1.70	2.60
Cu										
Co										
Sc										
V										
Cr										
Ni										
% Ol. added	9.40	30.80	25.70	7.20	9.40	7.20	17.30	12.70	20.80	17.30

North Fiji Basin

number	10A	10B
SiO2	48.76	49.38
TiO2	1.26	2.13
Al2O3	13.97	15.14
Fe2O3	2.14	1.80
FeO	7.70	6.49
MnO	0.19	0.17
MgO	12.81	10.97
CaO	10.50	9.77
Na2O	2.27	2.62
K2O	0.27	1.03
P2O5	0.15	0.49
L.O.I.		
H2O-		
rest		
total	100.02	99.99
Cs		
Pb		
Rb	4.50	23.20
Ba	45.40	346.00
Sr	149.00	363.00
La	4.99	31.53
Ce	12.80	63.74
Pr	1.72	7.15
Nd	8.62	30.66
Sm	2.42	5.89
Eu	0.89	1.87
Gd	3.13	5.89
Tb		
Dy	4.15	5.63
Ho		
Er	2.59	3.17
Yb	2.41	2.41
Lu		
Y	25.50	28.00
Th		
U		
Zr	76.30	197.00
Hf		
Sn		
Nb	6.40	52.10
Cu		
Co		
Sc		
V		
Cr		
Ni		
% Ol. added	11.60	6.20